SANDIA REPORT

SAND95–1318 • UC–800
Unlimited Release
Printed July 1995

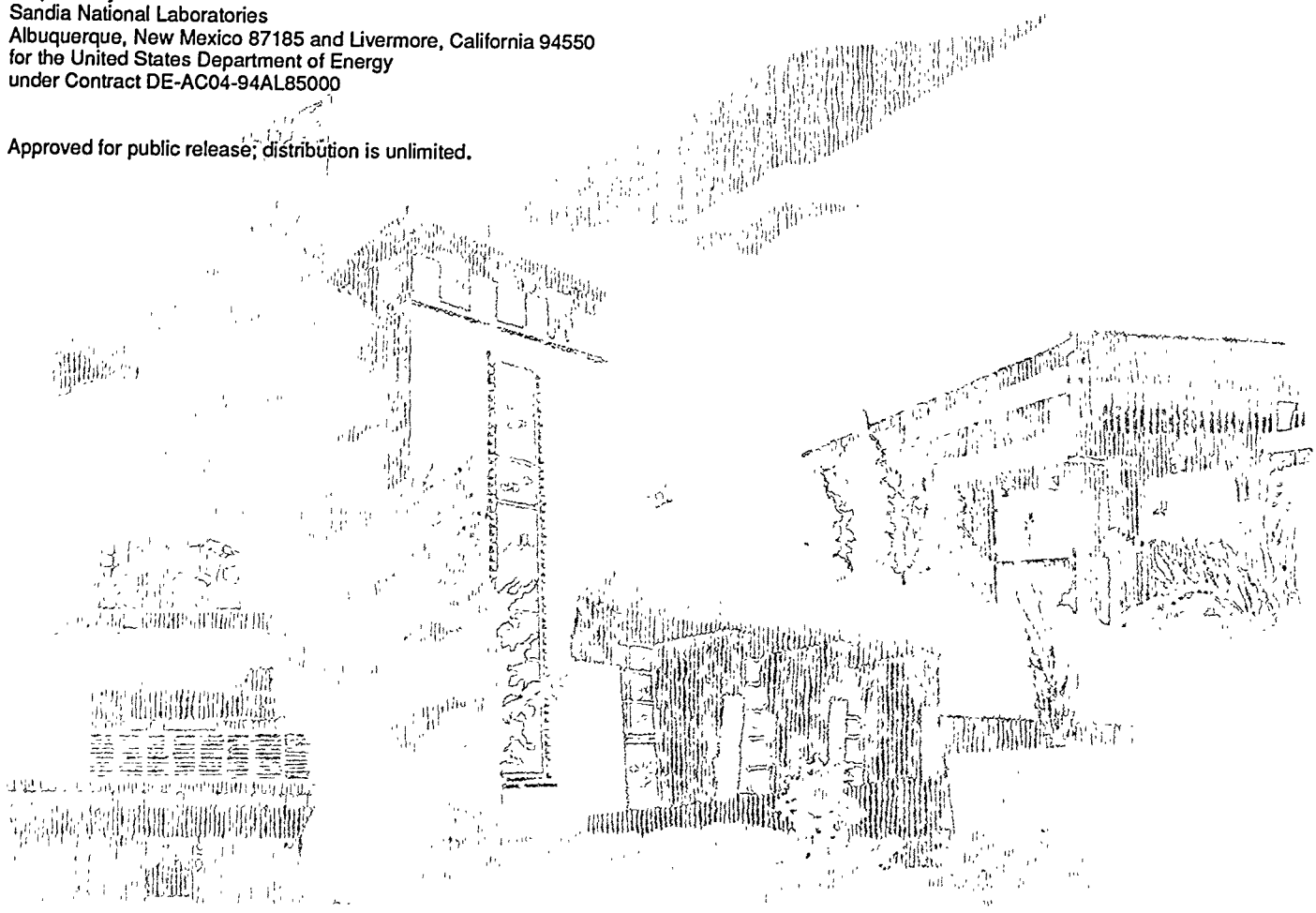
Materials and Process Engineering Projects for the Sandia National Laboratories/Newly Independent States Industrial Partnering Program

Volume II

Frank J. Zanner, William C. Moffatt

Prepared by
Sandia National Laboratories
Albuquerque, New Mexico 87185 and Livermore, California 94550
for the United States Department of Energy
under Contract DE-AC04-94AL85000

Approved for public release; distribution is unlimited.



SF2900Q(8-81)

Issued by Sandia National Laboratories, operated for the United States Department of Energy by Sandia Corporation.

NOTICE: This report was prepared as an account of work sponsored by an agency of the United States Government. Neither the United States Government nor any agency thereof, nor any of their employees, nor any of their contractors, subcontractors, or their employees, makes any warranty, express or implied, or assumes any legal liability or responsibility for the accuracy, completeness, or usefulness of any information, apparatus, product, or process disclosed, or represents that its use would not infringe privately owned rights. Reference herein to any specific commercial product, process, or service by trade name, trademark, manufacturer, or otherwise, does not necessarily constitute or imply its endorsement, recommendation, or favoring by the United States Government, any agency thereof or any of their contractors or subcontractors. The views and opinions expressed herein do not necessarily state or reflect those of the United States Government, any agency thereof or any of their contractors.

Printed in the United States of America. This report has been reproduced directly from the best available copy.

Available to DOE and DOE contractors from
Office of Scientific and Technical Information
PO Box 62
Oak Ridge, TN 37831

Prices available from (615) 576-8401, FTS 626-8401

Available to the public from
National Technical Information Service
US Department of Commerce
5285 Port Royal Rd
Springfield, VA 22161

NTIS price codes
Printed copy: A21
Microfiche copy: A01

DISCLAIMER

Portions of this document may be illegible in electronic image products. Images are produced from the best available original document.

SAND95-1318
Unlimited Release
Printed July 1995

Distribution
Category UC-800

INTERIM REPORT

MATERIALS AND PROCESS ENGINEERING PROJECTS FOR THE SANDIA NATIONAL LABORATORIES/NEWLY INDEPENDENT STATES INDUSTRIAL PARTNERING PROGRAM

Volume II

Frank J. Zanner, William C. Moffatt
Sandia National Laboratories
Liquid Metal Processing Department
Albuquerque, NM 87185

Abstract

In July, 1994, a team of materials specialists from Sandia and U. S. Industry traveled to Russia and the Ukraine to select and fund projects in materials and process technology in support of the Newly Independent States/Industrial Partnering Program (NIS/IPP). All of the projects are collaborations with scientists and Engineers at NIS Institutes. Each project is scheduled to last one year, and the deliverables are formatted to supply U. S. Industry with information which will enable rational decisions to be made regarding the commercial value of these technologies. This work is an unedited interim compilation of the deliverables received to date.

DISTRIBUTION OF THIS DOCUMENT IS UNLIMITED

MASTER

FOREWORD

This book is a compilation of reports written by Ukrainian and Russian investigators under 30 contracts between Sandia National Laboratories (Sandia) and institutes in the Ukraine and the Urals region of Russia. Projects focus on materials and process engineering, more specifically coating technologies and process metallurgy; technologies of projects selected are those thought to have the most promise for direct US private sector investment. Projects last one year; their results should allow businesses to make sound decisions about the value of the technologies studied. Information on all of the projects is given in the following table. The table is followed by detailed statements of work and copies of reports received for each project. In some instances the statement of work stands alone because at this date deliverables have not been received.

We are grateful to many people who contribute to the success of this effort. The group which traveled to Russia and the Ukraine to evaluate technologies and place contracts at the institutes included:

- Lee Bertram (fluids and plasma technology) -- Sandia
- Nancy Davis (contracting) -- Sandia
- Harry Saxton (materials) -- Sandia
- Rod Williamson (plasma and melting processes) -- Sandia
- Frank Zanner (liquid metal processing) -- Sandia
- Dale McIntyre (coatings) -- Optex Communications, formerly Sandia
- Jack Simon -- American Society for Metals and General Motors
- Tanya Golub (logistics) -- Kaiser Research

Dennis Croessmann, Sandia's Industrial Partnering Program project manager, provided administrative support; John Hnatio, the Department of Energy project manager for the Newly Independent States/Industrial Partnering Program, provided the funds and the vision that made this effort possible. Project technical monitors include Bill Moffatt (Sandia) and the team that traveled to Russia and the Ukraine. Cincinnati Milacron, United Technologies, General Motors, Pratt & Whitney and Teledyne Allvac have provided specimens or technical guidance or services for these projects. We are grateful to Academician Gennady Mesyats from the Russian Academy of Sciences (Urals Branch) for arranging technical presentations at institutes he runs.

When the projects are completed we plan to publish a collection of final reports. Call us if you have questions about the technologies or institutes.

Editors: Frank J. Zanner, Sandia
William C. Moffatt, Sandia

Materials Projects in the SNL NIS - Industrial Partnering Program

Number	Proposal Title	SNL PI	SNL PI Phone	NIS Country	NIS Institution	NIS PI
SNL-023	The Effect of Melt Nuclei on the Properties of Alloy 718 Castings	Brian Damkroger	845-3105	Russia	Urals Polytechnic Institute, Ekaterinburg	E Tretyakova
SNL-024	Review of Liquid Metal Processing Research in the FSU	Mike McGuire	845-3105	Russia	Moscow Steel & Alloys Institute, Moscow	L Romonav
SNL-025	Development of Face Coat Materials for Investment Casting Titanium	Mike Maguire	845-3105	Russia	Chelyabinsk Polytechnic Institute, Ekaterinburg	B Kulakov
SNL-083	Thermal Physical Properties of Liquid Metals	Frank Zanner	845-3085	Russia	Ural Mining and Geology Academy, Ekaterinburg	Vladislav E. Zinov'ev
SNL-084	Step-by-step Deformation of Metal Alloys	Frank Zanner	845-3085	Russia	Chelyabinsk State University of Technology, Chelyabinsk	G. I. Koval
SNL-085	Development of a Method of Growing Band-like single crystals of Molybdenum (Mo) and Tungsten (W)	Frank Zanner	845-3085	Russia	Institute of Physics of Metals, Ekaterinburg	Eugene Romanov
SNL-086	Directional Solidification of Ni-Based Eutectic Alloys and High Purity Ti3Al Single Crystals Using An Annular Electron Beam Gun	Rodney Williamson	845-3105	Ukraine	Institute of Metal Physics, Kiev	Oleg M. Barabash
SNL-087	Purification of Molten Metals by Application of Electric Fields	Rodney Williamson	845-3105	Russia	Institute of Metallurgy, Ekaterinburg	A. V. Kaybichev
SNL-088	Effect of Volatile Alloy components on the Vacuum Arc Remelting Process	Rodney Williamson	845-3105	Russia	The Research and Development Institute of Metallurgy, Chelyabinsk	Felix J. Shved
SNL-089	Melting, Refining and Casting of Ti-Based Alloys in an Electron-Beam Furnace with Electromagnetic Stirring	Rodney Williamson	845-3105	Ukraine	Institute of Foundry Problems, Kiev	Sergey V. Ladkhin
SNL-090	Electron Beam Spray Casting of Dense Metallic and Ceramic Coatings	Rodney Williamson	845-3105	Ukraine	E.O. Paton Electric Welding Institute, Kiev	Nikolai Trigub
SNL-091	Characterization of a Metal Vapor Arc Burning On Nickel and Nickel-Magnesium Cathodes	Rodney Williamson	845-3105	Russia	High Current Electronics Institute, Tomsk	Yuri D. Korolev
SNL-092	Novel Large Deformation Processes	Harry Saxton	845-8739	Russia	Institute of Metallurgy, Ekaterinburg	Petr Savintsev
SNL-093	Continuous Casting of Tool Steels	Frank Zanner	845-3085	Russia	Urals Polytechnical Institute, Ekaterinburg	Sergey Burkin
SNL-094	Amorphous Palladium (Pd)-based Alloys	Harry Saxton	845-8739	Russia	Institute of Metallurgy, Ekaterinburg	Vatolin
SNL-095	A Novel Accelerated and Ecologically-Friendly Method for the Production of Wear Resistant Coatings of iron Boride on Steels	Bill Moffatt	844-7062	Russia	Institute for Electrochemistry, Ekaterinburg	A. A. Ivanovich
SNL-096	Development and Production of Advanced Cutters for Super-Alloys	Frank Zanner	845-3085	Ukraine	Bakel Institute of Superhard Materials, Kiev	I. B. Chernov
SNL-097	Investigation of the Electronic Properties and Varistor Effect in Novel Diamond Compacts	Harry Saxton	845-8739	Ukraine	DonBass Civil Engineering Institute, Makeveka	Nikolai Samsonenko

Materials Projects in the SNL NIS - Industrial Partnering Program

Number	Proposal Title	SNL PI	SNL PI Phone	NIS Country	NIS Institution	NIS PI
SNL-098	The Use of a Unique Super-Heated Steam Treatment for the Enhancement of the Tribological Properties of Ferrous and Non-Ferrous Alloys	Bill Moffatt	844-7062	Russia	Chelyabinsk State University of Technology, Chelyabinsk	Herman Vyatkin
SNL-099	Multilayer Coatings for Improved Tribological Performance	Bill Moffatt	844-7062	Russia	Institute of Metal Physics, Ekaterinburg	A. Vladimirov
SNL-100	Multilayer coatings composed of alternating layers of Cu/Fe and Cu/TiC	Bill Moffatt	844-7062	Ukraine	Paton Electric Welding Institute, Kiev	Anatol V. Demchishin
SNL-101	Functionally Graded Interfaces for the Enhancement of the Performance of Hard Coatings on Austenitic Stainless Steel and Titanium Alloys	Bill Moffatt	844-7062	Russia	High Current Electronics Institute, Tomsk	Sergei Bugaev
SNL-102	Surface Treatments for the Enhancement of the Performance of Diamond Like Coatings (DLC) on Tool Steels	Bill Moffatt	844-7062	Russia	Institute of Electrophysics, Ekaterinburg	N. V. Gavrilov
SNL-103	Application of Wear Resistant Coatings to Tools Using Novel Diamond Coating and Attachment Processes and Explosive Detonation Deposition Processes	Bill Moffatt	844-7062	Ukraine	Institute for Superhard Materials, Kiev	Mariy Voronkin
SNL-104	Diffusion Barriers/Nucleation Surfaces for Chemical Vapor Deposition (CVD) of Diamond on Tool Steel Surfaces	Bill Moffatt	844-7062	Russia	Institute of Metal Physics, Ekaterinburg	Vladimir Vykhodets
SNL-105	Synthesis of Polycrystalline Diamond Films Using Super High Frequency Plasma Deposition	Harry Saxton	845-8739	Ukraine	Donbass Civil Engineering Institute, Makeveka	Nikolai Samsonenko
SNL-106	High Energy Electron Beam Treatment for the Enhancement of the Tribological Properties of Tool Steels, Cemented Carbides, and Nitride Coated Tool Steels and Cemented Carbides	Bill Moffatt	844-7062	Russia	High Current Electronics Institute, Tomsk	Vladimir P. Rotshtei
SNL-107	Genetic Bond Between the Melt Properties and the Properties of an Industrial Aluminum Alloy	Frank Zanner	845-3085	Russia	Institute of Metal Physics, Ekaterinburg	Irena Brodova
SNL-108	Growth of Nickel Base Single Crystal Alloys at High Pressure	Lee Bertram	(510)294-1545	Russia	Institute of Metal Physics, Ekaterinburg	Vladimir O. Esin
SNL-109	Damage/Healing Theory as Applied to Self-Healing Bearings and to Semi-Continuous Wire Drawings	Lee Bertram	(510)294-1545	Russia	Mechanical Engineering Research Institute (IMACH), Ekaterinburg	Eduard Gorkunov
SNL-110	Investigation of the Role of Ectons in the Vacuum Arc	Lee Bertram	(510)294-1545	Russia	Institute of Electrophysics, Ekaterinburg	Gennady Mesyats
SNL-111	Measurement of Viscosity of Liquid Metals	Frank Zanner	845-3085	Russia	Institute of Metallurgy, Ekaterinburg	Viatcheslav Lisii

Project Title: Novel Large Deformation Processes
Principal Investigator: Petr Savintsev
Institute of Metallurgy
Ekateringburg, Russia
AM-7667

CLAUSE 1 - STATEMENT OF WORK

Tasks:

The Contractor shall:

1. Describe the four (4) profiled stamp process as typically applied to aluminum data. Include a description of equipment used, alloys (Russian alloys V65 & D16) tested, reductions achieved, resulting microstructures and mechanical performance. Provide a report including representative data and analysis. Also, provide three (3) material samples each of V65 & D16. The dimensions of the samples will be:

30mm x 300mm
15mm x 300mm

2. Conduct large deformation processing study on the nearest Russian equivalent 304L stainless steel, and establish the largest possible single pass deformation that occurs at ambient temperature. Fabricate and provide samples to Sandia at 25, 50 and 75% of this maximum deformation as identified above.

3. Measure the tensile properties and characterize the microstructures, along with the hardness profiles of the samples identified in Task 2. Hardness measurements shall be taken at sufficient intervals to accurately measure the variance in hardness. Provide a final report that describes the results of the above activities.

NOVEL LARGE DEFORMATION PROCESSES.

TASK 1.

The given report contains description of equipment used for metal treatment by four (4) profiled stamps, some information about D16 and B65 alloys under investigation and data on microstructure and mechanical properties of resulted deformed samples.

Last years the intense development of new methods of metal's deformation and the improvement of existing ones providing high mechanical propeties of final products at large degrees of deformation takes place in the field of metal treatment by pressure. Such methods of reduction combining different kinds of deformation as upset and shift, upset and angular strain etc. are considered to be promising in the given direction.

Radial forging is widely applied today to manufacturing of articles from special metals and alloys including hardly deformed materials. This method provides all-sided type of workpieces reduction. However it is characterized by some disadvatages as well. The main one is the essential irregularity of tensely deformed state in the hearth of deformation resulting in nonuniform structure of treated metals at low degrees of deformation. The increase of radial forging efficiency is achieved by different ways. For example, a working tool is subjected to a complicated movement. Such approach allows to realize the scheme of combined loading of workpieces providing their best structure.

A similar scheme of deformation is used in the forging machines SACK and DANIELI and in the pass forging machine (GFM) as well. In the first two cases the vertical shift of the tool is combined with the shift in transversal direction. The pass forging machine GFM has a complicated shift of the tool in longitudinal direction according to the principle of machine's operation. However, the usual upset by inclined stamp is realized here in the process of loading without application of shift deformations along the axis of a workpiece.

The carried out analysis of different kinds of radial forging indicated that one way of process efficiency growth is the application of complicated movement to working tool providing upset of workpiece without simultaneous longitudinal shift. This way leads to minimization of deformation's ununiformity and correspondingly allows to achieve high mechanical properties of deformed material. The optimum scheme of deformation for all-sided strain with actiive use of friction at the tool-workpiece interface provides higher deformations in one passage at room temperature.

This principle of metal's manufacturing by pressure serves as the base for suggested scheme of workpiece's deformation by means of simultaneous reduction by four profiled stamps (figure 1) on an arch with the given radius in the direction of workpiece's movement (figure 2) with big crushing.

Common view of machine using the described principle of working tool movement is given on figure 3. In its usual variant this unit is known as pointing machine (model AVS, KIESERLING). The technical characteristics of AVS machine are given in the table 1.

Table 1. Tecnical characteristics of AVS machine

Model AVS	16	25	40	63	100
Forming capasity, Mp	4×16	4×25	4×40	4×63	4×100
Numbe of strokes per min	900	800	710	630	560
Max. stock dia., mm	60	75	90	115	170
Rating of motor, kW	11	15	22	30	45
Feeding speed, mm/sec.	0-70	0-70	0-100	0-100	0-100

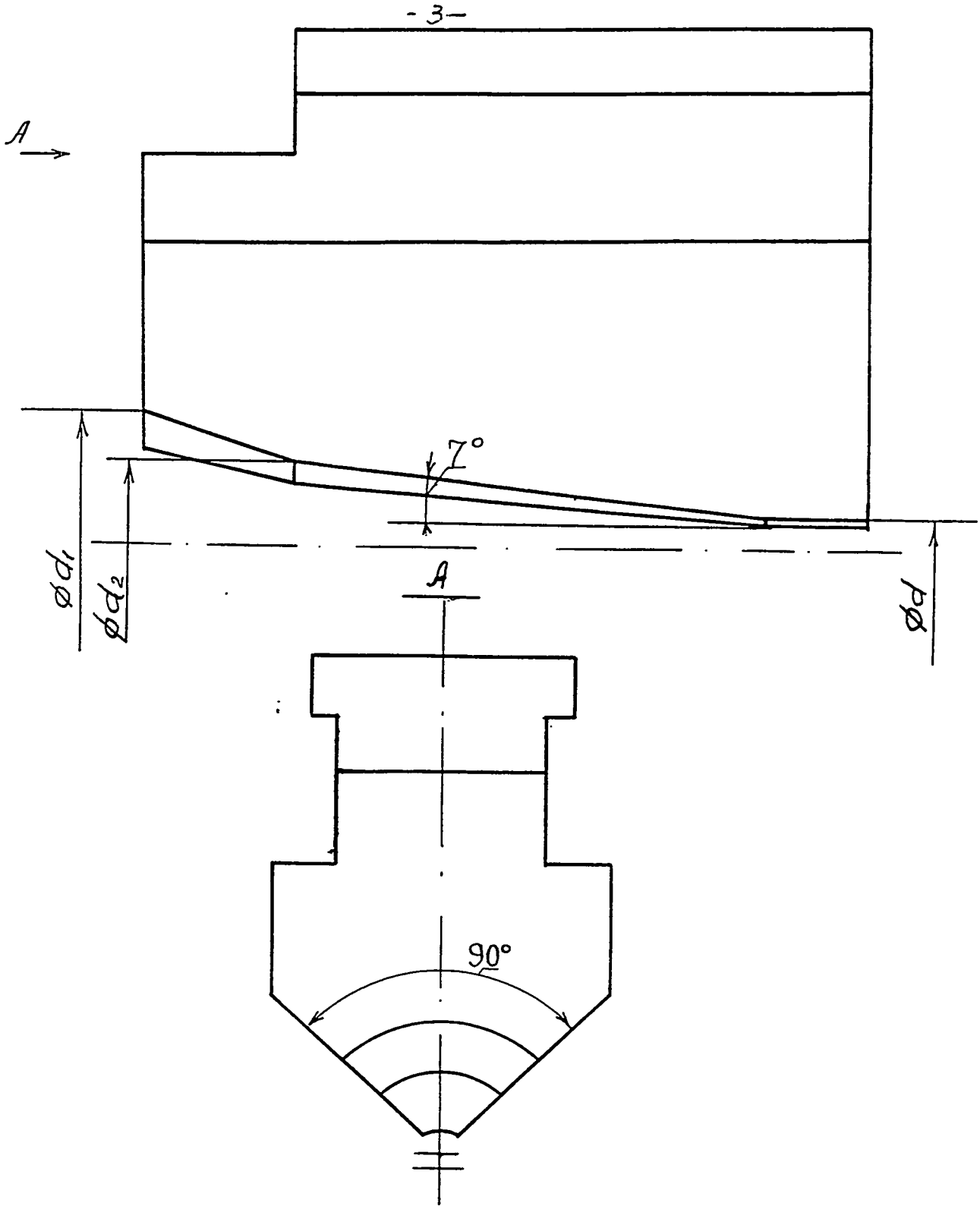


Figure 1. Stamping tool.

d_1 - diameter of entrance cone; d_2 - diameter of working cone; d - diameter of working part for gauging.

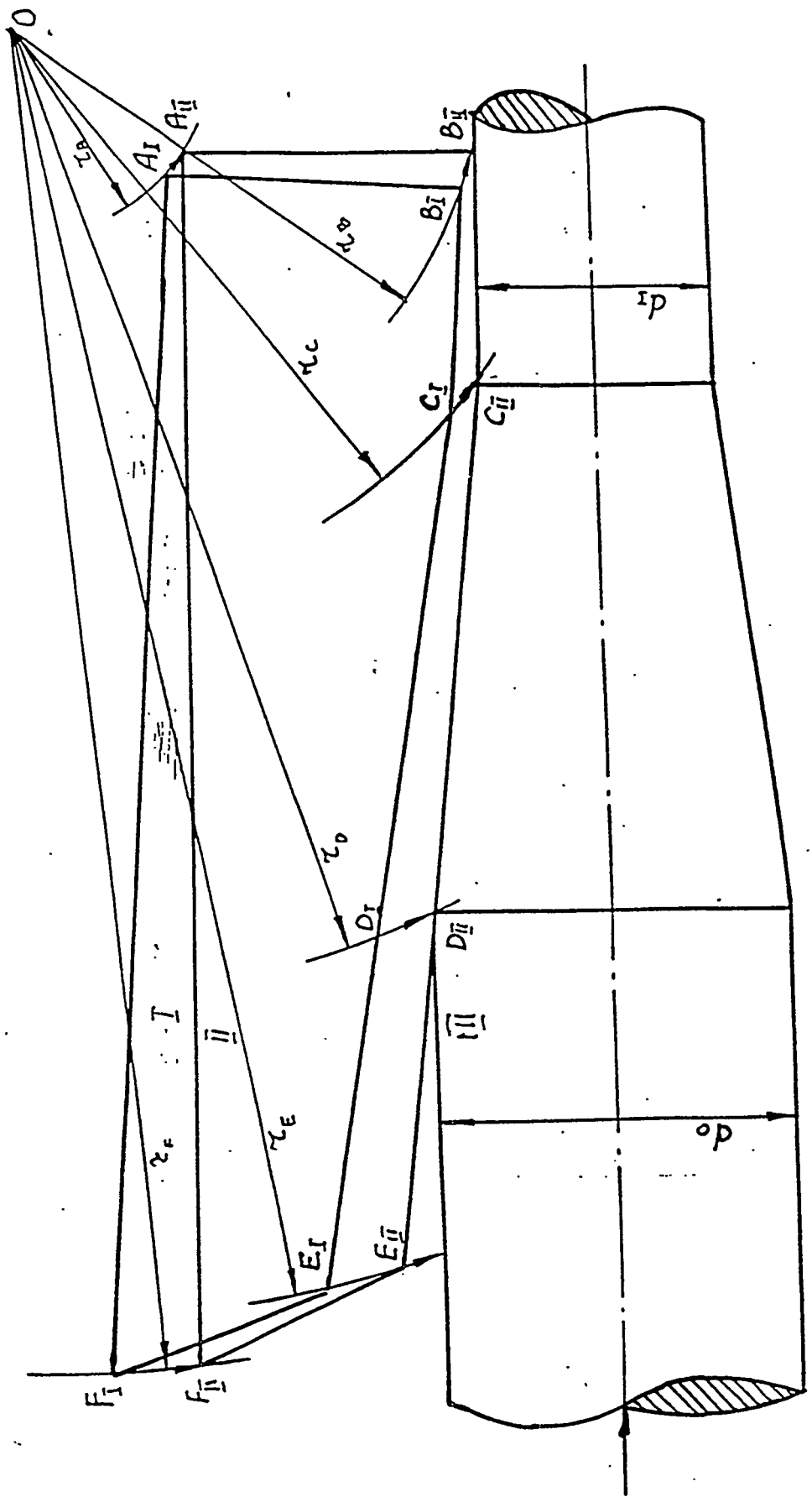


Figure 2. Scheme of movement the stamping tool.

$\overline{I}$ - apper position; $\overline{II}$ - lower position; d_o - initial diameter; d_I - final diameter; O - conditional centre of revolving tool.

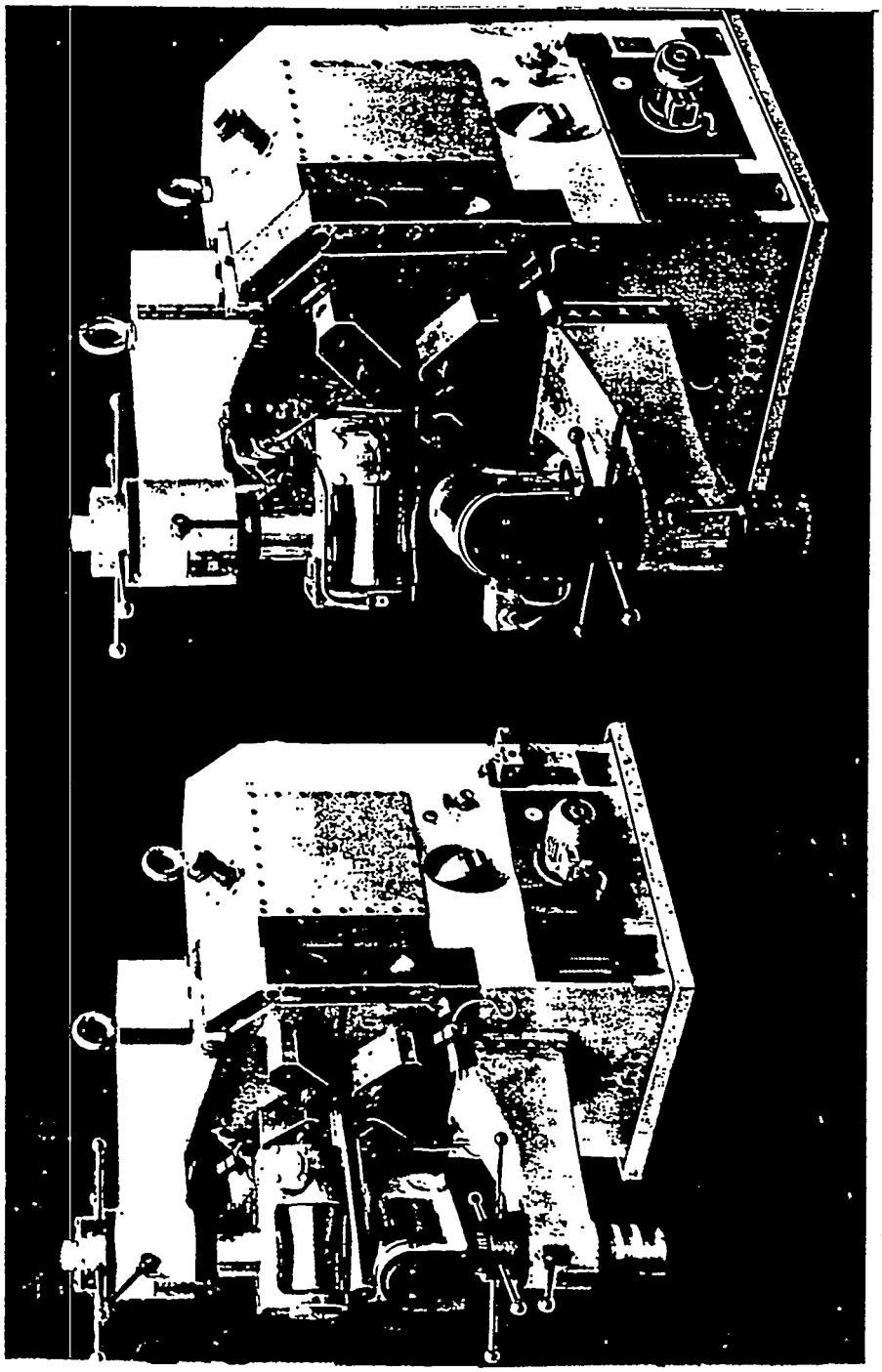


Figure 3. Machine AVS.

The movement of the 4 tools is operated via excentrics. A hollow shaft is driven from an A.C. motor by means of vee belt and flywheel, the shaft on which four excentric bushes are fitted being set in roller bearings (fig.4). The stroke movement of the excentrics is transmitted to four rocking arms which pivot around bolts fixed on the machine body. At the front end of the rocking arms, which protrude from the machine body, there is a tool take up. Rapid tightening of tools by means of a locking button permits tool changing in the shortest possible time. Thus the circular closing motion of the tools offers considerable forming possibilities. The length of the material which has to be reduced can be set as required on an adjustable stop in conjunction with a limit switch. This limit switch also operates the return of the workpiece.

THE STUDY OF ALUMINIUM ALLOYS WORKPIECES DEFORMATION ON AVS MACHINES

The process of manufacturing by pressure was studied using D16 and B65 aluminium alloys as the materials to be deformed. The chemical compositions of these alloys and their mechanical properties are given in tables 2 and 3 correspondingly.

Table 2. Chemical compositions of D16 and B65 alloys (wt%).

Alloy	Al	Cu	Mg	Mn	max.				
					Fe	Si	Ni	Zn	Ti
D16	bal	3.8-4.9	1.2-1.8	0.3-0.9	0.5	0.5	0.1	0.3	0.1
B65	bal	3.9-4.5	0.15-0.3	0.3-0.5	0.2	0.25	-	0.1	0.1

The study of the influence of deformation's degree on mechanical properties was conducted using D16 alloy. In this case pressed and heat-treated rod 30 mms in diameter was taken as the initial sample.

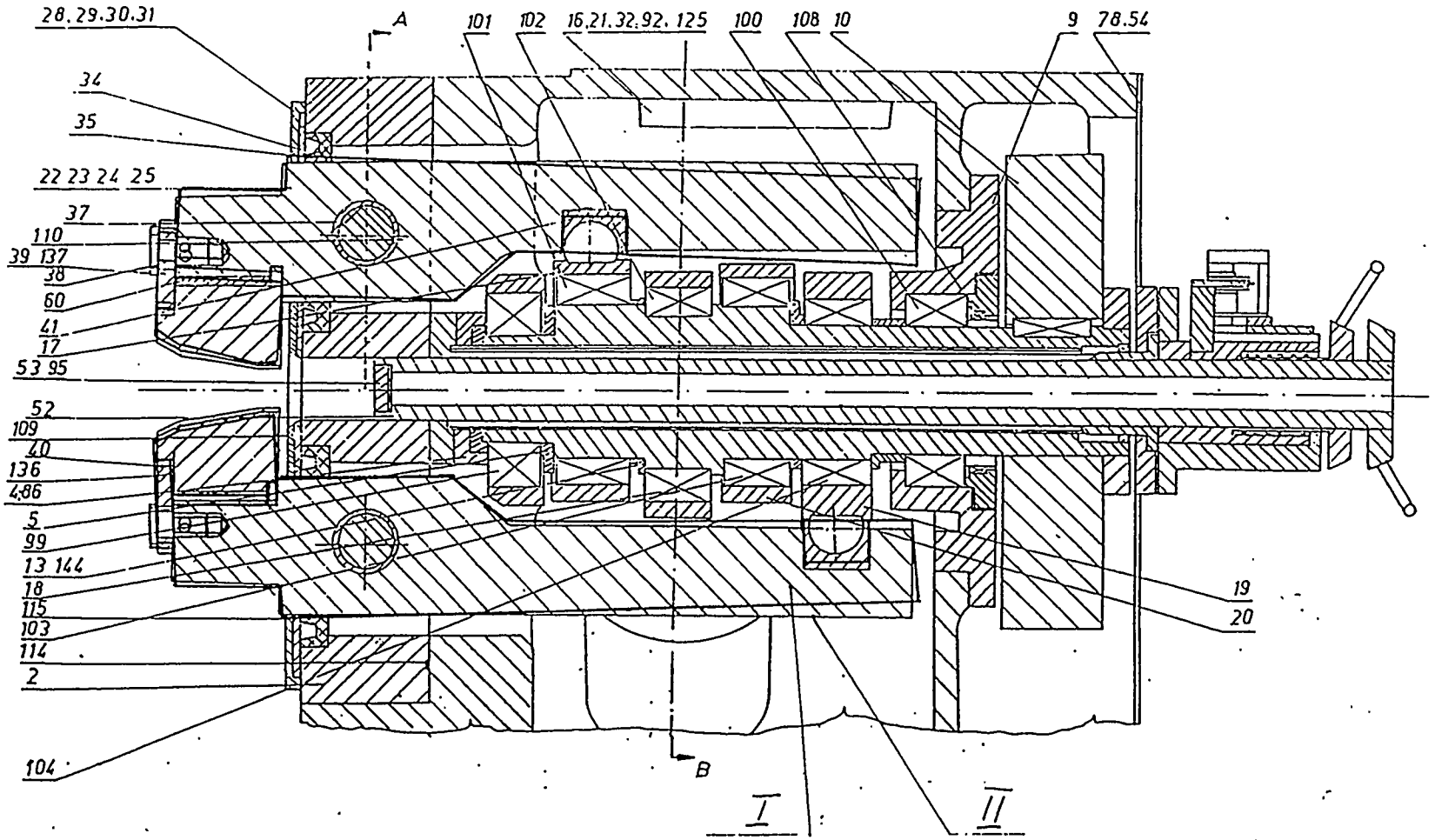


Figure 4. Section of forging bloc.

I - upper position;
II - lower position.

Table 3. Mechanical properties of D16 and B65 alloys.

Alloy	Yield strength, MPa	Tensile strength, MPa	Elongation, %	Reduction in area, %
D16	110	210	18	30
D16T	280	400	8-10	15
B65	250	400	20	30

The following order of reduction was used:

1. Diameter 29.6 (initial)---------->
2. Diameter 28.0 (degree of deformation 10,5)--->
3. Diameter 25.4 (degree of deformation 26,5)--->
4. Diameter 23.0 (degree of deformation 39,5)--->
5. Diameter 21.0 (degree of deformation 48,5)--->
6. Diameter 18.0 (degree of deformation 63,0)--->
7. Diameter 14.6 (degree of deformation 75,5)--->
8. Diameter 10.0 (degree of deformation 88,5).

The total number of passages covering the range of reduction from workpiece's initial diameter 29.6 mm to final diameter 10 mm was equal to 7. Deformation of workpieces was achieved with the help of AVS-63 machine having a working corner of tool's cone 7 degrees at room temperature without intermediate heat-treatments. Reduction was conducted using forced rotation of the workpiece around its longitudinal axis. It should be noticed that the workpiece's deformation from initial diameter 29.6 mm to diameter 10 mm (degree of deformation 88,5%) in one passage is also possible. However, this leads to excess complication of the reduction's process and results in bad surface of deformed workpiece.

Strength properties of deformed workpieces were measured on standard rupture test samples cut out from central parts of workpieces. Results are shown in the table 4. The influence of defor-

mation's degree on mechanical properties is illustrated by figures 5-9. The growth of deformation's degree increases tensile strength, 0.2 yield strength and hardness. Moreover, the lowering of plastic characteristics with minimum of elongation at 30 % deformation is observed.

Table 4. The influence of mechanical properties of D16 samples on deformation

Sample	Degree of def. %	Yield stren. MPa	Tens. stren. MPa	Elong. %	Reduct. in area, %	Hard. HB, MPa
1	0	126	230	18	20	624
2	10.5	248	250	7.0	17.5	721
3	26.5	260	268	5.0	12.5	732
4	39.5	253	270	7.0	12.5	743
5	48.5	248	274	8.0	12.5	752
6	63.0	258	289	8.0	12.5	785
7	75.5	272	304	8.0	12.5	814
8	88.5	354	383	7.4	12.5	1070

Metallographic investigations showed that structure of the workpieces under study consists of solid solution with inclusions of intermetallic phases. The initial material has fibrous structure stretched in the axial direction and is characterized by lined arrangement of intermetallic phases (figure 10a-b). Intermetallic inclusions have predominantly stretched form with linear dimensions 2.5-40 μm in longitudinal section and 2.5-10

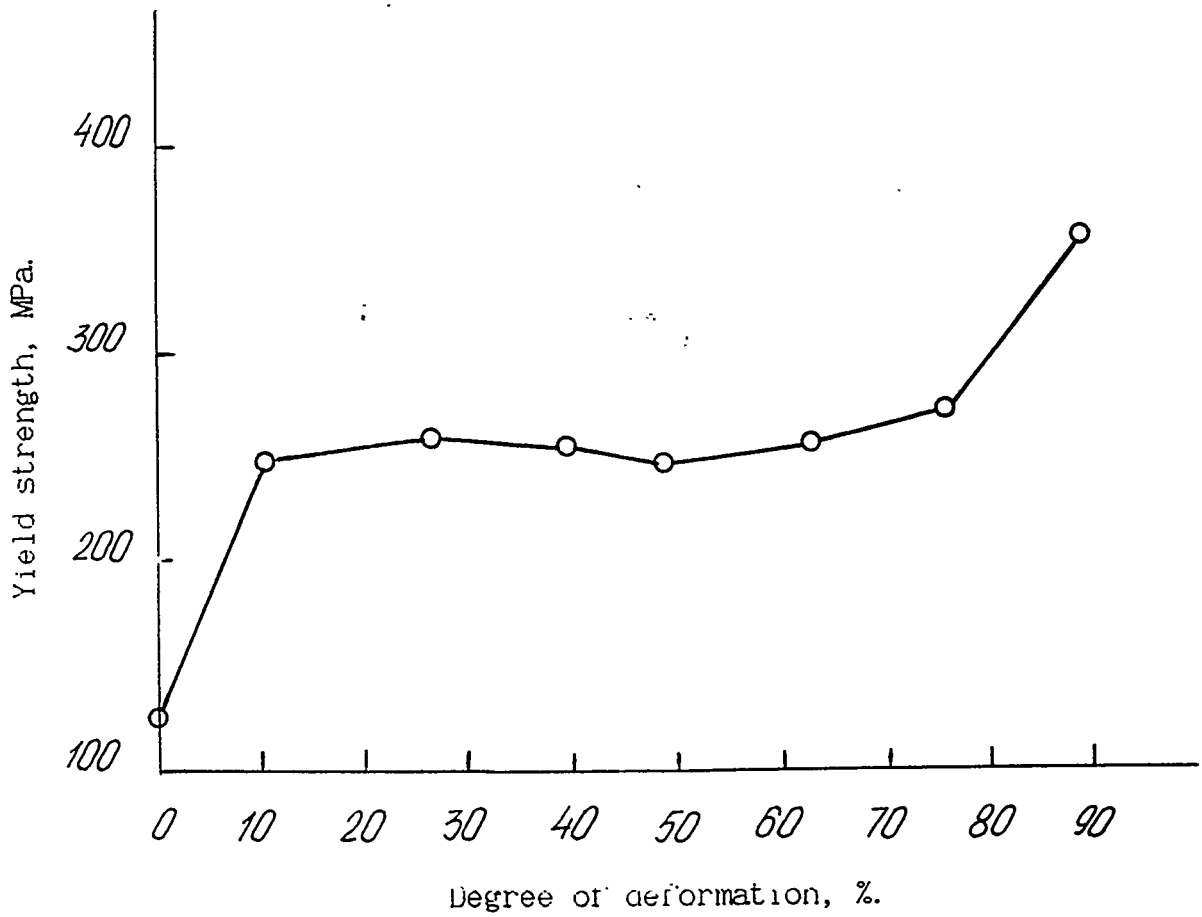


Figure 5. The dependence of yield strength on degree of deformation samples, alloy D16.

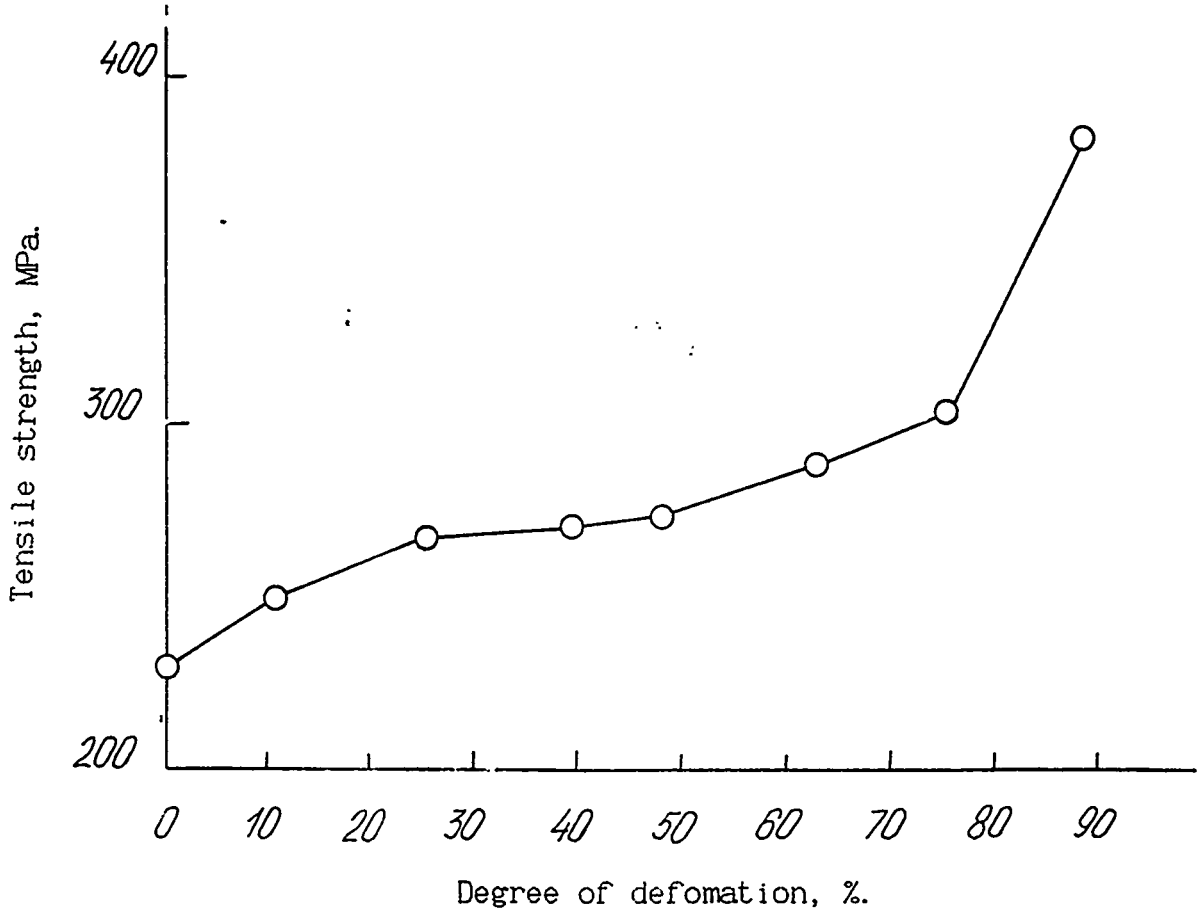


Figure 6. The dependencee of tensile strength on degree of deformation for samples, alloy D16.

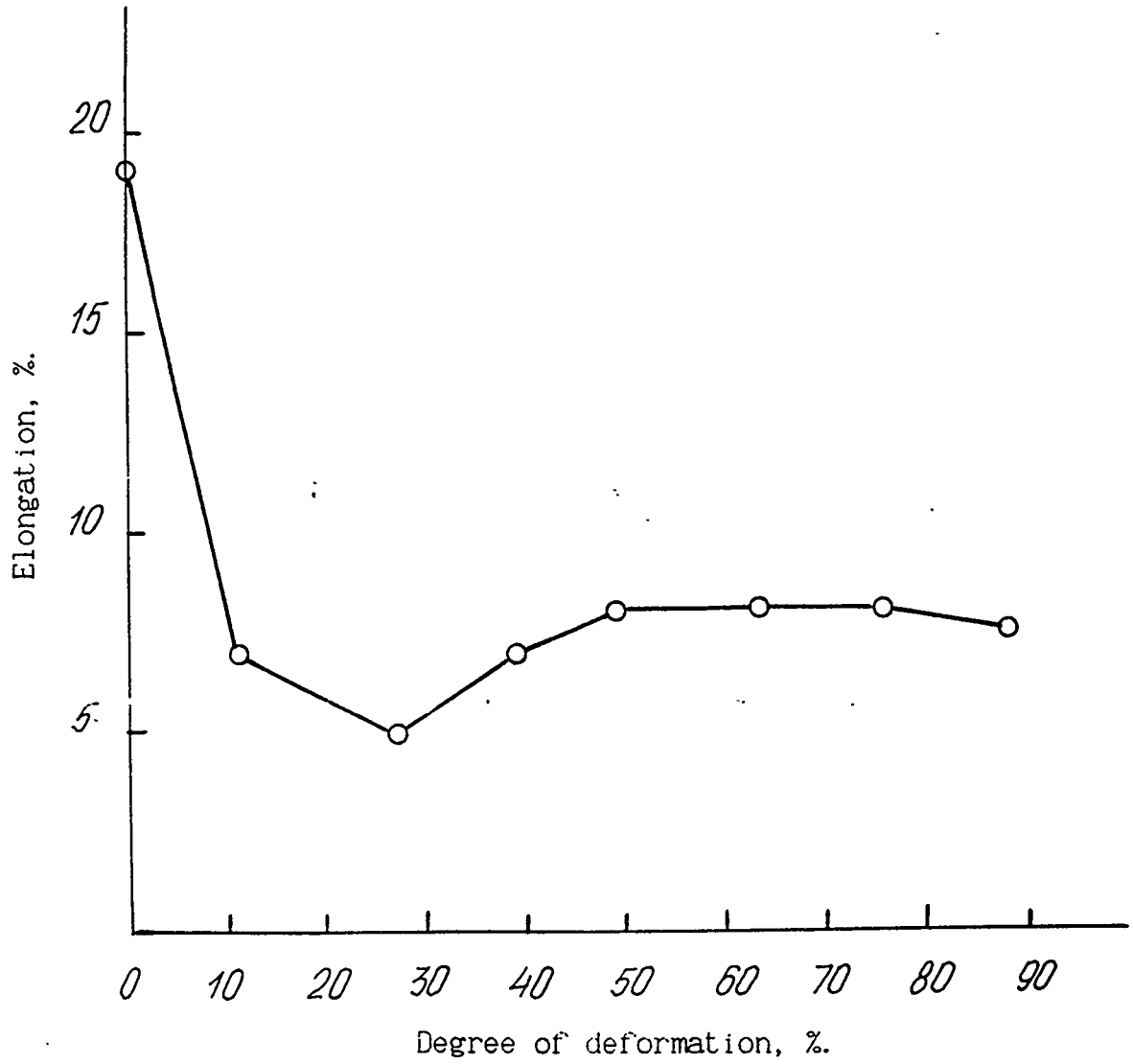


Figure 7. The dependence of elongation on degree of deformation for samples, alloy D16.

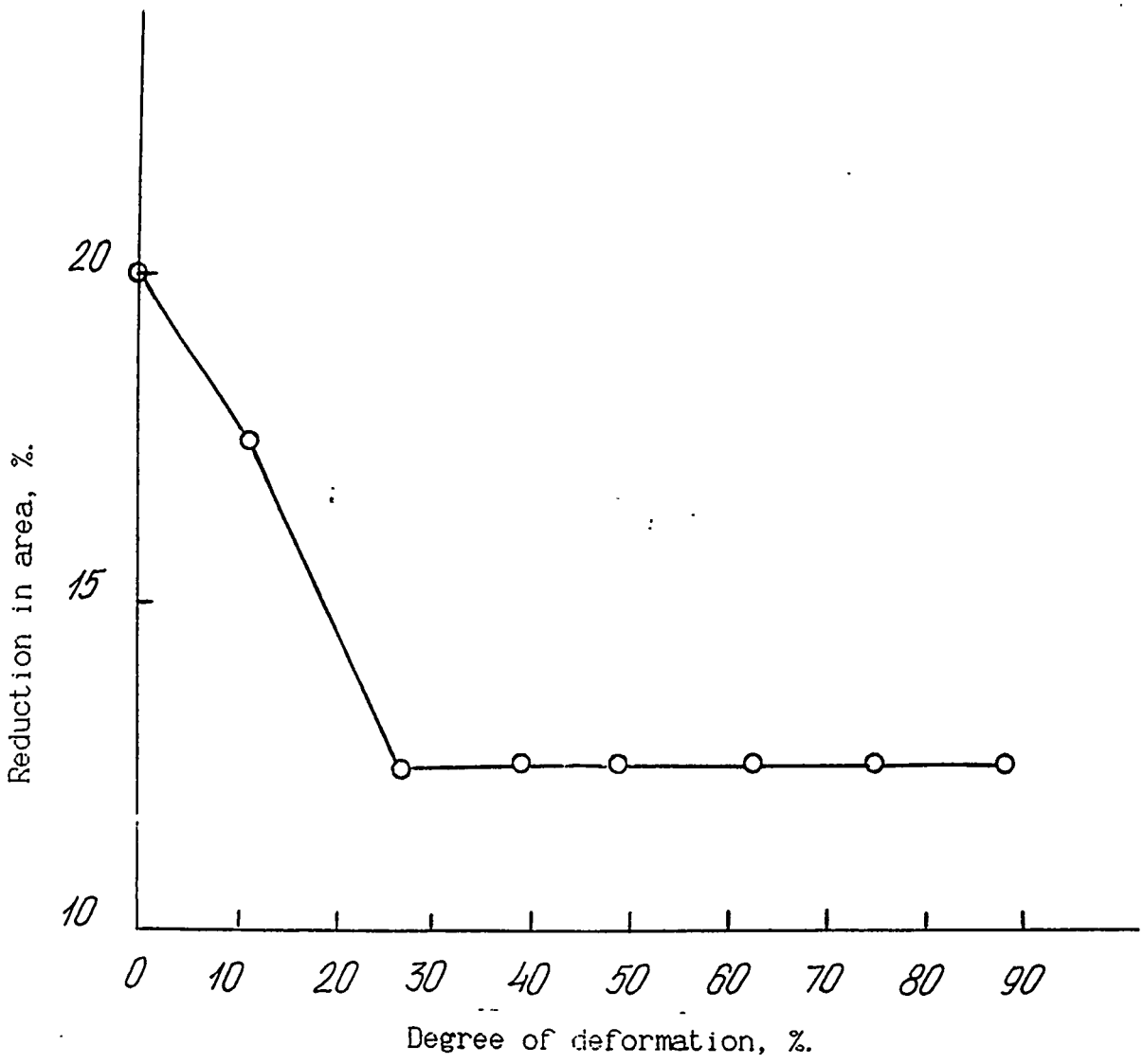


Figure 8. The dependence of reduction in area on degree of deformation for samples, alloy D16.

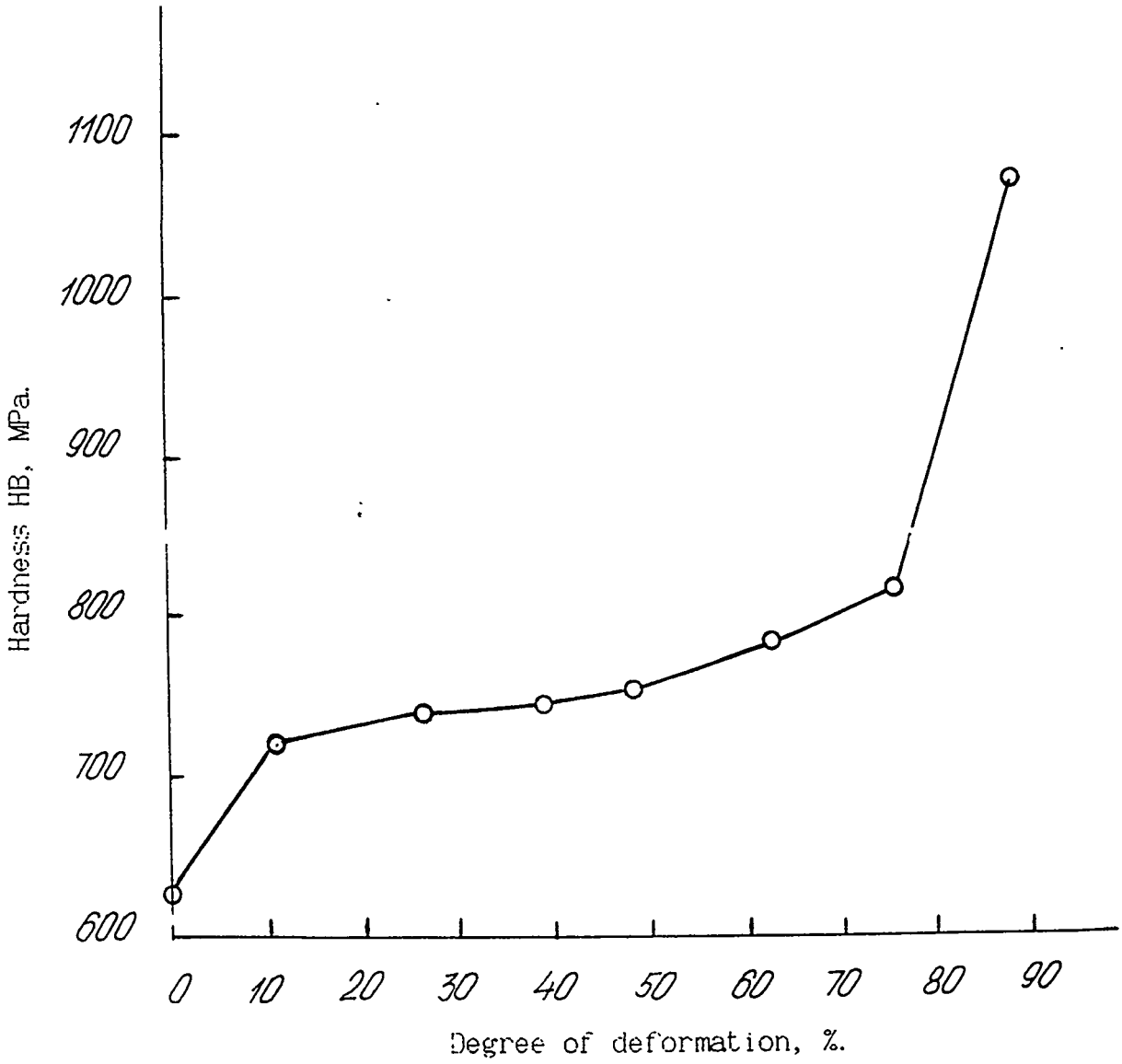


Figure 3. Thee dependece of hardness on degree of deformation for samples, alloy D16.

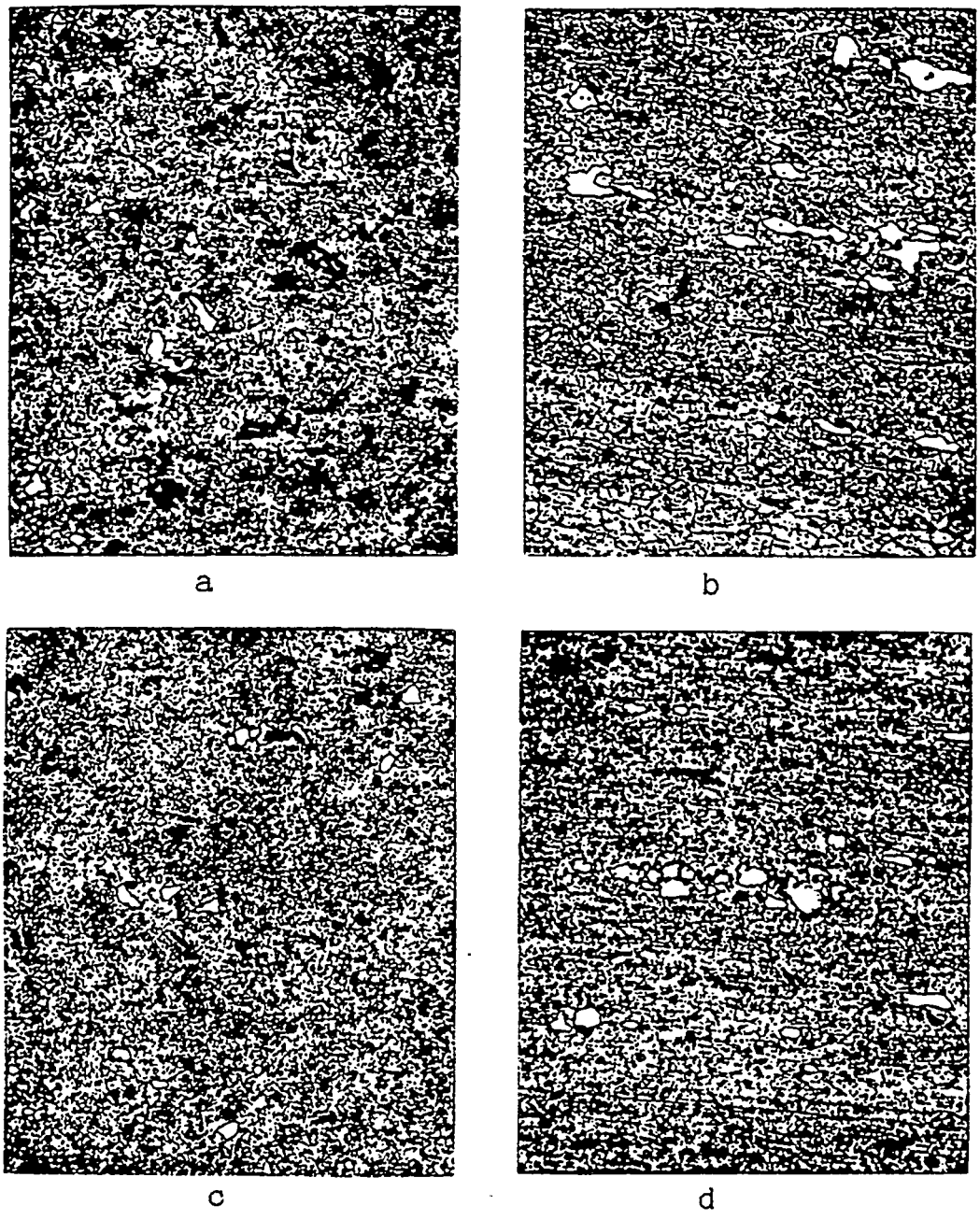


Figure 10. Microstructure of deformed samples, alloy D16 (initial diameter 30 mm).
Initial: a) transversal section;
b) longitudinal section.
Degree of deformation 48,5%:
c) transversal section;
d) longitudinal section.

μm in transversal one.

During workpiece's reduction material acquires more fine-fibrous structure and redistribution of intermetallic compounds takes place (figures 10 c,d; 11 a-d). The growth of deformation's degree leads not only to the change of intermetallic phases distribution character, but to the change of their dimensions and form as well. Meanwhile linear structure is maintained at all degrees of deformation just up to 88,5 %. Crushing of intermetallic phases begins to be observed already at insignificant deformation; at maximum degree the form of inclusions either in longitudinal or in transversal sections is mainly equiaxial with the average dimension of approximately 8 μm.

The study of D16 alloy mechanical properties and structure dependence on deformation's degree showed that the optimum degree of deformation for workpieces 30 mm in diameter with the given composition, initial state and regime of reduction by profiled stamps at the angle 7^0 lies in the range of 50-70%.

MAKING OF EXPERIMENTAL WORKPIECES WITH THE LENGTH 300 MM FROM D16 AND B65 ALLOYS.

Experimental workpieces from D16 and B65 alloys were made on AVS-63 machine with the working corner of tool's cone 7^0 at room temperature and without intermediate heat-treatments. The workpiece 40 mm in diameter, whose properties are given in the table 5 (example 1), was used in the role of initial material for preparation of experimental sample 30×300 mm from D16 alloy. The workpiece 30 mm in diameter was taken as initial material for preparation of samples from D16 alloy at deformation's degrees 55% and 70%. Its properties are given in the table 5 (example 3). Experimental samples from B65 alloy were prepared from the workpiece 40 mm in diameter (table 5, example 6). For manufacturing of samples from B65 alloy at deformation's degrees 55% and 70% the workpiece 40 mm in diameter mechanically turned on 30 mm in diameter was also used.

The following order of reduction was used:

1. For experimental sample diameter 30 mm:

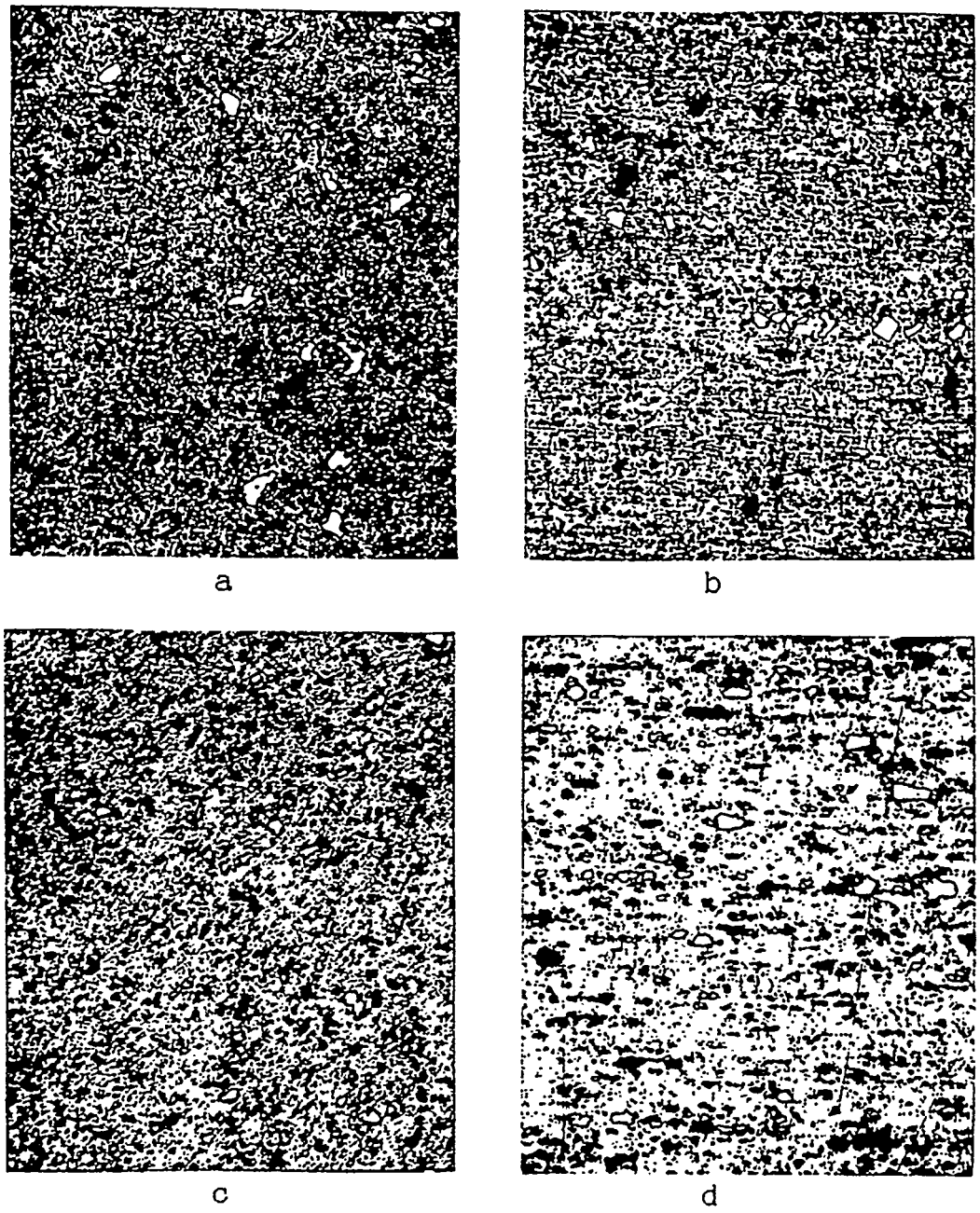


Figure 11. Microctructure of deformed samples, alloy D16.
Degree of deformation 75,5%:
a) transversal section;
b) longitudinal section.
Degree of deformation 88,5%:
c) transversal section;
d) longitudinal section.

Diameter 40.0 mm (initial)---------->
Diameter 35.5 mm (degree of deform. 23.5%)------>
Diameter 30.0 mm (degree of deform. 42.0%).

2. For experimental sample diameter 20 mm:
Diameter 30.0 mm (initial)---------->
Diameter 25.4 mm (degree of deform. 26.5%)------>
Diameter 20.0 mm (degree of deform. 55.5%).

3. For experimental sample diameter 16.5 mm:
Diameter 30.0 mm (initial)---------->
Diameter 25.4 mm (degree of deform. 26.5%)------>
Diameter 20.0 mm (degree of deform. 55.5%)------>
Diameter 16.5 mm (degree of deform. 70.0%).

Strength properties of deformed workpieces were measured on standard rupture test samples cut out from central parts of workpieces. Results obtained for the samples from D16 alloy show (table 5) that the values of tensile strength, 0.2 yield strength and hardness at the same degrees of deformation are higher in comparison with the properties of those given earlier (table 4). Such difference is likely to be connected with another orders of reduction and other initial properties of D16 workpiece 40 mm in diameter. The dependence of strength properties of experimental samples from B65 alloy on deformation's degree has the same character as in the case of D16 samples deformed from initial diameter 30 mm (table 4).

The microctructure of initial workpiece from D16 alloy 40 mm in diameter is simular to the structure of the workpiece 30 mm in diameter. However, it is characterized by bigger number of large inclusions of intermetallic phases (25-40 μm) and by more rough structure (figure 12 a,b). The changes of material's structure taking place during reduction are analogous to those described above. Large inclusions are crushed, but still they have big dimensions as compared with the structure of the samples with the same degree of deformation (figure 12 c,d). The structure of the samples deformed with degree 55-70% is similar to given earlier (figures 10,11,13) structure of material with the same degree of

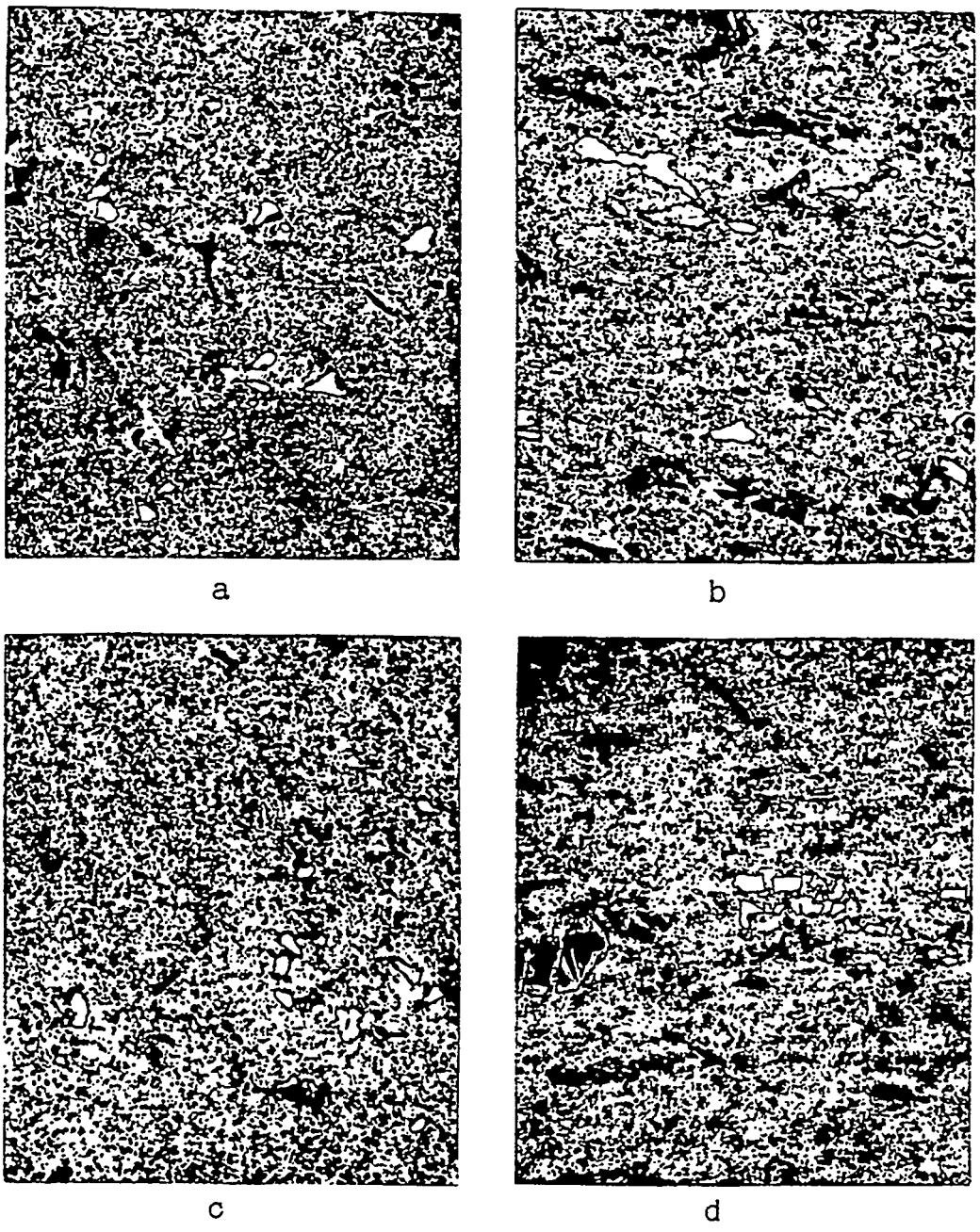


Figure 12. Microstructure of deformed samples, alloy D16 (initial diameter 40 mm). Initial: a) transversal section; b) longitudinal section. Degree of deformation is 42%: c) transversal section; d) longitudinal section.

deformation.

Table 5. Mechanical properties of D16 and B65 alloys samples.

Sample	Initial diam., mm	Degree of def. %	Yield stren. MPa	Tens. stren. MPa	Elong. %	Reduct. in area %	Hard, HB, MPa
			D16				
1	40.0	0	179	309	14.5	15.0	763
2	40.0	42.0	366	372	5.5	7.5	938
3	30.0	0	126	230	18.0	20.0	624
4	30.0	55.5	277	291	6.0	13.5	783
5	30.0	70.0	319	339	4.5	10.0	849
			B65				
6	40.0	0	114	200	22.0	32.5	497
7	40.0	42.0	265	269	8.5	25.0	670
8	30.0	55.5	265	273	8.5	27.5	700
9	30.0	70.0	291	297	5.5	22.0	763

Microstructure of B65 alloy presents by itself a solid solution with inclusions of intermetallic phase CuAl; (figure 14 a,b). Finely dispersed inclusions of this phase having round shape and dimension about 1 μm are uniformly distributed either in longitudinal or in transversal sections. Larger inclusions of intermetallic phase are concentrated into groups. Their dimensions in transversal section are 3-8 μm (figure 14 a). In longitudinal direction they have certain orientation and their dimensions are

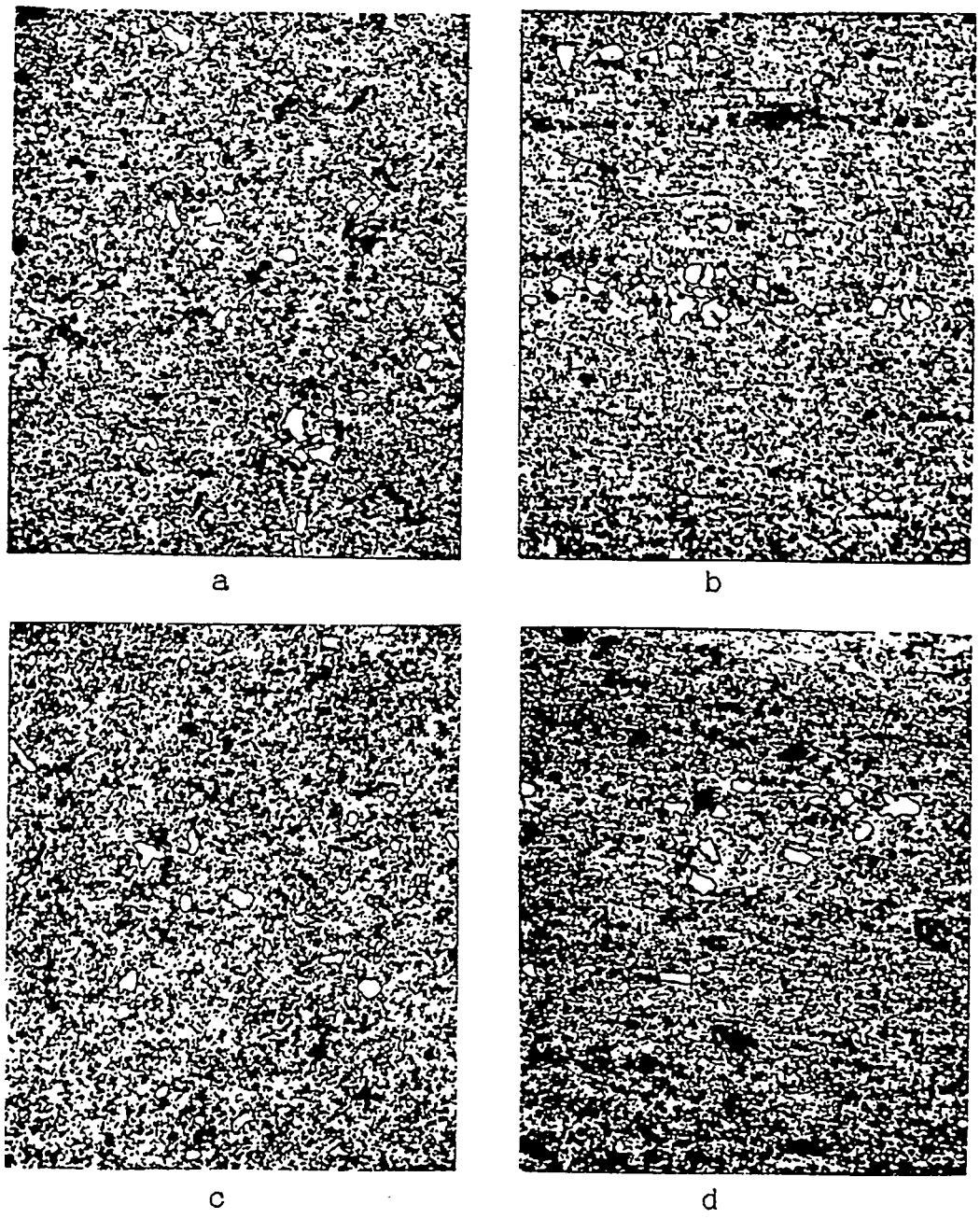
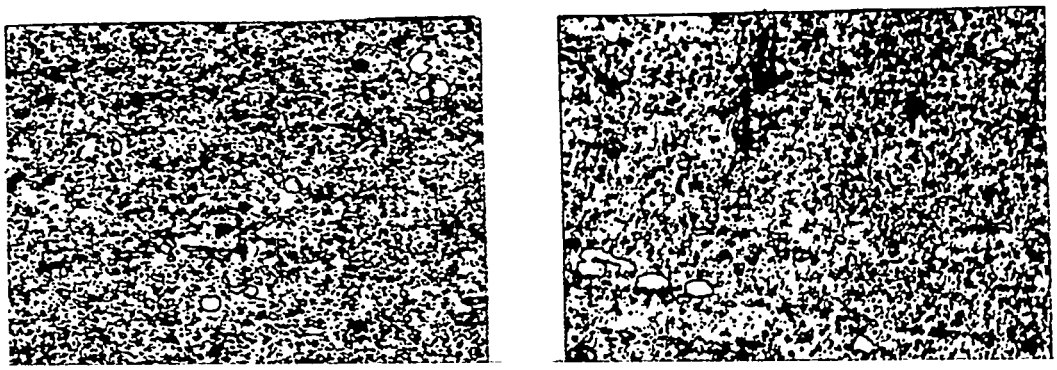
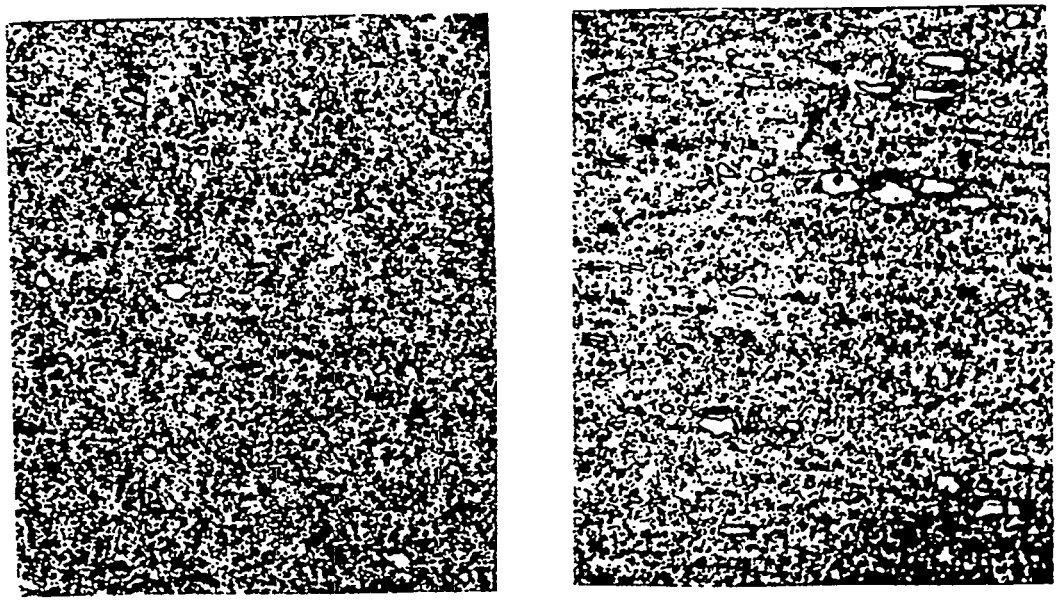
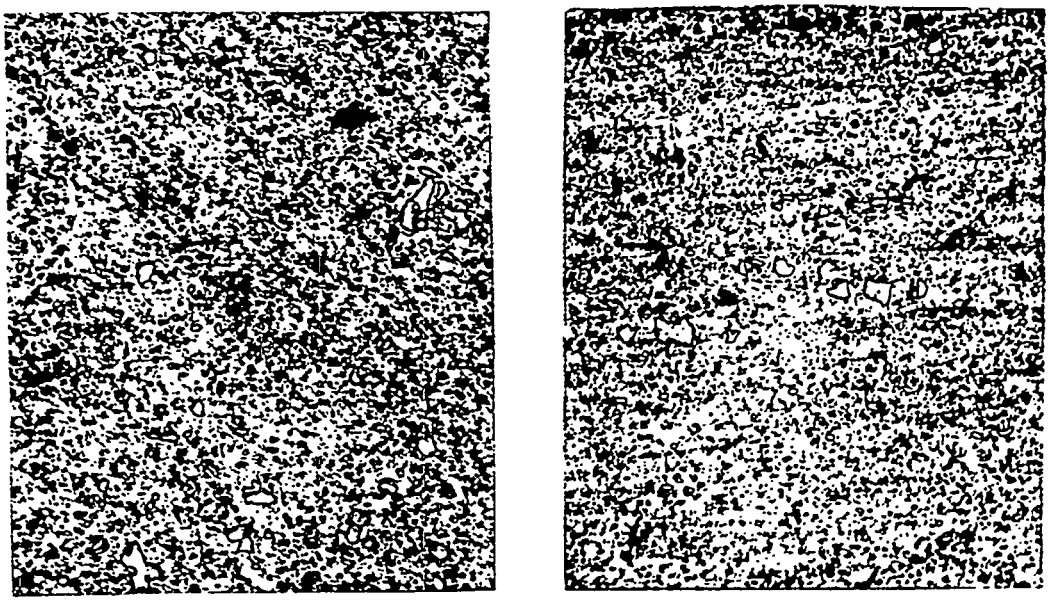


Figure 13. Microstructure of deformed samples, alloy D16 (initial diameter 30 mm).
Degree of deformation 55 %:
a) transversal section;
b) longitudinal section.
Degree of deformation 70 %:
c) transversal section;
d) longitudinal section.





a b



c d

10-40 μm (figure 14 b).

Workpieces reduction leads to crushing of large inclusions (to 5-8 μm), but their linear structure stays invariable (figures 14c,d; 15). At larger degrees of deformation (up to 70%) redistribution of inclusions and change of the character of their arrangement in volume of material are taking place besides further crushing (figure 15 c,d).

Thus, the study of deformation of workpieces from D16 and B65 alloys showed, that the structure and strength properties of the samples treated by suggested method are essentially improved. Moreover, the level of properties and the quality of structure depend to a marked degree on dimensions, composition and structure of the initial workpiece's material and on the order of deformation. The optimum range of deformation's degree will depend on composition, structure, mechanical properties and dimensions of initial workpieces and on advanced requirements to manufactured materials.

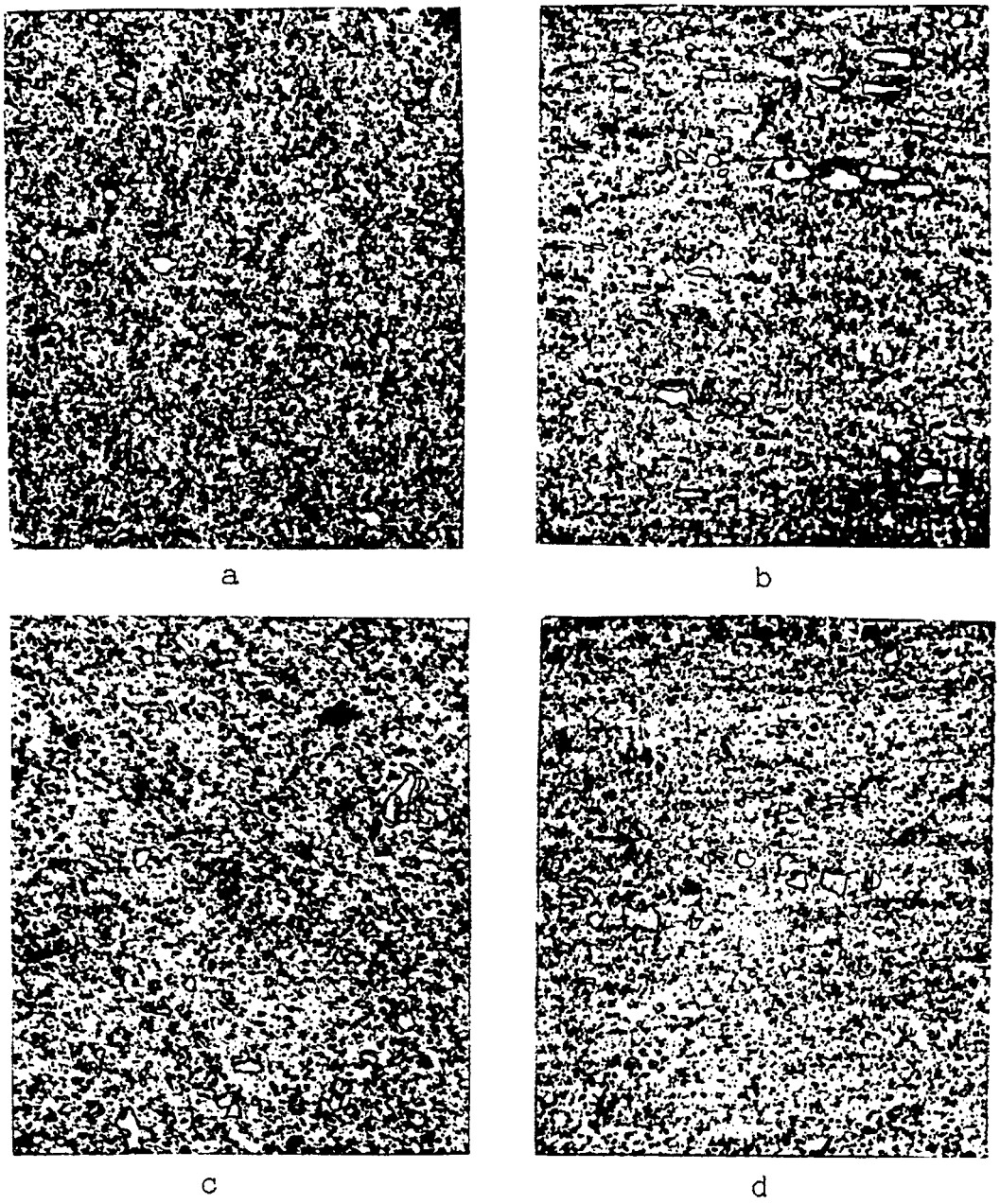


Figure 15. Microstructure of samples deformed, alloy B65 (initial diameter 30 mm).
Degree of deformation is 55,5%:
a) transversal section;
b) longitudinal section.
Degree of deformation is 70,0%:
c) transversal section;
d) longitudinal section.

Project Title: Continuous Casting of Tool Steels with Plastic Deformation
Principal Investigator: Sergey Burkin
Urals Polytechnic Institute
Ekateringburg, Russia
AM-7668

CLAUSE 1 - STATEMENT OF WORK

Tasks:

The Contractor shall:

1. Provide a complete technical description of a continuous casting and deformation pilot facility and provide three (3) typical (typical refers to geometric characteristics) metal samples demonstrating process capabilities from previous work along photomicrographs.

2. Provide 100kg of a 120-160 mm casted bar of Russian equivalent of an American tool steel H-11 (as specified by Sandia).

Project Title: Amorphous Palladium (Pd)-based Alloys
Principal Investigator: Nikolai Vatolin
Institute of Metallurgy
Ekateringburg, Russia
AM-7669

CLAUSE 1 - STATEMENT OF WORK

Tasks:

The Contractor shall:

1. Provide a report detailing previously developed information that characterizes the performance, microstructure, and chemistry of Pd-based hydrogen filter materials, including representative data and analysis.

2. Provide the following material samples of Pd-based alloys used for hydrogen filter materials:
Pd-based alloys with the impurity atoms: Ag, Au, Cu, In, V, Pt
Pd-based alloys with large impurity concentration of noble metals
Ni (nickel) and Ti (titanium) based alloys

3. Develop a Materials Model that hypothesizes the enhanced filter performance of the material. Provide a report that explains the model and the results.

4. Using the model, determine the point at which the filtering diffusivity and conductivity of this material are equally optimized. Provide a report that includes a data analysis describing how well and how fast Hydrogen is filtered under these optimum conditions. Also provide material samples.

Project Title: A Novel Accelerated and Ecologically-Friendly Method for the Production of Wear Resistant Coatings of Iron Boride on Steels.
Principal Investigator: A. A. Ivanovich
Institute for Electrochemistry
Ekateringburg, Russia
AM-7670

CLAUSE 1 - STATEMENT OF WORK

Background:

Electochemical methods have been used to produce iron-boride coatings on ferrous-based alloys, however, standard techniques used for boridizing steels utilize environmentally unfriendly reactive salts and often require extended treatment times. The Contractor has addressed theses drawbacks by developing unique, ecologically friendly boridizing salts that more rapidly generate a hard and tough iron-boride coating on ferrous alloys. This project will demonstrate the industrial utility of this unique boridizing process for enhancing the tribological properties of ferrous-based metal cutting and metal working tools.

Tasks:

The Contractor shall:

1. Prepare and submit an initial report describing the unique borodizing process developed by the Contractor. The report shall summarize the experimental work conducted to date to measure the friction, wear and lifetime of the coatings on ferrous alloys. References to published work shall also be included.

2. The Contractor and Sandia shall mutually determine three (3) ferrous alloys for the purpose of experimentation within two months after Contact execution.

Experimentation shall be carried out on samples made from the nearest Russian equivalent to the American alloys chosen for the experiments.

Develop borodizing treatments that will optimize the wear resistance of the alloys.
Measure the wear resistance and hardness of the treated materials. Using optical metallography and x-ray diffraction, characterize the treated areas.

Provide a brief interim report (approx. 4 pages in length) describing the experiments performed and initial property characterization results.

Treat four (4) test samples for each of the three alloys, to yield optimum wear resistance. The test samples shall be approximately 4cm in diameter and between 2-5mm thick. Provide the samples to Sandia.

3. The Contractor shall treat the Sandia supplied tools in the same manner as for Task 2 and return the tools to Sandia. The Contractor shall also provide a final report on the experimentation data and results for the entire project.

INSTITUTE OF HIGH TEMPERATURE ELECTROCHEMISTRY
URAL BRANCH OF RUSSIAN ACADEMY OF SCIENCES

ECOLOGICALLY HARMLESS WASTE-FREE TECHNOLOGY FOR BORATING OF STEEL PARTS IN SALT MELTS

RUSSIA
Ekaterinburg

INSTITUTE OF HIGH TEMPERATURE ELECTROCHEMISTRY

URAL BRANCH OF RUSSIAN ACADEMY OF SCIENCES

R E P O R T

On the Contract Number AM - 7670
Amendment Number 01
Date November 17, 1994

ECOLOGICALLY HARMLESS WASTE - FREE TECHNOLOGY FOR BORATING OF STEEL PARTS IN SALT MELTS

Task 1

Principal investigator:
Ia.B. Chernov

Investigators:
N.G.Ilyushchenko
A.I.Anfinogenov

Ekaterinburg

ECOLOGICALLY HARMLESS WASTE-FREE TECHNOLOGY FOR BORATING OF STEEL PARTS IN SALT MELTS

Goal

The study is aimed at development of a technology for strengthening of machine parts and tools with the use of a thermochemical treatment which would answer the modern requirements imposed on production methods. The requirements include primarily ecological safety, non-waste production, saving of energy resources, the use of cheap raw materials and quantity-produced equipment, better conditions of labour, mechanization of works in full-scale production, and profit-ability.

A Review of Related Scientific and Technical Developments

Borating is a thermochemical treatment which consists in saturation of the surface layers of parts with boron during heating in a certain boron-containing medium. It is realized to improve hardness and abrasive resistance.

The temperature and the time of holding in the saturation medium ensure diffusion of boron into steel, which is accompanied by formation of iron borides FeB and Fe_2B (Fig.1). Alloying elements, for example, chromium and manganese, form borides $(Fe_{1-x-y}Cr(Mn)_xC_y)B$ and $(Fe_{1-x-y}Cr(Mn)_xC_y)_2B$ whose structure is similar to that of the borides FeB and Fe_2B.



Fig.1. Typical structure of a boride layer (FeB, Fe_2B) on steel U8A [W1-0,8C Special].[1] x450

[1] Here and henceforward the steel grades are given according to the classification adopted in Russia. Steel grades between brackets comply with USA standart AISI [23 - 24].

The choice of a particular borating method depends on adaptability of the method to production, conditions of manufacture, configuration, dimensions of treated parts and degree of their hardness improvement.

Borating is most effective for tools and machine parts running under strong wear conditions, without dynamic loads, and which have a relatively simple shape. The last requirement eliminates spalling at angles and portions with abrupt changes in cross-section.

Numerous publications deal with development of borating methods, study of the structure of surface layers, and the influence of alloying elements in steel, temperature and time on the borating kinetics [1-8].

Under industrial conditions borating is realized in powders, liquid and gaseous media.

Borating in Powders of Boron-Containing Materials

Powders of various boron-containing materials are used for borating: boron carbide, ferroboron, amorphous boron. "Inert" additions (aluminium or magnesium oxide, chamotte, etc.) are introduced into the powders to preclude sintering. Activators (NH_4Cl, KF, NaF, KBF_4, AlF_3, etc.) are added to the saturation mixture to accelerate the borating process. The merits of the technology are simplicity, accessibility, and possibility of realizing the process in furnaces of any type.

The drawbacks of the technology consist in its low production capacity, high labour intensity of preparatory works (preparation of processing mixtures and packing of products in containers), dustiness of working places, necessity of recovering the powders on their multiple use, insufficient heat resistance of the containers, frequent nonoxidizing heating of borated parts for hardening.

Borating in Gaseous Atmospheres

Borating is usually realized in vapours of borane (B_2H_6) or boron trichloride (BCl_3).

A large drawback of the gaseous borating is the use of toxic and explosive mixtures, the need of special equipment, and nonuniformity of the layers produced.

Electrolysis Borating.

A borax melt or molten borax with various additions is used for electrolysis.

This method has been most widely adopted in industry.

The shortcomings of the method are as follows: the use of direct current; low corrosion resistance of crucibles, enrichment of the melt with iron, which stops the borating process; large removal of borax with the treated parts; surfaces of borated parts are difficult to wash; graphite electrodes occupy much of the working space of the bath, this reducing the number of parts loaded for treatment. Large crucibles are to be made of high-temperature steels, a circumstance which incurs heavy expenses.

Liquid Borating in a Salt Melt

Liquid borating in a salt melt is realized in high-temperature steel crucibles with external heating or in electrode salt baths with refractory lining.

In the former case the melt base is borax or borax with various salt additions and a powder of boron-containing materials or boron reducers [9, 10]. A low resistance of the crucibles at high temperatures, scarcity of high-temperature steels, high energy consumption by the furnaces, and extra costs of purification works and processing of wastes suppress application of the method.

In the latter case halogenide melts, mainly chloride-fluoride and chloride-fluoride-oxide melts, with addition of boron compounds are used [11-16].

A drawback of the method is the use of harmful fluoric compounds.

A common shortcoming of the above-mentioned borating methods is expensive arrangements on provision of environmental protection.

A Brief Characteristic of a Waste-Free Technology of Liquid Borating [22]

In order to provide a closed cycle of utilization of raw materials and wash water and also to eliminate discharge of toxic wastes to the environment, the researchers at the Institute of High-Temperature Electrochemistry, Ural Division of Russian Academy of Sciences, have worked out a new technology for strengthening of machine parts and tools by borating in a melt of calcium chloride with a powder of amorphous boron or magnesium polyboride in electrode salt baths which are used in industry for nonoxidizing heating of metal subject to thermal treatment. The chloride melt

does not attack the high-refractory lining.

Borating of iron and steel in the calcium-chloride melt with a boron powder is conceived as follows.

A fine powder of amorphous boron or magnesium polyboride always has an oxide film of B_2O_3 on its surface. When the powder is added to the molten calcium chloride, the oxide film dissolves in the melt. At high temperatures boron reduces ions of the dissolved trivalent boron to lowest-valence ions:

$$2\ B^{3+}(\text{melt}) + B\ (\text{solid}) \longrightarrow 3\ B^{2+}(\text{melt}) \qquad (1)$$

Ions of bivalent boron disproportionate and form iron alloys according to the following scheme:

$$3\ B^{2+}(\text{melt}) + 2\ Fe\ (\text{solid}) \rightleftharpoons 2\ B^{3+}(\text{melt}) + Fe_2B\ (\text{solid}) \qquad (2)$$

$$3\ B^{2+}(\text{melt}) + Fe_2B\ (\text{solid}) \rightleftharpoons 2\ B^{2+}(\text{melt}) + 2FeB\ (\text{solid}) \qquad (3)$$

A chemical analysis of the melt (Table 1), which was performed repeatedly during a month of the salt bath operation (melt volume 0.08 m^3, melt weight 0.18 t), shows that the melt contains small amounts of boron and calcium oxides but they do not accumulate greatly.

Table 1

Sample No.	Time (days)	B_2O_3 (mass %)	CaO (mass %)
1	0	1.80	0.92
2	10	2.50	1.43
3	15	2.65	1.26
4	20	2.43	1.83
5	25	2.80	1.58
6	30	2.64	1.65

The process takes place in an electrode salt bath at a temperature of 1073 to 1273 K during 0.5-5 hours depending on the steel grade and the required thickness of the layer. Parts that require thermal treatment are quenched in a quenching bath with an aqueous solution of calcium chloride. Parts are tempered in tempering furnaces to remove quenching stresses and to achieve a preset hardness and then they are washed in water to remove salts.

The principle of the technology is that borating and quenching baths contain one and the same salt – calcium chloride. Calcium chloride and the powder of magnesium polyboride, which cover the parts, are transferred together with hot parts into the quenching bath where the substances are readily washed off the parts during quenching.

As is seen from the technological scheme, the calcium chloride solution and magnesium polyboride can be recovered from the quenching bath, dried, calcined, and returned to the borating bath.

With this procedure, the technology is adaptable to production conditions and is ecologically friendly. The calcium chloride solution almost completely replaces quenching mineral oils which are harmful to environment and are fire-hazardous.

Figure 2 depicts a waste-free technological scheme of borating and thermal treatment of parts:

- Borated parts, which require quenching, undergo thermal treatment in a quenching bath containing an aqueous solution of calcium chloride.

- To remove stresses and to achieve a preset hardness after quenching, parts are tempered in tempering furnaces at a temperature of 353 to 873 K depending on the steel grade and application (items 5-6).

- Subsequent to tempering the parts are washed in baths (items 3-4), dried, and inspected for serviceability.

- Parts, which do not require quenching, are air-cooled (item 9), washed in baths (items 3-4), dried, and inspected for serviceability.

- When parts are quenched in the bath (item 2), a surplus calcium chloride (in excess of the assigned concentration) and magnesium polyboride are accumulated. The supersaturated solution is extracted, boiled down in the evaporator (not shown), calcined in the furnace (item 5), and is returned to the borating bath (item 1) or placed in sealed containers for future use.

- Water evaporates from the quenching bath (item 2) owing to heating from quenched parts. For this reason water is added to the bath (2) from the bath (3) and to the bath (3) from the bath (4). Service water is poured into the bath (4).

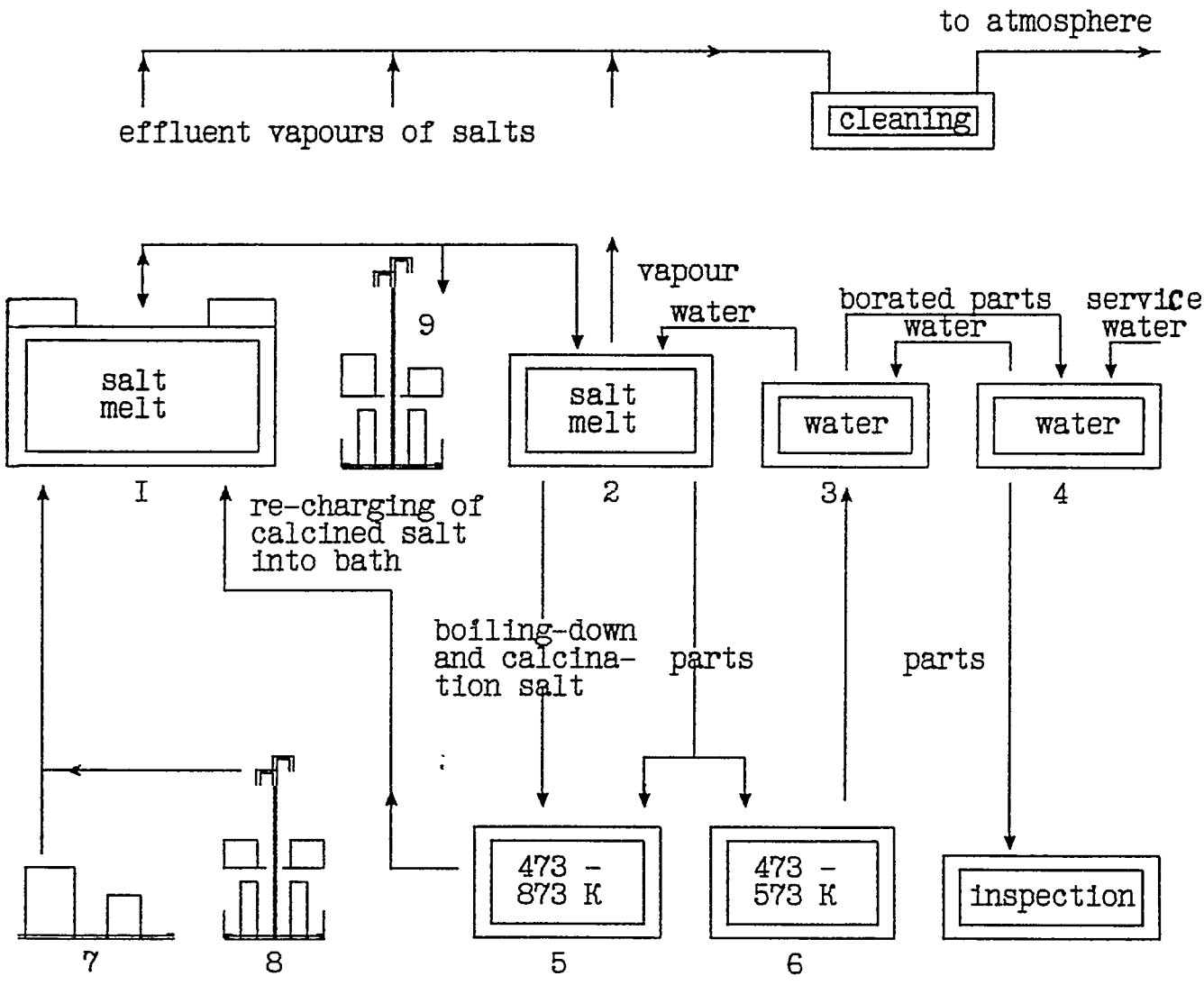


Fig.2. Waste-free technological scheme of borating and thermal treatment of parts:

1 - electrode salt bath (borating);
2 - quenching bath;
3 - washing bath;
4 - final washing bath;
5 - electric furnace for calcination of salt and tempering of parts;
6 - electric furnace for tempering of parts;
7 - 8 -preparation of chemical agents and parts;
9 - cooling of parts which do not require quenching.

- The borating bath (item 1), cooling racks (item 9), the quenching bath (item 2), and the tempering furnaces (items 5-6) have an exhaust ventilation system providing for cleaning of the effluent gases and removal of dust. Recovered products are calcined and returned to the borating bath.

This borating technology has been tested on constructional steels 20 [C1020], 45 [C1045], 40Ch [5140], CchCh15 [E52100], 30ChGSA; tool steels U8A [W1-08C Special], 9ChC, ChVG, Ch12F1 [D2]; tool steels for hot working 5ChNV, 5ChGM, 3Ch3MF, 4ChMFS, 3Ch2V8 [H21], etc. The choice of these steels was governed by the possibility of borating drawing, bending, moulding and knurling tools, rolls, and other parts.

The following conclusions have been drawn from the tests performed under industrial conditions at two enterprises located in the town of Ekaterinburg:

- The melt ensures a high rate of borating, which is about 30% higher than that in the borax melt;
- The bath lining is not attacked;
- Heating of the melt and maintaining it at the working temperature require much less electric power than in other borating methods where external heating is used.

Literature and experimental data were used to calculate the relationship between the density and concentration of aqueous solutions of calcium chloride at temperatures from 293 to 353 K [18, 19, 20]. This made it possible to assign the concentration of calcium chloride in the quenching bath in strict accordance with the solution density.

When an aqueous solution of calcium chloride of different density was tested as a quenching medium for the UIOA, ChI2M, 5ChNM, CchChI5 and 40Ch steels, the following was found:

- stirring of the solution is unnecessary;
- sludging of the solution does not take place;
- the cooling capacity weakly depends on temperature (298-373 K). As the solution temperature is raised, the maximum of the heat transfer coefficient shifts to the region of higher temperatures (433-633 K);
- borated and quenched parts can be washed easily in cold

water. No surface corrosion is observed after borated parts have been dried.

The use of the calcium chloride solution instead of mineral oils as the quenching medium does not impair mechanical properties of borated steels and in some cases the properties, for example, such parameters as hardenability and hardening capacity, are even improved. Strength characteristics of the steels are enhanced and formation of quenching cracks is less probable [19, 20].

Ecology

The sources of harmful matter are:

- electrode salt bath;
- hot parts transferred from the borating bath to the quenching medium.

Vapours of calcium chloride and hydrogen chloride are released to the environment.

Literature sources [21] provide no data on harmful effect of calcium chloride in the atmosphere and water reservoirs. The vapour pressure of molten calcium chloride at temperatures of 1073 to 1273 K is insignificant (0.01 mm Hg at 1223 K) [18].

The maximum permissible concentration of amorphous boron and magnesium polyboride (B, MgB_x) is 10 mg/m^3 [21].

Gaseous effluents are drawn by the exhaust ventilation system where the effluents are cleaned. The accumulated concentrate of calcium chloride is boiled down, calcined, and returned to the borating bath.

So the technology is rendered ecologically harmless and waste free.

Local Protection of Parts from Borating

Since mounting faces of borated parts cannot be machined under a full-scale production, a special-composition putty, which is applied with a brush, was tried for local protection of parts. The putty protects well the surfaces of parts from coating deposition. For example, the mounting hole (where the putty was brushed on) of a roller made of steel grade 40Ch has no boride coating after borating, while the coating thickness on the working surface of the roller is 120-140 μm.

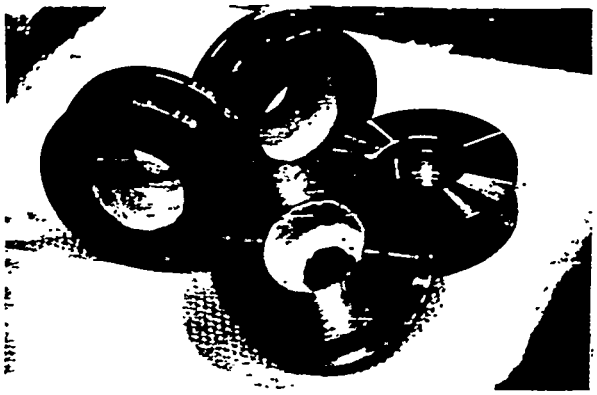


Fig.3. Roller with the putty applied prior to borating.

The putty is indifferent to the melt, does not crack, and is readily washed off with water after borating.

Subsequent to borating and thermal treatment the mounting faces of parts, which were protected with the putty, were brought to the assigned dimensions on a lathe using a T5K10 cutting tool when the base metal hardness was HRc=30 and using a T15K6 cutting tool when the base metal hardness was HRc=40.

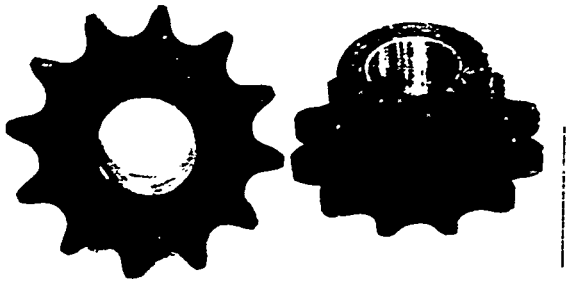


Fig.4. Borated sprockets (45 steel) Left: putty on the mounting face after washing. Right: the mounting hole is brought to the assigned dimension using a T15K6 cutting tool.

The borated layer exhibits a high hardness. Hardness depends on the borating temperature and chemical analysis of steel. For different steels and given different borating regimes hardness of the boride FeB is within 15700 to 19600 MPa and that of Fe_2B is within 12750 to 14700 MPa.

Adhesion of the borated layer to the base metal is not inferior to that of the carburized layer.

The surface roughness changes insignificantly after borating: usually it is one class lower than the original surface. The surface may be finished using diamond pastes and tools.

Changes in dimensions of tools and machine parts after borating are determined by heating and cooling conditions and chemical analysis of steel. In the case of borating combined with quenching heating changes in dimensions of parts are due to simultaneous action of various factors and comprise increments in dimensions resulting from formation of the boride layer and volume changes associated with formation of retained austenite and martensite. Surface layers change when the iron lattice is transformed into the boride lattice, a factor which contributes most to changes in linear dimensions of parts. Given the same conditions of borating, the increase in dimensions for every steel grade is constant and depends directly on the boride layer thickness. Therefore it can be allowed for in the dimensions of parts to be borated (Table 2):

$$\Delta L = KX ,$$

where ΔL is the increase in linear dimensions;
X the layer thickness;
K the constant.

For different grades of steel the constant K has the following values:

Steel grade	K			
	1073 K	1123 K	1173 K	1223 K
45	–	0.13	0.16	0.16
U8A	0.32	0.20	–	0.19
5ChNM	–	0.18	–	–
ChVG	–	0.26	–	0.25
3Ch2V8	0.28	0.27	–	0.20

Table 2

Finally finished parts should be subjected to borating considering an increase in dimensions by 15–30 μm per 100 μm of the layer thickness.

Wear Resistance of Steels Borated in a Calcium Chloride Melt

Abrasive wear

Borated steels 40, U8A and 5ChNM were tested. Samples of the same steels, which were subjected to a usual quench-hardening, were studied simultaneously. As compared to the quench-hardened samples, the wear was 2,6 and 2.5 times as low in the case of steel grades 40, U8A and 5ChNM respectively.

Results of Industrial Tests of Borated Tools and Machine Parts

Table 3

Borated parts	Steel grade	Results
1	2	3
1. Mold plates of lime-sand brick machines	Carburized, 20 [C1020]	Resistance increased by 3 to 5.7 times. Number of bricks produced: 504000 to 940000 pcs using borated plates; 165000 pcs using non-borated plates
2. Dies and punches of bending, drawing and forming press tools	U8A [W1-0,8C Special]	Resistance of press tools increased by 4 to 10 times. Quality of the products improved thanks to absence of scores, scratches and overpeening
3. Punch	U8A [W1-0,8C Special]	136700 can lids of stainless steel were stamped (40000 pcs using chromized punch). Resistance of the punch increased by 3.5

1	2	3
		times. Stainless steel does not stick to the punch
4. Guides and axles of forging machines (AVCh-25; 40; 63). Chain shafts of 0-50 tf drawbench	40Ch [5140]	Resistance of guides, axles and chain shafts increased by 2.2, 3 and 2.5 times respectively
5. Dies of drawing and bending press tools	U8A [W1-0,8 Special]	Resistance increased by 3 to 7 times when drawing stainless-steel parts. The labour productivity is 5 times as high owing to a lower sticking
6. Press tools for hot working	3Ch2V8 [21] 5ChNM	Resistance increased by 2.5 times
7. Parts working under abrasive wear in the manufacture of electrodes of alkaline batteries	U8A	Resistance increased by 10 times
8. Thread guides textile manufacture	St 3	Resistance increased by 3 times. Fluffiness of threads is decreased

1	2	3
9. Threading rolls for cutting thread 18x4-8c	ChI2FI [D2]	Quench-hardened rolls last 500-800 cuttings; borated rolls last 2900-3600 cuttings. Resistance increased by 4.5 to 7.1 times
10. Dies for hot heading of socket wrenches	5ChNM	Resistance increased by 2.2 to 3 times
11. Injection moulds	5ChNM 3Ch2V8 [H21]	Resistance increased by up to 3.5 times owing to nonsolubility of borides in aluminium melt

REFERENCES

1. L.S. Lyakhovich, L.G. Voroshnin. Borating of Steel. M.: Metallurgiya, 1967. 120 p.
2. L.G. Voroshnin, L.S. Lyakhovich. Borating of Steel. M.: Metallurgiya, 1978. 239 p.
3. V.P. Glukhov. Boride Coatings on Iron and Steels. Kiev: Nauk. Dumka, 1970. 208 p.
4. L.G. Voroshnin. Berating of Industrial Steels and Irons: Handbook. Minsk: Beards, 1981. 205 p.
5. N.S. Gorbunov. Diffusion Coatings on Iron and Steel. M.: Izd-vo AN SSSR, 1958. 208 p.
6. A.N. Minkevich. Thermochemical Treatment of Metals and Alloys. M.: Mashinostroeniye, 1965. 492 p.
7. L.S. Lyakhovich, L.G. Voroshnin, G.G. Panich, E.D. Scherbakov. Multicomponent Diffusion Coatings. Minsk: Nauka i Tekhnika, 1974. 288 p.
8. Thermochemical Treatment of Metals and Alloys: Handbook. Ed. L.S. Lyakhovich. M.: Metallurgiya, 1981. 424 p.
9. Cert.Authorship 393373, USSR, MKI C 23 C 9/10. A Method for Thermochemical Treatment of Metals /N.G. Ilyuschenko et al./ Filed 2.07.71. Publ. 10.08.73, Bull. Inv. No.33.
10. Cert.Authorship 533671, USSR. MKI C 23 C 9/10. A Borating Melt /N.G. Ilyuschenko et al./ Filed 7.05.73. Publ. 30.10. 76, Bull. Inv. No.40.
11. Cert.Authorship 779438, USSR. MKI C 23 C 9/10. A Melt for Borating of Steel Parts /G.I. Belyayeva et al./ Filed 5.12. 78. Publ. 15.11.80, Bull. Inv. No.42.
12. E.A. Smolnikov, L.M. Sarmanova. Borating of Tools in Electrode Baths./ Metalloved. i termicheskaya obrabotka metallov. 1984, No.3, p.p. 8-10.
13. E.A. Smolnikov, L.M. Sarmanova. Borating of Steel in Composition-Efficient Salt Melts./ Metalloved. i termicheskaya obrabotka metallov. 1987, No.1, p.p. 41-45.
14. Cert.Authorship 996515, USSR. MKI C 23 C. A Method for Borating of Steel Products /E.A. Smolnikov et al./ Filed 20.02.81. Publ. 15.02.83, Bull. Inv. No.6.

15. Cert.Authorship 1206335, USSR. MKI C 23 C 9/10. A Method of Preparing an Electrode Bath for Nonelectrolysis Borating /E.A. Smolnikov et al./ Filed 24.12.82. Publ. 23.01.86, Bull. Inv. No.3.
16. Patent 3326863 (ZO,TH), C 23 C 9/10. Salzbad zur Stromloßen erzeugung verschleißfester Boridschichten /H.H. Beyer, U. Baudis, P. Biberbach, W. Weber/ Filed 26.07.83. Publ. 7.02. 85.
17. Concise Handbook of Chemistry. Kiev: Naukova Dumka, 1987.
18. Properties of Inorganic Materials. Handbook. p.3206. L.: Khimiya, 1983.
19. Quench-hardening of Structural Steels in Chloride-Based Cooling Media./ Metalloved. i termoobrabotka metallov, No.9, 1989.
20. G.T. Boleko, A.O. Bannykh, N.I. Kobasko. A Comparison Assessment of the Effectiveness of Water-Based Cooling Media./ Metalloved. i termicheskaya obrabotka, No.10, 1986.
21. Noxious Substances in Industry. v.3, Khimiya, 1987.
22. Patent 2004617 (RU), C 23 C 8/42. A Method for Thermochemical Treatment of Steel Products /Ya.B. Chernov, A.I. Anfinogenov, N.G. Ilyuschenko/ Priority dated 15.06.92.
23. Nachslagewerk "Stahlschlussel", 5.auflage. Verlag "Stahlschlussel", Marbach a/n Bundesrepublik Deutschland, 1960.
24. Handbook of steel grades. M.: Gosudarstvennoe nauchno-tekhnicheskoe isdatelstvo literatury po tsuernoi metallurgii, 1963.

Project Title: Development and Production of Advanced Cutters for Super Alloys.
Principal Investigator: Igor Petrusha
Bakal Institute for Superhard Materials
Kiev, Ukraine
AM-7671

CLAUSE 1 - STATEMENT OF WORK

Background:

The lifetime of cutters presently used for machining super alloys is limited because of the severe tribo-chemical interactions that occur between the tools and work pieces. The Contractor shall utilize their unique experience in developing new Cubic-Boron-Nitride (C-BN) tool materials and manufacturing tools to produce advanced cutters for Ni-based super alloys. This effort is a nonprofit research and development project.

Tasks:

The Contractor shall:

1. Investigate the interaction of C-BN based cutters with Ni-based super alloys at high cutting speeds and feeds. The mechanical properties that are to be evaluated include hardness, fracture toughness and diametric compression strength of the materials. The variation in wear resistance of the cutting tools with cutting tool material and cutting conditions shall also evaluated in machining KhN77TYuR cast alloy of hardness 3.86 GPa HV (the alloy composition being Ni-73.2, Cr-22.15, Si-0.34, Fe-2.03, Mo-1.05, Al-0.18, Ti-0.35, W-0.2%) and PG-10N01 powder gas-thermal coating having a hardness off 55-62 HRC (the composition being Ni-70, Cr-40 to 20, B-2.8 to 3.4, Si-4 to 4.5, Fe-4 to 4.5%). Provide a report that summarizes the evaluation of the microstructure and mechanical properties, and the variation in wear resistance of the cutter materials.

2. Provide ten (10) sample cutters made of the cutting materials demonstrating the lowest wear rate as identified in Task 1. Final dimensions and geometry of the cutters shall be agreed upon by the Contractor and Sandia within eight (8) month of Contract execution.

A final report detailing the results and conclusions of this project shall be provided.

REPORT AT TASK 1 OF THE CONTRACT AM - 7672

1. INTRODUCTION.

The development of a semiconductor engineering puts forward demand to devices, wich can work with the pulses different polarity. Such devices are necessary for the absorption energy switching pulses with the purpose of the stabilization voltage and protection apparatus and elements of circuits. It demand of creation nonlinear resistors with symmetric current-voltage characteristic and large disperse of the power.

Such nonlinear elements with symmetric characteristics name varistors. They permit to create the schemes of stabilization voltage, limitation of currents, switching, memory, protection from overvoltage, spare suppretion on contacts, multiplication of frequency, circuit of peak and frequent modulation of signals, circuit control electroluminescent indicator and liquid crystal displays and etc.

Main cause of a spoilage of a existing varistors on the basis traditional materials (carbides, oxides) is electrical break-down. Electrical break-down under the action of electrical fields and temperature. Electrical break-down result to unreversibility growth electrical conductivity and decrease threshold voltage. "Degradation" varistors take place. "Degradation" and electrical break-down are connected with drift impurity and defects, i.e. to ionic conductivity in intercrystalline transition. There is destruction of surface states forming potential barriers.

Main causes of these processes are the high mobility of ions in oxides and high temperature, which the canals in the substance at electrical break-down has. Besides, this large gradient temperature between the canal discharge and varistor materials can make destruction them [1].

These factors force to conduct searches new materials with best characteristics for the manufacturing varistors.

2. SUBSTANTATION OF CONDITIONS OF CHOICE OF DIAMOND MATERIALS AS WORKING SUBSTANCE OF VARISTORS.

Achievement in the field of synthesis and processing of diamond materials at high pressure and temperatures, and as well the development of synthesis diamond films from a gas phase. we consider, open a way to a diamond in electronics and in power electronics in particular.

PHYSICAL PROPERTIES OF A DIAMOND [2]. The diamond is a material with covalence bonds. In it there are not ions. Hence, there is not ionic conductivity. It also has unique set of physical properties: high thermal conductivity (higher than at copper), high thermal stability, high electrical strength. low factor diffusion of impurity, resistance to aggressive environments (does not interact with water solutions of acids, salts, alkalies), high radiating stability, which surpasses in 10 - 100 time stability than silicon [3]. Besides the diamond is accessible to various technological effects and processes. Natural single crystals diamond at high voltage already have in itself nonlinear current-voltage characteristics [3]. Besides during synthesis of a artificial diamond it is possible to operate value of its specific resistance in very wide limits (from units Ω·cm up to 10^{14} Ω·cm) [4]. Thus, the diamond is a material, which should give attention with the purpose of development on its basis of effective varistors.

CHOICE OF DIAMOND MATERIALS FOR VARISTORS. Natural diamonds for electronics not adaptable to streamlined production. Their physical properties including electrical have large spread. Therefore we have payd our attention to synthetic diamonds.

At present they receive the synthetic diamonds from a graphite [5] and from hydrocarbons [6]. Recently they are very intensive investigating processes of synthesis diamond films from a gas phase at low pressure [7]. At manufacturing of synthetic diamonds will be formed mainly small-sized crystals.

For needs processing and mountain industry diamond industry arrange with technologies baking of a diamond small-sized crystals in compacts of the

various sizes and forms. They also use diamond ceramic in electronics to takeaway a heat[4] .

Our analysis of data [4,8] on processes baking of diamond materials conditions baking under determined has shown, that at baking small-sized crystals join with one another intercrystalline borders is also diamond material. Specific resistance of diamond compacts equally about 10^{14} Ω·cm at temperature of the baking to 1400 C and pressure 5,5 GPa. With increase of temperature of a baking the resistance of compacts decreases.

The thermal conductivity of diamond compacts below, than it is in single crystals of natural diamonds. But thermal conductivity compacts is higher yet than at copper. High thermal conductivity of a diamond promotes fast disperse of a warm from a canal electrical break-down to a volume of a device. It protects a device from destruction. Our researches (unpublished) of a destructions of a diamond at pulsing laser have showed, thatdiamond materials have high mechanical strength.

3. RESEARCH OF THE VARISTOR EFFECT IN DIAMOND MATERIALS.

As diamond has many unque electronic properties, we have beran to study possibilities of application of diamond materials in electronics, eletrotechnic calculation technic and automatic [9].

RESEARCHED SAMPLES. We investigate natural single crystals of a diamond, natural diamond powders with the size of a grain from 1 up to 57μm, synthetic diamonds, made at high pressure and temperatures without introduction of impurity and with additives doping elements B, Zr, N, P, As, Al. The synthetic diamonds were investigated two types: made from graphite with metals solvent Ni, Co, Fe, Cr, Mn [10] and from hydrocarbons (naphthalene) without metals solvent [11]. Research of the varistor effect in synthetic diamond films, made from a gas phase at low pressure is begun in our laboratory.

METHODS OF RESEARCH. We in this work used X-ray diffruction research of perfection and structure of diamond materials. For determination electronic imperfection, which have brokend carbon bonds, we apply a electronic spin resonance (ESR). The electrical characteristics of diamond materials are investigated in a wide interval of voltage (from 0 up to 6 kV). For standardization of received results during study samples are placed in vacuum.

In work by us were investigated initial diamond crystal powders and diamond compacts, baking from these initial materials.

4. RESULTS OF EXPERIMENTAL RESEARCHES.

NATURAL DIAMOND POWDERS. By us are investigated diamond powders with the size of a grain 1μm, 8μm, 34 μm, 57 μm.

These powders were studied by a method ESR [12,13]. Diamond powders received by a split of natural diamond crystals. At splitting will be formed predominary small plate with planes (111) or (123). On these planes there are broken carbon bonds on the surface atoms. Electrons on such bonds cause resonant absorption of microwave-field quantums. The intensity of this absorption has allowed to determine surface density of broken off bonds. It is equal about 10^{14} bond/cm^2. These broken off carbon bonds at baking of the compacts can probablly influence on formation of their electrical characteristics.

For study of stages of compacting was taken natural diamond powder with the size of a grain 20 μm. In a initial powder is recorded ESR a spectrum from broken off bonds on a surface of small-sized crystals. X-ray diffruction spectrums recorded on X-ray apparatus with Cu-tube. All lines of a diamond with the good spliting copper doublet are received. The second stage - cold compress of the diamond powder at general pressure 8 - 9 GPa. ESR research have shown, that the number paramagnetic centres (broken off bonds) has decreased. X-ray data specify on that the size of particles has not changed at this stage, and number of defects was increased, which have arisen

in small-sized crystals as a result of plastic deformation. The electrical measurements have shown sharp fall of resistivity of diamonds compacts after baking. It is pursuant to work [4], where is established, that at baking of diamond powders at temperatures higher 1500 C resistivity up to units Ω·cm see drops with 10^{14} Ω·cm. The authors explain this process with graphitization of the diamond particles. However our discovery of formation of electronic properties of a diamond with extended structural defects (review is contained in the report on contract N7680) permits us to assert following. At baking of diamond particles higher 1500 C plastic deformation form extensive dislocation system, which is the reason of high conductivity compacts. This process opens new possibility of control with electrical parameters compacts without the introduction of impurity. The similar results are received at baking of diamond crystal powders of synthetic diamond, received from a graphite at high temperatures and pressure [4]. In this work is established(installed), that a maximum of density compacts at pressure 5,5 GPa receive at temperature baking about 1400 C. High structural quality of diamond compacts receive from of diamond crystal powders with size of a grain 5-7μm [8].

We have cerried other group of experience with use of synthetic diamonds, made from hydrocarbons without metals solvent [11].

To features of these synthetic diamonds concern following: Small-sized crystals are free from metals solvent, but contain as a impurity a hydrogen. First condition provides clealiness of diamond particles from magnetic conducting components, second condition, containing hydrogen, should result to reduction of number of broken carbon bonds.

X-ray research of this group of diamonds and compacts from them have shown, that the processes of the compacting cause the same structural features, that are observed at compacting of natural and synthetic diamonds, made from graphite at high pressure and temperatures.

The ESR-researches have shown the smaller contents of paramagnetic centres, connected with surface or structural defects, possessing broken off

carbon bonds. The latter has found reflection in electrical properties of this group of diamonds and compacts from them.

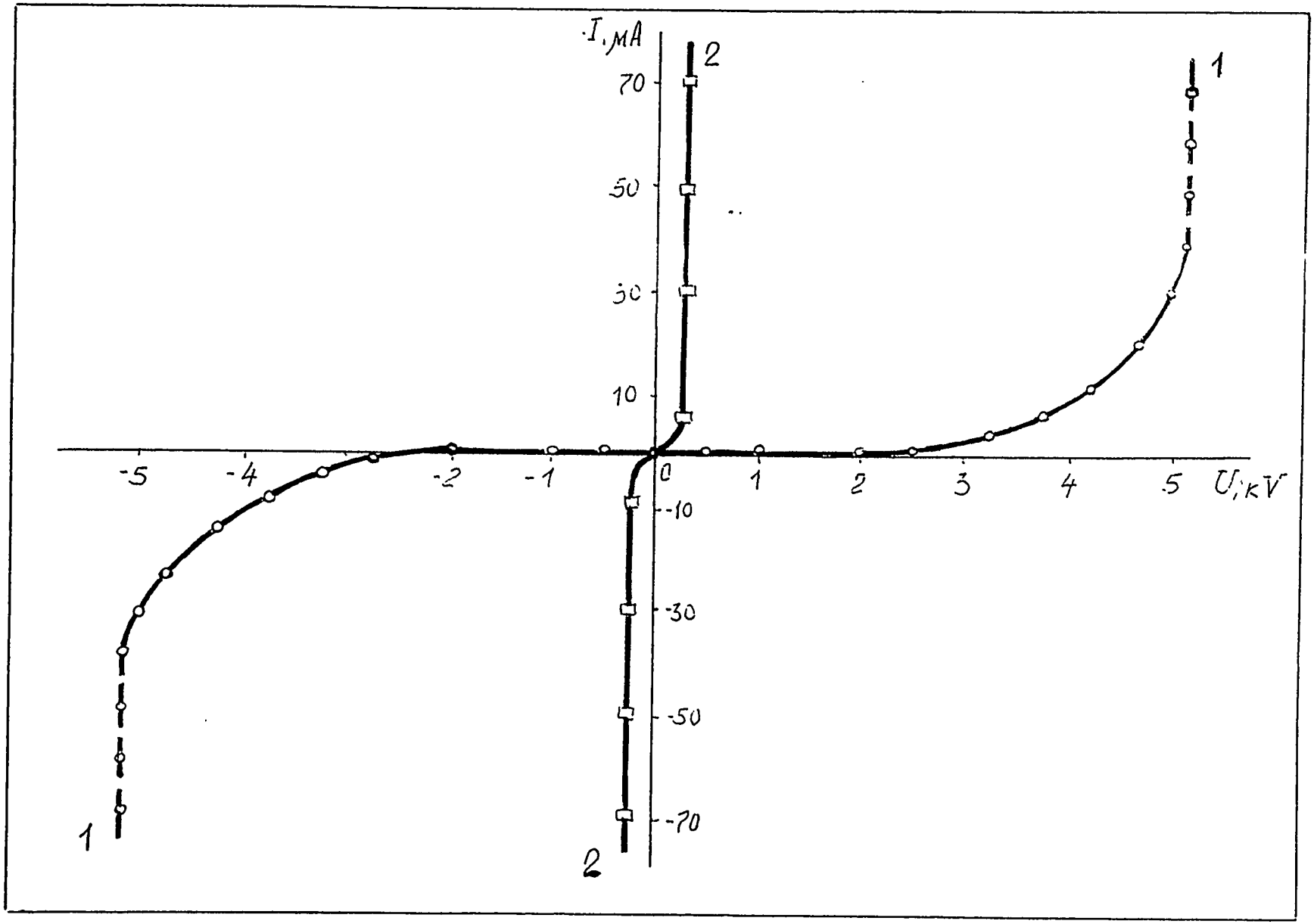
Compacts, made on the basis of diamonds from hydrocarbon at p=8 - 9 GPa and t = 1500 C have large resistance (> 10^{10} Ω·cm). Current-voltage characteristics, measured in wide interval voltage, have shown their symmetry depending on polarity of a voltage and display nonlinearity at voltage more than 1000 B.

For experience compacts were produced with a diameter of 3mm and height 1,5 - 2 mm. The surface these compacts after baking was cleared from a graphite with boiling till 6 hours in $HClO_4$. Technology of drawing of electrical contacts on face of a surface samples is fulfilled by us: them served aquadag, silver paste, conducting glues on the basis Ni, cover from Ti and Ni, put magnetron spattering.

At of research of dependence of a current from a voltage of a electrical field in compacts by us we were established, that borders of section a diamond - metal is very weak depend on electrical fields, and nonlinear electrical characteristics a material diamond compacts has.

Besides, we were investigated processes of electrical break-down. In our experiments was established, that after each electrical break-down the electrical characteristics are restored. So after five-divisible electrical break-down the residual voltage (electrical break-down) remained within the limits of 84 % (2700 - 3000 B).

With the purpose of management of voltage opening of varistors during synthesis diamond powders and them baking are received compacts with specific resistance from 10^2 up to 10^{14} Ω. From current-voltage of the characteristics is established, that the current is proportional U^{β}, where β - degree of nonlinearity. We receive a factor of nonlinearity from 1 up to 80. So, for a current 2 mA is received β = 25, and classification voltage 50 V. On Fig. 1 are submitted current-voltage of the characteristic high-resistance compacts (1) and low-resistance compacts (2).


I, мА
70
50
30
10
-10
-30
-50
-70
-5
-4
-2
-1
0
1
2
3
4
5
U, kV
1
2
1
2

5. CONCLUSION.

Our researches of electronic properties of a diamond, discovery of gears of formation of its electronic properties permit to assert, that the diamond can become a perspective material of a electronic engineering. Thus can be used as natural diamonds and diamond powders, as synthetic diamonds, made at high temperatures and large pressure.

On the basis above stated at a given stage it is possible to make following conclusions:

1. To use in electronics of small-sized natural and synthetic diamonds it is necessary to apply them compacting at high temperatures (up to 1400 C) and large pressure (5,5 GPa).
2. Diamond compacts have nonlinear symmetric current-voltage the characteristics.
3. The specific resistance compacts can be operated over a wide range (from 10^{14} Ω·cm up to units Ω·cm).
4. Large factors of nonlinearity b permit to create on the basis diamond compacts varistors with the various characteristics.
5. The electronic devices created on the basis diamond compacts can dissipate in 10 - 100 time large power, than other conventional materials. It will allow to reduce dimensions and weight of devices.
6. Electronic devices, created on basis diamond compacts will have greater radiating stability, as the diamond is subject radiation destraction in 10 - 100 time less, than other materials electronic of a engineering.
7. Diamond compacts as well as diamond do not interact with chemical agresive environments (acids, alcalies, salts).
8. It is possible to believe, what expediently to expand the program of researches on use diamond materials in electronics, electrotechnics, automatics, computer technics.

LITERATURE

1. Kh.S.Valeyev, V.B.Kvaskov. Nonlineal metalloxyde semiconductors. Energoatomizdat. Moscow (Russian), (1983), 159 p.

2. The Properties of Diamond. Ed. S.E.Field.- London etc.: Acad.press. (1979).

3. Diamond in electronic technics. Moscow, Energoatomizdat, (1990), 248p.

4. N.V.Novikov, D.V.Fedoseyev, A.A.Shulzenko et.al. - Synthesis of diamonds. Naukova dumka. Kiev(Russian), (1987), 159 p.

5. F.P.Bundy. Diamond synthesis and behavior of carbon at very high pressure and temperatures. - Ann. Acad. J. Sci., 105, N 17, (1964), pp.951 - -982.

6. E.N.Yakovlev, O.A.Voronov, A.V.Rachmanina. Synthesis of the diamonds from hydrocarbons. - Sverchtverdiye materiali, N 4, (Russia), (1984), pp.8 - - 11.

7. B.V.Spitsyn. Chemical crystalisation of the diamond. Doctor of Science Dissertation. Moscow, (1993), 53 p.

8. B.I.Resnic. Forming of the structure and properties of the dielectric diamond ceramic on the base of the aggregate powders. Doctor of Philosophy Dissertation, Odessa, (1991), 173 p.

9. Report on the contract AM - 7680.

10. N.D.Samsonenko, V.G.Chulga, Yu.A.Litvin. Electron paramagnetic resonance on the defects with nonimpurity character in diamonds.- Synthetisheskiye almazi N 3, (1970), pp.22-26.

11. N.D.Samsonenko, V.V.Tokiy, S.V.Gorban, I.V.Selskaya. EPR- and X-ray diagnostic in the technology of the make compacts on base of the nature and synthetic diamonds. Abstracts. Vsesoyusnaya konferencia "Perspectives of the application of the diamonds in electronics and electron technic", Moscow, Energoatomizdat, (1991), pp.70 -71.

12. N.D.Samsonenko, E.V.Sobolev. Electron paramagnetic resonance stipulated diamond surface. - Pis'ma Zh.Eksp.Teor.Fiz.,5, (1967), pp.304 - 307.

13. N.D.Samsonenko, G.V.Zhmychov, V.Sh.Zon et.al. Characteristic features of the electron paramagnetic resonance centers of diamond. - Zhurnal Strukturnoi Khimii, 20, (1979),pp.1116 - 1118.

Project Title: Investigation of the Electronic Properties and Varistor Effect of Novel Diamond Compacts.
Principal Investigator: Nikolaie Samsonenko
Dunbass Civil Engineering Institute
Makeveka, Ukraine
AM-7672

CLAUSE 1 - STATEMENT OF WORK

Background:

The Dunbass Civil Engineering Institute has developed novel processes for manufacturing diamond based varistor devices. The properties of the diamond used in varistors depends on the doping and microstructural defects generated in the diamond material during processing. Varistors based on diamond materials may be used for voltage/surge protection and may continue to operate after several voltage surges.

This project is nonprofit research and development effort between Sandia and the Dunbass Civil Engineering Institute.

Tasks:

The Contractor shall:

1. Without revealing any proprietary data (know-how), prepare and deliver a report outlining the generated aspects of how the Contractor manufactures diamond-based varistor materials. The report shall also summarize results collected to date on the electronic properties of the diamond-based materials.

Six samples of existing small varistors and large varistors shall be supplied. The Contractor and Sandia shall mutually determine the type of samples that shall be provided, within one-month after date of Contract.

2. Study, by means of x-ray diffraction and electronic paramagnetic resonance, the defect structure of diamond compacts. Defect characterization shall include:
grain size determination and
electronic and varistor properties.
Provide a brief report (10 pgs. or less) detailing the results of the investigation as described above.

3. Measure the influence of doping of the I-V characteristics of diamond-based varistors. Develop working ohmic contacts for the varistor samples and provide 20 samples, with working ohmic contacts, to Sandia. The dimensions of

the samples shall be mutually determined within eight months after Contract execution.

Provide a final report that summarizes the experimental results and provides conclusions on the work performed.

Project Title: The Use of a Unique Super-heated Steam Treatment for the Enhancement of the Tribological Properties of Ferrous and Non-ferrous Alloys.
Principal Investigator: H. P. Vyatkin
Chelyabinsk Polytechnic Institute
Chelyabinsk, Russia
AM-7673

CLAUSE 1 - STATEMENT OF WORK

Tasks:

The Contractor shall:

1. Provide a report that describes:
the general design and operation of the super-heated steam treatment
previous work performed by the Contractor on the characterization of the tribological and corrosion properties of super-heated steam treated ferrous and non-ferrous alloys

2. The Contractor shall provide a report describing the experiments conducted, described as follows. Steam-treat and characterize plain-carbon and tool steel samples. (Sandia and the Contractor shall mutually determine the specific alloys to be treated within two months after Contract execution.) Experiments shall be carried out to identify the steam treatments that will optimize the wear resistance of the two alloys. The wear rate and friction coefficient of the alloys shall be measured. The microstructure of the best performing coatings on each alloy shall be characterized using X-ray diffraction and transmission electron microscopy.

The Contractor shall provide three samples of each of the two alloys, which shall be treated under conditions agreed upon by Sandia and the Contractor. The sample dimension will be approximately four(4) cm in diameter and between two(2) and five(5) mm thick.

3. A brass alloy shall be steam-treated and its tribological properties characterized. (Sandia and the Contractor shall agree on the brass alloy to be treated within 6 months of the beginning of the contract.) Experiments shall be carried out to identify the steam treatments that will optimize the wear resistance of the alloy. The same wear resistance, friction coefficient and microstructural measurements identified in Task 2 for steel alloys shall be applied to the steam-treated brass samples. Three samples of the same dimensions identified in Task 2 shall be supplied for the steam-treated brass alloy samples.

The Contractor shall provide a final report on the experimentation data and results for the entire project.

Chelyabinsk State University

REPORT

contract AM-7673 from October 10, 1994

"The use of a unique super-heated steam treatment for the enchancement of the tribological properties of ferrous and non-ferrous alloys"

(Task 1)

Principle Investigator H.P.VYATKIN

Chelyabinsk
1994

THE USE OF A UNIQUE SUPER-HEATED STEAM TREATMENT FOR ENHANCEMENT OF THE TRIBOLOGICAL PROPERTIES OF FERROUS AND NON-FERROUS ALLOJS

1. General statements of metal treatment by superheated water steam

One of the most important problems the science and technolody face is the corrosion and wear control of metal products. At present, the main way for solving the problem is the application of the protective coating by means of various techniques, particularly, by steam-thermal oxidation. The technique under consideration proved to be ecologically pure, harmless, quite simple for implementation, and, besides, no expensive materials are required.

The process of steel oxidation in water steam may be presented in terms of the following reaction [1]:

a) at the temperatures below 843 K;

$$3Fe + 4H_2O \rightarrow Fe_3O_4 + 4H_2,$$

b) at the temperatures above 843 K

$$Fe + H_2O \rightarrow FeO + H_2,$$
$$3FeO + H_2O \rightarrow Fe_3O_4 + H_2.$$

Since the process of high temperature oxidation is accompanied by the formation of solid products as a result of the reaction, it is influenced not only by the chemical reaction at the metal-oxide film phase boundary, but by the processes of solid-state diffusion and those of reagent transfer. Thus, oxidation of metals in superheated water steam proceeds through a series of successive stages [2,3]:

1. Reactions at phase boundaries:

a) molecule dissociation of non-metals along with chemisorption of the products formed;

b) incorporation of chemisorbed ions into the oxide lattice either directly or by combining with the metal ions released from the lattice;

c) transfer of metal ions from the metal or alloy phase into the oxide lattice;

d) reactions between the ions of non-metals and those of metals at the metal-oxide phase boundary.

2. Processes of crystal nuclei formation.

3. Diffusion of cations and ions induced by the gradient of the chemical potential or interdiffusion of the two in opposite directions through the oxide layer, taking place:

a) through the defects of the coating lattice:

b) through grain boundaries or pores.

The oxidation rate is determined by the slowest stage from those considered above.

In most cases the growth of oxide films follows either the linear law or the parabolic one. Thus, at the initial moment when the thickness of the oxide coating is small, and the rate of reagent diffusion is very high, these are the processes at the phase boundary (kinetic control) which are considered to be the limiting stage. The oxidation rate, in such a case, is detemined by the linear equation in the form of:

$$\frac{\Delta m}{S} = k_1 \tau,$$

where Δm - specimen mass change, S - specimen area, k_1 - oxidation rate constant, τ - time.

As the processes of oxidation and scaling proceed to form the scale of the proper thickness, it is the diffusion that becomes the limiting stage, the linear law gradual-ly going over into the parabolic one:

$$\left(\frac{\Delta m}{S}\right)^2 = k_2 \tau.$$

During the intermediate phase, oxidation proceeds under diffusion-kinetic control, the oxidation kinetics following the time law, accoding to Evans [7]:

$$\frac{\Delta m}{S}\frac{1}{k_1} + \left(\frac{\Delta m}{S}\right)^2 \frac{1}{k_2} = \tau.$$

While forming the gas-proof bubbles in the scale, the oxidation process, sometimes, may follow the logarithmic law [4]:

$$\frac{\Delta m}{S} = k_3 \lg \tau + k_4.$$

In the above equations determining the process of metal oxidation the constants of oxidation rates depend upon a great number of factors, namely, the initial state of the metal, the rate of the oxidation medium motion, the medium pressure, but, first of all, upon the temperature.

The temperature influence upon the metal oxidation process is diverse. On the one hand, the oxidation rate is determined either by the temperature dependence of the chemical reaction rate constant k_1 (under the kinetic control over the oxidation process) or that of the diffusion coefficient (under the diffusion control). On the other hand, the change of the oxidation temperature results in that of the

phase composition of the scale as well as the phase composition and structure of the metal being oxidized.

The phase composition of the scale on the iron surface is determined by the diagram of the iron-oxygen state [5], according to which two temperature ranges for iron oxidation are to be considered. At the temperatures above 843 K, the scale , to a great extent, consists of FeO, the thin external layer consisting of Fe_3O_4 and Fe_2O_3 .

As for mechanical defects such as cracks and bubbles, they are often observed in the oxide layers formed in air or oxygen, as opposite to the oxide layers formed in water steam [6]. The dense oxide film having no mechanical de-fects and attained in water steam prevents from further oxidation, change of the chemical composition as well as decarburation of the steel being oxidized.[8,9].

2. The implementation of treating the steel products by superheated water steam

Steam-thermal oxidation of specimens up to the temperature of 1273 K was carried out at the unit presented schematically in Fig. 1.

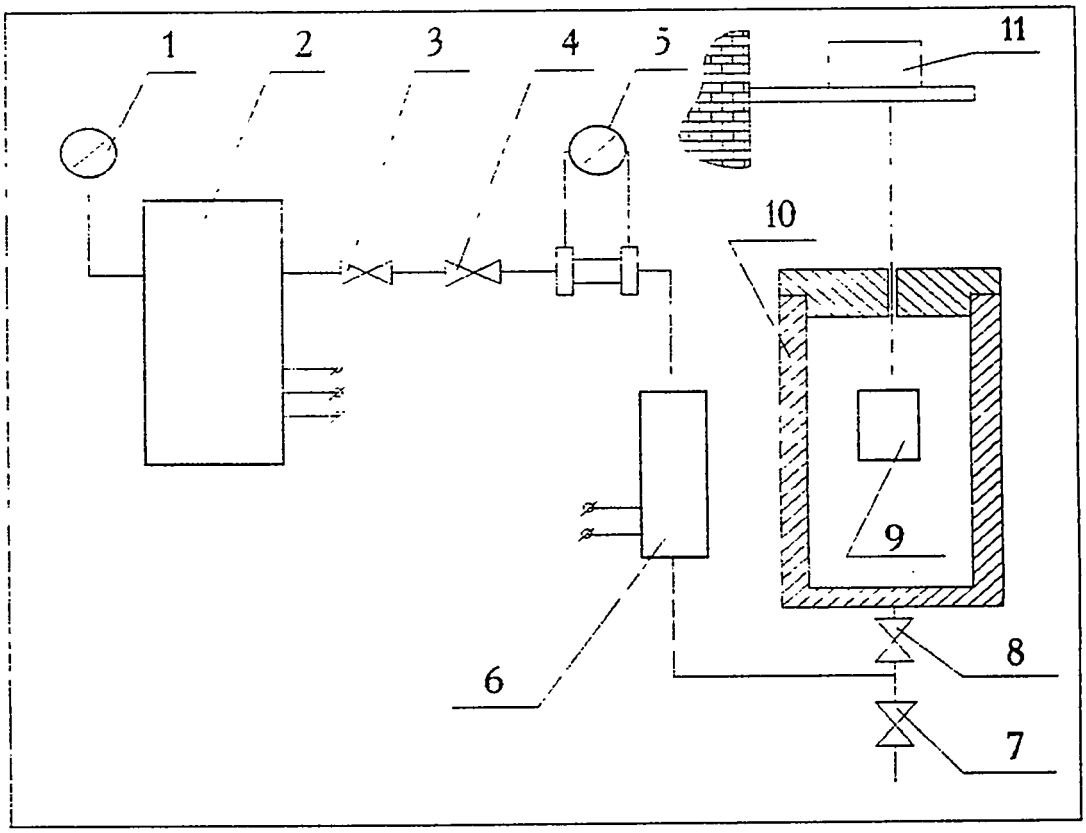


Fig.1. Experimental plant scheme

Water steam with the excessive pressure of $3.85 \cdot 10^5$ Pa superheated up to 383...393 K was obtained in the BK-75 autoclave (2). The steam flow rate was controlled by the throttle valve (4) in the range of $0...3,5 \cdot 10^{-3}$ kg/s. The calibrated plate and the differential manometer were used to measure the rate (5). The pressure in the autoclave was controlled and kept in preset ranges by the electric contact manometer (1).

From the autoclave steam entered the superheater (6) shaped like a stainless steel coil placed in a pipe electric furnace. The steam temperature at the superheater output was 773 K. It was controlled by a thermocouple. The additional steam heating up to the oxidation temperature was carried out in a stainless steel coil placed in a furnace.

The superheated steam was delivered from the bottom into the working space of the СШОЛ-1.1,6/12 furnace with the capacity of $2,5 \cdot 10^3$ W.

The preset temperature of the working space was kept with the accuracy of ±1,5 K. The measurements showed that the temperature difference along the height of the working space did not exceed ±3 K, the time for heating the specimen with the thickness of $3 \cdot 10^{-3}$ m up to 1073...1273 K was 30 s.

Fig 2 is a scheme of the technological process for steam-thermal oxidation.

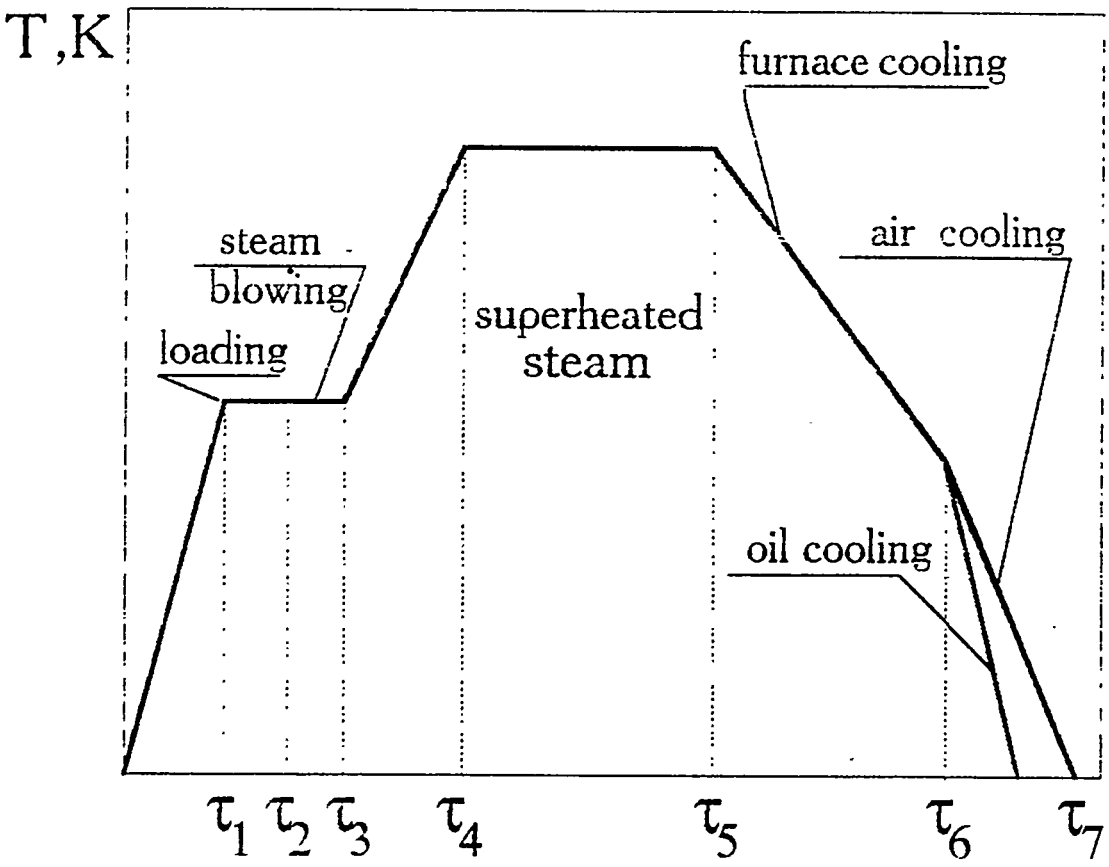


Fig.2. Diagram of steam-thermal oxidation technological process

where τ_1 - time of heating the furnace up to the temperature of product charge, τ_2 - time of soaking the products at the charge temperature without fee-ding water steam, τ_3 - time of soaking the products at the charge temperature with water steam blowing, τ_4 - time of heating the products up to the temperature of steam-thermal oxidation. τ_5 - time of soaking the products at the temperature of steam-thermal oxidation, τ_6 - time of cooling the products in other media.

All the specimens are degreased before oxidation.

3. The kinetics study of forming the oxide coating on carbon and tool steels

Table 1 presents the chemical composition and critical temperature points of the alloys studied.

Таблица 1.

Steel grade	Element contents, mass %										Critical points, K	
	C	Mn	Cr	W	Mo	V	Ni	Co	S	P	A_{C_1}	A_{C_3}
Ст.3	0,19	0.37	0,12	-	0,03	-	0,16	-	0,03	0,01	1003	1143
Ст.10	0.11	0.54	0.09	-	0.02	-	0.08	-	0.25	0.01	1003	1163
08кп	0.07	0.52	0.11	-	0.02	-	0.20	-	0.12	0,01	1003	1168
Р6М5	0,88	0.50	4.10	6,2	5,1	1,9	-	4.9	0.03	0,03	1113	1143

The critical points of polymorphial transformations in steels were found by the dilatometric technique with the rares of heating the specimens equal to those of oxidizing. The gravimetric technique was used to study the oxidation kinetics by means of continuous recording the increase in the mass of a specimen. The latter to be tested was placed on the platinum hanger in the furnace reaction space. The measurement results were processed on a computer. To the end of excluding the influence of the external mass transfer (the steam motion rate in the furnace reaction space) upon the oxidation kinetics, the critical state of the steam motion was determined experimentally, its maximum value being 0,2 m/s. The results were found to be in a good agreement with those obtained before [10], Fig.3. In the ex-periments to follow the steam motion rate in the furnace reaction space was kept far higher the critical one.

The kinetic dependences obtained through the studies of carbon steels are presented in Fig. 4,5,6. The results show that the initial stage of oxidation at all the oxidation temperatures follows the linear law

$$\frac{\Delta m}{S} = k_1 \tau,$$

where Δm - increase in the specimen mass, kg, S - area of the oxidized surface, m^2, k_1 - linear constant of the reaction rate, $kg \cdot m^{-2} \cdot s^{-1}$, τ - oxidation period, s.

Then, the oxidation law goes over into the power one:

$$(\Delta m / S)^n = k_2 \tau.$$

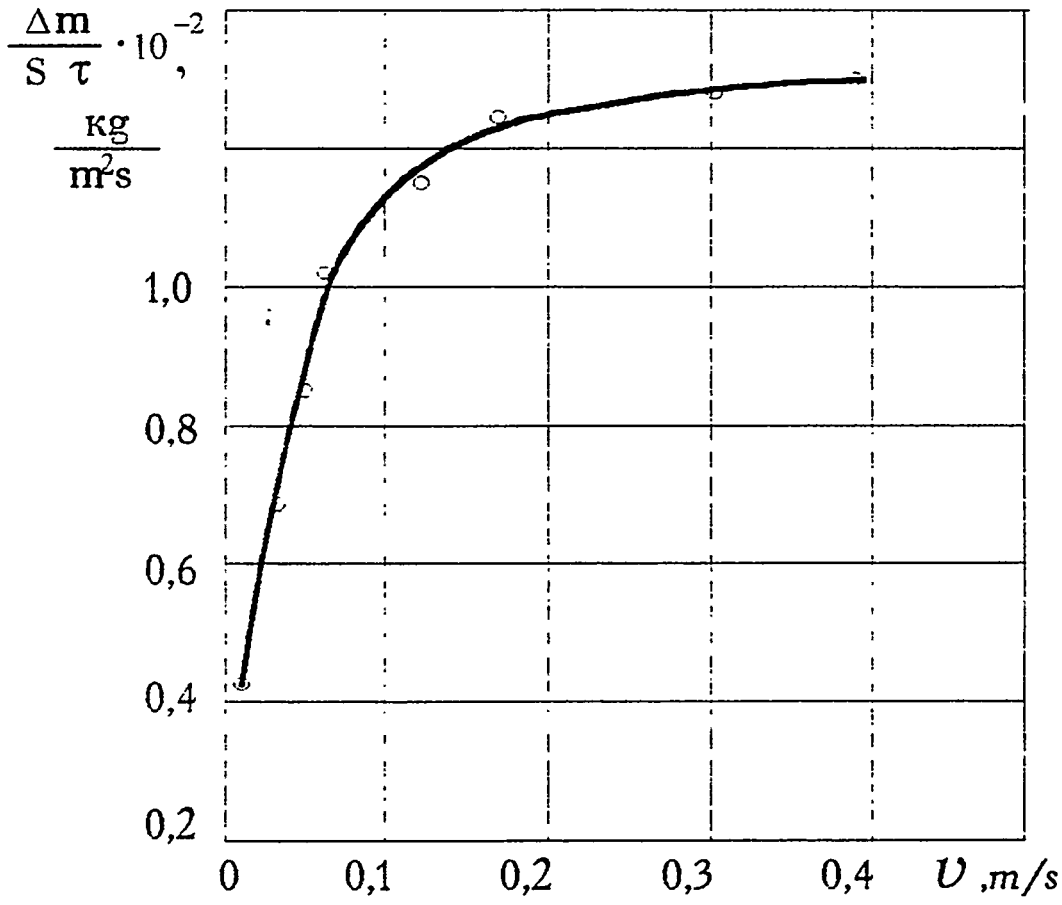


Fig.3. Steam rate influence upon carbon steel oxidation (T=1473 K, t=40 minutes)

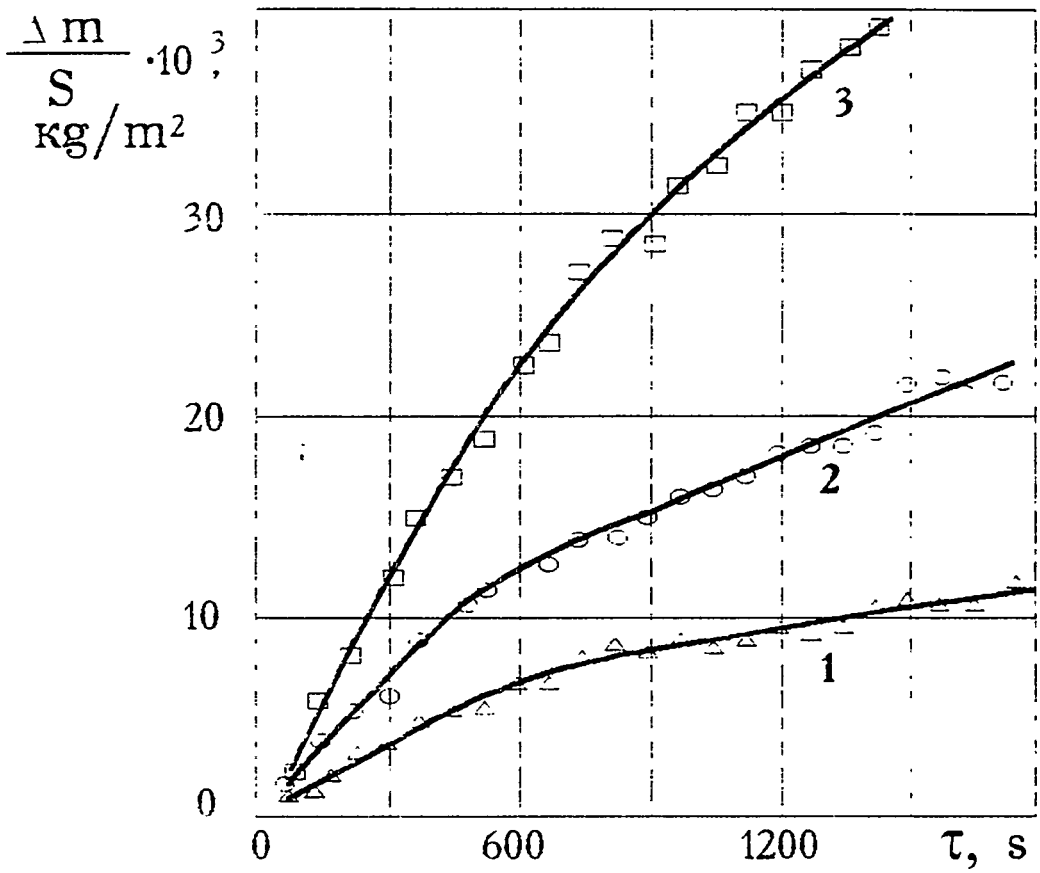


Fig. 4. Steel oxidation kinetics for the temperatures of 1.- 873 K, 2.- 973 K, 3.- 1073 K

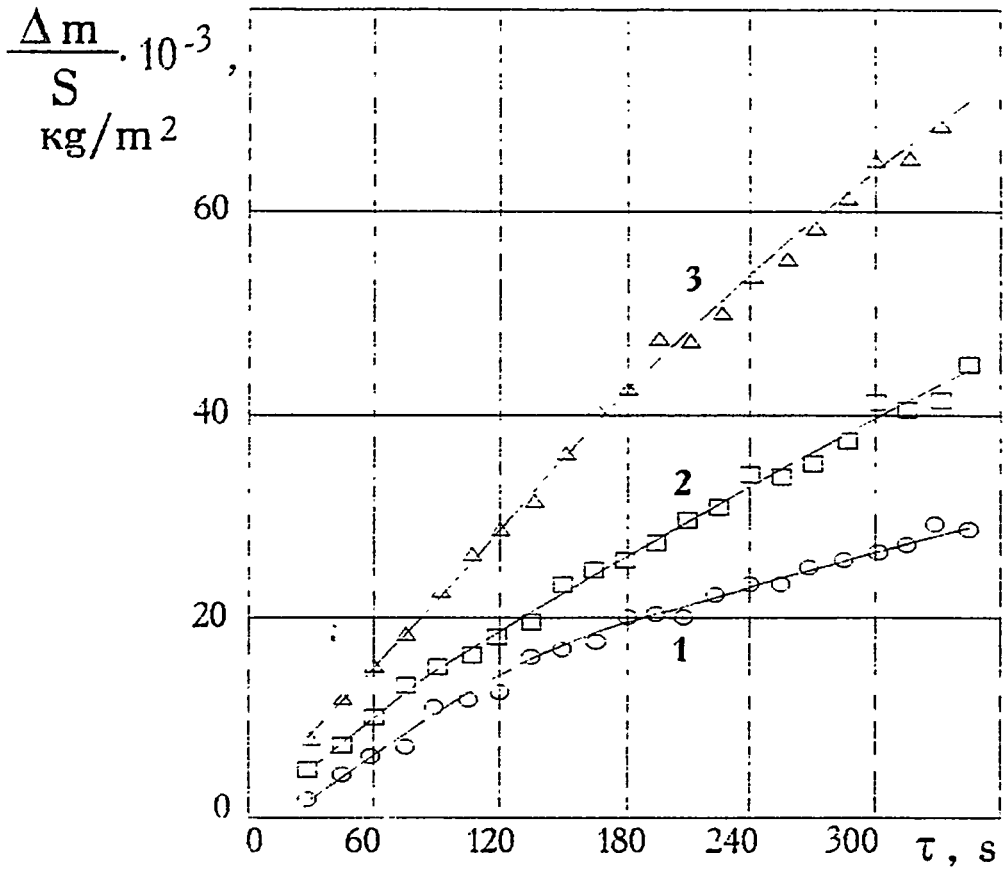


Fig.5. Steel oxidation kinetics for the temperatures of 1.- 1173 K, 2.- 1223 K, 3.- 1273 K

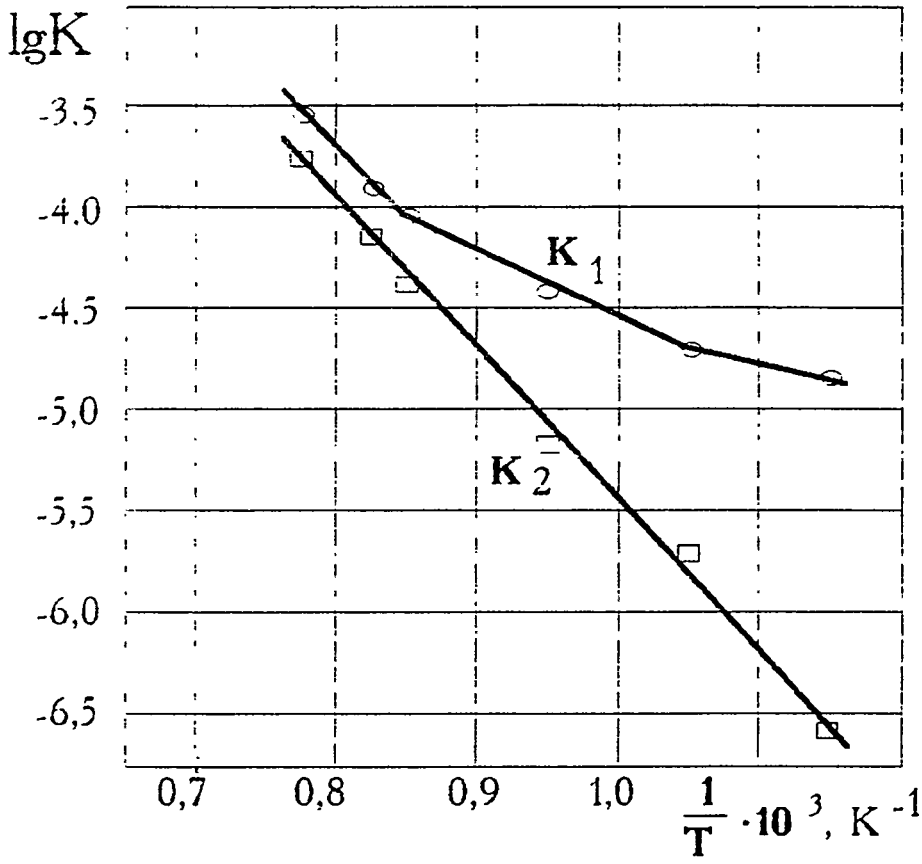


Fig.6. Oxidation rate constant temperature dependence
(K_1 -according to the linear law, K_2 - according to the power law)

Consider the initial oxidation stage. The linear nature indicates the formation of the porous coating, the porosity study (Fig. 7) confirming the fact. Now, the oxidation reaction rate [4] or, in other words, the transfer of iron ions into the oxide through the metal-oxide boundary (i.e., the processes taking place at the phase boundary) is stated to be the control stage.

The dependence of the linear constant of the reaction rate upon the temperature in the coordinates log k_1 – 1/T (Fig. 6) takes the form of the polygonal line, the oxidation abnormalities being observed at the temperatures of 1003 K as well as in the range of 1150 K The former corresponds to the initial stage of $\alpha \rightarrow \gamma$ transformation (point A_{C_1}), the latter to the final stage (point A_{C_3}).

The study of the P6M5 tool steel (Fig.8) revealed the comparable nature of the oxidation kinetics.

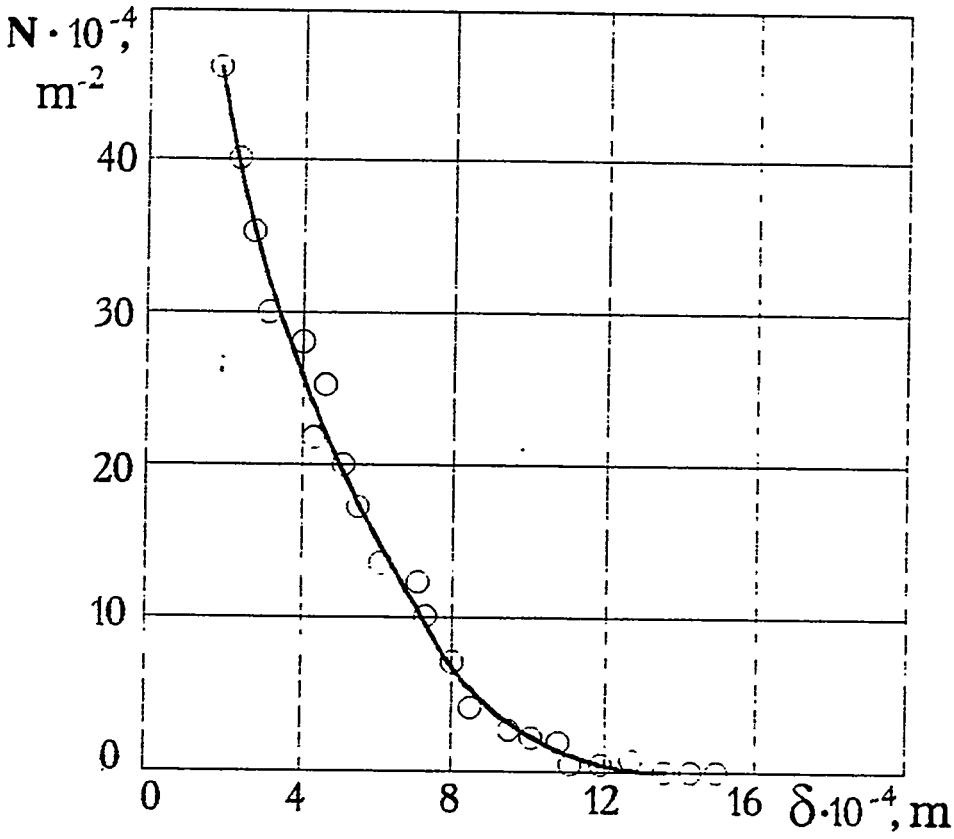


Fig. 7. Oxide coating porosity as a function of thickness

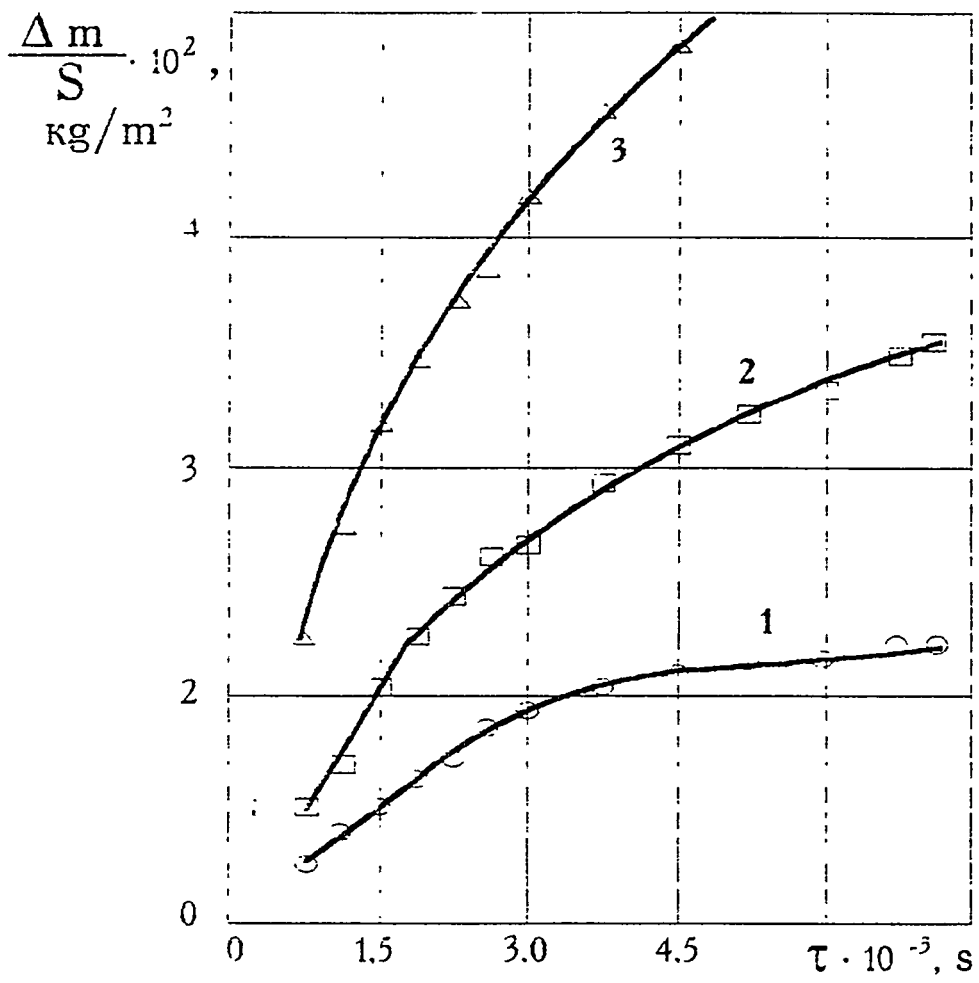


Fig.8. R6M5-Steel oxidation kinetics for the temperatures of 1.- 823 K, 2.- 873 K, 3.- 973 K

The analysis of the temperature dependence of the linear constant makes it possible to conclude that at the initial oxidation stage, that of formation of thin, porous films, the "metal-substrate" state as well as the oxide formation reaction are the most essential factors. In such a case, the oxidation process may be assumed to be limited by the transfer of iron ions from the lattice into the oxide through the "metal-scale" boundary as well as by the chemical reaction rate at the "scale-gas" boundary. Thus, speeding up the coating formation may be possible due to the change of the metal energy state.

The deformation or phase hardening of the metal before oxidation permit speeding up the coating formation at the cost of the decrease in the energy barrier in transferring the iron ions into the oxide through the "metal-scale" boundary [11]. The preliminary treatment mentioned above decreases the period of the oxidation initial stage and thereby the total period of oxidation.

Further oxidation of steel causes the linear law of oxidation to go over into the power one with the power index of $1<n<2$. Regardless of the oxidation temperature, the aforementioned takes place with the same specimen gain in weight per surface unit equal to $(14,2...18,0)\cdot10^{-3}$ kg/m^{-2} , which corresponds to the coating thickness of $(11...14)\cdot10^{-6}$ m.

The comparison of the data obtained with those on the coating porosity studies (Fig. 7) makes it possible to conclude that with the coating thickness of $(11...14)\cdot10^{-6}$ m the through pores in the coating are not observed.

Thus, the formation of the pore-free coating with the proper thickness makes the diffusion rate of the iron ions through the scale quite comparable with that of the processes at the phase boundary. The above mentioned results in the change of the oxidation law.

The dependence of the power constant k_2 of the reaction rate upon the temperature in the coordinate log k_2 - 1/T is linear and has no breaks. It may be expressed by the equation:

$$k_2 = A \cdot \exp\left(-\frac{E}{RT}\right) = 260 \cdot \exp\left(-\frac{151500}{RT}\right),$$

where A - pre-exponential multiplier, kg·m·s^{-1}, E - effective activation energy, J·mole^{-1}.

This means that in oxidizing steel in water steam following the power law the state of the metal being oxidized does not influence upon the process. The diffusion of the iron in the scale as well as the chemical reaction rate of the oxide formation may be considered to be the only limiting stages of oxidation, since the rate of the steam motion is found without taking into account any influence of the external mass transfer. In addition, since the processes of adsorption, dissociation and chemisorption proceed at the high rate.

Thus, the studies of the oxide coating formation kinetics made it possible to reveal the main mechanisms of this process. In addition, the dependences obtained enable to determine one of the main technological parameters of steel oxidation, namely, the treatment period for creating the coatings with high protective properties.

4. Influence of the steam-thermal oxidation conditions upon the corrosive resistance and tribological properties of steels

4.1. Carbon steel

The corrosive resistance of oxidized specimens was tested in main water at the temperature of 1073 K (that of maximum corrosion rate of iron in water). The change of the specimen mass per surface unit in 500 hours was assumed to be the corrosion index. In addition, electrochemical studies by means of a potentiostat were carried out. Now, the corrosion current was asssumed to be the index.

The relative corrosion rate was found on the basis of the study results. In the first case, it was the ratio of the increase in the oxidized specimen mass to that in the non-oxidized one, the second case being the ratio of the corrosion current of the oxidized specimen to that of the non-oxidized one.

The phase composition of the oxide coating was studied on the X-ray difractometer. The adhesive strength was determined by means of the ordinary breakaway. The decarburation depth was determined on the specimen cross-section by means of the microscope 'Epignost'.

The protective properties of the oxide coating are characterized by the corrosive resistance as well as the adhesion to the metal protected. Fig. 9 presents the dependence of the corrosion rate of the oxidized Ст.3-steel upon the temperature of the steam-termal treatment. Fig. 10 is the dependence of the adhesive strength of the oxide coating attained under the same conditions.

The analysis of the dependences presented indicates that the temperature range of 773...1273 K may be subdivided into the three ones: 773...Ac_1 (1003 K); Ac_1...Ac_3 (1143 K) and above Ac_3. The first one includes the common oxidation temperatures of 773...923 K at which the oxide coatings with the high protective properties are formed.The nature of the corrosive resistance transformation in this temperature range indicates that the emergence of FeO in the composition of the oxide coating doesn't result in decreasing its anticorrosive properties. As a result of steam thermal oxidation, FeO formed possesses high density and good adhesive properties.

With the further increase in the oxidation temperature, the corrosion rate increases significantly and achieves its maximum at 1073 K (the period of oxidation is above 5 min.). At the temperature of Ac_3 the corrosion rate tends to decrease achieving its minimum in the temperature range of 1273 K (the third temperature range).

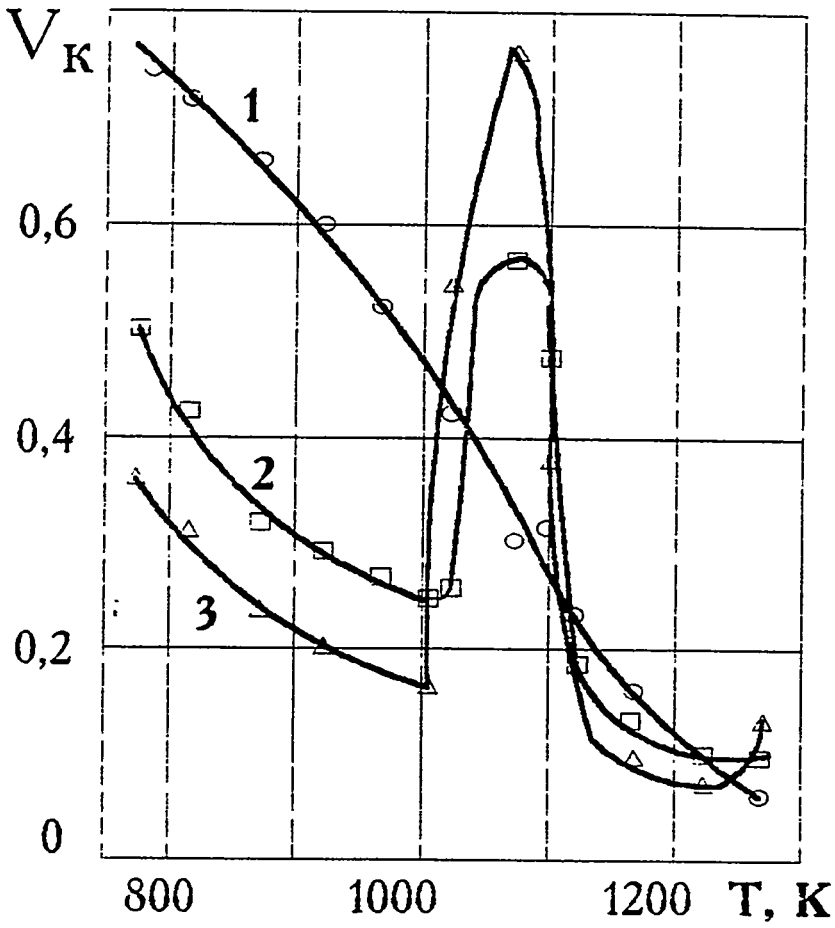


Fig. 9. Oxidation periods:
1. - 300 s, 2.- 600 s, 3.- 1200 s

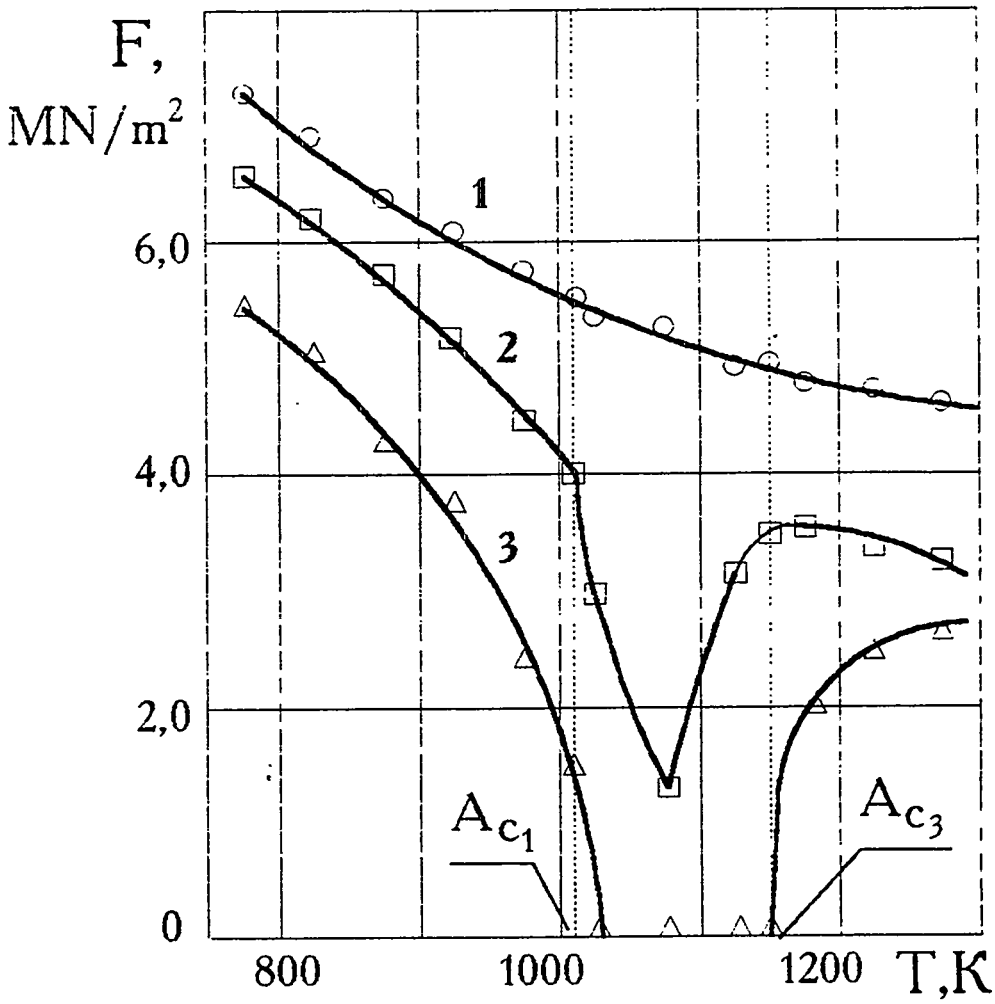


Fig. 10. Adhesion strength of the oxide coating. Oxidaition periods: 1. - 300 s, 2.- 600 s, 3.- 1200 s

The maximum corrosion rate in the temperature range of Ac_1...Ac_3 is due to the weak adhesion of the coating. The destruction of the oxide coating as well as worsening of the adhesion may be supposed to be the consequence of the lattice reconstruction as a result of $\alpha \rightarrow \gamma$ transformation in the oxidized steel. Then the adhesion properties, the number of defects in the coating and, hence, the corrosion rate of the specimens treated at the temperatures of Ac_1...Ac_3 would depend upon the extent of $\alpha \rightarrow \gamma$ transformation and, hence, upon the oxidation period. The above mentioned concerns the dependences in Fig. 9 and 10. The dilatometric studies, however, showed that the time to complete the $\alpha \rightarrow \gamma$ transformation was

1...1,5 min for the temperature of 1073 K. This means that the specimens studied experienced the complete phase transformation during all the three ranges. However, in a specimen being oxidized for 5 min in the temperature range of Ac_1... Ac_3 the destruction of the coating and, hence, the increase in the corrosion rate were not observed.

Thus, the polymorphial transformation alone cannot be considered to be the reason for the abnormal increase in the corrosion rate in the temperature range of Ac_1...Ac_3 .

Another possible reason for the destruction of the oxide coating is considered to be the formation of CO and CO_2 under the scale as a result of decarburation of the surface layers of the oxidized metal. The highest decarburation rate is observed in the intercritical temperature range of Ac_1...Ac_3 [12]. The latter supposition was confirmed by the study of the depth dependence upon the temperature and time, the highest depth of the decarburized layer with steam-thermal oxidation being observed at the temperature of 1073 K (Fig. 11).

The longer the oxidation period, the thicker the decarburized layer is. For instance, decarburization was not observed at the oxidation time of 5 min. Neither it was observed at the temperatures above Ac_3 .

Comparable dependences for the corrosion rate and adhesive strength were obtained for 45 and 08 КП steels [13-16].

Thus,

1) FeO-containing protective coatings obtained on steels in superheated water steam possess high anticorrosive and adhesive properties;

2) to obtain the oxide coatings with high protective properties, at the oxidation temperature being above Ac_3, the oxidation period may be reduced to 5 min.

4.2. Tool steel (Р6М5)

On the specimen surface oxidized in the temperature range of 773...973 K the homogenous, smooth, glitter oxide film was formed. At the higher oxidation temperatures of 1073...1173 K, bubbling, peeling and spalling effects of the oxide film were observed on the specimens with the oxidation period exceeding that of the linear law (1073 K, τ>800 s; 1123 K, τ >700 s; 1173 K, τ >600 s).

High hardness is considered to be one of the main requirements the tool must meet. Since the tempering was supposed to be carried out in the superheated steam medium to the end of achieving uniform oxidation of the tool as well as in-

creasing its corrosion and operation resistance, the measurements of hardness were performed for each oxidation condition, the results being presented in Fig. 12.

According to the experiment results one may conclude that the temperature of steam-thermal oxidation for tool steels should not be raised above 873 K.

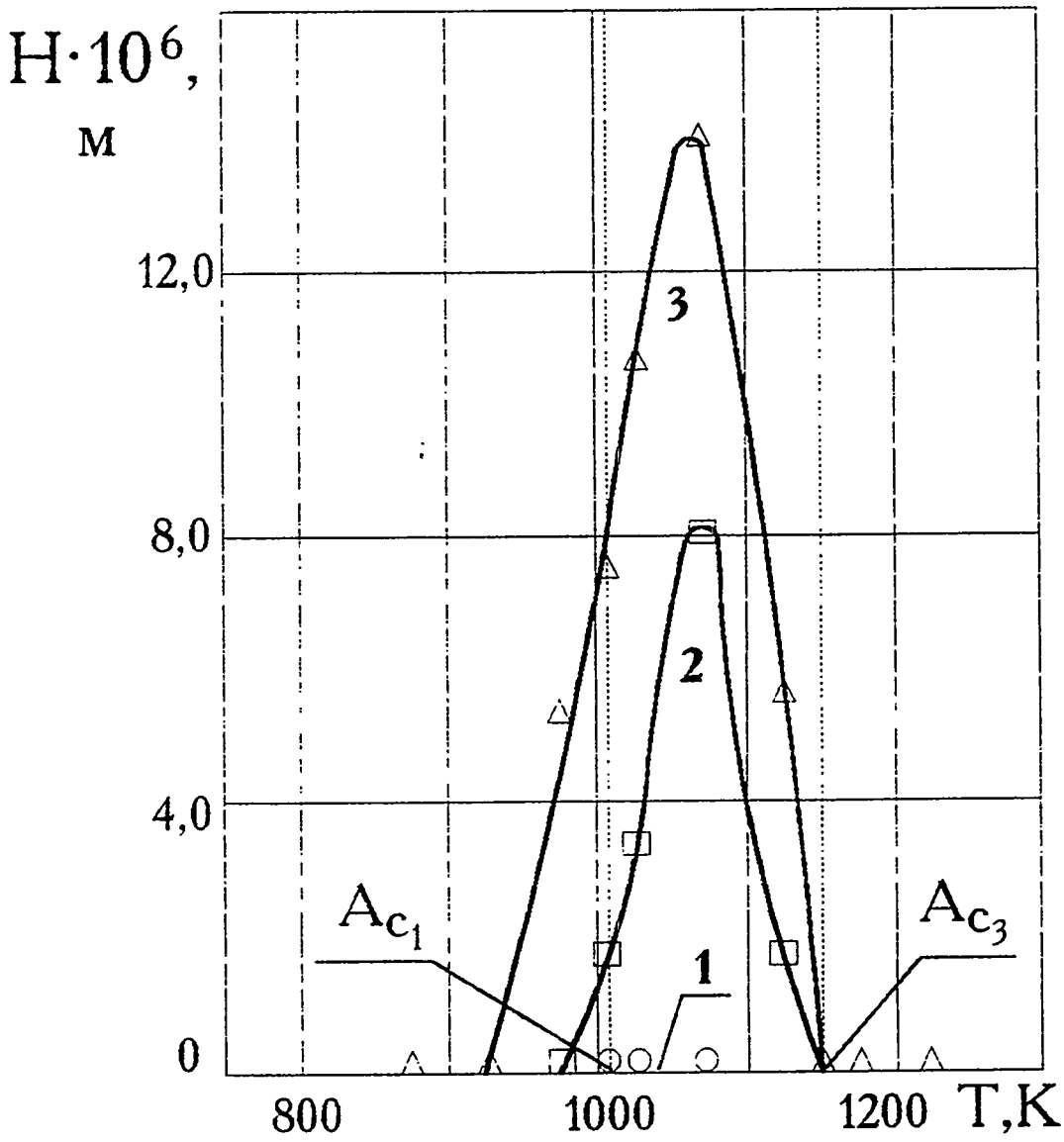


Fig 11. Ferrite layer thickness as a function of the treatment temperature Oxidation periods: 1. - 300 s, 2.- 600 s, 3.- 1200 s

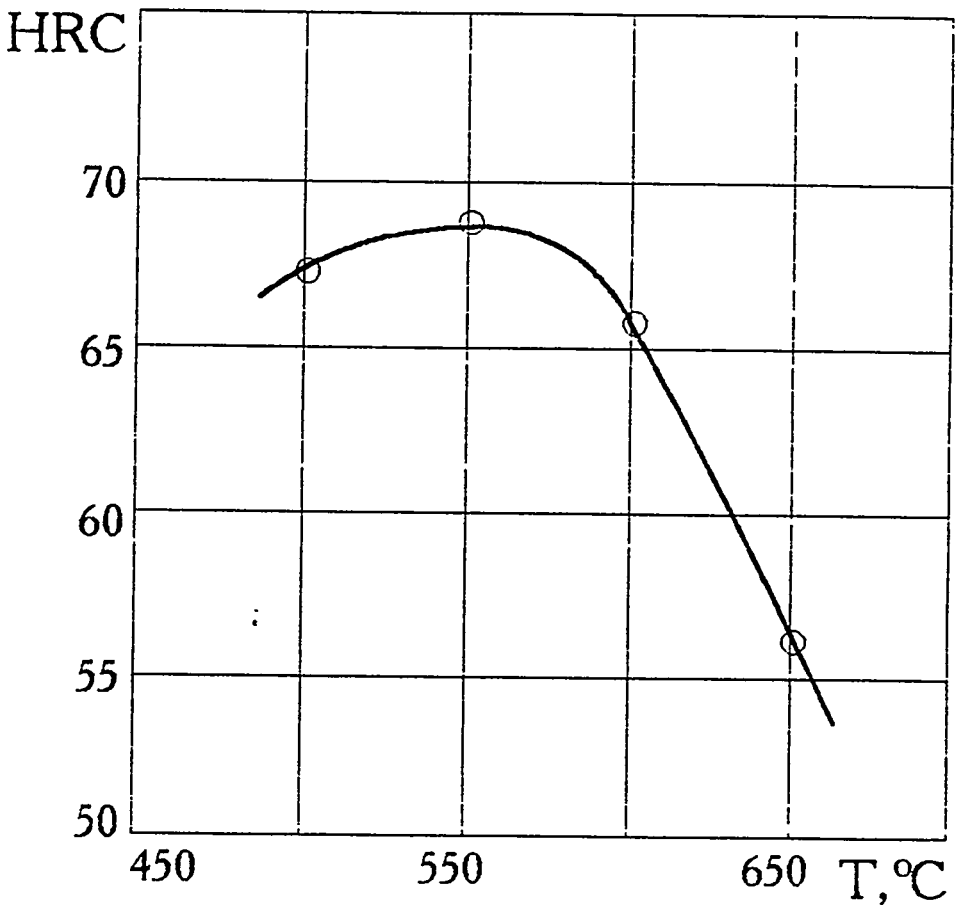


Fig. 12. R6M5-Steel specimen hardness as a function of the tempering temperature (tempering time - 1 hour)

Fig. 13 presents the results of the corrosion tests of specimens. The specimens oxidized at the temperatures above 1023 K were not tested, since the oxide film there was destructed. The corrosion tests showed that the temperature rise as well as the increase in the oxidation period lead to the decrease in the corrosion rate. The latter is likely to be due to the formation of the thicker, pore-free film. At the temperature above 923 K, however, the corrosive resistance either slightly increased, or even decreased at long oxidation periods. This is due to the worsening of the thick film adhesive properties as well as their porosity.

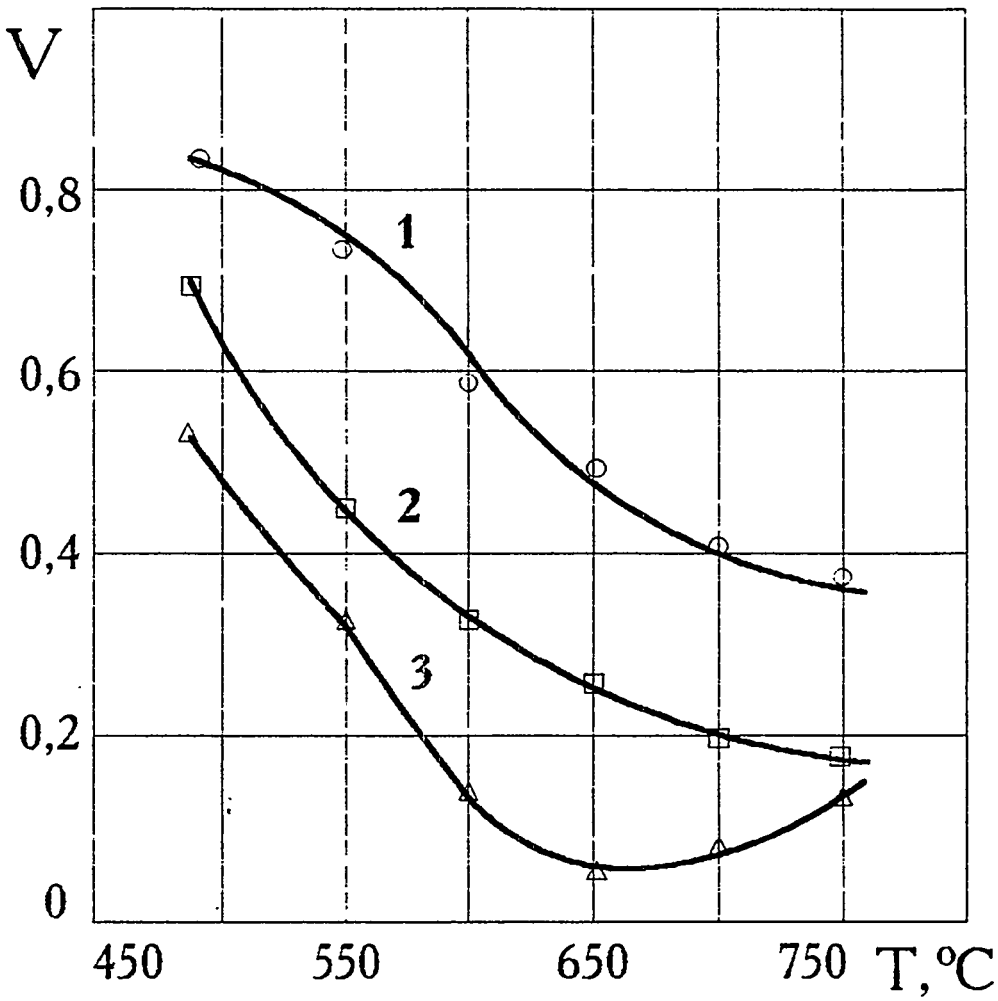


Fig. 13. Relative corrosion rate as a function of the oxidation temperature Treatment periods: 1.- 600 s, 2.- 1800 s, 3.- 3600 s

Thus, to the end of increasing the corrosive resistance it is not reasonable to raise the oxidation temperature above 973 K.

The strength of the film adhesion with the specimen surface as well as its antiscouring properties were studied on a dry friction unit. The best results were obtained in testing the specimens oxidized at the temperatures of 823,873 and 923 K with the oxidation period of 3,2 or 1 hours respectively. With the load of 2 kg/sm^2 the emergence of scoures on the non-oxidized specimens was observed in 5 min, while on the oxidized ones they were not observed at all even in 60 min of testing.

In addition, the studies were carried out to the end of determining the temperatures where the adhesion of the tool (specimens) surface with the 45-steel

being treated was observed. The temperature for the non-oxidized specimens was 973 K, for the oxidized ones 1073...1173 K.

Thus, the presence of the oxide film on the tool steel surface results in improving the antiscouring properties of the latter, as well as in increasing the temperature of adhesion with the steel being treated and, hence, in improving the tool wear-resistance.

Finally, the wear-resistance tests of the tool made of P6M5-steel in treating 45-steel were carried out. The full-scale tests confirmed the conclusion of this paper and showed that the wear-resistance of the drill increased by a factor of 2...3 in oxidizing in water steam.

Conclusion

The studies carried out demonstrated that the wear-resistance of the cutting tool made of P6M5-steel increases by a factor of 2...3 in case of simultaneous operations of tempering and oxidation in superheated water steam, the corrosive resistance increasing by a factor of 5...8. The experiments on improving the corrosive resistance of carbon steels gave far exciting results.

The kinetic dependences of the oxidation process were determined. This makes it possible to find the optimal parameters of the technological steam-thermal oxidation process. It should be noted, however, that in this case, more thorough studies of the influence of different technological oxidation parameters upon the operation properties of the tool are to be carried out. Special attention here should be paid to the choice of the cooling conditions as well as to the phase composition of the oxide film formed.

References

1. Arharov V.I. Oxidation of metals at high temperatures.- M.: Metallurgizdat, 1945.- 171 p.

2. Hauffe K. Reactions in solid bodies and on their surface. M.: IL, 1962, V.1.- 415 p.

2. Hauffe K. Reactions in solid bodies and on their surface. M.: IL, 1963, V.2.-273 p.

4. Zhook N.P. The theoretical course of corrosion and metal protection. M.: Metallurgia, 1976.- 472 p.

5. Vol A.E. The structure and properties of binary metallic systems.- M: Nauka, 1976, V.2.- 655 p.

6. Tikhomirov V.I., Ipatyev V.V., Gofman I.A. Micrographic studies of the iron oxidation kinetics// The rate of scaling on metals and alloys: LGU Proceedings.- L.: 1954, V.1.-p.7-20.

7. Evans Yu. N. Corrosion, passivity and protection of metals.- M.: Metallurgizdat, 1941.- 866 p.

8. Borisenko S.A., Filipova N.M. Thermal treatment in water steam// MTOM.- 1959, N6.- p.17.

9. Korolyov G.G., Alexandrovich B.L.,Goldvasser M.I. Annealing of specimens in water steam//Machine tools and tools.- 1959, N11.- p.38-39.

10. Popov A.A., Mihalyov M.S. On kinetics of the ferrite formation in decarburizing carbon and alloyed steels// FMM.- 1959, V.7, N2.-p.198-208.

11. The preliminary thermocyclization influence on the carbon steel oxidation rate./ V.A.Achlustin, G.P.Vyatkin, Yu.B.Peisahov, Yu.N.Teplyakov. In "Automation of industrial power systems and power equipment".-Chelyabinsk: ChPI.- 1985.-p.105-107.

12. Oxide coating corrosive resistance./V.A.Achlustin, G.P.Vyatkin, R.E.Chirkova, E.Yu.Kurkina.-In "Phisical and chemical principals of metallurgical processes".- Chelyabinsk: ChPI.- 1987.-p.40-43.

13. Patent USSR (Claim of right) N1070211. The steel products oxidation way.- V.A.Achlustin, G.P.Vyatkin at al. - 1.10.1983.

14. Patent USSR (Claim of right) N1201346. The austenite steel oxidation way.- V.A.Achlustin, G.P.Vyatkin at al. - 1.09.1985.

15. Patent USSR (Claim of right) N1297490. The carbon steel products oxidation way.- V.A.Achlustin, G.P.Vyatkin at al. - 15.10.1987.

16. Patent USSR (Claim of right) N1217008. The carbon steel products oxidation way.- V.A.Achlustin, G.P.Vyatkin at al. - 8.11.1985.

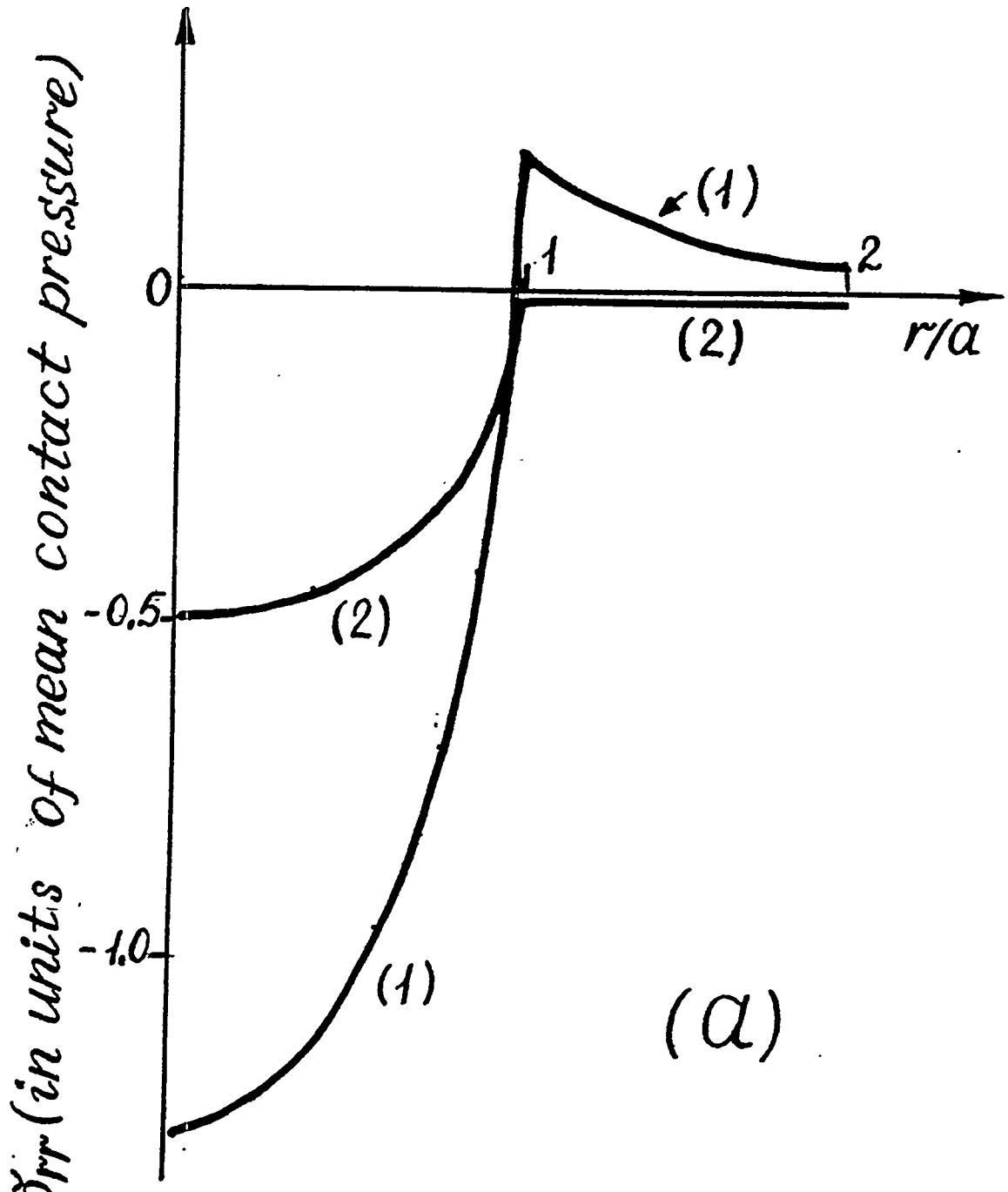


Fig. 3a

AM 7674 Abia.

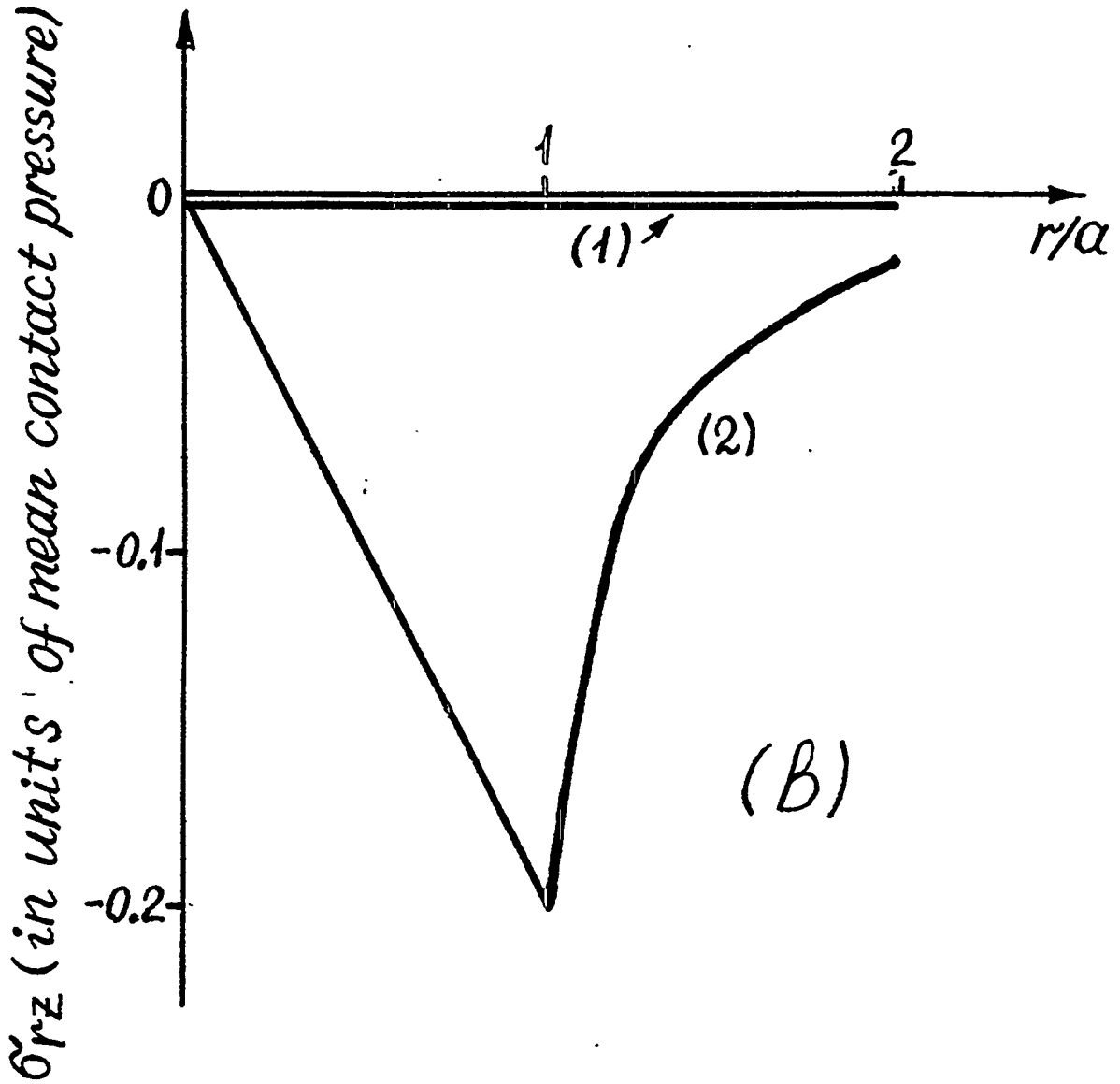


Fig. 36.

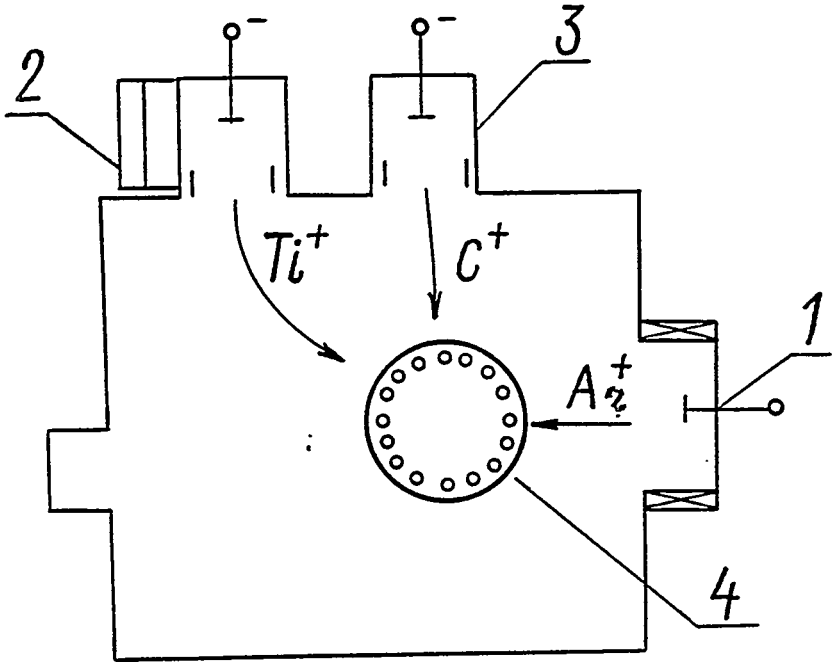


Fig. 4

AM 7674

Project Title: Multilayer Coatings for Improved Tribological Performance
Principal Investigator: A. B. Vladinerov
Institute of Metal Physics
Ekateringburg, Russia
AM-7674

CLAUSE 1 - STATEMENT OF WORK

Objective:

The objective of this work is to determine if layering a hard material and a soft material in a sputtered multilayer thin film will enhance tribological performance. The sputtering shall be carried out using a unique jet magnetic separation arc source.

Tasks:

The Contractor shall:

1. Provide a report that describes:
the operation of the magnetic separation arc source
previous work performed by the Contractor on multilayer coatings for tribological applications

2. Optimize the deposition conditions for Diamond Like Carbon (DLC) and Copper (Cu) films on tool steels, and measure the hardness, wear resistance, and friction coefficient of DLC and CU films. Within two months after the commencement of work Sandia and the Contractor shall mutually determine what tool steels shall be coated. The Contractor shall provide a report on the experimentation data and results.

3. Deposit alternating multilayers thin films of Cu and DLC. The total film thickness shall be 10 microns or less. The layer thickness shall vary from 500 angstroms to 1 micron. The hardness, wear resistance, and friction coefficient of the multilayer films shall be measured. The Contractor shall provide a report on the experimentation data and results.

4. The Contractor shall provide a final report summarizing all experimental results.

PREVIOUS STUDIES PERFORMED BY THE CONTRACTOR ON TRIBOLOGICAL PROPERTIES OF MULTILAYER COATINGS

The principal goal of our studies [1-9] is a maximum practical realization of unique tribological properties of diamond-like coatings (DLC's), which possess a high hardness and low friction coefficients. The focus was on the reasons responsible for the failure of the "coating - substrate" system. Investigations of DLC's on metal and nonmetal substrates, which were performed mainly on our test installation for wear in a jet of abrasive particles [1,2,4] , showed that the DLC material wears little if at all and the "DLC - substrate" system fails owing to cracking and peeling of the coating. Optimization of the sample pretreatment methods and deposition of a thin (about 0.1 of the DLC thickness) adhesion titanium sublayer allowed production of sufficiently stable DLC's on steel, which were used for hardening of cutting tools [6]. A further increase in the service life of DLC's can be achieved through preliminary modification of the substrate with the help of ionic implantation, which adds to adhesion reactivity of the surface and hardness of the metal surface layer. Initial experiments yielded positive results [8]. At the same time our investigations provided evidence that another way exists to raise efficiency of DLC's as wear-resistant coatings of tools and parts of friction pairs.

1.1. For the sake of comparison we took two materials to

AM 7674 ABeal

determine an optimal adhesion sublayer titanium, which is a carbide-forming material tending to form strong chemical bonds with carbon, and aluminum, which is almost chemically neutral to carbon. As far as adhesion is concerned, we expected a much greater adhesion of the DLC to steel in the case of the titanium sublayer.

Samples (stainless steel, sublayer 0.2-0.3 μ thick, and DLC 2-3 μ thick) were tested in a jet of corundum particles [5]. A different area of the sample received the same portions of the abrasive at different speeds of particles. The speeds V_b, at which first traces of the coating peeling are observed, and V_e, at which the coating disappears completely, were registered. The results are given in the Table. As it turned out, aluminum at least is not inferior to titanium as the sublayer. Most probably, of crucial importance here is a high plasticity of aluminum, which lowers stresses arising in the "DLC - substrate" system when a hard particle strikes. Thus a favorable effect of a ductile interlayer between the coating and the substrate was revealed.

1.2. Friction tests were staged on the ШХ-15 steel with a DLC (2 μ) to determine the influence of the substrate hardness on the coating breakdown process [9]. Two lots of samples having hardness HRC 60 - 62 and HRC 35 - 38 were produced using different tempering regimes. Under the friction tests the samples performed 1000 double strokes (2 x 4) cm on the X12M steel at each of the loads chosen (3 - 15)kg/cm^2. Friction coefficients f were

measured during the tests (Fig.1). Every cycle of 1000 strokes the weight loss was determined and the coating surface was examined visually. Samples from both lots of the uncoated steel were tested simultaneously under the same conditions. Portions of the DLC on the soft steel peeled even at a minimum load but part of the coating remained on the surface even at P = 14 kg/cm^2. As was expected, the coating on the hard steel peeled at larger loads, P = 14 kg/cm^2 . Hence the results presented in Fig.2. However, what deserves attention here is not a higher stability of the DLC on the hard steel but the fact that fragments of the coating on the soft steel continued functioning even after the coating has disintegrated: they lowered a little the friction coefficient and considerably inhibited wear of the sample. Disintegration of the DLC on the hard steel under an increased load almost immediately returns the friction coefficient and wear rate of the sample to the values typical of the steel without the DLC (Figs 1 and 2). From here it follows that a soft substrate under the DLC can add considerably to wear resistance (especially under large loads) thanks to separate DLC fragments, which are pressed down into the substrate and thus are reliably fixed therein. In this situation we have a structure similar to diamond particles in a soft base. This has long been used in grinding wheels and electrolytic coatings with diamond particles.

1.3. We have performed initial calculations on the influence of a hard coating on the stress field arising in a sample under a

concentrated external load. It turned out that a hard coating changes qualitatively the distribution of stresses responsible for formation of cracks and, finally, for the breakdown of the sample's surface. Such coating (Fig.3a) essentially eliminates radial tensile stresses σ_{rr} at the surface of contact with the loading body (indenter). This precludes formation and development of surface microcracks. However, a negative effect also takes place: tangential stresses σ_{rz} appear at the coating/substrate interface and the stresses tend to tear off the coating (Fig.3b). A traditional method used to inhibit peeling of the coating consists in improvement of adhesion. However, another way is possible: provision of an additional layer of a softer material between the hard coating and the substrate. This layer will, first, redistribute tangential rupture forces throughout the layer thickness and, second, lower σ_{rz} as a result of plastic flow. So, initial calculations make one look for an optimal combination of a hard strengthening layer and a soft damping layer in order to bring the breakdown to a minimum under preset external effects.

1.4. The service life of the coating is affected greatly by how the force is transmitted from the counterbody to the coating. The point is that the surface of a coating, in particular of a DLC, is never perfect. As the coating first contacts the counterbody, overstresses arise on the coating surface at projections and the overstresses form a system of cracks representing future centers of the coating peeling. During this

initial period, which is called "running-in" in practice, friction coefficients of DLC's are never found to be low. In the above-described experiments with the ШХ-15 steel having a DLC friction coefficients were equal to 0.3 - 0.4 during the first 100 strokes.

Penetrating into the counterbody whose hardness is always lower than that of the DLC, projections on the DLC even can cause spalling of the substrate material together with the coating given good adhesion to the substrate. During our studies [6] we observed such catastrophic breakdown of DLC- hardened milling cutters, which was accompanied by a sharp increase in the cutting force.

During the "running-in" period an improvement in the tribological characteristics of the DLC's was achieved thanks to smoothening of the original DLC relief, for which purpose the sputtered coating underwent ionic etching in an active gas [9]. However, another method can be proposed: a layer of material that easily lends itself to plastic deformation is provided between the coating and the counterbody. In the course of "running-in" this layer ensures a more uniform redistribution of stresses and inhibits transmission of forces from the counterbody to the strong brittle DLC at projections. This method of improving tribological characteristics of surfaces with a DLC was verified experimentally.

We prepared steel friction pairs of the "shaft-bushing" type. Some bushings were copper-plated. Tests were performed on a СМЦ-1

friction bench at the Institute of Mechanical Engineering, Ural Division of Russian Academy of Sciences. Cup grease was used as a lubricant. "A combination of the shaft, which was hardened before deposition of diamond, and a copper- plated bushing showed the best results. Even when the friction bench developed a maximum possible load of 500 kg, the pair functioned properly without cooling at different, including maximum, test speeds (1400 r.p.m.). The friction coefficient was 0.0045." (An extract from the report presented by the test laboratory.)

So, we have serious reasons to believe that of unquestionable interest are coatings where a ductile layer is placed both under and over the hard diamond-like coating, i.e. multilayer coatings of the "DLC - soft material" type. Other researchers also began to use this method of producing coatings with high tribological properties ("Diamond Films'94" Conf., Il Chiocco, Italy, September 25-30, 1994, Reports 2.100, 12.040).

In our investigations we took copper as the soft material as it does not form chemical compounds with carbon. This was a deliberate choice so that we could consider only mechanical properties of the layers and disregard their mutual chemical interaction when analyzing the results.

Multilayer coatings will be deposited on samples of a hard (HRC 62 - 65) molybdenum- and tungsten-alloyed tool steel grade P6M5. (The steel grade is given according to the nomenclature adopted in Russia.)

The contractor has a vacuum sputtering installation outfitted with several sources for production of multilayer coatings.

VACUUM SPUTTERING INSTALLATION.

A vacuum sputtering installation is used for deposition of strengthening, wear-resistant and decorative coatings. The installation ensures ionic cleaning of the surface of parts to be treated, deposition of a metal sublayer and sputtering of a wear-resistant diamond-like coating in a single vacuum cycle. The installation is shown schematically in Fig.4.

2.1. Ionic etching source.

For preliminary cleaning of the surface to be treated the installation is provided with an ionic etching source where the voltage is adjusted in steps from 800 to 2500 V and the current rating is from 0.1 to 0.5 A. As soon as the required pressure of 10^{-3} Pa is built up in the working chamber (approx. 1 hour after the installation has been turned on), the processing gas is fed into the chamber and the source is switched on. The substrate material determines the operating regime of the source (voltage, current, gas pressure) ensuring optimal conditions of etching (etching rate, temperature limits, etc.).

AM 7674 ABay.

2.2. A magnetic-separation arc source for deposition of metal layers.

An electric-arc evaporator with separation of the plasma flux in a magnetic field is used for deposition of metal layers. The maximum power of the evaporator is 5 - 6 kW.

The operating principle of the evaporator consists in erosion of the material from moving cathode spots which appear when the electric arc glows. The magnetic field of the stabilizing coil keeps the cathode spots on the end-face surface of the cathode. An arc discharge is initiated during pulse evaporation of the metal film from the surface of the igniter electrode. Subsequently the discharge goes from the igniter electrode to the main discharge between the cathode and the anode.

The magnetic field of the focusing coil is used to focus the plasma flux of the arc discharge. To ensure that the evaporated flow of the material is deposited on the surface of the treated parts only as ions and not in the form of droplets, a magnetic separation of plasma is used in the evaporator. The essence of the separation is that the flow of the material in the droplet phase travels in a straight line and is deposited on the near-by walls of the chamber and internal surfaces of the evaporator. Ions of the evaporated material are deflected towards the turret mounting holders of the samples. Elimination of the droplet phase ensures production of better - quality coatings. The source can be used to deposit nitride, carbide and oxide coatings by the method

of reaction deposition. The source allows deposition of metal and nitride coatings at relatively low temperatures. This is very important for deposition of wear - resistant coatings on tool steel as in this case no tempering takes place and therefore hardness is not impaired. In the installations designed for sputtering of nitride coatings the substrate temperature generally is not lower than 500^{o}C.

Our installation and sputtering regimes permit production of metal and nitride coatings with good adhesion at relatively low temperatures. Under the chosen regimes the sputtering rate is 2-3 Å/s.

The nuclear reaction method was used to determine the content of gas impurities in the deposited metal layer. Measurements were made for a titanium coating 1μ thick. As is known, titanium is a getter material which absorbs gas impurities from the ambient atmosphere. An analysis showed that even such a getter material as titanium contains not more than 0.1 at.% oxygen, while nitrogen was not detected at all. This fact attests that our installation and sputtering regimes make it possible to produce pure metal coatings.

2.3. A pulse-arc source for sputtering of DLC's.

A pulse generator of carbon plasma is designed to deposit carbon coatings on the surface of treated parts. The generator comprises a water-cooled holder of a graphite cathode, a ring

anode, and two igniter electrodes. The igniter electrodes initiate the main discharge at the graphite cathode. A pulse (the pulse repetition frequency is from 1 to 35 Hz) electric- arc discharge forms a carbon plasma whose ions are accelerated in the electric field and are deposited on the substrate surface. The mean energy of carbon ions is about 80 eV, a fact which makes unnecessary an additional acceleration of ions by applying a negative potential to the substrate. A pulse character of the sputtering process, which is distinguished for long pauses, allows a better removal of heat from the condensation zone. The last fact ensures formation of diamond- like structures over a wider temperature interval. A study of the substrate temperature as a function of the pulse repetition frequency showed that the DLC is formed at a temperature not exceeding $300^{o}C$. The deposition rate is 0.75 Å/pulse. At this rate a DLC 2-3 μ thick can be produced over a relatively short period of time (1 hour). An analysis performed by the nuclear reaction method showed absence of oxygen and nitrogen in the DLC.

2.4. Sample holder.

At the top and at the bottom the installation chamber (0.3 m^3) has rotating turrets with water - cooled rotating seals. This makes it possible to lower the temperature during the sputtering process. A relatively large number of the seals (54) provides for the most rational use of the chamber volume at a

maximum number of parts to be treated.

References

1. Klotsman S.M., Kovsh A.S., Kovsh L.M., Kuzmina E.V., Mukhametkhaziev R.R., Plotnikov S.A., Trakhtenberg I.Sh., and Feigin D.M. - Protective diamond-like coatings on quartz. Fizika i khimiya obrabotki materialov, 1991, No. 6, p.p. 113- 116.

2. Gorpinchenko S.D., Klotsman S.M., Kuzmina E.V., Plotnikov S.A., and Trakhtenberg I.Sh. - Wear resistance of diamond- like coatings. - Surface and Coating Technology, 1991, v.47, p.p. 201-208.

3. Trakhtenberg I.Sh. and Gorpinchenko S.D. - Determination of wear resistance of hard coatings. - Treniye i Iznos, 1993, v.14, p.p. 907-913.

4. Gorpinchenko S.D., Klotsman S.M., Kuzmina E.V., Plotnikov S.A., and Trakhtenberg I.Sh. - Friction, wear and service properties of i-C coatings on steel. - Diamond and Related Materials, 1992, v.1, p.p. 619-622.

5. Gorpinchenko S.D., Plotnikov S.A., and Trakhtenberg I.Sh. - Wear of diamond-like and other hard coatings on steel in a jet of corundum particles. - Abstracts of 3rd European Conference on Diamond, Diamond-like and Related Coatings, Aug. 31 - Sept.

AM 7674 Abrasion.

4, 1992, Heidelberg, Germany, p.13.112.

6. Trakhtenberg I. Sh., Plotnikov S. A., Vladimirov A. B., Liberman Ya. L., Kanalina V. A., Boborykin V. A., and Leizerov V.M. - Service properties of cutting tools hardened with a diamond-like coating. - Diamond and Related Materials, 1993, v.2, p.p. 1434-1438.

7. Arbuzov V.L., Vladimirov A.B., Vykhodets V.B., Davletshin A.E., Plotnikov S.A., Trakhtenberg I.Sh., Rubshtein A.P., Gorpinchenko S.D., and Kuzmina E.V. - Practical use of strength and anticorrosion properties of amorphous carbon thin films. - Diamond and Related Materials, 1994, v.3, p.p. 775-778.

8. Gorpinchenko S.D., Trakhtenberg I.Sh., Bakunin O.M., Plotnikov S.A., Nechaev A.A., Mizgulin V.N., and Gavrilov N.V. - Breakdown of a-C coatings on ion-implantation- modified metal alloys with a jet of abrasive particles. - Diamond and Related Materials, 1994, v.3, p.p. 779-782.

9. Trakhtenberg I.Sh., Plotnikov S.A., Bakunin O.M., Yakovleva S.G., Nechaev A.A., Gorpinchenko S.D., Korshunov L.G., Gavrilov N.V., and Mizgulin V.N. - The effect of additional treatment on tribological properties of a-C coatings on metals. - Abstracts of 5th European Conference on Diamond, Diamond-like and Related Materials, Sept. 25 - Sept. 30, 1994, Il Chiocco, Italy, p.9.089.

AM 7674 Авт.

Table

Characteristic speed, m/s	Substrate material	Dimensions of abrasive particles, portion weight		
		120 μ, 1 kg	120 μ, 0.5 kg	70 μ, 1 kg
V_b	Ti	12	13	20
	Al	11	12	23
V_e	Ti	22	25	28
	Al	22	23	29

AM 7674 Abrasf.

FIGURE CAPTIONS

Fig.1. The friction coefficient f on the X12M steel as a function of the specific load applied to the samples of the ШХ-15 steel (curves 1 and 2) and to the samples of the same steel with a DLC (curves 3 and 4) at the substrate hardness HRC 60 -62 (curves 1 and 3) and HRC 35 - 38 (curves 2 and 4)

Fig.2. The ratio between the friction wear on the X12M steel of the samples of the ШХ-15 steel with a DLC and that of the samples of the same steel without a DLC depending on the specific load at HRC 60 - 62 (curve 1) and HRC 35 - 38 (curve 2)

Fig.3. Radial (a) and tangential (b) stresses as a function of the distance to the center of the contact area when a spherical indentor acts upon the elastic half - space. a - radius of the contact area, (1) without coating, (2) with an absolutely hard thin coating

Fig.4. Diagram of the vacuum sputtering installation: 1 - ionic etching source; 2 - magnetic - separation source for deposition of metal layers; 3 - pulse - arc source for sputtering of diamond - like coatings; 4 - sample holder

AM 7674 Abs.

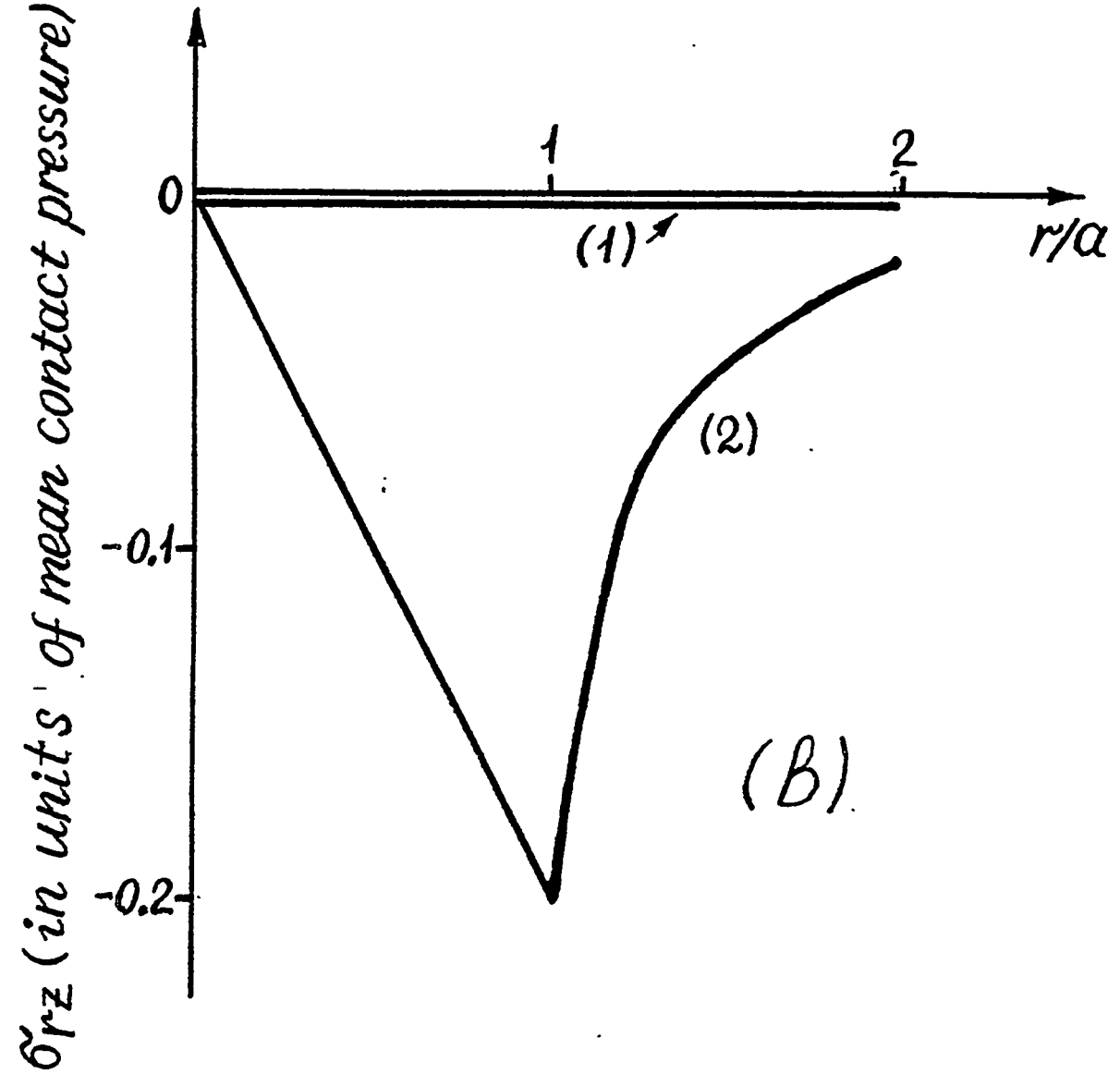


Fig. 36.

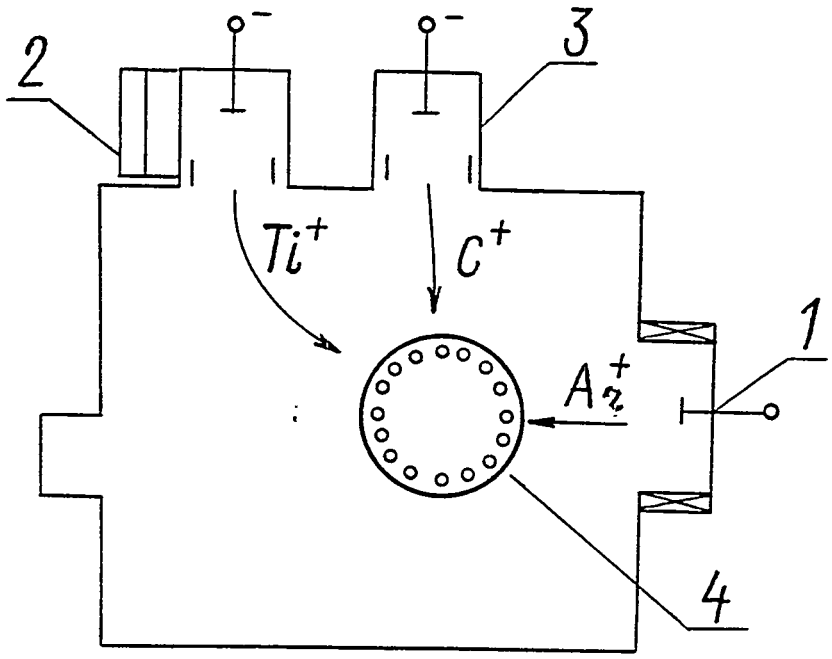


Fig. 4

AM 7674 Abrof.

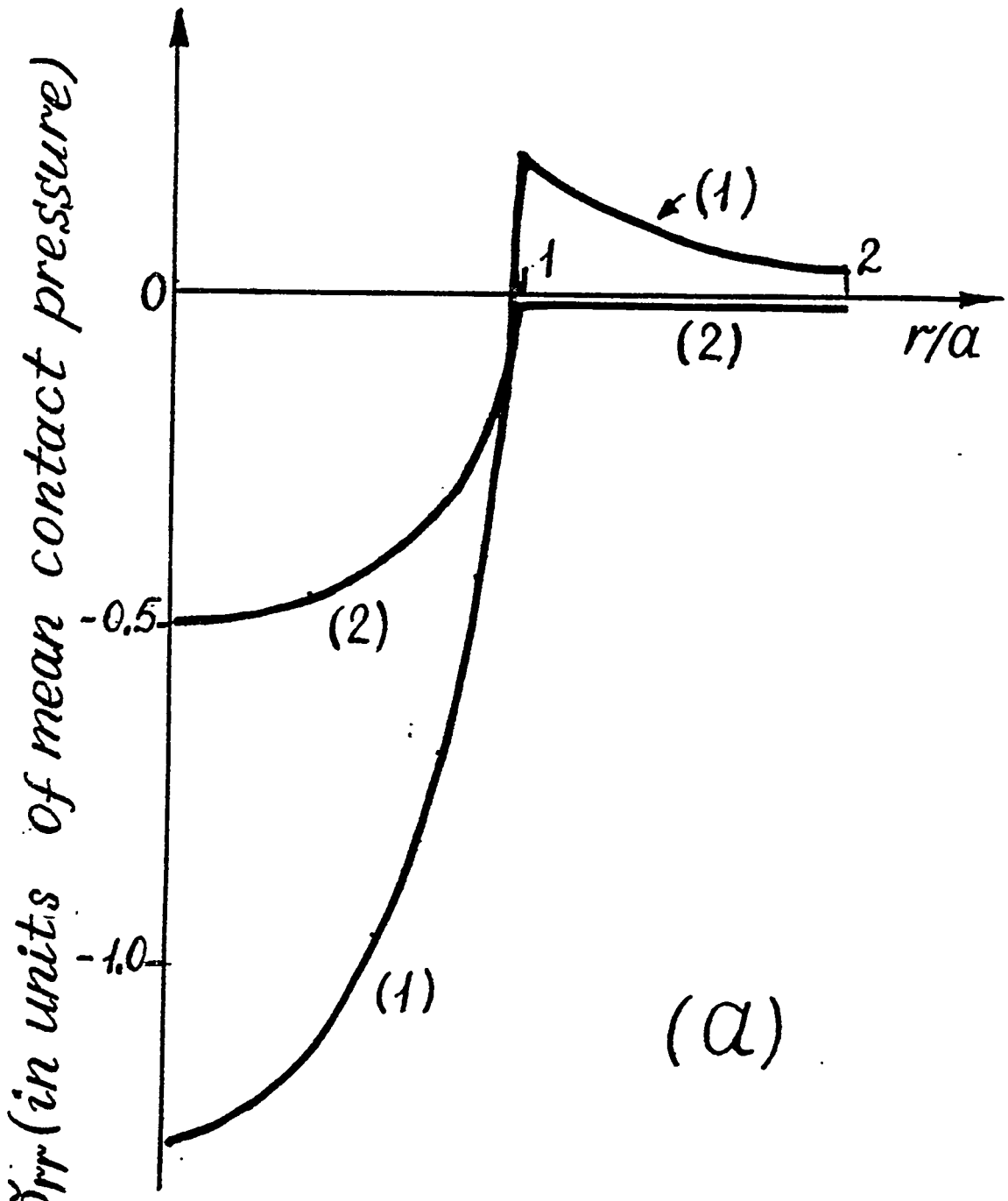


Fig. 3a

AM 7674 Abia.

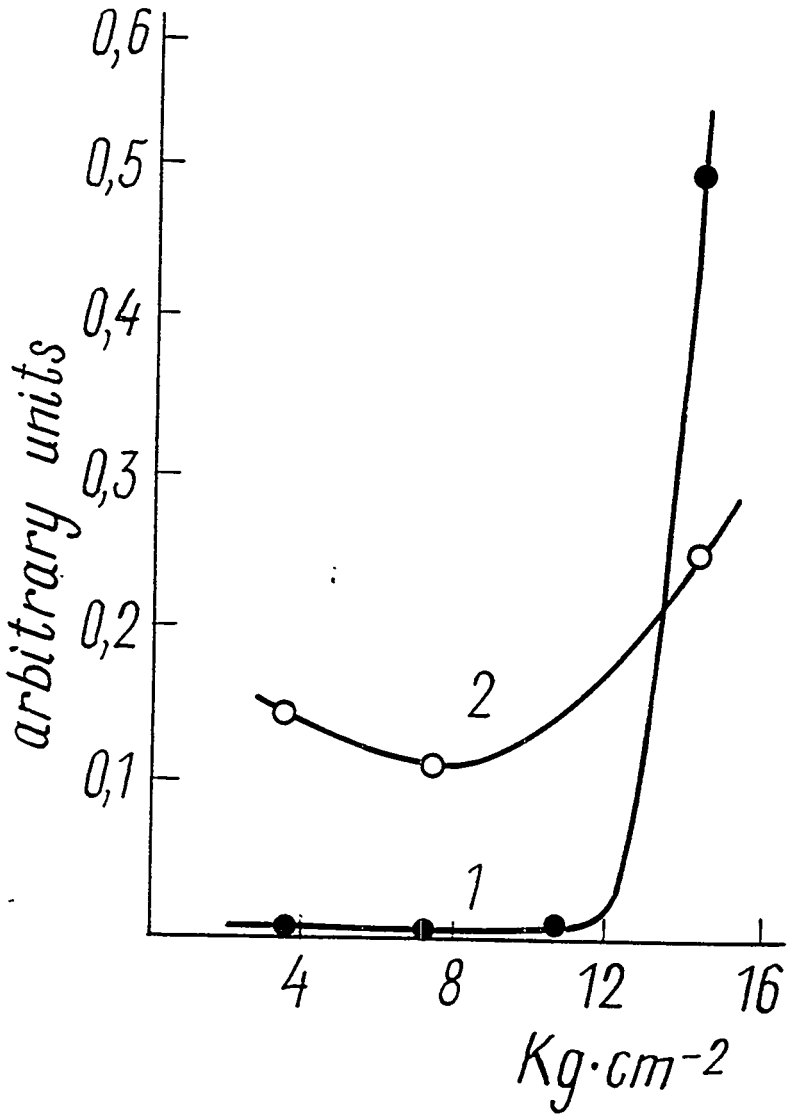


Fig. 2

AM 7674 Abst.

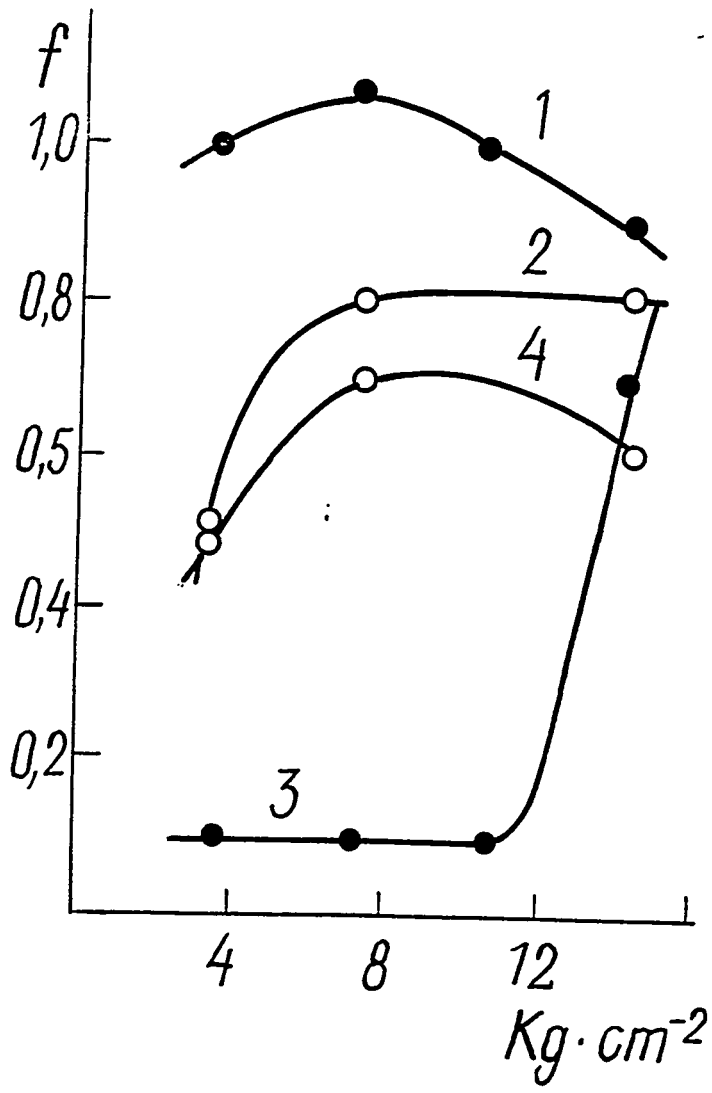


Fig. 1

AM 7674 Abrog.

REPORT

on the 2nd Stage of Works Performed under the Contract AM-7674 Concluded with the Sandia National Laboratories Under the provisions of the contract AM-7674 the following works were to be performed at the second stage:

1. Production of tool-steel samples and preparation of the surface of the samples for coating deposition.

2. Selection of conditions for sputtering of metal and diamond- like films.

3. Measurement of the microhardness and friction coefficients and staging of wear tests.

1. SAMPLES

The P6M5 tool steel was taken as the starting material of the samples, on which the film sputtering regimes were optimized and friction tests were performed. The composition of the steel was as follows, weight %: 5.5-6.5 W, 0.8-0.88 C, 3.8-4.4 Cr, 1.7-2.1 V, 0.5 S, and 0.4 Mn [1]. This steel has been widely used as the material of various cutting tools. It is analogous to the AISI-3343 steel containing (weight %) 6.6 W, 5.0 Mo, 1.9 V, 4.0 Cr, and 0.9 C [2].

The steel was subjected to a thermal treatment, which is generally used for tools, under the following conditions:

- annealing at 840-860° C;

- cooling at a rate of ^{40} C per hour to 720-730^0 C;

- holding for 4 hours, minimum;

- air cooling at a rate of 50^0 C per hour to 600^0 C [1].

The microstructure of the steel (Fig.1) was a tempered martensitic matrix with spheroidal (1 to 15 mcm) carbide inclusions.

The samples were shaped as plates measuring (15 x 15 x 2.5) mm. The surface of the samples was ground and polished on a hard-alloy block using successively diamond pastes with the grain size of 20 to 1 μ.

Since the goal of the study is to produce films that would havepractical applications, it is necessary to provide good adhesion of the films to the surface of the samples. After the mechanical treatment the polished samples have a stressed surface layer contaminated with the abrasive material. To remove the adrasive material, the samples were etched electrochemically in a chlorine-acetic electrolyte (90 % glacial acetic acid and 10 % perchloric acid at the current density of approx. 0.5 A/cm^2).

A relief was always formed on the surface owing to a different rate of etching of the martensitic matrix and carbide inclusions. For preliminary experiments we used samples with different time of electrochemical etching (10 times) and the corresponding relief ($\approx$ 1 μ and $\approx$ 7 μ).

In order to determine the best method of the surface pretreatment, the diamond-like films (DLFs) sputtered on samples with the original mechanically polished or electrochemically etched surface were tested for mechanical resistance. For details of the DLF sputtering see subsection 2.3. Here we shall note only that two DLF

sputtering methods were used: 1) without ionic bombardment (method 1); 2) with a periodic oxygen-ion bombardment during sputtering (method 2). All the samples received DLFs of the same thickness (3 μ).

The preliminary experiments yielded the following results. The films, which were sputtered on overetched surfaces with therelief of about 7 μ, cracked and peeled off at once. This was observed for both sputtering methods. The film sputtered on the mechanically polished surface exhibits a weak adhesion. The best results were obtained for the films deposited on the surfaces, which were subject to a slight (12 sec) electrochemical etching (see Table 1).

The last method, that is, electrochemical etching for 12 sec, was used subsequently to prepare all the samples for sputtering.

Figure 2 depicts a typical section of a profilogram of such surface. The peaks observed in the profilogram correspond to carbide inclusions. These inclusions project over the matrix for about 0.5 μ. Figure 3a shows a typical structure of the original surface of the samples as seen through a scanning electron microscope (SEM).

Microhardness of the starting samples was measured. It was the same for all the samples and equaled (950 ± 80) kg/mm^2 (the load on indentor - 20g.).

Samples of the X12M steel were prepared additionally using the same procedure. The X12M steel differs from the P6M5 steel in a lower content of carbides. The composition of the X12M steel is as follows, weight %: 1.45-1.65 C, 0.15-0.35 Si, 0.15-0.40 Mn, 11.00-12.50 Cr, 0.15-0.80 V, and 0.40-0.60 Mo [1]. This steel is used generally as the material of die tools. Microhardness of these samples is somewhat smaller than that of the P6M5 steel samples and equals (820 ± 70) kg/mm^2 .

Subsequently samples of the P6M5 steel were used for optimization of sputtering conditions and preliminary experiments on sputtering of Cu, Ti and DLFs.

2. SELECTION OF CONDITIONS FOR SPUTTERING OF METAL AND DIAMOND-LIKE FILMS

The films were deposited in a vacuum plant whose design and operating principle were described in the previous report. Before placing into the vacuum chamber, the samples were subject to an ultrasound cleaning in suds, were washed in a water flow, and rinsed in distilled water heated to 80^0 C. Then the samples were dried in a vacuum cabinet at a temperature of 200^0 C for 5 min.

The samples were mounted in special holders and placed into the vacuum chamber on a turret, which rotated during sputtering. The working space of the chamber was evacuated to a pressure of $1.3 \cdot 10^{-3}$ Pa or better and then sputtering commenced. Sputtering of the coatings includes three basic processes: 1) ionic cleaning; 2) sputtering of metal films; 3) sputtering of DLF.

2.1. IONIC CLEANING

The surface of the samples underwent ionic cleaning before each sputtering procedure. The ionic cleaning was realized using a relevant source in an argon atmosphere at a pressure of ($2 \cdot 10^{-2}$ - $6 \cdot 10^{-2}$) Pa with a negative bias (U) applied to the samples. The argon ion bombardment caused heating of the samples. The absence of the sample's surface overheating was the main criterion that determined the choice of ionic etching conditions. The overheating could lead to a loss in the steel hardness and impairment of the mechanical properties of the diamond-like

coating. To avoid a loss in the steel hardness, the temperature should not go in excess of 500° C, but to preserve the mechanical properties of DLFs, it is desirable not to heat the samples over 300° C.

A chromel-alumel thermocouple was used to measure the temperature (T) of motionless samples (with the turret stopped). Heating of rotating samples is always lower.

The experiments showed that at U = 800 V T 300° C, while at higher voltages the temperature rises. Subsequently all the sputtering procedures involved ionic cleaning at U = 800 V for 1 hour. The source current was about 10 mA.

The fact that the steel retains its initial microhardness subject to ionic cleaning under this regime is the main testimony to the absence of the sample's overheating (Table 2).

The ionic cleaning rate V was determined using two methods:

a) by the loss of the weight of the check samples: V = (2.7 ± 0.5) Å/s;

b) by the magnitude of the step in the profilogram (part of the sample's surface was covered): V = (3.0 ± 0.5) Å/s.

The values of V agree within the measurement error.

Figure 2 shows a section of a sample with such step. The thickness of the layer removed from the sample's surface by ionic bombardment was (1.0 - 1.2) μ.

Figure 3b illustrates a section of the sample's surface after ionic etching. Note a greater density of carbide inclusions compared to the sample, which was not subject

to ionic etching (Fig.3a). This is due to the fact that the rate of etching of the martensitic matrix is higher than that of the carbide inclusions. The matrix is etched around carbides, this leading not only to a greater projection of the carbides over the surface but also to emergence of new carbides on the steel surface. As is seen from the profilogram, the surface roughness increases approx. 1.5 times at the given regimes of ionic cleaning.

2.2. SPUTTERING OF METAL FILMS

Sputtering of metal films commenced immediately after the ionic cleaning unit was turned off. The films were deposited using an electric-arc evaporator with a magnetic separation of the plasma flux.

Conditions for sputtering of copper and titanium were optimized during the preliminary experiments. It was required to produce films with good adhesion to the sample's surface, determine the film growth rate, and measure the sputtering temperature.

Our measurements showed that the temperature depends mainly on the magnitude of the negative potential applied to the samples during sputtering. At U = -800 V the temperature is 300^0 C. At higher voltages the temperature rises (550^0 C at U = 2000 V). Subsequently all the metal films were deposited at U = -800 V, with the source arc current being 100 A.

The film sputtering rate was determined using two methods:

1) By the difference in the weight of the check samples before and after sputtering.

2) Observation of the fracture of the check samples through a scanning electron microscope.

The values of the sputtering rate determined by both methods were the same: (9 ± 0.5) Å/s for copper and (7.5 ± 0.5) Å/s for titanium.

The content of carbon, nitrogen and oxygen in the sputtered films was found by the method of nuclear reactions on a beam of deutons with an energy of 900 keV. No nitrogen and carbon were detected, while the content of oxygen did not exceed 0.1 at.%.

We measured microhardness of the samples with metal films of different thickness (see Table 2). The microhardness represents an effective quantity dependent on the substrate hardness. Naturally, the effective microhardness is less, the lower the load and the thicker the sputtered metal film (Fig.4).

2.3. SPUTTERING OF DIAMOND-LIKE FILMS

DLFs were sputtered on a predeposited titanium sublayer using a pulse carbon-plasma generator. The sublayer thickness was (0.3 - 0.4) μ. The use of titanium for the sublayer is determined by good adhesion of titanium to the metal surface and its ability to form carbides and, as a consequence, strong chemical bonds with the carbon film.

The temperature of motionless samples (with the turret stopped) was measured as a function of the sputtering regime and the DLF growth rate. Thin (≈ 1000 A) films were sputtered under different operating regimes of the pulse generator (the pulse frequency was varied between 1 and 30 Hz), with simultaneous measurements of the temperature. Figure 5 shows the temperature of the sample's surface vs the sputtering frequency (rate). As is seen, the film temperature does not exceed 300° C at frequencies lower than 20 Hz.

Subsequently all the DLFs were sputtered at a frequency of 10 Hz, which allowed maintaining the sputtering temperature at 300° C or lower.

The DLF sputtering rate was determined by two methods:

1) Optical interferometric methods were used for thin ($\approx$ 1000 Å) films purposefully deposited on glass substrates.

2) Observation of the fracture of thick (several microns) films through an electron microscope.

The values of the DLF sputtering rate determined by both methods agreed within the measurement error and were equal to (0.7 - 0.8) Å/pulse.

Figure 6 shows a microphotograph of a fracture of a sample with a DLF about 4.5 μ thick (60000 pulses at a frequency of 10 Hz).

The content of residual gases (oxygen, nitrogen) in the DLFs was determined in the same way as in metal films. No oxygen and nitrogen were detected in the DLFs.

We tried to measure microhardness of the samples with the DLFs. With a maximum permissible load at the indenter (200 g), impressions could not be measured through an optical microscope with a magnification of 150 power.

Figure 7 displays a microphotograph of the surface of a sample with the DLF. This appearance of the surface is typical of the diamond-like coatings [3]. The visible light inclusions correspond to the largest fragments of the diamond-like form of carbon, which is a dielectric.

The tribological tests of the DLFs produced by the given technique showed that the DLFs possess a rather low (0.09) friction coefficient on steel and exhibit a high resistance to loads (see Table 3). However, one might attempt to improve the tribological properties of the DLFs. One of the possible ways of doing so is a periodic bombardment of the growing DLF with ions of certain gases (argon, oxygen, nitrogen). This treatment of the surface will provide:

a) smoothing of the surface relief and, as a result, a decrease in the friction coefficient [4], particularly at small loads;

b) an increase in the number of diamond-like nuclei (especially in the case of oxygen bombardment) thanks to etching of nondiamond forms of carbon [5, 6];

c) partial removal of stresses.

We have staged experiments on determination of the DLF surface etching rate in the atmosphere of argon, oxygen or nitrogen. Figure 8 shows the variation of the film thickness vs the time of bombardment with gas ions at a pressure of (4.2 · 10-2) Pa. The etching rate was 0.3 Å/s for Ar, 0.1 Å/s for N_2, and 0.5 Å/s for O_2.

Proceeding from these results, we adopted a different method of the DLF sputtering: Every 5000 pulses the film surface was bombarded with oxygen ions for 1 minute during sputtering. After sputtering of the DLF was complete, the film surface was bombarded with argon ions for 5 minutes. As was expected, this sputtering method provided lower friction coefficients of the DLFs on steel (see Table 4).

3. FRICTION TESTS OF SAMPLES WITH METAL AND DIAMOND-LIKE FILMS

The samples with sputtered coatings were tested according to the following scheme: The samples reciprocated on the surface of a counter-body (plate of the X12M steel, hardness HB = 255) under certain loads in air without lubrication. Roughness of the counter-body working surface was 1 mcm. The average gliding speed was 0.07 m/s and the working stroke was 40 mm. Five hundred double strokes were made under every load. The friction force was measured, this allowing calculation of the friction coefficient f as the quotient of the friction force by the normal load P. The friction force measurement error was 10 %, maximum.

After each test the loss of the sample's mass was determined by weighing on an analytical balance. The weighing accuracy was 0.15 mg. The test was stopped when a marked loss of the sample's mass was evident and the friction coefficient f increased greatly. Our observations showed that these phenomena corresponded to the stage of a complete wear of the coating. In this way we determined the critical load the coating can stand to.

The friction coefficient of the uncoated steel samples on the counter-body surface was 0.65.

Table 4 gives the steady values of f under different loads P for the coated samples. The same table shows the limiting loads, at which the coating is still preserved. In the foregoing (section 1) these results were used for selection of the steel surface pretreatment for sputtering and for comparison of the DLFs deposited by two different methods.

We have tested an experimental multilayer coating 3 μ thick comprising alternating layers of copper and diamond-like films of the same thickness ($\approx$ 1000 Å). This coating proved to have friction coefficients on steel higher than those of the uncoated samples and disintegrated under small loads (3 kg). Such tribological characteristics make the copper + DLF system little promising for practical

applications. The use of titanium as the metal component of the multilayer coating is much more preferrable. The titanium coating on the samples (P6M5 steel) has lower values of f than the uncoated steel. With this in view, we prepared a multilayer coating 3 μ thick based on the titanium-diamond system and comprising alternating layers of the DLF and the metal 1000 A thick each. The results of the friction tests performed on this coating are presented in Table 4. It turned out that the coating possesses a low friction coefficient, which approximates that of the DLFs, and does not disintegrate under loads up to 30 kg. These tentative results make expedient the study of the tribological properties of the multilayer coatings of the metal-diamond type on tool steels. The multilayer coatings shall be based on titanium and the DLF. It seems worth searching further for the optimal structure of such coatings in the direction of increasing the ratio between the DLF layer thickness and the titanium layer thickness.

CONCLUSION

So, the outcomes of the 2nd stage of works performed under the contract AM-7674 can be summarized as follows:

1. Tool-steel samples have been produced and the surface of the samples has been prepared for sputtering.

2. Conditions for sputtering of diamond-like and metal (Cu, Ti) coatings on tool steel have been determined.

3. Diamond-like, metal and certain multilayer coatings have been sputtered on the samples under the conditions selected.

4. Microhardness and friction coefficients under different loads have been measured.

5. It was found that the DLFs possess high hardness, low friction coefficients and excellent adhesion to the tool steel.

6. It was shown that titanium is preferrable to copper in development of multilayer coatings with a metal component.

REFERENCES

1. Tool Steels. Handbook., M.: Metallurgiya, 1977, p.127.

2. Metals Handbook, 8th Edition, American Society of Metals, Metals Part,1973, v.8, p.95.

3. Frenklin Chan-Han Hong et al., Diamond and Related Materials, 2 (1993), p.365-372.

4. I.Sh. Trakhtenberg et al., Abstract "Diamond Films-94", Il Chioco, Italy, 23-30 September, 1994, 9.089.

5. K. Miyoshi et al., J.Appl.Phys., 74 (1993), p.4446.

6. Y. Lifshitz et al., Diamond and Related Materials, 1994, to be published.

~~FIGURE CAPTIONS~~ AM-7674

FIGURE CAPTIONS

Fig.1. Microphotograph of the structure of the P6M5 steel surface made through an optical microscope. X500

Fig.2. Typical section of a profilogram of the surface of a sample: a) after electrochemical etching (12 sec); b) after ionic cleaning in argon (t = 1 hour)

Fig.3. Microphotograph of the structure of the sample's surface taken through a scanning electron microscope: a) after electrolytic etching, X500; b) after ionic cleaning (t = 1 hour, V = -800 V), X500

Fig.4. Microhardness of the samples vs thickness of the titanium film

Fig.5. Temperature of the samples vs frequency of impulse

Fig.6. Microphotograph of the fracture of a sample with the DLF taken through a scanning electron microscope

Fig.7. Microphotograph of the surface of a sample with the DLF taken through a scanning electron microscope

Fig.8. Variation of the DLF thickness as a function of the time of bombardment with gas ions (● - nitrogen, ■ - oxygen, ▶ - argon). Pressure = $4.2 \cdot 10^{-2}$ Pa, J = 10 mA

Table 1. Limiting loads DLF disintegration

DLF sputtering method	Surface pretreament	Limiting load, kg
Sputtering of DLFs w/o periodic ionic bombardment (method 1)	Mechanical polishing +electrolitic etching	> 100
	Mechanical polishing	10 - 20
Sputtering of DLFs with periodic ionic bombardment (method 2)	Mechanic polishing + electrolitic etching	> 100
	Mechanical polishing	50

Table 2 . Microhardness of samples with different coatings

Surface type	Microhadness under different loads, kg/mm^2	
	20 g	50 g
Surface of P6M5 steel after ionic cleaning	980 ± 120	860± 50
Titanium coating (0,5 μ)	820 ± 120 760 ± 80	780 ± 70 860 ± 40
Titanium coating (1 μ)	730 ± 100	820 ± 40
Titanium coating (2 μ)	630 ± 40 650 ± 40	720 ± 60 720 ± 50
Copper coating (1 μ)	750 ± 140	830 ± 60
Copper coating (2 μ)	560 ± 90	670 ± 180

Table 3. Friction coefficients of the DLFs on steel under the load of 10 kg

Surface treatment method	Coating type	f
Electrolitic etching	DLF, method 1	0,10
	DLF, method 2	0,08
Mechanical polishing	DLF, method 2	0,32
	DLF, method 2	0,10

Table 4. Steady values of the friction coefficient (f) for coated samples under different loads (P)

Coating type	P, kg	f
DLF (3 μ) method 1	10	0,10
	20	0,13
	30	0,10
	40	0,12
	60	0,13
	80	0,11
	100	0,09
DLF (3 μ) method 2	5	0,07
	10	0,09
	15	0,08
	20	0,10
	30	0,09
	40	0,10
	60	0,11
	80	0,11
	100	0,09
Cu + DLF (3 μ)	1	0,65
	2	0,90
	3	1,10
Titanium (2 ,5 μ)	1	0,20
	2	0,26
	3	0,3
Ti + DLF (3 μм)	1	0,09
	2	0,09
	3	0,09
	5	0,09
	10	0,09
	20	0,20
	30	0,22



Fig. 1 Microphotograph of the structure of the P6M5 steel surface made through an optical microscope. X500

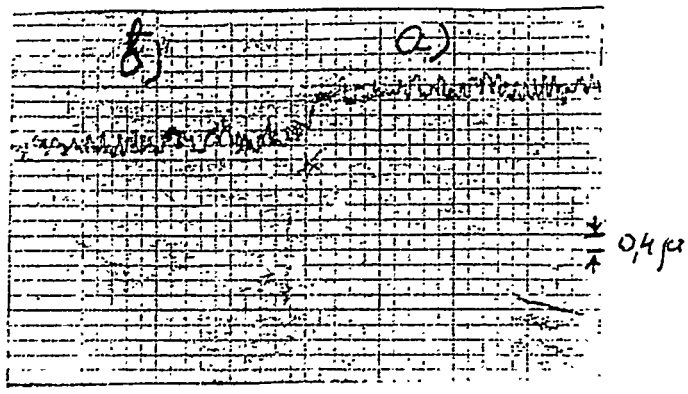
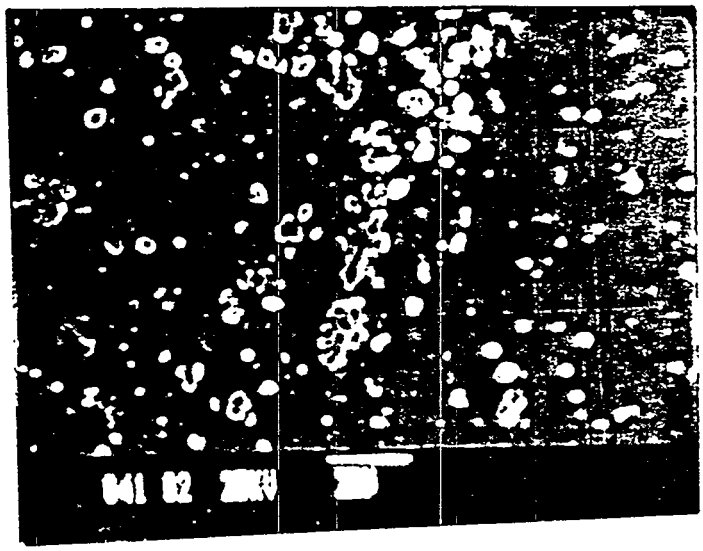
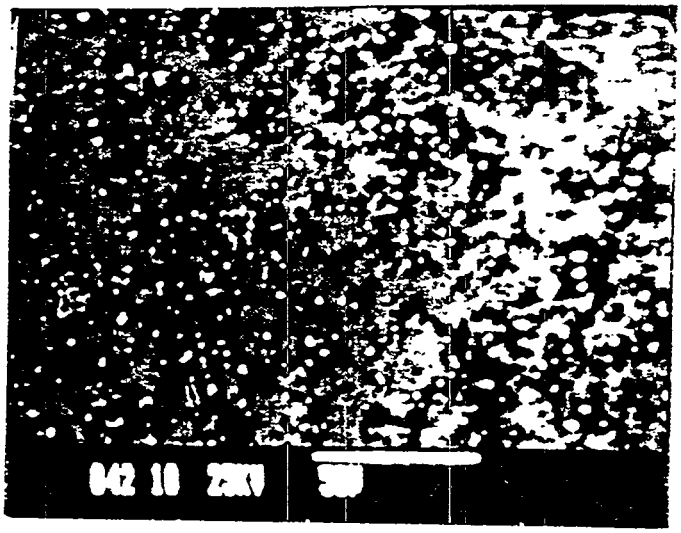


Fig. 2 Typical section of a profilogram of the surface of a samle: a) after electrolytic etching (12 sec); b) after ionic cleaning in argon (t = 1 hour).



a)



b)

Fig. 3 Microphotograph of the structure of the sample's surface taken through a scanning electron microscope: a) after electrolytic etching, X500; b) after ionic cleaning (t = 1 hour, U = - 800 V), X500.

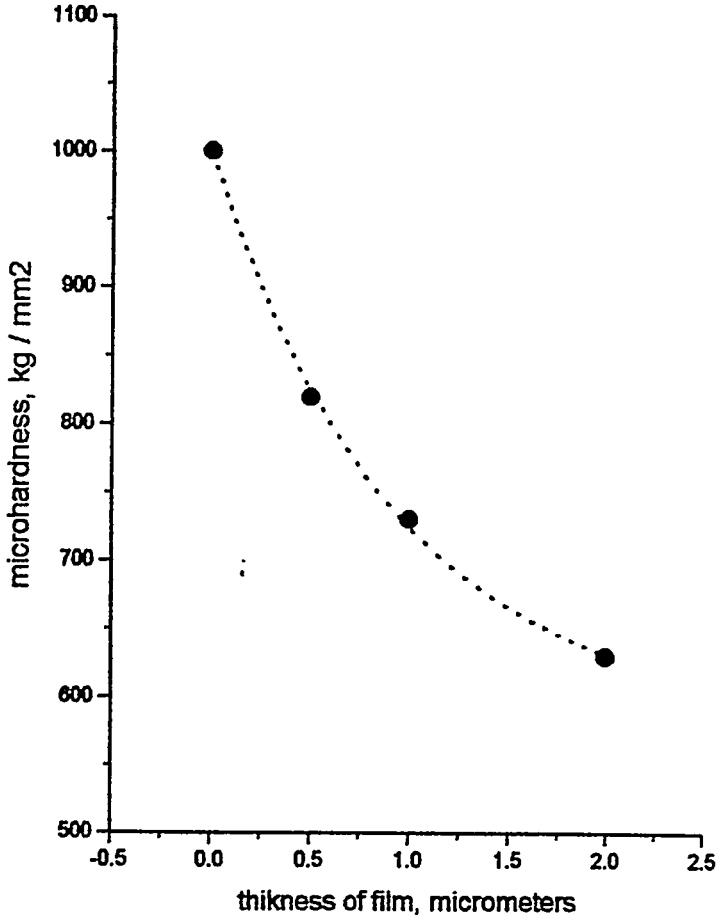


Fig. 4

Microhardness of the samples vs thickness of the titanium film.

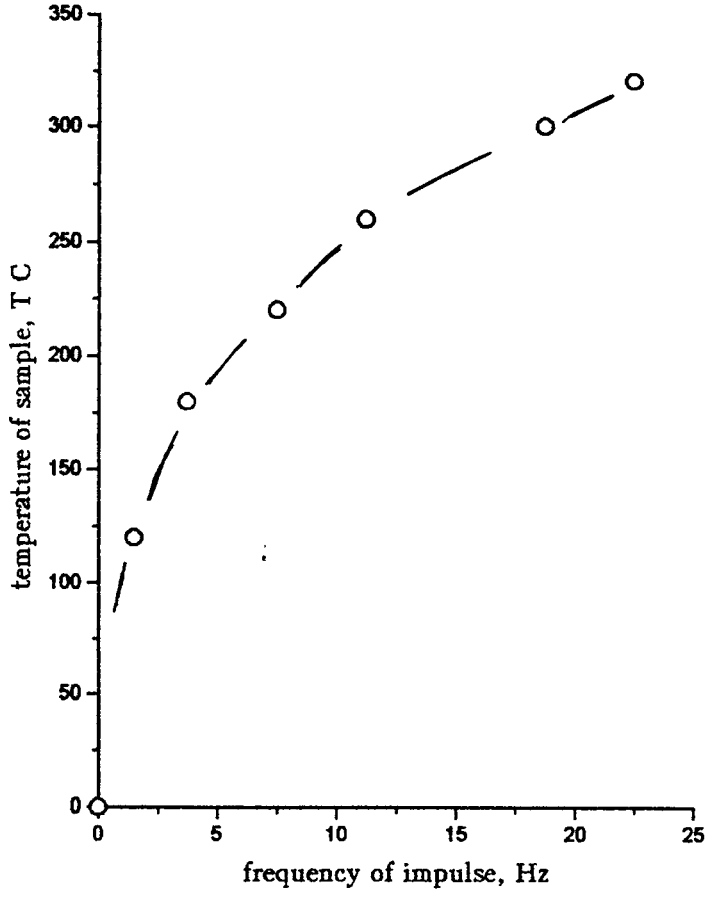


Fig. 5

Temperature of the samples vs frequency of impulse.

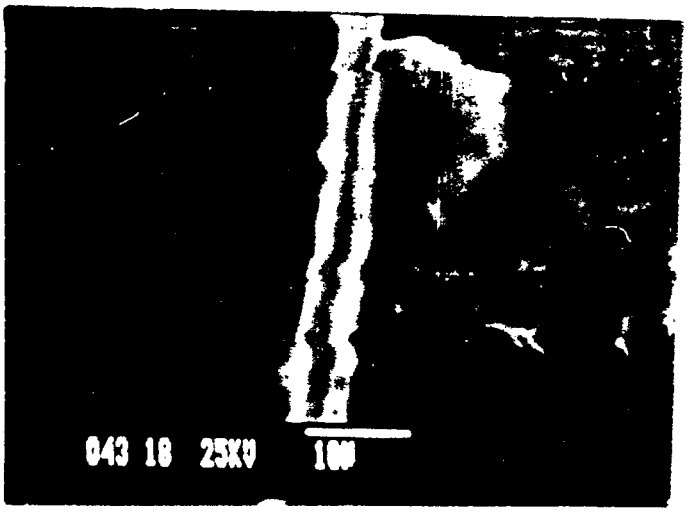


Fig. 6 Microphotograph of the fracture of a sample with the DLF taken through a scanning electron microscope. X 1500

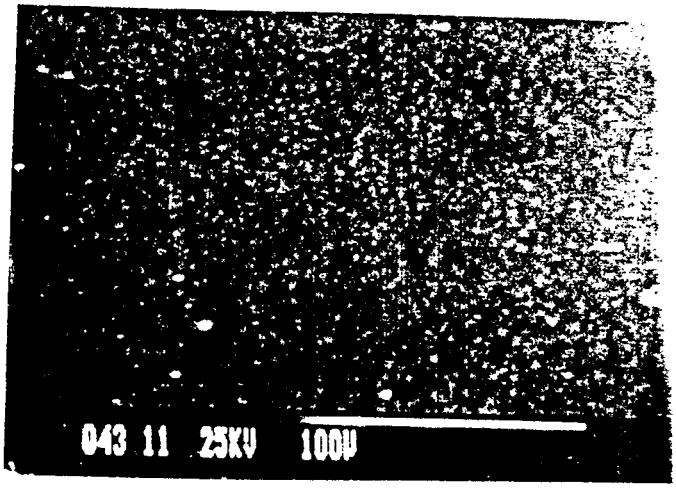


Fig. 7 Microphotograph of the surface of a sample with the DLF taken through a scanning electron microscope. X500

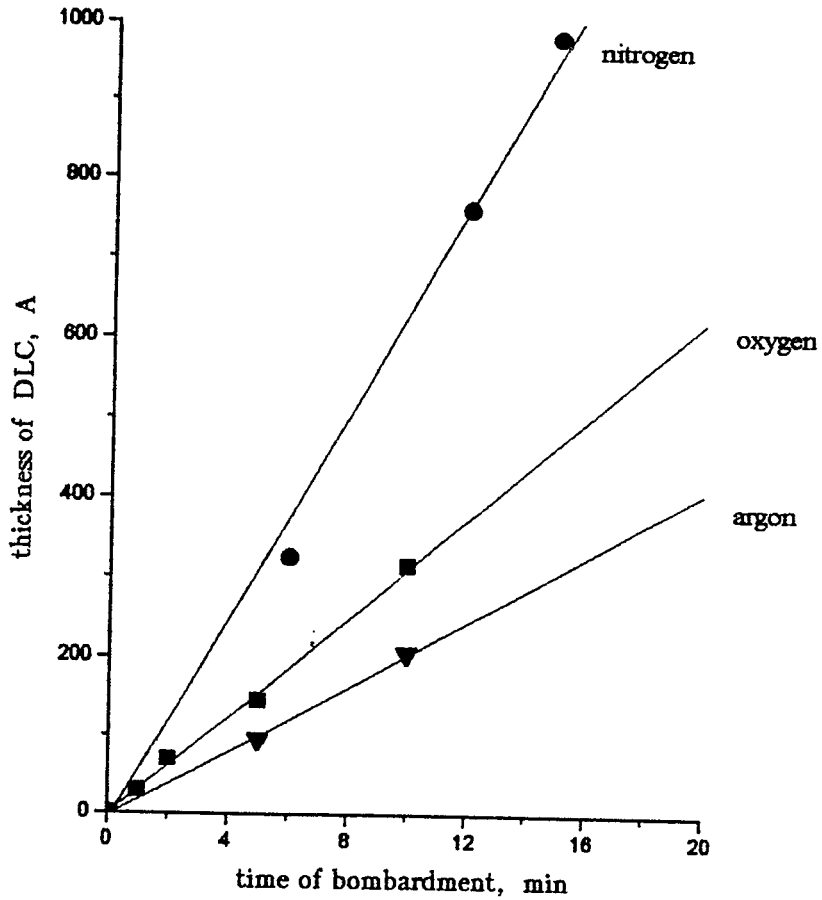


Fig. 8

Variation of the DLF thickness as a function of the time of bombardment with gas ions (● - nitrogen, ■ - oxygen, ▶ - argon). Pressure = $4.2*10^{-2}$ Pa, I =10mA.

Project Title: Multilayer coatings composed of alternating layers of Cu/Fe (Copper/Iron) and Cu/TiC (Copper/Titanium Carbide).
Principal Investigator: Anatol Demchishin
Paton Electric Welding Institute
Kiev, Ukraine
AM-7675

CLAUSE 1 - STATEMENT OF WORK

Tasks:

The Contractor shall:

1. Provide a report detailing previously obtained information about the relationship between the microstructure and mechanical properties of microlaminated materials.

2. Provide four (4) samples of each of the following materials:

Cu/Fe multilayered structures with different thickness of microlayers (0.1 - 10(m), and

Cu/TiC multilayered structures with the different thickness of microlayers (0.1 - 10(m).

NOTE: The samples shall be 4cm in diameter and between 2-5mm thick.

3. Conduct tests (1) investigating the relationship between the microstructure and mechanical properties of the Cu/Fe and Cu/TiC systems, (2) investigating the microstructure of the Cu/Fe and Cu/TiC systems using transmission electron microscopy and x-ray diffraction, and (3) measuring the microhardness of all samples. Provide a letter report of all results.

4. Provide a final report that provides data analysis and conclusions from all work performed herein.

Document No AM-7675
Report on the Task 1 of the Clause 1
May 31, 1995

Microlaminate materials -- a structure and mechanical properties.

INTRODUCTION

A progress, achieved in the technology of the thin film production, allowed to produce a new class of materials -- composite micro laminated structures with the alternating thin layers of different components. Such structures have unique mechanical, electric, magnetic and other properties. This type of materials is widely used in a practice -- from the clarifying or reflective optical coatings to the independent class of thin film materials applied in the microelectronics and computing technique.

There are some methods of producing such type of composite materials: an electrolytic deposition [1], a pack foil rolling [2], a pack sheet melt impregnation [3], a vapour phase condensation of materials in vacuum [4].

The physical processes of an evaporation with the subsequent condensation of substances in vacuum have the widest possibilities in the production of microlaminated materials. PVD vacuum techniques allow to construct the material by means of the regulated assembling of separate atoms and, therefore, knowing the program of this assembling it is possible to fabricate the materials with in advance planned structure and properties.

Depending upon the layer structures and the interlayer boundary type the microlaminated materials can be divided on:

-composites with sharp interlayer boundaries and randomly oriented crystallites (for example Nb/Ge);

-composites with the sufficiently clear interlayer boundaries but the layers are epitaxialy connected with each other (for example Nb/Cu);

- composites with the relatively fluent change of a component concentration across the thickness of layer (for example Ni/Cu) [3,4,5,6] (Fig.1).

The thickness of microlaminated materials may range from hundredths to hundreds micrometers. In case of application of the condensed compositions as protective, strengthening or construction coatings the laminate thickness changes from tenth fractions to tens micrometers.

A great number of multylayered composite materials were created during solving a problem of an increase of a real strength of solids [2,3,7,8]. Such structures have unique mechanical properties that are to be different of the bulk material properties [9].

The basis of the structural strengthening is a formation of the interphase and intercrystalline interfaces that are to be the most effective barriers for the dislocations. A creation of dislocation barriers and regulation of distances between them allow to control the strength and the plasticity of film type materials. Because of that material condensation in vacuum are of great interest since the crystallization in that case take place in conditions of high supercoolings and supersaturations. As a result the polycrystal films contain at certain conditions practically all known defects of crystal structure, have an ultrafine microstructure and their strength considerably exceeds the strength of bulk materials. A possibility to control the density and the type of defects within the wide range and, as a consequence, the level of the obtained strength creates good prospects for the wide application of film compositions as the engineering materials and protective coatings.

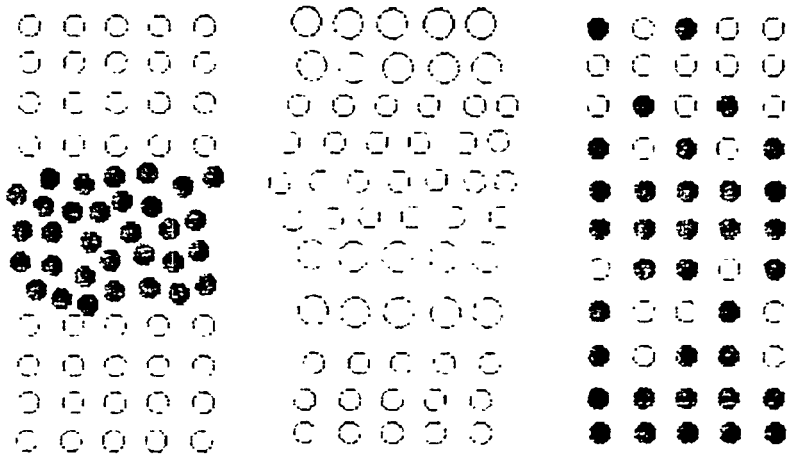


Fig. 1. Schematic representation of degree of order in various classes of layered materials.

The perspectiveness of microlaminate materials as a new class of materials is beyond of doubt. However their application is limited because it is not known what sings and ratios of components have to be used in order to combine the material pair properties for the achievement of the maximum strengthening. Little is known about the deformation mechanism and the phenomena that define their properties.

FABRICATION METHODS OF MICROLAMINATE COMPOSITIONS

The main requirements to components of the produced microlaminate compositions are as follows: the absence of the mutual solubility of the components in a solid state, the substantial difference in mechanical characteristics, the high stability of properties for the strengthening component, the high interlayer adhesion [10]. Hence the various methods are used for the fabrication of microlaminate compositions.

- The production of the microlaminate materials by means of a pack foil rolling:

3-5 layered films with laminate thickness up to 0.01 μm were obtained with this method. The technique for preparing of multilayered films consisted of the following steps: a 10 μm thick aluminum foil was placed between two copper sheets of the 1 mm thickness each of ones. The three layer pack was rolled up to 20 μm thickness. After that operation the thickness of the aluminum lamina was reached 0.1μm. If it was necessary to obtain the 0.01 μm aluminum lamina thickness then the 20 μm thick copper -- aluminum -- copper pack was placed once more between 1 mm copper sheets and the cycle was repeated.

3 - layered Al - Au - Al foils were produced by the same technique.

The rolling was made with the slow speed and the billet temperature did not exceed 30°C in order to prevent the formation of the alloy. Attempts of the production of the thinner films were unsuccessful. The reason was because of the fragmentation of the continuous layer to the islands under the influence of the tension force and residual stresses. The thinner film the lower temperature of the fragmentation is beginning. The small islands have the polygonal shape that indicate on the fragmentation in a solid state [2,11-22].

There are reports about the fabrication of layered composite materials by means of a pack sheet melt impregnation [3].

- The production of the multilayered structures by means of an electrolytic deposition: the multilayered structures can be produced by means of the impulse electrolytic deposition from one and the same electrolyte. This technique is based on the phenomenon that the balanced potentials of reduction of many metals are of a great difference. The non-magnetic elements (copper, silver, gold, et al) are deposited at very small negative potentials of a cathode, whereas the magnetic metals (iron and the elements of its group) are deposited at the relatively high negative potentials. The potential difference during the deposition of the magnetic

and non-magnetic materials can reach 600 mV and still more. The Ni/Cu and Co/Cu structures were obtained in such a way - a composition gradient at the interlayer boundary has a sufficiently sharp change. The total composite thickness was 15 - 20 um, the laminate thickness -- some tens of nanometers. The deposition was produced during -- 20 hours [1].

- The production of the multilayered structures by means of a material condensation in vacuum: the method of the vacuum deposition allows to make the multilayered condensates practically of any combinations of metals, alloys and non -- metals within the range of the composition and the physical -- mechanical properties, to produce multilayered coatings and foils including the hardly deformed materials. The productivity of this technique and the spectrum of materials used for the fabrication of multilayered compositions by this method considerably exceed all the rest methods. So the method of the material condensation in vacuum is the most prospective one for the production of the microlaminated materials.

THE PRODUCTION OF MICROLAYERED STRUCTURES BY MEANS OF THE MATERIAL CONDENSATION IN VACUUM.

The evaporation and sputtering of materials with the subsequent condensation in vacuum are the physical vapor deposition processes. The aim of this technique is the formation of thin films or coatings.

When evaporated in vacuum the material is heated in a crucible by means of radiation, eddy currents, thermal effect, electron beam bombardment, laser beam or electrical discharge [23]. The method of a direct evaporation is the most universal one. The evaporation is carried out from one or several independentevaporators. The vapors are condensed then on the substrate with a zero potential. The perfect method of heating to be considered for the material evaporation in vacuum is an electron beam bombardment.

Considering the structural elements of PVD materials it should be noted the possibility of a direct synthesis of intermetallides and refractory compounds such as TiC, SiC by means of independent evaporation of initial constituents and subsequent condensation of vapor flows on the heated substrate. The lower synthesis temperatures are observed when being deposited compared with the bulk compound formation temperatures during pressed powder sintering of initial

substances. For example the condensates with the TiC structure are formed during deposition of titanium and carbon vapor flows at the 650°C substrate temperature. Microlaminated condensates which are consisting of the alternating micron or submicron lamellae of different metals non-metals belong to materials with untraditional structural elements. It is possible to vary within the wide range the properties of microlaminated systems by means of a material and thickness lamella option and by keeping of physic-chemical conditions of compatibility including a satisfactory adhesion between the interphase surfaces.

When sputtered in vacuum a material-target with the solid surface is bombarded by the gas ions generated in a glow discharge and the separate atoms or atom clusters of the target material are knocked out and deposited on the substrate Ions of different elements are used for the ion bombardment of a target including ions of the material target. The ion gives the part of its energy to the atoms of a crystal lattice at a moment when it strikes the target surface. The sputtering of the material surface takes place when the ion energy exceeds some threshold value. The sputtering is accelerated as the ion energy is increased. The main amount of sputtered particles are the neutral atoms. A fraction of the charged particles is about 1% [23-26].

The main attention is paid to the deposition rate when being considered the item of the PVD application. The deposition rate during the evaporation is on some orders more than that during the sputtering. Methods of physical vapor deposition of metallic and non-metallic materials allow to obtain the microlaminated composites consisting practically of any combination of the alternating laminates: metal-metal, metal-oxide, metal-carbide, metalboride, ets.

Microlaminated condensates are produced by turn electron beam evaporation of components from crucibles and their vapor deposition on the substrate [27].

Another method of production of microlaminated coatings and foils is a simultaneous electron beam evaporation of constituents out of separate crucibles. Initial materials are either the ingots or the sintered powder billets of a cylindrical shape that are placed into the water-cooled copper crucibles. Water-cooled rods push the evaporated materials in order to feed the liquid metal bath. The two sources of the evaporated materials are separated by a water-cooled vertical shield hat separates the vapor flows and prevents intermixing of the two vapors. The vapors are condensed onto a rotating disk type substrate located above the shield. In case of the multilayered foil production the substrate is preliminary coated with the layer of an antiadhesive material that ensures the easy separation of the condensate from the substrate. The substrate is heated by a scanning electron beam from the back side and its temperature is measured in calibration runs using a

thermocouple welded onto its surface. The volume fraction of each material is controlled by adjusting the evaporation rate of the respective material, and the individual layer thickness is controlled by adjusting the rotation speed of the substrate in the range of 0.05-200 revolutions per minute. The method allows to deposit the multilayered coatings onto the different wares. In this case the holders of the appropriate machine parts are mounted instead of the substrates in a vacuum chamber [28]

In case of the multilayered condensate fabrication with the alternation of three or more components the electron beam evaporation is made with the application of the programmed capacity control of the electron beams directed onto the crucibles. In such a case one of the electron beam gun is working in an evaporation regime and the rest ones -- in a heating regime. After the expire of the given by program time the capacities of the electron beams are switched over and the next component is evaporated and so on. The sun total of such switchings determines the laminate thickness and succession of their alternation within the fabricated multilayered composite [29].

The method of the microlayered condensate production by means of the simultaneous component evaporation from two crucibles and subsequent deposition on the stationary substrate through the window of a rotating shutter is described [30].

COMPOSITION, STRUCTURE AND MECHANICAL PROPERTIES OF DEPOSITED MICROLAMINATES.

Microlaminate compositematerials offer potential as high strength high toughness material with isotropic properties in the plane of the sheet. In view of these mechanical properties, microlaminates have been extensively investigated in recent year to establish their structure-property relationships.

The microstructure and composition profiles of the deposits were studied in most cases with the use of combined methods: by optical micrography, scanning electron microscopy, X-ray diffraction and electron microprobe analysis [31-35].

The researches have allowed to investigate the layer microstructure, the interlayer composition gradient, the diffusion coefficients of elements in the process of annealing.

The thickness of the EB PVD microlaminated composites was varied in the range of 10-100 μm. The mechanical trials of films are substantially differed from the analogous tests of bulk materials. The film samples for tensile tests are usually cut

in the shape of rectangular ribbons. Their sizes have to be similar to the standard ones. The necessity of the use of films with the uniform thickness stipulates the application of tension specimens with the small gauge length. In the case of films under discussion tensile tests were carried out on specimens cut from the deposited sheets that were 2-4 mm in width and 6-15 mm in gauge length [36,37]. If being properly carried out tensile tests of the plane samples should be made under several main conditions: the registration of the small efforts and deformations, the reliable fastening of specimens in claws without their damage, the thorough centering of claws, the low rate displacement (shift) of movable claws [30,38].

The strengthening features of microlaminated composites have not obtained yet the synonymous interpretation. According to Ashby's model [39], the strain rate is increasing substantially in two-phase system that have a different deformation ability of the constitutive phases. As a result the deformation gradients with the wave length equal to the interphase distance are formed. The presence of a such situation is led to the accumulation of the so-called geometrically necessary dislocations (g-dislocations). Their density is determined by regimes of a joint deformation of the heterogeneous phases. The defects are different from the statistically accumulated dislocations (s-dislocations) stipulating the deformation strengthening of monocrystals. The density of g-dislocations that are generated during the plastic deformation is determined by the geometric distance of sliding (λ). This parameter is a structure feature of the material and does not depend on the plastic deformation. For the heterogeneous materials the value is determined by the distance between the strengthening phases. This parameter is similar to the slide length (Λ) of s-dislocations in homogeneous crystals. When $\lambda \ll \Lambda$ (i.e., λ is less than some microns) it ought to wait the substantial influence of that parameter on the processes of the dislocation accumulation and therefore on the strengthening. The total dislocation density is determined by the summary quantity of dislocations of both types. An amplitude of internal stresses created by dislocations is limited with transversal sliding processes. Therefore the long distance stresses determine strengthening at about 1 - 2% deformations and after that their value does not change substantially. The strengthening effect of the thin films deposited on the surface of a crystalline substance comes to the two main mechanisms: a fastening of the dislocation surface sources and a suppression sliding by means of the barrier creation preventing a way out of dislocations on the crystal surface. The efficiency of the film as a dislocation barrier depends on the difference of elastic constants of a film and a crystal -- substrate, film strength and its structure [40]

The strengthening features can be observed taking as an example a composite which consists of an electropolished copper foil coated with chrome at both sides.

The thickness of the copper foil and the average grain size were 20±3 μm and 12±2 μm respectively. The thickness of the chrome coating (h) was varied from 0.02 to 1.3 μm, that corresponds to the volume content of chrome from 0.2 to 13%. In this case next meanings of composite mechanical properties are obtained:

h, μm	0	0.05	0.08	0.3	0.5	1.3
YS, MPa	36	37	43	60	95	150
UTS, MPa	80	185	190	205	210	185
δ, %	20	16	13.5	12.5	11	4.5

An increase of the Cr coating thickness h from 0.02 to 1.3 μm leads to the considerable change of properties.The yield strength grows up more than 4 times, the elongation is decreased in 4.5 times [41,42].

A tension diagrams show that a cracking of the chrome surface films starts at 0.7-0.9% relative elongation. Correspondent stresses are 1.7-2.2 GPa that considerably exceed the strength of the bulk material and this phenomenon is typical for the thin condensated layers [8].

The main reason of the substantial increase of composite yield stresses is a high strength of chromium films

X-ray studies of non-deformed samples revealed considerable compressive stresses in surface chrome films which are decreased with the growth of the film thickness. The value of compressive stresses reaches 1.3±0.2 GPa for 0.08 μm thick films. When the thickness of the deposited chromium films was increased up to 0.5 μm the values of compressive stresses were decreased up to 250±50 MPa. This is related to the stress relaxation at the expense of a substrate deformation (the copper foil). At the same time when the thickness of the chromium films reaches ~ 0.1 mm the values of copper foil yield stress don't depend on the film thickness and grow up on 20% in comparison with the uncoated copper foil [42].

The investigation of the coper foil with the double-sided chromium coating was fulfiled in order to study the influence of the interphase surfaces on the deformation processes [41].The foil thickness was varied within the range of 5-300 μm and the chromium film thickness from 0.05 to 1.5 μm that corresponds to the 1-2% volume content of chromium. Metallographic studies have shown that the average grain size is close to the foil thickness. The average yield stresses of coated and uncoated foils were determined. A considerable increase of a yield stress starts at the ~ 50 μm thickness of a coated foil. For the foil with the 5 μm thick coating the values of yield stress reach 80 MPa and for the uncoated foil -- 40 MPa. Thus the considerable contribution of interphase boundaries is revealed within the range of 5-50 μm thicknesses of a coated foil and these boundaries are the effective barriers to the moving dislocations.It means that the composite

resistance to the deformation can substantially exceed the value calculated according to the additivity ratio. This effect increases with the decreasing of the composite layers thickness.It is revealed under condition of a substantial difference of elastic characteristics and yield stresses of layer components and also of a good adhesion between them.

The structure and properties of the multilayered composites are determined by the two main parameters:a volume content of the strengthening phase and the thickness of the constitutive layers.For example,the ultimate tensile strength and microhardness of the multilayered Ni/SiO composite grow up as the volume content of the strengthening phase is increased. The volume fraction of the strengthening phase was varied by means of a change of the SiO layer thickness from 0.02 to 0.8 μm (Fig.2). A maximum SiO content was limited because of the brittleness of the multilayered composites [8,13,44].

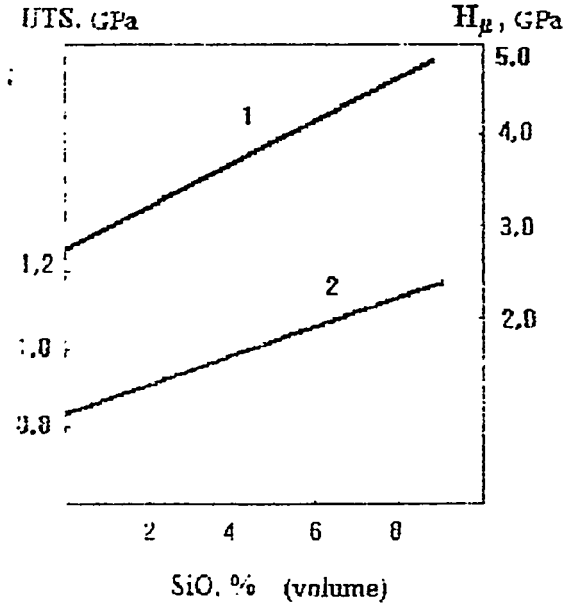


Fig.2. Dependence of the microhardness (1) and UTS (2) of the Ni/SiO microlayered composites on the volume content of the strengthening phase.

The strong dependence of strengthening characteristics on the laminate thickness is the feature of microlaminate composites. For example the strengthening characteristics of the Cu/Cr composite are increased in 7 times (a yield strength and microhardness) when the copper layer thickness is decreased from 12 to 0,1 μm. A thickness decrease of the composite laminates results in reducing of plasticity. The values of the ultimate tensile strength and yield strength practically

coincide when the laminate thickness of copper is equal to 0.1 μm [45]. The structure investigation of microlaminate composites has shown that a decreasing of the laminate thickness at the constant parameters of a deposition leads to the structure dispersing. When changed the copper laminate thickness of the Cu/Cr composite from 1.5 to 0,1 μm the mosaic subgrain size is decreased almost 6 times. The thickness of the copper and chromium layers was varied in the range 12-0.1 and 1-0.01 μm respectively. The crystallite sizes of laminates in the investigated interval are determined by the layer thickness. The structure dispersing in composite materials starts at considerably layer thickness (≤10 μm) in comparison with the single layered condensates (≤2 μm) [45].

The substrate type and the character of its bond with the deposited film substantially influence on the structure of the formed layers [46-48]. The bond increasing of adsorbed atoms with a substrate leads to decreasing of the nucleus critical sizes and increasing of the density nucleation. Therefore at the consecutive deposition of copper laminates onto the chromium laminates that have more fine structures and a strong adhesion with copper the processes of crystallite growth can be considerably delayed in comparison with the films deposited onto the neutral substrates. The dislocation nets formed on both interphase surfaces limit the mobility of crystalline boundaries during a condensation and a subsequent heat treatment of the microlaminate composites. The characteristic feature of the Cu/Cr composites is a high structure stability after an annealing. The annealing of the Cu/Cr composites at 500°C practically does not influence on the structure of the 10 μm thick copper layers. The similar heat treatment of the single layered copper films leads to a quintuple grain growth (from 0.5 to 2.5 μm).

Changing the type of the interlaminate interfaces and the laminate thickness of composites it is possible to control the structure and properties of multilayered composite materials.

The high temperature stability of the multilayered composites is determined by the stableness against the mutual diffusion of their components. Otherwise the microlaminated composite turns into an alloy of the appropriate components during the long-termheating at high temperatures. The production of the Cu/Cr composite at the deposition temperatures more than 500°C causes some diffusion dissolution of interlayer boundaries. Composites of the metal-oxide or metal-carbide systems are more perspective in this respect.

The investigation results of the Ni/SiO components and the single layered nickel condensats put on annealing trial up to 700° C show the considerable stabilization of the composite strengthening characteristics. The composites after annealing are 2.5 times stronger in comparison with the single-layered films [44]. The ultimate

tensile strengths of the multilayered composites and the pure nickel films decreased on 20% and 2 times respectively at the 600 C test temperature [44]. The presence of interphase surfaces leads to the suppression of the recrystalization process in nickel laminates of the microlayered Ni/SiO composites. As a result the strength of the nickel laminates in the microlayered Ni/SiO composite is considerably higher in comparison with the strength of the single-layered nickel films. This effect increased substantially with raising the test temperature.

According to the data shown in reference [49] it is possible to control in a wide range the mechanical properties of microlaminated materials by means of a thickness variation of the alternating matrix and high modulus laminates. Three types of microlaminated copper-molybdenum materials of 1.2-1.4 mm thickness were considered. All types of the materials had the same molybdenum laminate thickness -- 1.1 μm. The copper laminate thickness was 1.8, 5.0 and 7.0 μm. The volume fraction of the molybdenum was equal to 0.38, 0.18 and 0.13 respectively. **Figure 3** shows the yield strength (YS) values of these composites, molybdenum and copper films as a function of the temperature.

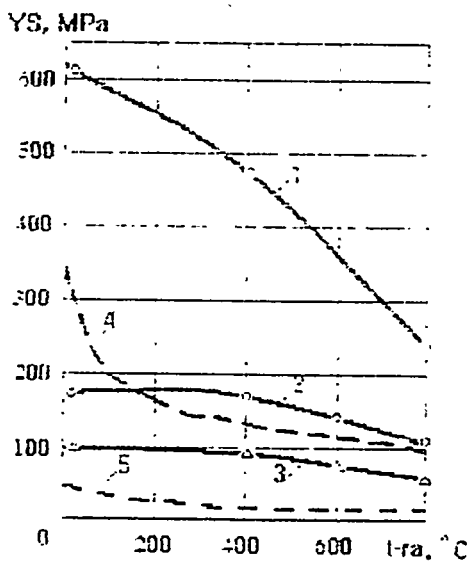


Fig.3. Temperature dependence of the yield strength of the **Cu/Mo** microlaminated composites. The thickness of Mo laminates is constant: 1.1 μm. The thickness of Mo laminates is constant: 1.1 μm. The Cu laminate thickness is variable: 1 -- 1.8 μm; 2 -- 5.0 μm; 3 -- 7.0 μm; 4 and 5 -- YS of the single-layered Mo and Cu films respectively.

As follow from the data given in **Fig.3** the yield strength of the **Cu/Mo** microlaminated material even at relatively small volume fraction of **Mo** (0.38) considerably exceeds the yield strength of the single-layered Mo.

It is determined experimentally that **YS** of the Cu-Cr and Cu-Mo microlaminated materials at a fixed Cu:Cr and Cu:Mo volume fraction ratio of about 0.5 can be presented in such relation:

$$\sigma_{YS} = \sigma'_{YS} + \frac{30 \cdot G \cdot b}{h} \cdot f \quad ,$$

where σ'_{YS}, G and b are the yield strength, shear modulus and Burger's vector of the crystal lattice of high modulus materials respectively, h is the layer thickness and f -- the volume fraction of the high modulus material in the composite. Therefore the high strength of the microlaminated materials can be achieved even at relatively not high values of shear modulus of the high modulus material. It is possible to create the systems without chemical dissociation at high temperatures because of a component mutual diffusion at the expense of a material selection for alternating laminates. By means of a layer thickness adjustment it is possible to minimize the laminate disintegration caused by reduction of an interphase surface total area and the laminate transforming to the more equilibrium shape of polyhedral grains. Multilayered Ti-**Ti-16%Al** condensates were studied in [27]. A titanium has a good plasticity while a **Ti-16Al** alloy has a low elongation at room temperature. A component deposition was fulfiled onto the substrate heated up to 750°C. A mean width of column crystallites in Ti and Ti-16Al layers was 12 and 4 μm respectively. Annealing an 1000°C during 4 hours has led to a diffusion activation, disappearance of a microlaminated structure and formation of a homogeneous solid solution. The microhardness of this composite independently on the layer thickness was within the range of 3800-4000 MPa and it decreased after annealing to 3200-3300 MPa. The ultimate tensile strength increased from 750 to 830 MPa when the Ti and **Ti-16Al** layer thickness were changed from 4 to 22 μm and from 22 to 4 μm respectively while a relative elongation increased from 0 to 4%. Microlayered condensates of such composition have the heightened strength characteristics at room temperature.

Increasing of a pure titanium layer thickness has led to the growth of their plasticity. Simultaneously the thermal stability is inherent in the multilayered composites of such type.

The layer interphase surfaces of heterogeneous materials are effective barriers on ways of the thermal activated dislocation movement in creep conditions. This factor is the reason of a high heat resistance of the multilayered materials [50-53].

Multilayered Fe-Cr-Mo/Cu and Fe-Cr-Mo/BrCr-08 (chromium bronze-0.8) condensates were studied in [51]. The Fe-Cr-Mo layer had a next composition: 22-25% Cr, 4-5% Mo, Fe - the rest. A total thickness of the condensates was 0.9 - 1.2 mm, the laminate thickness -- 0.5-33 mm. The substrate temperature when deposited -- 600 °C.

Copper laminates consisted of the equiaxial crystallites with the grain size being equal to the laminate thickness while Fe-Cr-Mo laminates consisted of the fine columnar crystallites. There were clear marked interlaminate boundaries.

The creep of these condensates was measured as a function of the laminate thickness. The multilayered Fe-Cr-Mo/Cu composites with the laminate thickness of 5 μm had a minimum rate of a steady creep that was equal $2 \cdot 10^{-3}$ 1/h. An annealing at 950°C during 5 hours didn't change the microlayer structure and because of that it was not observed an increase of creep. An improvement of the high temperature strength of the microlaminated vacuum condensates in comparison with the similar properties of the separate components is caused by the barrier effect of the interlaminate boundaries. An interface between the copper and Fe-Cr-Mo phases that have FCC and BCC lattice respectively is an effective barrier for the dislocation movement [51].

Microlaminate Cr/Cu condensates were produced at the substrate temperature of 600 °C. A total thickness of the condensates was up to 0.5 mm while the laminate thickness of the component was varied within the range 0.2-25 μm. Metallography investigations have shown that copper grains have an equilibrium share. The mean grain size changes proportionally to the laminate thickness. Copper and chromium laminates consist of the columnar crystallites. The height of these crystallites quals to the laminate thickness within the range 1-20 μm. A width of the chromium crystallites is almost constant and equals 0.80 μm in the 5-25 μm thickness range. A sharp decrease of the crystallite width up to 0.48 μm or less takes place when the laminate thickness is changed within the range of 0.5-1.0 μm. A width of the diffusion zone between the laminates is about 1 μm. A chromium content in the copper laminates is more than a copper content in the chromium laminates. A fatigue resistance that is determined on the base of $5 \cdot 10^7$ cycles makes 170 MPa for the condensates with the 25 μm laminate thickness and this parameter increases till 220 MPa for the condensates with the 1 μm laminate thickness [52].

It was observed that the ultimate tensile strength and microhardness increased with decreasing laminate thickness of the microlaminate Cr/Cu condensates. The plasticity and creep rate of the Cr/Cu composites decreased with decreasing laminate thickness. The heightened values of mechanical properties were obtained for the limits of 0.5-1.5 μm at the 600 - 700°C testing temperature [52].

Annealing at 1050°C during 2 hours led to formation of a transitional zone of 1.5-2.0 μm thick between the microlayers of a high modulus and matrix phases. A creep rate of the annealed samples tested at 800°C decreased with increasing a molybdenum content. Samples with the 0.20-0.22 molybdenum volume fraction

had the best high temperature strength. In this case the grain size of the Mo microlayer was equal to the microlayer thickness.

The high temperature strength of the microlaminate Ni alloy /NbC condensates was studied as a function of an alloying extent of the Ni matrix microlayers by the Co, Cr, Al, Mo elements [53]. An optimum composition of the matrix microlayers that ensured the maximum high temperature strength at the 800°C testing temperature was found, namely the Ni – 15 Cr – 6 Al – 5 Mo alloy.

An oxidation resistance of the microlayered Mo/Cr condensates was investigated in [54]. The condensates were prepared by simultaneous evaporation of chromium and molybdenum using two electron beam sources. The substrate temperature was maintained at 970-1000°C. The microlayer thickness was varied between 5.0-10μm for chromium and 7-14 μm for molybdenum, with the overall thickness of the deposited sheet ranging from 0.9 to 1.0 mm. The diffusion zone between Cr and Mo microlayers was about 1.5 μm. High mechanical properties and the oxidation resistance of the microlayered coating were observed.

Structure-property relationships in microlaminate Ni/TiC condensates were studied in [55, 56]. The thickness of the composite coating was about 250 μm with the laminate thickness being varied in the range of 0.1-11 μm. Optical and scanning electron micrographs showed discrete layers of nickel and TiC in the composite material and the electron microprobe confirmed the presence of alternating Ni and TiC layers with negligible interdiffusion. It was found that the strength increases with increasing percentage of TiC and the variations in YS and UTS with composition and layer thickness in tests at room temperature and 600°C follow the same pattern.

A hardness is an important characteristic of the microlaminated structures. Microhardness measuring of the microlaminate TiC/TiB2 condensates has shown its dependence on the alternating layer thickness [57]. Maximum values of microhardness were about 31 GPa at laminate thickness 0.8-0.9 μm TiB2 volume fraction was equal 0.5-0.6. A bending strength of the composites had maximum values at the same content of the components.

SUMMARIZING REMARKS AND CONCLUSIONS.

A fabrication of the microlaminate composite materials is a perspective direction of obtaining composites whose mechanical properties can considerably exceed the mechanical ones of the bulk materials. The evaporation techniques allow to program the fabricated composites and consequently the physical-mechanical properties of the created deposited composites. At the same time the greatest difficulties during the practical use of deposited materials are connected with the production of objects with the reproduced and controllable properties.

Strengthening of themicrolaminate deposited materials is based on the formation of the interphase surfaces that are the most effective barriers to dislocations. The PVD techniques allow to adjust a distance between these barriers and thus to

change the physical and mechanical properties of the composite materials within the wide range.

The composites of metal/oxide system have a high thermal stability while the Cu/Cr materials have unique elastic properties and a good electric conductivity. The highly strengthened film composites can be used as functional coatings for the increase of a fatigue strength and wear resistance of bulk materials.

The evaporation-PVD techniques give wide possibilities for the realization of substructures with the unique physical and mechanical properties.

REFERENCES

1. В.М.Федосюк, М.У.Шелег, О.И.Касютич "Многослойные магнитные структуры" - Зарубежная радиоэлектроника, 1990, N5, с.83-97.

2. Копань В.С., Лысенко А.В. - ФММ, 1970, т.29, 3, с.663-664.

3. Гиндин И.А., Сомов А.И., Стародубов Я.Д. и др. - ФХОМ, 1970, N6, с.82-85.

4. Мовчан Б.А., Малашенко И.С. "Жаростойкие покрытия,осаждаемые в вакууме".-Киев: Наук.думка, 1983.- с.

5. Charles M. Falco: Metallic Multilayers and superlattices - 5th General Conference of Condensed Matter Division European Physical Society. Berlin. Germany 18-22 March 1985.

6. Charles M. Falco and Ivan K. Schuler. Artificial Metallic Superlattice. In "Novel Materials and Techniques in Condensed Matter", ed. by G.W. Crabtree and P.D. Vashishta, North Holland, New York, 1983.

7. Пинес Б.Я., Нгуен Саун Тянь.- ФММ, 1965, т.19, N 6, с.899-906.

8. Палатник Л.С., Ильинский А.И.- УФН, 1968, т.95, N 4, с.613-645.

9. Алехин В.П. Физика прочности и пластичности поверхностных слоев материалов.-М.: Наука, 1983. 230с.

10. Ильинский А.И., Лях Г.Е.- Заводская лаборатория, 1978, т.44, N12, с.1507-1511.

11. Копань В.С., Лысенко А.В. "Об электросопротивлении и механических свойствах многослойных композиций на основе меди и алюминия" - Физ.мет.иметалловедение., 1970, т.29, N 3, с.1074-1080.

12. Копань В.С., Лысенко А.В., Клименко А.Г. "Исследование переходной зоны медь-алюминий при холодной сварке давлением."-Вторая Всесоюзная конференция по холодной сварке металлов давлением. -Киев: Изд. Института электросварки им.Е.О.Патона, 1970, с.41-45.

13. Копань В.С., Лысенко А.В. "О механических свойствах многослойных композиций на основе алюминия,меди,олова и кадмия". Физ.мет. и металловедение, 1970, т.29, N 3, с.663-666.

14. Копань В.С., Лысенко А.В. "О влиянии твердых покрытий меди ,кадмия,олова,свинца,цинка и графита на деформирование алюминиевых слоев в многослойных композициях"- Вопросы физико-химической механики материалов.- Львов: Изд.Львовского университета, 1969, с.19-20.

15. Копань В.С., Лысенко А.В. "О некоторых физико-механических свойствах многослойных композиций алюминий-свинец и алюминий графит"- Физика и химия обработки материалов, 1973, N 4, с.104-109.

16. Лысенко А.В. , Копань В.С., Михалко В.Д., "О микро-и макропластической деформации в некоторых двухкомпонентных многослойных композициях на основе алюминия.- Металлофизика, 1973, вып.45, с.34-37.

17. Копань В.С., Майборода В.П., Хорунов В.Ф.и др. "Многослойные композиции никель-медь и медь-пермалой" -Вестник Киевского университета.серия физика. 1974, N 5, с.30-33.

18. Копань В.С., Майборода В.П. "Зависимость механических и магнитных свойств многослойных материалов никель серебро от толщины слоя и состава"-- Металлофизика. 1973, вып.48. с.89-93.

19. Копань В.С., Майборода В.П. "Свойства композитных слоистых материалов сталь-серебро"-- Порошковая металлургия, 1974, N 6, с.40-45.

20. Копань В.С., Майборода В.П. "Прочность слоистых материалов никель-серебро"-- Порошковая металлургия, 1974, N 5, с.81-83.

21. Майборода В.П., Копань В.С. "Свойства тонкослойного проката сталь-медь"-- Известия АН УССР, Металлы, 1973, N 3, с.132-135.

22. Майборода В.П., Копань В.С. "Прочность на разрыв многослойных композиций медь-сталь"-- Вестник КГУ, серия "Физика", 1975, N16, с.9-11.

23. Технология тонких пленок: Справочник. В 2-х т./Под ред.Л.Майссела и Р.Глэнга.-- М.: Сов.Радио,1977-- Т.1. 664с.

24. Каминский М. "Атомные и ионные столкновения на поверхности металла"-- М.: Мир, 1967. 506с.

25. Майссел Л.И. "Нанесение тонких пленок катодным распылением" В кн.: Физика тонких пленок: В 8-и т., М.: Мир, 1968, т.3. с.58-127.

26. Плешивцев Н.В. "Катодное распыление"-- М.: Атомиздат, 1968. 343с.

27. Гречанюк Н.И., Кривасов А.К., Мовчан Б.А. " Исследование структуры и свойств микрослойных вакуумных конденсатов Ti/Ti-16% Al" -- Пробл.спец.электрометаллургии. 1984, вып.21, с.50-52.

28. Щербицкий В.В., Гречанюк Н.И., Кучеренко П.П. "Электронно-лучевая установка для получения многослойных материалов"-- Пробл.спец.электрометаллургии. 1982. вып.16, с.51-53.

29. Бадиленко Г.Ф., Мищенко В.П., Николаев Ю.В. "Получение микрослойных конденсатов на электронно-лучевой установке с применением ЭВМ"-- Пробл.спец.электрометаллургии. 1986. N 1. с.37-41.

30. Ivan K. Schuller and Charles M. Falco, in "Inhomogeneous Superconductors -- 1979", ed. by D.U. Gubser. T.L. Francavilla et al. American Institute of Phisics, New York, 1980.

31. Палатник Л.С., Фукс М.Я., Косевич В.М. "Механизм образования и субструктура конденсированных пленок"--М., Наука, 1972. 320 с.

32. "Электронная микроскопия тонких кристаллов"/ Хирш П.,Хови А. Николсон Р. и др., М.: Мир, 1968. 574 с.

33. Точицкий Э.И. "Кристаллизация и термообработка тонких пленок. Минск: Наука и техника. 1976. 376с.

34. Черемский П.Г., Бурлакова М.В., Ильинский А.И. и др.-Металлофизика, 1980, т.2, N6, с.92-95.

35. Кириенко В.И., Ильинский А.И., Савченко И.А. -- УФЖ, 1980, т.25, N12, с.2056-2058.

36. Донник И.Г. "Механические испытания металлов. М.: Машиностроение, 1962. 150 с.

37. Фридман Я.Б. "Механические свойства металлов"-- Т.2. М.: Машиностроение,1974. 368 с.

38. Ильинский А.И., Лях Г.Е. -Заводская лаборатория, 1978. т.44, N12. с.1507-1511.

39. Ashby M.F. --Phil.Mag., 1970, v.21, N170, p.399-424.

40. Иванов В.Е., Сомов А.И., Тихоновский М.А.-- В кн. "Защитные высокотемпературные покрытия" -- Л.: Наука, 1972, с.291-305.

41. Ильинский А.И., Палатник Л.С., Подтележников А.А. -- ФТТ. 1977, т.19, с.1836-1837.

42. Ильинский А.И. Подтележников А.А. - ФХОМ.1980, N6, с.71-73.

43. Палатник Л.С., Ильинский А.И., Сапелкин Н.П.-- ФТТ.1966, т.8, с.2515-2517.

44. Ильинский А.И., Палатник Л.С., Билетченко Н.М., Синельникова Р.И.- ММ, 1971, т.32, N6, с.1312-1313.

45. Ильинский А.И., Подтележников А.А., Шмыгарев Ю.М.- Металлофизика, 1981, т.5, с.133-135.

46. Тур Р.Э.- В кн.: "Физика тонких пленок":Пер.с англ. М.: Мир, 1967, т.1, с.224-274.

47. Чопра К.П. "Электрические явления в тонких пленках": Пер.с англ. М.: Мир. 1972. 435с.

48. "Поверхности раздела в металлических композитах": Пер.с анг./ Под ред.Меткалфа А.М.: Мир, 1978, т.1. 438с.

49. Мовчан Б.А. "Композиционные материалы.осаждаемые из паровой фазы в вакууме"/ Новые металлические материалы: Сб.науч.тр.- Киев: ИЭС им.Е.О.Патона. 1989. с.34-47.

50. Movchan B.A., Bunshah R.F. "Structure/property relationahips in microlaminate condensates//Proc.the seventh international conference on vacuum metallurgy.--Tokyo, 1982, -P.96-109.

51. Бернадская И.В., Нероденко Л.М., Мовчан Б.А. "Высокотемпературная ползучесть микрослойных конденсированных материалов на основе железа" - Пробл.спец.электрометаллургии, 1985, N4, с.35-40.

52. Смагленко Ф.П., Луговской Ю.Ф., Дидикин Г.Г. " Структура и механические свойства микрослойных конденсатов Cr/Cu при циклическом нагружении"-- Пробл.спец.электрометаллургии, 1989. N 4, с.52-57.

53. Белявин А.Ф., Нероденко Л.М., Мовчан Б.А. "Структура и механические свойства микрослойных жаропрочных материалов системы Ni-Al-Mo" - Пробл.спец.электрометаллургии, 1990, N1. с.52-56.

54. Бадиленко Г.Ф., Мовчан Б.А. "Жаростойкость многослойных конденсатов системы Mo/Cr" -- Пробл.спец.электрометаллургии, 1986, N2. с.39-43.

55. Bunshah R.F., Sans C., Deshpandey C., et al. "Structure-property relationships in microlaminate TiC/Ni condensates". Thin Solid Films, 96 (1982) 56-66.

56. Sans C., Deshpandey C., Doerr H.J.. et al. "Preparation and properties of TiC/Ni microlaminates". Thin Solid Films, 107 (1983), p.345-351.

57. Movchan B.A., Demchishin A.V.. Badilenko G.F.et al. "Structure-property relationships in microlaminate TiC/TiB2 condensates". Thin Solid Films,97 (1982) 215-219.

Project Title: Functionally Graded Interfaces for the Enhancement of the Performance of Hard Coatings on Austenitic Stainless Steel and Titanium Alloys.
Principal Investigator: S. P. Bugaev
High Current Electronics Institute
Tomsk, Russia
AM-7676

CLAUSE 1 - STATEMENT OF WORK

Objective:

The objective of this work is to improve the performance of diamond titanium nitride (DTN) films by modifying the substrate material on which they are deposited. The substrate modification will be carried out using a unique high flux, low energy ion beam source developed by the Contractor.

Tasks:

The Contractor shall:

1. Provide a report that describes:
the ion source that will be used in the experiment
work that has already been performed using the ion source for surface modification, and
previous work that has been performed to enhance the adhesion f TiN (titanium nitride) coatings.
The report shall also include references to published literature.

2. Perform surface modification experiments in accordance with the following specifications:
implementation doses shall range from 1016 atoms/cm3 to 1017 atoms/cm3
N shall be implanted into Ti alloys - (The Contractor shall choose the alloy to be implanted.)
Ti and N shall be implanted into stainless steel. Sandia and the Contractor will jointly determine the type of stainless steel early in the Contract performance.
The microstructure of the modified samples shall be analyzed using transmission electron microscopy.
Hardness of the surface shall be measured.

The Contractor shall provide a report of the experimentation data and results.

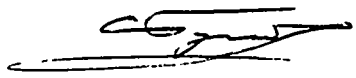
3. Coat modified surfaces in accordance with the following specifications:
Titanium Nitride coatings shall be deposited using the vacuum arc technique
the micro-hardness of the samples will be measured

The Contractor shall provide six (6) samples of the material, and a final report analyzing all experimental results.

FUNCTIONALLY GRADED INTERFACES FOR THE ENHANCEMENT OF THE PERFORMANCE OF HARD COATING ON AUSTENITIC STAINLESS STEEL AND TITANIUM ALLOYS

Scientific Report

according to contract number AM-7676 on october 1994

Principal Investigator  S.P. Bugaev

professor

Tomsk 1994

List of the participants

in the experimental and theoretical investigations

High Current Electronics Institute, Tomsk

1. P. M. Schanin — professor
2. N. N. Koval' — senior scientists
3. D. P. Borisov — post graduate
4. G. Yu. Yushkov — scientist worker
5. A. V. Visir' — jr. scientist worker
6. A.G.Nikolaev — jr. scientist worker

Siberian Phys-Technical Institute, Tomsk

1. A. D. Korotaev — professor
2. A. N. Tyumentsev — professor
3. Yu. P. Pinzhin — senior scientist

1 Equipment for metallic surface modification

The progress in new technologies for the surface modification of construction materials through ion implantation stimulates the refinement of the available ion sources and the development of essentially new devices of this type. In "metallurgical" implantation, as distinct from the ion implantation into semiconducting materials, the requirements on the ion beam purity are substantially reduced; however, ion beams of high current density therewith are needed to produce the necessary exposure dose $\sim 10^{16} - 10^{17}$ cm^{-2}. On the other hand, the emission current of these ion sources is lower compared to those used for heating the plasma in thermonuclear reactors, and the sources in theirselves must be simple, reliable, adaptable to manufacture and service, in order that the required ion beam parameters be provided along with the low cost of the source.

To produce gas ion beams, various types of low-pressure discharge can be used. However, the highest gas ion beam current I_i per unit power (with the total power P_i deposited into the discharge system) is produced by arc-based ion sources, notwithstanding their specific design features (Fig. 1). To make the production of ion beams in such systems more efficient, conditions are generally created in the discharge system such that electrons could oscillate in an axial magnetic field localized in the region of a hollow anode.

A vacuum-arc cathode spot has in fact an unlimited emissive power and, despite the high current density [1], it operates overall on a cold cathode surface. This is why such generators are insensitive to the increase in pressure related to an emergency gas bleed-in and show rather high efficiency (up to an ampere of ion current per a kilowatt of power deposited into the discharge system). A cathode spot ejects directed plasma jets consisting of the cathode material [2]. The ion current of all species present in the anode plasma of a vacuum arc is about 8% of the total arc current, which is generally of the order of 10^2 A [3]. Owing to the above peculiarities, the vacuum-arc-based metallic ion sources are used more extensively as compared to other known types of source [4].

However, in designing vacuum-arc sources it is necessary to solve a number of essential problems. For the pulsed operation of the source, stable initiation of vacuum-arc cathode spots for a long time must be ensured since this process determines the continuous operation time for an ion source. The widely used technique for the initiation of a vacuum arc by a discharge over a dielectric surface seems to be able to ensure stable operation of the source within 10^6 pulses. However, the use of backup cathodes, like in the type MEVVA [4] and Raduga [5] ion sources, may extend these limits. A promising technique is the initiation of

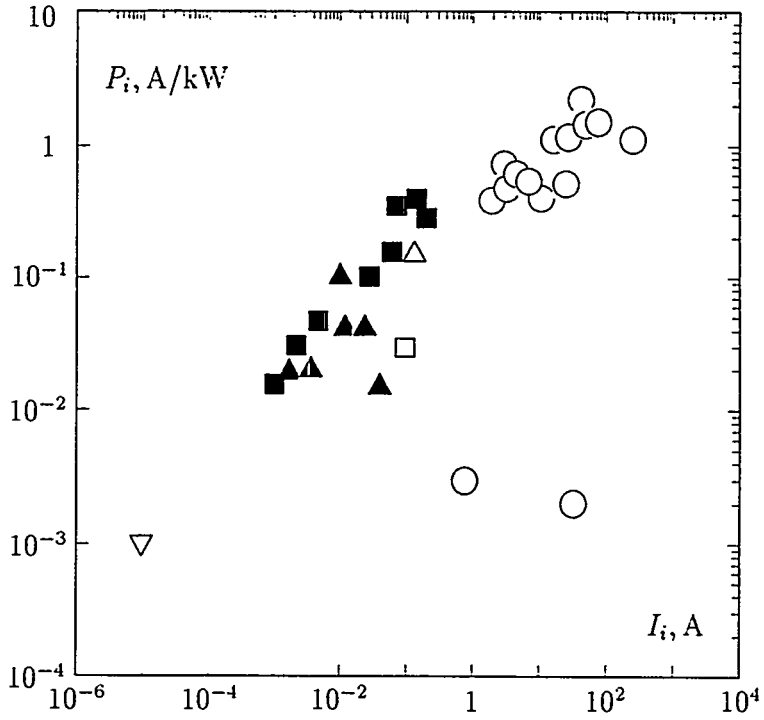


Fig. 1. Energy efficiency of gaseous ion source with an arc discharge (○), a glow discharge (□), a high-frequency discharge (△), and laser ionization (▽). The shaded symbols refer to constant ion sources and the unshaded ones to pulsed ion sources.

an arc by an auxiliary low-current gas discharge whose pulse duration is substantially shorter than that of the main arc. This initiation technique is rather reliable, and the contamination of the metallic ion beam with gaseous ions is insignificant (proportional to the $I_p\tau$ product for the auxiliary discharge). Another problem is concerned with the provision of a uniform distribution of the implanted ion dose over the irradiated surface. However, for wide-aperture beams, the distribution of the ion current density generated by the cathode spot is governed by the $\cos\theta$ or $\cos^2\theta$ law [1]. Therefore, with no influence of the ion source optical system, the ion current density in the beam will obey the same law, i.e., the distribution will be rather far from uniform. Moreover, since for hollow-anode arc discharges at pressures of $10^{-4} - 10^{-1}$ Pa the anode fall potential is as a rule negative, ions may go away from the plasma both to the anode cavity surface and to the plasma electrode, which reduces the efficiency of the ion source.

1.1 The Titan ion source

The Titan ion source combines the principles for gaseous ion production realized in sources of the duoPIGatron type [6] and for metallic ion production in sources of the MEVVA type [6]. This allows one not only to produce gaseous and metallic ion beams simultaneously

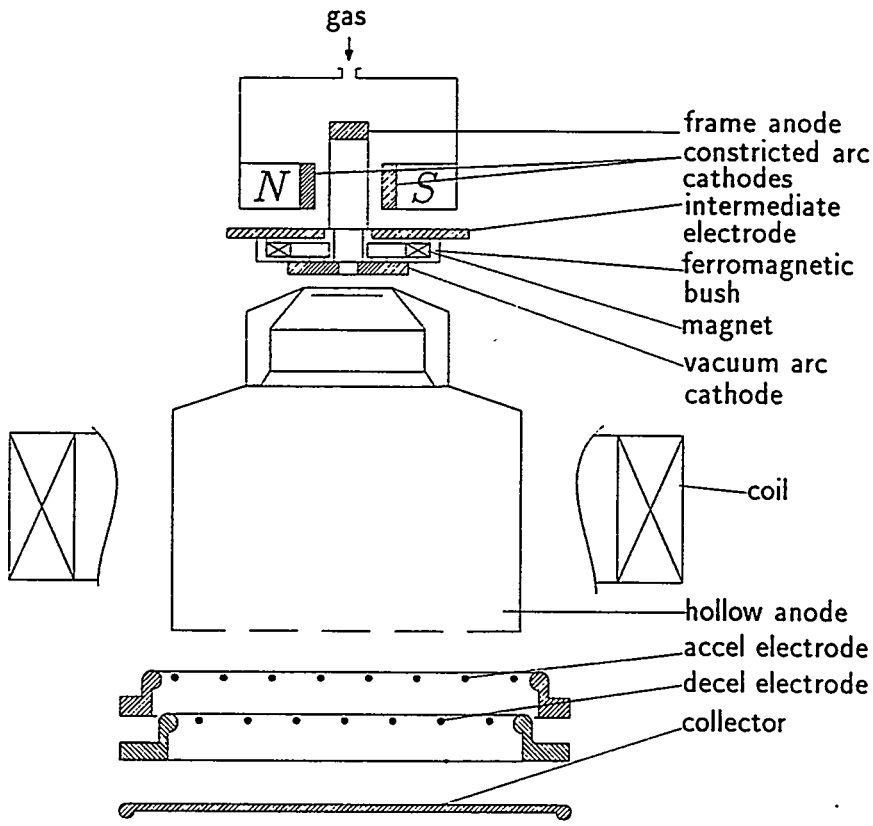


Fig. 2. Electrode system of the ion source.

in a single source but also to solve the problem of stable initiation of vacuum-arc cathode spots at the cathode surface beneath the plasma generated by a 20-μs auxiliary low-current discharge [7, 8]. The continuous operation time of the device therewith is increased to over 10^7 pulses.

1.1.1 The principle of operation of the ion source

The electrode system of the source is shown schematically in Fig. 2. Constricted-arc cold cathodes are placed in a discharge chamber into which a working gas flow is feeded at a flow rate of $10^{-3}-10^{-2}$ Pa·m^{3}s^{-1}. The pressure in the discharge chamber therewith is an order of magnitude greater than the pressure in the vacuum chamber, which in our experiments was $9\times10^{-3}-10^{-1}$ Pa. The cold cathodes are mounted one opposite the other on a magnetic core in which a magnetic flux is produced by arch dc Sm-Co magnets. Between the cold cathodes a frame anode is fixed on the auxiliary electrode. The cathodes and the frame anode form a Penning cell. The auxiliary electrode contains a ferromagnetic insert with a constriction channel of diameter 7 mm and length 10 mm. At the exit of the constriction channel, the vacuum-arc cathode is fixed. The insert serves as a magnetic core for the "arch"-configured

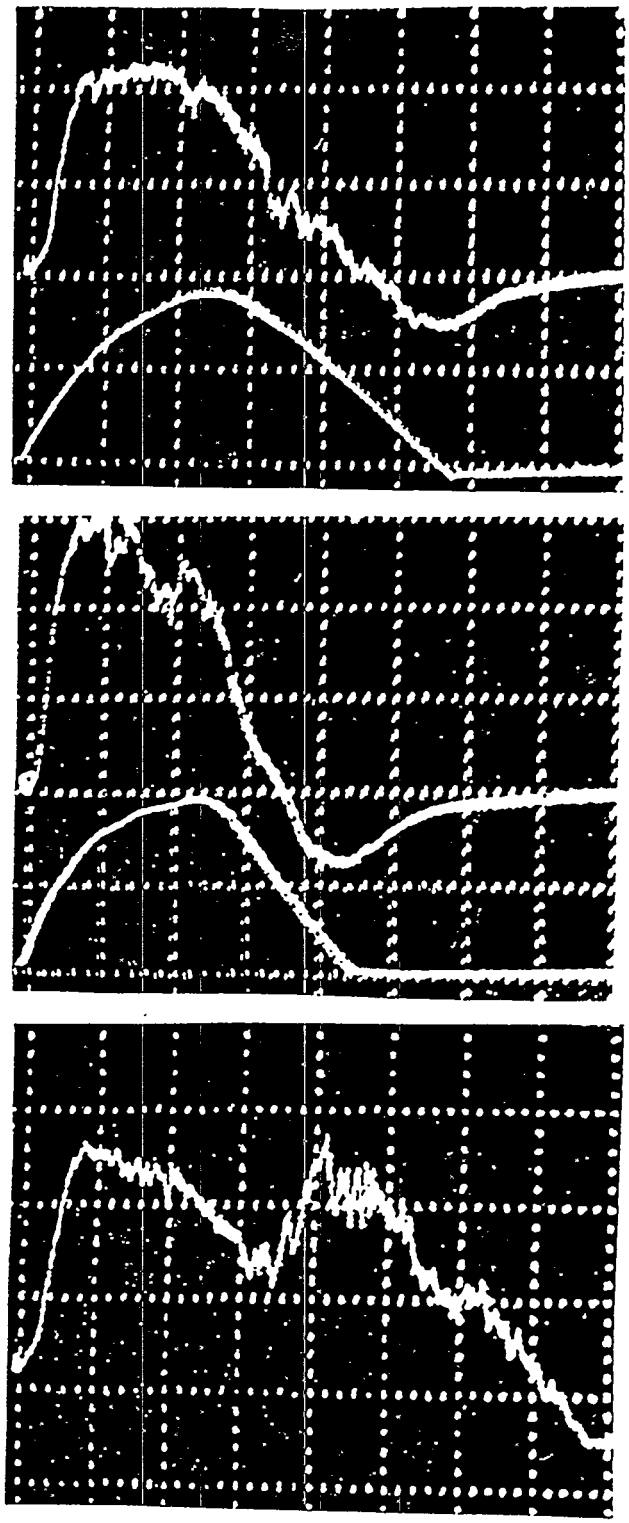


Fig. 3. Current pulse waveforms for the ion beam (upper trace) and the discharge (lower trace) for sources with a constricted arc (*a*), a vacuum arc (*b*), constricted and vacuum arcs (*c*). Scales for: time – 100 μs/div; beam current – 0.2 A/div; discharge current – 10 (*a*) and 50 A/div (*b*). Working gas – argon; vacuum arc cathode – Ta.

magnetic field produced by the Sm-Co ring magnet. The hollow anode common for two discharges is covered on its emission end with a fine grid of diameter 12 cm. The grid and the hollow anode are made of stainless steel. The axial magnetic field in the hollow anode region is produced by a short solenoid placed on the vacuum chamber of the ion source.

Ions are extracted by a dc accelerating voltage of up to 80 kV applied between the hollow anode being at high positive potential and the grounded acceleration electrode. The accelerated ion beam is received by a collector. To cut off the secondary electrons knocked out the ion beam from the collector surface, a dc voltage of the order of 2 kV negative with respect to the collector voltage is applied to the cutoff electrode.

Once an auxiliary discharge has been ignited and a pulsed voltage has been applied between the cold cathodes and the hollow anode, a constricted arc is initiated between them. In the constricted arc, plasma is generated through the ionization of the working gas by the electrons accelerated in the double layer formed at the inlet of the constriction channel. The gas-discharge plasma fills the hollow anode, and ions are extracted from the plasma surface stabilized by the emission grid. Typical waveforms of the currents of a constricted discharge and of the ion beam produced by this discharge are presented in Fig. 3a.

A voltage applied between the vacuum arc cathode and the hollow anode after the ignition of an auxiliary discharge initiates a vacuum arc between these electrodes, and cathode spots are formed on the cathode surface. During the operation of the vacuum arc, the cathode material plasma coming from the cathode spots fills the hollow anode cavity, and a metallic ion beam is produced in the same manner as a gaseous ion beam. Typical current waveforms for this case are presented in Fig. 3b. The location of cathode spots on the cathode surface is stabilized by the "arch" magnetic field.

The constricted arc and the vacuum arc may operate simultaneously or separately. In the former case, the discharges are initiated one after the other, and both gaseous and metallic ions can be produced in a single pulse (Fig. 3c). Since the discharges are powered from independent power supplies and the processes of plasma generation in these discharges are distinct and not interrelated, the density of each plasma species in the hollow anode, and hence the gaseous–to–metallic ion current ratio for the extracted ion beam, can be controlled by varying the discharge currents. To increase the ion current extracted from the discharge plasma, a magnetic field produced by a 20-mT solenoid is applied to the anode region.

The ion extraction system consists of three grids. The first (plasma) grid whose diameter is equal to the diameter of the hollow anode is at the potential of the hollow anode. Two other grids form an acceleration-deceleration system made from metallic filaments stretched

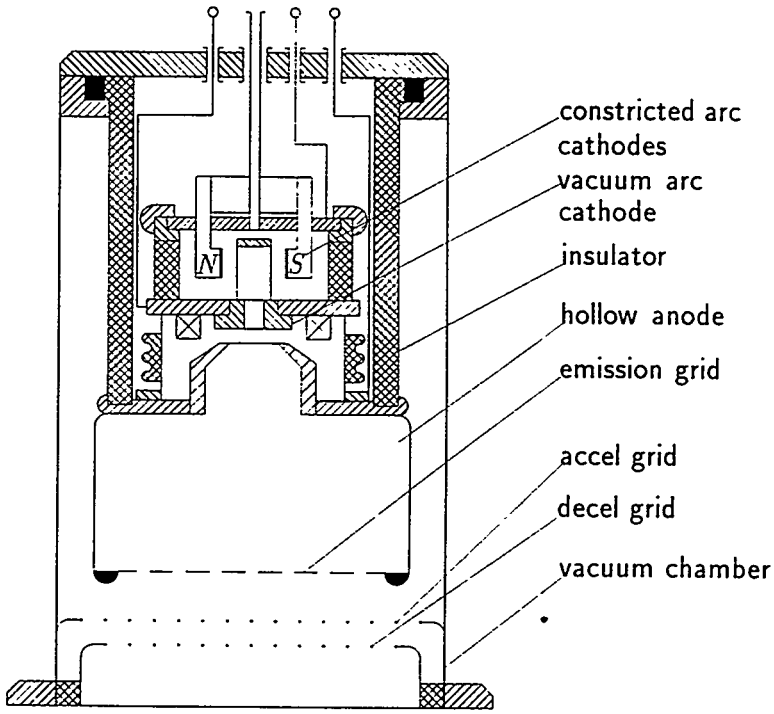


Fig. 4. Schematic of the Titan ion source.

in parallel to each other. The high geometrical transparency precludes significant ion losses in the ion-optical system of the source. The ion beam produced is transported to the collector placed at a distance of 0.5–1 m from the source.

1.1.2 Construction and parameters of the ion source

The construction of the ion source is shown schematically in Fig. 4. The discharge chamber is made of nonmagnetic stainless steel and housed in metal-ceramic (type 22KhC) cases. Used as materials for the constricted arc cathodes are magnesium or aluminum-magnesium alloys including more than 50% magnesium.

The working gas is feeded into the discharge chamber, being at high accelerating potential, through a polyethylene pipe of inner diameter 1 mm under an excessive pressure of 2–10 atm. Between the pipe and the discharge chamber a calibrated leaker is placed which represents a porous Al_2O^3 ceramic pellet through which the working gas enters the discharge chamber. Electrical insulation in this system is provided by the excessive pressure of the working gas in the pipe, and the working gas flow rate is controlled by varying this pressure.

The vacuum arc cathode of diameter 20–30 mm and thickness 1–8 mm made of the material whose ions are wanted to be obtained is mounted on the intermediate electrode. The hollow anode of diameter 20 cm and length 10 cm is made of stainless steel sheet of

thickness 0.7 mm. The plasma anode is attached to the bottom end of the hollow anode. On the anode top end a hollow graphite electrode having the form of a cone is mounted. The electrode hole diameter on the side faced to the cathode is 25–30 mm, and the distance between this electrode and the cathode is 2–8 mm. Using graphite as a material for this electrode avoids the discharge instabilities related to the formation of anode spots on the electrode surface.

The discharge chamber is placed inside the base insulator rated for operation at a total accelerating voltage of 80 kV. The high-voltage insulator is filled with transformer oil. This not only ensures the required electric strength over its inner surface but also allows efficient cooling of the discharge chamber units during the operation of the ion source. The oil is cooled with water flowing through a thin-walled bellows which serves simultaneously as an oil concentrator. With water cooling the oil temperature in a prolonged operation of the ion source is no more than ~ 60 °C.

The acceleration unit consists of two tungsten grids of transparency ~95%. The top grid is grounded, while the bottom one is at the secondary electron cutoff voltage. The grid assembly and the hollow anode are demountable, so the cathodes can be replaced not disassembling the ion source.

The trigger pulse from an auxiliary discharge is formed on discharging a capacitor through a step-up transformer. To produce the constricted and vacuum arc pulses, artificial pulse-forming lines switched by thyristors and discharged through pulse transformers insulated to hold-off the total accelerating voltage are used, which provide maximum discharge currents of 50 and 200 A with a pulse duration of 400 μs at the transformers' outputs. Using a dc accelerating voltage circuit with a partially discharged capacitor precludes the problems related to the matching of the accelerating voltage with a variable load. The absence of controlling and adjusting elements being at a higher voltage with respect to the ground makes the accelerator convenient to service.

The master oscillator allows one to change discretely the pulse repetition rate (f_p = 10, 25, and 50 Hz), to switch on or off one of the discharges, and to shift smoothly the vacuum arc ignition time with respect to the time of initiation of the constricted discharge. To monitor the process of ion implantation, a control-measuring microprocessor system is used which measures the implanted ion doze, the target temperature, and the treatment time and stops the irradiation process once anyone of these parameters has achieved a specified value.

Constructionally, the power supply system of the Titan ion source includes a control rack and a high-voltage power source. The control rack houses the low-voltage part of the electric

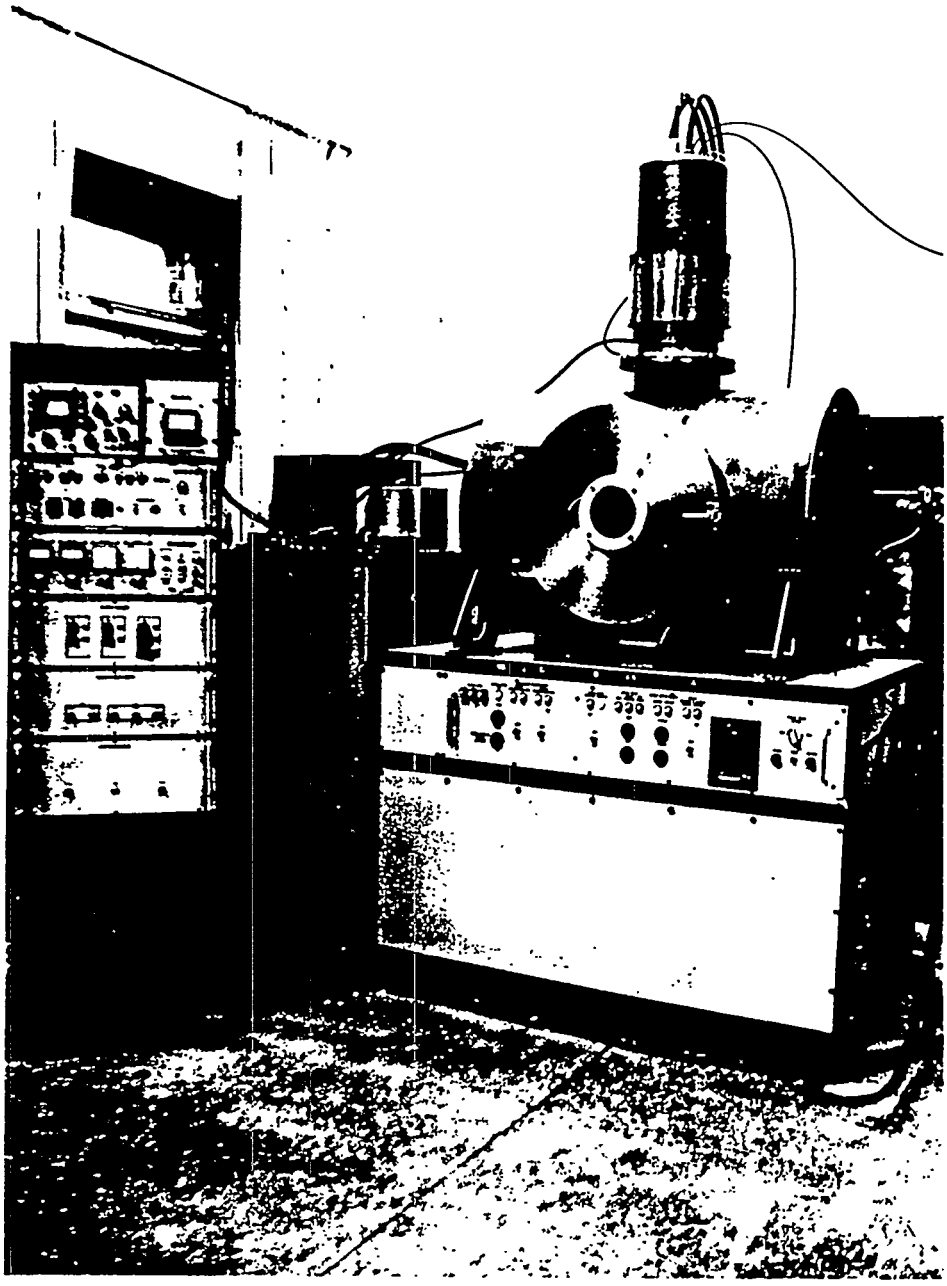


Fig. 5. General view of the Titan ion system.

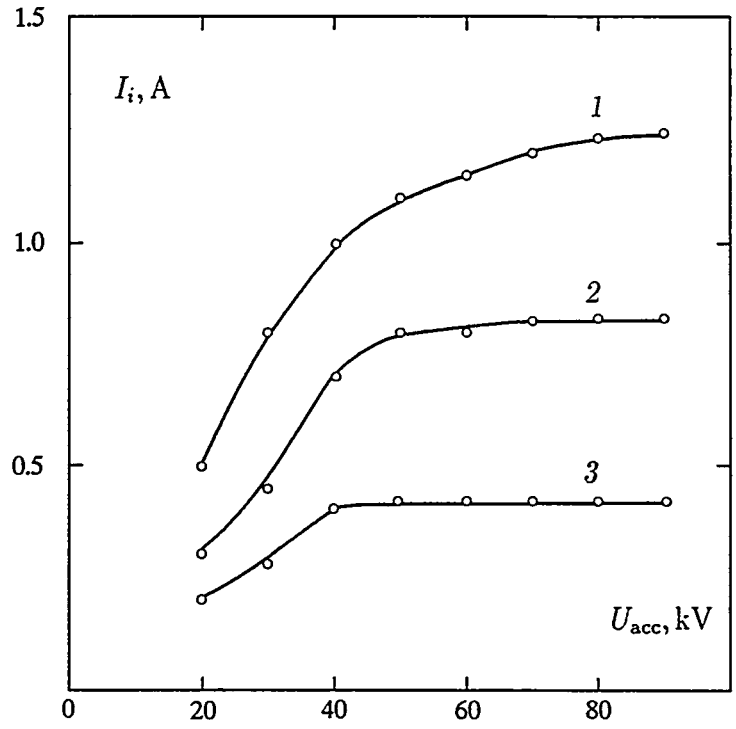


Fig. 6. Current-voltage characteristics of the ion source: (1) $I_d = 60$ A (Ta); (2) $I_c = 15$ A (N); (3) $I_d = 20$ A (Al).

circuit, the control and adjustment units, and the power supply of the cutoff electrode. The high-voltage unit includes dividing pulse transformers and a dc accelerating voltage source. A photograph of the ion source is given in Fig. 5.

The current-voltage characteristics (CVCs) of the ion source (Fig. 6), as distinct from those presented in Ref. 9, have no maximum; this is related to a feature of the ion-beam-forming system used in the ion source. The saturation portion of the CVC testifies to an efficient cutoff of secondary electrons. The attainment of saturation depends on the relation between the acceleration gap spacing, the accelerating voltage, and the plasma parameters. As the accelerating voltage is decreased, saturation is attained at a lower accelerating voltage; as the plasma density in the hollow anode is increased, saturation is observed at a higher accelerating voltage. The magnitude of the ion current extracted from the plasma depends on the mesh size of the emission grid. For the Titan source, the maximum ion current up to 1 A has been achieved for both gaseous and metallic ions.

1.1.3 Ion beam formation

The application of the magnetic field produced by the solenoid to the discharge anode region not only increases the ion current but also changes the current density distribution over the beam cross section. As the magnetic field is increased, the maximum current density at the

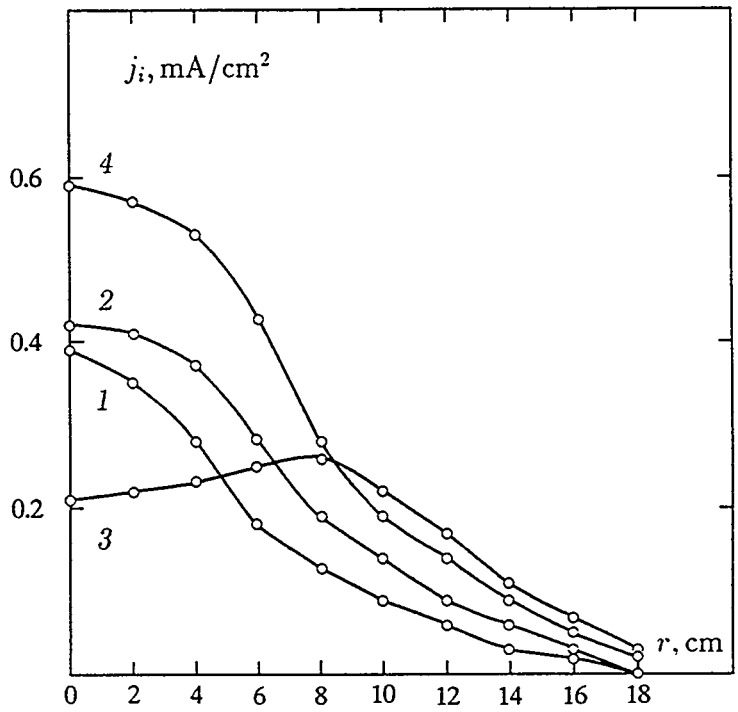


Fig. 7. Cross-sectional ion current density distribution for the constricted arc current I_c = 20 A (working gas N_2). U_{accel} = 40 (1, 2, 3) and 80 kV (4); B = 0 (1), 15 (2), and 40 Gs (3, 4).

center decreases and the distribution becomes more uniform (Fig. 7). As the magnetic field is further increased, a current density minimum appears in the distribution, corresponding to the beam center. This effect becomes not so pronounced with increasing accelerating field or with decreasing acceleration gap spacing.

The above change in the ion current density distribution is due to the penetration of plasma through the emission grid into the acceleration gap. If the relation between the acceleration gap spacing d, on the one hand, and the applied accelerating voltage U and the plasma parameters, on the other hand, satisfies the inequality

$$d < \frac{2}{3}\left(\frac{\varepsilon_0}{0.4}\right)^{1/2}\left(\frac{2}{q_i k T_e}\right)^{1/4}\frac{U^{3/4}}{n^{1/2}},$$

the plasma emission boundary is fixed by the grid and the acceleration gap has a plane-parallel geometry. In this case the current density distribution over the ion beam cross section is determined by the plasma density distribution near the emission grid. Application of a magnetic field to the hollow anode region increases the plasma density. For both the vacuum arc plasma and the constricted discharge plasma therewith the increase in plasma density is a maximum at the system axis. So a situation occurs where condition (1) is fulfilled only at the edge of the emission grid and, owing to the increase in plasma density, it is violated in the center. In this case the plasma boundary is no longer be fixed by the emission grid,

and plasma penetrates into the acceleration gap. The plane plasma boundary transforms into a convex one and this, in combination with the configuration of the accelerating grid, redistributes the accelerating field in such a way that it becomes defocusing for the ion beam in its center. This is turn deforms the cross-sectional current density distribution. As the accelerating voltage is increased, the plasma boundary shifts beyond the emission grid, and the defocusing of the ion beam disappears.

A partial defocusing of the ion beam allows a more uniform cross-sectional current density distribution to be produced. It is possible therewith to vary the distribution, with the acceleration gap geometry and the accelerating voltage being kept the same, not only by controling the discharge current but also by varying the applied magnetic field strength. Since both the accelerating electrode and the cutoff electrode have a high geometrical transparency and the defocusing of the ion beam does not cause a noticeable increase in the ion losses on the these electrodes, this makes it possible to use a magnetic field for controling the ion current density distribution over the beam cross section.

1.1.4 Technological capabilities of the Titan ion source

Using the Titan with an accelerating voltage of 10–80 kV, He, Ne, Ar, Xe, N, C, Mg, Al, Ti, Cu, Nb, Cr, Fe, Co, Ni, Zn, Sn, Sm, Ta, W, Re, Y, Bi, Po, and Mo ion beams of cross-section area ~200 cm^2 have been produced. The average rate of dose build-up was $\sim 10^{16}$ $cm^{-2}min^{-1}$ at a pulse repetition rate of 50 Hz. To produce ions of nonconducting substances like B or Si, cathodes made of TiB_2, LaB_2, crystalline Si, or doped Nb were used.

The scope of technological applications of an ion source is determined by its operational capabilities. To find the limits within which the gaseous-to-metallic ion content ratio in the beam produced by the Titan ion source can be controlled, the Rutherford backscattering (RBS) technique was used. A silicon plate was implanted with Ar and Ta ions at an accelerating voltage of 60 kV and an ion current density of ~2 mA/cm^2. The concentration of the impurities implanted into the specimen by the ion beam was measured using the backscattering spectra of α-particles of energy 1.8 MeV. The obtained RBS spectra (Fig. 8) correspond to the modes of operation of the ion source with the respective waveforms given in Fig. 3.

An analysis of the given RBS spectra as well as the RBS spectra for carbon and beryllium specimens implanted with nitrogen and titanium ions has shown that when only gaseous ions are generated, the content of the atoms of the vacuum arc cathode material in the specimens is less than 0.05 at.% of the content of the embedded gas atoms. The contamination of the

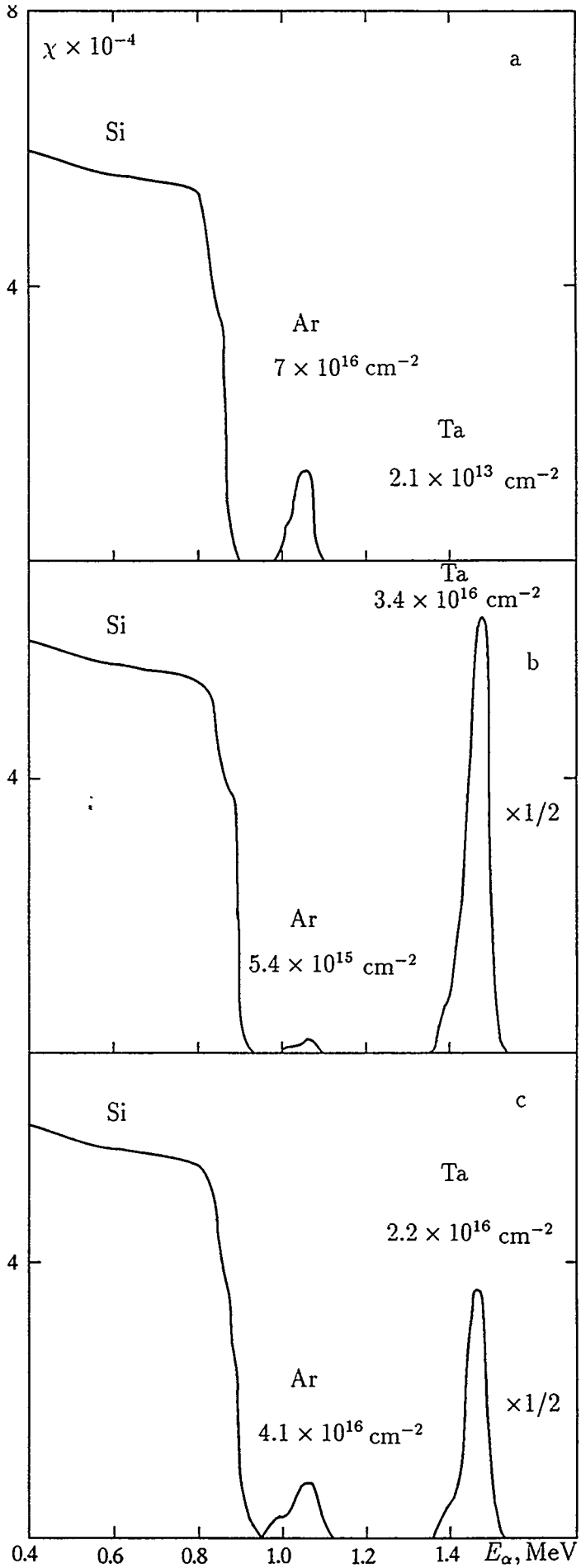


Figure 8: Spectra of backscattering of the α-particles $E_\alpha = 1.8$ MeV) from the surface of silicon implanted with ions of Ar (a), Ta (b, and Ar and Ta (c).

gaseous ion beam with metallic ions is related in this case to the sputtering of the vacuum arc cathode material in the constriction channel under its bombardment with the gaseous ions of the constricted discharge plasma.

On implantation with metallic ions, the content of gaseous impurities is 5–20 at.% of the content of the implanted atoms of the vacuum arc cathode spot. Metallophysical investigations have shown that in this case these impurities appear for the most part not due to the generation of gaseous ions in the discharge but due to the recoil implantation caused by the interaction of the accelerated metallic ions with the gas atoms adsorbed on the target surface during the interpulse intervals.

For the implantation by the ion source producing a beam consisting of both gaseous and metallic ions, the RBS spectra show the presence of embedded atoms of both the plasma-generating gas and the vacuum arc cathode material, and their content ratio correlates with the ion current ratio in the beam and varies on varying the constricted discharge and the vacuum arc currents.

It should also be noted that the ion-beam-forming system used in the ion source, which consists of tungsten filaments stretched in parallel to each other and subjected to the bombardment by the accelerated beam ions causing their sputtering, contaminates the beam insignificantly, and the concentration of tungsten atoms on the specimen surface is less than 10^{-4} at.%.

1.2 Setup for deposition of coatings with treating the surface with an ion beam

The experimental setup (Fig. 9) designed for deposition of coatings on materials and articles by the vacuum ion-plasma technique with treating the surface with charged particle flows incorporates the principal units as follows:

(1) an operating vacuum chamber with a manipulator,

(2) a vacuum pump system,

(2) a system for bleeding-in the working gas,

(3) an arc vaporizer with a power supply,

(4) an arc vaporizer with a magnetic separator and a power supply, and

(5) a gaseous ion source.

The vacuum chamber (Fig. 10) is a 600 × 600 × 600 mm cube. On one side wall of the chamber there is a connection for a vacuum pump. The opposite side wall serves as a door for loading specimens. On the top of the vacuum chamber, the ion source is mounted. On

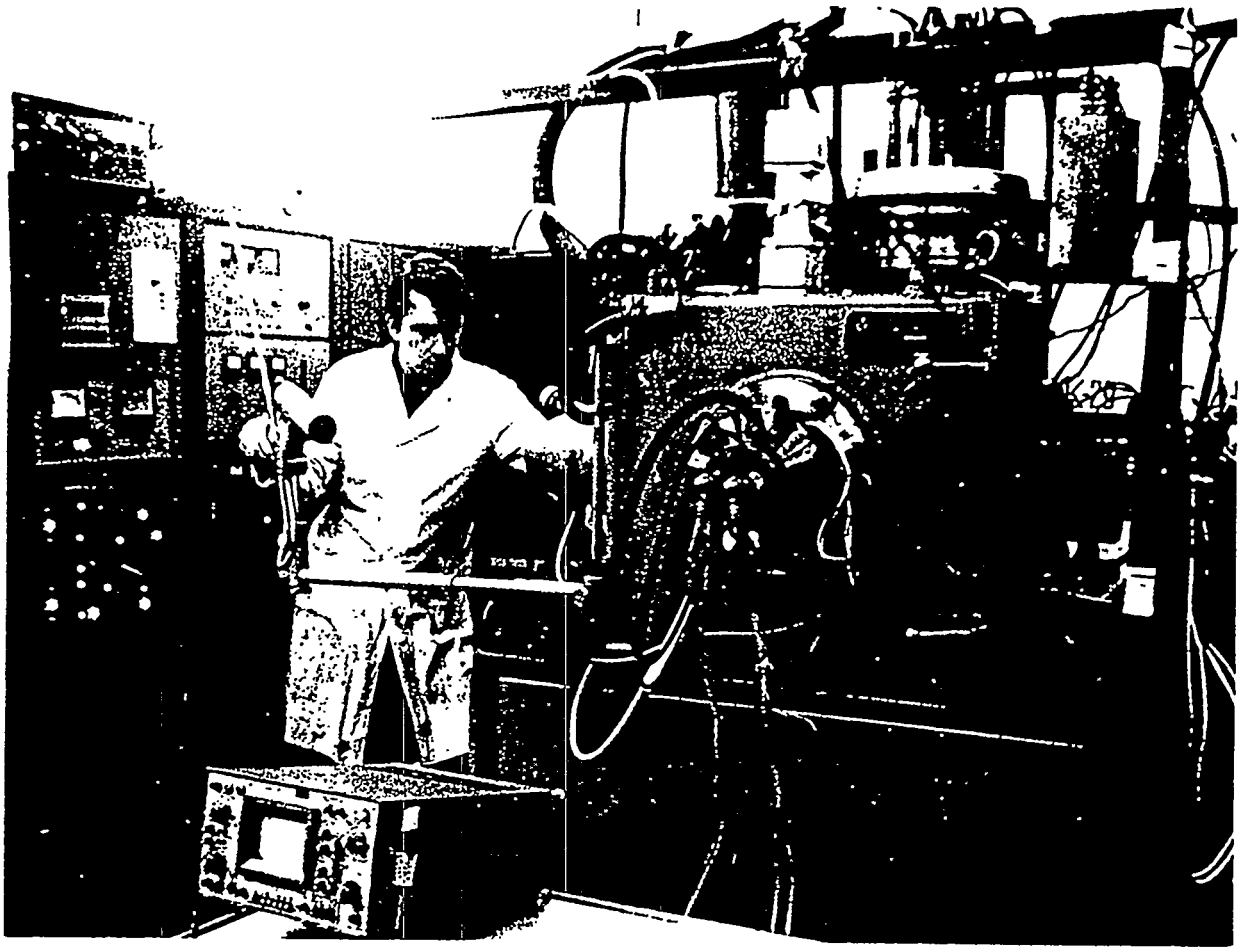


Fig. 9. General view of the coatings deposition system.

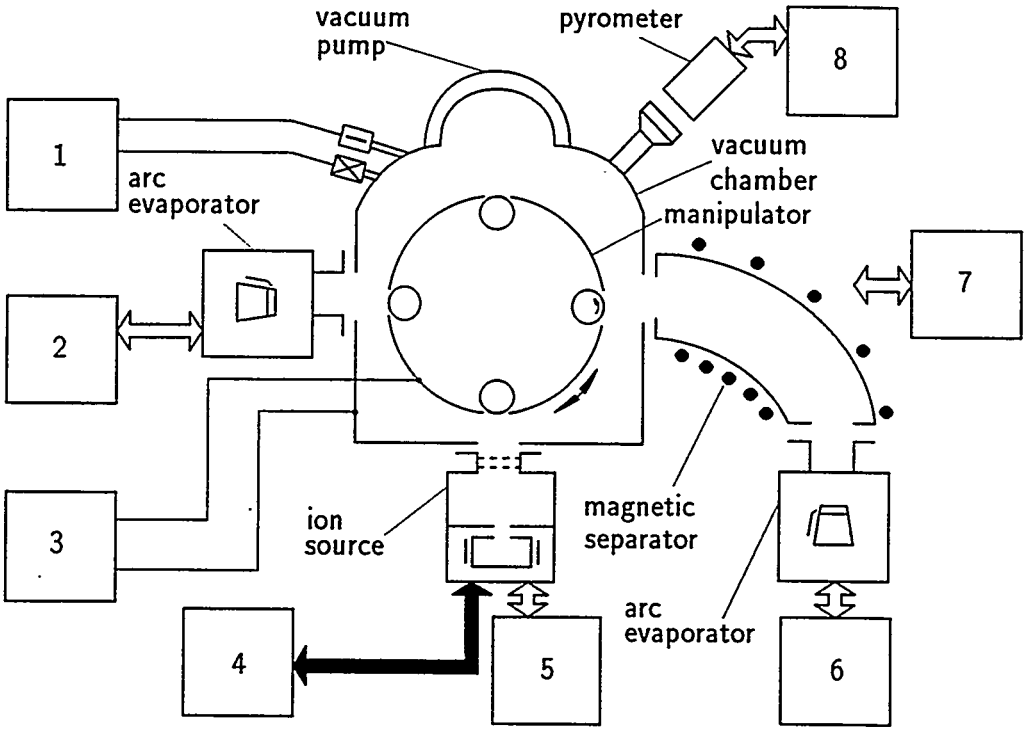


Fig. 10. Block diagram of the deposition system: 1 – vacuum meter; 2, 6 – power supplies of the arc evaporators; 3 – power supply of the manipulator; 4 – power supply of the ion source; 5 – gas feed system; 7 – power supply of the magnetic separator; 8 – power supply of the pyrometer.

two other side walls, the arc vaporizers are attached. One of the vaporizers is furnished with a magnetic separator. The manipulator, which is a planetary gear designed for 12 positions arranged in a centrally located circle of radius 200 mm, is mounted on the bottom of the vacuum chamber. The manipulator has an electric drive whose revolutions are controllable from zero to 15 rpm. The manipulator table is insulated from the vacuum chamber. This makes it possible to apply to it a dc voltage from a special source controllable from zero to 1200 V.

The vacuum chamber is roughly pumped to 1 Pa by a fore pump at a rate of 150 ℓ/s. Further pumping to a pressure of 10^{-3} Pa is performed by an oil diffusion pump at a rate of about 2000 ℓ/s; at the output of this pump two fore pumps each operating with a pumping rate of 5 ℓ/s are set. Pressure is measured by an ionization thermocouple vacuum gage. The working gas is bleeding in the vacuum chamber with the use of a double-channel automatic gas-bleed-in system with a working pressure range from 10^{-3} to 10 Pa and a maximum gas flow rate, with the leak completely open and with atmospheric pressure at its inlet, of no less than 7×10^{-2} m^{3}Pa/s.

The main element of the arc vaporizer (Fig. 11) is a cathode made as a truncated cone

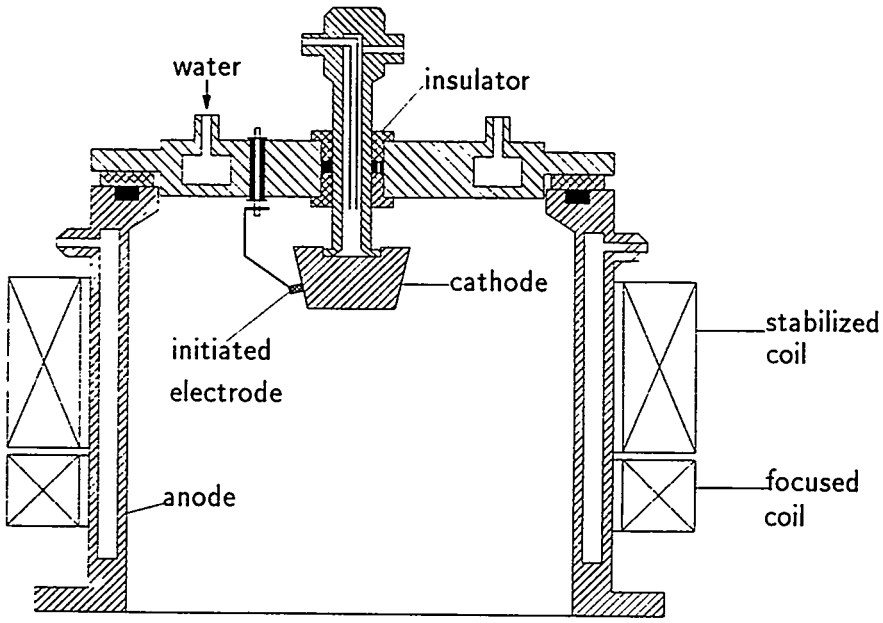


Fig. 11. Schematic of the arc evaporator.

with a base diameter of 80 mm, an inclination angle of 8°, and a height of 45 mm. The working face of the cathode is about 70 mm in diameter. The cathode is cooled with running water. On its side wall, an arc trigger unit is mounted which represents a ceramic insulator of diameter 6 mm and length 6 mm attached to the cathode with a spring-loaded contact. On application to the cathode of a ~6 kV trigger pulse, a breakdown over the ceramic surface occurs and a cathode spot appears on the cathode side wall. The cathode is placed in a magnetic field; under the action of this field, the cathode spot moves on the cathode face causing the cathode material to sputter. Varying the magnetic field of the focusing coil permits one to can control the dimensions of the deposition region. The arc is powered from a three-phase rectifier producing a current of up to 100 A. The arc operating voltage is 30–40 V. The coating deposition rate is 4 μm/h. Another arc vaporizer designed like that described above is furnished with a magnetic separator. The separator represents a tube of inner diameter 180 mm made of nonmagnetic steel and bent through 90 deg. The tube carries a winding made of copper tie of cross section 16 × 4 mm^2 and having 30 turns. Through the winding the arc discharge current is passed. The separator is insulated from the vacuum chamber. A bias voltage of ~50–70 V is applied to the separator from a special power source.

A schematic diagram of the ion source designed to treat a surface prior to and during the process of coating deposition is given in Fig. 12. The source consists of a hollow anode made as a cylinder of diameter 200 mm and length 200 mm with three plasmogenerators fixed

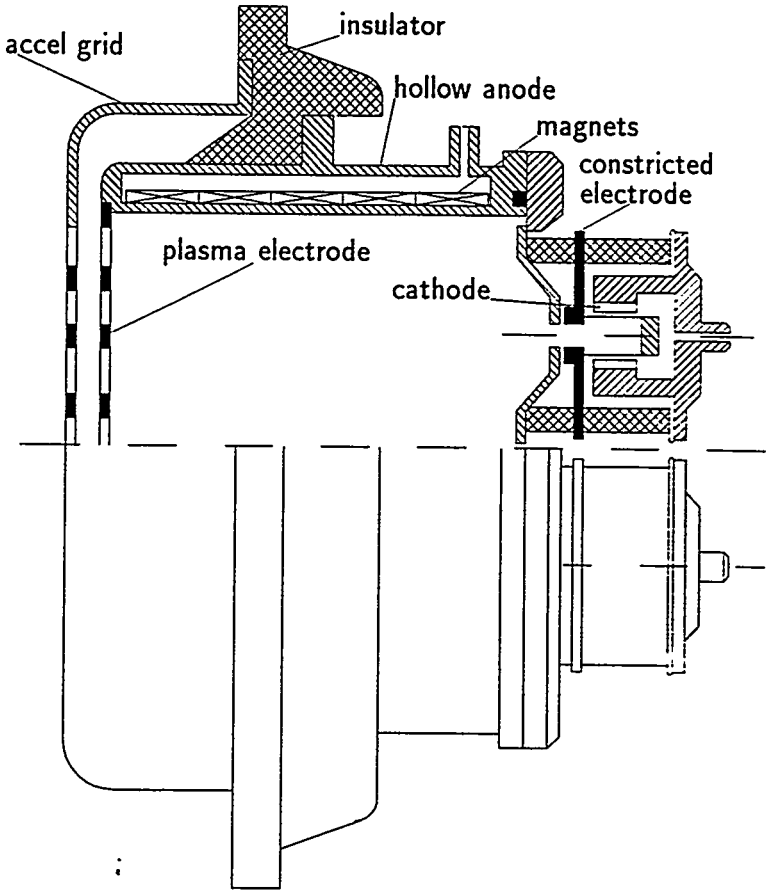


Fig. 12. Schematic diagram of the ion source for surface treatment.

at its end face. The plasmogenerators are constructed in Penning cells and their operation is based on the geometrical constriction of an arc [1]. In the anode cavity a peripheral magnetic field is produced by constant samarium-cobalt magnets each 35 × 10 × 4 mm in size, placed on the side wall into 16 longitudinal slots spaced at 40 mm [2]. The magnetic field distribution and a fragment of the "magnetic wall" are shown in Fig. 13. (Curve 1 is the distribution of the azimuthal field component B_θ along the radius at the magnet center. The working gas (Ar, Ne, air) is bleeded at a flow rate of up to 30 mPa·m^{3}s^{-1} through controllable leaks into the plasmogenerators which communicate with the anode cavity only through the constriction channels of diameter 4–6 mm. Thereby a pressure difference is produced between the Penning cell, on whose cathodes a cathode spot operates, the anode region of the discharge, and the acceleration gap. With low pressures in the hollow anode and in the acceleration gap, the pressure difference is favorable to the initiation of an arc and assists in keeping a high electric strength of the acceleration gap between the end emitter electrode of the hollow anode and the accelerating multiaperture graphite electrode which are spaced 5–10 mm. The plasma emitter is fixed on a bushing insulator rated at a voltage

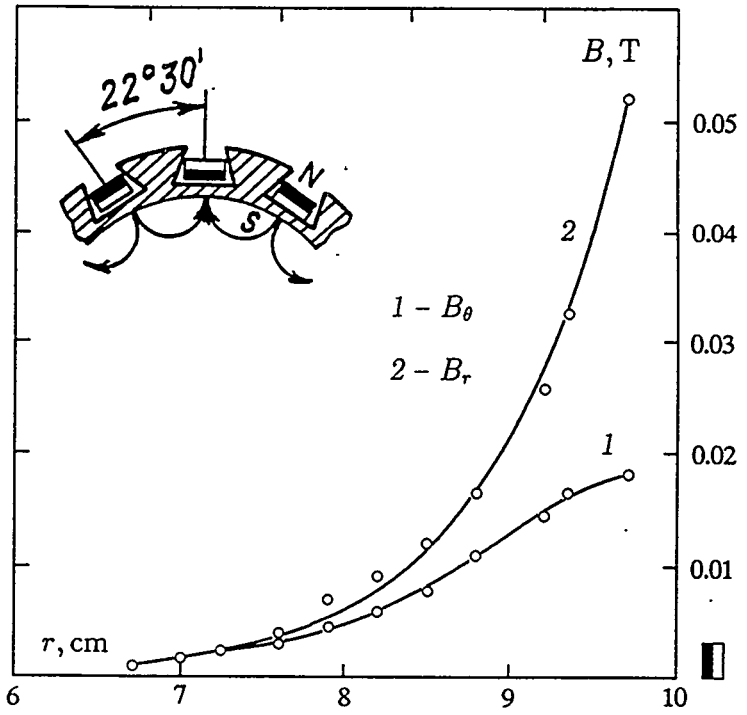


Fig. 13. Magnetic field distribution and a fragment of the "magnetic wall".

of 30 kV. To accelerate electrons, a multiaperture electrode is used which is at a distance of 5 mm from the plasma electrode and has holes aligned with those of the latter. The current of accelerated ions is measured by a Rogowski coil connected into the grounded collector circuit.

The power supply system of the ion source includes the power supplies of the discharge and the acceleration gap and the negative bias source for the electrode cutting off secondary electrons for the source operating in the ion beam generation mode.

A capacitor charged through charging resistors from a controllable high-voltage rectifier to 5–30 kV is connected to the acceleration gap through a low-ohmic resistor. The power supply unit of the discharge consists of three identical arc power supply circuits connected to three plasmogenerators. Each pulse-forming circuit is a double-step system and switch on the discharge triggering channel and the arc current pulse-forming channel. The discharge triggering pulse has a duration of 5 μs and a peak voltage of 10 kV. The main arc current pulse of controllable peak voltage 300–600 V and FWHM duration $\sim$ 50 μs is formed in the secondary winding of a pulse transformer in switching the capacitor into its primary winding. The pulse transformers are constructed in ferrite rings and placed in a tank filled with transformer oil which ensures an insulation rated at the total accelerating voltage and efficient cooling. Power is feeded to the plasma emitter through cables. The current pulse repetition rate is adjusted within a range from 1 to 500 s^{-1} with the use of a master oscillator

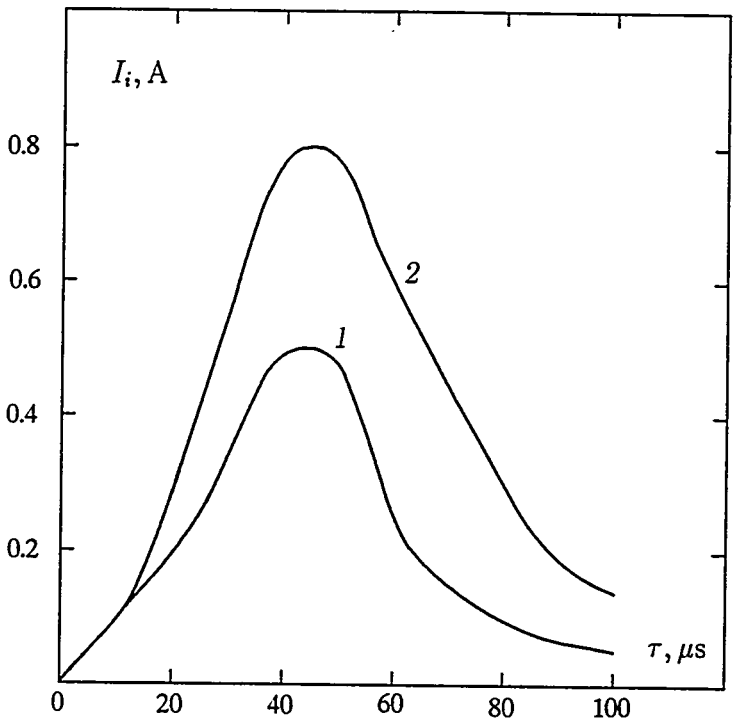


Fig. 14. Ion beam current waveforms recorded with (1) and without a peripheral magnetic field (2) for a discharge current of 150 A and an accelerating voltage of 10 kV.

applying sync pulses to the trigger electrodes of switching thyristors.

On application of negative pulses generated by the discharge power supply unit at the cathodes of the plasmogenerators, constricted arcs having a common anode region are initiated. In 3–6 μs the discharge goes over into a low-voltage stage with an operating voltage of 70–90 V and a current of 75–150 A and continues to operate during 50 μs producing plasma. The anode cavity is filled with this plasma whose emission boundary is fixed with the use of a fine grid applied on the multiaperture emitter electrode having 750 holes each 5 mm in diameter.

The accelerating multiaperture electrode has holes of diameter 5.5 mm aligned with those in the emitter electrode. So configured extraction system, when properly positioned, ensures efficient current passage through the acceleration system. The beam current is modulated by modulating the discharge current at a constantly applied accelerating voltage. The beam power can be controlled by varying independently one of the three parameters: the accelerating voltage, the discharge current, and the pulse repetition rate, which widens the technological scope of the source.

Figure 14 presents typical ion beam current waveforms recorded with (1) and without a peripheral magnetic field (2) at a discharge current of 150 A and an accelerating voltage of 10 kV. The peripheral magnetic field hampers the electron outcome to the side walls of the

hollow anode thereby improving the conditions for ionization, increasing the plasma density and hence the ion beam current.

The gaseous ion source produces a beam of diameter 200 mm with the cross-sectional current density distribution uniform within ±20%. The accelerated ion energy varies within a range from 5 to 20 kV and the beam current peaks at up to 1 A for the pulse duration 50 μs and repetition rate from 1 to 500 s^{-1}. The source can be switched into the electron beam generation mode by inverting the polarity of accelerating voltage.

2 Modification of the surface microstructure and properties under ion implantation using the Titan ion source

The use of the Titan ion source for surface modification calls for material science studies in various operating modes. At the moderate pressures 1×10^{-4} to 5×10^{-5} Torr used in this case, gaseous components are intensively absorbed at the surface of the article under implantation. The element and phase composition of the article may be changed as desired, as a result of ion mixing and diffusion saturation of the surface with the gas medium components, by varying the partial pressure of a needed component. This, first, offers the possibility to attain an optimal phase-structure state of the surface layer with lower doses as compared to the ion sources used up to now and, second, to realize in fact multielement doping on implantation of a single type of ions (e.g., metallic ions). An evaluation of the possibilities of the Titan-type sources to modify the surface of a metallic materials requires that its phase-structure composition be completely revealed for varied irradiation conditions and doses. These studies with invoking transmission electron microscopy and local diffraction analysis for the surface layer are a prime necessity in revealing the mechanisms of the modification of physicomechanical properties and in developing prediction methods and procedures for choosing optimal conditions (modes) of ion-beam treatment of materials when using technological implanters. This is of particular importance for high-productivity modes of ion implantation (increased current densities and ion energies) since in this case diffusion processes, the processes of nucleation and growth of secondary phases, take on great significance. Nevertheless, the studies where the structure of the modified surface layer was completely revealed for particular ion sources and various modes of their operation and various doses still have been comparatively lacking. Our investigations are distinguished by the fact that they offer completely revealing the structure of the modified surface layer using the most informative direct methods for material examination.

As mentioned above, in the Titan-type sources, under ion implantation with a specified type of metallic or gaseous ions, occurs in fact multielement doping of the surface layer. Moreover, these sources offer the possibility to perform multielement implantation with metallic and gaseous ions. Finally, multielement implantation can be accomplished using a composite multicomponent cathode serving as an ion source in pulsed vacuum-arc implanters. The mechanism for the multielement implantation and its technological potentialities call for investigation. This type of investigation constitutes a part of our studies on ion-beam treatment of metallic materials being under way.

Even with extensive material science investigations associated with ion-beam modification of materials, in particular with the problem of hardening of the surface layer, the achievements and the concepts developed in the strength and plasticity science for crystalline materials are invoked by no means insufficiently. In contrast to other research groups, we in our theoretical analysis of both the phase-structure states and the physical and mechanical properties of ion-doped materials are based on the achievements, ideas, and physical models of the strength and plasticity science.

Most interesting, in our opinion, is the extension of the ideas related to the high-strength state of heterophase alloys and alloys highly doped with embedded impurities [12–17] to the ion implantation problems. In metallic alloys with high contents of embedded impurities (oxygen, carbon, nitrogen, boron, etc.) and fine particles of carbides, nitrides, borides, etc., a significant reduction of the mobility of individual dislocations is achieved [12–17]. As a result, first, the processes of dislocation relaxation should be suppressed and high-energy nonequilibrium dislocation substructures with a high level of internal stresses and their gradients should be formed. Second, it should be expected that, along with the dislocation (translational) mechanisms for the deformation in an ion-doped layer with uniquely high overstaturation of embedment solid solutions and volume fractions of fine dispersive phases, rotational (disclination) deformation mechanisms may be operating. Accordingly, for actual conditions of high-dose implantation, the formation of unrelaxed dislocation-disclination substructures, typical of high-strength state, which are responsible for the abnormally high curvature of the lattice, should be expected. Their evolution with the involvement of point defect flows in local gradient fields of normal mechanical stresses dominates the formation of nanophase substructures (dispersion of the lattice).

The above structures, besides their own significance, are precursors for the solid-phase amorphization of the surface layers in some alloys under higher-dose implantation. In this connection we intend to analyze the processes involved in the solid-phase amorphization of

metals and alloys under ion implantation and to make attempts to predict the possibility of amorphization for particular systems.

Nowadays, in the strength and plasticity science rather workable physical models and theories for substructural, solid-solution, and disperse hardening are developed which relate the strength capabilities of materials with the defect density, the impurity density in the solid solution, the characteristics of the secondary phases, etc. This allows a theoretical prediction of the hardening effects and hence a choice of desired dopants, alloy compositions, and treatment techniques aimed at the attainment of required mechanical properties. These achievements in the plasticity science, however, have not been used up to now as applied to the modification of alloys by ion implantation. We in our work intend to use in full measure the modern theories of hardening to solve the problems of the modification of the properties of alloys under ion implantation with the aim to choose the type of ions, their dose, and the conditions of implantation for a particular case.

The experimental results obtained to date demonstrate considerable capabilities of the ion-beam surface modification with the use of the Titan ion source and the new approaches and principles of this type of surface modification.

2.1 Ion mixing

Using the Titan ion source it is possible to vary in a wide range those ion-beam treatment parameters which control the efficiency of ion mixing of the gas components absorbed on the target surface and the structure-phase transformation in the modified layer. The parameters most important from this viewpoint are the nature of the implanter gas medium, the partial pressures of species in this medium, the target temperature, and the atomic weight of the ions.

Electron microscopy of specimens subjected to ion implantation in the modes presented in Table 1 [18] has shown that for the modes with beam treatment in vacuum and in argon (modes I and II, Table 1), the most important feature common for both modes is the presence of released Mo_2C (Fig. 15). An increased carbon concentration in the ion-doped layer is also testified by the data of an elementary analysis (Fig. 16, curves 1 to 3). The result of ion beam treatment at $T \leq 500$ K in the environment of nitrogen (modes III.1 to III.3 in Table 1) is enrichment, owing to ion mixing, of the surface layer with nitrogen, with carbon concentration being somewhat lower (Fig. 16, curves 4). The principal phase observed microscopically therewith is fcc molybdenum nitride Mo_2N (Fig. 17). The volume fraction of Mo_2C particles is insignificant.

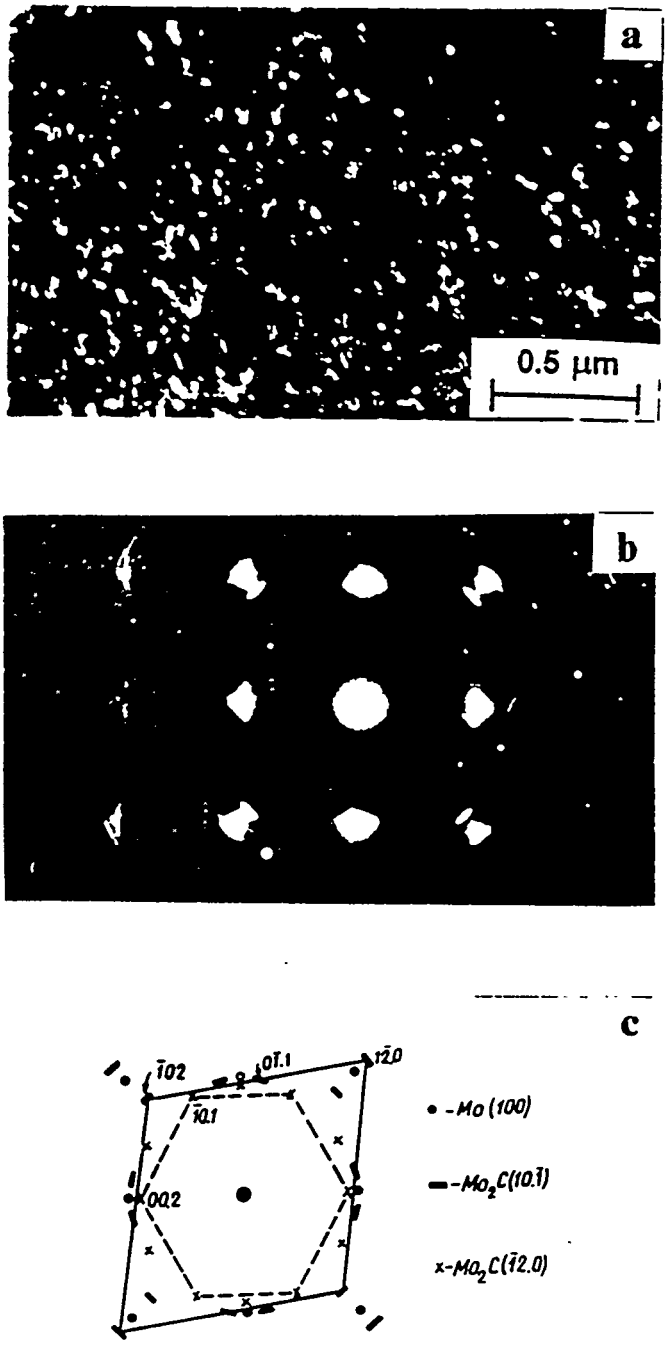


Fig. 15. Mo_2C particles (a), a microdiffraction pattern of the ion-doped layer in molybdenum taken after ion-beam treatment by mode II (b), and its schematic (c).

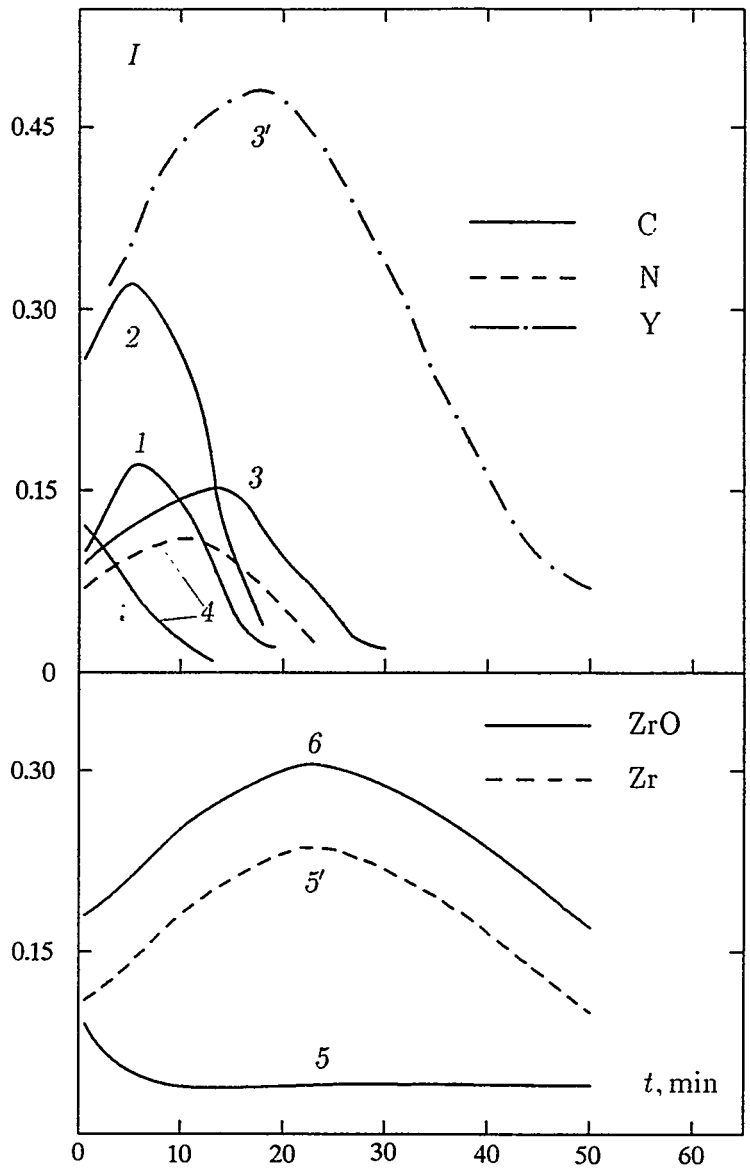


Fig. 16. Distribution profiles for the relative intensities of secondary ions versus the time of sputtering of the surface of molybdenum after ion implantation by modes I.1 (curve 1), I.3 (curve 2), II (curves 3 and 3′), III.1 (curve 4), III.4 (curves 5 and 5′), and III.4 + 1273 K for 40 min (curve 6).

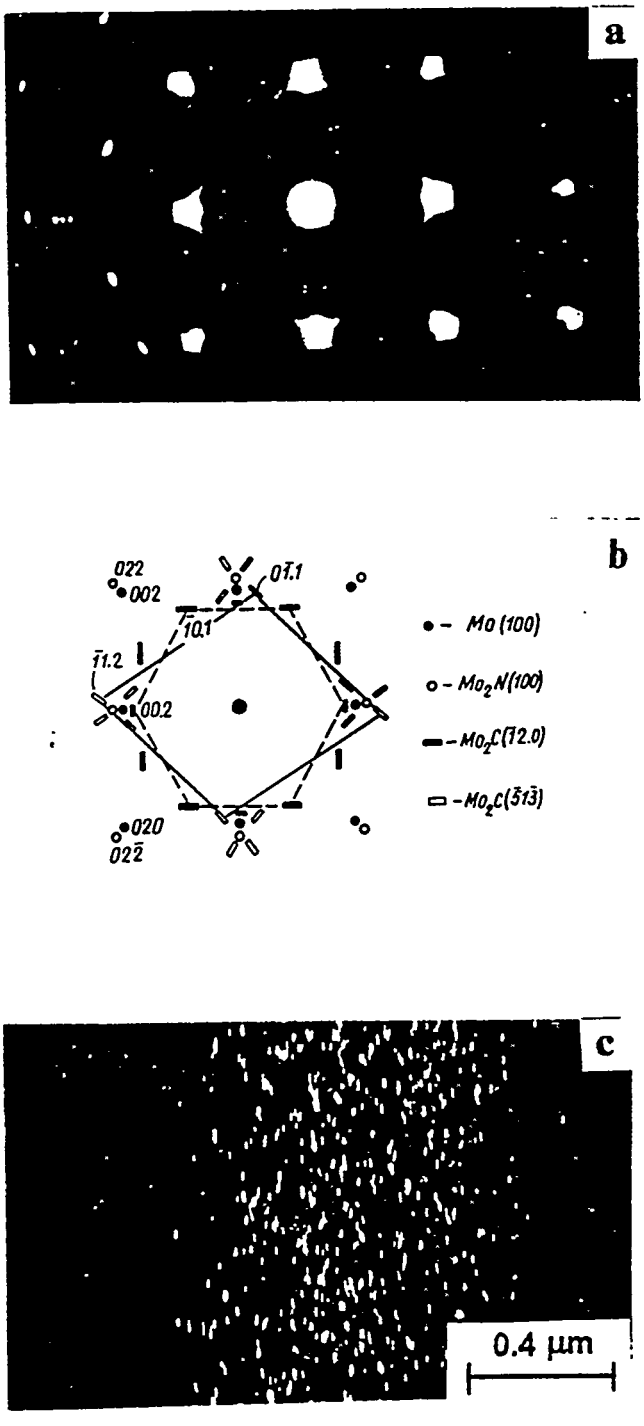


Fig. 17. A microdiffraction pattern of a heterophase (Mo + Mo_2N + Mo_2C) surface layer (*a*), its schematic (*b*), and a dark-field image of Mo_2N particles (*c*) taken after ion implantation of molybdenum by mode III.2.

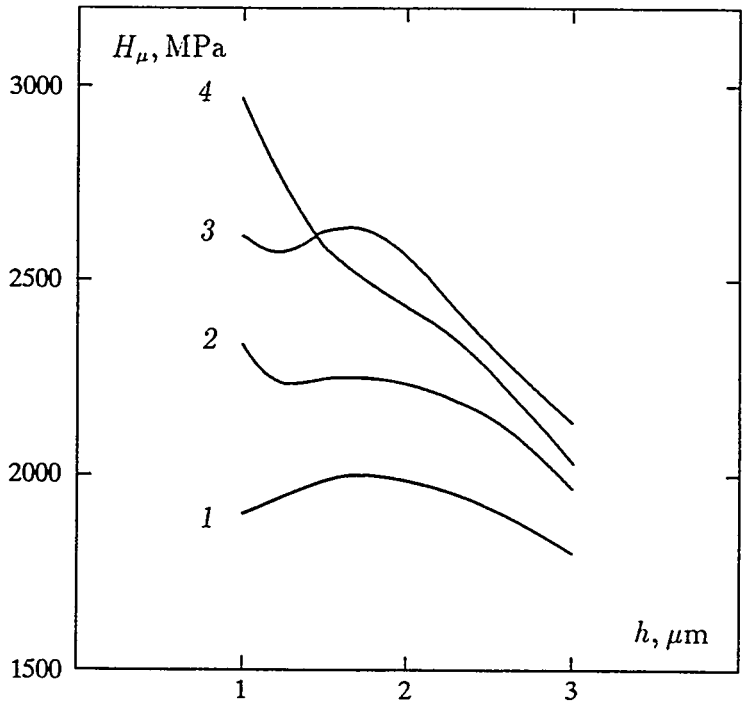


Fig. 18. Microhardness of the surface layer in untreated molybdenum (1) and after implantation with the ions of a (TiB_2)Fe composite cathode at a nitrogen pressure of 2×10^{-4} (2, 3) and 5×10^{-4} Torr (4) with $D = 10^{16}$ (2, 4) and 2×10^{17} cm^{-2} (3).

Table 1. Ion implantation modes
(irradiation dose $D = 10^{17}$ cm^{-2}, pressure 2×10^{-4} Torr)

Mode	Gas type	Ion type	Ion energy, E, keV	Pulse frequency, f, Hz	Pulse current density, j, mA/cm^2	Target temperature, K
I.1	air	Y	60	50	1	370
I.2	air	Mo	60	50	1	360
I.3	air	Pb	60	50	1	370
II	Ar	Y	60	50	2	670
III.1	N	Y	60	50	2	660
III.2	N	Zr	60	5	2	520
III.3	N	Zr	30	50	2	480
III.4	N	Zr	60	50	2	800

For the above ion implantation modes, the formation of embedded phases as a result of ion mixing of the implanter gas components is one of the main processes in the modification of the structure-phase state of an ion-doped layer. It is highly important therewith that

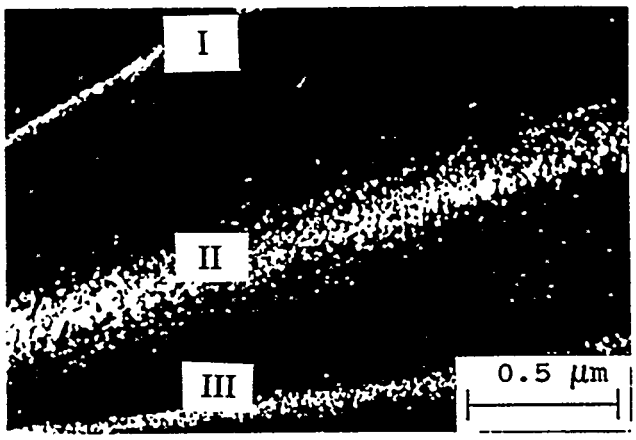


Fig. 19. Dark-field images in several active reflections (of bcc, fcc, and hcp phases) of the surface layer of molybdenum after implantation with composite cathode ions at a nitrogen pressure of 5×10^{-4} Torr. I: $\bar{g} = \langle 110 \rangle$ Mo, foil plane {111}; II: $\bar{g} = \langle 111 \rangle$ fcc Mo_2N, foil plane {110}; III: $\bar{g} = [111]$ hcp Mo_2N, foil plane $(2\bar{1}.0)$.

an efficient modification of the microstructure with increasing the surface layer hardness ia attained with a low implantation dose ($D \simeq 10^{16}$ cm^{-2}). It has been shown [19–21] that with this D value the implantation of molybdenum with the ions of a $(TiB_2)Fe$ composite cathode in nitrogen results in the formation of a Mo_2N-based solid layer of thickness ~300 Å in the ion-doped zone and a substantial increase in microhardness (Fig. 18, curve 2).

Increasing the partial pressure of nitrogen form 2×10^{-4} to $\sim 5 \times 10^{-4}$ Torr with D kept constant, $D \simeq 10^{16}$ cm^{-2}, results in the formation of a molybdenum-nitride-based double-layer coating (doped with the composite cathode elements, carbon, and oxygen) of thickness ~700 to 1000 Å with fcc and hcp lattices (Fig. 19). The surface layer hardening effect therewith (Fig. 18, curve 4) is no less pronounced than that observed with $D = 2 \times 10^{17}$ cm^{-2}. This coating has a zero porosity and, owing to the absence of localized boundaries between the nonmetallic layers and the matrix, a high adhesive strength.

It has been established [19, 20] that an important parameter in the ion-beam treatment, which may aid to the production of highly doped surface layers with low ($\sim 10^{16}$ cm^{-2}) irradiation doses is the mass of the implanted ions; increasing this parameter makes ion mixing much more efficient. This can be illustrated by the observation that the carbon concentration in the surface layer of molybdenum doubles (Fig. 16, curves 1 and 2) as the

ion mass is increased from 88 (Y^+, curve 1) to 207 (Pb^+, curve 2).

When analyzing the temperature effect on the phase-structure states in ion-doped layers with ion mixing, it is necessary to take into account, first, the possibility of variation of the adsorptive activity of the target surface with respect to various gas medium components and, second, the temperature effect on the kinetics of phase formation.

It has been established [18] that the change in the reactivity of molybdenum with respect to nitrogen and carbon with increasing the target temperature from 500 (modes III.2 and III.3) to 800 K (mode III.4) is responsible for the change in the nature of the second phase in the ion-doped layer, such that in this layer after ion-beam treatment in mode III.4, instead of molybdenum nitrides (as observed after the ion-beam treatment in modes III.2 and III.3, Fig. 17), solid Mo_2C films are found (Fig. 5 in Ref. 18) notwithstanding the high nitrogen concentration in the implanter chamber.

An analysis [18] has shown that in steels and Mo-based alloys within the high-doze ion implantation temperature range (300–800 K) the kinetic conditions for the release of embedded phases based on the target elements are fulfilled. This is due the rather high diffusion mobility of the embedded elements that controls the formation of these phases. The substantially lower diffusion mobility of the implanted replacing elements (Pb, Zn, Y) precludes the release of secondary phases based on these elements and should provide for the formation of highly concentrated nonequilibrium solid solutions of the implanted elements showing low solvability with respect to the target material.

According to the above-said, under the above conditions of ion implantation and mixing, as revealed by electron microscopy, nothing but matrix-element-based embedded phases are released (Figs. 15, 17, and 19). The implanted replacing elements (Y – curve 3′, Fig. 17; Zr – curve 5′, Fig. 17) therewith are in solid solution. As can be seen from Fig. 17, their concentrations are much higher than the equilibrium solvabilities of these elements in Mo. The latter is unambiguously confirmed by the fact that oxides of these elements (curves 5 and 6, Fig. 17) are formed during the heat treatment process after ion implantation, which has been revealed by electron microscopy (Fig. 4 in Ref. 18) and secondary ion mass spectroscopy. It has also been unambiguously evidenced [18] that nonequilibrium solid solutions of embedded elements are formed in the ion-doped layer of molybdenum.

Thus, the ion mixing of the gas medium elements adsorbed on the surface of the ion-doped layer results in the formation in this layer of both nonequilibrium solid solutions of these (and implanted) elements and embedded phases based on them to the extent that solid layers of nonmetallic phases, doped multilayer coatings included, are formed. The capabilities of

the Titan ion source to vary the ion implantation parameters within wide limits make it possible to produce the above phase-structure states with comparatively low (up to 10^{16} cm^{-2}) irradiation doses and thus substantially increase the productivity of the ion-beam treatment.

2.2 Multielement ion implantation using composite cathodes

In working out this line, we have realized two approaches. The first approach is related to the fact that the Titan pulsed ion source is capable of producing, sequentially or simultaneously, metallic and gaseous ion flows of varied intensity. The second one is based on the development and use of multicomponent composite cathodes of required composition.

Cathodes of this type were developed, first, with the aim to form in the surface layer of a target fine particles of carbides, borides, and silicides of transitional elements like TiB_2 or WC when reactive elements are in deficit or absent in the target material and, second, to make possible the ion implantation of low-conductivity elements (Si, S).

For the ion implantation of silicon we have developed a method for increasing the conductivity of silicon cathodes by forming eutectic compositions of the Si-$MeSi_2$ (Me-V, Nb, etc.) type with directed fibers. The special cathode structure (with regular interphase boundaries) enhances their conductivity and promotes the operation of an arc.

Using these cathodes for ion implantation in argon or in vacuum results in amorphization of the surface layer with the particles of Mo_2C, Mo_3Si, and $MoSi_2$ formed in the lower-lying layer. As a result of the multielement ion implantation Si^++Ni^+ in nitrogen, SiN and Mo_2 nitride particles are released in the ion-doped layer along with molybdenum silicide; the amorphization of the surface layer therewith is suppressed. The surface layer represents a silicon-doped nanocrystalline solid film based Mo_2N on fcc nitride.

Ion alloying of the surface layer of molybdenum with boron and titanium (Fig. 20) is attached with metal-ceramic binder of the (TiB_2)Fe type, produced by self-spreading high-temperature synthesis. In this case, under the conditions of ion mixing, the composition of the solid layers of embedded phases of the Mo_2N type can also be modified (Fig. 19).

For efficient disperse hardening of steels with WC particles, a metal-ceramic cathode of the "tungsten carbide with a Co binder" type has been proposed. An investigation performed has shown that during ion implantation first released from the cathode material are tungsten and carbon having close ionization potentials. Ion-beam treatment of cutting tools with ion-plasma TiN coatings with the use of this cathode increases the durability of the tools 2–3 times.

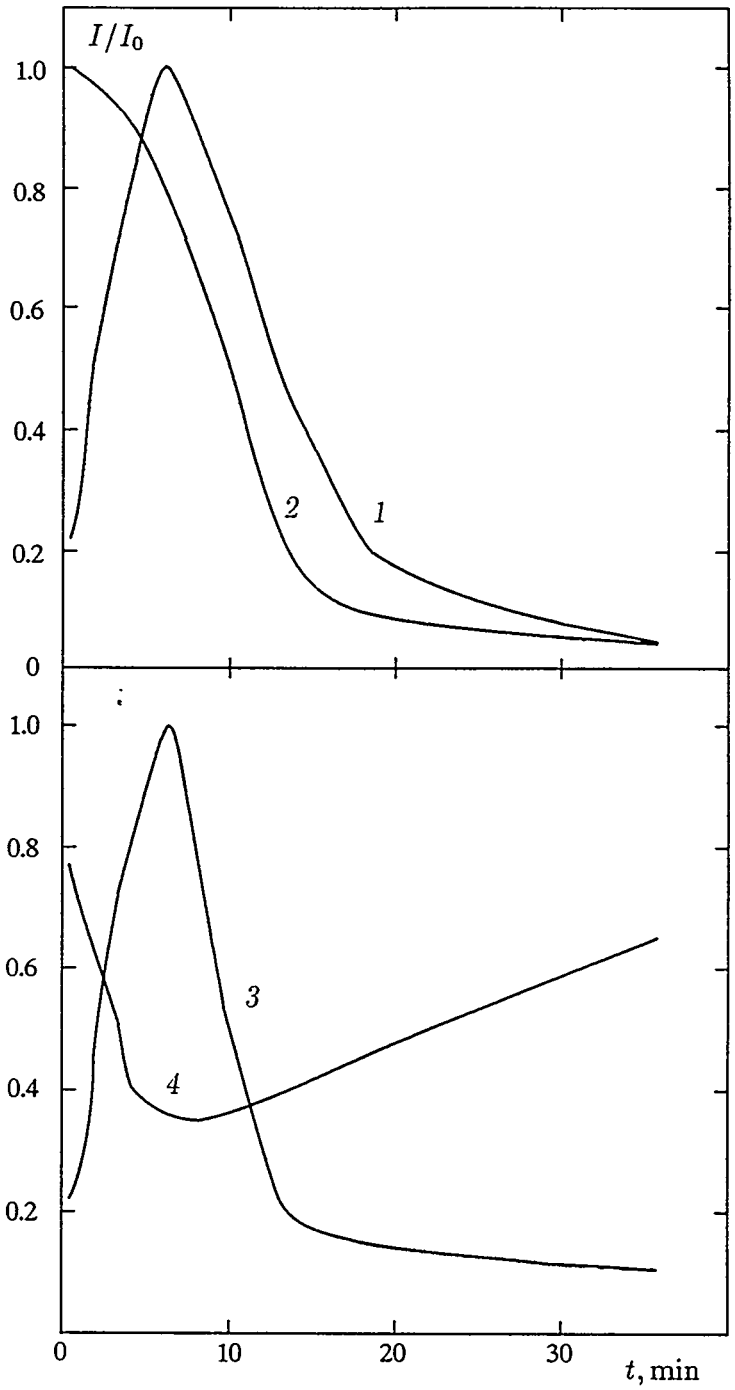


Fig. 20. Distribution profiles for the relative intensities of secondary ions in molybdenum after implantation with the ions of a $(TiB_2)Fe$ composite cathode: 1 – B, 2 – N, 3 – Ti, 4 – Mo.

Thus, using composite cathodes and the multielement ion implantation technique substantially extends the scope of modifying the microstructure of surface layers with a wide spectrum of structure-phase states including nonequilibrium solid solutions; released fine particles of embedded phases (nitrides, carbides, borides, silicides); solid layers of nonmetallic phases with a varied element composition: thin multilayer coatings of embedded phases; completely amorphized layers, etc.

2.3 Dose dependencies of structure-phase states

A series of investigations performed by the contract executers have revealed some regularities in the formation of structure-phase states, depending on the irradiation dose ($D = 10^{16} - 5 \times 10^{17}$ cm^{-2}), under various conditions of ion implantation.

With intense ion mixing (see Subsec. 2.1) these regularities depend on D only weakly and are determined in the main by the partial pressures of the gas medium components, the implanted ion mass, and the target temperature.

However, for the conditions where the efficiency of ion mixing is low (small masses of ions, low temperatures and partial pressures of reactive elements in gas media) it was managed [18–25], using a wide spectrum of ions (gaseous N^+ ions and metallic Cu, Pb, Mo, Ti, Zr, and Y ions and metalloids such as C, Si, and S), to reveal some general regularities for the formation of structure-phase states depending on the irradiation dose. These regularities are as follows:

1. For the irradiation dose $(1 - 2) \times 10^{16}$ cm^{-2}, whatever the type of implanted ions, the decisive factor in the modification of the ion-doped layer is accumulation of lattice defects such as dislocations, point defects, or their clusters (Fig. 21a,b).

2. For the dose $\sim 5 \times 10^{16}$ cm^{-2}, the dominant factor in this type of modification is the formation in the ion-doped layer of disperse secondary phases in high volume percentages (Fig. 21c,d) released both due to the ion doping with implanted elements and as a result of ion mixing. The latter is the more substantial, the greater the implanted ion mass.

3. A highly important factor in the modification of a structure-phase state, whose importance is enhancing with increasing irradiation dose, is the formation of highly nonequilibrium solid solutions of embedded and replacing elements with a limited solvability of the target material.

4. The formation of fine heterophase structures with a high volume percentage of the second phase and of highly nonequilibrium solid solutions ensures a high level of internal stresses in the ion-doped layers and, with irradiation doses on the order of 10^{17} cm^{-2}, results

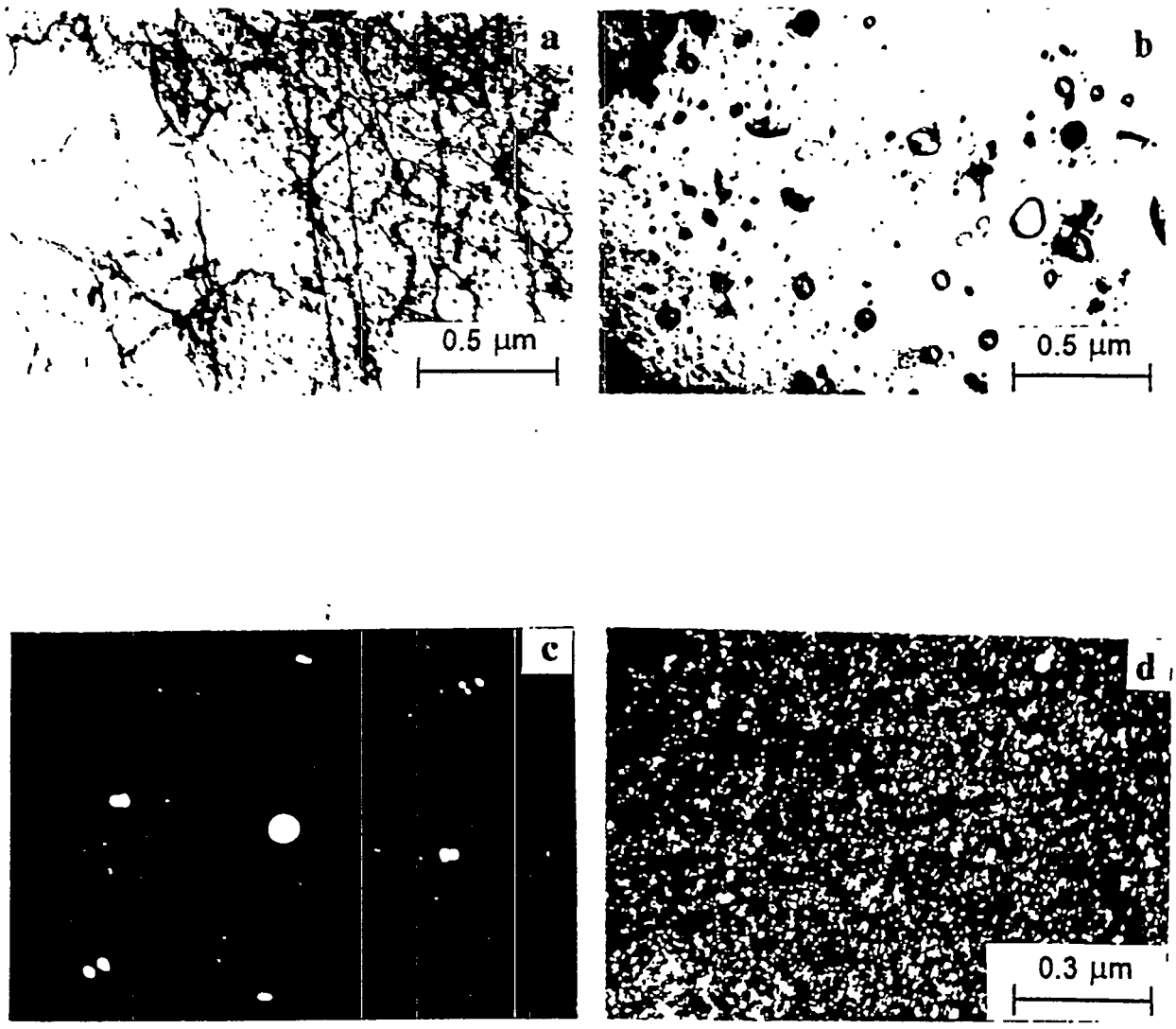


Fig. 21. Microstructure of the surface layer of molybdenum after implantation with carbon (*a*, *b*) and nitrogen ions (*c*, *d*) with doses 10^{16} (*a*, *b*) and 10^{17} cm^{-2} (*d*). *b* – specimens were annealed after implantation at 1200 K for 30 min; *c* – a microdiffraction pattern of the two-phase Mo-M-$_2$N layer; *d* – a dark-field image of Mo_2N particles.

as a rule in the formation of high-energy structural states with a high defect density and a highly curved lattice (see Subsec. 2.4).

5. The features of the subsequent relaxation of the above states are determined by the element and phase composition of the ion-doped layer, and with the highest ($\geq 10^{17}$ cm^{-2}) irradiation doses they may give rise to amorphization of the surface layer (see Subsec. 2.6) or its dispersion into nanometer-sized grains (see Subsec. 2.4).

2.4 High-energy defect structures in ion-doped layers

With ion implantation doses $D \geq 10^{17}$ cm^{-2}, and under the conditions of ion mixing even with $D \simeq 10^{16}$ cm^{-2}, a structural state is formed, in the ion-doped layers which is characterized, first, by a high density of effective obstacles to the sliding of dislocations (highly doped nonequilibrium solid solutions, disperse particles of high-strength nonmetallic phases, forest of dislocations) and, second, by extremely high nonuniform internal stresses.

As applied to similar states formed in the process of plastic deformation of high-strength metallic alloys, we have developed a concept of a high-strength state [12–17] according to which the accumulation of defects under the above conditions is accompanied by the formation of a new type of substructures with an unusually high (up to 1 rad/μm) curvature of the lattice [12–14, 16]. Subsequent relaxation of these high-energy substructures occurs with an active participation of collective (rotational) modes of plastic deformation and nonequilibrium point defects moving in high nonuniform stress fields [15, 16]. An original electron microscopic method for the location and measurement of various components of the bending-torsion tensor in states with highly curved lattice has been worked out [13, 14].

Proceeding from the concept developed and using the above method, an electron microscopic study and an analysis of the regularities of the formation of highly defective substructures in ion-doped layers with a high volume percentage of embedded phases and with highly-doped versaturated solid solutions have been carried out [18, 21, 23]. It has been established that:

1. High-energy defective substructures with a high (up to 1 rad/μm) curvature of the lattice are truly found in the mentioned structural states after high-dose ($(2-5)\times 10^{17}$ cm^{-2}) implantation of C^+ (Fig. 22a), Si^+, Si^++N^+ ions into molybdenum as well as a result of ion mixing in a (TiBr)Fe cathode treated with an ion beam with doses from 10^{16} to 10^{17} cm^{-2}.

2. An important source of the high stresses and their moments that provide the formation of the above substructures are internal stresses appearing in the process of release of secondary phases with high parameters of disbalance between the lattices of the phase and the

matrix. This is unambiguously evidenced by the correspondence between the directions of the maximum curvature vectors of the molybdenum lattice and molybdenum-nitride-based solid layers (Fig. 22b) and the directions of the maximum moments appearing in the process of secondary phase release [21].

3. No less important are the gradients of internal stresses appearing as a result of a strong in-depth variation of the lattice parameter (Fig. 22a) with a nonuniform distribution of the dopant in a highly nonequilibrium Mo-C solid solution observed experimentally. The latter is confirmed by the regular gradual variation of the lattice parameter in molybdenum on varying gradually the azimuthal component of the lattice orientation (Fig. 22a).

4. According to the notions developed in Refs. 12, 14, 18, 21, the formation of high-energy substructures with a highly curved lattice in ion-doped layers appears to be possible owing to the efficient suppression in them of the dislocation relaxation of nonuniform internal stresses.

5. Under these conditions, an additional mechanism for their relaxation is quasi-viscous mass transfer occurring through the drift of nonequilibrium point defects in nonuniform stress fields [12, 15]. The high density of point defects under the conditions of ion implantation substantially facilitates this process. It has been shown [16] that the efficiency of the above mechanism for moment relaxation is the higher, the smaller are the dimensions of the reorienting structural elements.

6. The statements in items 4 and 5 are associated with the experimentally established [21, 23] fact that the relaxation of a substructure with high continuous disorientations during the process of ion implantation or subsequent thermal treatment (Fig. 22c) results in a dispersion of the lattice of the ion-doped layer onto the nanometer-sized grains with a wide spectrum of disorientations.

The approaches, ideas, and mechanisms for the formation of high-energy and nanocrystalline structural states are highly important for the physics and practice of ion-beam surface modification for the reasons as follows:

First, the high nonequilibrium of these states is responsible for the newly discovered features of their behavior under various external actions, under the conditions of mechanical loading, plastic deformation and destruction included.

Second, it is well known that changing crystals into the nanocrystalline state may change their physical properties not only quantitatively but also qualitatively; therefore, this is one of the most efficient ways to modify the properties of a surface under ion implantation. In particular, the formation of nanocrystalline structures may serve as a highly efficient means

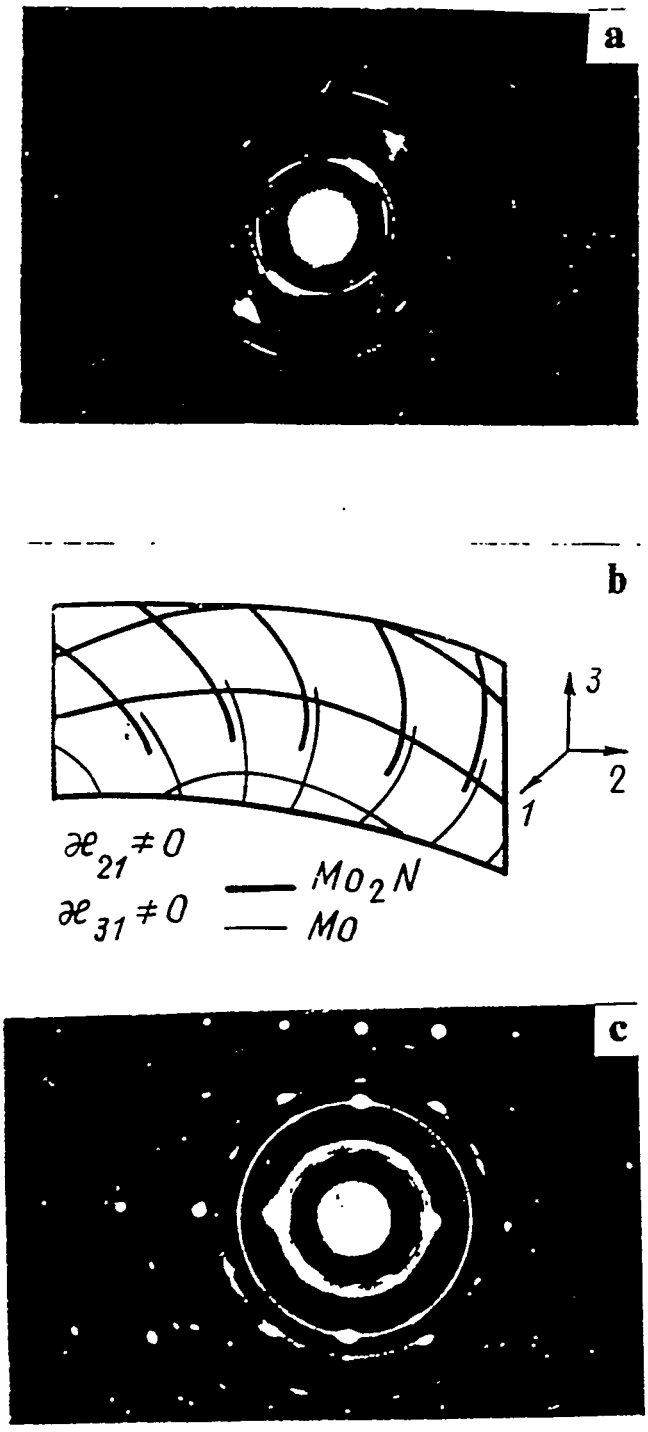


Fig. 22. A microdiffraction pattern of a zone with a high azimuthal curvature of the molybdenum lattice with a variable lattice parameter, taken after implantation with Cu (*a*); a scheme of gradual disorientations in Mo and in the solid MO_2N layer after the ion mixing upon implantation with the elements of a $(TiB_2)Fe$ composite cathode (*b*), and a microdiffraction pattern of the nanocrystalline surface layer in molybdenum after implantation with Cu ions and annealing at 1200 K for 30 min(*c*).

for increasing the destruction viscosity of ceramics.

Third, the high-energy and nanocrystalline states may play an important part as intermediate states in the amorphization process, determining the amorphization regularities and mechanisms under ion implantation. This problem is discussed in Subsec. 2.6.

2.5 Physical analysis of the nature of hardening

The hardening effects in the surface layer under ion implantation are generally related to all changes in the structure and composition of this layer. Meanwhile the data we have obtained make it possible to estimate the contribution of each factor, namely, the high defect density, the doping of the solid solution, and the formation of secondary phase particles.

In particular, we have estimated the efficiency of the above hardening mechanisms on the example of the implantation of N^+ and C^+ ions into molybdenum with irradiation doses from 2×10^{16} to 10^{17} cm^{-2}.

The strain hardening calculated by the formula

$$\Delta G_d = \alpha G b \sqrt{\rho},$$

where α= 0.20–0.33, G is the shear modulus for molybdenum, $b = /3\langle III\rangle$ is the Burgers vector for dislocations, and ρ is the dislocation density, for the experimentally found $\rho \leq 10^{10}$ cm^{-2} yields $\Delta\sigma_d \leq 150 - 200$ MPa.

The effect of the solid-solution hardening of molybdenum with carbon or nitrogen have defied proper estimation. However, based on the data of our earlier analysis [12] for Nb-O and Nb-N systems, with the concentration of the mentioned impurities in the molybdenum solid solution being 1 at.%, the hardening can be estimated as $\Delta\sigma_{[N,C]} \simeq 400 - 500$ MPa.

Depending on the mechanism for the interaction of the glide dislocations with the particles, the dispersion hardening can be estimated by the formulas

$$\Delta\sigma_{GH} = bG\varepsilon^{3/2}(rf/b)^{1/2}$$

for the case where the particles are cut through by the dislocations or

$$\Delta\sigma_{Or} = \frac{Gb}{\pi(D_s - 2r_s)} \ln\left(\frac{x}{r_0}\right)$$

for the case where the dislocations pass over the particles. Here, r is the particle radius ($r \leq 50$ Å), f is the volume fraction of the particles, $\varepsilon = \Delta a/a$, $\Delta a = a_{ph} - a$ is the difference between the lattice parameters of the phase and the matrix, $D_s = r_s(\pi/f)^{1/2}$, $r_s = r\sqrt{2/3}$, and $x = 2r_s$ to $D_s - 2r_s$. Estimates show that for the doses 2×10^{16} and

10^{17} cm^{-2} $\Delta\sigma$ values for the case where the particles are cut through by the dislocations are, respectively, $\Delta\sigma^1_{GH} = 2000 - 2500$ MPa and $\Delta\sigma^2_{GH} = 5000 - 6000$ MPa and for the case where the dislocations pass over the particles $\Delta\sigma^1_{Or} = 250 - 300$ MPa and $\Delta\sigma^2_{Or} = 800 - 1000$ MPa.

Thus, it should be expected that for the nitrogen or carbon dose $\sim 2 \times 10^{16}$ cm^{-2} the yield strength in the implanted layer will increase by $\Delta\sigma_s \simeq 600 - 800$ MPa, while for the dose 10^{17} cm^{-2} it will increase by $\Delta\sigma_s \simeq 1500 - 1800$ MPa. The decisive contributions to the hardening of the modified layer therewith are from the solid-solution hardening with embedded impurities and the dispersion hardening with nitride and carbide particles. The analysis performed testifies to the high efficiencies of hardening under ion implantation with this type of particles.

2.6 Amorphization of metals and alloys under ion implantation and ion mixing

The problem under discussion is of importance in theory and applications. The theoretical importance is associated with the possibility to study the solid-phase amorphization reaction with controllable variations in the composition, atomic ordering, and the state of the defect subsystem in the alloy and to investigate the kinetics of the amorphization and the preceding structural states. Thereby the role played by thermodynamic, structural, and kinetic factors in the development of amorphization with atom mixing in alloys can be estimated along with the elaboration of methods for predicting the possibility of amorphization of tool and work materials. The applied (technical) importance of solving this problem is related to the production of surface layers with high strength and corrosion resistance, a low friction coefficient, and unique magnetic and other physical properties. The formation of an amorphous layer on a surface for providing high adhesion of coatings, for accommodation of the physical and mechanical properties of the coating and the base, and for producing coatings with optimal complex and nanophase structures is of fundamental importance. We have performed a physical analysis of the problem of amorphization of metals and alloys by ion implantation and ion mixing [25]. It has been shown that it makes sense to classify amorphizable alloys as "metal-metalloid" systems, intermetallides, heterophase alloys, and alloys with a high positive heat of mixing. It has been concluded that it is impossible to amorphize, using the above techniques, pure metals with the exception of those having structural modifications only slightly differing by the free energy in the liquid phase (gallium at $T \leq 10$ K). The impossibility to amorphize pure metals and solid solutions with an unlimited solvability are related, first, to the formation in the latter, with the dislocation density $\rho \geq 10^{11}$ cm^{-2},

of low-energy dislocation substructures of the cellular or fragmented (nanocrystalline) type and, second, to the impossibility to achieve critical concentrations ($C_{cr} = 2 \times 10^{-2}$) of vacancies because of their spontaneous recombination in collision cascades (with the atomic volume of the spontaneous recombination being $\omega \approx 100$).

A review [25] of the now available experimental data, first, shows that an important role in the achievement of the energy state of crystals necessary for their amorphization is played by the chemical component of the internal energy of the alloys. Second, based on the results of our own studies the conclusion is made that a substantial contribution to amorphization is from high-energy dislocation-disclination substructures since the dislocation relaxation is suppressed upon ion implantation as a result of the formation of embediment solid solutions with an abnormally high content of the embedded impurity and heterophase alloys containing ultrafine particles of carbides, nitrides, borides, and oxides.

It is also concluded that it is impossible to amorphize ceramics with a simple cubic lattice (e.g., TiN, TiC, ZrC, etc.) not producing additional doping, in particular, with oxygen or hydrogen, and to efficiently amorphize ceramics with a complex lattice (Si_3N_4, Al_2O_3, etc.) with a comparatively low implantation dose.

Based on our investigations and analysis [23–25], principal ideas have been formulated concerning the choice of the ion type and the ion implantation conditions and dose for specific metallic systems, which are intended to be embodied in forming a desired amorphous phase at the "base-coating" interface, in producing graded structures in the base prior to depositing a coating, and in solving the problems related to the formation of complex and nanophase structures of coatings. Specific examples of the solution of these problems will be presented in reports on subsequent stages of work within the frames of the present project.

2.7 Ion-beam-assisted deposition of TiN coatings enhancing their adhesion

An enhanced adhesive strength of TiN-type coatings can be achieved through the activation and cleaning of the surface by low-energy ions, ion mixing of intermediate adhesive layers, and modification of the microstructure and internal stresses of the coatings during their deposition assisted by ion-beam irradiation (ion-assisted deposition, IAD).

In our opinion, important factors in the enhancement of the adhesive strength of a coating therewith are, first, the reduction of the gradients of mechanical and thermophysical properties of the "base-coating" composition at the interface; second, the formation of nanocrystalline, amorphous-crystalline, and entirely amorphized structural states of the base and the coating, and, third, the use of these structural states as interfaces between the coating and

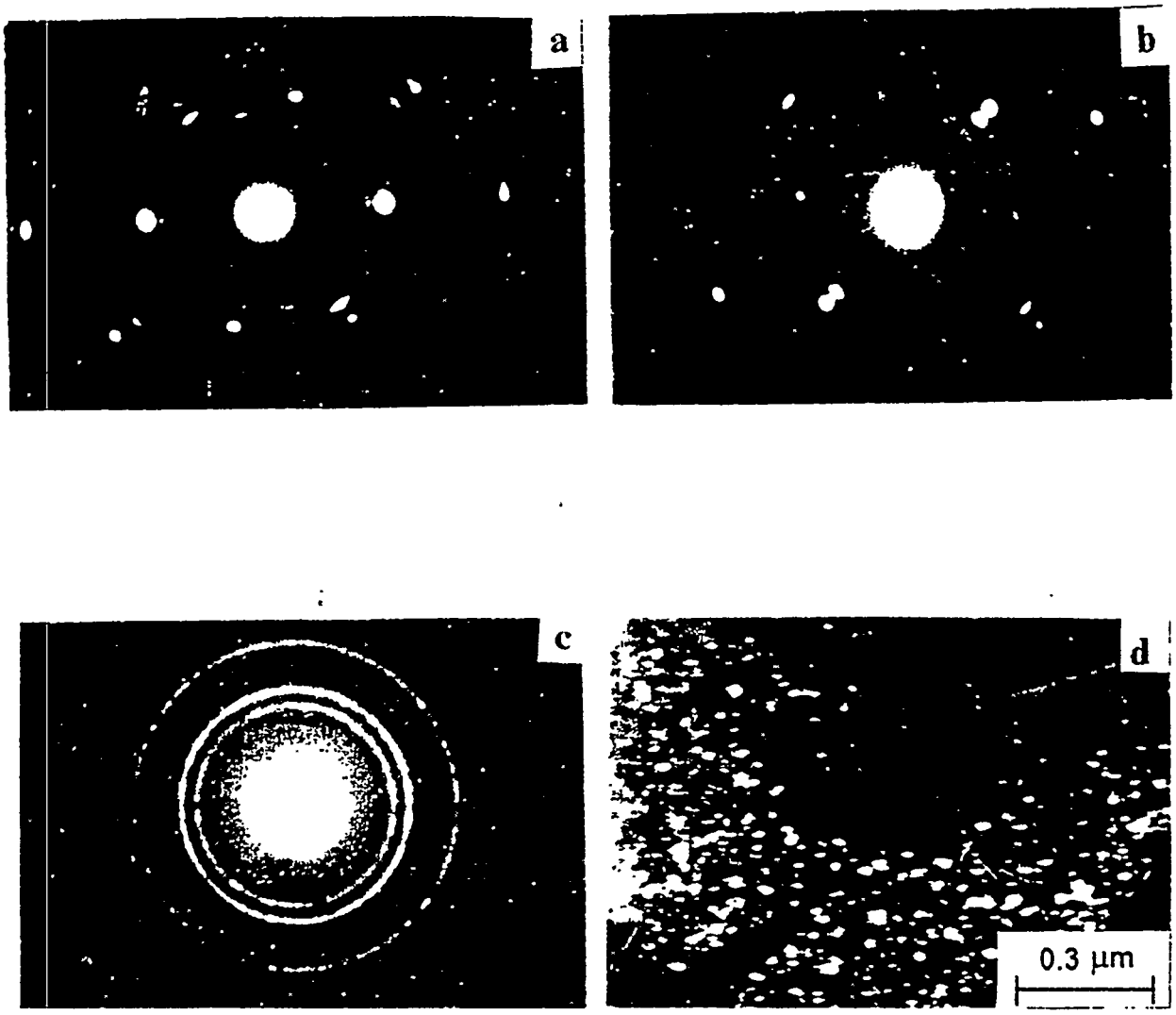


Fig. 23. A microdiffraction pattern of the intermediate (base-coating) layers γ-Fe + TiN (*a*) and γ-Fe+TiN+amorphous phase (*b*), formed in the process of ion-reactive deposition of titanium combined with ion implantation, a microdiffraction pattern of a TiN coating produced by arc ion-plasma technique (*c*), and a dark-field image of the nanocrystalline structure (*d*).

the base. In doing this, ion-beam modification of the microstructure and properties of both the coating and the base material.

It has been shown above that it is basically possible to produce a base with graded structure and properties by way of high-dose implantation of Ni^+ ions for Mo-based alloys (similar structures can also be created for Ti-based alloys) or multielement implantation (e.g., $Ti^+ + N^+$ or $Zr^+ + N^+$) for Fe-based steels and alloys. As the surface is approached, the graded structure changes in the sequence as follows: regions of high dislocation density – a solid solution doped with nitrogen atoms – a heterophase system combining a matrix highly doped with nitrogen and nitride particles – a nanophase layer of titanium nitride.

The possibility to vary in a wide range the ion implantation conditions and modes, offered by the Titan ion source makes it possible to produce the above state not only in the base but also in the deposited coating. Let us illustrate this on the example of the ion-reactive deposition of titanium at a nitrogen pressure of $\sim (1-5) \times 10^{-4}$ Torr. During this deposition combined with implantation of nitrogen ions at high rates of dose gathering for the ion implantation and a partial pressure of nitrogen of $\sim 5 \times 10^{-4}$ Torr, thin epitaxial layers having the structure of titanium nitride are formed on the surface of austenitic stainless steel (Fig. 23a). A decrease in the rate of N^+ dose gathering or in the partial pressure of nitrogen results in the formation of an amorphous phase based on titanium nitride (Fig. 23b) doped with carbon and oxygen. Treatment modes resulting in the formation of a heterophase composition of the amorphous phase with the TiN crystalline phase were realized. In the process of vacuum-arc deposition of titanium nitride in nitrogen, nanocrystalline TiN coating with a crystallite size of some tens of nanometers are formed for a small (some fractions of a micrometer) thickness of the coating (Fig. 23c, d).

Thus, using the Titan ion source and the IAD technique, structural states varying from epitaxial titanium nitride layers of nanocrystalline and completely amorphized TiN-based interlayers can be produced at the "base-coating" interface. These capabilities make it possible not only to modify the structural state of the intermediate layer to enhance the adhesive properties of the coating but also to produce multilayer compositions of nanocrystalline, amorphous, and amorphous-crystalline heterophase compounds.

The use of the Titan ion source for IAD allows, in addition to the structural state modification, a variation of the element composition of the coating produced by the techniques of multielement ion implantation (simultaneous implantation of metallic and gaseous ions, using composite cathodes) and ion mixing of the elements of controllable gas media.

References

1. Vacuum Arcs: Theory and Application. Ed. by J.M. Lafferty. Wiley, N.Y. 1980.
2. V.M. Khoroshikh, I.I. Aksenov, and I.I. Konovalov, Zh. Tekh. Fiz., 1988, V. 58, P. 1220-1226.
3. C.W. Kimblin, Proc. IEEE, 1971, V. 59, P. 546-560.
4. I. Brown, Rev. Sci. Instr., 1992, V. 63, P. 2351-2364.
5. A.I. Ryabchikov, Rev. Sci. Instr., 61 (1990) 641-645.
6. S.P. Bugaev, E.M. Oks, P.M. Shchanin, and G.Yu. Yushkov, Prib. Tekh. Eks., 1992, V. 63, P. 2422-2425.
7. H. Shiraishi, I.G. Brown, Rev. Sci. Instr., 1990, V. 61, P. 3775-3782.
8. Ion Sources with Plasma Emitter. Ed. by Yu.E. Kreindel. Nauka. Novosibirsk 1983.
9. A.T. Forrester, Large Ion Beams: Fundamental of Generation and Propagation. Wiley, N.Y. 1988.
10. F.A. Smidt and G. Hubler, Nucl. Instr. and Methods in Phys. Res., 1993, V. 80/81, P. 207-216.
11. A.D. Korotaev, A.N. Tyumentsev and V.F. Sukhovarov, Dispersion Strengthening of Refractory Metals. Nauka, Novosibirsk 1989.
12. V.Ch. Gonchikov, A.N. Tyumentsev, and A.D. Korotaev, The Physics of Metals and Metallography, 1987, V. 63, No 3.
13. V.Ch. Gonchikov, A.N. Vergazov, and A.D. Korotaev, Ibid., 1987 V. 64, No 1.
14. A.N. Tyumentsev, V.Ch. Gonchikov, A.D. Korotaev et al., Ibid., 1989, V. 67, No 3.
15. A.D. Korotaev, A.N. Tyumentsev, V.Ch. Gonchikov, and A.I. Olemskoi, Rus. Physics J., 1991, V. 37, No 3.
16. A.N. Tyumentsev, V.V. Manako, and A.D. Korotaev, Ibid., 1994. V. 37, No 12.
17. A.N. Tyumentsev, A.D. Korotaev, and S.P. Bugaev, Ibid., 1994. V. 37, P. 452-461.
18. A.N. Tyumentsev, Yu.P. Pinzhin, and A.D. Korotaev, Nucl. Instr. and Methods in Phys. Res., 1993, V. 80/81, P. 491-495.
19. A.N. Tyumentsev, Yu.P. Pinzhin, A.D. Korotaev et al., The Physics of Metals and Metallography, 1992, V. 68, No 9.

20. A.N. Tyumentsev, Yu.P. Pinzhin, A.E. Bekhert, A.D. Korotaev et al., Ibid.. 1992, V. 68, No 9.

21. A.D. Korotaev, Yu.R. Kolobov, and A.O. Savchenko, Phys. Res., 1988, No 8, P. 210-212.

22. V.G. Abdrashitov, A.E. Bekhert, A.D. Korotaev et al., Poverkhnost, 1993, No 5, P. 141-152.

23. A.D. Korotaev, A.N. Tyumentsev, A.E. Bekhert, and S.P. Bugaev, Rus. Phys. J., 1994, V. 37, No 2, P. 109-114.

24. A.D. Korotaev and A.N. Tyumentsev, Ibid., 1994, V. 37, No 8.

Contents

1 Equipment for metallic surface modification **3**

1.1 The Titan ion source 4

1.1.1 The principle of operation of the ion source 5

1.1.2 Construction and parameters of the ion source 8

1.1.3 Ion beam formation 11

1.1.4 Technological capabilities of the Titan ion source 13

1.2 Setup for deposition of coatings with treating the surface with an ion beam . 15

2 Modification of the surface microstructure and properties under ion implantation using the Titan ion source **22**

2.1 Ion mixing 24

2.2 Multielement ion implantation using composite cathodes 31

2.3 Dose dependencies of structure-phase states 33

2.4 High-energy defect structures in ion-doped layers 35

2.5 Physical analysis of the nature of hardening 38

2.6 Amorphization of metals and alloys under ion implantation and ion mixing . 39

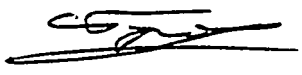
2.7 Ion-beam-assisted deposition of TiN coatings enhancing their adhesion . . . 40

References **42**

PHASE - STRUCTURE TRANSFORMATIONS IN AN AUSTENITIC STAINLESS STEEL AND IN TITANIUM ALLOYS IN THE PROCESS OF ION - BEAM MODIFICATION OF THE SURFACE

Scientific Report on Task II Performed under Contract AM - 7676
of October 10, 1994

"FUNCTIONALLY GRADED INTERFACES FOR THE ENHANCEMENT OF THE PERFORMANCE OF HARD COATINGS ON AUSTENITIC STAINLESS STEEL AND TITANIUM ALLOYS"

Principal Investigator  S.P.Bugaev
professor

Tomsk 1995

List of the participants in the experimental and theoretical investigations

High Current Electronics Institute, Tomsk

1. P. M. Schanin --- professor
2. N. N. Koval' --- senior scientists
3. D. P. Borisov --- post graduate
4. G. Yu. Yushkov --- scientist worker
5. A. V. Visir' --- jr. scientist worker
6. A.G.Nikolaev --- jr. scientist worker

Siberian Phys-Technical Institute, Tomsk

1. A. D. Korotaev --- professor
2. A. N. Tyumentsev --- professor
3. Yu. P. Pinzhin --- senior scientist
4. Yu.I. Pochivalov --- senior scientist
5. A.F. Safarov --- post graduate

Contents

Introduction 4

1 Test materials and techniques 4

2 Results 5

2.1 Features of the phase-structure states of the ion-doped layers formed in austenitic stainless steel upon irradiation with $Ti^+ + N^+$ ions 5

2.2 Modification of the Microstructure of Titanium Alloys on Ion Implantation 16

3 Conclusions 20

References 21

Introduction

The microstructure and properties of the intermediate (between the substrate and the coating) layer are of the highest importance in improving the performance of the surface of a metal or alloy in the process of deposition of wear-resistive and protecting coatings of the TiN type. On the one hand, this factors is responsible for the adhesive strength of the coating and on the other hand, it allows a modification of the substructure and properties of the coating as such.

In view of the above-said, the methods for improving the performance of coatings we are developing are based on the idea to modify the microstructure and properties of the intermediate layer mentioned above with the use of ion-beam techniques for the modification of the substrates surface (ion implantation, ion mixing) simultaneously with the deposition of coating.

The Titan ion source, when operated in the modes ion implantation (i.i.) and ion mixing (i.m.) of the components of the implanter gas medium, provides great scope for modification of the ion-doped surface layer. Our investigation [1-6] and analysis of the results [7,8] form the basis for the production in alloys under ion-beam treatment of a wide spectrum of specified phase-structure states such as states with solid-solution, dispersion and strain strengthening; nanocrystalline, amorphous and crystalline-amorphous layers of non-metallic phases; high-energy defect structures with a high curvature of the crystal lattices, etc.

Thus, strong possibilities of modifying the microstructure and properties of the intermediate (between the substrate and the coating) layer are opened up. First, the formation of the above phase-structure states in the substrate makes it possible to harness the idea of producing in this layer graded structures with monotonicly varying mechanical and thermal properties to provide good adhesive capabilities of the coatings. Second, the possibility to produce amorphous, nanocrystalline and crystalline-amorphous layers on the substrate surface is of principal importance for providing high adhesion of the coating and adjustment of the physical and mechanical properties of the substrate and the coating. Third, the above layer, when formed, may substantially modify the structural state and properties of the coating.

The results of the investigation into the regularities of variation of the structure and properties of TiN coatings under ion irradiation will be presented in the final report under the contract. The present report deals with the results that illustrate the capabilities of the modification of the phase -structure states of the substrate under the conditions of high-dose i.i. performed simultaneously with i.m. of specially deposited thin films or components of the implanter gas medium.

1 Test materials and techniques

In terms of the contract, the targets used to perform ion-beam modification of the surface layer followed by deposition of TiN coatings were made of type X17H14M austenitic stainless steel (Fe-17.2Cr-14.4Ni -2.3Mo-1.1Mn) and type

BT-6 (Ti-6Al-3.5V) and BT-9 (Ti-6Al-2Zr-3.2Mo-0.3Si) titanium alloys (numbers denotes percents by weight). Specimens to be irradiated were 20x20 mm plates of various thickness (0.2, 1.0, 2.5, and 6.0 mm). Prior to irradiation, the specimen surface was polished mechanically or electrolitically. The ion-beams treatment in the Titan pulsed arc implanter was carried out with an accelerating voltage E=30 or 60 kV, pulse repetition rate ν =10 Hz, pulse ion current density j_i=1mA/cm^2, and pulse duration τ_p≈400 μs. The implanter gas medium was produced by pumping out of the air with a diffusion pump to a pressure P≈10^{-4} Torr and dosed filling of nitrogen needed to produce an arc, which increased the pressure to P≈(2-4)*10^{-4} Torr. Austenitic stainless steel specimens were irradiated simultaneously with Ti^+ and N^+ ions in an about 1:1 ratio. The ion implantation of titanium alloys was performed with N^+ ions and, in the mode of multicomponent i.i., with nitrogen and with components of a (TiB_2)Fe composite cathode . The radiation dose was varied from 10^{16} to 10^{17} cm^{-2}.

An important parameter of the phase-structure modification at i.i. is the target temperature which was monitored in the process of treatment and varied from 300 to 700K. The latter was accomplished by varying the ion beam power density or, in steady irradiation modes, the specimen thickness and the heat removal conditions.

To change the features of the interaction of the surface with elements of the implanter gas medium, some austenitic stainless steel specimens were covered prior to i.i. with thin (~10-30 nm) Ti or TiN films using ion beam reactive or ion-plasma deposition.

The phase-structure state of the ion-doped layers produced was investigated by transmission electron microscopy combined with electron diffraction phase analysis. Specimens for the electron microscopy of ion-doped layers were prepared by one-sided jet electropolishing. The characteristics of the phase-structure state were investigated as functions of the distance from the specimen surface on subsequent ion sputtering of surface layers of varied thickness.

The efficiency of hardening of the surface layer was evaluated by measuring the microhardness as a function of the load on the indenter with the use of a special attachment to the type NEOPHOT-21 metallographic microscope.

2 Results

2.1 Features of the phase-structure states of the ion-doped layers formed in austenitic stainless steel upon irradiation with Ti^+ +N^+ ions

In the process of irradiation of austenitic stainless steel with Ti^+ +N^+ ions, the change in the composition of the surface layer of thickness a few hundreds of angstroms is determined not only by the effect of i.i. of Ti and N but also by the effect of ion mixing of the components of the implanter gas medium. The most active component of this medium which is intensely adsorbed on the target surface is oxygen. As a result, in the surface layer an interstitial phase of complex composition, (FeCrNiTi)O_xN_y, is formed whose structural state is determined by the target temperature in the i.i. process.

Mode I : Ti^+ +N^+ ions, E=30 kV, ν =10 Hz, j_i=1mA/cm^2, τ_p=400 μs, D=3*10^{16} -2*10^{17} cm^{-2}, and T~400-450 K .

Electron microscopy has revealed a surface layer having, a nanocrystalline structure. Analysis of the electron-diffraction patterns of this layer (Fig. 1a) has shown that its lattice is similar to that of Fe_3O_4 with the structure Fd3m (Table 1). The crystallite size therewith is not in excess of ~5-10 nm. The surface layer is observed to include chaotically disoriented crystallites (see Fig. 1a). In the layer adjacent to the substrate, the lattice of the nonmetallic phase is oriented relative to the lattice of the substrate (Fig. 1b) in such a way that the {400} and {440} planes of this phase are parallel to the {200} and {220} planes, respectively, of the fcc lattice of the austenitic steel. Dark-field electron microscopy of the reflections from the fcc austenite revealed, in the zone adjacent to the oxynitride layer, an fcc austenite region with a high (~10^{11} cm^{-2}) dislocation density (Fig. 1c).

Mode II : all parameters are the same as in mode I except the target temperature T=300 K .

The reduction of the target temperature from 400-450 K to room temperature leads to the fact that ion-beam treatment causes the formation on the surface of a structureless amorphous oxynitride layer which gives diffusion maxima of intensity in electron diffraction patterns (Fig. 2a). The structure of the adjacent metallic surface layer is therewith similar to the highly defective structure shown in Fig. 1c.

Mode III : treatment in mode II followed by short-time annealing at T=773K.

After thermal treatment during 15 min at T=773 K, the fine structure of the amorphous surface layer changes. An electron diffraction patterns of this layer subjected to this type of treatment is given in Fig. 2b. The electron scattering pattern seen here can be identified (see also Table 1) as the result of the diffraction on very fine particles having the type Fd3m lattice and parameters coinciding to ±0.002 nm with those of the Fe_3O_4 phase. The diffraction line broadening due to the small particle size therewith is so large that the diffraction maxima from the type {220} and {311} planes overlap to form a broad "diffusion" maximum of intensity (see Fig. 2b). The crystallite sizes estimated by the breadth of the {400} diffraction maximum are not in excess of d≈2-3 nm. Since for these d values the volume fraction of "amorphous" intercrystallite boundaries is comparable with that of the crystalline component, this structural state may be defined as a crystalline-amorphous state.

Thus, in the surface layer of austenitic stainless steel subjected to i.i. with Ti^+ and N^+ ions on the Titan ion source, an oxynitride of complex, variable in depth composition of the $(FeCrNiTi)O_xN_y$ type is formed which, depending on the treatment temperature, may include an amorphous, crystalline-amorphous, or nanocrystalline state. Between this layer and the substrate, an intermediate epithaxial layer of this phase can be produced which in turn would contact with a layer of γ austenite with a high dislocation density.

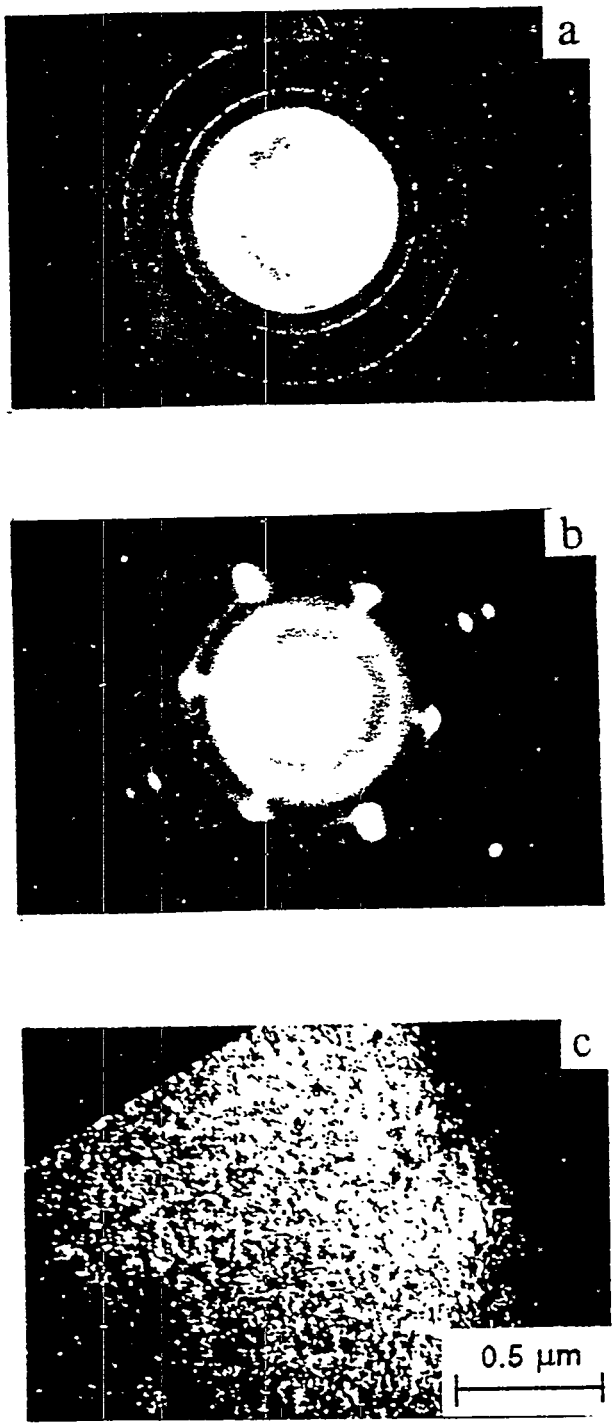


Fig.1. Microdiffraction patterns (a.b) and dark-field image (c) of the surface layer of stainless steel after ion-beam treatment in mode I. a - diffraction from the surface layer of TiN; b - diffraction from the layer being in contact with the base.

Table 1. Interplane distances: tabular values for Fe_3O_4 and TiN [9] and measurements for the second phases formed on ion-beam treatment.

$d_{tabul.}$, nm						$d_{measur.}$ (±0.002 nm)				
Fe_3O_4			TiN			Fig.1a,b	Fig.2b	Fig.3a	Fig.4b,d	Fig.7b
hkl	d	I	hkl	d	I					
111	0.485	6	111	0.244	75	—	—	0.485	0.245	0.244
220	0.297	28	200	0.211	100	0.299	diffuse	0.298	0.210	0.212
311	0.253	100	220	0.149	50	0.253	halo	0.252	0.150	0.149
222	0.242	11	311	0.127	25	—	—	—	0.127	0.126
400	0.210	32	222	0.122	10	0.209	0.208	0.211	0.121	0.120
422	0.171	16				—	—	—		
511	0.161	64				0.160	—	0.161		
440	0.148	80				0.149	0.150	0.148		

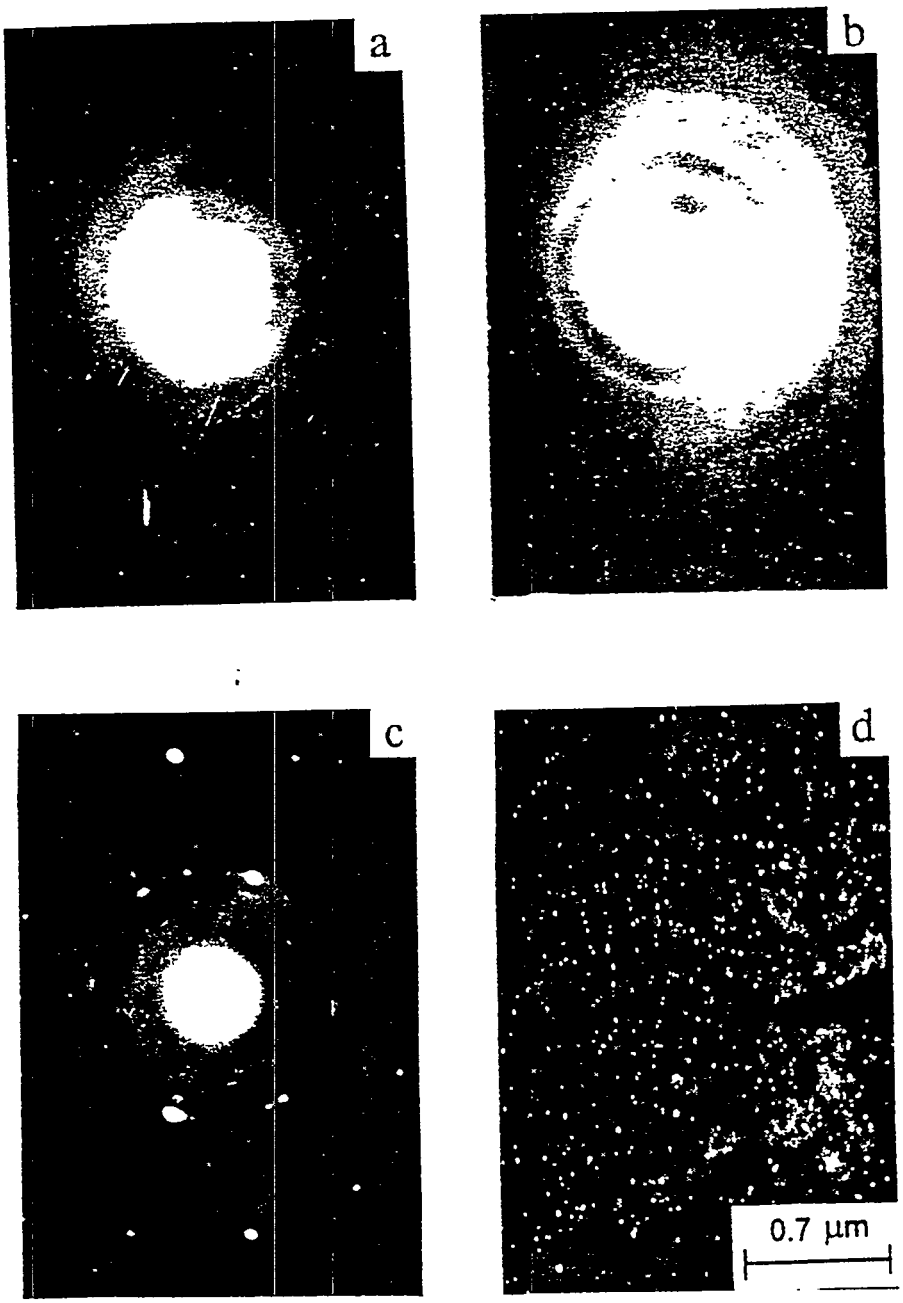


Fig.2. Electron-diffraction patterns of the surface layer of stainless steel after i.i. in modes II (a) and III (b) followed by thermal treatment at 1173 K (c); d - dark-field image of the nanocrystalline phase after i.i. and annealing at 1173 K

The above sequence of phase-structure states together with a variation of their fine structure in the process of ion-beam treatment, which offers the possibility to efficiently adjust the physical and mechanical properties of the substrate and the coating, may increase significantly their adhesive strength.

An important factor for increasing the performance of coatings are the thermal stability of the amorphous and nanocrystalline structural states formed on ion-beam treatment as well as the temperature intervals in which these states have been formed. As shown above, after i.i. in modes I, II, and III, the modified layer keeps its amorphous-crystalline structure at comparatively high (800 K) temperatures (see Fig. 2b). However, the upper limit of the temperature interval within which a completely amorphized layer forms is comparatively low (< 350 K).

In view of the above, we have made an attempt to stabilized the amorphous state in modified layer by varying its composition, namely by increasing the titanium concentration through ion-reactive deposition of this material on the surface of stainless steel prior to ion-beam treatment.

Modes IV: i.i., in modes I and III, of the surface of stainless steel covered with a titanium layer of thickness no more than 20-30 nm at various temperatures (300-700 K).

As a result of this treatment at T<550 K, an amorphous phase layer is observed on the specimen surface; a microdiffraction pattern for this layer is similar to that given in Fig. 2a. The analysis performed allows the supposition that the composition of this layer corresponds to a titanium-based oxynitride, TiO_xN_y , doped with the base components (predominantly with iron) as the result of ballistic ion mixing and ion-stimulated diffusion. Activation of these processes by increasing target temperature results in that at T>600 K a nanocrystalline layer of the second phase (Fig. 3a,b) enriched with iron and having the type Fd3m crystalline structure with parameters close to those of the Fe_3O_4 oxide (Table 1) is formed on the target surface. Thus, the deposition of titanium prior to i.i. heightens substantially (from 350 to 550 K) the upper limit of the temperature interval within which a completely amorphized surface layer forms.

Modes V: i.i. in modes similar to modes I and III at E=60 kV with ion-plasma deposition of thin (≈20 nm) TiN layers prior to ion-beam treatment

The deposition of thin titanium nitride films on austenitic stainless steel prior to i.i. seems to be a promising way for increasing the coating performance for many reasons. First, this may reduce the activity of the stainless steel surface with respect to oxygen and prevent the enrichment of the intermediate layer with this element in subsequent i.i. Second, the structural state and properties of the coating at its boundary with the base, i.e., in the zone that determines the adhesive strength of the coating, can be modified substantially in the process of i.i. Third, owing to ion mixing in this zone, the gradients of the concentrations of the base and coating components can be reduced, which is also favorable for the adhesive strength of the coating. Finally, when the thickness of the layer deposited prior to i.i. is not in excess of the projected ranges of the implanted elements, the structural state of the base can be modified substantially as well.

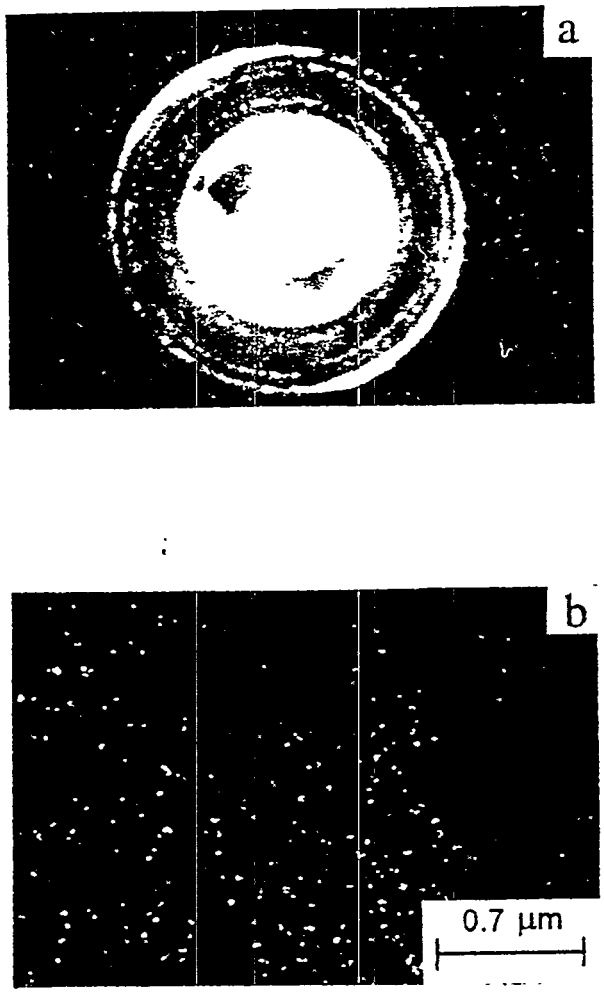


Fig.3. Diffraction patterns (a) dark- field image (b) of the surface layer of stainless steel after ion-reactive deposition of titanium followed by i.i. at 650 K.

The effect of ion beam treatment on the microstructure of the contact zone between the base and the TiN coating is revealed by a comparison electron-microscopic examination of a specimen immediately after the deposition of TiN and after deposition followed by ion implantation. The study has shown that in the process of ion-plasma deposition of titanium nitride on the surface of stainless steel , a nanocrystalline layer of this phase forms (Fig. 4a,b, Table 1) the crystallite size being d=5 nm. In the layer contacting with the base, along with the formation of chaotically disoriented nanocrystals, there take place nucleation and growth of titanium nitride having epithaxial character which is indicated by the diffraction maxima of TiN strictly oriented with respect to the reflections of γ- austenite in ring-shaped electron- diffraction patterns (see Fig. 4b). Subsequent ion implantation has no effect on the phase composition of the surface layer (Fig. 4c,d, Table 1) but modifies substantially its fine structure. Let us discuss the most important points of this modification.

1. Ion implantation reduces significantly the level of internal stresses in the contact zone between the coating and the base. These stresses are indicated immediately after the deposition of the coating by a significant bend of the thin foil; the bending of the foil leads to the formation of narrow extinction contours of γ-austenite reflections in electron-microscopic images (see Fig. 4a). After i.i. (see Fig 4c), the width of extinction contours at the foil edges increases by no less than an order of magnitude, which testifies to the respective decrease in the strength of the internal stresses.

2. After ion-beam treatment, it is difficult to localize electron-microscopically the interface between the coating and the base (see Fig. 4c) that can readily be observed immediately after the deposition of TiN (see Fig. 4a). This testifies to significantly reduced structural gradients in this zone.

3. Ion implantation increases substantially the volume fraction of the nitride phase epithaxially oriented with respect to the base. The latter is indicated by more intense diffraction maxima for the epithaxially oriented nitride phase (see Fig. 4b,d) and by a stronger dark-field electron-microscopic contrast at these maxima (see Fig. 4a,c).

4. Ion-beam treatment increases the grain size in the deposited nanocrystalline TiN film by about an order of magnitude (from 5 to 50 nm, see Fig. 4a,c). This favors structural softening of the high-strength coating on the contact surface.

5. In the process of ion-beam doping of base with implanted elements ($Ti^{+}+N^{+}$) and ion mixing at the base-coating interface, the generation of high-density dislocation is observed in the surface layer of the γ- austenite. The latter is indicated in the base once the TiN film has already been deposited. However, the character of the dislocation structure (long, strain dislocations, Fig. 5a) testifies to the fact that the dislocations have formed as a result of the relief of internal stresses (see Sec. 1) in the thin foils during and after their preparation. The dislocation density therewith is no more then $\rho=10^{10}$ cm^{-2}. For the dislocations generated in ion-beam treatment, their density is greater by an order of magnitude and reaches $\rho=10^{11}cm^{-2}$ (Fig. 5b).

The latter results in a noticeable strain strengthening of the base ($\Delta\sigma=\alpha Gb\rho^{1/2}=G/300$, were $\alpha=0.3$, G is the shear modules of the base material, and

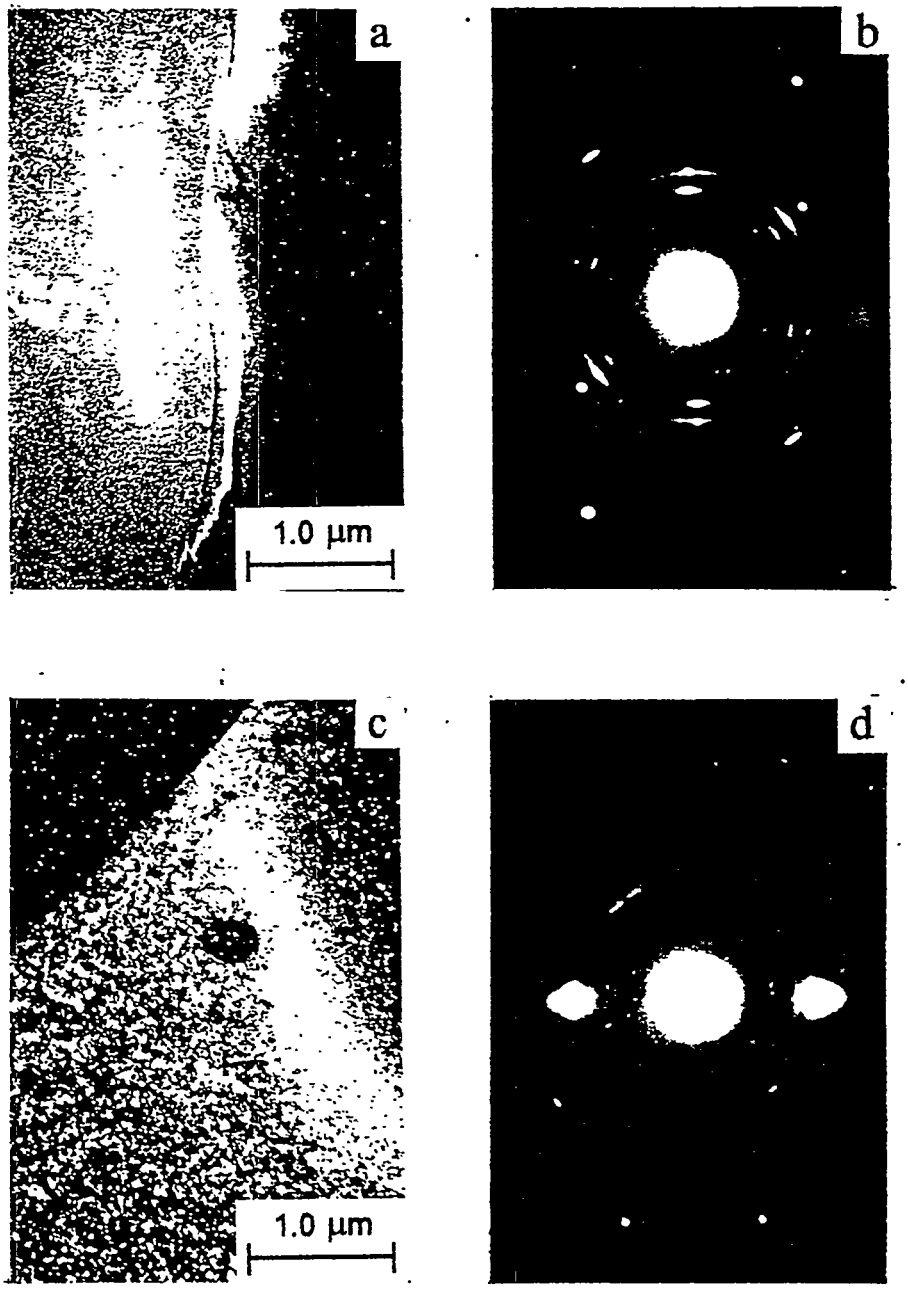


Fig.4. Microstructure (a,c) and microdiffraction patterns (b,d) of the base-coating contact zone after ion-plasma deposition of a thin nitride layer (a,b) and subsequent i.i. (c,d). a,c - dark- field image in the reflections of γ-austenite and TiN.

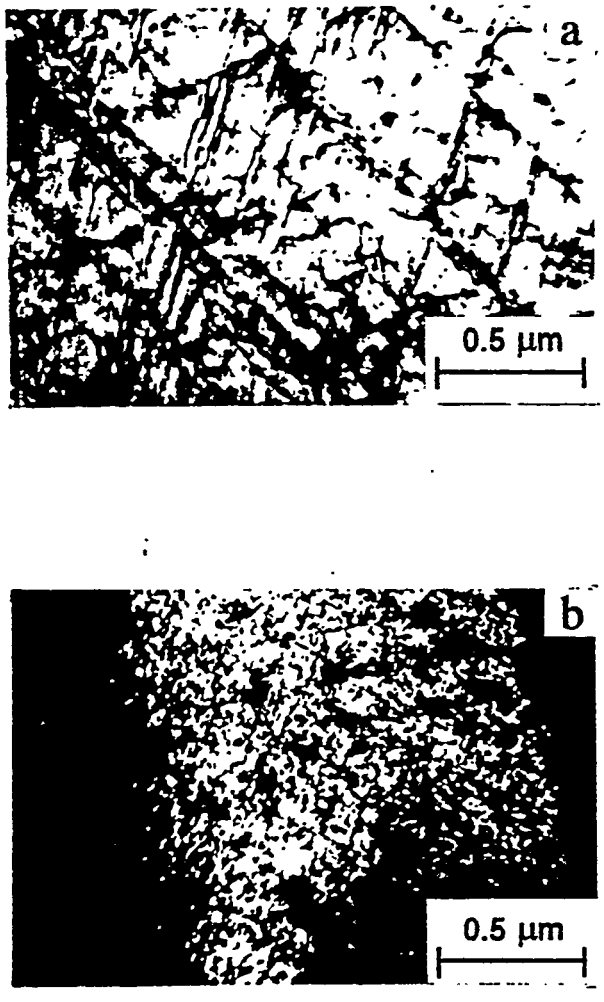


Fig.5. Dislocation structure of the surface layer of stainless steel after deposition of a thin TiN film (a) and subsequent i.i.(b).

b is the Burgers vector for dislocations). In combination with the solid-solution hardening of the γ-astatine with nitrogen and the substructural softening of the coating (see Sec. 4), this reduces significantly the gradients of mechanical properties in the contact zone between the base and the coating.

Thus, the deposition of the thin nitride layers followed by ion-beam treatment makes it possible to lower significantly the level of internal stresses at the base-coating interface, to reduce the structural gradients and the gradients of mechanical properties in this zone, and to stimulate the epithaxial character of the junction between the base and the coating. Evidently, all this should increase the adhesive strength of the coating.

The above results also show that the deposition of TiN on the surface of stainless steel prevents the formation of oxygen-containing compounds of the interstitial phases. An expected, this seems to be related to the fact that the nitride phase layer serves as an efficient barrier which hinders the interaction of the base surface with the oxygen of the implanter gas medium and reduces the efficiency of the ion mixing of the components of this medium during i.i.

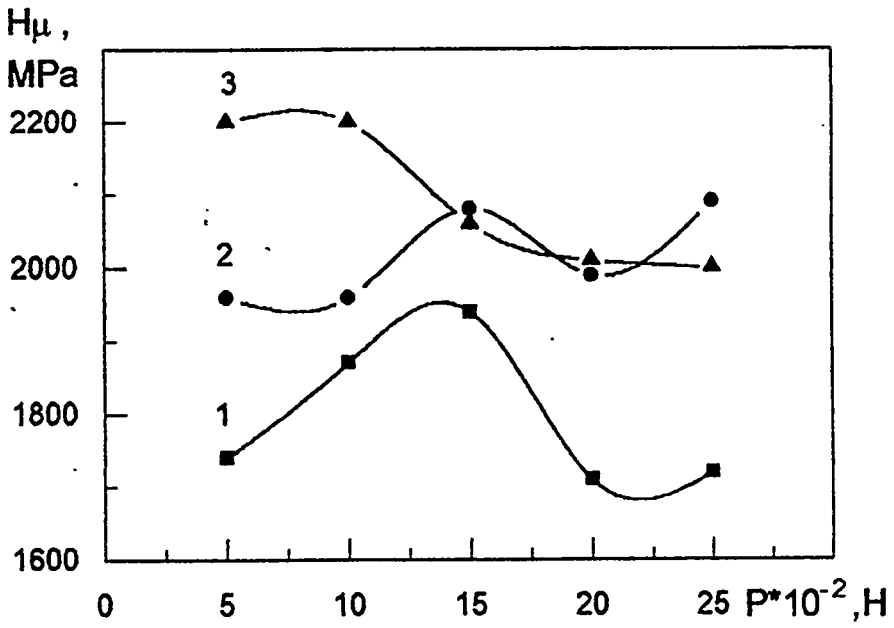


Fig.6. Microhardness of the surface layer of stainless steel as a function of the load on indenter , measured in the initial state (1), after deposition of a nitride layer (2), and after subsequent i.i. (3).

Despite the small thicknesses of the deposited nitride film and the ion-doped layer in the stainless steel base, microhardness measurements at small loads reveal a noticeable strengthening ($\Delta\sigma$ = 500 MPa) of the surface layer after ion-beam treatment (Fig. 6). The microhardness therewith increases both after the deposition of a thin TiN layer (curve 2 in Fig. 6) and as a result of the subsequent ion implantation (curve 3 in Fig. 6). The latter seems to be due to the strain and solid-

solution strengthening of the base in the process of ion implantation and ion mixing (see the above discussion).

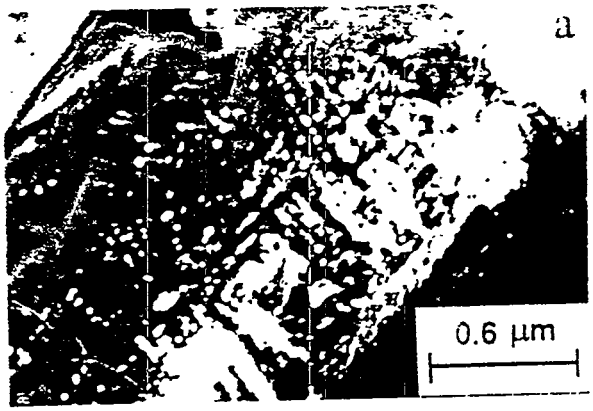
2.2 Modification of the Microstructure of Titanium Alloys on Ion Implantation

The doping of titanium alloys with nitrogen by ion-beam treatment in the modes discussed in Sec.1 results in the formation of solid surface layers of TiN δ-nitride having an fcc lattice. An example of such a layer of thickness ~100 nm formed in the type BT-9 alloy doped with nitrogen ions in combination with the components of the $(TiB_2)Fe$ composite cathode is given in Fig. 7. The substantial azimuthal disorientations in the TiN layer seen in an electron diffraction pattern (Fig. 7b) as well as the character of the dark-field contrast (Fig. 7a) unambiguously testify to the dispersion of the TiN lattice into mutually disoriented submicroareas of the nanometric scale. The nature of the dispersion of the surface nitride layer is associated with high nonuniform stresses appearing and relaxing during phase transformations. (We have discussed these stresses in detail as applied to the formation of such layers in molybdenum in Refs. 3 and 8).

These high nonuniform stresses also cause a qualitative change of the defect substructure in the underlying titanium layer. After ion implantation, in the originally monocrystalline microvolumes of this layer, disoriented substructures of various types are observed. The features of their fine structures are determined by the temperature of the target in ion-beam treatment.

At comparatively low (<450 K) temperatures, these structures are high-energy defect structures with strongly curved lattices. The azimuthal disorientations that reach some tens of degrees at distances of the order of 1 μm are illustrated by Fig. 8a. A dark-field analysis of the disorientations (Fig. 8b) performed by a specially developed technique [10] has failed to indicate any local boundaries of disorientations in the microvolumes examined. It follows that the substructure formed in the surface layer has high continuous disorientations; its lattice curvature being $K=0.5\ \mu m^{-1}$ and the excess density of dislocations of the same sign $\rho_{\pm}=\rho_{+}-\rho_{-}=|K/b|=2*10^{11}\ cm^{-2}$. It has been shown [10-12] that in order that such a structure be formed it is necessary that, first, high nonuniform internal stresses be available and, second, their dislocation relief be efficiently suppressed. For the i.i. of titanium, the former is attained owing to the phase transformation Ti+N→TiN that goes with a significant spatial disparity between the TiN second phase and the matrix. The latter is the result of the significant precipitation (with TiN particles) and solid solution (with nitrogen) hardening in the ion-doped layer. In combination with the high strain strengthening in the substructure with the large curvature of the lattice, this substantially reduces the gradients of mechanical properties at the Ti-TiN interface.

Increasing target temperature promotes the dislocations and diffusion stress relief. As a result, after i.i. at T=700 K, the surface layer is observed to disperse into nanometer-scale grains (50 to 500 nm with an average diameter d=100 nm; see Fig. 9b,c) with large-angle disorientations (Fig. 9a). Thus, varying the target temperature in i.i. of titanium, one may widely vary the structural state of the surface layer, the internal stresses in the layer, and the strength properties of the composition in the Ti-TiN contact zone.



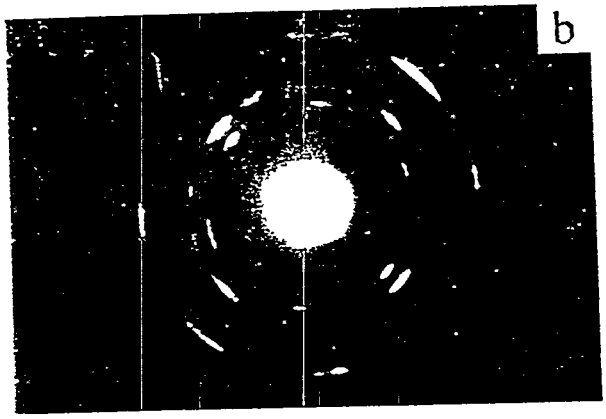


Fig.7. Dark- field micrograf (a) and microdiffraction pattern (b) of titanium nitride in the type BT-9 alloy after ion implantation.

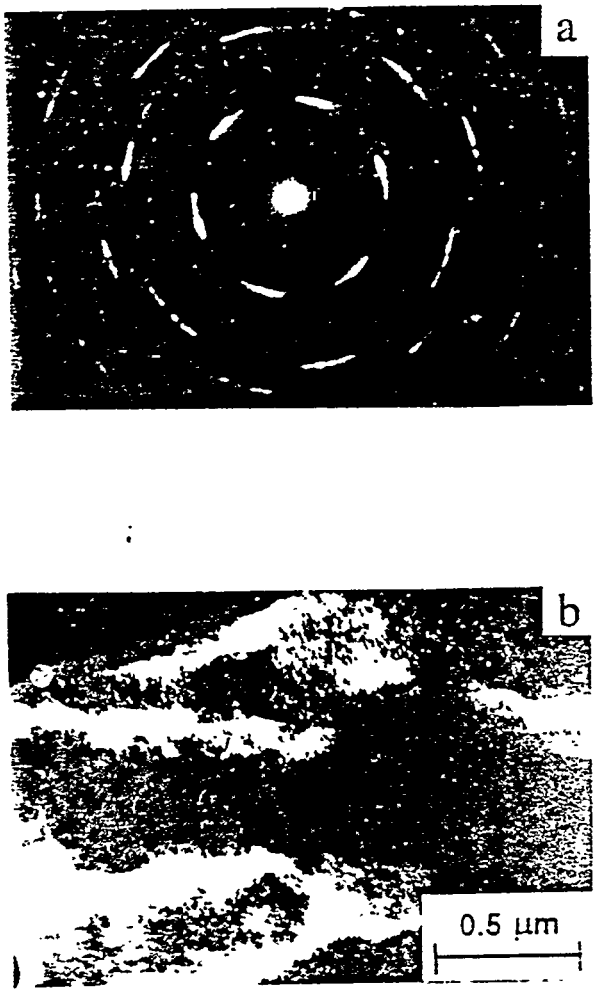


Fig.8. Microdiffraction patterns (a) and dark-field image (b) of the microstructure of the Ti surface layer after implantation with nitrogen ions at 450 K.

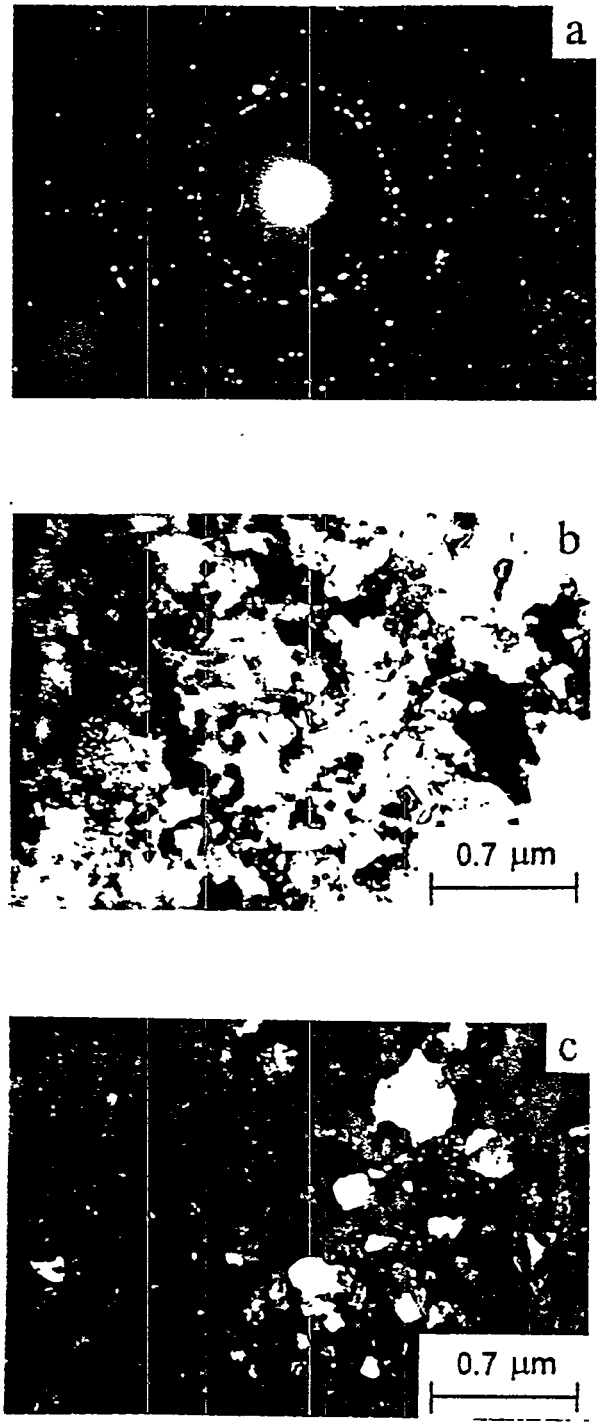


Fig.9. Electron-diffraction pattern (a) and microstructure (b.c) of the Ti surface layer after implantation with Ti+N ions at 700 K: b - light-field image, c - dark - field image in the reflections of the dispersed layer.

An important feature of the surface layer microstructure, as follows from electron microscopy, is the absence of a sharp boundary between the target material and the solid layer of TiN δ-nitride which gradually changes into the matrix with decreasing the volume fraction of the interstitial phase. The latter implies high adhesive strength at the Ti-TiN interface. The nanocrystalline structure of TiN should be beneficial for increasing the viscosity of fracture of this phase.

The decreased structural and mechanical gradients at the interface between Ti and TiN, the nanocrystalline structure of the latter as well as the possibility to control the structural state and the mechanical properties in the Ti-TiN contact zone offer promise for using i.i. to create intermediate (between the base and the coating) graded layers which increase the adhesive strength and performance of TiN coatings on titanium alloys.

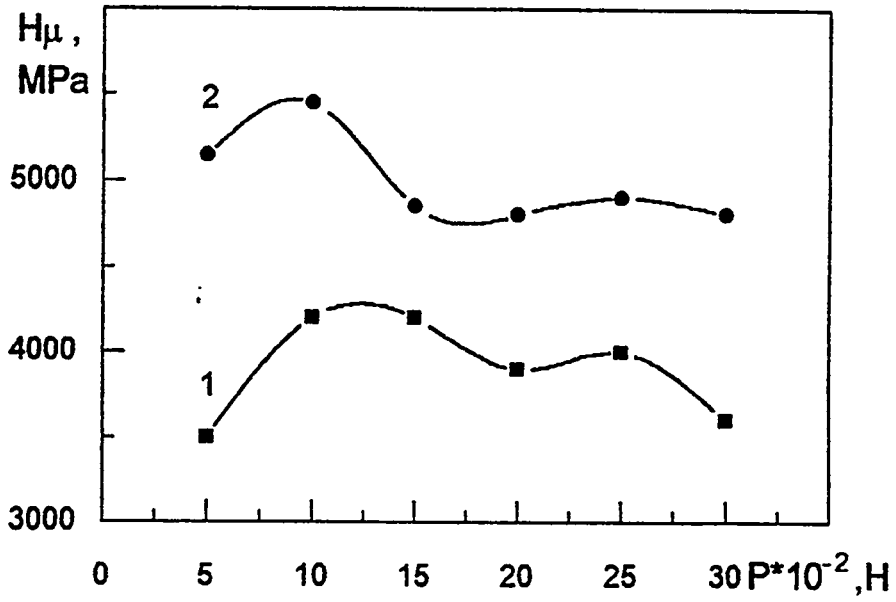


Fig.10. Microhardness of the surface layer of BT-9 alloy as a function of the load on the indenter , measured in the initial state (1), and after i.i. (2).

The i.i. modes discussed above are also of independent (irrespective to subsequent deposition of coatings) interest for increasing the performance of titanium alloy surfaces. This is testified by the experimental evidence that the surface hardness of the type BT-9 alloy appears to be substantially increased on ion implantation (Fig. 10).

3 Conclusions

As a result of the above-described investigation it has been established that high-dose i.i. combined with ion mixing of the components of the Titan implanter gas medium and with deposition of thin (a few tens of nanometers) TiN or Ti films is an efficient technique for production of amorphous, crystalline-amorphous, and

nanocrystalline structural states of varied composition in the intermediate (between the substrate and the coating) layers as well as for the modification of internal stresses at the coating-base interface. The features of the phase-structure state of the modified intermediate layers depend not only on the ion beam parameters (power density, ion energy, radiation dose, etc.) and the composition of the implanter gas medium but also on the target temperature. The temperature dependence is so strong that for austenitic stainless steel qualitative changes may appear in the fine structure of the modified layer when the temperature is changed by only a few tens of degrees. This offers the possibility to control the phase-structure states and properties of the intermediate (between the substrate and the coating) layer to improve the performance of the coating. For this purpose, the following techniques for modification of the intermediate layer have been developed:

1. Implantation of austenitic stainless steel with $Ti^+ + N^+$ ion combined with ion mixing of the oxygen from the implanter gas medium adsorbed on the surface. This treatment results in the formation of intermediate layers of oxynitrides being in the amorphous, crystalline- amorphous, or nanocrystalline state with simultaneous solid-solution and strain strengthening of γ-austenite and reduction of the gradients of the composition mechanical properties.

2. The above treatment combined with ion-reactive deposition of titanium which extends the temperature interval for the formation of an amorphous intermediate layer.

3. Ion-plasma deposition of a thin nitride film followed by ion-beam modification of the film and ion mixing. This treatment prevents the formation of oxygen-containing interstitial phases in the intermediate layer and provides significant reduction of the internal stresses and the gradient of the microstructure and mechanical properties of the composition at the interface of the substrate (stainless steel) and the TiN coating .

4. Ion implantation of titanium alloys with nitrogen or with nitrogen together with titanium or components of composition cathodes of the type $(TiB_2)Fe$. This treatment provides the formation of TiN-based thin nanocrystalline coatings as intermediate (between the substrate and the coating) layers, significant strain and solid-solution strengthening of titanium, and reduction of the mechanical property gradients in the intermediate layer.

The above structural states can be utilized as intermediate (between the coating and the substrate) layers in various techniques of production of titanium-nitride-base coating. Their efficiency in the improvement of the performance of ion-plasma-deposited TiN coatings will be investigated at the next stage of the work under the contract.

References

1. AN Tyumentsev, Yu.P. Pinzhin, and A.D. Korotaev, Nucl. Instr. and Methods in Phys. Res., 1993, V. 80/81, P. 491-495.

2. A.N. Tyumentsev, Yu.P. Pinzhin, A.D. Korotaev et al., The Physics of Metals and Metallography, 1992, V. 68, No 9.

3. A.N. Tyumentsev, Yu.P. Pinzhin, A.E. Bekhert, A.D. Korotaev et al., Ibid., 1992, V. 68, No 9.

4. A.D. Korotaev, Yu.R. Kolobov, and A.O. Savchenko, Phys. Res., 1988, No 8, P. 210-212.

5. V.G. Abdrashitov, A.E. Bekhert, A.D. Korotaev et al., Poverkhnost, 1993, No 5, P. 141-152.

6. A.D. Korotaev and A.N. Tyumentsev, A.E. Bekhert, and S.P. Bugaev, Rus. Phys. J., 1994, V.37, No 2, P. 109-114.

7. A.D. Korotaev and A.N. Tyumentsev, Ibid., 1994, V. 37, No 8.

8. A.N. Tyumentsev, A.D. Korotaev, and S.P. Bugaev, Ibid., 1994, V. 37, P. 452-461.

9. S.S. Gorelik, L.N. Rastorguev, Yu.A. Skakov. Roentgenographic and Electronographic Analysis of metals. Supplement. (in Russian), Metallurgya, Moscow (1963)

10. V.Ch. Gonchikov, A.N. Tyumentsev, and A.D. Korotaev, The Physics of Metals and Metallography, 1987, V. 63, No 3.

11. A.D. Korotaev, A.N. Tyumentsev and V.F. Sukhovarov, Dispersion Strengthening of Refractory Metals. Nauka, Novosibirsk 1989.

12. A.D. Korotaev, A.N. Tyumentsev, V.Ch. Gonchikov, and A.I. Olemskoi, Rus. Physics J., 1991, V. 37, No 3.

Project Title: Surface Treatments for the Enhancement of the Performance of Diamond-like Coatings (DLC) on Tool Steels.
Principal Investigator: N. V. Gavrilov
Institute of Electrophysics
Ekaterinburg, Russia
AM-7677

CLAUSE 1 - STATEMENT OF WORK

Tasks:

The Contractor shall:

1. Provide a report that describes:
the design and operation of the ion source
previous work performed by the Contractor on strategies to improve the adhesion and performance of DLC films on tool steels

2. Conduct ion implantation studies using the following parameter ranges:
species: N (nitrogen) and C (carbon)
substrate temperature = 200(C to 700(C, dose = 1017 to 1019 ions per cm2, and frequency = 10 to 50 Hz ;
depth distribution of C & N shall be determined using nuclear reaction analysis

The Contractor shall provide a report description of the experiments conducted.

3. Coat the implanted substrates with DLC using arc evaporation at a rate of approximately 2 microns per hour. The coating thickness shall range from 3 to 5 microns. The substrate temperature during deposition shall be approximately 200(C. The microhardness and wear resistance of the implanted and coated shall be characterized. The Contractor shall provide a final report on the experimentation data and results.

Doc. 7677

PREVIOUS WORK PERFORMED BY THE CONTRACTOR ON STRATEGIES TO IMPROVE THE ADHESION AND PERFORMANCE OF DLC FILMS ON TOOL STEELS

Our previous investigations were connected in the main with searching for the ways of a maximum possible realization of strength characteristics of carbon diamond-like coatings (DLC's) so that a maximum effect is obtained in their practical applications [1-8].

We refined methods for correct measurement of the wear resistance of thin coatings [1-3] and designed an installation for testing of samples in a jet of abrasive particles, which is produced by a centrifugal accelerator [4]. Ten samples can be tested simultaneously in the installation at the speed of abrasive particles from 5 to 100 m/sec and the incidence angle from 20 to 90°.

In our investigations of the wear of samples with DLC's we never observed wear of the coating material itself. Cracking and peeling of the coating are responsible for the failure of the sample's surface with DLC (Fig.1).

In the case of hard brittle materials (for example, quartz, germanium, tungsten-cobalt alloys) the main factor that determines stability of DLC's is adhesion to the substrate [1, 2, 4, 8]. On softer materials (for example, stainless steel, permalloy) peeling of the coating is preceded by its cracking as a result of deformation of the substrate under the DLC [4, 7]. So, the problem resides in provision of conditions favorable for the best possible adhesion of the coating to the strengthened surface rather than in refinement of the methods used to condense the coating. For this reason the strategy adopted by us for the most comprehensive use of DLC's as strengthening coatings was realization of all the procedures that contribute to improving stability of the "DLC - substrate" system. These include chemical pretreatment of the substrate, argon ionic cleaning prior to sputtering, and deposition of a thin (about 0.1 of the DLC thickness) titanium sublayer [5]. Tests in a jet of abrasive particles served to assess adhesion of the coating to the substrate. At a constant speed of the particles the number of the abrasive portions N causing appearance of the first traces of peeling was determined. Otherwise a different area of the coating received the same portions of the abrasive at different speeds. The speeds V_B and V_E , which correspond to the beginning of peeling and complete peeling respectively, were registered.

For example, an additional distillation of the organic detergents used for preliminary cleaning of the substrates increased V_B from 12 to 14 m/sec and V_E from 18 to 23 m/sec in the case of the system "stainless steel - DLC (5 μ)". The variation of V_B and V_E for the samples in a single series of tests was two times as low [5]. As a result, it was possible to produce sufficiently strong DLC's on tool steels and to test cutting tools (milling cutters) over a wide range of operating conditions [6]. Subsequently, a stable increase in the service life of the tools (approx. by 2 times) allowed a successful use of the DLC's for strengthening of milling cutters, taps and knives under real conditions of production.

However, the above-mentioned measures for adhesion improvement (thorough cleaning of surfaces, titanium sublayer) have been almost exhausted. It was necessary to look for other methods of strengthening the "DLC - substrate" system. In this respect a very promising direction was modification of the system using ionic implantation, which is one of the known methods of surface strengthening. The implantation showed promise in terms of the physical processes determining properties of surface layers of the material since it allows one to:

1) change the chemical, structural and phase compositions;

2) produce an additional system of lattice defects (point defects, dislocations) that can

improve hardness;

3) increase reactivity of the surface thanks to ionic bombardment.

The implantation is also promising from the viewpoint of technological equipment (if the technology yields positive results) because it permits sputtering of the DLC and implantation modification to be performed in situ, i.e. in a single vacuum cycle avoiding an intermediate exposure of the item's surface to the air.

We have performed initial experiments aimed at determining the influence that implantation of nitrogen and carbon ions (30 keV) has on adhesion of DLC's 2 to 3 μ thick to metal substrates [8]. Hard substrates were samples of the tungsten- cobalt alloy BK6 (designations are given accorging to the nomenclature adopted in Russia), which is used as a material of carbide tools, while soft substrates were samples of the austenitic chromium-nickel stainless steel 12X18H10T.

As before, DLC's were sputtered from a graphite target using the method of vacuum pulse arc discharge [2, 4-7]. Microhardness of the substrates (a diamond pyramid, loads up to 200 g) and characteristics of the coating adhesion to the substrate N, V_B and V_E in a jet of corundum particles were measured.

Experiments on ion-beam modification of the DLC proper (nitrogen implantation) did not yield positive results. As the irradiation dose was increased, stability of the DLC on the stainless steel lowered (Fig.2) and graphitization developed in the coating. This was determined, in accordance with literature data, by a characteristic change in the form of the Raman spectrum and by the shift of the entire spectrum to the long-wave region.

A different result was obtained when the DLC was sputtered on a preliminary implanted substrate. As the irradiation dose was increased, adhesion of the coating to the substrate improved (Figs 3 and 4). Note that in the case of the hard alloy microhardness of the substrate did not increase at least (Fig.4), a fact which shows that the effect was achieved owing to an improved adhesion.

In the case of the soft stainless steel the basic role in a higher stability of the DLC on the implanted substrate could belong to strengthening of the material under the coating and, as a consequence, to a decrease in the deformation and formation of cracks in the DLC (Fig.3).

During experiments dealing with the influence of the temperature regime of carbon implantation in the stainless steel (the temperature was controlled by changing the pulse repetition rate of ion beam current) upon the DLC stability (Fig.5) we examined distribution of the carbon concentration in the implantation zone [9]. Measurements were made using a light-ion accelerator by the method of nuclear reactions on a 900-keV deuton beam.

It turned out that in all the implanted substrates the surface concentration of carbon was practically the same - about 5 %. Therefore a considerable influence of variations in adhesion on the observed improvement of the DLC stability is hardly probable. At the same time it was found that the width of the carburization zone increases (up to 3 μ at 460°C) with the samples temperature during ion implantation. This fact explains the observed (Fig.5) increase in microhardness of the substrates and accounts for an improved stability of the DLC primarily by a lower deformation of steel under the coating.

So, we showed that the effect of strengthening of the metal surface with a hard diamond-like coating can be enhanced using preliminary implantation of carbon and nitrogen in the substrate. This provides a serious reason to stage more comprehensive studies in this direction, in particular on samples of tool steels with the aim of elucidating the prospects of developing an effective

technology for surface strengthening of tools.

Such study is the subject of the work we are currently engaged in. The sample materials will be as follows:

1. High-speed steel P6M5. The steel is used for all types of cutting tools used to machine carbon and medium-alloy structural steels and for gear- and thread-cutting tools used to machine stainless steels.

Composition (% by mass): C 0.80-0.88, Cr 3.8-4.4, W 5.5-6.5, V 1.7-2.1, Mo 5.0-5.5; HRC 63-65.

2. Cold-working die steel X12M. The steel is used for production of rollers, drawholes, dies and punches.

Composition (% by mass): C 1.45-1.65, Si 0.15-0.35, Mn 0.15- 0.40, Cr 11.0-12.5, V 0.15-0.30, Mo 0.40-0.60; HRC 57-63.

REFERENCES

1. Klotsman S.M., Kovsh A.S., Kovsh L.M., Kuzmina E.V., Mukhametkhaziev R.R., Plotnikov S.A., Trakhtenberg I.Sh., and Feigin D.M. - Protective diamond-like coatings on quartz. Fizika i khimiya obrabotki materialov, 1991, No.6, p.p. 113-116.

2. Gorpinchenko S.D., Klotsman S.M., Kuzmina E.V., Plotnikov S.A., and Trakhtenberg I.Sh. - Wear resistance of diamond- like coatings. - Surface and Coating Technology, 1991, v.47, p.p. 201-208.

3. Trakhtenberg I.Sh. and Gorpinchenko S.D. - Determination of wear resistance of hard coatings. - Treniye i Iznos, 1993, v.14, p.p. 907-913.

4.Gorpinchenko S.D., Klotsman S.M., Kuzmina E.V., Plotnikov S.A., and Trakhtenberg I.Sh. - Friction, wear and service properties of i-C coatings on steel. - Diamond and Related Materials, 1992, v.1, p.p. 619-622.

5. Gorpinchenko S.D., Plotnikov S.A., and Trakhtenberg I.Sh. - Wear of diamond-like and other hard coatings on steel in a jet of corundum particles. - Abstracts of 3rd European Conference on Diamond, Diamond-like and Related Coatings, Aug. 31 - Sept. 4, 1992, Heidelberg, Germany, p.13.112.

6. Trakhtenberg I.Sh., Plotnikov S.A., Vladimirov A.B., Liberman Ya.L., Kanalina V.A., Boborykin V.A., and Leizerov V.M. - Service properties of cutting tools hardened with a diamond - like coating. - Diamond and Related Materials, 1993, v.2, p.p. 1434-1438.

7. Arbuzov V.L., Vladimirov A.B., Vykhodets V.B., Davletshin A.E., Plotnikov S.A., Trakhtenberg I.Sh., Rubshtein A.P., Gorpinchenko S.D., and Kuzmina E.V. - Practical use of strength and anticorrosion properties of amorphous carbon thin films. - Diamond and Related Materials, 1994, v.3, p.p. 775-778.

8. Gorpinchenko S.D., Trakhtenberg I.Sh., Bakunin O.M., Plotnikov S.A., Nechaev A.A., Mizgulin V.N., and Gavrilov N.V. - Breakdown of a-C coatings on ion-implantation- modified metal alloys with a jet of abrasive particles. - Diamond and Related Materials, 1994, v.3, p.p. 779-782.

9. Trakhtenberg I.Sh., Plotnikov S.A., Bakunin O.M., Yakovleva S.G., Nechaev A.A., Gorpinchenko S.D., Korshunov L.G., Gavrilov N.V., and Mizgulin V.N. - The effect of additional treatment on tribological properties of a-C coatings on metals. - Abstracts of 5th European Conference on Diamond, Diamond-like and Related Materials, Sept. 25 - Sept. 30, 1994, Il Chiocco, Italy, p. 9.089.

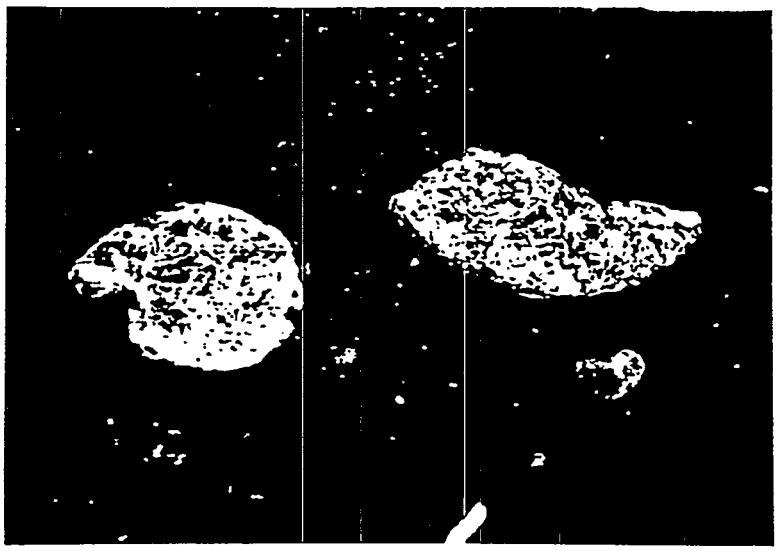


Fig. 1. Typical pattern of breakdown of DLC on stainless steel by corundum particles (DLC thickness 2 μ on Ti-sublayer, particles speed 13 m s^{-1}, particle size about 120 μ, incidence angle 90°), 200^{x}.

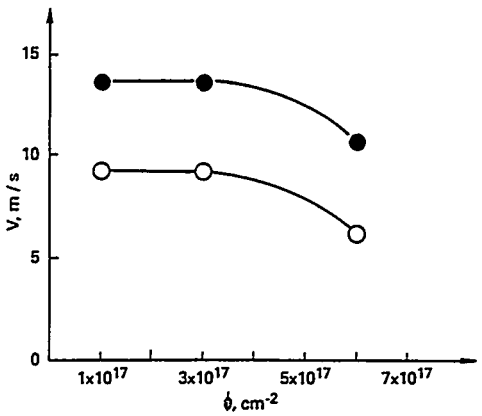


Fig. 2 Resistance of DLCs approximately 3 μm thick on stainless steel 12X18H10T to a jet of abrasive particles after irradiation of the coatings with 30 keV nitrogen ions. Mass of the portions of corundum particles is 1 kg; particle dimension, approximately 120 μm; incidence angle, 90°. ○, V_b (=speed of abrasive particles at which coating starts peeling); ●, V_e (=speed of abrasive particles at which coating is stripped completely).

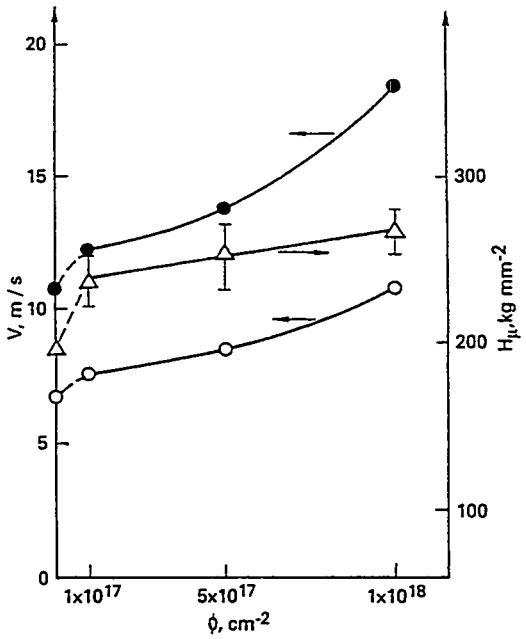


Fig. 3 Resistance of DLCs approximately 3 μm thick on stainless steel 12X18H10T implanted with 30 keV nitrogen ions to a jet of abrasive particles. The implantation temperature of the specimens is approximately 600 °C. Mass of the portions of corundum particles is 1 kg; particle dimension, approximately 120 μm; incidence angle, 90°. ○, V_b (=speed of abrasive particles at which coating starts peeling); ●, V_c (=speed of abrasive particles at which coating is stripped completely); △, microhardness of stainless steel after irradiation with N^+ ions.

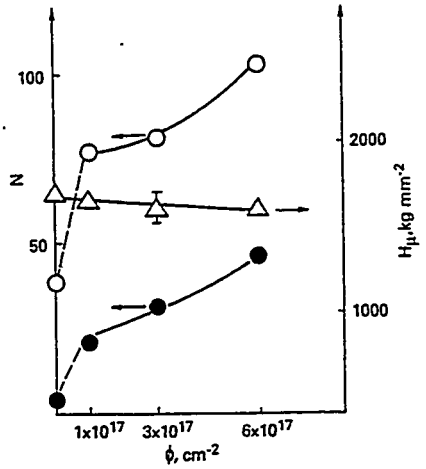


Fig. 4 Abrasive particle resistance of DLCs approximately 3 μm thick on BK60 alloy implanted with 30 keV nitrogen ions at a fluence Φ. The implantation temperature of the specimen is less than 100 °C. Mass of the portions of corundum particles is 1 kg; particle dimension, approximately 120 μm; incidence angle, 45°; speed of abrasive particles, 45 m s^{-1}. ●, N_b (the number of abrasive portions for which the coating starts peeling); ○, N_e (the number of abrasive portions for which the coating is stripped completely); △, microhardness of BK60 alloy after irradiation with N^+ ions.

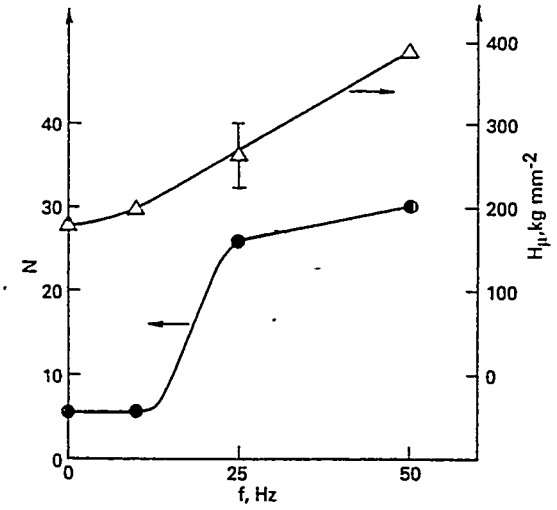


Fig. 5 Abrasive-particle resistance of DLCs approximately 2 μm thick on stainless steel 12X18H10T implanted with 30 keV carbon ions at a fluence of 5×10^{17} cm^{-2} and irradiation frequency f. Frequencies 10, 25 and 50 Hz correspond to the specimen temperatures 250, 400 and 460 °C. Mass of the portions of corundum particles is 1 kg; particle dimension, approximately 120 μm; incidence angle, 45°; speed of abrasive particles, 10 m s^{-1}. ●, N_b (number of abrasive portions for which the coating starts peeling); △, microhardness of stainless steel after irradiation with C^- ions.

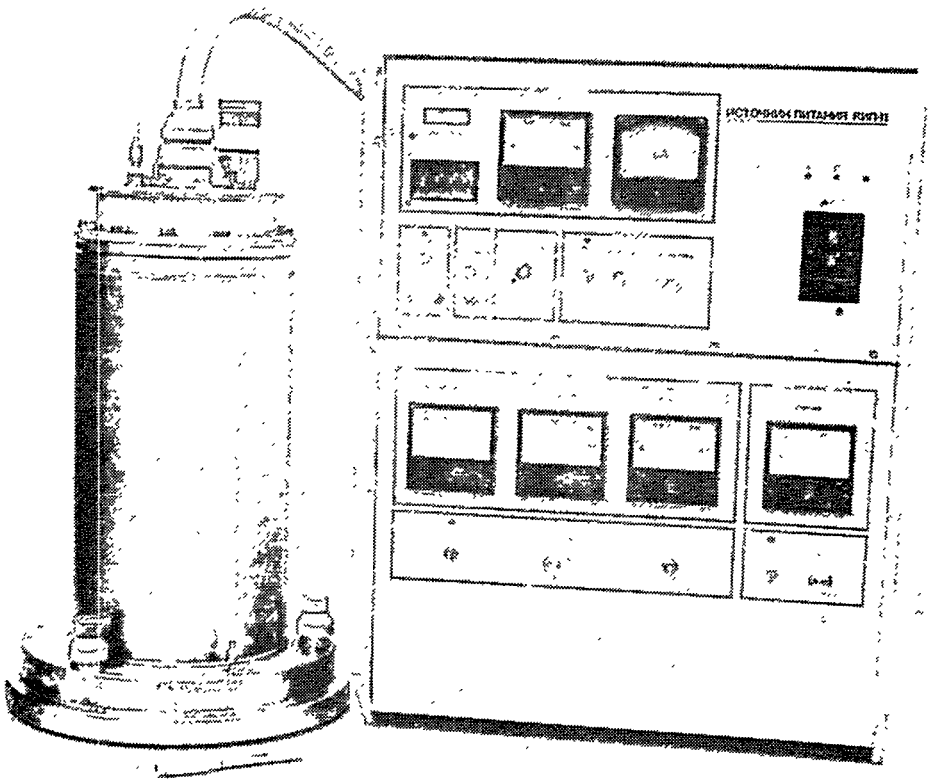


Fig.5

Doc. 7677

ПРЕДЫДУЩИЕ РАБОТЫ ИСПОЛНИТЕЛЯ ПО СТРАТЕГИИ УЛУЧШЕНИЯ АДГЕЗИИ И СВОЙСТВ DLC НА ИНСТРУМЕНТАЛЬНЫХ СТАЛЯХ

Основной темой проведенных ранее исследований был поиск путей реализации потенциально высоких прочностных свойств углеродных алмазоподобных покрытий (DLC) с целью получения максимального эффекта при их практическом использовании [1-8].

Были усовершенствованы методы корректного измерения износостойкости тонких покрытий [1-3] и создана установка для испытаний в струе абразивных частиц, образуемой с помощью центробежного ускорителя [4]. Установка позволяет испытывать одновременно 10 образцов в диапазоне скоростей абразивных частиц от 5 до 100 м/сек и углов атаки от 20 до 90°.

В наших исследованиях процесса изнашивания образцов с DLC мы никогда не наблюдали износа собственно материала покрытия. Разрушение поверхности образца с DLC всегда происходит путем растрескивания и отслаивания покрытия (рис. 1).

На твердых хрупких материалах (например, кварц, германий, вольфрам - кобальтовые сплавы) основным фактором, определяющим устойчивость DLC, является адгезия к подложке [1, 2, 4, 8]. На более мягких материалах (например, нержавеющая сталь, пермаллой) отслоению покрытий предшествует его растрескивание вследствие деформации подложки под DLC [4, 7]. Таким образом, проблема состоит не столько в совершенствовании методов конденсации этого покрытия, сколько в создании условий для его наилучшего закрепления на упрочняемой поверхности. Поэтому стратегическим направлением наших работ по наиболее полному использованию DLC как упрочняющего покрытия нами было выбрано проведение всех процедур, способствующих повышению устойчивости системы DLC - подложка. Сюда относится предварительная химическая очистка подложки, ионная очистка аргоном перед напылением, осаждение тонкого (около 0.1 от толщины DLC) подслоя титана [5]. В качестве критерия прочности сцепления покрытия с подложкой служили испытания в струе абразивных частиц. При постоянной скорости частиц фиксировалось количество порций абразива N, приводящих к первым следам отслаивания. В другом варианте каждый раз на свежий участок покрытия направлялись одинаковые порции абразива, но с разными скоростями. Фиксировались скорости V_B и V_E - скорости начала отслоения и, соответственно, полного отслоения покрытия с испытываемого участка. Например, дополнительная дистилляция органических моющих средств, применяемых для предварительной очистки подложек, привела для системы нержавеющая сталь - DLC (5 мкм) к росту V_B от 12 до 14 м/сек и V_E от 18 до 23 м/сек. При этом в 2 раза сократилась вариация V_B и V_E между образцами в одной серии испытаний [5]. В результате удалось получить достаточно прочные DLC- покрытия на инструментальных сталях и испытать в широком диапазоне условий эксплуатации режущий инструмент (фрезы) [6]. Стабильное увеличение ресурса инструмента (примерно в 2 раза) позволило в

дальнейшем успешно применить DLC для упрочнения фрез, метчиков, ножей в реальном производстве.

Однако упомянутые выше меры улучшения адгезии (тщательная очистка поверхностей, титановый подслой) были практически исчерпаны. Следовало искать дальнейшие пути упрочнения системы DLC - подложка. В этом смысле весьма перспективным направлением была модификация этой системы путем ионной имплантации, являющейся одним из известных способов поверхностного упрочнения, Имплантация была перспективна с точки зрения физических процессов, определяющих свойства приповерхностных слоев материала, поскольку она :

1) Позволяет изменять элементный, структурный и фазовый состав поверхностных слоев.

2) Создает дополнительную систему дефектов кристаллического строения (точечных дефектов, дислокаций), способных повысить твердость.

3) Может повысить химическую активность поверхности, как следствие ионной бомбардировки.

Имплантация перспективна и с точки зрения аппаратурного оформления технологии (если таковая даст положительный результат), поскольку принципиально позволяет провести и напыление DLC, и имплантационную модификацию в одной вакуумной установке, т.е. в одном вакуумном цикле без промежуточного контакта поверхности изделия с воздухом.

Нами были проведены первые эксперименты по влиянию имплантации ионов азота и углерода (30 КэВ) на прочность сцепления DLC толщиной 2 - 3 мкм с металлическими подложками [8]. Примером твердой подложки служили образцы вольфрам - кобальтового сплава ВК6 (применяется как материал твердосплавных резцов), а мягкой - аустенитная хромо - никелевая нержавеющая сталь 12Х18Н10Т.

DLC напылялись, как и ранее на металлы, с графитовой мишени методом вакуумного импульсного дугового разряда [2, 4-7].

Измерялась микротвердость подложек (алмазная пирамида, нагрузки до 200 г), а также характеристики прочности сцепления покрытий с подложкой N, V_B и V_E в струе абразивных частиц корунда.

Эксперименты по ионной модификации собственно DLC (имплантация азота) не дали положительного результата. С ростом дозы облучения устойчивость DLC на нержавеющей стали падала (рис. 2), а в самом покрытии проходил процесс графитизации, что обнаружено было, в согласии с литературными данными, по характерному изменению формы Рамановского спектра и сдвигу всего спектра в длинноволновую область.

Другой результат был получен на образцах, на которых DLC напылялось на предварительно имплантированную подложку. С ростом дозы облучения (рис. 3, 4) возрастало сцепление покрытия с подложкой. При этом на твердом сплаве (рис. 4) микротвердость подложки по крайней мере не возрастала, что указывало на получение эффекта за счет повышения адгезии.

На мягкой нержавеющей стали основную роль в повышении устойчивости DLC

на имплантированной подложке могло сыграть упрочнение материала под покрытием и, как следствие, уменьшение деформации и образования трещин в DLC (рис. 3).

В экспериментах по влиянию температурных условий имплантации углерода в нержавеющую сталь (температура регулировалась изменением частоты следования импульсов тока пучка ионного имплантера) на устойчивость DLC (рис. 5) было исследовано распределение концентрации углерода в зоне имплантации [9]. Измерения были проведены с помощью ускорителя легких ионов методом ядерных реакций на пучке дейтонов 900 КэВ.

Оказалось, что поверхностная концентрация углерода во всех имплантированных подложках была практически одинаковой, - около 5%, что делало маловероятным существенное влияние изменения адгезии на наблюдаемое повышение устойчивости DLC. В то же время было обнаружено, что с ростом температуры имплантации возрастает (до 3 мкм при 460°C) ширина науглероженной зоны.

Это объясняет наблюдаемое (рис. 5) повышение микротвердости подложек и объясняет повышение устойчивости DLC, в основном, уменьшением деформации стали под покрытием.

Таким образом, нами было показано, что эффект упрочнения поверхности металла твердым алмазоподобным покрытием может быть усилен предварительной имплантацией углерода и азота в подложку. Это служит серьезным основанием для проведения более подробных исследований в этом направлении, в частности, на образцах инструментальных сталей с целью определения перспектив создания эффективной технологии поверхностного упрочнения инструмента.

Такое исследование и является предметом проводимой нами работы. В качестве материала для образцов будут служить:

1. Р6М5 - быстрорежущая сталь. Применяется для изготовления всех видов режущих инструментов для обработки углеродистых и среднелегированных конструкционных сталей, зуборезных и резьборезных инструментов для нержавеющих сталей.

Состав (% по массе): C 0.80 - 0.88; Cr 3.8 - 4.4; W 5.5 - 6.5; V 1.7 - 2.1; Mo 5.0 - 5.5, HRC 63 - 65.

2. Х12М - штамповая сталь для холодного деформирования. Применяется для изготовления роликов, волок, матриц и пуансонов.

Состав (% по массе) C 1.45 - 1.65; Si 0.15 - 0.35; Mn 0.15 - 0.40; Cr 11.0 - 12.5; V 0.15 - 0.30; Mo 0.40 - 0.60, HRC 57 - 63

ЛИТЕРАТУРА

1. Клоцман С.М., Ковш А.С., Ковш Л.М., Кузьмина Е.В., Мухаметхазиев Р.Р., Плотников С.А., Трахтенберг И.Ш., Фейгин Д.М. - Защитные алмазоподобные пленки на кварце. - Физика и химия обработки материалов, 1991, N 6, стр. 113 - 116.

2. S.D. Gorpinchenko, S.M. Klotsman, E.V. Kuzmina, S.A. Plotnikov and I.Sh. Trakhtenberg - Wear resistance of diamond - like coatings. - Surface and Coating Technology, 1991, V.47, pp. 201 - 208.

3. Трахтенберг И.Ш., Горпинченко С.Д. - Определение износостойкости твердых покрытий. - Трение и износ, 1993, Т. 14, стр. 907 - 913.

4. S.D. Gorpinchenko, S.M. Klotsman, E.V. Kuzmina, S.A. Plotnikov and I.Sh. Trakhtenberg - Friction, wear and service properties of i-C coatings on steel. - Diamond and Related Materials 1992, V. 1, pp. 619 - 622.

5. S.D Gorpinchenko, S.A. Plotnikov, and I.Sh. Trakhtenberg - Wear of diamond - like and other hard coatings on steel in a jet of corundum particles. - Abstracts of 3rd European Conference on Diamond, Diamond - Like and Related Coatings, Aug 31 - Sept. 4, 1992, Heidelberg, Germany, p 13.112.

6. I.Sh. Trakhtenberg, S.A. Plotnikov, A.B. Vladimirov, Ya.L. Liberman, V.A. Kanalina, V.A. Boborykin, and V.M. Leizerov - Service properties of cutting tools hardened with a diamond - like coating. - Diamond and Related Materials 1993, V.2, pp. 1434 - 1438.

7. V.L. Arbuzov, A.B. Vladimirov, V.B. Vykhodets, A.E. Davletshin, S.A. Plotnikov, I.Sh. Trakhtenberg, A.P. Rubstein, S.D. Gorpinchenko and E.V. Kuzmina - practical use of strength and anticorrosion properties of amorphous carbon thin films. - Diamond and Related Materials 1994, V.3, pp. 775 - 778.

8. S.D. Gorpinchenko, I.Sh. Trakhtenberg, O.M. Bakunin, S.A. Plotnikov, A.A. Nechaev, V.N. Mizgulin, and N.V. Gavrilov - Breakdown of a-C coatings on ion-implantation-modified metal alloys with a jet of abrasive particles. - Diamond and Related Materials 1994, V.3, pp. 779 - 782.

9. I.Sh. Trakhtenberg, S.A. Plotnikov, O.M. Bakunin, S.G. Yakovleva, A.A. Nechaev, S.D. Gorpinchenko, L.G. Korshunov, N.V. Gavrilov and V.N. Mizgulin - The effect of additional treatment on tribological properties of a-C coatings on metals. - Abstracts of 5th European Conference on Diamond, Diamond - Like and Related Materials, Sept. 25 - Sept. 30, 1994, Il Chiocco, Italy, p. 9.089.

ПОДПИСИ К РИСУНКАМ

Рис. 1. Типичная картина разрушения DLC на стали струей частиц корунда (DLC толщиной 2 мкм на титановом подслое, скорость частиц 13 м/с, средний диаметр частиц 120 мкм, угол атаки 90°). Увеличение 200^x.

Рис. 2. Устойчивость DLC толщиной приблизительно 3 мкм на нержавеющей стали 12Х18Н10Т к воздействию пучка абразивных частиц после имплантации в покрытие ионов азота с энергией 30 КэВ. Масса порции корундовых частиц 1 кГ, размер частиц около 120 мкм, угол атаки 90°. o - V_b (скорость абразивных частиц, при которой покрытие начинает отслаиваться); • - V_e (скорость абразивных частиц, при которой покрытие отслаивается полностью).

Рис. 3. Устойчивость DLC толщиной приблизительно 3 мкм на нержавеющей стали 12Х18Н10Т, имплантированной ионами азота с энергией 30 КэВ. к воздействию пучка абразивных частиц. Температура образцов во время имплантации примерно 600°С. Масса порции корундовых частиц 1 кГ, размер частиц около 120 мкм, угол атаки 90°. o - V_b (скорость абразивных частиц, при которой покрытие начинает отслаиваться); • - V_e (скорость абразивных частиц, при которой покрытие отслаивается полностью); △ - микротвердость нержавеющей стали после имплантации ионов азота.

Рис. 4. Устойчивость DLC толщиной приблизительно 3 мкм на сплаве ВК6, имплантированном ионами азота с энергией 30 КэВ и дозой Ф, к воздействию пучка абразивных частиц. Температура образцов во время имплантации ниже 100°С. Масса порции корундовых частиц 1 кГ, размер частиц около 120 мкм, угол атаки 45°, скорость абразивных частиц 45 м/с.• - N_b (число порций абразива, при котором покрытие начинает отслаиваться); o - N_e (число порций абразива, при котором покрытие отслаивается полностью); △ - микротвердость ВК6 после имплантации ионов азота.

Рис. 5. Устойчивость DLC толщиной приблизительно 2 мкм на нержавеющей стали 12Х18Н10Т, имплантированной ионами углерода с энергией 30 КэВ, дозой $5{\cdot}10^{17}\mathrm{cm}^{-2}$ и при частоте импульсов тока пучка f, к воздействию пучка абразивных частиц. Частоты 10, 25 и 50 Гц соответствуют температурам образцов 250, 400 и 460°С. Масса порции корундовых частиц 1 кГ, размер частиц около 120 мкм, угол атаки 45°, скорость абразивных частиц 10 м/с. • - N_e (число порций абразива, при котором покрытие начинает отслаиваться); △ - микротвердость нержавеющей стали после имплантации ионов углерода.

THE DESIGN AND OPERATION OF THE ION SOURCE

Introduction

An ion source is the key part of technological ion - beam installations. It must fulfil the requirements of a high productivity and a reliability, but the most of currently available powerful gas - ion - beam sources are based on gaseous discharges with a thermoionic cathode, which has a short lifetime in the case of poor vacuum and reactive gas media [1]. This decreases the reliability of such ion sources and restricts their scope for a technological use.

Our approach to the development of technological ion - beam sources for a surface modification of metals and alloys by the high - dose implantation of ions is based on the use of low - pressure high - current cold-cathode discharges to produce a dense and uniform plasma with a large surface of ion emission and a high density of emission current. This makes possible to form broad beams with high current and to ensure the long lifetime of ion beam sources and their ability to operate in rather poor vacuum conditions.

We currently perform researches and develop the technological ion-beam sources based on a pulse glow discharge with hollow cathode in magnetic field [2]. The use of a pulse mode decreases the possibility of the glow-to-arc transition, that ensures the stable generation of high - current beams. Using the pulse mode it is easy to control the average ion - beam current and the temperature mode of treated specimens because the variation of the pulse repetition rate does not effect on the ion beam formation and does not require to change the parameters of the ion beam optics. Besides, the use of the pulse - repetitive mode substantially simplifies the circuitry and design of a discharge power supply, because of the possibility to omit a short - circuit protective gear and to use a compact insulating pulse - transformer.

Ion sources based on the glow discharge have more simple design of a discharge system and more high lifetime of a cathode comparing with the gas - ion sources based on an arc discharge with a shielded cathode spot, which had been developed earlier [3]. Lower noise levels of discharge voltage and current symplify the problem of the ion beam formation.

Ion emitter based on glow discharge

The ion emitter has been developed using the discharge electrode system of the "inversed magnetron" type (Fig. 1). The discharge operates between a hollow cathode 1 with covered ends and a rod anode 2 in magnetic field created by solenoid 3. The cathode is a stainless steel cylinder having a length and a diameter of 150 mm. A tungsten rod 3 mm dia is used as the anode. The glow discharge in this system has some features [2,4], which determine the properties of the ion emitter.

1) The use of the hollow cathode, thin rod anode and transverse magnetic field causes electron oscillations and an efficient plasma generation even at low gas pressures ($\leq 10^{-1}$Pa).

2) The use of weak magnetic fields with magnetic induction B$\sim$1 mT ensures the low noise - level of the discharge current and voltage and the high efficiency of the ion extraction from the discharge plasma.

3) The igniting voltage of the discharge only slightly exceeds its operating voltage even under low gas pressures, that enables to exclude a discharge initiation system and substantially

simplifies the design and power supply circuit of the emitter.

4) The discharge can operate both in a high - current pulsed mode and in a continuous one. An upper current limit is restricted by the glow - to - arc transition.

5) The uniformity of an electron emission from the cold cathode with large area surface (1000 cm^2) and the stable operation of the high - current discharge in weak magnetic fields ensure the generation of the uniform stable dense plasma in a large volume. It makes possible to form the large - area surface of the plasma ion emitter with the high density **j** of the ion current and the uniform distribution of **j** over the emitting surface.

6) The large operating surface of the cathode ensures its long lifetime and permits the emitter to be operated for a long time even when carbon - containing gases are used as feed ones.

The ion emitter based on glow discharge operates by the next way. A feed gas (argon, oxygen, nitrogen, etc.) is filled into the cathode cavity with the flow rate of $1\text{-}3\cdot10^3 cm^3 atm/hour$. The gas pressure **p** in a vacuum chamber evacuated by a pump with an effective pumping rate of 2000 l/s is equal to $3\text{-}9\cdot10^{-2} Pa$. Magnetic field in the interelectrode gap is created by the solenoid. The discharge is ignited by a pulse power supply with the voltage amplitude of up to 1800 V. The delay time of the glow discharge ignition decreases with the rise of the gas pressure and the voltage amplitude. It also depends on **B** and in the conditions of our experiments is within range of 1 - 100 μs. The discharge voltage is a function of the gas type and pressure, magnetic induction, pulse current, pulse repetition rate and is equal to 500 - 900 V.

When the source is started up for the first time after an assembly, then it is necessary to clean the cathode from surface contaminations. To pre - burn the cathode the pulsed voltage applied between the cathode and the anode is increased step-by-step up to the end of the glow-to-arc transitions. There is no need to pre-burn the cathode under the following operation of the source. The pulse glow discharge current Id reaches the value of up to 15 A at the pulse duration of 1 ms without arcing under the normal operation of the ion source.

The current density of the ions extracted from the plasma through the holes at the cathode end reaches the value of up to 15 mA/cm^2. The spatial and temporal nonuniformities of **j** do not exceed $\pm 10\%$ within a circle 100-mm dia. The typical distribution of the ion emission current density is shown in Fig. 2.

Ion beam optics

To form the broad beams with an ion energy of up to 40 keV and a pulsed current density of up to 10 mA/cm^2 the electrostatic multiaperture three-electrode ion beam optics with plane-parallel electrodes are used. The cathode end (Fig. 1) plays the role of the plasma electrode and has a high potential. A negative potential (2 - 3 kV) preventing the penetration of secondary electrons into an accelerating gap is applied to an accelerating electrode 4. A decelerating electrode 5 is grounded. Each electrode contains 140 holes 8 mm in diameter arranged hexagonally on an area of 120 cm^2. The length of the accelerating gap is equal to 12 - 15 mm, decelerating gap one amounts $\sim$5 mm. The thickness of the stainless steel electrodes is equal to 1.5 - 3 mm.

The transformation of the beam consisting of the number of beamlets into an uniform large cross-section beam is provided at a beam drift length ($\sim$150 mm) due to the large angular divergence of the beamlets (about 5 - 10 degrees). The beam cross-sectional area at the distance of 150 mm from the optics is about 150 cm^2. The typical radial profile of the beam current

density is shown in Fig. 3. The total beam current Ib of Ar, N_2, O_2, C_3H_8 - ions reaches 1 A.

Convergent beams with a high current density at a target are formed by spherical ion - beam optics. Such system containes two electrodes of equal radius of curvature of 250 mm, but having different spacing between 5-mm-dia holes. The beamlets converge in the drift zone, where electric fields are absent and the space charge of the beam is neutralized by the electrons of the beam plasma, that promotes the focusing of the beam. The 30-keV ion beam with the current density of up to 1 A/cm^2 in a crossover 1 - 2 cm dia near the axes of the system has been obtained.

The mass-charge composition of the ion beams has been studied using a 180° - magnetic spectrometer. The studies have shown that the content of the cathode material ions in the beam is below the sensitivity threshold of the used method ($\leq 1\%$). When C_3H_8 is used as the feed gas, the ion beam mass-spectrum contains 3 main groups of peaks corresponding to $C_1H_X^+$, $C_2H_Y^+$, $C_3H_Z^+$ with relative amplitudes of 10%, 54% and 36%, accordingly.

The value of $\mathbf{I}_b$ increases when **B** decreases (Fig. 4) and so the efficiency of the ion extraction from the plasma, determined as $\alpha = \mathbf{I}_b/\mathbf{I}_d$, reaches the maximum value of 0.07 at the lowest possible values of **B**. The value of α is approximately equal to the ratio of the emission hole total area (70 cm^2) to the cathode surface one. The beam current is modulated by low frequency (30 - 40 kHz) modes. The amplitude of these modes does not exceed 10% of the current value and goes to zero at minimal values of **B**.

Design and circuitry of the ion source

The electrode system of the ion source is placed in a grounded case consisting of a cylinder 200 mm dia and 550 mm in length and two flanges. The accelerating electrode and the grounded decelerating electrode of the ion beam optics are attached to the bottom flange by which the source is mounted on the vacuum chamber. A high - voltage insulator with metal - ceramic joints is attached to the top flange. An interelectrode insulation is made of ceramics. The discharge system electrodes are mounted on the high - voltage insulator and are forced - cooled by water or by contact with a transformer oil. The cooling water, feeding gas and electric cable entries are disposed inside the high-voltage insulator. Teflon tubes 1.5 m in length are used to feed the gas and water to the high-voltage electrodes.

The circuitry (Fig. 1) of the ion source includes a discharge power supply (DPS), d.c. accelerating power supply (APS) and a cut-off voltage source (CVS). The discharge power supply is based on a low-impedance (2.5 Ohm) artificial LC - line forming 1-ms pulses. The pulsed line is charged up to 300 V and is commutated to the discharge gap by a thyristor through a pulse insulating transformer increasing the voltage 6 times. The pulse repetition rate is adjusted in steps from 3 up to 50 1/s. D.c. high voltage is varied continuously from 0 up to 40 kV. A storage capacitor of C = 0.4 μF is used to maintain the accelerating voltage about constant during the pulse. The secondary electron cut-off d.c. voltage is equal to 2 - 3 kV. The ion - beam system, which incorporates the ion source and all power supply sources is shown in the Fig. 5.

The ion beam dose monitoring is ensured by the use of a small - aperture (0.2 - 1 cm dia) Faraday cup to measure the local density of the beam current nearby a treated specimen and a counter of the beam current pulses or, for more precise measurements, an electrical charge integrator.

Conclusion

In conclusion we shortly summarize main paramerers of the developed ion source:

1. Accelerating voltage	up to 40 kV
2. Pulsed ion - beam current	0.3 - 1 A
3. Pulsed discharge current	5 - 15 A
4. Pulse duration	1 ms
5. Pulse repetition rate	3 - 50 pps
6. Average beam current	0 - 50 mA
7. Feed gas	Ar, N_2, O_2, C_3H_8, NH_3 etc.
8. Gas pressure	0.025 - 0.2 Pa
9. Beam cross-sectional area	150 cm^2

The developed system can operate in a continuous mode too. Broad (150 cm^2) continuous beams of low energy (2 - 3 keV) ions with a current of up to 150 mA are used for cleaning of surfaces before a coating deposition. The sources have the simple design and power supplies, high reliability and long lifetime, this being due to the use of the cold-cathode discharge needing no initiating system.

REFERANCES.

1. H. R. Kaufman, Technology and applications of broad - beam ion sources used in sputtering. Part 1. Ion source technology. J. Vac. Sci. Technol., 21, 725 (1982).

2. N. V. Gavrilov, V.N. Mizgulin, S. P. Nikulin, A. V. Ponomarev, A technological ion source with hollow cathode in magnetic field. 10 th International Conference of High Power Particle Beams. Book of Abstracts, 61 (1994).

3. N. V. Gavrilov, Yu. E. Kreindel', O. A. Shybin, Periodically - pulsed source of high - power electron and ion beams. Pribory i technika experimenta [in Russian], 3, 130 (1991).

4. N. V. Gavrilov, S. P. Nikulin, Investigation of striking characteristics of pulsed low - pressure discharge in magnetic field. Proceedings of XVI Int. Symp. on Discharges and Electrical Insulation in Vaccuum, 118 (1994).

Figure captions

Fig. 1. Electrode system and circuitry of the ion source.

Fig. 2. Typical distribution of the ion emission current density.

Fig. 3. Typical radial profile of the beam current density.

Fig. 4. Dependance of the beam current on magnetic induction.
1 - p = 0.03 Pa, 2 - p = 0.06 Pa.

Fig. 5. Ion-beam system incorporating the ion source and all power supplies.

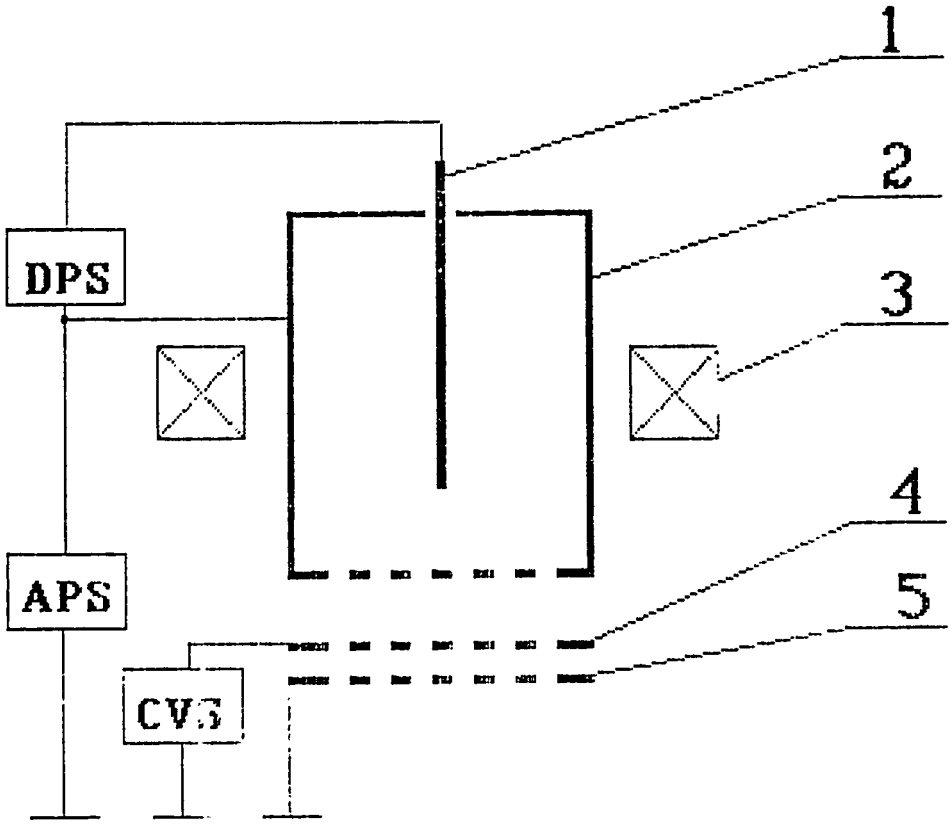


Fig. 1.

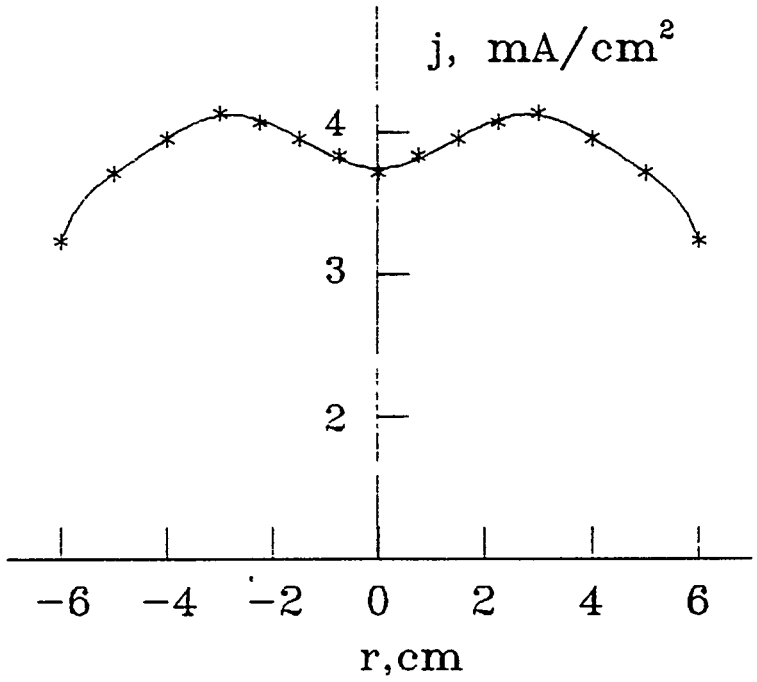


Fig. 2.

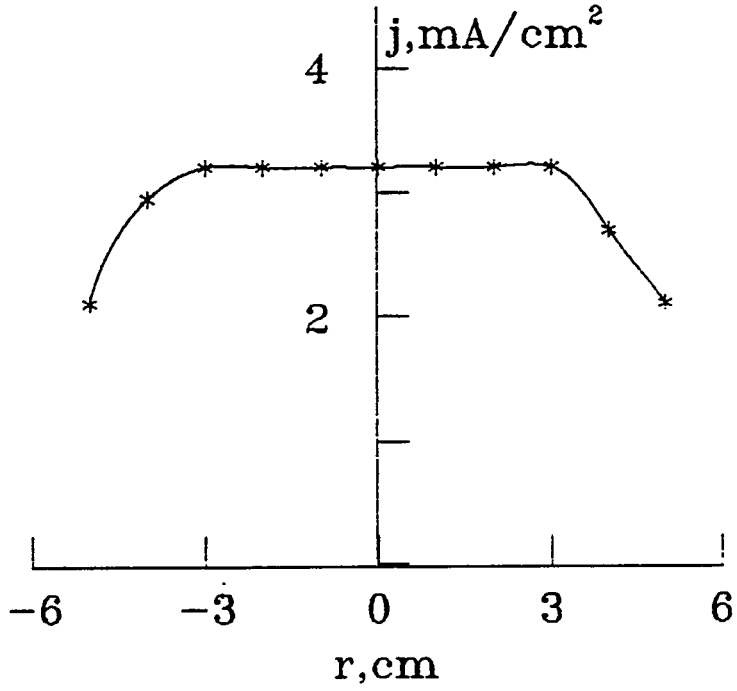


Fig. 3.

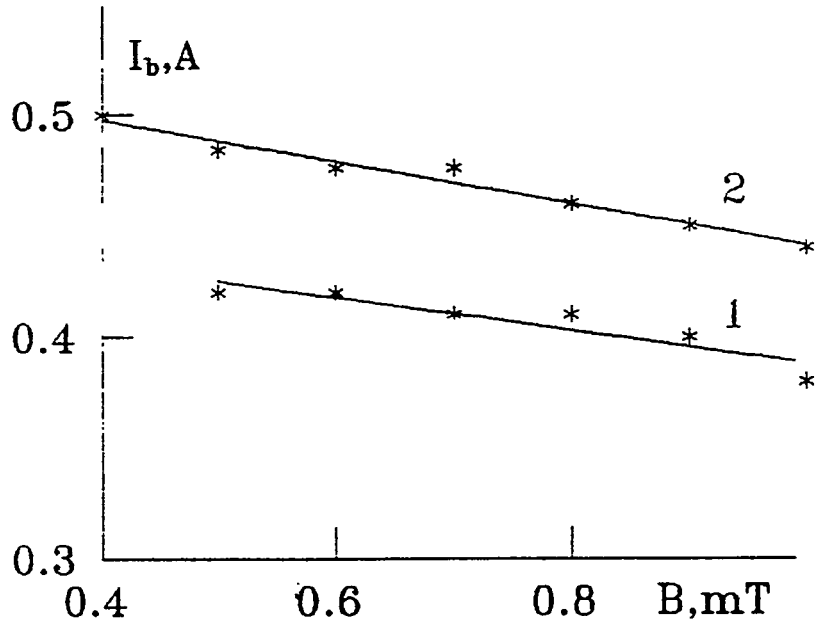


Fig. 4.

DOC. 7677

КОНСТРУКЦИЯ И РАБОТА ИОННОГО ИСТОЧНИКА

ВВЕДЕНИЕ

Источник ионов является основным элементом технологических ионно-лучевых установок. Он должен отвечать требованиям высокой производительности и надежности, однако большинство разработанных к настоящему времени мощных источников ионов газов основаны на использовании газовых разрядов с накаливаемым катодом, который имеет ограниченный срок службы в условиях несовершенного вакуума и в присутствии химически активных газов [1]. Это уменьшает надежность таких ионных источников и ограничивает возможность их технологического использования.

Наша концепция разработки технологических источников ионов для модификации поверхностей металлов и сплавов высокодозной ионной имплантацией основывается на использовании сильноточных разрядов низкого давления с холодными катодами для генерации плотной и однородной плазмы с большой поверхностью ионной эмиссии и высокой плотностью эмиссионного тока. Это позволяет формировать ионные пучки большого сечения со значительным током и обеспечивает высокий ресурс и надежность ионных источников, их некритичность к вакуумным условиям.

В настоящее время нами осуществляются исследования и разработки технологических ионно - лучевых систем на основе импульсного тлеющего разряда с полым катодом в магнитном поле [2]. Использование импульсного режима снижает вероятность перехода тлеющего разряда в дуговой, что способствует устойчивой генерации сильноточных пучков. В импульсном режиме значительно упрощается управление средним током пучка и температурным режимом обработки образцов, поскольку изменение частоты повторения импульсов не влияет на формирование пучка и не требует изменения параметров ионной оптики. Кроме того, использование импульсно-периодического режима существенно упрощает схему и конструкцию источника электрического питания разряда, так как позволяет исключить узел защиты от коротких замыканий и использовать малогабаритный импульсный разделительный трансформатор.

Ионные источники, основанные на тлеющем разряде, имеют более простую конструкцию разрядной системы и более высокий ресурс катода по сравнению с источниками ионов газов, основанными на дуговом разряде с экранированным катодным пятном, которые были разработаны ранее [3]. Более низкие уровни шумов разрядного напряжения и тока упрощают проблему формирования ионного пучка.

ИОННЫЙ ЭМИТТЕР НА ОСНОВЕ ТЛЕЮЩЕГО РАЗРЯДА

Эмиттер ионов был разработан с использованием электродной системы типа "обращенный магнетрон" (рис. 1). Разряд горит между полым катодом 1 с закрытыми торцами и стержневым анодом 2 в магнитном поле соленоида 3. Катод выполнен из нержавеющей стали и имеет форму цилиндра, длина и диаметр которого равны 150 мм. В качестве анода используется вольфрамовый пруток диаметром 3 мм. Тлеющий разряд в такой системе обладает рядом особенностей [2,4], определяющих свойства плазменного эмиттера:

1) использование полого катода, анода из тонкого прутка и поперечного магнитного поля обусловливает возникновение осцилляций электронов и эффективную генерацию плазмы даже при низких ($p \leq 0.1$Па) давлениях газа;

2) при использовании слабых магнитных полей с магнитной индукцией B~1 мТл обеспечивается минимальный уровень шумов напряжения и тока разряда и высокая эффективность извлечения ионов из разрядной плазмы;

3) напряжение зажигания такого разряда даже при низких давлениях газа лишь незначительно превышает напряжение его горения, что позволяет исключить систему инициирования разряда и существенно упростить конструкцию эмиттера и схему его электрического питания;

4) разряд может функционировать как в импульсном сильноточном, так и в непрерывном режимах. При этом максимальный ток разряда ограничен переходом в дугу;

5) равномерная электронная эмиссия холодного катода с большой (около 1000 см^2) рабочей поверхностью и устойчивое горение сильноточного разряда в слабых магнитных полях обеспечивают генерацию стабильной однородной плотной плазмы в больших объемах. При этом обеспечивается формирование большой рабочей поверхности плазменного эмиттера с высокой плотностью ионного тока **j** и равномерным распределением **j** по эмиссионной поверхности.

6) большая рабочая поверхность холодного катода обеспечивает значительный срок его службы и делает возможной продолжительную работу эмиттера при использованиие углеродсодержащих рабочих газов.

Ионный эмиттер на основе тлеющего разряда работает следующим образом. В катодную полость подается поток (1-3·10^{3}см^{3}атм/час) газа (аргон, азот, кислород и др.). При этом давление газа в вакуумной камере, откачиваемой насосом со скоростью откачки 2000 л/сек, составляет 3-9·10^{-2}Па. С помощью соленоида в разрядном промежутке создается магнитное поле. Разряд зажигается при подаче импульса напряжения амплитудой до 1800 В от импульсного источника питания. Время запаздывания зажигания тлеющего разряда уменьшается при увеличении давления газа и амплитуды импульса напряжения. Оно также зависит от B и в условиях наших экспериментов находится в пределах 1 - 100 мкс. Напряжение горения разряда является функцией вида газа и его давления, магнитной индукции, амплитуды тока, частоты повторения импульсов и может составлять 500 - 900 В.

При первоначальном запуске источника после сборки разрядной системы необходимо очистить поверхность катода от загрязнений. Для кондиционирования катода между электродами прикладывается импульсное напряжение, которое ступенчато увеличивается до полного прекращения переходов тлеющего разряда в дугу. При последующей работе источника необходимости в тренировке источника не возникает. В рабочем режиме работы источника импульсный ток тлеющего разряда I_d без перехода в дугу достигает 15 А при длительности импульса 1 мс.

Плотность тока эмиссии ионов, извлекаемых из плазмы через отверстия в катодном торце, достигает в импульсе до 15 мА/см^2. Пространственная и временная неоднородности распределения плотности эмиссионного тока в пределах круга диаметром 100 мм не превышает ±10%. Типичное распределение плотности тока эмиссии ионов показано на рис. 2.

СИСТЕМА ФОРМИРОВАНИЯ ПУЧКА

Для формирования ионных пучков большого сечения с энергией ионов до 40 кэВ и плотностью тока в импульсе до 10 мА/см^2 используются электростатические многоапертурные трехэлектродные ионно-оптические системы с плоскопараллельными электродами. Катодный торец (Рис. 1) играет роль плазменного электрода и находится под высоким потенциалом. Отрицательный потенциал (2 - 3 кВ), предотвращающий проникновение вторичных электронов в ускоряющий зазор, прикладывается к ускоряющему электроду 4. Замедляющий электрод 5 заземляется. В каждом электроде сделано 140 отверстий диаметром 8 мм, размещенных гексагонально на площади 120 см^2. Ускоряющий зазор составляет 12 - 15 мм, замедляющий зазор - около 5 мм. Электроды толщиной 1,5 - 3 мм выполнены из нержавеющей стали.

Трансформация многолучевого пучка в однородный пучок большого сечения обеспечивается на длине дрейфа пучка (~150 мм) за счет значительной угловой расходимости отдельных лучей (5 - 10°). Площадь сечения пучка на расстоянии 150 мм от оптики около 150 см^2. Типичный радиальный профиль распределения плотности тока пучка показан на рис. 3. Полный ток пучка I_b ионов аргона, азота, кислорода и ионов углеродсодержащих газов достигает 1 А.

Для формирования сходящихся пучков с высокой плотностью тока на мишени используются сферические системы формирования. Такая система содержит два электрода с одинаковым радиусом кривизны 250 мм, и различным расстоянием между отверстиями диаметром 5 мм. Лучи сходятся в зоне дрейфа, где отсутствуют электрические поля, а пространственный заряд пучка компенсируется электронами пучковой плазмы, что облегчает фокусировку пучка. В такой системе был получен пучок ионов с энергией 30 кэВ и плотностью тока до 1 А/см^2 в кроссовере диаметром 1 - 2 см, расположенном вблизи оси системы.

С использованием 180° - магнитного спектрометра проведен анализ масс-зарядового состава пучков. Исследования показали, что содержание ионов материала катода в пучке не превышает предела обнаружения используемого ме-

тода анализа (менее 1%). При использовании в качестве рабочего газа C_3H_8 пучок содержит три основные группы пиков, соответствующих $C_1H_X^+, C_2H_Y^+, C_3H_Z^+$ с относительной амплитудой 10%, 54% и 36%, соответственно.

Величина I_b возрастает с уменьшением B (Рис.4) и таким образом эффективность извлечения α ионов из плазмы, определяемая как отношение $\alpha = I_b/I_d$, максимальна при минимальной индукции магнитного поля и достигает 0,07. Величина α приблизительно равна отношению суммарной площади отверстий в эмиттерном электроде (70 $см^2$) к площади поверхности катода. Ток пучка промодулирован низкочастотными (30 - 40 кГц) колебаниями. Амплитуда этих колебаний не превышает 10% от величины тока и близка к нулю при минимальных значениях B.

КОНСТРУКЦИЯ И СХЕМА ЭЛЕКТРИЧЕСКОГО ПИТАНИЯ ИСТОЧНИКА

Электродная система источника размещается в заземленном корпусе состоящим из цилиндра диаметром 200 мм и длиной 550 мм и двух фланцев. На нижнем фланце корпуса, с помощью которого источник устанавливается на вакуумной камере, закреплены ускоряющий и заземленный замедляющий электроды системы формирования пучка. На верхнем фланце крепится высоковольтный изолятор с металлокерамическими спаями. Межэлектродная изоляция выполнена из керамики. Электроды разрядной системы смонтированы на высоковольтном изоляторе и принудительно охлаждаются прокачкой воды или с помощью трансформаторного масла. Вводы охлаждающей воды, рабочего газа и кабельный ввод размещаются внутри высоковольтного изолятора. Газ и вода подаются к электродам, имеющим высокий потенциал, через фторопластовые трубки длиной 1,5 метра.

Схема электрического питания ионного источника (рис. 1) включает импульсный источник питания тлеющего разряда и источники постоянного ускоряющего напряжения и напряжения отсечки вторичных электронов. Источник питания разряда выполнен на основе искусственной низкоомной (2,5 Ом) импульсной LC - линии , формирующей импульсы тока длительностью 1 мс. Импульсная линия заряжается до напряжения 300 В и коммутируется на разрядный промежуток тиристором через повышающий импульсный разделительный трансформатор с коэффициентом трансформации 1:6. Частота повторения импульсов регулируется дискретно в пределах 3 - 50 Гц. Постоянное ускоряющее напряжение плавно регулируется в пределах 0 - 40 кВ. Накопительная емкость C = 0,4 мкФ используется для поддержания постоянства ускоряющего напряжения в течение импульса. Напряжение отсечки вторичных электронов составляет 2 - 3 кВ. Общий вид ионно-лучевой системы, включающей источник ионов и все источники электропитания, показан на рис. 5.

Контроль дозы облучения производится с использованием цилиндра Фарадея с малой входной апертурой (0,2 - 1 см), измеряющего локальную плотность тока пучка вблизи облучаемого объекта, и счетчика числа импульсов тока пучка, либо, для более точных измерений, интегратора электрического заряда.

ЗАКЛЮЧЕНИЕ

В заключение кратко обобщим основные параметры разработанного ионного источника.

1. Ускоряющее напряжение	до 40 кВ
2. Импульсный ток ионного пучка	0.3 - 1 А
3. Импульсный ток разряда	5 - 15 А
4. Длительность импульса	1 мс
5. Частота повторения импульсов	3 - 50 Гц
6. Средний ток пучка	0 - 50 мА
7. Рабочие газы	Ar, N_2, O_2, C_3H_8, NH_3 и др.
8. Давление газа	0.025 - 0.2 Па
9. Поперечное сечение пучка	150 $см^2$

Разработанная система может работать также и в непрерывном режиме. Широкие (150 $см^2$) непрерывные пучки ионов низкой энергии (2 - 3 кэВ) с током до 150 мА используются для очистки поверхностей перед нанесением покрытий. Источники имеют простые конструкцию и схемы источников питания, обладают высокой надежностью и сроком службы, что обусловлено использованием разряда с холодным катодом, не нуждающегося в системах инициирования.

ЛИТЕРАТУРА

1. H. R. Kaufman, Technology and applications of broad - beam ion sources used in sputtering. Part 1. Ion source technology. J. Vac. Sci. Technol., 21, 725 (1982).

2. N. V. Gavrilov, V.N. Mizgulin, S. P. Nikulin, A. V. Ponomarev, A technological ion source with hollow cathode in magnetic field. 10 th International Conference of High Power Particle Beams. Book of Abstracts, 61 (1994).

3. Н. В. Гаврилов, Ю. Е. Крейндель, О. А. Шубин, Источник мощных электронных и ионных пучков импульсно - периодического действия. Приборы и техника эксперимента, 3, 130 (1991).

4. N. V. Gavrilov, S. P. Nikulin, Investigation of striking characteristics of pulsed low - pressure discharge in magnetic field. Proceedings of XVI Int. Symp. on Discharges and Electrical Insulation in Vaccuum, 118 (1994).

ПОДПИСИ К РИСУНКАМ

Рис. 1. Электродная система и схема электрического питания ионного источника

Рис. 2. Типичное распределение плотности тока ионной эмиссии

Рис. 3. Типичный радиальный профиль распределения плотности тока пучка

Рис. 4. Зависимость тока пучка от магнитного поля
1 - p = 0.03 Па, 2 - p = 0.06 Па

Рис. 5. Общий вид ионно-лучевой системы

CONTRACT AM-7677

REPORT ON TASK 2

The contractual works envisage investigations into the strength properties of the "steel substrate - diamond-like coating" system produced by preliminary implantation of nitrogen or carbon ions into the steel and subsequent deposition of the diamond-like coating (DLC). The goal of the study is to optimize the conditions of the substrate treatment and coating deposition with the aim of elaborating a highly efficient technology for improvement of the service properties of tools.

The following works were to be done at the given stage: preparation and certification of the samples of two grades of tool steels differing in their initial physico-mechanical properties; implantation of nitrogen and carbon ions at temperatures of 200-700°C and doses of 10^{17}-10^{19} cm^{-2}; determination of the depth distribution of the implanted ions using the nuclear reactions method.

PREPARATION OF THE SAMPLES

1. The **P6M5** high-speed steel is used as a material for the manufacture of all kinds of tools for machining of carbon and medium-carbon structural steels or gear-cutting and thread-cutting tools for stainless steels. The steel composition is as follows (mass %): **C** 0.8-0.88, **Cr** 3.8-4.4, **V** 1.7-2.1, **W** 5.5-6.5, **Mo** 5.0-5.5.

It is analogous to the AISI-3343 steel having the following composition: **C** 0.9%, **Cr** 4.0%, **V** 1.9%, **W** 6.6%, **W** 5.0% [Metals Handbook, 8th Edition, American Society for Metals, Metals Park, Ohio - v.8, p.95].

The samples measuring 15x15x2.5 mm were subjected to a thermal treatment, which was similar to the one used for the tools:

1) annealing at 840-860°C;

2) cooling to 720-730°C at a rate of 40°C per hour;

3) holding for 4 hours, minimum;

4) cooling to 600°C in air at a rate of 50°C per hour [Tool Steels. Handbook. Moscow, Metallurgiya, 1977, p.127].

To remove the stressed surface layer, after mechanical grinding and polishing with diamond pastes the samples were subjected to electropolishing in a solution containing 90 % glacial acetic acid and 10% perchloric acid for 12s at a voltage of 30 V.

As is seen from Fig.1a, after this treatment the surface of the P6M5 samples is made up of different-dimension (1 to 15 μm) spheroidal inclusions in the matrix representing a tempered martensite with the Me_7C_3 and $Me_{23}C_6$ carbides.

Figure 2a shows a profilogram of this surface. The observed roughnesses, which correspond to the carbide inclusions, do not exceed 0.5 μm in height.

The microhardness of the prepared samples was 950±80 kg/mm^2.

The microhardness was measured on a "ПМТ-3" instrument using a Vickers diamond pyramid.

2. The **X12M** die steel for cold deformation. It is used as a material for the manufacture of rollers, drawing dies, dies and punches. The steel composition is as follows (mass %): 1.45-1.65 **C**, 0.15-0.35 **Si**, 0.15-0.40 **Mn**, 11.0-12.5 **Cr**, 0.15- 0.30 **V**, 0.40-0.60 **Mo**.

The steel samples measuring 15×15×4 mm were made according to the same technique as the P6M5 steel samples. The thermal treatment regime was as follows:

1) annealing at 850-870°C;

2) cooling to 700-720°C at a rate of 40°C per hour;

3) holding for 3-4 hours;

4) cooling to 550°C in air at a rate of 50°C per hour [Tool Steels. Handbook. Moscow, Metallurgiya, 1977, p.43].

As is seen from the microphotograph (Fig.1b), the microstructure of X12M is analogous to that of P6M5, but the carbide inclusions are larger (5 to 30 μm) and are spaced a greater distance from one another.

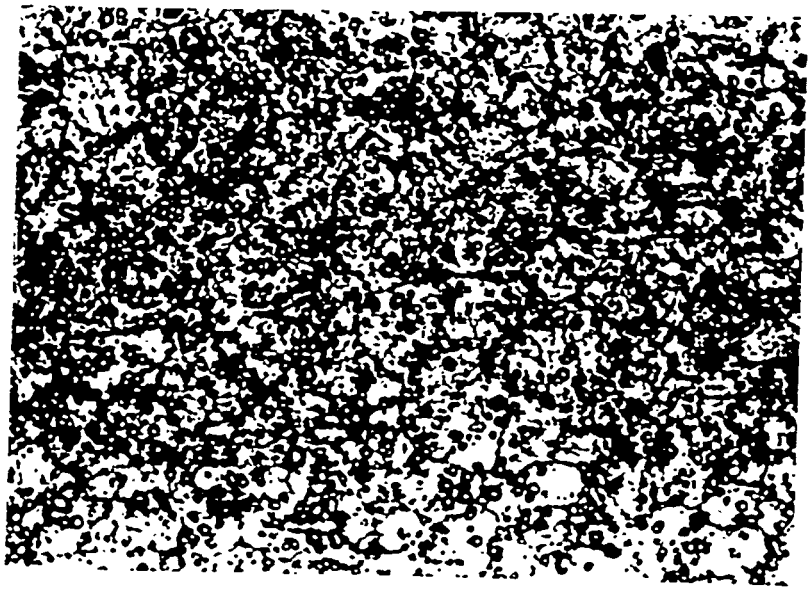
Figure 2b shows a profilogram of the surface of a X12M steel sample. As in the case of the P6M5 steel, the observed roughnesses, which correspond to the carbide inclusions, do not exceed 0.5 μm in height.

The microhardness of the prepared samples was 820±70 kg/mm2.

IMPLANTATION OF NITROGEN AND CARBON

The ion source, which was described in detail in the report on the first stage of the contractual works, was used in the experiments.

The ion source utilized N_2 and C_3H_8 as the feed gases. The analysis of the mass-charge composition of the ion beams, which was performed using an "MX-7303" radio-frequency monopolar spec-

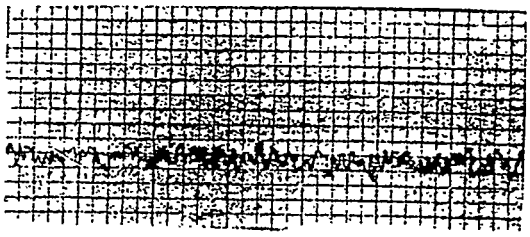


a

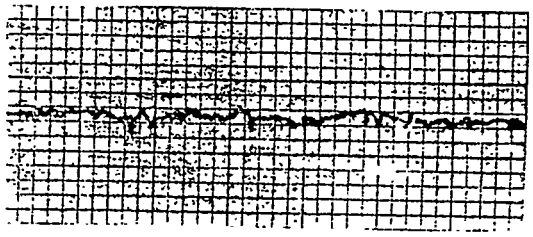


b

Fig. 1. Microphotographs of the structure of the P6M5 (a) and X12M (b) steel surfaces made through an optical microscope (x 500).



a



b

Fig. 2. Typical section of a profilogram of the sample surfaces: a - P6M5, b - X12M. Scale division = 0.4 μm.

trometer, showed that the content of impurities in the beam (caused by the use of an oil-diffusion vacuum pump) does not exceed fractions of a percent. In the case of nitrogen ion implantation the beam contains both atomic and molecular nitrogen ions in comparable quantities (Fig.3). If C_3H_8 is used as the working gas, the beam contains a wide spectrum of the products from a partial dissociation of C_3H_8 molecules (Fig.4). So, when propane is used, the beam includes ionized fragments of C_3H_8 molecules possessing different mass and atomic composition but having the same energy determined by the accelerating voltage of the ion source. When accelerated ions strike against a solid surface, they dissociate further and, as a result, a wide energy spectrum of the implanted carbon and hydrogen atoms is formed.

For implantation the samples were mounted in a bulky copper holder within a maximum homogeneity of the ion beam. The irradiation dose was measured using a Faraday cap fixed in the center of the holder at the beam axis. The beam inhomogeneity don't exceed 10 % at the central part of the beam cross-section about 70 - 80 mm in diameter. To lower heating of the copper holder by broad beam, a stainless-steel screen with an opening 50 mm in diameter was installed above the holder at a distance of ~30 mm. Four to eight samples were treated simultaneously with one and same dose but at different temperatures.

The samples were heated by the ion beam and no additional heaters were used. The difference in the temperatures of the irradiated samples was achieved thanks to different thermal resistance of the contacts between the samples and the holder. Part of the samples were placed freely on the collector, while the others were pressed to the collector through different spacers. Since the heat removal conditions were different, similar samples were heated to different temperatures under the same exposure. The temperature of each sample was checked using chromel-alumel thermocouples welded to the side surface of the sample. The typical temperatures that set in after ~5 min of irradiation are given in Table 1.

A typical dependence of the temperature on the implantation time is depicted in Fig. 5.

The distribution of nitrogen and carbon in the near-surface zone of the samples was examined by a nondestructive method using nuclear reactions $^{14}N(d,\alpha_1)^{12}C$ and $^{12}N(d,p)^{13}C$. A Van de-Graaf accelerator produced a beam of deuterons with an energy of 0.9 MeV. The depth distribution of the **N** and **C** concentrations was determined from the energy spectra of the nuclear reaction products.

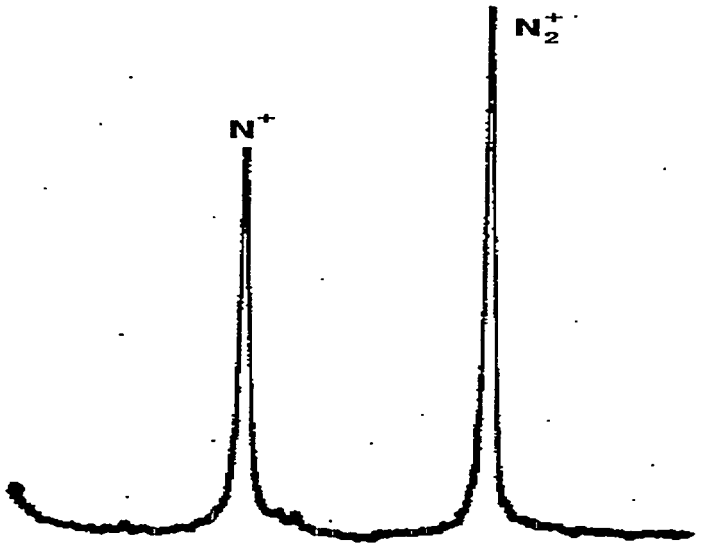


Fig. 3. Mass-charge spectrum of ions for N_2 feed gas

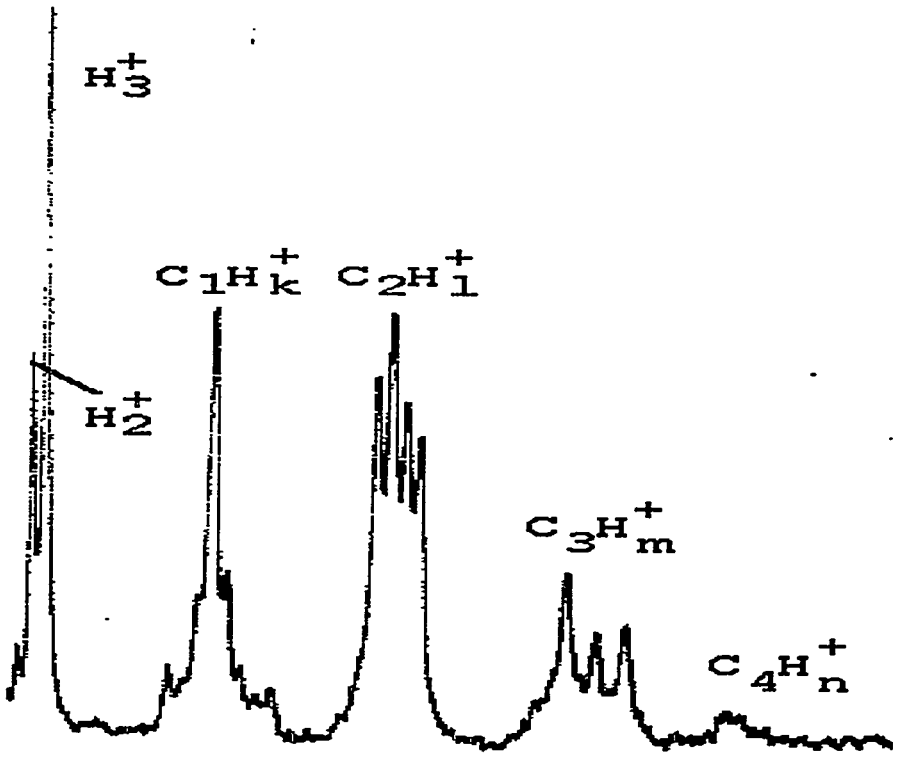


Fig. 4. Mass-charge spectrum of ions for feed gas C_3H_8.

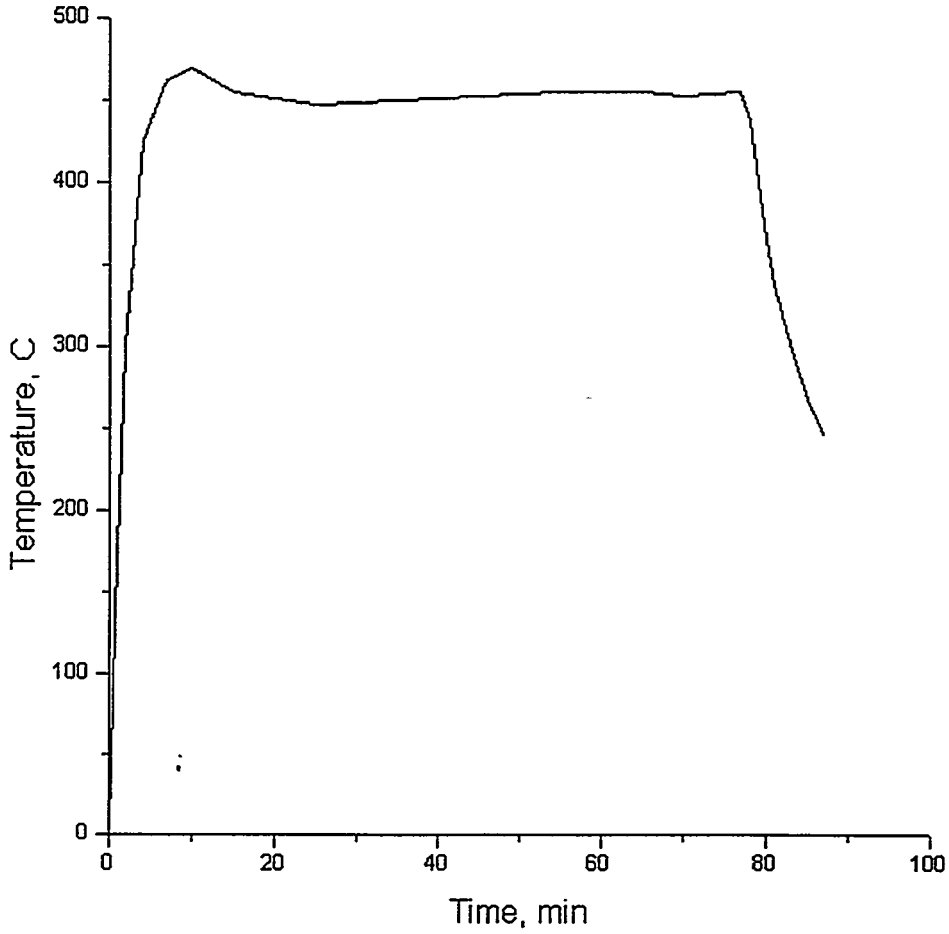


Fig. 5. Typical dynamics of heating and cooling of sample during implantation.

Table 1. Temperatures of the samples during implantation of nitrogen ions (beam pulse density j = 7 mA/cm^2, frequency f = 25 Hz, pulse duration = 1 ms, ion energy = 30 keV)

Sample No.	Spacer shape and material	Temperature,°C
1	Indium	96
2	Stainless steel 0.4 mm thick	273
3	Ni-Cr alloy (ring dia.10 mm wire 1 mm thick) ,	477
4	Ni-Cr alloy (ring dia.10 mm wire 0.1 mm thick) ,	570
5	Screwed loosely, w/o spacer	615
6	Placed freely, w/o spacer	695

The starting samples of the P6M5 and X12M steels and a $TiN_{0.82}$ sample with a uniform distribution of nitrogen served as references in the case of carbon and nitrogen respectively. Up to a depth of 2.5 μ the concentration determination error was 10-15% of the measured value, while at greater depths the error increased sharply.

EXPERIMENTAL RESULTS AND DISCUSSION

The ion implantation in the P6M5 and X12M steels was realized under the following conditions:

- nitrogen and carbon ion energy — 30 keV
- ion beam current density — 1-10 mA/cm^2
- pulse duration — 1 ms
- pulse repetition frequency — 10-50 Hz
- dose — 10^{17} - 10^{19} cm^{-2}
- temperature of the samples — 50-800°C
- implantation time — 5-80 min

Figure 6 and Appendix 1 furnish data on the implantation conditions for all samples. It should be noted that the given values of the ion irradiation dose were determined from the electric charge of the ion beam per unit area of the surface dur-

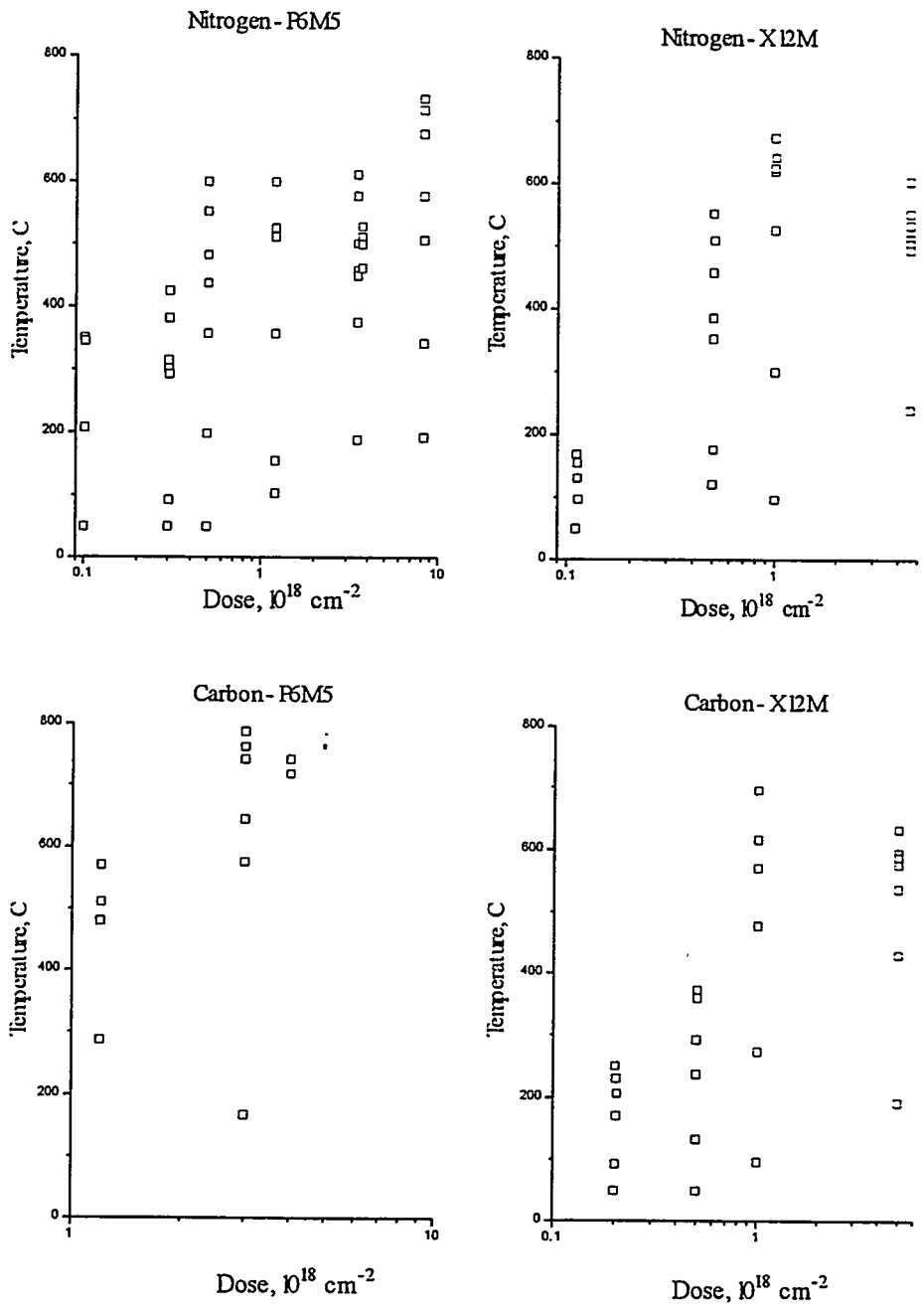


Fig. 6. Implantation regimes for samples prepared.

ing irradiation. Considering the complex ions present in the beam and sputtering of the sample's surface during implantation, the dose of implanted ions can differ essentially (up to 3 times) from the irradiation dose.

The concentration of carbon and nitrogen in the near-surface zone rises with the irradiation dose. In the case of a low - temperature implantation, the implanted particles diffuse little if at all and the particles are registered in the near-surface layer up to 100 nm thick. This value is determined by the depth resolution of the nuclear reactions method and slightly exceeds the projective path of the ions. Maximum surface concentrations of the implanted particles are achieved at temperatures of about 200° C. In assumption of a uniform distribution of the particles in a layer 100 nm thick they are estimated at 25-30 at.% under a dose of 3.5 10^{18} cm^{-2}.

Figures 7 -9 displays typical profiles of the depth distribution of carbon and nitrogen concentrations measured using the nuclear reactions method. Appendix 2 gives measured concentrations of implanted particles for the most characteristic regimes of ion implantation.

As the temperature is raised, the surface concentration of both carbon and nitrogen drops in both steels to several atomic percents owing to a diffusion flow to the bulk of the sample (Fig.8). At high temperatures of the samples (X12M, dose 10^{18} cm^{-2}, 700° C) the surface concentration of carbon drops during implantation to the level existing in the starting samples.

The diffusion-induced growth of the concentration of the implanted particles at a depth up to 2.5 μm becomes pronounced at temperatures above 300° C. This thickness of the modified layer is sufficient for a considerable change in the mechanical properties of the surface and ensures a correct measurement of the microhardness. The depth distribution of the particles is characterized by a drop of the concentration to a certain almost constant level in a layer about 1 μm thick (Fig.8).

Table 2 gives mean values of excess (compared to the initial value) concentrations of carbon and nitrogen in the zone where they are almost constant (0.9 - 2 μm).

The given results suggest that the temperature dependences of carbon and nitrogen concentrations in the near-surface layer of the samples differ greatly.

The nitrogen content grows with temperature in both steels (under a constant dose): 5-6 at.% in the X12M steel (dose of 4.6 10^{18} cm^{-2}) and 2.5-4 at.% in the P6M5 steel (dose of 1.2 10^{18} cm^{-2} - 3.5 $10^{18}cm^{-2}$). Oppositely, the concentration of carbon

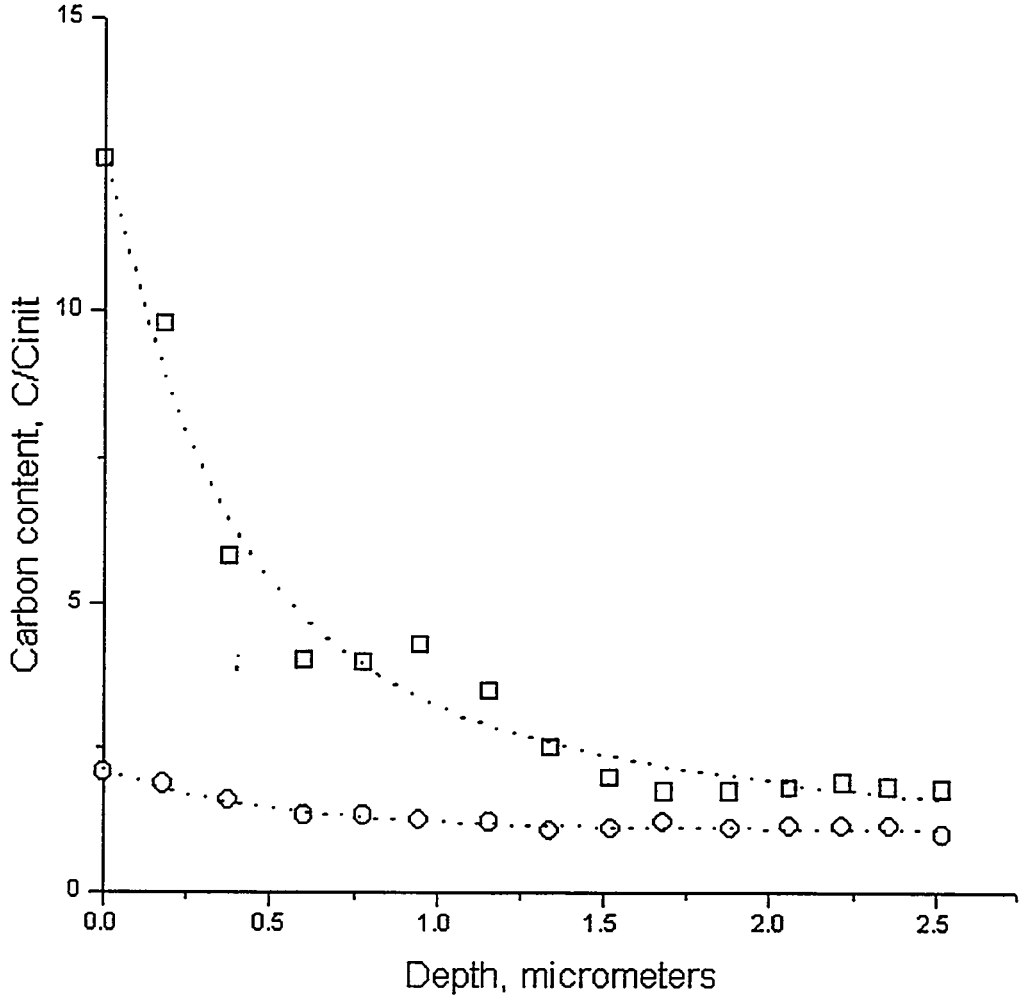


Fig.7. Depth distribution of Nitrogen in P6M5 steel.
□ - dose $5 \cdot 10^{18}$ cm^{-2}, temperature 430 °C; o - $1 \cdot 10^{18}$ cm^{-2}, 480 °C

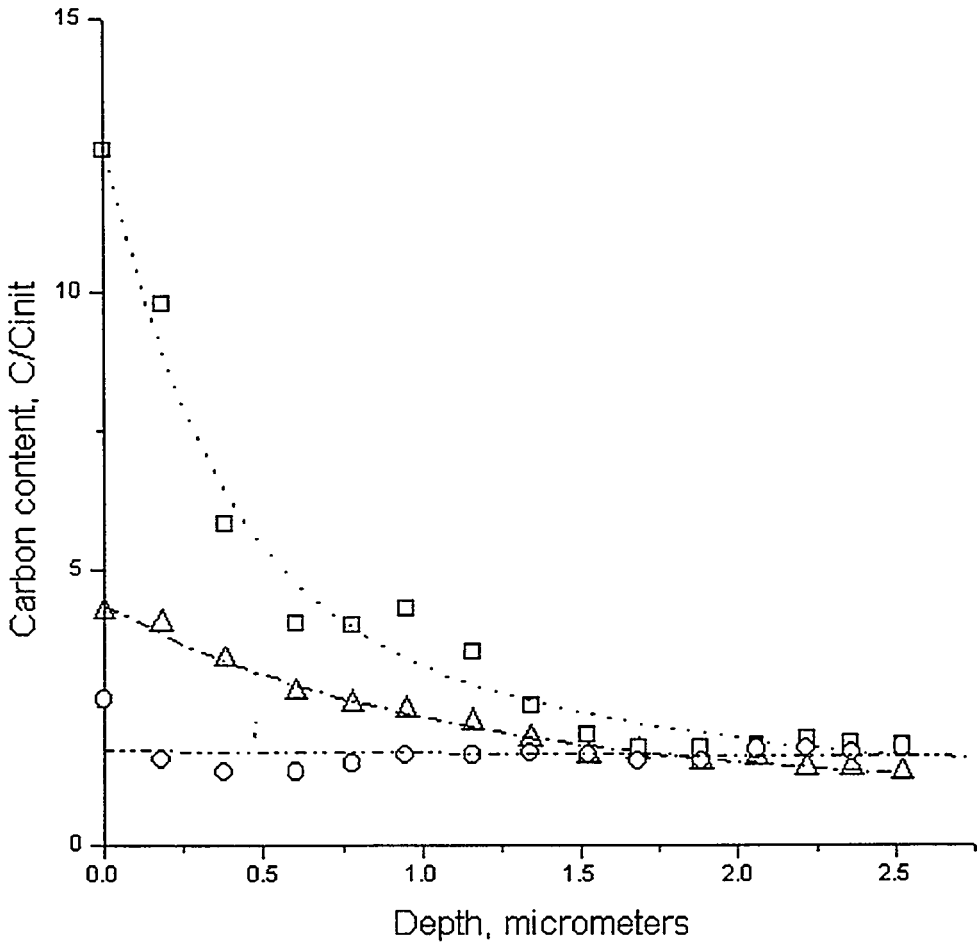


Fig.8. Depth distribution of Carbon in X12M steel.Dose 5 $\cdot 10^{18}$ cm^{-2}, □ - 430 °C, Δ - 540 °C , o - 630 °C

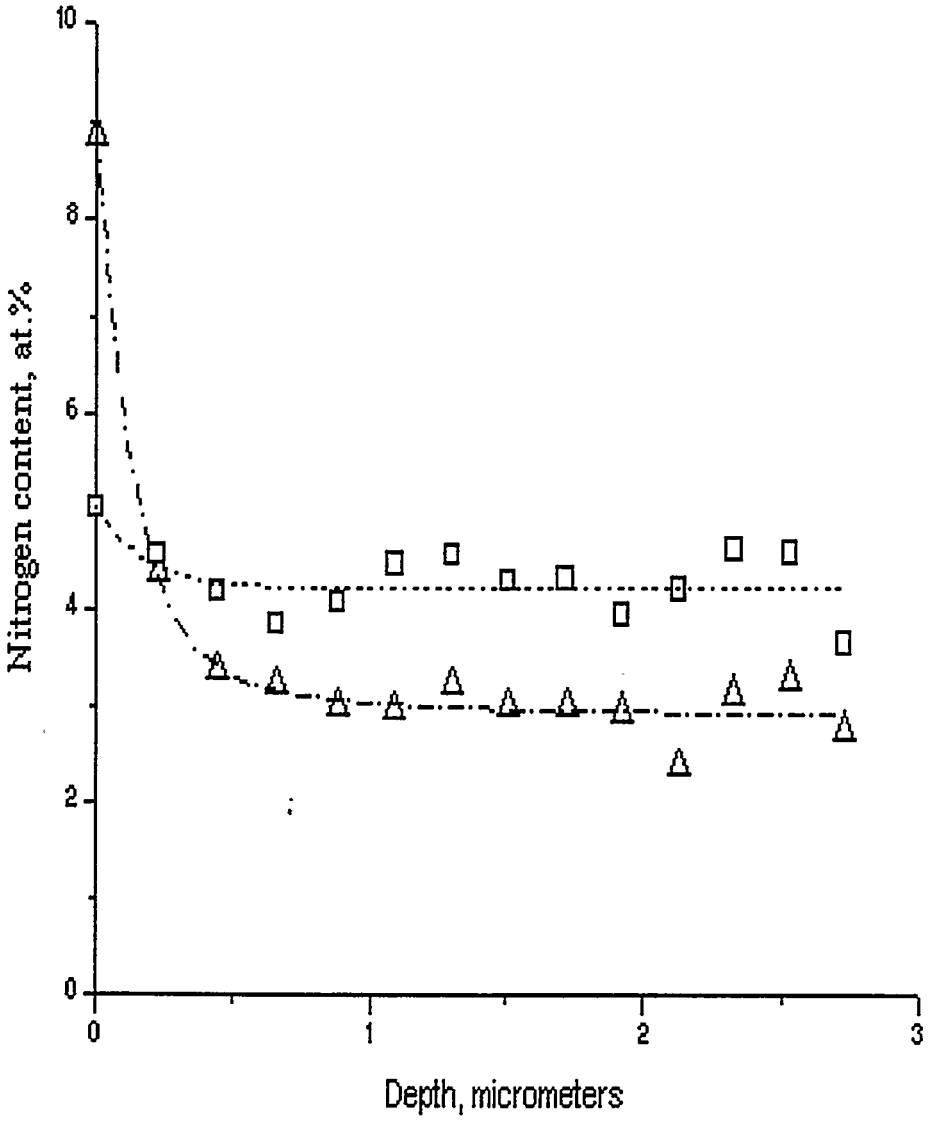


Fig.9. Depth profiles of Nitrogen in P6M5 steel.
Temperatures during implantation :Δ - 380 °C, □ - 610 °C

implanted in the sample drops with temperature in both steels from 9 at.% to 4 at.% (X12M, 5 10^{18} cm^{-2}, 430 and 630°C) and from 2 at.% to nearly zero (P6M5, 2 10^{18} cm^{-2}, 200 and 700°C).

Table 2: Mean concentrations of carbon and nitrogen implanted into the near-surface layer of the P6M5 and X12M steels

P6M5					X12M				
ions	dose cm^{-2}	temperature °C	zone of average, μm	mean concentration at.%	ions	dose cm^{-2}	temperature °C	zone of average, μm	mean concentration at.%
N		360	1.09-2.13	2.47	N	$5 \cdot 10^{17}$	380	1.09-2.13	0.54
N	$1.2 \cdot 10^{18}$	510	1.09-2.13	2.22	N	$4.6 \cdot 10^{18}$	490	1.09-2.13	5.34
N	$1.2 \cdot 10^{18}$	520	1.09-2.13	2.85	N	$4.6 \cdot 10^{18}$	600	1.09-2.13	6.38
N	$1.2 \cdot 10^{18}$	600	1.09-2.13	3.17	C	$1 \cdot 10^{18}$	100	0.95-2.06	1.3
N	$3.5 \cdot 10^{18}$	380	1.09-2.13	2.92	C	$1 \cdot 10^{18}$	270	0.95-2.06	1.53
N	$3.5 \cdot 10^{18}$	450	1.09-2.13	3.37	C	$1 \cdot 10^{18}$	480	0.95-2.06	0.94
N	$3.5 \cdot 10^{18}$	500	1.09-2.13	3.12	C	$1 \cdot 10^{18}$	700	0.95-2.06	-0.41
N	$3.5 \cdot 10^{18}$	580	1.09-2.13	3.84	C	$5 \cdot 10^{18}$	430	0.95-2.06	8.9
N	$3.5 \cdot 10^{18}$	610	1.09-2.13	4.29	C	$5 \cdot 10^{18}$	540	0.95-2.06	5.08
C	$5 \cdot 10^{17}$	100	0.9-1.7	1.09	C	$5 \cdot 10^{18}$	630	0.95-2.06	3.66
C	$5 \cdot 10^{17}$	500	0.9-1.7	0.57					
C	$1.2 \cdot 10^{18}$	500	0.95-2.06	0.99					
C	$2 \cdot 10^{18}$	200	0.9-1.7	2.2					
C	$2 \cdot 10^{18}$	700	0.9-1.7	0.34					
C	$3 \cdot 10^{18}$	580	0.95-2.06	2.08					

So, the measured concentration profiles of carbon and nitrogen in the implanted samples of the P6M5 and X12M tool steels show that we have produced two groups of samples for convenient analysis of the influence of implantation on the strength properties of the steels with DLC. A low-temperature implantation, which practically changes only the surface composition, can affect the said properties only as a result of a change in the adhesion interaction between the surface and the coating. A high-temperature implantation, where diffusion causes a change in the composition of the near-surface zone to a depth of several microns, can exert its influence by changing the mechanical properties of the material under the coating. In this case the diffusion processes can lead either to strengthening of the steels as a result of saturation with carbon and nitrogen or to their weakening caused by the tempering processes. Figure 10 illustrates the influence of the treatment temperature on the microhardness of the implanted and back surfaces of the samples. The unimplanted surface keeps a constant microhardness up to the temperatures of tempering and then is decreased sharply. The microhardness of the implanted surface increased considerably when temperature is rised and reach the maximum values near the 500 °C.

CONCLUSION

The results of the 2nd stage of the contractual works are as follows:

- 1. Samples of two grades of tool steels, namely the P6M5 high-speed steel and X12M die steel, have been prepared and certified.
- 2. Carbon and nitrogen have been implanted over broad intervals of temperatures (50 - 700°C) and doses ($1\ 10^{17}$ - $8.3\ 10^{18}$ cm^{-2}).
- 3. The distribution of carbon and nitrogen concentrations in the near-surface zone up to 2.5 μm thick has been measured. It was shown that the character of the distribution depends on particular implantation conditions (dose and temperature). This makes it possible to analyze the influence of implantation on the strength of the "tool steel - diamond-like coating" system.

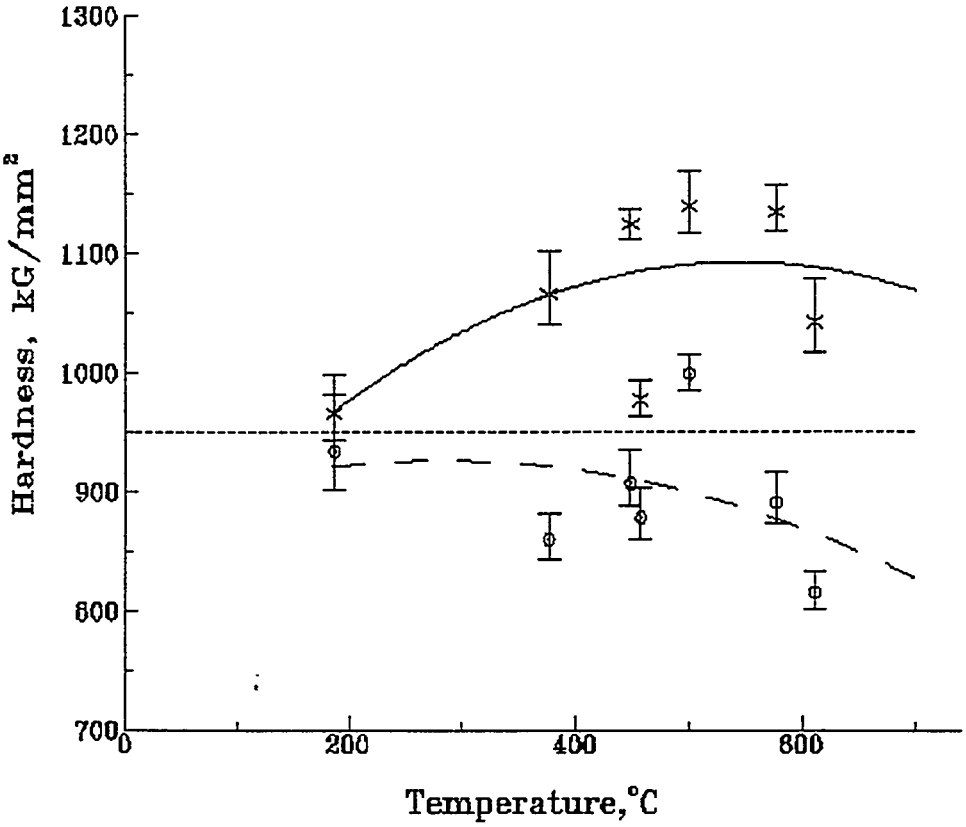


Fig. 10. Microhardness of P6M5 steel implanted by Nitrogen ions vs temperature during implantation. Dose is of 3.5 10^{18} cm^{-2},
* - implanted sides, o - back sides of specimens,
---- - initial average microhardness.

Appendix 1. Modes of ion implantation.

carbon - P6M5				carbon - X12M				nitrogen -P6M5				nitrogen -X12M			
Dose 10^{-18} cm^{-2}	Frequency, Hz	Temperature, °C	Time min	Dose 10^{-18} cm^{-2}	Frequency, Hz	Temperature, °C	Time min	Dose 10^{-18} cm^{-2}	Frequency, Hz	Temperature, °C	Time min	Dose 10^{-18} cm^{-2}	Frequency, Hz	Temperature, °C	Time min
1.2	25	290	26	0.2	10	50	10.5	0.1	25	50	3	0.11	10	50	5.3
1.2	25	480	26	0.2	10	250	10.5	0.1	25	210	3	0.11	10	170	5.3
1.2	25	510	26	0.2	10	90	10.5	0.1	25	350	3	0.11	10	130	5.3
1.2	25	570	26	0.2	10	230	10.5	0.1	25	350	3	0.11	10	150	5.3
3	50	170	27	0.2	10	170	10.5	0.3	10	50	15.5	0.11	10	100	5.3
3	50	790	27	0.2	10	210	10.5	0.3	10	90	15.5	0.5	25	120	12
3	50	640	27	0.5	25	50	10	0.3	10	310	15.5	0.5	25	550	12
3	50	760	27	0.5	25	130	10	0.3	10	300	15.5	0.5	25	180	12
3	50	580	27	0.5	25	240	10	0.3	10	380	15.5	0.5	25	350	12
3	50	740	27	0.5	25	290	10	0.3	10	290	15.5	0.5	25	380	12
3	50	790	27	0.5	25	360	10	0.3	10	420	15.5	0.5	25	460	12
4	50	740	22	0.5	25	370	10	0.5	25	50	9	0.5	25	510	12
4	50	720	22	1	50	100	12	0.5	25	200	9	1	50	100	12
4	50	720	22	1	50	700	12	0.5	25	440	9	1	50	680	12
				1	50	270	12	0.5	25	360	9	1	50	300	12
				1	50	570	12	0.5	25	550	9	1	50	620	12
				1	50	480	12	0.5	25	480	9	1	50	520	12
				1	50	620	12	0.5	25	600	9	1	50	620	12
				5	50	190	60	1.2	25	100	17	1	50	640	12
				5	50	430	60	1.2	25	150	17	4.6	50	240	54
				5	50	540	60	1.2	25	360	17	4.6	50	600	54
				5	50	590	60	1.2	25	510	17	4.6	50	510	54
				5	50	580	60	1.2	25	520	17	4.6	50	500	54
				5	50	590	60	1.2	25	600	17	4.6	50	490	54
				5	50	630	60	3.5	25	190	52	4.6	50	530	54
								3.5	25	380	52	4.6	50	550	54
								3.5	25	460	52				
								3.5	25	450	52				
								3.5	25	580	52				
								3.5	25	500	52				
								3.5	25	610	52				
								3.7	25	460	77				
								3.7	25	530	77				
								3.7	25	510	77				
								3.7	25	500	77				
								8.3	50	190	65				
								8.3	50	340	65				
								8.3	50	500	65				
								8.3	50	720	65				
								8.3	50	680	65				
								8.3	50	580	65				
								8.3	50	730	65				

Appendix 2. Depth distribution of concentration of carbon and nitrogen implanted into P6M5 and X12M steels according to nuclear microanalyse.

Table 2.1. Changes of carbon concentration after C implantation in P6M5 referenced to initial concentration.
Delta - concentration measurements error.

Depth micrometers	580 C C/Cinit.	$3\delta10^{18}$ delta	500 C C/Cinit.	$1,2\delta10^{18}$ delta
0	1.95	0.02	1.76	0.02
0.18	1.87	0.02	1.59	0.02
0.38	1.72	0.03	1.42	0.02
0.6	1.66	0.04	1.36	0.03
0.78	1.65	0.05	1.36	0.05
0.95	1.67	0.07	1.37	0.06
1.16	1.74	0.09	1.42	0.08
1.34	1.72	0.11	1.35	0.09
1.52	1.82	0.14	1.4	0.12
1.68	1.63	0.14	1.09	0.13
1.88	1.3	0.13	1.09	0.12
2.06	1.65	0.19	1.42	0.17
2.22	1.51	0.17	0.91	0.14
2.36	1.76	0.23	1.44	0.19
2.52	1.54	0.21	1.17	0.15

Table 2.2. Changes of carbon concentration after C implantation in P6M5 referenced to initial concentration.

Depth	$2\delta10^{18}$ 200C	$5\delta10^{17}$ 100C	$2\delta10^{18}$ 700C	$5\delta10^{17}$ 500C
0.1	3.7	2.25	1.01	0.56
0.3	2.3	1.85	1.12	0.88
0.5	1.4	1.44	1.13	1.06
0.7	1.35	1.35	1.1	1.16
0.9	1.7	1.4	1.1	1.28
1.1	1.64	1.3	1.05	1.18
1.3	1.65	1.3	1.02	1.13
1.5	1.7	1.3	1.06	1.13
1.7	1.76	1.4	1.08	1.2
1.9			1.08	1.17

Table 2.3. Changes of nitrogen concentration after N implantation in X12M referenced to initial concentration.
Delta - concentration measurements error.

Depth micrometers	490 C	$4.6\tilde{o}10^{18}$	600 C	$4.6\tilde{o}10^{18}$	380 C	$5\tilde{o}10^{17}$
	at.%	delta	at.%	delta	at.%	delta
0	8.25	0.22	10.38	0.25	5.02	0.16
0.22	5.89	0.16	9	0.2	2.36	0.09
0.44	4.9	0.15	7.76	0.19	1.62	0.08
0.66	4.6	0.15	6.84	0.19	1.5	0.08
0.88	4.99	0.17	6.44	0.2	1.26	0.08
1.09	5.13	0.2	6.55	0.23	0.89	0.08
1.3	5.49	0.23	6.45	0.25	0.92	0.09
1.51	5	0.25	6.27	0.28	0.63	0.08
1.72	5.39	0.2	6.65	0.33	0.36	0.06
1.92	5.43	0.33	6.57	0.37	0.15	0.04
2.13	5.62	0.39	5.76	0.4	0.28	0.08
2.33	5.17	0.45	4.24	0.4	0.26	0.07
2.53	5.98	0.56	4.2	0.46	0.43	0.13
2.73	4.14	0.52	3.9	0.5	0.66	0.2

Table 2.4. Changes of carbon concentration after C implantation in X12M referenced to initial concentration. Dose 10^{18} cm^{-2}. Delta - concentration measurement error.

Depth micrometers	700 C	10^{18}	270 C	10^{18}	480 C	10^{18}	100 C	10^{18}
	C/Cinit.	delta	C/Cinit.	delta	C/Cinit.	delta	C/Cinit	delta
0	1.04	0.01	4.27	0.038	2.08	0.02	3.44	0.03
0.18	1.13	0.01	2.84	0.026	1.88	0.02	2.58	0.02
0.38	1.22	0.02	1.84	0.024	1.59	0.02	1.81	0.02
0.6	1.24	0.02	1.45	0.028	1.33	0.03	1.44	0.03
0.78	1.29	0.04	1.44	0.038	1.33	0.04	1.41	0.04
0.95	1.28	0.05	1.44	0.051	1.26	0.06	1.39	0.05
1.16	0.89	0.04	1.38	0.062	1.22	0.04	1.28	0.06
1.34	0.91	0.05	1.22	0.068	1.07	0.09	1.16	0.07
1.52	0.87	0.06	1.27	0.08	1.1	0.1	1.16	0.07
1.68	0.84	0.07	1.22	0.091	1.21	0.11	1.15	0.09
1.88	0.85	0.08	1.17	0.097	1.11	0.12	1.11	0.09
2.06	0.87	0.09	1.11	0.107	1.14	0.15	1.29	0.12
2.22	1.11	0.11	1.12	0.12	1.15	0.16	1.1	0.11
2.36	0.92	0.1	1.1	0.12	1.14	0.16	1.05	0.11
2.52	1.13	0.13	1.05	0.12	0.98	0.19	1.09	0.13

Table 2.5. Changes of carbon concentration after C implantation in X12M referenced to initial concentration.
Dose 5 10^{18} cm^{-2}. Delta - concentration measurements error.

Depth	430 C		630 C		540 C	
micrometers	C/Cinit.	delta	C/Cinit.	delta	C/Cinit.	delta
0	12.62	0.1	2.65	0.02	4.22	0.04
0.18	9.79	0.08	1.57	0.02	4.01	0.03
0.38	5.82	0.07	1.33	0.02	3.38	0.04
0.6	4	0.07	1.34	0.03	2.77	0.05
0.78	3.98	0.09	1.5	0.04	2.55	0.06
0.95	4.26	0.13	1.63	0.06	2.44	0.08
1.16	3.51	0.14	1.65	0.07	2.22	0.09
1.34	2.52	0.12	1.66	0.09	1.92	0.1
1.52	1.98	0.11	1.65	0.1	1.62	0.1
1.68	1.74	0.12	1.54	0.11	1.71	0.12
1.88	1.74	0.13	1.52	0.12	1.5	0.12
2.06	1.8	0.18	1.72	0.15	1.59	0.14
2.22	1.89	0.17	1.74	0.16	1.4	0.14
2.36	1.81	0.17	1.68	0.16	1.4	0.14
2.52	1.78	0.19	1.77	0.19	1.3	0.15

Table 2.6. Changes of nitrogen concentration after N implantation in X12M referenced to initial concentration.
Dose 1.2 10^{18} cm^{-2}. Delta - concentration measurements error.

depth	520 C		510 C		360 C		600 C	
micrometers	at.%	delta	at.%	delta	at.%	delta	at.%	delta
0	4.51	0.21	4.77	0.27	4.92	0.27	4.71	0.27
0.22	2.8	0.17	2.88	0.17	2.83	0.17	3.02	0.18
0.44	2.96	0.19	2.76	0.19	3.65	0.22	3.2	0.2
0.66	2.83	0.2	2.09	0.17	3.06	0.22	2.41	0.19
0.88	2.38	0.21	2.36	0.21	2.62	0.22	3.06	0.24
1.09	2.56	0.25	1.96	0.21	2.11	0.22	2.98	0.27
1.3	2.69	0.3	2.42	0.28	2.79	0.31	3.16	0.33
1.51	2.82	0.36	2.59	0.34	2.68	0.35	3.47	0.41
1.72	2.69	0.4	2.57	0.39	2.38	0.37	3.79	0.48
1.92	3.11	0.56	1.51	0.37	2.92	0.54	3.52	0.6
2.13	3.25	0.73	2.28	0.6	1.96	0.55	2.11	0.58
2.33	1.69	0.54	1.69	0.54	2.25	0.64	1.32	0.47
2.53	3.35	0.89	1.56	0.6	2.23	0.72	1.79	0.64
2.73	1.96	0.81	1.96	0.81	1.96	0.81	2.6	0.94

Table 2.7. Changes of nitrogen concentration after N implantation in X12M referenced to initial concentration.
Dose 3.5 10^{18} cm^{-2}. Delta - concentration measurements error.

depth, micrometers	450 C		610 C			380 C		580 C	
	at.%	delta	at.%	delta	delta	at.%	delta	at.%	delta
0	6.37	0.19	5.04	0.17	0.17	8.88	0.23	4.85	0.16
0.22	3.67	0.12	4.56	0.14	0.12	4.39	0.14	4.23	0.13
0.44	3.15	0.12	4.19	0.14	0.12	3.36	0.12	3.91	0.13
0.66	3.14	0.13	3.85	0.14	0.12	3.21	0.13	3.56	0.13
0.88	3.22	0.14	4.07	0.16	0.13	3	0.13	3.68	0.15
1.09	3.36	0.16	4.46	0.18	0.15	2.96	0.15	3.74	0.17
1.3	3.34	0.18	4.54	0.21	0.17	3.21	0.18	3.96	0.2
1.51	3.46	0.2	4.29	0.23	0.18	3.01	0.19	4.16	0.23
1.72	3.51	0.23	4.31	0.27	0.22	3	0.22	3.78	0.25
1.92	3.29	0.26	3.94	0.29	0.26	2.94	0.24	3.63	0.27
2.13	3.23	0.29	4.21	0.34	0.3	2.37	0.25	3.76	0.32
2.33	3.46	0.37	4.61	0.43	0.33	3.13	0.35	4.65	0.43
2.53	4.05	0.46	4.58	0.49	0.34	3.28	0.4	4.05	0.46
2.73	2.76	0.48	3.66	0.48	0.36	2.76	0.42	3.72	0.49

Project Title: Application of Wear Resistant Coatings to Tools Using Novel Diamond Coating and Attachment Processes and Explosive Detonation Deposition Processes
Principal Investigator: Dr. Mariy A. Voronkin
Institute for Superhard Materials
Kiev, Ukraine
AM-7678

CLAUSE 1 - STATEMENT OF WORK

Background:

This project will demonstrate the use of the coating and attachment technique on commercially available stone and metal cutting and polishing tools. The project will also demonstrate the capabilities of the unique explosive detonation deposition process developed at the Institute. This work is a non-profit research and development effort between the Contractor and Sandia National Laboratory.

Tasks:

The Contractor shall:

1. Prepare and submit an initial report reviewing the Institute's previous work on coating and attaching diamond particles to copper, cobalt, iron, and nickel based alloy substrates and its work on improving the properties of tools using the explosive detonation coating process. This report shall not reveal know-how but shall emphasize, when possible, the factors that make these technologies developed by the Institute novel compared to currently used commercial processes.

2. Provide twenty four (24) tools that have been coated with diamond powders using the techniques developed at the Institute. Six (6) each of four (4) different tools will be coated. The specific type of tools will be agreed upon by the Contractor and Sandia within three (3) months of the beginning of the contract. A letter report summarizing the work performed to coat the tools will also be supplied.

3. Provide twenty four (24) tools that have been coated with the explosive detonation process developed by the Institute. Six (6) each of four (4) different tools will be coated. The specific type of tools and coatings will be agreed upon by the Contractor and Sandia within six (6) months of the beginning of the contract. A letter report summarizing the work performed to coat the tools will also be supplied.

NATIONAL ACADEMY OF SCIENCES OF THE UKRAINE
INSTITUTE FOR THE SUPERHARD MATERIALS
LABORATORY OF THE COATING TECHNOLOGY

Contract AM-7678 from January 03, 1995.

APPLICATION OF WEAR RESISTANT COATING TO TOOLS USING NOVEL DIAMOND COATING AND ATTACHMENT PROCESSES AND EXPLOSIVE DETONATION DEPOSITION PROCESSES

Step 1 Prepare and submit an initial report reviewing the Institute's previous work on coating and attaching diamond particles to copper, cobalt, and nickel based alloys substrates and its work on improving the properties of tools using the explosive detonation coating process.

Investigators:

Dr. Mariy A. Voronkin
Dr. Ivan V. Bondar'

KIEV 1995

Introduction

Different types coatings are effective for solving various problems of materials science engineering.

The achievements of the Laboratory of Coating Technology of the Institute for Superhard Materials in applying both thin composite coatings to diamond powder in order to improve the powder retention in a tool bond and thick strengthening wear-resistant composite coatings on large substrates are listed below.

The efficiency of diamond tool usage is defined by its high wear-resistance and productivity. The strength of grain retention in the tool body is the main factor, responsible for the efficiency of the grain use.

Since beginnings of 70's of past century up to now diamonds are intensively used in rock destructive tools, and all this time the methods of diamond retention in tools have been improved. At first large natural diamonds (carbonates) from 0,5 to 2 carats in weight were used. They were mounted in a soft matrix. Then tools were developed, in which smaller size diamonds (20 to 60 pcs per carat) were used. With this purpose, methods of securing diamonds in cast matrixes, and later of sintering by powder metallurgy were developed, that are considerably cheaper and reliable. The further investigations were aimed at the development of various bonds, in which diamond grains were sintered. These are resin and various metal bonds. Diamond is a very inert modification of carbon, which reacts poorly with other materials. One of the ways of solving this problem is the applying of coatings to the diamond grain surface. The expediency of using coatings is convincingly proved by world practice of application nickel-coated diamond powders in resin bond grinding tools [1]. Under heavier working conditions, however, where metal bond tools are used and especially under the conditions of intensive abrasive wear and large shock loads occurring in stone working, wheel dressing and drilling, the efficiency of the use of nickel-coated diamond is low, as the electrochemical technology of coating provides neither a strong retention of diamond grains in a bond nor an effective protection of grains from harmful effects during both the sintering of diamond layer and in tool operation.

Thus, the necessity of development of new technologies of applying coatings is obvious. They should ensure a strong retention of grains in diamond-containing layer of a tool and their protection from harmful effects during both sintering in various bonds and tool operation. For many years already such works are conducted at the V.Bakul Institute for Superhard Materials of the National Academy of Sciences of Ukraine.

1. Application of metal coatings on a diamond powders

Up to now a large experience is accumulated in application of metal coated diamond powders. As it is seen from reviews of patents [2-6], which look at 120 patents on problems associated with diamond powder coatings, transition metals are most often used for metal coatings. Chemical elements used to coat diamond powders are listed in Table 1.1 [2-6]. As reported in the literature, the transition groups IV, V, and VI metals are most frequently used as coating materials.

Diamond powders with various coatings were tested for tools in different bonds and different conditions of operation. Production tests were conducted of tools with diamonds coated with iron group metals and their-base alloys as well as with some carbide-forming metals and their compounds (Table 1.2). As it follows from the

advertizing materials, only nickel and copper coatings deposited by electrochemical method have found a wide application. The simplicity and ease of this method facilitated its wide implementation in production technology of resin bond diamond grinding tools. Other types of metallization have found only a limited application and call for further research and development.

Table 1.1 Chemical Elements Used for Metal Coating of Diamond Powders

									Al	Si
Ti	V	Cr	Mn	Fe	Co	Ni	Cu	Zn		
Zr	Nb	Mo				Pd		Ag		Sn
Hf	Ta	W				Pt		Au		Pb

Table 1.2 Metal-Coated Diamond Powders and their Application Areas

Metal coating	Powder	Tools	Application
Nickel, copper	AC-M Ukraine CDA-30 N, CDA-55 N, CDA÷50 C, DXDA-11 MC De Beers RVG-D, CSG-11, RVG-880, RVG-W56, RWG-30 General electric Co	Resin bond grinding wheels	Grinding hard alloys together with steel, Ni- and Cr-containing alloys, and difficult-to-machine stainless and tool steels
Adhesion-active alloys based on Cu-Sn, Ni-Ti Cu-Sn-Ti	AC-HT, AC-A, AC-MA Ukraine	Resin and metal bond grinding tools	Machining brittle materials: crystal, glass, ceramics
Refractory compounds TiC, WC, Mo 42 OC	AC-K Ukraine	Resin and metal bond grinding tools	Machining brittle nonferrous materials
Refractory metals Ti	SDAT De Beers	Saw blades, cut-off wheels	Cutting stone, concrete, refrectory materials

1.1. Functions of coatings on a diamond grain

During tool making and operation, a diamond grain is subjected to a lot of of chemical and physical effects, which worsen its properties.

Basic parameters describing a diamond grain as a microcutter are its mechanical properties: the strength, microhardness, and fracture toughness.

Many researchers have studied the effect of metallization on the value of the mean load destructing diamond grains [7-15]. The majority of them assumed, that when a coating is applied to a diamond powder, just this factor permits the service

life of a tool to be increased. As it is seen from the literature, actually all types of coatings increase the force required to destruct a diamond grain in a uniaxial compression. However, the value of a destructive loading increases (the effect of the grain hardening) differently depending of the material of a coating. The effect of a coating material strength, adhesion to a grain and other factors on this characteristics is not analyzed.

As this factor is given so much attention, we also have studied thoroughly the influence of a metallization on the grain strength. The strength of a grain is indirectly characterized by the value of a destruction force at the uniaxial compression. Various defects are present in a real grain. Just they define the value of the force destructing the grain. Let us consider the influence of a coating on the so-called effect of hardening diamond grain.

The increase in the destruction load value can be affected by a soft layer of the coating due to a more uniform distribution of load. This effect of a soft interlayer, probably, will be reflected in the results of dectruction load measurements when the coating thickness is commensurable with the surface roughness (places of the grain integrowth - tens of microns, cavities and protrusions - from units to a few tens of microns). Hence, such thickness of coatings affects the measurements of the mean destructive load. The further increase of thickness the effect action of a soft interlayer is insignificant and can manifest itself through the banding effect.

Two cases should be considered: the case, when a coating is not bonded with a grain by a strong bond, and the case when, on the contrary, the coating is firmly bound to the grain. In case of a destruction of a crystal with a metal coating, that is not firmly bonded to a grain, the deformation occurs along the shell length for the crack size with no destruction of the shell [15]. Hence, the coating receive a very small part of the load, as the deformation of the crystal itself is small. If the coating is firmly bonded to a grain surface, not the whole coating is deformed and destructed but only a part of it in the place of the crystal destruction. The force needed to destruct a thick coating can be commensurated with the force required for a destruction of the grain itself.

It is seen, that all the above effects occur at large thicknesses of coatings ($h>1$ μm). At the same time there is another large group of defects - sites of outputs of inclusions (microns), steps of growth (hundreds of nanometers), exits of dislocations (tens of nanometers). This group of defects is characteristic of strong types diamond (AC50, SDA80, and RWG, produced by CIS, De Beers and General Electric Co, respectively, and stronger), which are usual applied for stoneworking, dressing and drilling tools. The defects are a micron less in size. Hence, a coating just of such a thickness should affect the average powder destructive load. As the problem has not been adequately investigated, we consider such influence in more details.

Figure 1.1 shows histograms of destructive loads for the high-strength thermostable diamond powder AC132T 400/315: uncoated (b) and metallized with molybdenum (a). The metallization was performed using the magnetron sputtering method under predetermined conditions of the process. The average calculated thickness of the coating made 0.36 μm. The powder was tested for strength using uniaxial compression on DA-2 plant. The mean destructive load was determined based on three series of 50 grains each. The conditions of metallization are such, that only slight interaction exists between the coating material and diamond [25].

Thus, as it is seen from Fig. 1.1, such a metallization does not affect the force needed to destruct the high-strength ACT132T diamond. The mean destructive forces for metallized and unmetallized powders are virtually the same and make up

162 and 161 N, respectively. In Fig. 1.2 strength histograms are given of the same diamond powder with a coating applied under the technological conditions, under which at the diamond-coating interface, the process of carbide formation takes place and a transition carbide sublayer form, that provides both the strong diamond-coating cohesion and healing of the surface defects.

As it is seen from the Figure, for metallized crystals, the destructive force shifts to the large value region and the load required for destruction of some grains exceeds 420 N. The grain distribution on the histogram of loads for metallized powder is more uniform, and the average force of destruction is greater by the factor 1.41 and makes 228 N. For clearer representation, we consider the following characteristic a percentage of destroyed grains (Fig. 1.3). For less defective crystals, those, which require to be destructed the force exceeding 300 N, the difference between percentage of destroyed grains of unmetallized and metallized powder begins to decrease.

For the greater reliability of the above said, carefully selected defect-free crystals of this powder (Table 1.3) were also tested for strength. The strength of diamond grains was defined using the technique, described in [17], which permits the strength of perfect diamond crystals to be measured. The selected crystals were of a cubooctahedron habit. The supports were produced of the VK4 alloy. The average strength of unmetallized and metallized diamonds made 11,3 and 11,11 GPa, respectively, that confirms the suggested hypothesis.

The effect of coatings on the crystal strength was also examined using a Freitester device.

The conditions of cyclic impact load, occurring in working stone, dressing and drilling are simulated in the device. The effect of metallization on the value of the F-criterion is of no significance. The analysis of products of destruction, which remain on the sieve shows, that when tested, the grains are destroyed as a result of splitting angles. The analysis shows, that it happens due to shear impact loads. Therefore, under the given conditions of loading, the healing of defects does not affect the strength.

Thus, the healing of defects can really affect favorably the service life, if the tool works under the conditions of grain loading that corresponds to the uniaxial compression. одноосному to compression. But in view of the small hardening effect (the increase in strength up to 30 %), it can not be considered as decisive for the efficient application of metallized powders. At the work of a grain, neither the banding effect can exert a considerable influence, as the coating on the protruding grain is removed during the operation, nor the soft interlayer, as the bond acts as the soft interlayer irrespective of whether there is a coating or not. Therefore, all these effects responsible for strength are not defining the high efficiency of coatings on adiamond grain in an operating tool.

Many papers [9, 18-22] describe the studying protective functions of coatings at sintering diamond tools. They are the protection from the actions of high temperature, aggressive gas medium, in which the sintering occurs, and from the liquid phase component of the bond. All these factors somehow affect the change of diamond powder properties.

It is shown in [23] that at heating to a high temperature (1100 ^{o}C) even in a high vacuum, the strength of synthetic diamonds drops approximately by a factor of three. The authors state that this is associated with the inclusions of solvent-metals which enter the composition of a catalyst. The strength of the natural diamond is shown not to decrease practically at the above temperature.

Table 1.3 The Strength of the AC132T 400/315 Diamond Grinding Powder

Number	Size of contact area, μm lower	upper	Mean contact area, mm	Destruction load, kg	Strength of diamond kg/mm	GPa
		AC132T 400/315. Uncoated.				
1	280x224	272x224	0,618	57,0	921	9,0
2	288x224	240x224	0,0591	68,5	1158	11,3
3	312x256	312x240	0,0774	89,6	1158	11,3
4	288x264	280x192	0,0605	55,7	891	8,7
5	280x296	280x256	0,0773	94,4	1222	12,0
6	240x256	192x224	0,0518	67,2	1296	12,7
7	256x280	256x264	0,0696	93,4	1342	13,1
8	240x288	264x224	1,0645	81,0	1255	12,3
9	240x288	264x224	1,0653	81,0	1240	12,2
10	296x256	296x240	0,0734	84,5	1151	11,3
		AC132T 400/315 h=0,35 μm.				
1	272x216	240x256	0,0604	60,2	993	9,7
2	264x248	240x296	0,0685	94,9	1314	12,9
3	296x296	256x304	0,0828	83,1	1004	9,8
4	320x240	240x244	0,0706	80,2	1136	11,1
5	296x280	224x240	0,0676	91,1	1348	13,2
6	216x280	216x216	0,0536	72,5	1352	13,3
7	264x216	280x216	0,0588	67,7	1151	11,3
8	240x240	240x208	0,0538	60,2	1119	11,0
9	280x272	272x272	0,0751	58,6	781	7,7

We have investigated the influence of a molybdenum coating on the dynamic strength growth (Table 1.4). For this purpose, the AC80 250/200 diamond powder with and without coating was annealed in a hydrogen furnace at the temperature of 1150 °C for 10 min with a subsequent slow cooling. The annealing simulated the temperature conditions for sintering of a diamond-containing layer of drilling bits.

As it is seen from the table, the dynamic strength at annealing decreases much sharplier than the static strength at the uniaxial compression. The dynamic strength of as-annealed powder decreases more than fivefold. This is indicative of the prevailing influence of intracrystalline defects. The studies show that in actual processes of diamond tool manufacture the protective function of a coating is insignificant, as protective media are used. The strength of diamond drops basically due to internal inclusions and defects while the external factors here play a smaller role.

It is shown in [24] that in stone working, the large part of a grain does not perform the rock destructive function. The grain is retained in the diamond-containing layer of the bond provides the protrusion necessary for work. Therefore,

one of the main requirements, which ensures the efficient operation of a grain in a tool as a microcutter is its reliable retention in a bond.

Table 1.4 Test Resuls of the AC 50 315/250 Diamond Powder with a Different Thickness of Molybdenum Coating

Coating thickness, μm	Predeter - mined number of cycles	Mass of residue, cts	Necessory number of cycles	Strength criterion, F	Criterion mean of value	Root-mean-square deviation of the mean value
0,0	1000	1,05	1076	45		
0,0	1070	1,00	1070	44	44,5	0,5
0,3	1000	1,01	1015	42		
0,3	1000	0,98	971	40	41,0	2,0
0,6	1000	1,00	1000	42		
0,6	1000	1,00	1000	42	42,0	0,0
1,0	1200	0,87	997	42		
1,0	1000	1,02	1030	43	42,5	0,5

1.2. The interaction and strength of a metallized diamond grain adhesion to a metal bond

Depending on the conditions of operation, different bonds are used in the tool manufacture. They can be divided into three main groups: resin, vitrified and metal bonds. Tools in metal bonds are applied under heavy conditions, where the grain is subjected to high loads. For tools operating under impact loads (stone working, dressing and drilling), very hard metal bonds are used. These are copper-base bonds with cobalt addition, cobalt-base bonds with nickel or iron addition, and copper-base bonds with additions of W_2C and WC-Co alloys.

The reliability of a diamond grain retention in a bond depends on the contact interaction at the diamond-coating-bond interfaces. The retention of a grain is defined by the strength of a grain-bond adhesion. As diamond is rather inactive with metals, to solve the above problem, a metal-insulating coating is used that ensures the formation of chemical bond elements at the interface with diamond [25, 26]. We think it important to study how the intensity of carbide formation at the diamond-coating interface affects the strength of a metallized grain adhesion to the bond in a joint sintering and what is the effect of additives of, say, cobalt or other metal, which solve diamond actively.

To study a contact interaction at the diamond-coating-bond interface, a special device for measuring the strength of a metallized grain adhesion with a bond has

been developed. The device is made as an attachment to a VUP-4 vacuum station and is placed in the vacuum chamber (Fig. 1.4). The device allows us to sinter the crystal with a bond under a load in a high vacuum or in an inert medium and to measure the breaking off force when cooled to room temperature. Thus, the device makes it possible to simulate the diamond tool sintering conditions and to study the nature of a metallized grain-bond interaction.

Grains of the AC132T 400/315 diamond powder metallized under different technological conditions have been investigated. For metallization, molybdenum has been used which is a carbide-forming metal. Molybdenum carbides have a low microhardness and, hence, low brittleness. Perfect crystals were selected for testing. Due to this the measurement of the breaking off area with an object-micrometer using a microscope was made easier. The accuracy of the measurements was ± 8 μm. The mean value of the breaking off area was determined from four measurements. X-ray phase analysis was used to assess the quantity of a carbide phase at the diamond-coating interface and then the thickness of a carbide interlayer forming in the process of metallization under the given conditions was calculated.

The strength of adhesion and the nature of metallized grains interaction with different quantity of the carbide phase at the diamond-coating boundary with the bond, including 42 % Cu, 27 % Co, 15 % Fe and other additives. The sintering temperature of the above bond is 830 °C. The holding time was sufficient for sintering a press-fit bond layer and the crystal and made up 0.5 h. The mean calculated thickness of the molybdenum coating on these powders was 1 μm. The investigations of the coating adhesion show (Fig. 1.5) that the strength of the coating adhesion with diamond increases with the thickness of the intermediate carbide layer. With the thickness of a carbide layer above 80 nm, the adhesion strength increases only slightly. Therefore, the further increase of the carbide layer thickness is inefficient.

Figures 1.6a and 1.6b show surfaces of a metallized crystal breaking off the bond which are characteristic of low carbide phase powders. In this case, the calculated thickness of a carbide layer is 3-4 μm. It is seen from the Figure, that a molybdenum layer was broken off together with the bond. A very thin layer of molybdenum carbide remained at the crystal surface. It can be seen in the Figure as a lighter layer than the diamond and darker than the molybdenum coating one. The molybdenum carbide surface is even and smooth and the fact probably is responsible for its weak adhesion with an external molybdenum layer (σ = 40 MPa) and because of this the breaking off occurs along the carbide-metal interface. The strength of metallized grains adhesion with a bond increases with the carbide phase quantity at the diamond-molybdenum interface. Figure 1.7 exhibits breaking off surfaces characteristic of powders with a calculated thickness of the carbide layer of 10-15 μm. The adhesion of such crystals with the bond is 140 MPa. In this case, the breaking off occurs also at the carbide and molybdenum interface. Globular carbide structures are seen well in the Fig. They form at the places of defects, for instance, at the right corner along the crystal cleavage band.

The further growth of carbide structures of a transition layer facilitates the increase in the adhesion strength. Thus, for 70-80 nm calculated thickness of a carbide transition layer, the adhesion strength is 220 MPa. In this case, as is seen from Fig. 1.8a,b, the break off occurs mainly along the molybdenum layer - bond interface and the bond material. The coating broke off the crystal in individual places only (Fig. 1.8b). Hence, the adhesion of the coating with a diamond exceeds

220 MPa. As the breaking off occurs by the bond material, then the specific load of 220 MPa corresponds to the strength of a sintered bond.

1.3. The effect of molybdenum coating on diamond grain retention in the bond and the operation efficiency of stone working tools

In order to assess the efficiency of retention of metal-coated and uncoated diamond grains in a tool bond, the fractographic studies have been carried out of the surface of a section of a drilling bit with a notch fractured at the three-point load. The mode of fractured diamond grain distribution was examined in a phase contrast of the fracture structure employing a CamScan electron scanning microscope and shown in Fig. 1.9. The area of 1700x2500 μm was analyzed. The average amount of grains of the given fraction falling within such a section is found to be 88+7 pcs. The grain retention in the bond increases with the strength of adhesion of a coating with a grain and as a result, the per cent of fractured grains grows (see Table 1.5).

Table 1.5 Test Results of As-Annealed at 1150 °C Metal-Coated Diamond Powder

Coating thickness, μm	Predeter - mined number of cycles	Mass of residue, cts	Necessory number of cycles	Strength criterion, F	Criterion mean of value	Root-mean-square deviation of the mean value
			Initial powder without annealing			
0,0	2600	1,06	2800	116		
0,0	2800	0,99	2767	115	115,5	0,5
			As-annealing dimond powder			
0,0	700	0,81	550	23		
0,0	550	0,96	518	22	22,5	0,5
0,5	700	0,88	550	23		
0,5	600	0,99	525	22	22,5	0,5
1,0	700	0.82	475	21		
1,0	500	1,00	500	22	21,5	0,5

77 % grains of powders with adhesion of 220 MPa were fractured to one or other extent. Thus, the retention of a metal-coated grain in a metal bond depends mainly on the strength of the grain-coating adhesion. The influence of the retention of a metal-coated grain on the drilling bit service life was investigated. These tools are subjected to the most intensive impact loads and the tests proved that the

strength of a grain - bond adhesion affect greatly the tool service life. The subject of investigations were 59-mm diameter drilling bits made by infiltration of the AC 250/200 diamond powder having a given strength of adhesion. The tests were carried out on a laboratory stand. For a comparative evaluation of a wear resistance, the drilling conditions were chosen, under which a constant mechanical drilling rate of 3.8 m/h was kept, a 80 μm hole was made per a revolution, the rotational speed made 800 rev/min and that ensured a constant cutting speed of 2.11 mm/s. 0.6 m were drilled during each test.

The following characteristics were taken during tests: the penetration depth (by the stand limb) accurate to 1 mm, drilling power (by a three-phase wattmeter H396) accurate to 0.25 kW, wear by weight accurate to 10 mg. Granite of the 10 category of drillability was drilled.

Drilling with a constant rate has allowed us to reveal the effect of the adhesion strength between a coating and a diamond grain on the variation in the tool wear. The results of laboratory tests on wear resistance of the drilling bits are given in Table 1.6. The visual examination has shown that the process of the diamond break-in is fully ended in bits equipped with diamond powders of batches 1 and 2 after the first run already. The face of the sector became almost flat. Small regions of burns are observed. In this case, the power consumption is 4 kW. The curve of the power diagram exhibits many peaks, which is indicative of the unstable conditions of rock destruction and of a heavy wear of the bit matrix. The analysis of the structure of the segment working surface shows (Fig. 1.10b) that due to a weak retention of diamond in the bits of batches 1 and 2 (Table 1.7), the grains fall out. In this case, there appears an abrasive friction, which results in the overheating of the bit and the oxidation of the matrix. All this leads to a heavy wear of the matrix.

Table 1.6

σ, MPa	uncoated	40	140	220
Fractured grains, %	46	40	65	77

Better results were exhibited by bits equipped with powders of batches 3 and 4. A visual examination has shown that after the first penetration for 0.6 m both bits did not exhibit the whole run-in of the working elements. During the second penetration the bit wear is much lower as the working elements are mainly run-in. Thus, the results obtained in the second penetration are more reliable in evaluation the bit wear. Bits with coated diamonds having the strength of adhesion between a coating and a grain of $\sigma = 220$ MPa exhibit wear by a factor of 10.4 lower than that of bits with uncoated grains. Bits with a powder of batch 3 exhibit a somewhat higher wear $\sigma = 140$ MPa. This is because of the lower adhesion strength. From the energetic point of view, usage of these bits is more rational, as their power consumption is lower than that of the bits with uncoated diamond or bits with coated diamonds having lower strength of adhesion with the coating. Fractographic studies have shown that on the bit working surface, a relief forms, which destructs the rock intensely while a considerable protrusion of crystals from the bond decreases the bond wear and grain dislodging. Crystals protruding from the bond for more than one half are well retained by the bond.

Table 1.7 Service Life of Experimental Drilling Bits Equipped with Metal-Coated Diamond Powders Having Different Strength of Adhesion between the Grain and the Coating σ (according to laboratory tests)

№ batch	σ, MPa	Bit weight before the test, g	Bit weight after the test, g	Weight wear, g	Drillling power, kW
1	uncoating	433,770	430,540	3,230	4,0
		430,540	427,100	3,440	-"-
2	40	437,270	432,790	4,480	4,1
	-"-	432,790	428,710	4,080	4,1
3	140	437,720	435,410	2,310	3,6
	-"-	435,410	434,900	0,510	3,3
4	220	431,620	430,800	0,810	3,3
	-"-	430,800	430,480	0,320	3,1

2. Wear-resistant coatings by gas detonation

A gas detonation spraying relate to a group of gas-thermal methods, as well as a gas-flame and plasma methods. The gas-thermal methods [27-30] are characterized by high-energyeffect on the spraying material powder by a plasma flow or detonation products. As a result the powder acquires significant kinetic energy, melts partially and deposits on the article surface, thus forming a coating layer.

The control over the initial powder chemical composition, flow energy, and a gas medium composition at spraying permits obtaining coatings with required characteristics. In this series of methods, detonation coatings have the best technical parameters such as minimum porosity and gas permeability.

The possibility to enter in a jet various materials in turns permits one, prior to a deposition of a coating, to process the surface by coarse grain silicon carbide abrasive, thus cleaning it of chemically bound and adsorbed oxides.

This factor, inherent to the detonation method, and the greatest among the gas-thermal methods kinetic energy of the powder being sprayed (in detonation products of a gas mixture, the powder can pick up speed for several millisecond to 600 - 800 m/s, that is, considerably higher, than in a plasma-forming gas jet 100 - 150 m/s) provides the high adhesion strength of a coating with a substrate.

Also, the high temperature in the jet of detonation gases permits deposition of coatings of high-melting compounds and their based composite materials. At detonation spraying, however, there is no overheating of substrates, because of the

discreteness and short period of thermal effects of a gas powder flow. Under real conditions the temperature of sprayed articles does not exceed 150 °C.

These characteristics of the detonation method show its advantages for deposition coatings on surfaces, subjected to multifactory wear.

2.1. Peculiarities of the gas detonation spraying

The gas detonation technology of abrasive processing and coating deposition is designed for imparting specific properties to the article surfaces, which, as a rule, the substrate material does not have. It is used, for example, to increase the article wear resistance at a friction in various environments, intensive action of a loose abrasive, fretting-corrosion, as well as with the purpose of ensuring the necessary heat and corrosion resistance, electrical and thermal conductivity etc.

The detonation coatings are characterized by a high adhesion and cohesion strength and low porosity. The operational properties, chemical and phase compositions of materials being deposited change only slightly. Sprayed articles are not subjected to a considerable heating. Therefore, properties of construction materials, including those subjected to a thermal pretreatment, do not change.

In detonation-abrasive processing of surfaces, the deformation hardening of the article material occurs and a developed microrelief is formed. At the same time an oxide film or earlier applied coating is removed, and the surface is activated (as a result, its reactivity increases).

2.2. The essence of technology and characteristics of physical processes

The described technology is based on the use of detonation combustion energy of an explosive gas mixture for a directed acceleration and heating of powder material particles aimed at the processing of surfaces. At its realization, the detonation of an explosive mixture, formation and escape of a high-temperature gas powder flow, and physico-chemical interaction between individual particles of powder materials themselves, as well as with a gas medium and with the workpiece material take place.

The detonation provides the fastest increase of the gas temperature and pressure in a working space (detonation is a chemical conversion of an explosive, when a burning zone spreads in the form of a detonation wave, moving with the greatest possible speed, exceeding the sound velocity in this substance). After its completion a gas powder flow generates, that escapes in a critical regime out of the working chamber (tube) and affects the workpiece surface. The rate of particles in the flow can reach 80 - 1200 m/s.

During the acceleration, the powder is heated up to a temperature, the value of which depends on the particle sizes, characteristics of the powder material, technological parameters of the process and design features of the detonation equipment. Owing to the increase in a particle temperature, chemical reactions between elements, entering into the composition of a material being sprayed, and their interaction with the environment occur.

These processes are controlled regulating the technological parameters of detonation equipment.

At optimum conditions of the coating deposition, at the moment of the impact on the article surface, the particle temperature is close to that of the sprayed material melting, and the liquid phase content does not exceed the permissible values.

The particle adhesion with the workpiece surface occurs due to a number of processes, in particular, as a result of mechanical fixing, a chemical bond formation and a diffusion. The diffusion rate increases abnormally due to a pulse loading of the materials contact zone.

In abrasive treatment, the powder heating is a negative factor. In this case, the steps are taken to decrease the temperature and increase the abrasive particle rate. The distinctive feature of gas detonation technology processes is their extremely short duration. Thus, the detonation of an explosive mixture takes approximately $0{,}5 \times 10^{-3}$ s, the time of a shock interaction of each particle with the workpiece surface usually does not exceed 10^{-7} s. Thus, the spraying of a coating itself or a single treatment of a surface by a flow of abrasives takes no more than 10 milliseconds.

The including of operations associated with a gas detonation spraying of coatings and abrasive treatment into a technological cycle of a serial production requires a definite reorganization. The products to be gas-detonation treated are produced with the allowance made for the subsequent change of their sizes due to applying a coating of a given thickness (usually, no thicker than 0.5 mm). A special preparation of sprayed surfaces (etching, spinning, shot-blasting etc.) is not needed. It is desirable that the surface roughness should not exceed 100 μm. It means, that the last operation preceding the gas detonation can be turning or milling.

The sequence of the following operations depends on the choosing of coating and substrate materials, as well as on the state of a product surface. For example, if it is necessary to apply a coating of a hard alloy composite or aluminum oxide on a hardened steel substrate or any other coating on a surface with a scale or rust, the detonation-abrasive pretreatment is used. And only after cleaning the surface and a formation of a developed microrelief, the gas-detonation coating is sprayed.

Most often the grinding of an applied coating is the last operation of the technological cycle of manufacturing articles with gas-detonation coatings For this purpose, usual grinders equipped with superhard materials tools are used. In a number of cases, however, this operation is excluded, as the surface finish and the deposition accuracy of the required thickness layer can be sufficient for the product exploitation.

2.3. Coatings materials used for a gas-detonation spraying

To spray coatings, powders of metals, oxides, high-melting materials, metal alloys and composite materials are used. The powder grain size can be between 10 and 80 μm, but optimum size is 40-60 μm. The composite powders and alloys can be prepared beforehand, but can be used as the mixtures of components too.

The selection of a coating material depends on the area of application and function of the coating.

For restoration of worn-out regions and hardening of machine parts, alloys based on the iron group metals are most often used. For example, nickel self-fluxing alloys, containing chromium, boron and silicon. The structure of coating consists of a nickel-base matrix and hard inclusions of Ni and Cr carbides, borides, carbonitrides. It provides a combination of a high wear and corrosion resistance under various conditions of operation. Low melting temperature of the alloys (1000 °C) with the presence of the "solidus - liquidus" zone and fluxing alloying elements, such as boron and silicon, permits obtaining dense layers of these materials.

Oxides, high-melting compounds and composition on their base are used for obtaining of hard wear resistant layers with additional requirements for electrical resistance, thermal stability and a certain friction coefficient.

Compositions and properties of some coating materials, which have found a wide application, are given in Table 2.1

Table 2.1 Properties of some gas-detonation coating materials

Coating composition	Viccers hardness kg/mm^2	Max. using temperature in the oxidizer environment, °C	Coefficient of thermal expansion $\alpha*10^{-6}$, deg^{-1}	Time resistance to breakage $\sigma*10^2$, kg/sm^2	Modulus $\gamma*10^6$, $кг/см^2$	Porosity, %	Density g/sm^3
WC + 9% Co	1300	560	4.5	56.3	2.12	0.5	14.2
WC + 13% Co	1150	540	-	63.2	2.12	0.5-1	13.2
WC + 15% Co	1050	540	4.7	70.0	2.12	0.5-1	-
Al_2O_3	1000-1200	980	7.0	-	-	0.5-1	-
60%Al_2O_3 + 40%TiO_2	950	705	-	13.4	0.77	1	-
80%Cr_3C_2 + 20%NiCr	800	980	6.4	49.0	1.27	1	6.5
70%Cr_3C_2 + 30%NiCr	625	980	-	66.8	1.48	1	-
80%Cr_3C_2 + 20%Al_2O_3	925	870	-	10.5	0.56	1.5	-

Tungsten carbide (WC)-based coatings with a cobalt bond have a strong resistance to wear. The coating resistance to mechanical and thermal impacts increases with the Co-content.

Coatings, containing chromium carbide Cr_3C_2, have a high resistance to wear at high temperatures in a corrosion medium. A new multicomponent coating based on chromium and its compounds (trademark Sivil) is recommended as an antifriction one. It has a unique carrier ability (PV>800) and low wear (wear rate is less than $3x10^{-2}$ $\mu m/km^2$) in the wide range of loads from 10 to 100 kg/sm and sliding speeds between 0.5 and 20 м/s, the friction coefficient being no more than 0.02. The coating is most efficient when applied to both friction surfaces.

Oxide coatings (Al_2O_3) show the resistance to wear, chemical effect and oxidizing at high temperatures. Aluminum and titanium oxides mixtures are frequently used to

increase the density and decrease brittleness. The recent research by V. Marchuk (Dr. Sci. Dissertation, Kiev, 1994) shows, that the entering up to 50 % the $Na_2B_4O_7$ modifier additive into an oxide composition has a positive effect on tribotechnical characteristics of coatings. The additive reduces harmful technological residual stresses, increase the adhesion strength, somewhat reduces the microhardness of coating surface layers, and increases its wear resistance.

The earlier development of techniques for gasthermal deposition was based on single- and multicomponent compositions with regularly distributed phases with particles up to 10 μm in size. Powder materials for such coatings are produced by special technologies and are uniform in grain sizes.

Very frequently in engineering, it is, however, necessary to produce surfaces, which contain inclusions of hard particles of up to 150 μm in size distributed regularly over an uniform binder. Such surfaces can be used in pairs of friction, as heavy loaded footstep bearings, as highly wear-resistant and abrasive tool surfaces.

The obtaining of such coatings is technically possible by gasthermal technique. The binding alloy and large, for example abrasive, particles can be applied simultaneously from separate feeders in turn or from the same mechanical mixture.

Hard particles of diamond, silicon and boron carbides were used by us in experiments for producing abrasive and wear resistant surfaces. The particles previously clad by a metal to reduce a ricochet. The coating with 60 % SiC grains in a nickel binder was produced by us and was tested in a pair of friction with steel ШХ15 (the steel, which is used for manufacturing ball bearings, usually having a hardness 58-62 HRC).

A roller of the ШХ15 steel 50 mm in diameter and 2 mm in width at a speed of 1 m/s under the 300-N load interacts with a sample flat surface by Herz contact. The test conditions: the medium - a petroleum oil with additions of 1 weight % abrasive particles Al_2O_3 50 μm in size. 15000 revolutions of the roller were made during the tests.

A volume wear of the sample profile along a wear crater length (V, mm^3), coefficient of friction f, and the oil highest temperature during the test (^oC) were checked.

Gas detonation coatings of WC-15 %Co, Ni, Al_2O_3, Al_2O_3 -5% TiO_2, Al_2O_3 - 15% TiO_2 were tested for comparison with those of WC-6% Co and ШХ15. The test results are listed in Table 2.2.

The tests have shown, that the Ni + SiC coating exhibits the greatest wear resistance in an abrasive medium and the lowest coefficient of friction , i.e. the material with a tough matrix and strongly fixed hard particles. A low coefficient of friction and elastic-plastic properties of the matrix ensure the lowest interaction between microprotrusions of the surfaces being in friction. As a result, the temperature in the test zone increased only slightly.

Table 2.2

Materials Characteristics	WC + 15% Co	WC + 6% Co	Ni + SiC	Ni	Al_2O_3	IIIX15	Al_2O_3+ 5%TiO_2	Al_2O_3+ 15%Ti_2
$Vx10^{-3}$, мм^3	1.01	1.20	1.92	2.40	2.80	3.00	3.03	3.54
f	0.060	0.088	0.055	0.055	0.112	0.065	0.112	0.115
T,^oC	46	51	41	42	62	52	67	62

2.4. Equipment for deposition of gas detonation coatings

Several models of gas detonation installations for deposition of coatings have been developed in our laboratory. "Perun" is the trademark of all. The design documentation on installation "Perun-C" is given to a machine-building plant and the installation is produced in small series.

Technical solutions used in the development of the installation are made at the level of inventions and are patented. The "Perun-C" installation (Fig. 2.1) is a stationary detonation installation. It consists of five units, which are located in two soundproof premises. For its operation, the sources of gases under pressure, electric and water supplies are necessary.

The "Perun-M" installation (Fig. 2.2) is a small detonation installation with an increased independence. It contains a device for coating deposition, a manipulator of products, a soundproof chamber, and a control unit. It contains also a device for a metallization flow control. The chamber has a forced exhaust ventilation with a cyclone for trapping the powder. It can be operated in any industrial premise.

The "Perun-C" installation has no analogs in the world.

The main parameters responsible for the efficiency of gas detonation installations are the frequency of cycles and the area coated per a cycle. The value of the last parameter exceeds slightly the cross section area of gun barrel near the exit. The thickness of a coating deposited per a cycle is also of a great importance for the assessment of the equipment productivity. Numerical values of the above parameters, as well as other characteristics of the "Perun-C" and "Perun-M"installations are given in Table 2.3.

The "Perun-C" installation developed in our laboratory is characterized by the following features, in particular:

- the operation of the installation is possible using various working gases (as a fuel gas, except of conventional acetylene, propane-butane or hydrogen can be also used, and to carry the powder, blow-through the coil and barrel, to dilute the explosive mixture, nitrogen and com pressed air can be used);
- the process control device ensures a objective evaluation of the operation stability of a powder weigher by registration of changes in the powder contents changes of a high-temperature pulsing flow, permits the thickness or weight of a deposited coating to be predicted, controls the quality of the layers being formed (reveals hidden macrodefects, which arise at violation of the technology);

Таблица 2.3.

Characcteristics of "Perun-C" и "Perun-M" Istallation

№	Characteristics	Installation type	
		"Perun-C"	"Perun-M"
1	Frequency of covers deposition cycles, c^{-1}	3.33; 6.66	1.5
2	Gas-detonation gun lenght ,m	1.2; 0.6	0.5
3	Diameter of barrel duct,mm	20	13.5
4	Quantity of automatic scales	2	1
5	Area, deposited at one cycle,mm^2	320	150
6	Average thickness of one cover lay,μm	12	5
7	Using dases:		
	- combustible	C_2H_2; C_3H_8; H_2	C_2H_2; H_2
	- oxidizers	O_2	O_2
	- technological	N_2, air	-
8	Gases rate of flow, m^3/hour:		
	- acetylene, propane-butane	2.5	0.01
	- oxigen	5.0	0.1
	- compressed air or nitrogen	8.0	-
9	Clearences of deposited surfaces:		
	- lenght x widht, mm	1500 x 1000	80 x 90
	- diameter x lenght, mm	1500 x 3000	40 x 90
10	Gun manipulator presence	Yes	Yes
11	Number of controlled move coordinates	3	1
12	Article manipulator presence	No	Yes
13	Number of controlled move coordinates	-	3
14	Presence of work chamber with sound-proofing and ventilation tools	No	Yes
15	Special room for equipment's using	Box and console room	don't needed
16	Area for equipment, m^2	7	1
17	Clearences of installation (lenght x widht x height), mm	2050x2500x1115	870x650x1235
18	Weight of installation,kg	500	150

- a gas detonation gun by is equipped by two independently controlled powder automatic scales with increased capacity and this enables one to pass from the detonation-abrasive processing to the coating deposition mode without turning off of the installation, and simplifies considerably the processes of multicomponent coating formation and layer-by-layer deposition of various materials;

- a special nozzle on the installation barrel permits coating to be applied to internal surfaces of articles such as pipes of more than 130 mm in diameter at a depth down to 0,6 m (usually gasthermal methods allow the coating deposition on internal surfaces of pipes at a depth, not exceeding the pipe diameter);
- the design of the gas detonation gun barrel permits the explosive mixture to be set on fire on the sides of both the gun gate and the gun barrel. Due to this, the variation range of power characteristics of the pulse gas powder flows being generated is extended.

The operation cycle of the gun of a detonation installation.

The detonation-abrasive processing of articles and deposition of coatings is executed by a sequential effect of high-temperature pulse flows on the regions of articles, that are restored or hardened. Gas powder flows are formed periodically by the gun of a gas detonation installation as a result of operation of its working elements: electromagnetic pressure-operated valves and the ignition sparking plug. The sequence and duration of operation of the above elements is set by parameters of electrical pulses, generated by the gun control unit.

These pulses open pressure-operated valves installed in feed channels of explosive mixture components. Hence a combustible, oxidizing (and if necessary, a neutral) gases are supplied into a mixer, and then into the gun barrel. The pressure-operated valve of the powder scale operates when the barrel is being filled by the gas mixture. The transporting gas supplied through the valve acts on a powder of an abrasive or a being deposited material placed in the bunker, thus forming a gas-powder mixture, which is also supplied via the pipeline into the gun barrel. Then the mixer and the pipe, connecting it with the barrel, is filled by a neutral gas or air, which are supplied through the blow-through valve. After that an explosion of the gas mixture in the gun barrel is initiated by an electrical discharge excitation in the ignition interval of the sparking plug. Hereinafter the described cycle of the operation of the detonation installation is repeated.

The realization of the described operation cycle of the detonation installation and producing a coating with the required properties is impossible at arbitrarily given technological parameters.

The optimization of the detonation equipment operating mode implies strong restrictions on the following parameters:

- gas composition of the explosive mixture (with indication of the components and their ratio);
- the flow rate of the mixture, which affects the degree of filling the barrel;
- the distance of spraying or detonation-abrasive processing;
- the positioning of a cloud of the powder in the barrel at the instant of the explosion;
- the consumption of the transporting gas (flow rate);
- the dose of the powder.

The values of the above parameters depend on the granulometric composition of the abrasive powder or the material being deposited, its melting or dissociation points, chemical activity with respect to products of the explosive mixture detonation and environment as well as on the design characteristics of the installation: the barrel shape and sizes, the rate of gun cycles, the place and mode of the powder entry into the gun barrel, the place of the explosion initiation.

The improvement of the gas detonation technology implies: the the obtaining of the most efficient technological parameters of the process, i.e. productivity, efficiency of the powder material usage, gas consumption.

The solution of these tasks is provided by the strict compliance with the instructions of the application of the installation and technological instructions.

Our laboratory renders the engineering type services to customers (organization of the production bays and laboratories, training the customer stuff, starting and adjustment work) and consulting aid; applies the required coatings to the reference products, offers the equipment and know-how on applying coatings and detonation-abrasive treatment.

REFERENCES

1. "Revolutionary Russian for metal-clad diamond", Industial Diamond Quarterly,1972, no.2, p.25.
2. N.V.Balashova, "Abrasives with coatings", Almazy, 1973, issue 9, pp. 31-32.
3. V.M.Mogilevsky, E.M.Chistyakov, and M.D.Shakhnovich, "Coatings on grains of diamond and cubic boron nitride (a review of patents)", Sinteticheskie Almazy, 1974, issue 1, pp. 25-28.
4. G.P.Vovk, I.A.Lavrinenko, and Yu.V.Naidich, Methods of Formastion Coatings on Diamond and Cubic Boron Nitride [in Russian], Institute of Materials Science Problems of the UkrSSR Academy of Sciences, 1977.
5. I.G.Kalinina, N.V.Balashova, N.V.Prokhorov, et al., "Metallization of diamond powders: a review of foreign patents," Almazy i Sverkhtverdye Materialy, 1981, issue 8, pp. 11-13.
6. V.M.Mogilevsky, E.M.Chistyakov, and M.D.Shakhnovich, "Coatings on grains of diamond and cubic boron nitride (a review of patents)," Sverkhtverdye Materialy, 1981, no.2, pp. 38-42.
7. A.A.Ovchinnikov, V.L.Shirvo, and L.K.Sinysovsky,"Investigation of the influence of grain coatings on the wheel wear resistance," Almazy, 1972, issue 1, pp. 12-17.
8. A.A.Kolomiets, V.P.Marinin, S.O.Ovcharenko, et al., "Thermographic and strength characteristics of metal-clad powders of balas-type synthetic diamond," Rezanie i Instrument, 1977, issue 17, pp.84-87.
9. M.E.Mukhina, M.F.Yarmak, and V.V.Popov, "The effect of metal coating of CAM-grade diamond on the strength and efficiency of drilling tools," Almazy i verkhtverdye Materialy, 1975, issue 12, pp.6-8
10. I.P.Zakharenko, Yu.I.Nikitin, Yu.Ya.Savchenko, et al., "The effect of the degree of diamond metallization on the efficiency of resin bond wheels," Sinteticheskie Almazy, 1975, issue 5, pp.29-32.
11. M.Akaichi, H.Kanda, J.Saato, et al.," Sintering mechanism of diamond ," Oxford, 1980, vol.1, pp..551-553.
12. Kh.G.Tkhagapsoyev, B.S.Khapachev, Z.Zh.Berov, et al., "Metallization effect on the service life of a pencil," Almazy i Sverkhtverdye Materialy, 1977, issue 1, pp.9-11.
13. Yu.V.Naidich, I.A.Lavrinenko, G.P.Vovk, et al.,"Study of the strengthening effect of an adhesion-active metal coating on synthetic and natural diamond,", Almazy i Sverkhtverdye Materialy, 1974, issue 8, pp.18-22.
14. V.F.Grishachev, "The development of a method to apply coatings on diamond from a gas phase of transition metal galogenides and studying some properties of metal-coated diamonds," Author's Abstract of the Cand.Sci.(Eng.) Dissertation [in Russian], Moscow.
15. E.M.Chistyakov, A.A.Shepelev, T.M.Duda, and V.P.Chernykh, Tools of Metallized Superhard Materials [in Russian], Naukova Dumka, Kiev, 1982.
16. G.V.Samsonov (Ed.), Properties of Elements [in Russian], Metallurgiya, Moscow, 1976.
17. N.V.Novikov, V.I.Malnev and G.A.Voronin, "On the methods of determination of strength of diamond grinding powders," Sverkhtverdye Materialy, 1983, no.3, pp.24-27.
18. S.M.Fedotova, "Investigation of oxidation of synthetic and natural diamonds", Trudy VNIIASh, 1970, no. 11, pp.12-17.
19. V.A.Murovsky, A.M.Kutsovskaya, and E.M.Chistyakov, "The effect of a medim on the intensity of diamond burning," Sinteticheskie Almazy, 1971, issue 5, pp. 31-33.

20. V.F.Grishachev, V.P.Maslov, E.V.Prilutsky, et al., "Oxidation of diamonds having diffusion coatings of carbides of transition metals," Sverkhtverdye Materialy, 1984, no.2, pp. 30-32.
21. V.F.Grishachev, V.P.Maslov, E.V.Prilutsky, et al., "The effect of tungsten silicide coatings on oxidation resistance of diamonds," Almazy i Sverkhtverdye Materialy, 1982, issue 1, pp.2-3.
22. V.F.Grishachev, V.P.Maslov, E.V.Prilutsky, et al.,"Oxidation resistance of diamonds with coatings of chromium, molybdenum and tungsten carbides," Almazy i Sverkhtverdye Materialy, 1982, issue 3, pp. 1-3.
23. G.A.Voronin, V.I.Malnev, and G.F.Nevstruev, "The impact of inclusions on the high temperature strength of synthetic diamond," Sverkhtverdye Materialy, 1984, no.2, pp.33-37.
24. L.L.Mishnayevsky and A.V.Galkov, "Peculiarities of diamond wear in grinding titanium alloys," Sverkhtverdye Materialy, 1981, no.3, pp.56-62.
25. N.V.Novikov and I.V.Bondar', Surf. Coat. Technol., 46 (1991) 301-305.
26. N.V.Novikov, M.A.Voronkin and I.V.Bondar',Diamond and Related Materials, 3 (1993) 61-65.
27. V.V.Kudinov, "Plasma coatings", Nauka, Moscow, 1977.
28. A.Khasui, "Spraying technique", Mashinostroenie, Moscow, 1975.
29. M.H.Shorshorov, Yu.A.Kharlamov, "Physical - chemical basises of gas-detonation spraying of coatings", Nauka, Moscow,1978
30. S.S.Bartenev, Yu.P.Fedko, A.I.Grigorov, "Detonation coatings in the engineering industry", Mashinostroenie, Leningrad, 1982.
31. V.S.Klimenko,E.A.Astakhov, A.I.Zverev, "Investigation of processes, which take place in the materials with detonation spaying of coatings.",Anticorrosion coatings, Nauka, Leningrad, 1983, p .118-122

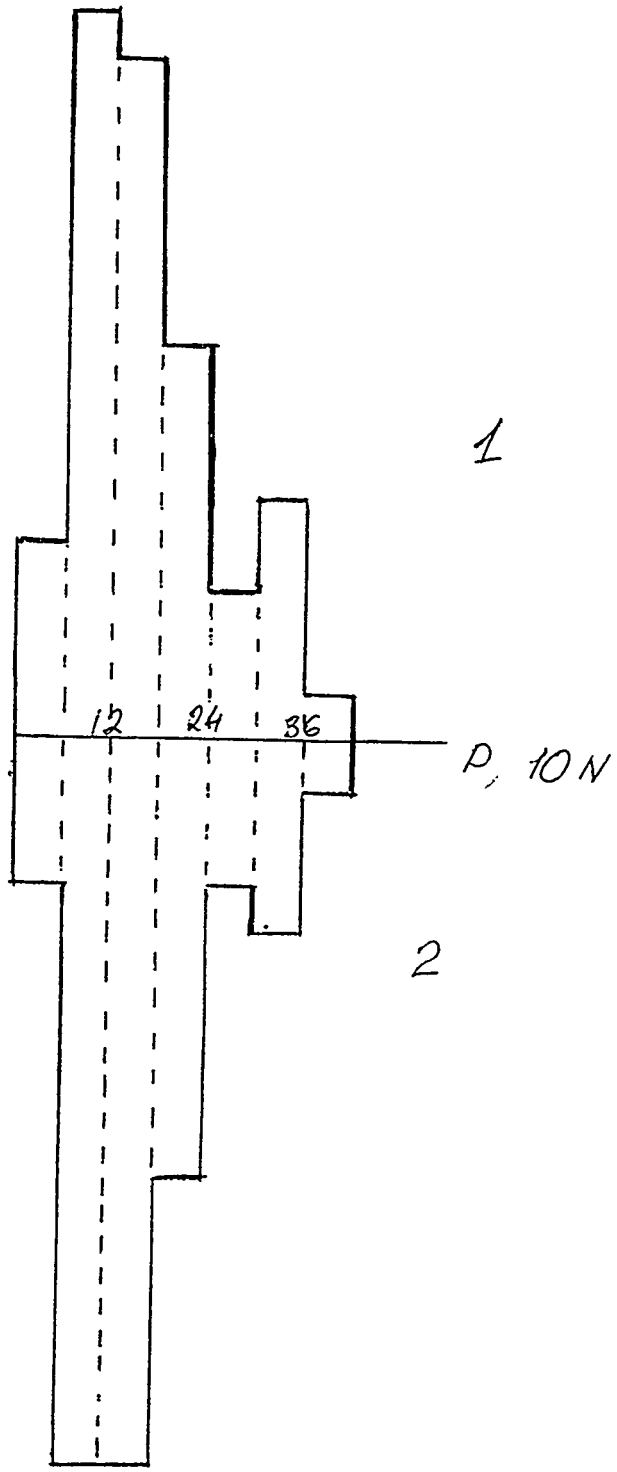


Fig. 1.1. A histogram of loads destructive for AC132T 400/315 diamond powder:
1 - uncoated,
2 - molybdenum-coated (h=0,36 μm, σ=40 MPa)

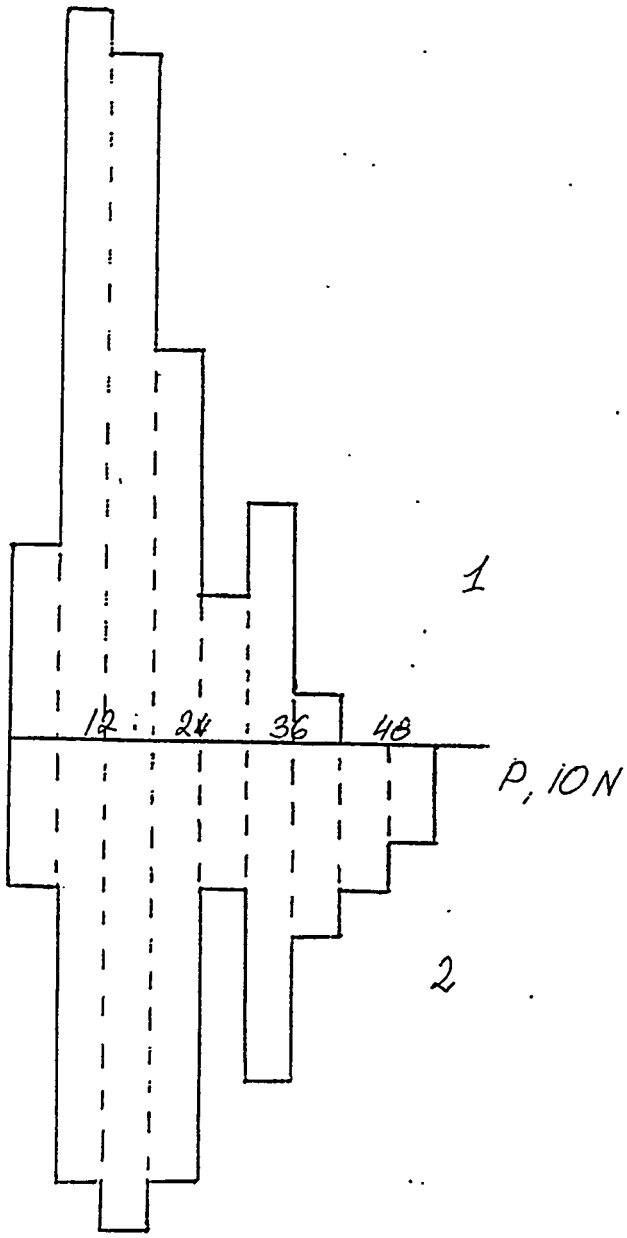


Fig. 1.2. A histogram of loads destructive for AC132T 400/315 diamond powder:
1 - uncoated,
2 - molybdenum-coated (h=0,36 μm, σ=220 MPa)

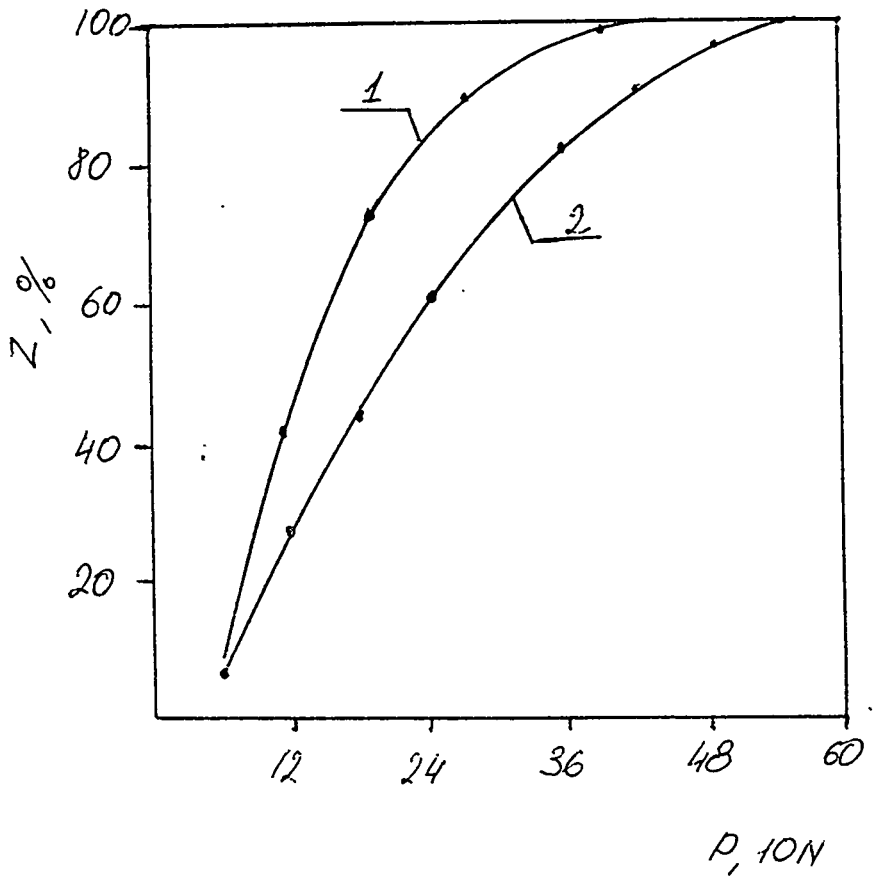


Fig. 1.3. A percentage of fractured grains (Z) in AC132T 400/315 diamond powder:
1 - uncoated,
2 - coated (h=0,36 μm, σ=220 MPa)
at a given value of a compressive force (P).

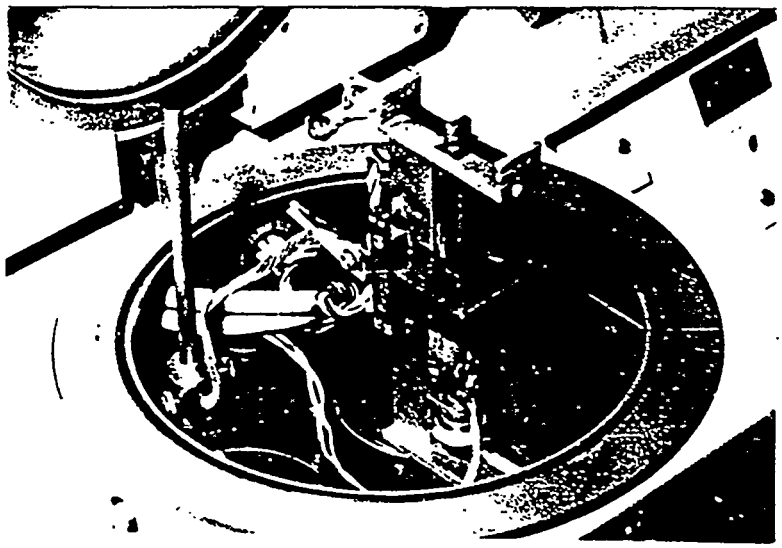


Fig. 1.4. A schematic view of the attachment for assessment of the strength of adhesion between a coating and a crystal.

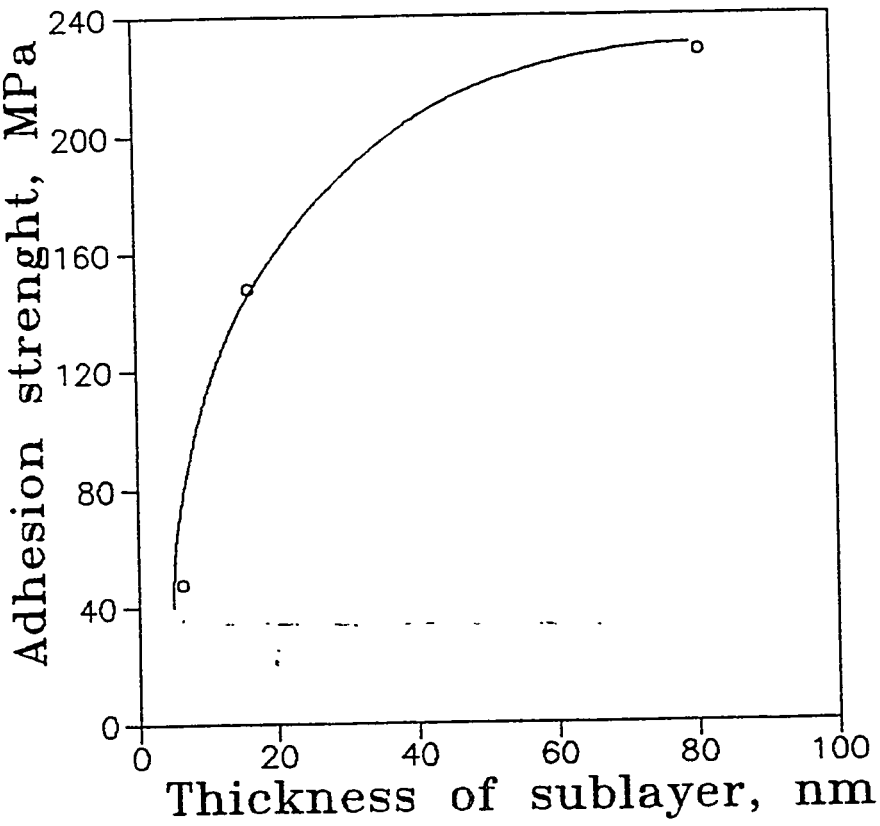


Fig. 1.5. Adhesion dependence on carbide sublayer thickness.

a.



b.

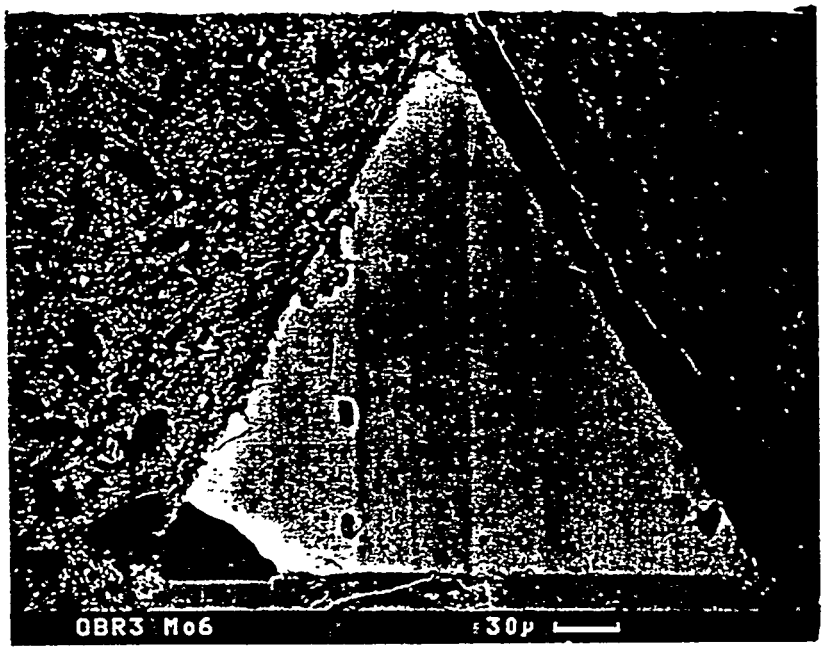
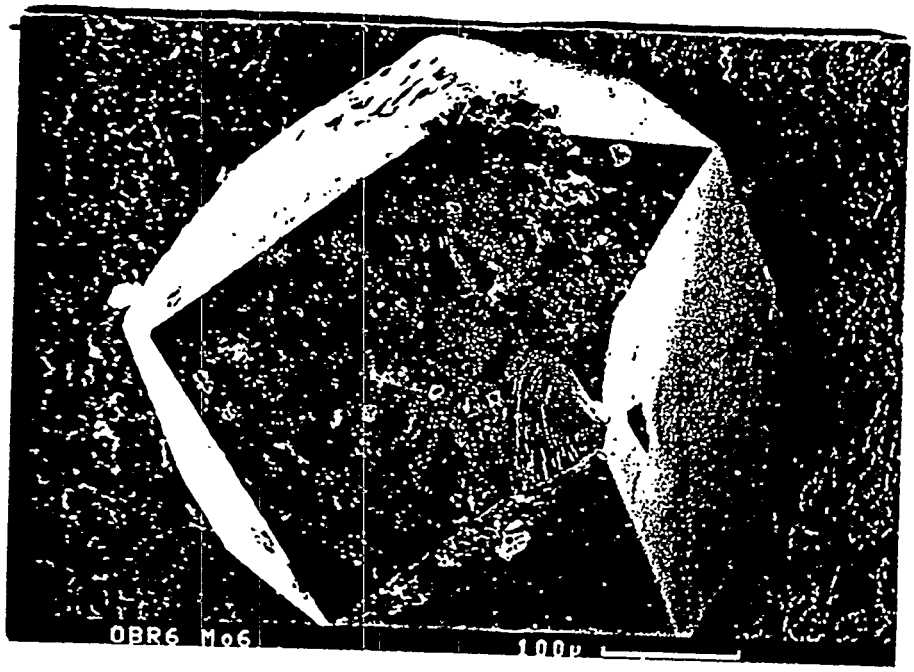


Fig. 1.6. Surface of breaking off (adhesion strenght of cover with grain $\sigma = 40$ MPa)
a) surface of breaking off on crystal
b) surface of breaking off on cover

a.



b.



Fig. 1.7. Surface of breaking off on crystal (σ=140 MPa)
a) without phase contrast
b) with phase contrast

a.



b.

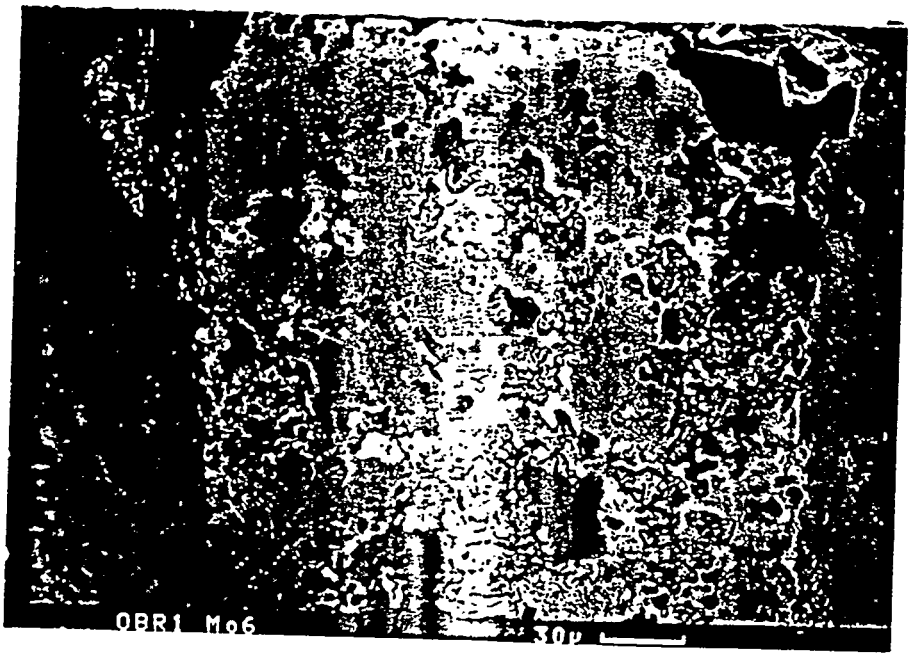


Fig. 1.8. Surface of breaking off on crystal (σ=220 MPa)
a) without phase contrast
b) with phase contrast

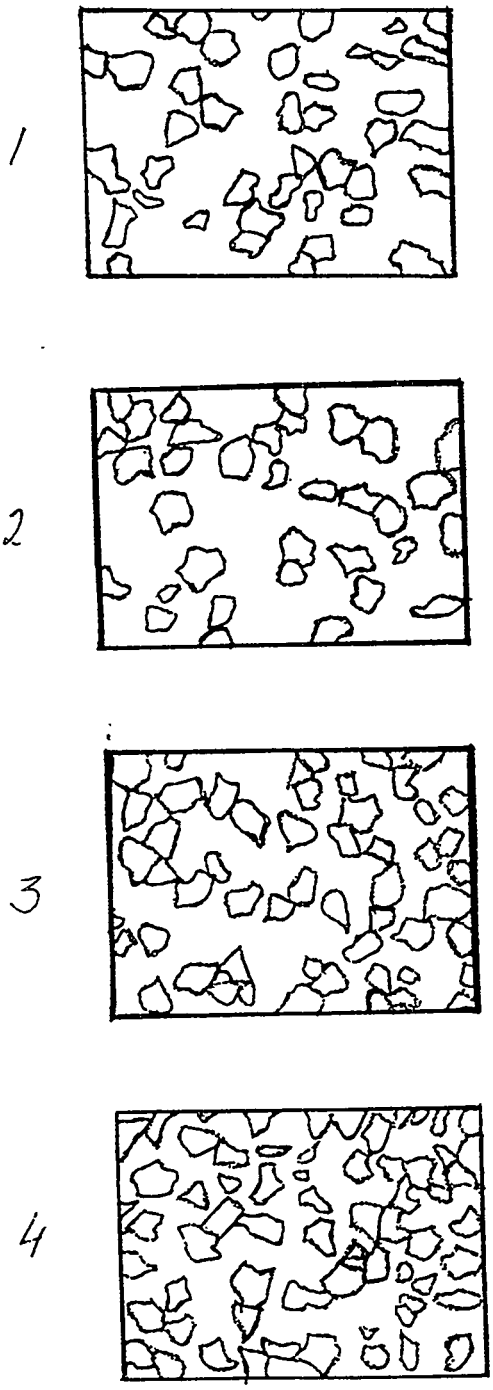


Fig. 1.9. Behavior of destroyed diamond grains distribution in the drill bit sector fracture, equipped by metallized diamonds with adhesion strenght:
1 - without metallization;
2 - σ=44 MPa;
3 - σ=143 MPa;
4 - σ=219 MPa;

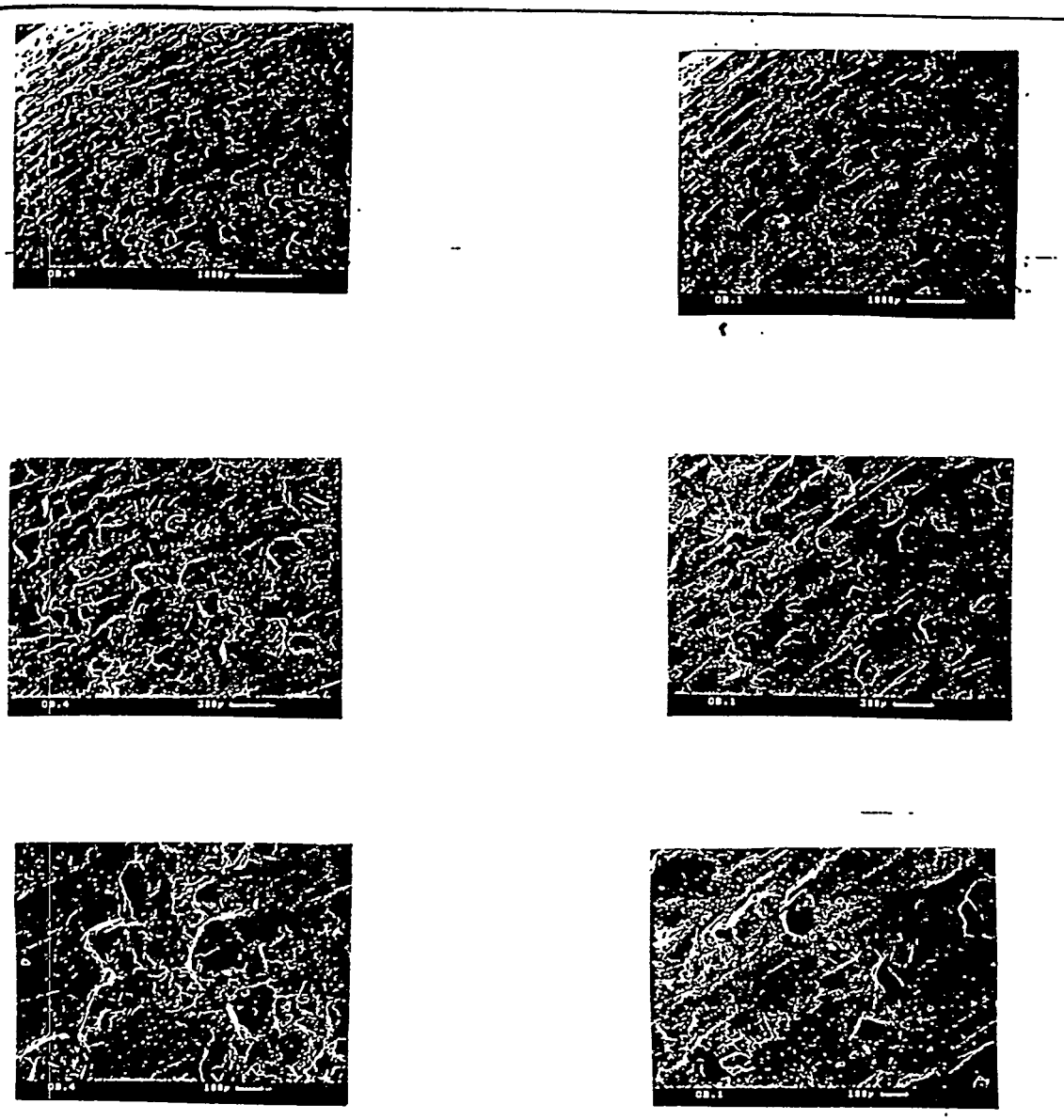


Fig. 1.10. The work surface of drill bit ВС05, equipped by metallized diamonds with adhesion strenght:

1 - σ=220 MPa;

2 - without metallization

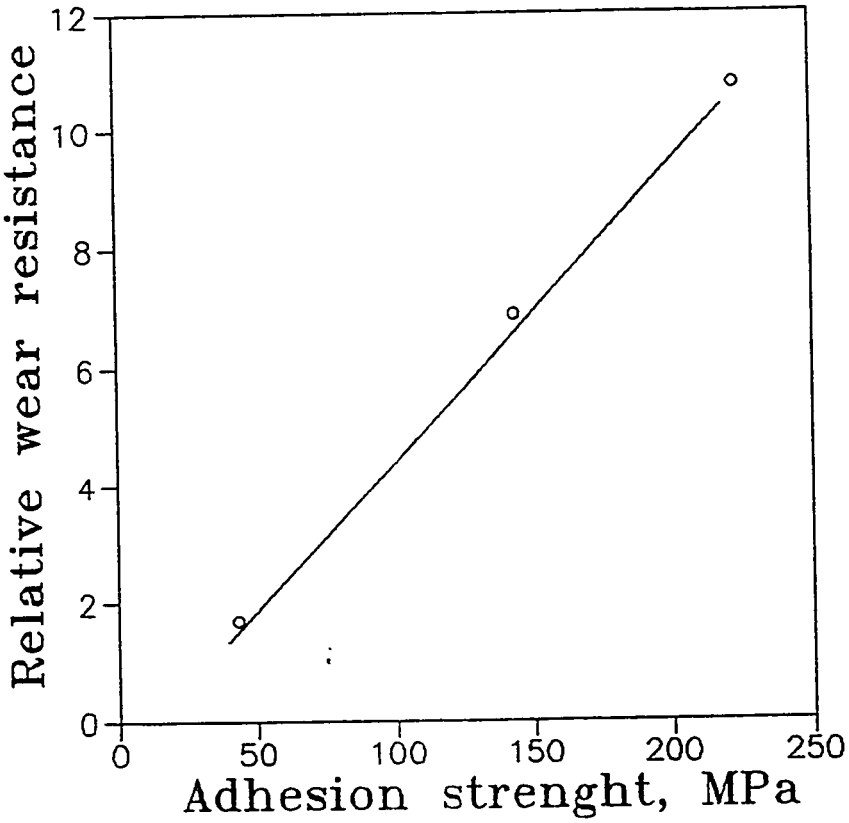


Fig. 1.11. The relative wear resistance of drill bits, equipped by metallized diamonds

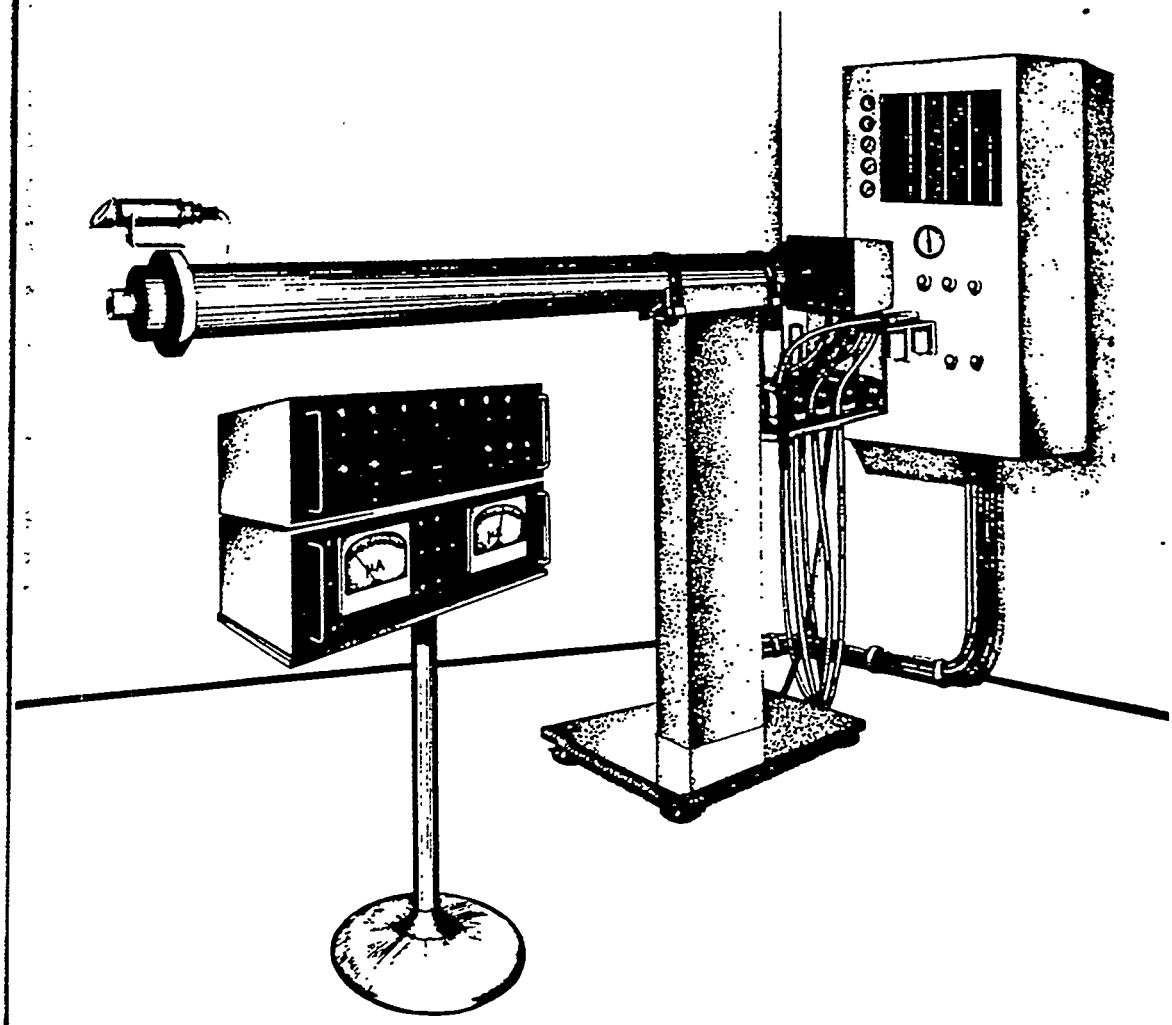


Fig. 2.1. The installation "Perun-C"

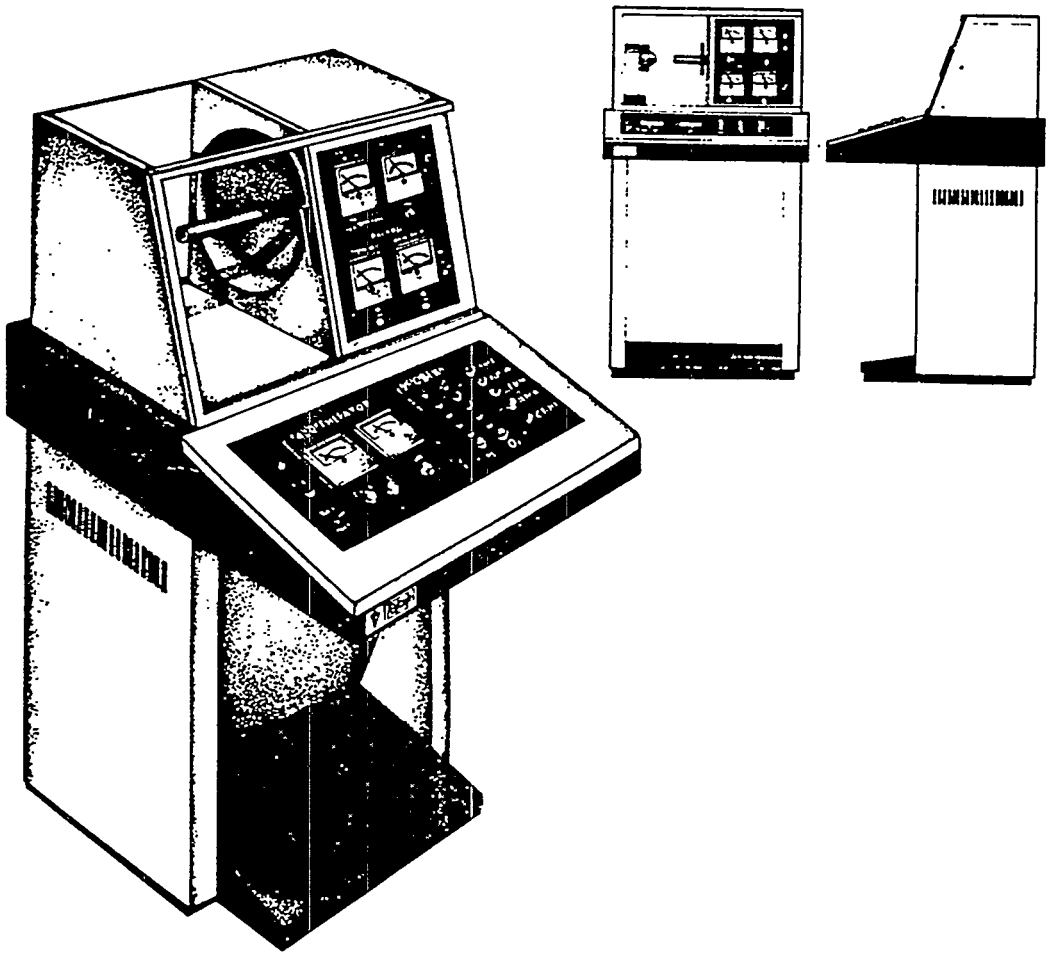


Fig. 2.2. The installation "Perun-M"

Project Title: Diffusion Barriers/nucleation Surfaces for Chemical Vapor Deposition (CVD) of Diamond on Tool Steel Surfaces.
Principal Investigator: Vladimir Vykhodets
Institute of Metal Physics
Ekaterinburg, Russia
AM-7679

CLAUSE 1 - STATEMENT OF WORK

Background:

Diamond coatings obtained by means of Chemical Vapor Deposition (CVD) are very prospective for metal working tools having extremely high service properties. However, tool steel is highly inconvenient material as a substrate for CVD of diamond. Carbon diffusivity in steel is too high at the temperature necessary for diamond growth. Therefore, the problem is to form on the surface of steel a layer which may act as a diffusion barrier for carbon during CVD.

Objective:

1. Develop methods for making the diffusion barrier layers on tool steel surface providing the conditions for CVD of diamond.

2. Develop methods of preparation of nucleation surfaces for CVD of diamond on the surfaces of the barrier layers.

Tasks:

The Contractor shall:

1. On the basis of data available from literature, and from the results previously obtained by the Contractor, define a number of compounds such as metal nitrides, carbides, oxides, etc., which may be used as diffusion barrier layers and nucleation surfaces of CVD of diamond. Candidate material will include TiN (titanium nitride), TiO (titanium oxide), TiC (titanium carbide), and VC (vanadium carbide). The Contractor shall choose corresponding techniques for formation of the layers including various deposition techniques and/or ion implementation. Provide a report that includes the above defined information.

2. Fabricate a set of samples of tool steel with diffusion barrier layers using various techniques. Study the properties of the layers including: structure, composition, adhesion, and temperature stability. Two samples, produced by each technique and with optimum wear resistance shall be provided. Sample dimension shall be approximately 4cm in diameter and between 2 and 5 mm in thickness. Prepare and provide the results in a report to Sandia.

3. Perform the experimental study of the penetration rate of carbon through the layers at high temperature using nuclear reaction analysis (NRA), and, if necessary, carbon radioactive tracers. Provide the results of the study in a report to Sandia.

4. Perform a study of nucleation on the surface of the barrier layer during CVD of diamond. Study the effects of various predeposition treatment on nucleation.

REPORT ON TASK 1

CONTRACT AM-7679 "DIFFUSION BARRIERS/NUCLEATION SURFACES FOR CVD OF DIAMOND ON TOOL STEEL SURFACES"

1. Introduction

Unique properties of diamond coatings produced using the CVD process make them promising for many practical applications. For this reason a great number of studies has been dedicated to solving the corresponding technological tasks. Much importance is attached to investigations dealing with deposition of CVD diamond coatings on tool steels. In the final analysis the point in question is development of efficient technologies which, as is expected, will ensure a tens-fold improvement in service properties of tools.

Deposition of a CVD diamond coating on steel is a complicated technological problem. All attempts to produce satisfactory-quality CVD diamond coatings directly on the surface of a tool steel have been a failure so far. Certain achievements have been due to the approach where an intermediate layer between steel surface and diamond coating is used having the properties of a diffusion barrier and providing a sufficient nucleation density during the CVD process. The main goal of our study is to ascertain the prospects of using of the interstitial phases like nitrides, carbides, metal oxides or a more complicated compound, e.g., carbonitride, as the sublayer for CVD of diamond. As will be shown below, literature contains scarce data on this issue.

At the first stage of the work much attention will be paid to a study of diffusion properties of the sublayers. The diffusion parameters will be considered as main criterion for the selection of more suitable compound from the set of candidate materials. The study of the diffusion of light impurities in solids have been one of the main directions of activity of PI and

his team for a long time [1-5].

In what follows we shall analyze the prospects of the use of interstitial phases as sublayers for CVD of diamond on tool steel. We consider literature and our data related to the problem of making the diffusion-barrier layers and surfaces with a high nucleation density during the CVD process.

2. Diffusion-Barrier Layers

It is possible to point out three basic approaches to production of diffusion-barrier layers for deposition of the CVD diamond on tool steels. The first approach is to choose the material for intermediate layer having low diffusion coefficient for carbon. Here one finds the following regularities. As a rule, the diffusion coefficients of interstitials in metals having a closely packed crystal lattice (face-centered cubic (FCC) and hexagonal closely packed (HCP) lattices) are much lower than those in metals with a bulk-centered cubic (BCC) lattice. Generally, diffusion coefficients of light atoms in the interstitial phases (carbides, nitrides etc.) are still lower. For interstitial mechanism of diffusion which is typical in metals, the diffusion activation energy depends in the main on the potential barrier separating two nearest equilibrium positions of an interstitial in the crystal lattice. In the interstitial phase the vacancy mechanism is more probable for carbon atoms in the metalloid sublattice. If there are no structural vacancies, an extra additive contribution to the diffusion activation energy takes place. The contribution is equal to the vacancy formation enthalpy. So, materials like carbides, nitrides, oxides, etc. must have low carbon diffusion coefficients, a fact which permits trying them as diffusion-barrier layers.

In the second approach, the diffusion-barrier layer is represented by carbon-containing material, which is characterized

by a high stability at the CVD process temperatures. In this case the diffusion barrier appears at the interface between the substrate and the sublayer, i.e. carbon passes little, if at all, into the substrate for the chemical binding energy of carbon in the intermediate layer is sufficiently high. It is this approach that is usually realized in practice for the CVD process. Actually, this is reduced to deposition of a sublayer of a refractory metal (generally tungsten or molybdenum) on the tool steel and then the CVD process is realized. Carbides of refractory metals thus formed exhibit a great thermal stability. This method was used, for example, in Refs [9-15].

One more possible approach to the formation of a diffusion-barrier layer is due to the fact that the diffusion process rate can decrease or increase considerably depending on the presence of motive forces in the crystal [7]. A change in the diffusion process rate by several orders of magnitude is quite possible in this case. By way of example we can cite our study [8], which shows that the rate of hydrogen removal from the titanium alloy drops sharply if a sufficiently high gradient of oxygen atoms concentration is provided beforehand in the near-surface layer of material. Probably, an analogous approach is applicable to diffusion of carbon. The method of gradient alloying might be fruitful in other respects too. Many physical and mechanical properties of the diamond coating and steel differ to a great extent and the gradient alloying of the intermediate layer might be beneficial to a smooth transition from characteristic to characteristic.

As follows from the foregoing, the materials such as TiN, TiC or TiO are promising for the formation of a diffusion-barrier layer for carbon. If necessary, the materials can be utilized in all the three approaches described above. The effectiveness of the TiN barrier layer is reported in Ref. [16].

Most probably, a diffusion barrier for iron atoms should also be provided to realize the CVD process. Some researchers

[17,18] note a positive effect of iron on the density of nucleation centers during the diamond growth, but In those studies silicon served as the substrate and therefore the corresponding results can hardly bear any relation to deposition of an intermediate layer on steels. Usually diffusion coefficients of the atoms forming substitutional solutions are the lower the higher is the melting point of the matrix material [19]. In this respect refractory metals are suitable materials for the diffusion-barrier layer. Carbides, oxides and nitrides of transition metals also have low diffusion coefficient for Fe. Of great importance can be the fact that the diffusion rate of iron atoms at the grain boundaries in the material will be much higher than the bulk diffusion rate [20]. It is of no use to calculate the corresponding contribution of the grain-boundary diffusion to the diffusion flow of iron atoms since the contribution depends on characteristics of grain boundaries, crystallite dimensions, and some other factors. Probably, it would be good to treat this problem by staging experiments on the samples prepared under the given Contract. For carbon no fast grain-boundary diffusion is expected.

3. Density of Nucleation Centers

General regularities determining the density of nucleation centers during the diamond growth have been still unclear. On the one hand, it was shown that during the CVD process a high nucleation density is found on metals which does not interact with carbon: for example, on copper and platinum [21]. On the other hand, a high density of nucleation centers is also observed on metals which are highly prone to carbide formation. These results were obtained for tungsten, molybdenum, tantalum and niobium [21]. Some researchers (see, e.g., [22]) note that oxides and nitrides of metals are also promising as materials having a high density of nucleation centers. It is noted that defects generated in titanium nitride during the CVD process act as additional nucleation centers. So, literature data do not permit

drawing a reasonable conclusion on the character of nucleation on the surface of oxides, carbides or nitrides. This problem is to be solved during the contractual works.

At the same time literature sources pay great attention to the methods of surface pretreatment, which make it possible to raise the density of diamond nuclei during the CVD process. We plan to test the methods in our study. The methods that seem most promising are:

- treatment of the surface with a jet of abrasive particles [23];
- treatment of the surface in a plasma discharge [24];
- polishing of the surface using a diamond paste [11] or silicon carbide [13,25];
  ultrasonic treatment of the samples in aqueous suspension of diamond dust [15];
- etching of the surface in a NaCl or NaF solution [11];
- deposition of a diamond-like film on the surface [35].

4. Adhesion of the Diamond Coating to the Intermediate Layer

A great difference in the linear expansion coefficients of diamond and steel brings about a problem of adhesion of the CVD diamond to a steel substrate. Literature gives the following ways of solving this problem:

A. Proper adhesion is achieved through brazing of the diamond coating to the substrate. This approach is realized, for example, in Refs [10,12,26]. We do not plan any study in this direction under the Contract.

B. Good adhesion is ensured thanks to a sufficiently strong binding of the coating to the substrate. This approach was used in numerous studies where the diamond coating is deposited on tools made of tungsten carbide [27-33].

C. An intermediate layer of a refractory metal is deposited on the surface of tool steel [15].

Proceeding from the available literature data it is difficult to predict adhesion properties of the surface of the diffusion-barrier layer selected for the CVD of diamond. There is evidence that the CVD diamond has a poor adhesion to the TiN surface [15,16]. Although a detailed study of the CVD diamond adhesion is outside the scope of the present Contract, a preliminary study will probably be necessary to analyze adhesion properties of the intermediate layer.

5. Samples for Investigations

To accomplish the Task 2, we plan to make a set of samples of tool steel with diffusion-barrier layers of following composition: TiN, TiO, TiC, ZrN, ZrO, ZrC. The method of electric arc sputtering of metal target is planed to be used for deposition of the layers. To form nitride, oxide or carbide, the deposition process is to be performed in the atmosphere of N_2, O_2 or C_2H_8, respectively. For comparative analysis of properties of this layers, we plan to make a set of samples of tool steel with Mo surface layer using the similar technique.

References

1. Vykhodets V. B., Klotsman S. M., Kurennykh T. E. et al., Fizika metallov i metallovedenie 1987, 63, 974 - 978.
2. Vykhodets V. B., Golubkov I. K., Klotsman S. M. et al., Fizika metallov i metallovedenie 1988, 66, 303 - 306.
3. Vykhodets V. B., Klotsman S. M., Kurennykh T. E. et al., Fizika metallov i metallovedenie 1989, 68, 723 - 727.
4. Vykhodets V. B., Kurennykh T. E., Trifonov K. V. et al., JETP 1994, 106, 2(8), 648 - 662.

5. Vykhodets V. B., Geld P. V., Demin V. B. et al., Fizika metallov i metallovedenie 1989, 68, 150-155.
6. Smirnov A. A. Theory of diffusion in institutional alloys, Naukova Dumka, Kiev, 1982, 167 p.
7. Manning J. Diffusion kinetics for atoms in crystals, Van Nostrand, Princeton, Toronto, 1968, 278 p.
8. Vykhodets V. B., Klotsman S. M., Kurennykh T. E. et al., Fizika metallov i metallovedenie 1989, 68, 733 - 737.
9. Polo M. C., Cifre J., Esteve J., Diamond and Related Materials, 1994, 3, 492 - 494.
10. Nesladek M., Asinari C., Spinnewyn J. et al,, Diamond and Related Materials, 1994, 3, 912 - 916.
11. Spinnewyn J., Nesladek M., Asinari C.,Diamond and Related Materials, 1993, 2, 361 - 364.
12. Kohzaki M., Higuchi K., Noda S. et al.,Diamond and Related Materials, 1993, 2, 612 - 616.
13. Steiner R.,Stingeder G., Grasserbauer M. et al., Diamond and Related Materials, 1993, 2, 958 - 962.
14. Fryda M., Benndorf C., Klages C.-P. et al., Diamond and Related Materials, 1992, 1, 558 - 562.
15. Shih H.C.,Sung C. P., Lee C. K. et al., Diamond and Related Materials, 1992, 1, 605 - 611
16. Weiser P. S., Prawer S., Diamond Films '94, Abstract Book of 5th European Conference on Diamond, Diamond - like and Related Materials, Il Ciocco (near Lucca), Tuscany, Italy, 25 - 30 September 1994, 9.028.
17. Kobayashi K., Mutsukura N., Machi Y. et al., Diamond and Related Materials, 1993, 2, 278 - 284.
18. Ahn J., Tan F. H., Tan H. S., Diamond and Related Materials, 1993, 2, 353 - 356.
19. Bokshtein B. S. Diffusion in metals, Metallurgy, Moscow, 43-44.
20. Adda Y., Philibert Y. La diffusion dans les solides, t.t. 1,2, Saclay, France, 1966, 1268 - 1273.
21. Kawarada M., Kurihara K., Sasaki K., Diamond and Related Materials, 1993, 2, 1083 - 1089.

C. An intermediate layer of a refractory metal is deposited on the surface of tool steel [15].

Proceeding from the available literature data it is difficult to predict adhesion properties of the surface of the diffusion-barrier layer selected for the CVD of diamond. There is evidence that the CVD diamond has a poor adhesion to the TiN surface [15,16]. Although a detailed study of the CVD diamond adhesion is outside the scope of the present Contract, a preliminary study will probably be necessary to analyze adhesion properties of the intermediate layer.

5. Samples for Investigations

To accomplish the Task 2, we plan to make a set of samples of tool steel with diffusion-barrier layers of following composition: TiN, TiO, TiC, ZrN, ZrO, ZrC. The method of electric arc sputtering of metal target is planed to be used for deposition of the layers. To form nitride, oxide or carbide, the deposition process is to be performed in the atmosphere of N_2, O_2 or C_2H_8, respectively. For comparative analysis of properties of this layers, we plan to make a set of samples of tool steel with Mo surface layer using the similar technique.

References

1. Vykhodets V. B., Klotsman S. M., Kurennykh T. E. et al., Fizika metallov i metallovedenie 1987, 63, 974 - 978.
2. Vykhodets V. B., Golubkov I. K., Klotsman S. M. et al., Fizika metallov i metallovedenie 1988, 66, 303 - 306.
3. Vykhodets V. B., Klotsman S. M., Kurennykh T. E. et al., Fizika metallov i metallovedenie 1989, 68, 723 - 727.
4. Vykhodets V. B., Kurennykh T. E., Trifonov K. V. et al., JETP 1994, 106, 2(8), 648 - 662.

REPORT ON TASK 2

Contract AM-7679 "Diffusion Barriers/Nucleation Surfaces for CVD of Diamond on Tool Steel Surfaces"

1. Introduction

Since the attempts to produce an adequate-quality CVD coating on the surface of tool steel have proved to be a failure, an approach has been advanced, according to which the steel surface receives an intermediate layer possessing properties of a diffusion barrier and providing a sufficient density of nucleation during the CVD process. The present contractual research is aimed at elucidating the prospects for the use of the interstitial phase (nitride, carbide, or oxide of metal or a more complicated compound) as the intermediate layer. The goal of stage 2 was to produce layers of metal carbides, nitrides or oxides on the surface of tool steel and to examine their properties, such as structure, composition, adhesion and thermal stability. Stages 3 and 4 will deal with analysis of the diffusion-barrier properties of the sublayers and examination of the nucleation characteristics when the CVD process is realized on these coatings. The last stages will possibly require certain changes in the coating deposition including changes in the thickness, conditions of deposition and chemical composition of the coatings. This will be done if the diffusion-barrier properties of the coatings or the diamond nucleation characteristics prove to be not quite acceptable.

The sequence of works performed on stage 2 and the structure of the report have been governed by the following considerations. The contract assignment does not specify characteristics of the tool steel receiving the coatings. Therefore we have selected two grades of steel referring to the class of high-speed steels. They are

characterized by a high or medium content of strong carbide-forming and non-carbide- forming elements (tungsten, molybdenum, vanadium, cobalt) at the carbon content of 0.7-0.9 mass %. The steels have been widely used for production of cutting tools operating under considerable forces and heating.

In our opinion, a high structural stability of these steels at characteristic temperatures and duration of the CVD process permits looking forward to good results. Certain differences in the chemical composition of the selected steels make it possible to assess sensitivity of the coating characteristics in question to the chemical composition of tool steel.

Section 2 of the report describes chemical compositions of the steels and pretreatment of the samples before coating deposition. At stage 2 layers of titanium carbide, oxide or nitride were deposited on the steel surface by different techniques. As distinct from the report on stage 1, now we thought it necessary to use two widely differing versions of the deposition technique. In addition to the method of electric-arc evaporation of the metal target in a gaseous atmosphere, which was described in the report on stage 1, we used the method of electron-beam evaporation of chemical compounds of metals in vacuum. We reasoned that the experience in the use of different sputtering techniques at the research stage will be of utility on subsequent transition to commercial technologies. Besides, we have dropped, for the time being, sputtering of molybdenum layers and layers of zirconium carbides and oxides. We thought it would be appropriate at the subsequent stages of the work, if the necessity arises. The sputtering techniques are described in section 3.

The study proceeded further according to the following scheme. First, we thought it necessary to vary the substrate temperature during sputtering as this factor can have a considerable effect on the coating adhesion to the steel surface. During deposition the temperature of the samples was close to room temperature or was much higher, amounting to several hundred degrees Celsius. Second,

after deposition all the samples were annealed for different time at the temperatures normally used for the CVD process. Such annealing treatments can also influence adhesion of the coating to steel. At this step the major information was derived by the method of nuclear microanalysis. The method permits a nondestructive determination of the distribution of carbon, oxygen and nitrogen in samples up to a depth of about 1 μm. Considering this factor, thickness of the coatings used in the given series of experiments was much smaller than 1 μm. The results of the experiments are presented in section 5. The same section contains adhesion data and data obtained with the help of optical microscopy. The latter reveal the structure of the coatings and steel layers adjacent to the coating.

In some instances thin layers of titanium carbide, oxide or nitride were deposited on silicon substrates. The temperature of the samples was close to room temperature. The use of the substrates whose atomic mass is less than that of titanium makes it possible to determine, by the nuclear microanalysis and Rutherford backscattering techniques, the chemical composition of the coatings having the formula of the TiC_x, TiN_x or TiO_x type. This information is difficult to obtain directly on steel samples using the nuclear microanalysis and Rutherford backscattering techniques. The corresponding data are presented in section 4. It is not improbable that the data of this kind will be given a particular attention at the subsequent stages. As expressed in the report on stage 1, in our opinion the best diffusion- barrier properties should be inherent in the coatings whose chemical composition is close to the stoichiometric one, e.g. to TiN. If this conjecture is confirmed, at stage 3 we will have to take measures to alter the chemical composition of the outer layers of the coatings. These measures can include, for example, changes in the deposition technique or post- deposition annealing of the samples in a gaseous atmosphere containing nitrogen (oxygen, carbon) atoms.

2. Preparation of steel samples.

An abrasive wheel was used to cut cylindrical samples about 30 mm in diameter and about 4 mm in height out of hot-rolled cylindrical steel billets. Flat surfaces of the samples were ground using abrasive wheels and then polished on a diamond paste with the dimension of abrasive particles decreasing in succession from 40 to 3 μm. Only the samples, which were intended for transfer to the Sandia Laboratory, had the size 30 x 4 mm. For the basic series of deposition and examination the samples were cut into four equal parts (their flat polished surfaces had the shape of a sector). Prior to deposition the samples were washed in ethyl alcohol. The chemical composition of the steels is given in Table 2.1.

Table 2.1.

Chemical composition of the steels

Steel grade (Russian classification)	Content of elements, mass %							
	C	Si	Mn	Cr	W	V	Mo	Co
P18 *	0.75	0.4	0.3	4.1	18.0	1.2	0.9	--
P6M5K5 *	0.84	0.3	0.3	4.0	6.5	1.9	5.1	5.1

* In the Russian classification of the grades of high-speed tool steels the letter P stands for tungsten, M for molybdenum, and K for cobalt. The figures after the letters denote an approximate content of the corresponding alloying element (mass %) in steel.

3. Deposition Techniques

3.1. Electron-beam evaporation technique.

The electron-beam evaporation technique was used for production of coatings of titanium oxide or carbide. The material for the coating deposition was pellets of titanium carbide and oxide compacted from powder with the particle dimensions of several microns. The pellets were compacted at room temperature under a pressure of 6 T/cm^2 without binding agents. The starting chemical composition of the

carbide particles was $TiC_{0.92}$ and that of the oxide particles approximated to TiO_2. Steel samples and silicon substrates were mounted in the immediate vicinity to each other in the vacuum chamber of the evaporation unit. Pellets of titanium oxide or carbide were spaced 10 cm from the steel samples. After evacuation to a pressure of 10^{-2} Torr the surfaces of the samples underwent ionic cleaning by discharge on residual gases for 5 minutes. Then the chamber was evacuated to a pressure of $2 \cdot 10^{-5}$ Torr. The carbide and oxide were sputtered at the electron beam current of about 100 mA and electron energy of 10 keV. Two deposition versions were realized: on "cold" and "hot" substrates. In the former case the temperature of the steel samples did not exceed $100^{o}C$. In the latter case the samples were mounted in a molybdenum holder, which served to heat the samples. The temperature of the substrates was about $600^{o}C$. Prior to deposition the samples were held at this temperature for nearly 20 minutes.

During the initial period of the pellet evaporation the samples were shielded with a screen and the evaporated matter could not get onto the samples. Then the pressure in the vacuum chamber was raised to 10^{-4} Torr. As soon as the vacuum conditions were stabilized, the screen was removed. The pressure in the chamber during the deposition process was $5 \cdot 10^{-5}$ Torr or lower. After process was complete, the samples cooled at the pressure of $2 \cdot 10^{-5}$ Torr for 30 min.

3.2. Electric-arc evaporation in a gaseous atmosphere.

The method of electric-arc evaporation was used for production of coatings of titanium oxide or nitride. The coating deposition procedure was as follows. Steel samples and silicon plates were placed in the vacuum chamber, which then was evacuated. As soon as a pressure of 10^{-5} Torr was reached, argon was leaked into the chamber up to a pressure of 10^{-2} Torr and the source of ionic etching was turned on. The surface of the samples was cleaned with Ar^{+} ions for 1 hour. With this technique, deposition on "cold" and

"hot" substrates was realized too. The substrates were heated thanks to the ionic bombardment of the sample surface. The difference in the conditions of deposition on "cold" and "hot" substrates was that in the latter case a negative potential of 2000 V was applied to the sample during ionic cleaning. In the former case the samples had a zero potential. The energy of the argon ions was 1 keV and the beam current density was 0.2 mA/cm^2. Subsequent to the sample surface pretreatment and the chamber evacuation a titanium sublayer 200 Å thick was deposited.

To produce nitride or oxide coatings, pure nitrogen or pure oxygen was leaked into the chamber up to a pressure of $1.2 \cdot 10^{-3}$ Torr or $6 \cdot 10^{-4}$ Torr respectively. Nitrides and oxides were formed by chemical interaction between titanium and the gases in the chamber. This method allows an easy control of the chemical composition of the coatings by changing nitrogen or oxygen pressure. In the case of "cold" sputtering the temperature of the samples did not exceed $100^{\circ}C$, while for the "hot" sputtering it was about $600^{\circ}C$.

4. Chemical Composition of the Coatings

Table 4.1 of this section gives the chemical composition of the coatings as formulas of the TiO_x, TiN_x or TiC_x type. These data were obtained for the procedure where thin films of oxides, nitrides and carbides were deposited on silicon substrates whose temperature was close to room temperature. Under these conditions the coating and the substrate interact little and therefore the data characterize the deposition process itself. It can be expected that the outer layers of sufficiently thick coatings on steels will have the same composition.

The film composition was determined using the methods of Rutherford backscattering (RBS) and nuclear reaction analysis (NRA). When only the RBS method is used, systematic errors are practically eliminated, but random measurement errors are rather large, because the spectral peak of the light element (carbon, nitrogen or oxygen)

is superimposed on the continuous spectrum of the silicon substrate. Reversely, when the RBS and NRA methods are used in combination, random errors can be reduced to a minimum, but the systematic errors associated with the use of data on the cross-sections of nuclear reactions and reference samples can be significant. Table 4.1 summarizes the results obtained by the RBS and NRA techniques. Possible systematic error of the determination of the chemical composition of the films is less then 10%. Later, if required, random and systematic errors can be lowered largely.

The following experimental conditions were realized for RBS and NRA physical measurements:

- the energy of the particles in the primary beam of deutrons was 0.9 MeV;

- the diameter of the beam was 1 mm;

- the beam current was 50 nA for RBS and 0.5 μA for NRA;

- the irradiation dose was measured using a secondary monitoring device representing a rotating target, which interrupted the beam for a certain period of time. Particles scattered by a thin gold film, which was deposited on the rotating target, were registered. The irradiation dose measurement accuracy was better than 1 %;

- products of nuclear interactions were registered using surface-barrier silicon detectors with the energy resolution of 15-20 keV;

- the detection angle for the products of nuclear reactions was 160°;

-the following nuclear reactions were used: $^{12}C(d,p)^{13}C$, $^{16}O(d,p)^{17}O^{*}$, and $^{14}N(d,\alpha_1)^{12}C$;

- the concentration of the atoms of light elements was measured within an accuracy of several percent on the average.

Table 4.1. Chemical composition of the coatings

Deposition technique	Oxide	Carbide	Nitride
Electron-beam evaporation	$TiO_{1.90}$	$TiC_{0.44}O_{0.47}$	---
Electric-arc evaporation in gaseous atmosphere	$TiO_{1.06}$	---	$TiN_{1.09}$

The data of Table 4.1 show that the method of electron-beam evaporation does not guarantee deposition of titanium-carbide coatings with a composition close to the stoichiometric one. In the other cases deposition of coatings of any composition is not a big problem.

5. Thermal Stability, Adhesion and Structure of the Coatings

To study the thermal stability of the coatings, thin oxide, carbide or nitride films were deposited on the steel samples, then the thickness of the films was measured in atoms (O, N or C)/cm^2 using NRA. After that the samples were annealed at the temperatures and duration typical for the CVD process. The chemical composition of the layers was measured NRA. The annealing treatment was realized in a quartz tube in a helium flow at a pressure of 1 atm. Before bleeding into the quartz tube, the helium gas was passed through a titanium sponge heated to 800^{o}C. This procedure was performed to remove oxygen from helium. At the same time the presence of nitrogen in helium was noted, a factor which led to doping of the coatings with nitrogen during annealing. We reasoned that it would make sense not to remove nitrogen from helium since its presence in the gaseous atmosphere during annealing made it possible to gain additional information about the relevant properties of the coatings.

The next task was to examine adhesion of the coatings. We found that the adhesion properties of the coatings were rather high and we had not appropriate adhesion testing equipment at our disposal. Then we designed a device, which permitted a comparative analysis of the adhesion properties of different coatings. The operating principle of the device is as follows. A truncated diamond pyramid with the angle between its lateral faces equal to 136° and the diagonal of the sample contacting platform equal to 75 μm was pressed against the test surface with the help of weights. The sample was mounted on a table, which moved relative the diamond pyramid at a speed of 3 mm/min. As a result, scratches appeared on the sample's surface. To assess the adhesion, a series of scratches was made on the surface of the test samples at the loads of 100, 200, 300 and 400 g. Subsequently a qualitative information about the character of interaction between the sample's surface and the diamond pyramid was obtained by observing the scratches through a microscope. Two criteria were used: First, we noted the load at which first symptoms indicating to peeling of the coating from the steel appeared (peeling onset). Second, the load at which peeling was complete was registered. Appearance of separate cavities at the scratch bottom was taken as the first symptoms of peeling. In the case of complete peeling the cavities covered almost all bottom of the scratch. We did not use loads in excess of 400 g as this could lead to breakage of the diamond pyramid. If complete peeling was not observed at 400 g, the load ">400" was indicated in the tables. Probably, the device we designed for adhesion tests is inferior in its characteristics to commercially available machines. However, it utilizes the same operating principles as its commercial counterparts and we believe our measurement results permit establishing basic laws of adhesion characteristics variation.

5.2. Results obtained for the coatings produced by electric-arc evaporation in a gaseous atmosphere

The major findings are summarized in Table 5.1. Along with the measurements presented in Table 5.1, we examined the structure of the coated samples using an optical microscope. Since thickness of the coatings was small, the structure was observed on "angle" microsections: the polished surface of the sample prepared for observation with the microscope was arranged at an angle of 5-10° to the plane surface of the coating. The microsections were prepared using emery cloth, diamond pastes and fine particles of chromium oxide. The microstructures were observed on unetched microsections and subsequent to a 10-15-s etching in a 4% solution of HNO_3 in alcohol. By way of example Fig.5.1 shows the structure of the P6M5K5 steel with coatings of titanium oxide and nitride. Three main areas can be distinguished on the microsections: (1) oxide or nitride coating about 0.1 μm thick; (2) a zone of weak etching adjacent to the coating. Even at large magnification power the fine structure does not show up in this zone. Thickness of the zone is comparable with that of the coating; (3) a transition zone. The latter is characterized by a larger number of weakly etched areas than in the starting sample. As in the starting sample, the main structural component of this zone is a ferrite-carbide mixture. The thickness of this zone is 2-3 times larger than that of the coating.

Let us comment on the results depicted in Table 5.1. As is seen, thickness of the oxide coating decreases markedly as the annealing time is increased. The fact that thickness of the coatings produced on "cold" substrates decreases at a faster rate can be attributed to the influence of the oxygen concentration gradient, because, when the coatings were deposited on a "hot" substrate, the samples were probably saturated with oxygen. Annealing of the samples with oxide coatings was also accompanied by doping of the coating with nitrogen from the gaseous phase. The measurements show that the

Table 5.1.

Thermal stability and adhesion of nitride and oxide coatings, the method of electric-arc sputtering in gaseous atmosphere.

Coating	Steel	Substrate temperature	Post-deposition annealing	Surface density 10^{17} atoms/cm^2		Adhesion test. Load, g	
				nitrogen	oxigen	Unset of peeling	Complete peeling
1	2	3	4	5	6	7	8
Titanium nitride	P6M5K5	Cold	as-deposited	7.03	1.06	100	300
			2h, 968^{0}C	7.78	1.20	100	300
			5h 15 min 968^{0}C	7.44	1.02	200 - 300	300
		Hot	as-deposited	7.56	0.69	100 - 200	300
			2h, 968^{0}C	5.88	0.70	100 - 200	300
			5h 15min 968^{0}C	5.62	0.66	300	>400
	P18	Cold	as-deposited	7.46	1.01	100	200
			2h, 968^{0}C	7.50	1.13	400	>400
			5h 15min 968^{0}C	7.27	0.94	300	400
		Hot	as-deposited	7.25	0.68	100	200
			2h, 968^{0}C	5.88	0.60	400	>400
			5h 15 min 968^{0}C	6.09	0.57	200 - 300	300
		Cold	as-deposited	The width of the coating was 2.5um, the composition of the coating had not been measured.		100	200
			2h, 962^{0}C			300 - 400	>400
		Hot	as-deposited			200	300
			2h, 962^{0}C			400	>400

Table 5.1. Continued

1	2	3	4	5	6	7	8
Titanium oxide	P6M5K5	Cold	as-deposited	--	2.75	300	400
			2h, 968°C	2.82	1.39	100	300
			5h 15 min 968°C	3.29	0.59	100	200
		Hot	as-deposited	--	12.58	200	>400
			2h, 968°C	2.10	9.73	100	200
			5h 15 min 968°C	4.20	7.64	100 - 200	200
	P18	Cold	as-deposited	--	3.35	100	300
			2h, 968°C	2.54	2.61	100	200
			5h 15 min 968°C	3.99	0.79	100	200
		Hot	as-deposited	--	15.15	100	400
			2h, 968°C	1.88	9.85	<100	100
			5h 15 min 968°C	3.43	6.94	100	200

atomic fraction of nitrogen in coatings on "cold" substrates is much higher than that in coatings on "hot" substrates. These data suggest this type of oxide coatings can hardly yield high diffusion-barrier properties in the case of the CVD process as well, because general regularities valid for diffusion of atoms of different light elements are alike. It can be stated also that adhesion of the oxide coatings to the substrates impaired after the annealing treatment, i.e. here the diffusion processes had an

unfavorable effect on adhesion. So, from the viewpoint of thermal stability, adhesion and, probably, diffusion- barrier properties, coatings whose composition is close to TiO are considered to be unpromising.

The regularities found for the nitride coatings differ markedly from those established for the oxide coatings. First, the nitride coatings are of high thermal stability. However, we cannot rule out the possibility that the thermal stability was maintained thanks to nitrogen supplied to the coating from the gaseous phase. This problem needs further consideration. We conceive of this mechanism as unlikely. Second, it is seen that the annealing treatment improved adhesion of the nitride coatings. This fact can be attributed to lowering of stresses in the samples during annealing. In our opinion, another important point is that high adhesion are achieved both on thin coatings (about 0.1 μm) and much thicker coatings (2.5 μm). Subsequently this will allow one to choose thickness of nitride coatings considering only the diffusion-barrier properties of the coatings.

5.3. Results obtained for the coatings produced by electron-beam evaporation.

The coatings produced by the electron-beam evaporation method have been examined in much less detail, because their characteristics proved to be unpromising for practical applications. The basic results are summarized in Table 5.2. As is seen from Table 5.2, the titanium- oxide coatings have a low thermal stability on both types of steels. This conclusion is confirmed also by the optical microscopic observations (Fig.5.2 shows that there are no oxide coating after the annealing treatment). One can see from Table 5.2 that the carbide coatings on "cold" substrates are thermally unstable either. Thickness of the carbide coating on a "hot"

Table 5.2.

Thermal stability of nitride and oxide coatings, the method of electron-beam evaporation.

Coating	Steel	Substrate temperature	Post deposition annealing	Atomic density of light element			
				Oxigen		Nitrogen	Carbon
				10^{17} at/cm^2	at. % ‡	10^{17} at./cm^2	10^{17} at./cm^2
Titanium oxide	P6M5K5	Cold	as-deposited	5.11	--	--	--
			1h, 971°C	--	0.86	2.93	--
			6h 17 min 971°C	--	0.86	3.98	--
		Hot	as-deposited	5.04	--	--	--
			1h, 971°C	1.81	--	2.97	--
			6h 17 min 971°C	--	1.29	4.14	
	P18	Cold	as-deposited	5.11	--	--	--
			6h 17 min 971°C	--	0.92	3.98	--
		Hot	as-deposited	5.04	--	--	--
			6h 17 min 971°C	--	0.86	3.64	--
Titanium carbide	P6M5K5	Cold	as-deposited	7.70	--	0.4	7.52
			1h, 971°C	no data	--	4.76	4.55
			6h 17min 971°C	--	2.7	15.0	--
		Hot	as-deposited	7.70	--	0.4	7.52
			1h, 971°C	no data	--	5.50	7.38
			6h 17min 971°C	3.51	2.3	16.0	7.46

‡ - average concentration in the near-surface layer ≈0.2 um thick.

substrate did not change during annealing. This distinction is probably due to saturation of the surface layers of steel with carbon during deposition. A point drawing one's attention is that annealing is accompanied by a strong doping of the coating with nitrogen and a decrease in the oxygen concentration of the coating. The optical microscopic data obtained for both deposition techniques are analogous. In all the cases (Figs 5.1 and 5.2) the microsections exhibit zones of weak etching near the steel surface and transition zones characterized by weakly etched components of the structure. Table 5.2 does not contain data on the P18 steel, because thin carbide coatings had peeled off the P18 steel in several hours after deposition. Taking into account the above results on thermal stability, we examined adhesion only of the carbide coatings deposited on "hot" substrates. This was done for the samples with the coating thickness of about 2.5 μm. The corresponding samples were not annealed. For both steels the onset of peeling was observed at the load of 200 g, while complete peeling was noted at 300 g. So, our findings described in this section suggest that the oxide coatings whose composition is close to TiO show no promise as diffusion barrier layers for CVD of diamond.As far as the carbide layers are concerned, the obtained results do not permit drawing a definite conclusion.

The present report on stage 2 does not contain a list of references as there was no special need in it. This is due to the specific features of the reading matter presented herein and a sufficiently detailed analysis of the literature data given in the report on stage 1.

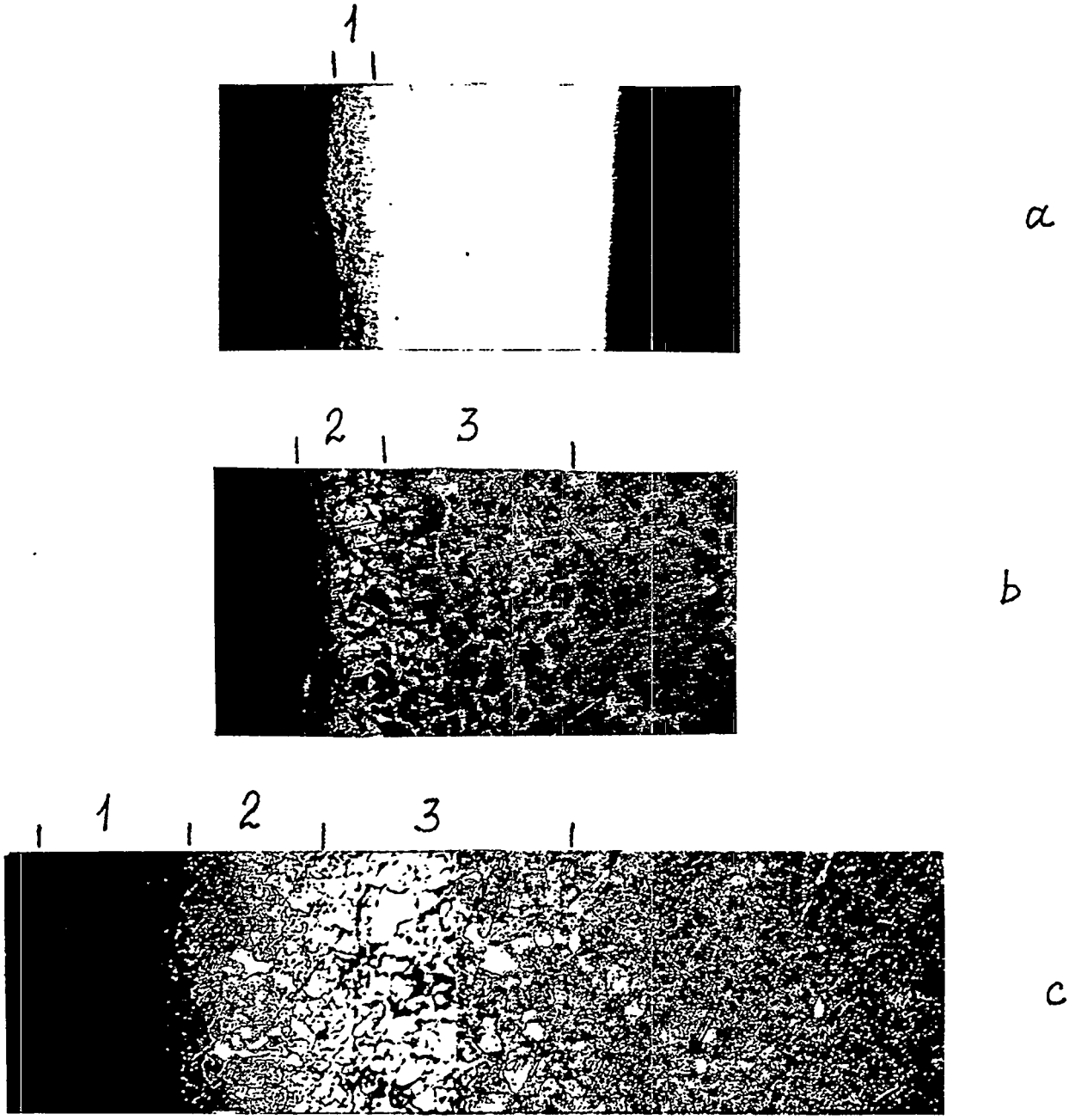
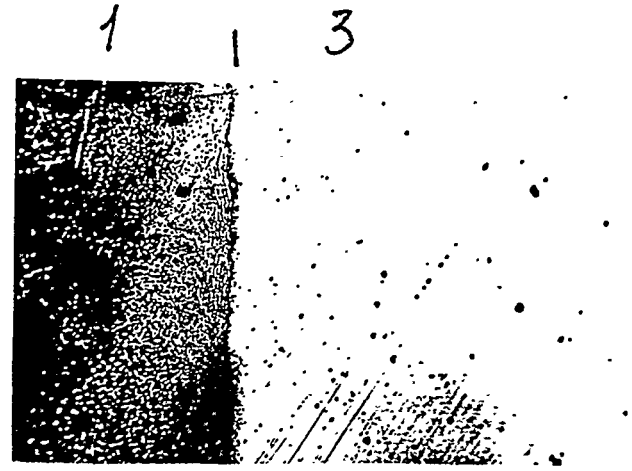
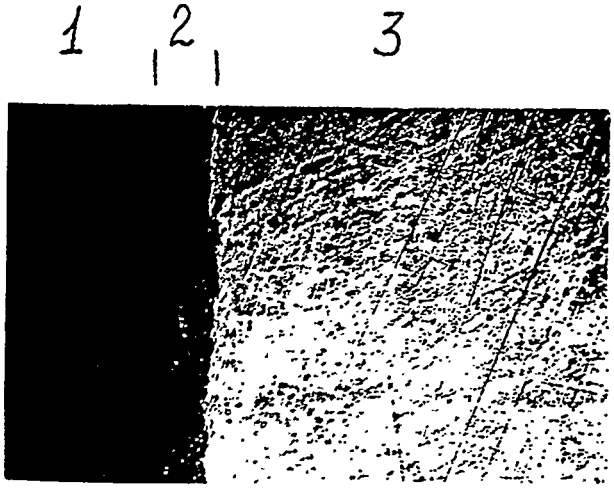


Fig.5.1.

The structure of the P6M5K5 steel with the coating.
The method of electric-arc sputtering in gaseous atmosphere,
"hot" substrate, post-deposition annealing 968° 5h 15min.
a) - oxide, non-etched microsection, ×100; b) - oxide, ×200;
c) - nitride, ×400.
1 - coating; 2 - zone of weak etching; 3 - transition zone.



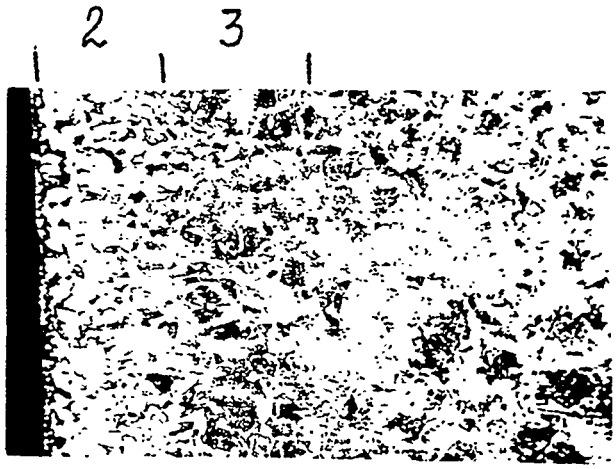
a



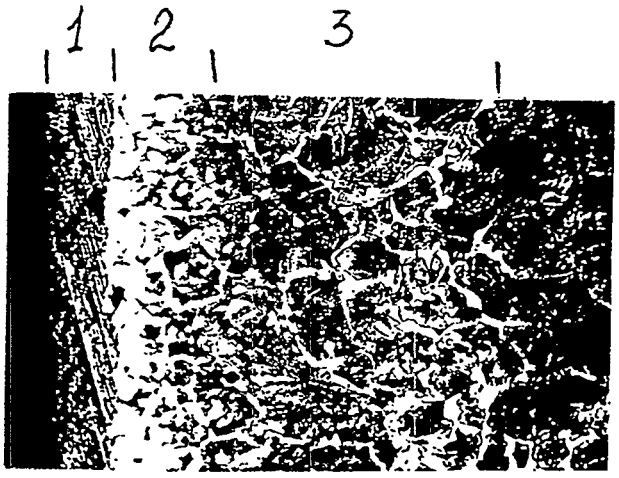
b

Fig.5.2.

The structure of the P6M5K5 steel with the coating.
The method of electron-beam evaporation, "hot" substrate, post-deposition annealing 971° 6h 17min, non-etched microsections.
a) - oxide, ×200; b) - carbide, ×200;
1 - epoxy composition; 2 - coating; 3 - steel.



a



b

Fig.5.3.

The structure of the P6M5K5 steel with the coating.
The method of electron-beam evaporation, "hot" substrate, post-deposition annealing 971^{o} 6h 17min.
a) - oxide. ×200; b) - carbide, ×200.
1 - coating; 2 - zone of weak etching; 3 - transition zone.

6. Conclusions

6.1. The coatings whose composition is close to TiO and TiO_2 produced using two different deposition techniques are unpromising for application as diffusion-barrier layers for the CVD process. This inference is primarily due to their low thermal stability.

6.2. The titanium-carbide coatings produced by electron-beam evaporation onto "hot" substrates are characterized by an adequate adhesion. The number of carbon atoms in such coatings changes insignificantly during annealing, i.e. thermal stability of the coatings is sufficiently high in this sense. At the same time these coatings differ greatly from the stoichiometric TiC in their chemical composition. For this reason they are capable of absorbing large amounts of oxygen and nitrogen atoms. As a result, the coatings actually represent oxicarbides, carbonitrides, or more complicated compounds. At this stage it is impossible to draw an unambiguous conclusion about the outlooks for these coatings as diffusion barrier layers for CVD of diamond.

6.3. In terms of thermal stability and adhesion properties the titanium-nitride coatings are deemed to be promising for deposition on tool steel prior to CVD of diamond.

6.4. The chemical composition of the coatings and sample pretreatment conditions will be optimized at stage 3 of the contractual works.

Appendix. Description of the samples delivered to the customer

1) Steel P18. Titanium-carbide coating 2.5 μm thick deposited by electron-beam evaporation. Deposition on a "hot" substrate - 2 pcs.

2) Steel P18. TiN coating 2.5 μm thick deposited by electric- arc evaporation in a gaseous atmosphere. Deposition on a "hot" substrate - 2 pcs.

3) Steel P18. TiN coating 2.5 μm thick deposited by electric-arc evaporation in a gaseous atmosphere. Deposition on a "cold" substrate - 2 pcs.

4) Steel P18. TiN coating 2.5 μm thick deposited by electric-arc evaporation in a gaseous atmosphere. Deposition on a "hot" substrate, annealing for 2 hours at t = 962°C in a helium flow - 1 pc.

5) Steel P18. TiN coating 2.5 μm thick deposited by electric-arc evaporation in a gaseous atmosphere. Deposition on a "cold" substrate, annealing for 2 hours at t = 962°C in a helium flow - 1 pc.

Contractor Representative

V. Vykhodets

Project Title: Synthesis of Polycrystalline Diamond Films Using Super High Frequency Plasma Deposition
Principal Investigator: Nikolai Samsonenko
Dunbass Civil Engineering Institute
Makeveka, Ukraine
AM-7680

CLAUSE 1 - STATEMENT OF WORK

Background:

By controlling microstructural defect production the semiconductor properties of the diamond films can also be controlled. The ability to influence the electrical properties of diamond films has important implications for varistor and integrated circuit applications. This project will utilize the Institute's previous expertise in depositing and characterizing films grown using CVD to explore the properties of diamond films deposited by super-high-frequency plasma (SHFP) assisted CVD. This project is a non-profit research and development project between the Donbass Institute and Sandia National Laboratories.

Tasks:

The Contractor shall:

1. Prepare and submit an initial report reviewing the Institute's previous work on depositing and characterizing the microstructure and electrical properties of diamond films deposited using CVD. References to published work shall be included.

2. Prepare and submit four (4) samples with diamond coatings grown by the Institute's conventional CVD process. The dimensions and type of substrates used for these samples will be agreed upon by the Contractor and Sandia within two (2) months of the beginning of the contract. The contractor shall also deliver a letter report summarizing initial X-ray diffraction, electron paramagnetic resonance, and electrical characterization results on the samples.

3. Prepare a deliver a report describing the operation characteristics of the super-high-frequency plasma generator and how it will be used for experiments in CVD diamond growth. The report shall also include a brief summary of other experiments conducted with similar sources and describe the advantages of using super-high-frequency (SHF) excitation of the plasma as compared to normal mega-hertz frequency excitation.

4. Prepare and deliver a final report on the microstructure, defects, and electrical properties of diamond films deposited using the SHF plasma assisted CVD method. Four (4) samples shall also be delivered to Sandia on substrates that are agreed upon by the Contractor and Sandia within 8 months of the beginning of the contract.

REPORT AT TASK 1 OF THE CONTRACT AM - 7680

1. INTRODUCTION.

Questions of the synthesis new materials with the semiconductor properties for electronics and pursuit of the new properties of traditional semiconductor materials and insulators are actual for electronics. In [1] they consider that for semiconductor electronics it follow to select of the materials with high relation Debye's temperature to bandgap. This relation is a measure chemistry and temperatur stability them. These considerations are leading to not large region of the period system of chemicl elements: B, C, N, Al, Si, P. They are giving to such materials as boron, diamond, silicon, boron nitride, boron phosphide, aluminium nitride and silicon carbide, wich are semiconductors with high temperature of the melting.

Therefore interest have growd to electron properties of the diamond since 1952 year, when they have finded semiconductor diamonds with low resistivity (25-10^8 Ω·cm). They have a hole electroconductivity. These crystals of the diamond have a name semiconductor diamonds. They are applying to type IIb diamonds [2-4].

Reserchers [5-7] are drawing only a admixture mechanism for the explanation of the unusual properties type IIb diamonds (low resistivity, special spectrums of the optical absorption, phosphorescence and other). However they are not able to explain many properties of the insulator diamonds and semiconductor diamonds only mixed with. There is not connection some optical elements.There is not comprehension of the cause polarisation effects in the diamonds. The energy of the acceptor centers in semiconductor diamonds not correspond to hydridgen model, photoconductivity of the type IIb diamonds have not satisfactory explanation. In nature there is not semiconductor diamonds with n-type conductivity.

Many researchers try to force the process of making electronic active elements of diamond. They consider that diamond is like usual semiconductors germanium and silicon in a formation of electronic properties.

Houwever, it is more intricate in the case of diamond. First of all diamond is an insulator with the wide gap. Secondly, the formation of energy states in the bandgap by impurities occurs quite differently from usual semiconductors. Thidly, the hard diamond lattice does not most impurity atoms to occupy a substitutonal positions in diamond lattice sites. A substitution is possible with carbon nearest neaghbours boron and nitrogen only.

So, the entering of nitrogen atoms into the diamond lattice is enough well studyd under electron spin resonance (ESR) investigations and optical ones [8-13]. The entering of impurity boron into the substitutional positions has been established in synthetic diamonds also [7]. Impurity atoms of nitrogen forms the bulk states of to 4 eV in diamond, i.e. these are the ciss-donors. There ara no any reliable data with respect to boron at the present time. The formation of boron energy states is imposed with other effects disguising the truth picture of energy spectrum. Above pointed out remarks make to return to study of an electronic properties of natural and synthetic diamonds and synthetic diamond films. One can to assume, that a progress in promotion of diamond into electronics will depends on undestanding of the forming electronic properties them.

2.DEFECTS IN NATURAL AND SYNTHETIC DIAMONDS.

IMPURITIES IN DIAMOND. A greate many impurities atoms (Al, Mg, Si, Fe, Cr, Co and other) are found in natural diamonds. Mineralogical study shows that these elements can be include in diamond as constituent components of inclusions (olivin, pirope, garnet,...) [14].

It has been determined by experiment that nitrogen (N) and boron (B) atoms, nearest neighbours to carbon (C), are included in diamond as impurities [7,8]. However, according to Schottky [15], in wide band gap insulator donor impurities form depth levels near edge of valence band - "ciss donors". Acceptor impurities form levels near to the middle of the bandgap, probably. Therefore influence of the impurities on electrical properties of diamond is weak. This scheme is distinguishing from one forming shallow levels in traditional semiconductors (Ge,Si,...).

POINT DEFECTS IN A CRYSTAL LATTICE. These are vacancies are found by ESR method at a light excitement with ease, according to Beldwin [16]. According to our datas on natural diamonds vacancies are less then 10^{12} cm^{-3} in number.

DISLOCATIONS. INTERGRAINE DISLOCATION BOARDERS (TYPE Ic AND IIb DIAMONDS). All diamond types containe a great many stretch defects - these are plate segregates with outline borderings by partial dislocations, dislocations of different types and dislocation boarders in mosaic diamonds [17,18]. As a rule, the dislocations cause displacements of a great many carbon atoms (> 10^{20} cm^{-3}) from their equilibrium position. Diamonds, plastically deformed in natural conditions are of a great importance for understsnding electronic properties. These are type IIb [19] and Ic [20,21] diamonds. The natural plastic deformation of type II diamonds results in a crystal mosaic. Borders between mosaic blocks consist of dislocation row (type IIb diamonds). The natural plastic deformation of type I diamonds result in a block form - in this case the plastic deformation is dificult because a presence of platelets, stoping one. Therefore type Ic structural defects are more complicated.

According to Shockley [22], dislocations in Ge and Si form dislocation acceptor centers, thet determine hole conductivity. Semiconductors type IIb and Ic diamonds have hole conductivity only [23].

3.ELECTRON SPIN\ RESONANCE ON DEFECTS IN DIAMOND.

ESR ON IMPURITY NITROGEN IN DIAMOND. Investigations of impurity nitrogen in natural and synthetic diamond had been devoted by many works [8-13]. One with optical researches have been established that main nitrogen entering form is nitrogen atom pairs placed in neighbour lattice sites in type Ib diamond. Paramagnetic nitrogen causes yellow colour of natural and synthetic diamonds.

ESR IN TYPE Ic AND IIb DIAMONDS. The plastic deformation forms line defects - dislocation. These defects in them cores have broken carbon bonds with unpaired electron spins that cause electron paramagnetic

resonance absorption [21. 24]. This electron spin resonance signal is like ESR on diamond surface [25,26]. It increases also with plastic deformations intensity of crystals. Type IIb diamonds have a similar ESR spectrum [27]. These diamonds was plastic deformation in natural conditions [19].

ESR IN NATURAL TYPE IIa AND SINTHETIC DIAMONDS PLASTICALLY DEFORMED IN LABORATORY. The plastic deformation have been carried out in a high pressure chamber at T = 1500 C and total pressure 50 kbar by pressing of small diamond crystals into sample surfaces. After the deformation the ESR spectrum have been found in type IIa diamonds similar to type IIb and Ic one [28].

The experiments with synthetic diamonds have been carred out as follows. During the sinthesis process Al has been introduced to connect nitrogen and decrease paramagnetic nitrogen and number. Nitrogen concentration has been decreased by two powers in magnitude. Wide lines of ESR spectrum of the paramagnetic nitrogen becomes 0,3 Oe.Then the samples have been deformed plastically at the same conditions as natural type II diamonds.

The ESR spectrum has been got with parameters similar to type IIb and Ic ones [24].

ESR IN SYNTHETIC DIAMOND FILMS. The ESR spestrum with to similar parameters has been found in epitaxial diamond film got in Spitcyn's laboratory. A diamond film mosaic have been caused by growth conditions [29]. Dislocation intergrain boundaries have caused resonance absorption too.

More compound spectrum from broken bonds on dislocations have been got and studied for polycrystalline films in our laboratory [30,31].

4.OPTICAL ABSORPTION IN DIAMONDS WITH DEFECTS.

OPTICAL ABSORBTION IN VISIBLE REGION SPECTRUM IN TYPE I, IIa, Ic DIAMONDS. How does the plastic deformation influence on optical absorbtion spestrums ? We have made a comparison the spectrum of the absorbtion of the type I, type Ic and type IIa diamonds in visible region. Nitrogen displaces the border of fundamental absorbtion band to long wave

range. The plastic deformation in natural and in laboratory [31] remove the border of fundamental absorbtion band to long wave range too. And plastic deformation decreas of transmition bands in range about 400 nm and 500 - 600 nm [32,33].

INFRARED SPECTRUM OF THE ABSORBTION IN PLASTIC DEFORMED DIAMONDS. Type Ic diamonds have bands of the absorbtion that are connected with nitrogen (7,8 μm; 8,3 μm; 9,1 μm; 20,8 μm) and bands that was appeared after plastic deformation in natural conditions [21] at wave lengthes: 2,43 μm; 3,40 μm; 3,56 μm; 4,10 μm; 6,00 μm. There are not nitrogen bands in type IIb diamonds, but there are bands at wave lengthes 1,83 μm; 2,43 μm; 3,40 μm; 3,40 μm; 3,56 μm; 4,07 μm; 6,00 μm [34].

These studies shous that general bands of the absorbtion for both type diamonds are not connected with admixture. They are stipulated with the complex defects that arise in diamonds at plastic deformation.

5.PHOTOCONDUCTIVITY IN DIAMOND WITH DEFECTS.

There is a direct connection between absorbtion and photoconductivity spectrum.

PHOTOCONDUCTIVITY IN TYPE Ic AND IIb DIAMONDS. The comparing the conduction spectrum of the type Ic diamond with one of the type I and IIa diamond allows to define new maximums at $\lambda \approx 500$ nm, $\lambda \approx 640$ nm and $\lambda \approx 890$ nm [33].

For mosaic type IIb diamonds photoconduction spectrum gives maximum at $\lambda \approx 640$ nm and $\lambda \approx 890$ nm in visible longwave range too [34]. These maximums are common with type Ic diamond one.

PHOTOCONDUCTION IN NATURAL TYPE IIa DIAMONDS AFTER DEFORMATION IN LABORATORY CONDITIONS. Type IIa diamonds have not any maximums of the photoconduction in wave range from 400 nm to 1000 nm. In deformation process formed defects are caused photoconduction maximum at $\lambda \approx 640$ nm, which have saw in type Ic and IIb diamonds [28].

PHOTOCONDUCTION IN THE SYNTHETIC DIAMOND FILMS. We have discovered that epitaxial diamond films have a mosaic structure wich is like structure type IIb diamond. For the first time we have discovered too maximum at $\lambda \approx 640$ nm in diamond epitaxial films [35]. It increases with film thickness. In indicates the existence of crystal lattice defects arised in plastic deformation process or growth. We consider they are dislocations. Later we have discovered the same spectrum of the photoconductivity in the polycrystalline diamond films, but with less intensity [36].

6.ELECTRICAL CONDUCTION IN DIAMOND.

INSULATING DIAMONDS. Champion [2] noted that ideal pure and perfect sample with $\Delta\varepsilon \approx 5,5$ eV would have resistivity about ^{70} Ω·cm. Really both natural and synthetic diamonds show $\rho \approx 10^{12} - 10^{15}$ Ω·cm. Such magnitude ρ corresponds to band gap wide of $\Delta\varepsilon \approx 2,0 - 2,5$ eV. The temperature dependences of σ on 1/T for type IIa diamonds are levels $\varepsilon_5 \approx$ 2,0 - 2,5 eV [33]. What determines diamond electrical properties ?

PLASTIC DEFORMED DIAMONDS. In plastic deformed type Ic and IIb diamonds the new level appears $\varepsilon_3 \approx 0,4$ -0,7 eV [4,21]. The lower diamond resistivity, the broader temperature range in wich electrical conduction defines the levels 0,4 -0,7 eV.

THE LABORATORY PLASTIC DEFORMATION DIAMONDS. The laboratory plastic deformation forming dislocation of type IIa diamonds, have led to the appearing of the 0,4 -0,7 eV level [28].

THE SYNTHETIC DIAMONDS FILMS. In the syntetic diamonds films having growth defects such as dislocations, levels at 0,4 -0,7 eV have been revealed too [33].

7. SUBBAND STRUCTURE OF DIAMOND.

So, dislocations are mainly defects at a plastic deformation. Moreover there are partial dislocations along an outline of platelet segregations in type I diamonds. A dislocation core is of great interest for electronics. The disturbance of periodicity at the plane perpendiculared to dislocation axis.

Shokly [37] predicted that dislocations having edge component have to make acceptor levels and p - type conduction.

Bonch - Brujevich [38] proved theoretically the existence of dislocation bands of energy in a semiconductor bandgap. A movement of electrical charge carrier along the dislocation bands is possible.

We have used by the experience of Messmer and Watkins [39], who proposed the MO LKAO method for a finding of electron energy spectrum in diamond with impurity nitrogen.

For solving similar task for diamond we have taken the carbon claster consisting of 34 atoms with 60 degrees dislocation. The calculation results have showed that the electron spectrum in the diamond claster with the dislocation differs from silicium one. In diamond the dislocation lead to a split off permitted energy bands : two Dislocation Filled Bands (DFB) and two Dislocation Empty Bands (DEB). Dislocation Acceptor Levels (DAL) have position between I DFB and I DEB. So, we consider that transitions from I DFB to DAL stipulat the electrical conduction dependence on temperature (with activation energy $\varepsilon_3 \approx 0,4$ -0,7 eV). Transitions from valency band to DAL give a photoconductivity of the plastic deformed diamonds at $\lambda \approx$ 0,64 μm (energy about 2 eV) and transitions from II DFB to DAL give a photoconductivity at $\lambda \approx 0,89$ μm (energy about 1,4 eV) [40].

The concentration of the dislocation ESR centers forming the dislocation acceptor levels is equal to 10^{13} - 10^{18} cm^{-3}. They have just to form the electronic properties of diamond.

We have used intensive plastic deformation and have got a high conductivity (~ 10^{-3} - 10^{-2} $\Omega^{-1} \cdot cm^{-1}$) in insulating diamonds [41].

Dislocations and dislocation structures in diamonds are key for the understanding of the electronic process in diamond crystalls.

Our discovery of the forming properties of the diamonds and achievement in the technology of the synthesies diamond films will be real progress for the applications of the diamond in the electronics.

8.ESR - DIAGNOSTICS FOR OPTIMISATION OF DEPOSITION PROCESSES OF DIAMOND FILMS.

The necessity of optimization of deposition processes of diamond films requires the development of new diagnostics methods of their structure and properties along with traditional ones. We have used new method of ESR-diagnostics of DF which allows, according to orientation dependence of characteristic points of complex ESR absorption spectral line, to detrmine both the parameters of anisotropic paramagnetic centres and the parameters of DF defect structure themselves.

We obtained following data on structure of paramagnetic centres [42] :

1. Studied paramagnetic centres, which stipulate resonance ESR - absorption, are unpaired electrons on broken bonds of carbon atoms, orientated along to direction [111]. The values $g_{\parallel}$ and $g_{\perp}$ have been calculated. $g_{\parallel[111]} = (2{,}0033 \pm 0{,}0005)$, $g_{\perp[111]} = (2{,}0025 \pm 0{,}0005)$.

2.According to results of experimental orientation dependence of the spectrum line for diamond film, we calculated the line's width ESR absorbtion in a single crystallite $\Delta H = (2{,}8 \pm 0{,}2)$ G.

We obtained the following data about real structure of diamond film itself:

1. It is established, that studted sample of diamond film being by partialy-oriented system of paramagnetic centres is the new object for ESR investigations, which differs by ESR line shape both from monocrystalline and polycrystalline objects (powder type).

2. Comparison of experimental data with results of phenomenological theory of ESR spectrum line shapes in partialy-oriented films shows, that studied sample has cone-like space distribution of symmetry axes of anisotropic paramagnetic centres. The altitude of this cone is the normal n to the film surfece, and the angle between the normal and the generating line of the cone χ is $(8 \pm 2)^0$. The direction of this line represets maximum deflection of axes f_i of primary orientation of anisotropic paramagnetic centres from the normal. The angle χ characterizes, respectively, the nutation disorientation of symmetry axes of paramagnetic centres in various crystallites.

3. According to results of azimuthal orientation dependeces, we can determine the degree of structure's anisotropy in the plane of film.

10.PERSPECTIVE OF THE SYNTHESIS OF THE DIAMOND FILMS FROM SHF-PLASMA.

There are various methods of the synthesis of the diamond films : hot filament activation plasma, plasma of the arcdischarge on direct current, plasma of the smouldering dicharge at the radiofrequency stimulation and other. But methode of the synthesis diamond film from superhigh frequency (SHF) plasma - is perspective [43,44].

Among modern sources SHF - plasma one using of the principe electron - cyclotron resonance (ECR) has very good perspective. It gives dense plasma (concentration of the electrons $n \geq 10^{12}$ cm^{-3}) at low pressure of the gas (10^{-1} - 10^{5} Pa). "Hot" electrons almost fully ionize of the neutral gas, and "cold" ions of the gas assisting to deposition of the products of the plasma chemical reactions.

Magnet insalation of the plasma from walls of the reaction camera and absence of the electrodes ability make of the superclean deposition materials.

In ECR - source of the plasma there is possibility operate with degree of the ionize of the atoms of the gas in magnet catch. This important significance for synthesis of the diamond films.

ECR-sources of the plasma may form thing films on the substrute with low temperature. And films have high quality. Besides diamond films take less hidrigen atoms than by other methods. Method with SHF plasma allows also make heterostructures of the diamond with other semiconductors that have low temperature of the melting. This method allows carry out ion cleaning surface of a substratums in united technology cycle, polish and exact treat surface of a diamond films and manufactures of the microelectronics.

SHF plasma allows to make thing films of the dielectrics semiconductors and metals.

Many scientists are studying properties of the diamond films that they make from SHF plasma. A review [43] is very solid. Outhors consider that

method of synthesis of the diamond films from SHF - plasma is perspective for manufacturing of the diamond electronics clements. They noted that this method allows to have gomoepitaxial good qualite layers of the diamond. It allows also bring DF boron atoms for creation acceptor centres. But a solution of the atoms P, Li, Na in diamonds is very low. It was not still had in diamond electroconductivity type n. They have had maximum rates of the growth DF at 975 C, but homoepitaxial DF the best quality were had at temperature 850 - 900 C. The most perfect DF were had on diamond surface (100). SHF - plasma method allows also to use technology processes of the microelectronics at the making electronics devices.

So today we have next problems:

1.Problems of the doping of the diamond.

2.Problem of semiconductor diamonds with n - type electroconductivity.

3.Problem of the growth perfect DF on strange substratums.

4.Problem of the electroconductivity diamond mechanisms.

We believe to solve these problems we must carry out complex experimental and theoretical stuyes of the synthesis DF and our conception of the forming electronic properties of the diamond with linear structure defects.

REFERENCES

1. Ch.E.Ryan. Perspectives on silicon carbide.- "Silicon Carbide 1980". Pergamon Press. (1969), p.1-12.

2. F.C.Champion. Electronic properties of diamond. London, Butterworthe, (1963), p.133.

1. I.F.H.Custers. The IIb diamond. - Physica,20,(1954), p.181-184.

2. I.F.H.Custers. Semiconductivity of type IIb diamond. - Nature, 176, (1955), p.173-175.

5. P.T.Wedepohl. On the nature of the acceptor centre in natural semiconducting diamond. - J.Phys.C. (Proc.Phys.Soc.), 1, (1968), p.1773 - 1774.

6. A.T.Collins, A.W.Williams. The nature of the acceptore centre in

semiconducting diamond. - Diamond Res., (1971), p.23-29.
7. V.S.Vavilov, A.A.Gippius and Ye.A.Konorova. Electrical and optical processes in diamond. Nauka (publishing house) Office of Physical Mathematical Literature. Moscow, USSR, (1985).
8. W.V.Smith, P.P.Sorokin, S.L.Gelles, C.J.Lacher. Electron spin resonance of nitrogen donors in diamond. - Phys.Rev., 115,(1959), p.1546-1552.
9. N.D.Samsonenko. On the distribution of the paramagnetic nitrogen's centres in some type I diamond. Solid State Phys., 6 (1964), p.3086-3088.
10. E.V.Sobolev, G.B.Bokiy, V.F.Dvoryankin, N.D.Samsonenko. On correlation of the optical and ESR - spectrums in nature type I diamonds. - Zhurnal Strukturnooi Khimii(USSR),5,(1964), p.557-561.
11. M.Ya.Scherbakova, E.V.Sobolev, N.D.Samsonenko, V.K.Aksenov. - Electron paramagnetic resonance of the ionisation nitrogen pair in the diamond. - Solid State Phys., 11, (1969), p.1364-1367.
12. E.V.Sobolev, N.D.Samsonenko, V.E Illin, V.K.Aksenov, M.Ya.Scherbakova. On advantage state of the nitrogen in natural diamonds. - Zhurnal Strukturnooi Khimii (USSR), 10, (1969), p.552-553.
13. E.V.Sobolev, Yu.A.Litvin, N.D.Samsonenko, V.E.Illin, S.V.Lenskaya, V.P.Butuzov. On state of the impure nitrogen in synthetic diamond. - Solid State Phys., 10,(1968), p.2266-2268.
14. S.I.Futergendler. X-ray study of the native diamonds and their inclusions of the minerals. - Author manuscript of the dissertation. Leningrad Mining Institut. Leningrad, (1964), p.18.
15. W.Schottky, F.Stockman. Vergleichende Betrachtungen uber die Natur der Storstellen in Halbleitern und Phosphoren. - Halbleiterprobleme. Fridrich Vieweg, Braunschweig, B.1, (1954), S.80-106.
16. J.Q.Baldwin. ESR of isolation vacancy in diamond.- Phys.Rev.Lett., 10, (1963), p.220-223.
17. T.Evans, C.Phaal. Imperfections in type I and type II diamonds. - Proc.Roy.Soc.A, (1962), p.538-544.
18. T.Evans, C.Phaal. Dislocation loops in diamond. - Phil.Mag., 1962, 7, p.843-846.

19. A.R.Lang.Internal Structure. In "The Properties of Diamond" edited by J.E.Field. Academic Press, London,NY,San Francisco (1979).
20.A.A.Urusovskaya, Yu.L.Orlov. On the nature of the plastic deformation of diamond crystals. Dokl.Akad.Nauk SSSR, 154 (1964) p.1099-1102.
21.N.D.Samsonenko,G.B.Bokiy, N.A.Shulga, V.I.Timchenko. About origin of the change electrical and optical properties of natural diamonds. Dokl.Akad.Nauk SSSR, 218, NO 6 (1974) p.1336-1339.
22.W.Shockley. Imperfection in nearly perfect cristals.- Phys. Rev., 91 (1953) p.228.
23.H.B.Dyer, P.T.Wedepohl. Electrical measurements on type IIb diamonds.- Proc. Phys. Soc.B, 69,(1956), p.410-412.
24.N.D.Samsonenko, V.G.Shulga, Yu.A.Litvin. Electron paramagnetic resonance on the non impurity deffects in diamond. -Sb.Sint. almazy (USSR),3,(1970), p.22-26.
25.N.D.Samsonenko, E.V.Sobolev. Electron paramagnetic resonance stipulated diamonds surface.- Pis'ma Zh. Eksp.Teor.Fiz., 5 (1967) p.304-306.
26.N.D.Samsonenko,G.V.Zhmykhov, V.Sh.Zon, V.K.Aksenov. Characteristic features of the electron paramagnetic resonance of the surface centers of diamond.- Translated from Zhurnal Strukturnoi Khimii, 20, NO 6 (1979) p.1116-1118.
27.M.D.Bell,W.J.Leivo. Electron spin resonance in semiconducting diamond.- J.Appl.Phys.,38 (1967) p.337-339.
28.N.D.Samsonenko, V.I.Timchenko, Yu.A.Litvin, G.B.Bokiy. Electron Propertiese of the natural Diamonds after Deformation in the Laboratory.- Dokl.Akad.Nauk SSSR,242,NO 2 (1978) p.826-828.
29.N.D.Samsonenko, L.L.Bujlov, T.A.Karpuhina, B.V.Spytsin, V.I.Timchenko. Photoconductivity and electron paramagnetic resonance on the deffects in the epitaxial diamond films. Sb.Sint. almazy (USSR),2,(1977), p.22-26.
30.N.D.Samsonenko, V.V.Tokiy, S.V.Gorban, V.I.Timchenko. Electron spin resonance spectroscopy of impure and pure structural defects in diamond.- Surface and Coatings Technology, 47 (1991) p.618-622.

31.V.V.Tokiy, N.D.Samsonenko, S.V.Gorban. Application of ESR to diamonds films. Preprint DonFTI-92-10, Donetsk,(1992), 28p.
32.C.Phaal. The absorbtion spectra and irradiarion of plastically deformed diamond.- Phil.Mag.,(1965), 11, p.369-378.
33.N.D.Samsonenko. Electron properties of the deffects in diamond.- Doctor of Science Dissertation. Moscow, (1985), p.377.
34.C.Johnson, H.Stein, T.Young, J.Wayland, W.Leivo. Photoeffects and related properties of semiconducting diamonds.- Phys.Chem. Solids, 25, (1964), p.827-836.
35.N.D.Samsonenko, V.V.Tokiy, V.I.Timchenko. Spectral dependence of photoconductivity in visible and infrared range on epitaxial diamond films. Diamond Films'91, Nice.France, Abstracts (1991), 12.53.
36.N.D.Samsonenko, V.A.Soroca, V.V.Tokiy, V.I.Timchenko. Spectral dependence of photoconductivity of polycrystalline CVD diamond films. Diamond Films'1993, Albufeira, Portugal, Abstracts (1993),12.083.
37.W.Shockley. Imperfection is nearly perfect crystals.-Phys.Rev., 91, (1953), p.228.
38.V.L.Bonch-Bruevich, V.B.Glassko. About the theory of electron state, connected with dislocations. Part I. Lineal dislocations. - Sov. Phys. Solid State, 3,(1961), p.36-46.
39.R.P.Messmer, G.D.Watkins. Molecular-orbital treatment for deep levels in semiconductors : substitional nitrogen and the lattice in diamond.- Phys.Rev.B, 7 ,(1964), p.2568-2590.
40.N.D.Samsonenko, V.I.Timchenko. The relations of the electron energy spectrum of dislocations with optical and electrical properties of the real crystal of diamonds . - Optical spectroscopy and ESR of the admixtures and defects in diamond. Kiev: ISM Academy Ukraine, (1986), p.8-13.(in Russian)
41.N.D.Samsonenko, G.B.Bokiy, V.A.Yemets et al. About electrical properties of the diamonds after deformation.-Sov.Crystallography, 25(6), (1980), pp.1300-1302.

42.V.V.Tokiy, N.D.Samsonenko, S.V.Gorban et. al. New ESR - diagnostic for optimization of deposition processes of diamond film.-2nd International Conference on the Applications of Diamond Films and Related Materials.Editors: M.Yoshikawa, M.Murakava, Y.Tzeng and W.A.Yarbroough. MYU. Tokyo, (1993). Printed in Japan, p.761-766.
43.G.Sh.Gildenblat, S.A.Grot and A.Badzian. The Electrical Properties and Devoice Applications of Homoepitaxial and Polycrysttalline Diamond Films.-Proceedings of the IEEE, vol.79, N 5, (1991), p.647-668.
44.A.S.Vus, A.M.Dudkina, V.A.Dudkin et. al. State of the working and perspective of the use ECR - source of the plasma for technology processesy forming of the film structure in microelectronics and optics.-Preprint N 90 - 22, Institute of the radiophysics and electronics Academy of the Ukraine, Kharkov, (1990), 55 p.(in Russian).

Project Title: High Energy Electron Beam Treatment for the Enhancement of the Tribological Properties of Tool Steels, Cemented Carbides, and Nitride Coated Tool Steels and Cemented Carbides.
Principal Investigator: V. P. Rostshtein
High Current Electronics Institute
Tomsk, Russia
AM-7681

CLAUSE 1 - STATEMENT OF WORK

Objective: The objective of the work is to demonstrate the effect of using high energy, pulsed ion beams on the tribological properties of tool materials, using a unique electron beam source.

Tasks:

The Contractor shall:

1. Provide a report detailing the design of the electron-beam source and previous work performed using the e-beam source. The report should also include all references to previously published work.

2. Treat the steel and carbide samples and tools {tools will be provided by Sandia) with the electron beam source in accordance with the following techniques and parameters. Provide a two page letter report outlining the results of the characterization data defined below. Return the treated tools to Sandia.

Characterize the treated samples utilizing the following techniques:
Optical Metallography
X-ray diffraction
Microhardness testing
Wear resistance testing

The electron beam parameters for treatment will be:
Pulse duration: (0.5 - 2(s)
energy density: (2-10 J/cm^2
number of pulses (5-50)

3. Deposit TiN (titanium nitride), ZrHfn (zirconium hafmium nitride), and W (tungsten) on tool steel and cemented carbide samples. Treat and characterize the coated samples using the same techniques and arameters described in Task 2. Provide a final report detailing the results and findings of Tasks 2 and 3.

November, 1994

High Energy Electron Beam Treatment for the enhancement of the tribological properties of tool steels, cemented carbides, and nitride coated tool steels and cemented carbides

Report

Contract AM-7681, issued by
the High Current Electronics Institute to SNL

Task 1

CIS contact: Senior Research Scientist
of HCEI V. P. Rotshtein, Ph.D.

Tomsk

List of the participants of the work

High Current Electronics Institute, SD RAS, Tomsk

1. V. P. Rotshtein, Ph.D. (Phys. & Math.)

2. D. I. Proskurovsky, Ph.D. (Phys. & Math.)

3. G. E. Ozur, Ph.D. (Phys. & Math.)

4. D. S. Nazarov

Siberian Physical-Technical Institute, Tomsk

1. V. I. Itin, Ph.D. (Phys. & Math.)

2. A. A. Tuhfatullin, Ph.D. (Phys. & Math.)

3. I. S. Kashinskaya, Ph.D. (Phys. & Math.)

Contents

1 INTRODUCTION 2

2 A low-energy high-current electron beam source (LEHCEB) 3

2.1 LEHCEB generation in explosive-emission-cathode plasma-filled diodes 3

2.2 LEHCEB source design and operation 5

2.3 Comparison of the LEHCEB source with its analogs 9

3 Surface hardening and improvement of the tribotechnical properties of steels and alloys treated by LEHCEB 10

3.1 Peculiarities of the formation of hardened layers in LEHCEB irradiated carbon steels 11

3.1.1 In-depth variation of the microhardness in the affected zone 11

3.1.2 Substructural changes and the mechanism of steel hardening 13

3.2 Modification of the tribotechnical characteristics of steels and alloys 15

3.2.1 Surface hardening and modification of the tribotechnical characteristics of the type ШХ15 steel 15

3.2.2 Effect of the pulsed e-beam treatment of metallic materials on the tribotechnical properties of metal-polymer friction couples 18

3.3 Increasing the durability of cutting tools, including those with wear-resistive coatings, by LEHCEB irradiation [29] 19

3.4 Other examples of using LEHCEBs for improving the operational features of parts and tools 24

4 Conclusion 25

A Designation of steel types 28

References 29

Abstract

The report describes a low-energy, high-current electron beam source designed for modification of the properties of material surface layers, that has no analog in perfomance. The use of a plasma-anode electron gun, special designed cathodes, a bipolar pulsed acceleration voltage, and a guide magnetic field has made it possible to produce 10–30 keV, up to 20 J/cm^2 , wide-aperture electron beams of duration up to 5×10^{-6} s with the reproducibility and uniformity high enough for technological applications.

The results of the application of such beams for surface hardening of steels, improvement of the tribotechnical characteristics of friction pairs, and for increasing the durability of cutting tools including those with nitride coverings.

1 INTRODUCTION

Low–energy (10–30 keV); high-current electron beams (LEHCEBs) are of significant interest for the modification of the properties of material surface layers by pulsed heating. In the process of such thermal processing, annealing, hardening, amorphyzation, melting, mixing of the film and substrate components, and evaporation may occur to result in the appearance of new properties of the surface.

In the mid 70-s, first accounts appeared that pulsed electron beams were used for surface hardening and annealing of metallic materials [1, 2] as well as for annealing of the implanted layers of semiconducting materials [3]. It could be anticipated that LEHCEBs will have become an alternative to laser beams owing to the more efficient conversion coefficient of the stored energy into the beam energy, the more intense absorption of the beam energy and the better controllability of its parameters. However, it has appeared that the production of wide-aperture LEHCEBs showing the cross-sectional uniformity and reproducibility high enough for technological purposes is a complicated problem. The minor advances in solving this problem attained up to now hindered the use of LEHCEBs in technology.

2 A low-energy high-current electron beam source (LEHCEB)

2.1 LEHCEB generation in explosive-emission-cathode plasma-filled diodes

Conventionally, LEHCEBs were produced in direct-action vacuum diodes with explosive-emission cathodes [4, 5]. These diodes are distinguished by their simple design and power supply. The specimen to be irradiated may be mounted on the anode (serve as an anode) or on a collector placed at the end of the drift channel (Fig. 1). Despite certain progress in the application of these diodes for the surface modification of materials, their use for technological purposes remains questionable because of some disadvantages inherent in this type of diode. In such diodes, the beam duration is typically no longer than 10^{-7} s, as it is limited by the time needed for the diode acceleration gap ($d_{k-a} \approx$ 1–2 mm) to be closed by the cathode and anode plasmas expanding to meet each other at a velocity of (2–3)$\times 10^6$ cm/s [5, 6]. Besides, the electron beams formed in direct-action diodes suffer from significant local nonuniformities which reflects the distribution of emission sites over the cathode surface [6].

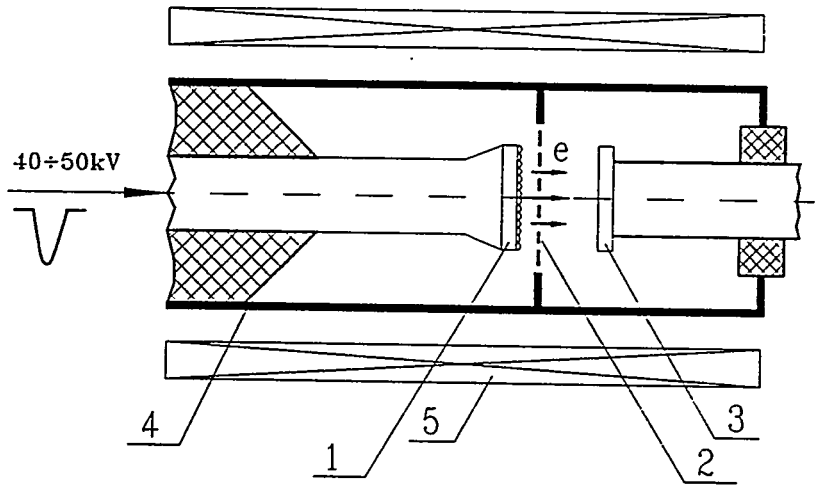


Figure 1: LEHCEB production in a vacuum diode [5]: 1 - explosive-emission cathode; 2 - grid anode; 3 - collector; 4 - vacuum chamber; 5 - solenoid.

Increasing the LEHCEB duration to $\approx 10^{-6}$ s makes it possible to solve the same problems of material modification and, at the same time, to substantially improve the uniformity of the energy

density distribution over the beam cross section.

The beam duration could be increased by proportionally increasing the length of the diode acceleration gap. This way is, however, unacceptable, as it requires that the accelerating voltage be proportionally increased to sustain a high ($\approx 5\times10^5$ V/cm) electric field at the cathode necessary to efficiently initiate explosive electron emission [6].

Promising for the creation of high electric fields at the cathode and the production of high-perveance electron beams are plasma-filled diodes. The authors of Ref.[7] were first to describe a high-current electron gun where the electron beam was formed in the double layer between the explosive-emission-produced cathode plasma and the preliminarily produced anode plasma, passed through the anode hole and got on the collector. With an accelerating voltage of $\approx$ 100 kV, an electron beam of duration $\approx 1.6\times10^{-6}$ s and current up to 40 kA was produced. The beam was highly nonuniform because of strong compression by the self magnetic field. It was used for the production of high-power X-ray flashes.

We have carried out a series of studies [8-11] which have allowed us to refine the mechanism for the formation of an LEHCEB in a plasma-filled diode (including with a guide magnetic field), and extend the accelerating voltage range toward lower values ($U \approx$ 10–30 kV) which makes the electron source X-radiation safe.

The mechanism of the LEHCEB generation in a plasma-filled diode seems to be as follows: The anode plasma (AP) produced by spark sources placed in a circle around the hole in the anode electrode fills the acceleration gap (diode) and the drift space (Fig. 2). The AP density is generally not high ($n_p \approx 10^{11}$–10^{12} cm^{-3}) and the temperature is not in excess of 1–5 eV. Nevertheless, the AP conductivity is high enough for the plasma to acquire the potential of the anode. Once the diode has been filled with plasma (generally in 1–4 μs), an accelerating voltage pulse is applied to the cathode and the electric field is concentrated within the near-cathode layer of ion space charge, whose thickness is much smaller than the cathode-anode distance. It should be noted that in order to stably initiate explosive electron emission uniform throughout the cathode surface with $U \approx$ 20–30 kV and $n_p \approx 10^{11}$–10^{12} cm^{-3}, we had to take some special measures [10] (application of a prepulse to the cathode, resistive decoupling in the cathode, etc.).

Once explosive emission has been initiated at the cathode and the cathode plasma has formed, the accelerating voltage is concentrated across the double layer between the cathode and anode plasmas. The electrons emitted by the cathode plasma are accelerated in the double layer and,

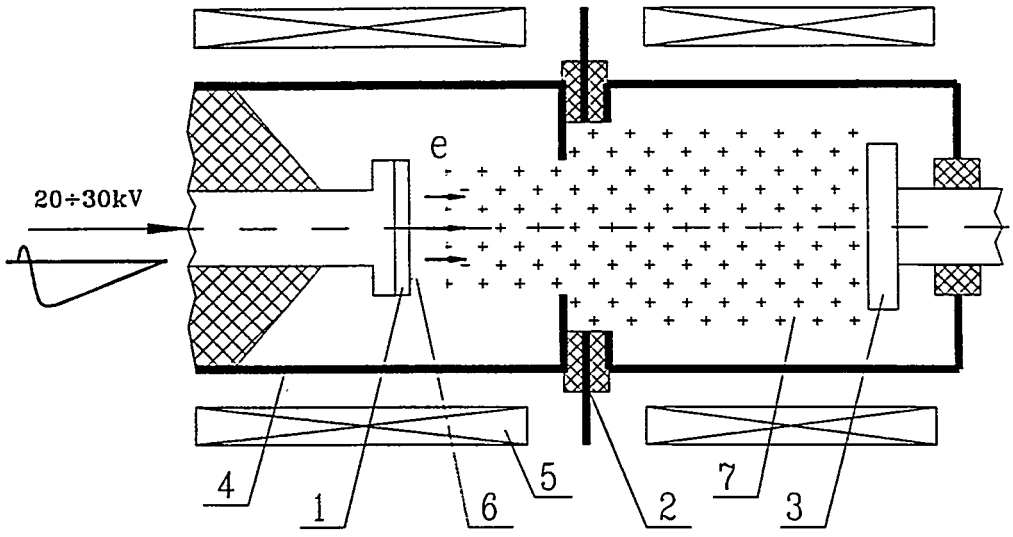


Figure 2: LEHCEB production in a plasma-filled diode [10]: 1- explosive-emission cathode; 2 - anode unit with spark plasma sources; 3- collector; 4- vacuum chamber; 5 - solenoid; 6 - cathode plasma; 7- anode plasma.

having passed through the anode electrode hole, get on the collector. The neutralization of the beam space charge by the AP ions sharply increases the electron flow perveance as compared to the vacuum systems for LEHCEB production and transportation. This allows the beam to be transported to much larger distances, which improves its uniformity and reduces the amount of the cathode and anode erosion products getting on the target. With no guide magnetic field H_z, the creation of a quasi-homogeneous AP column is hampered since the AP is injected predominantly transverse to the field lines. Nevertheless, our investigations [8-11] have demonstrated that for $H_z < 5$ kOe it is possible to obtain a satisfactorily uniform AP density distribution and hence workable beam parameters. Given below is a description of the LEHCEB source we had created, that was used to modify the surface layers of materials and articles.

2.2 LEHCEB source design and operation

A block diagram of the electron source is given in Fig. 3. Cathode 1 is made of an array of resistors consisting of a graphite base and a ceramic envelope [10]. Also used was another type of cathode, a graphite disk covered with a clothlike velvet. The emitting area of the cathode was 5–6 cm in diameter. Anode 2 is made of stainless steel and represents a diaphragm having in its center a hole of diameter 6–7 cm which serves to permit the passage of the beam. The diode acceleration gap

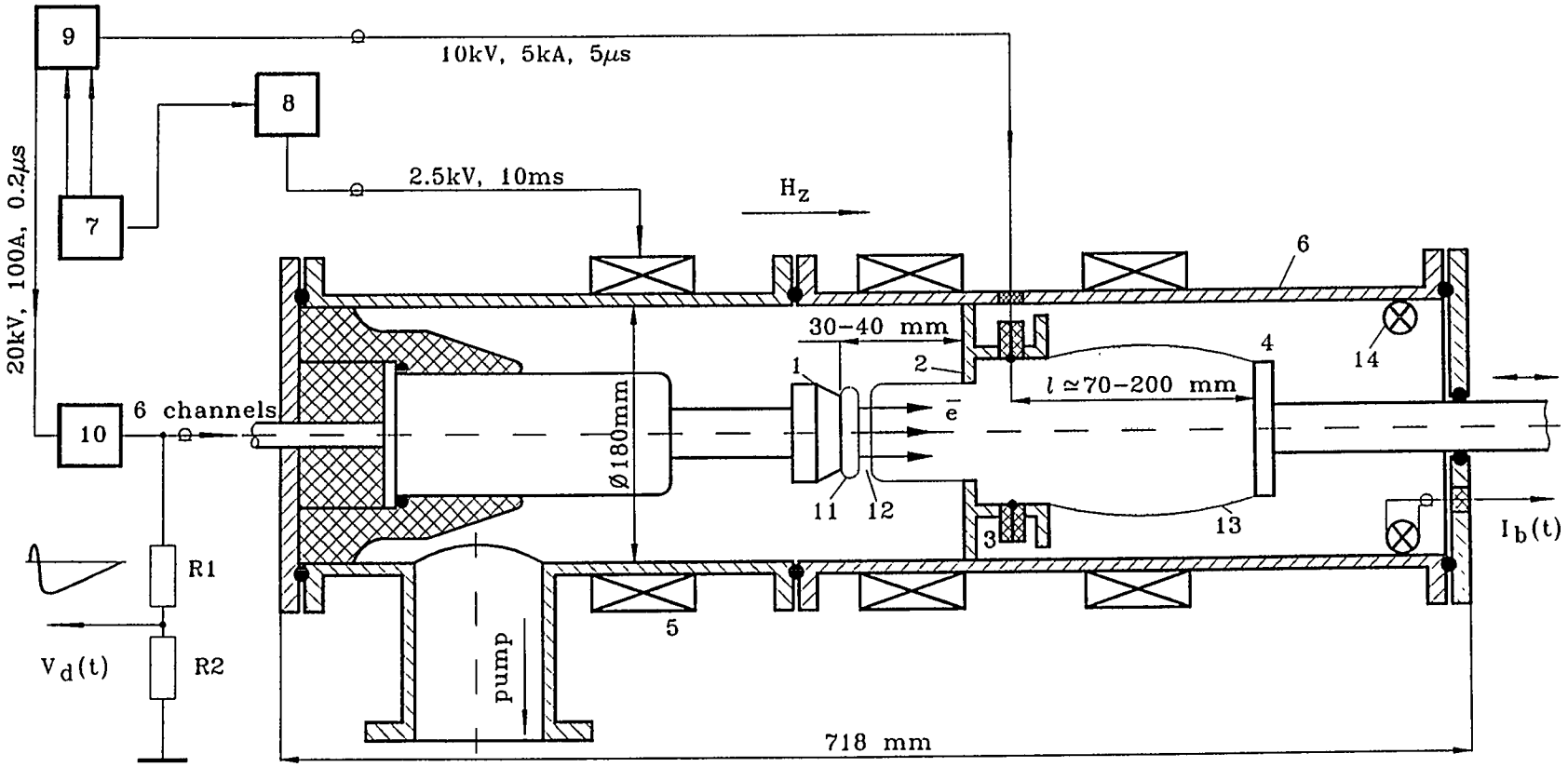


Fig.3. Block-diagram of the electron source. 1 – cathode; 2 – anode; 3 – plasma spark sources; 4 – collector; 5 – solenoid; 6 – vacuum chamber; 7 – control unit; 8 – solenoid power supply unit; 9 – trigger unit; 10 – pulse generator; 11 – cathode plasma; 12 – double layer; 13 – anode plasma; 14 – Rogovsky coil; R1, R2 – voltage monitor.

can be made 1.5–4 cm long. Behind the anode 2, plasma sources 3 are placed around the hole. Each plasma sourse consists of a resistor with its end grinded out to the graphite base. Plasma was generated as a result of a flashover along the surface of the resistor ceramic envelope, which went over into an arc discharge. Thus, the anode plasma mainly contains carbon ions. The electron beam was transported through the anode plasma to collector 4 placed at a distance of 5–20 cm from the plasma sources. The collector also serves as a holder for the article under treatment. To prevent the electron beam from pinching, an applied magnetic field up to 0.3 T is used, which is created by solenoid 5 placed outside vacuum chamber 6.

Initially, a trigger pulse from control unit 7 is applied to solenoid power supply 8. In 4.5×10^{-3} s, when the magnetic field reaches its maximum, a trigger pulse from unit 7 is applied to two-channel ignition unit 9. An aperiodic current pulse of amplitude 2–5 kA and duration 5×10^{-6} s is applied from the first channel of unit 9 to the plasma sources. Then, with a delay of $(1–3)\times10^{-6}$ s, an iginting pulse is applied from the second channel of unit 9 to high-voltage pulse generator 10. The generator produced a pulse of special form, consisting of a short positive prepulse and a negative main accelerating voltage pulse. The generator capacitance was $(0.4\text{-}1.2)\times10^{-6}$ F. The use of a prepulse in combination with the above-described types of cathode and external guide magnetic field makes it possible to produce uniform electron beams at an accelerating voltage of $\approx$ 10 kV [8-11].

The diode voltage was measured by a resistive voltage divider. A Rogowski coil was used to measure the diode current and the collector current. The energy density distribution over the beam cross section was measured using a sectioned calorimeter based on calibrated thermal resistors of the KMT-17 type. The beam autographs were taken on titanium and stainless-steel foils.

Figure 4 gives typical waveforms of diode voltage V_d , diode current I_d , and collector current I_b . The high-current diodes has the feature that the electrons in the beam produced show a continuous energy spectrum ranging from a maximum corresponding to the accelerating voltage peak to zero. This feature should be taken into account in analyzing the thermal conditions in the surface layers of the treated material. The thermal conditions can be varied in a wider range than it is possible with pulsed laser or ion beams by varying the pulse peak electron energy and duration. By varying the n_p profile, the cathode shape, and the guide magnetic field configuration, we were able to attain a satisfactorily uniform energy density distribution over the beam cross section. A typical cross-sectional energy density distribution obtained with the use of a sectioned calorimeter is given in Fig. 5. The beam autographs on foils represent uniformly molten-off circular regions whose

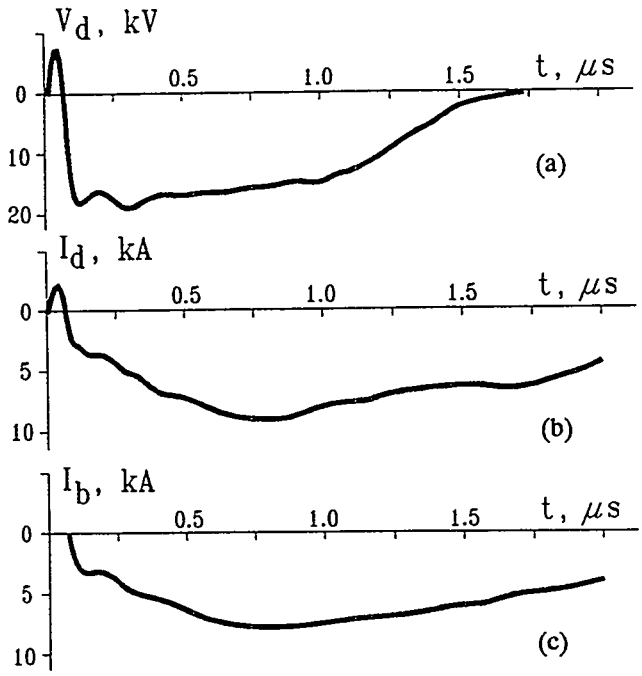


Figure 4: Typical waveforms of diode voltage (a), diode current (b) and collector current (c).

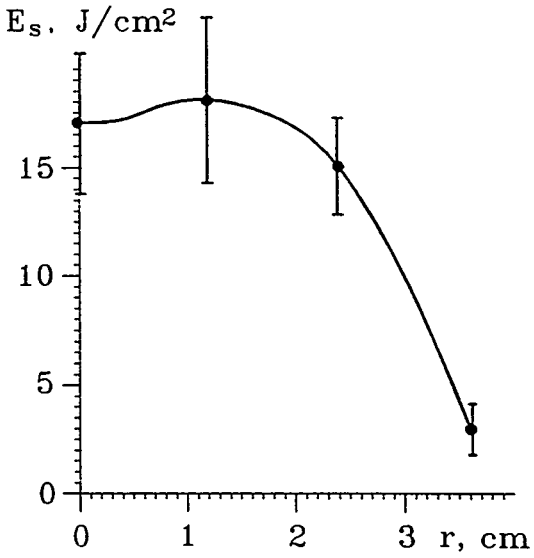


Figure 5: Beam-cross-section energy density distribution.

diameter corresponds to the beam diameter. The back side of the foil shows no visible changes. This is evidence that the LEHCEBs is a surface energy source.

The efficiency of conversion of the energy stored in the pulse generator into the beam energy was about 30–40%.

2.3 Comparison of the LEHCEB source with its analogs

Table 1: parameters of devices for pulsed electron-beam thermal treatment of materials.

Parameters of devices	[4]		[12]	[13]	Our source
	Type 1	Type 2			
Capacitor charge voltage, kV	5–300	5–100	10–50	30–200	10–40
Beam current, кA	1–40	1–10	1–6	3–15	5–15
Pulse duration, μs	0.08	0.06	0.05	0.05–0.2	0.2–5
Maximum beam energy, J	300	20	20	100	200
Beam cross section, cm^2	5–100	5–25	1–25	5–15	5–40
Acceleration gap length, cm	0.1–0.2	0.1–0.2	0.1–0.2	0.1–0.4	1.5–4
Distance from anode to collector, cm	<1	< 1	<1	<2	5–20

Table 1 lists the characterictics of the known electron sources for pulsed electron-beam thermal treatment of material surface layers and the source described above.

A comparison of these data shows that the described electron source offers the following advantages:

(1) the capability of producing LEHCEBs of long duration;

(2) radiation safety;

(3) simple high-voltage pulsed equipment and technology;

(4) the possibility to place the article under treatment at a significant distance from the anode.

For the two-year-long service of the source more than 2×10^5 shots have been performed with no serious failures that would require labor and time consuming repairs. The source is simple to operate and needs a vacuum as low as 10^{-4} Torr. Photographs of the entire setup are given in Fig. 6.

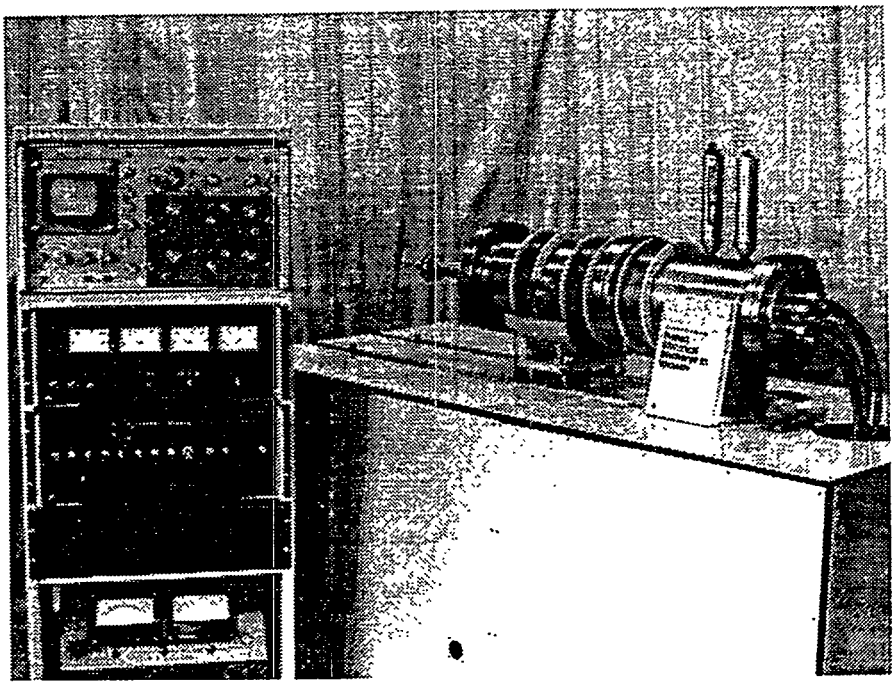


Figure 6: The LEHCEBs source.

3 Surface hardening and improvement of the tribotechnical properties of steels and alloys treated by LEHCEB

The surface condition determines many of the physical, chemical and mechanical properties of a material. For instance, the destruction of a workpiece in the process of service starts more often from its surface due to corrosion, wear, fatigue cracking, etc. Therefore, one of the urgent problems in material science and technology is purposeful modification of material surface layers.

As mentioned above, a highly efficient means for this modification is offered by low-energy, high-current electron beams. This section will describe the principal features and the qualitative mechanism for the formation of the hardened layers in LEHCEB irradiated steels. Some preliminary results indicating the promise of using LEHCEBs for surface treatment of articles and tools,

namely for hardening steel or alloy-made articles, including the improvement of the tribotechnical characteristics of friction couples, and for increasing the strength of cutting tools.

3.1 Peculiarities of the formation of hardened layers in LEHCEB irradiated carbon steels

It has been shown [14-21] that in the surface layer of a metallic material exposured to an LEHCEB a zone with modified physical, chemical, and mechanical properties is formed. The changes in the structure and phase state and in the mechanical properties of the material in the depth of the affected zone are related to the fast (up to about 10^9 K/s) heating of the surface layer up to the melting point and over and to its subsequent fast (up to about 10^9 K/s) cooling through heat conduction as well as to the generation and propagation of a stress wave appearing due to thermoplasticity [18, 22]. Adjacent to the surface is a heat affected zone (HAZ) which is formed mainly due to high temperatures. Beyond the HAZ, a substantial part is played by the deformation processes caused by the propagating stress wave. By varying the LEHCEB parameters, it is possible to vary the contribution of each factor to the total hardening effect and thus functionally grade the material structure and properties.

Temperature calculations and experiments have shown that the most interesting for applications are LEHCEBs of duration $\tau_p \approx 10^{-6}$ s and power density 10^6–10^7 W/cm^2. For $\tau_p < 10^{-7}$ s, the stress wave amplitude becomes substantially higher, which increases the probability of destruction for brittle and high-strength materials, such as semiconductors and hardened steels. For $\tau_p > 10^{-5}$ s, on the contrary, the probability of the formation of high-strength metastable structures decreases due to a decrease in the rates of heating and cooling of the surface layer. It should also be noted that in fact no studies on surface modification were performed with laser and ion beams having parameters close to those of LEHCEBs, which is related to the fact that no sources of such beams with the required parameters are available [23, 24].

3.1.1 In-depth variation of the microhardness in the affected zone

Detailed measurements of in-depth microhardness H_μ profiles have made it possible to reveal some regularities which we consider on the example of steel 45 irradiated with an LEHCEB with $\tau_p \approx 0.8$ μs [17].

1. Upon irradiation of a preliminarily quenched steel having the structure of martensite, a

hardened zone of thickness up to 250–300 μm with two pronounced maxima of microhardness H_μ^m is formed in the surface layer (Fig. 7). In this hardened zone four characteristic regions can be distinguished. The first region adjacent to the surface is in fact a HAZ. In regions II and IV, the microhardness H_μ^m reaches abnormally high values ($\approx$ 1600 kg/mm^2). The microhardness in region III is close to or somewhat higher than the original microhardness of the material.

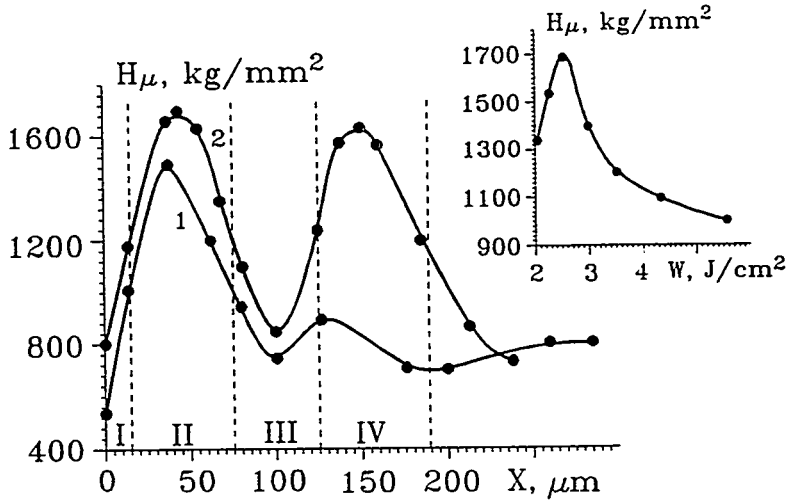


Figure 7: In-depth distribution of microhardness for a pre-hardened steel 45 specimen irradiated by an LEHCEB with τ_p = 0.7 μs, E_s = 2.5 J/cm^2 (1 - N = 1, 2 - N = 300; inset - the maximum microhardness in region II as a function of energy density for N = 300.

2. As the number of shots N is increased, the degree of hardening increases with the highest rate of increase in the region of the second maximum (see Fig. 7).

3. Increasing the pulse interval decreases the maximum values of microhardness in regions II and IV and causes these regions to shift into the bulk of the target (Fig. 8).

4. With increasing energy density the run of the curves $H_\mu(x)$ does not change. In this case the maximum H_μ^m values initially increase reaching a maximum of about 1700 kg/mm^2 at E_s = 2.5 J/cm^2 and then decrease (see Fig. 7, the inset). Examination of the surface state has shown that the H_μ^m maximum is achieved in the mode where the surface was initially molten off.

5. As the tempering temperature for a preliminary quenched steel is increased, the hardening retains its nonmonotonic character but the degree of hardening decreases. LEHCEB irradiation of an unquenched steel results in only a slight increase in microhardness (H_μ = 300–400 kg/mm^2) at a depth of about 30 μm.

As the pulse duration was incresed to 5 μs, the run of the curves $H_\mu(x)$ remained unchanged;

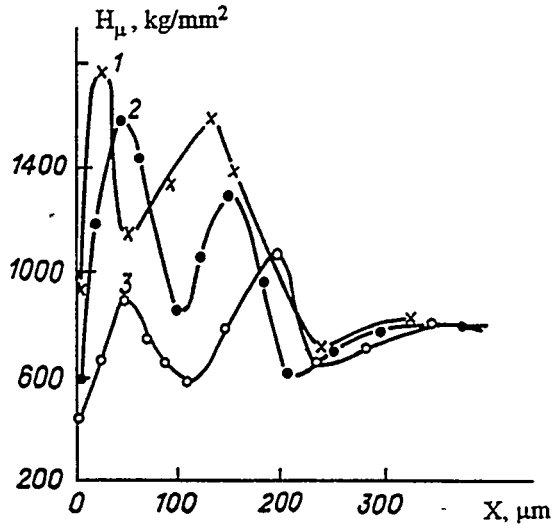


Figure 8: In-depth distribution of microhardness for a as-hardened steel 45 samples irradiated by an LEHCEB at different intervals between pulses: Δt = 6 (1); 15 (2) и 60 s (3); (τ_p = 0.7 μs, E_s = 2.5 J/cm^2, N = 200).

however, the microhardness maxima shifted into the specimen bulk and the degree of hardening decreased in all regions. As a contrast, in the subsurface layer whose thickness increased from 10 to 20 μm with increasing τ_p the microhardness was found to reduce compared to its initial value, that is martensite tempering took place.

Upon LEHCEB irradiation of alloyed steels (ШХ15, X12M, P6M5 types and other), most of the above regularities retain; the structures with an abnormally high microhardness produced therewith are more resistive to wear and tempering compared to carbon steels.

3.1.2 Substructural changes and the mechanism of steel hardening

As shown in Sec. 3.1.1, LEHCEB irradiation hardens most efficiantly preliminary quenched steels having the structure of martensite. An investigation of the structure and phase state of the affected zone in steel 45 irradiated in the mode with initial melt off of the surface (0.8 μs, 2.5 J/cm^2) [19, 20] has shown that the HAZ has a thickness of about 10 μm. This zone consists of three characteristic layers; the first one of thickness $\approx$ 0.2 μm has been formed as a result of superfast ($\approx 10^9$ K/s) quenching from melt. This layer has a nanocrystalline structure (grain size 30–100 nm) and consists off γ- and α- phases. The absence of martensite crystals in this layer is related to the fact that the grain size is smaller than the critical size ($\approx 10^{-4}$ cm) required for martensite to nucleate [25]. It should be noted that a similar nanocrystalline structure is formed in the surface layer of 0-1-type

tool steel (USA), preliminarily quenched from melt, on irradiation with an intense ion beam [26].

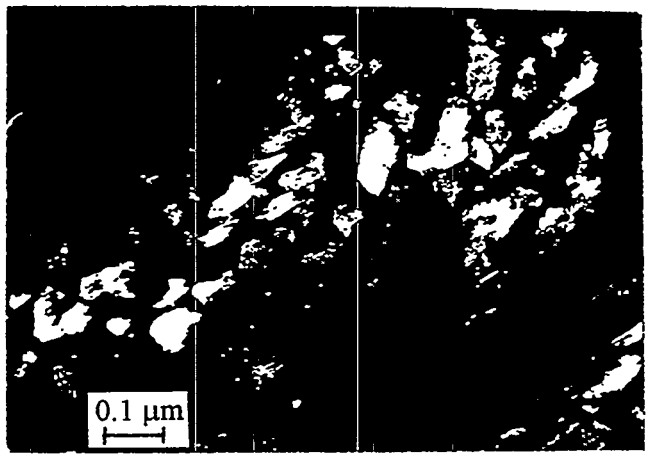


Figure 9: The TEM dark-field image in reflex [110] α-Fe of presurface layer of steel 45, quenched from the melt($\tau_p = 0.8$ μs, $E_s = 2.5$ J/cm^2).

Beyond the HAZ, the structural and phase changes are entirely determined by the interaction of the bipolar stress wave with the material. Layer-by-layer electron microscopy [18, 20] has shown that in regions II, III, and IV (see Fig. 7) substantial changes in the defect structure of the martensite phase take place.

In the region of the first maximum, an increased dislocation density, twinning and fragmentation of martencite crystals, and enhanced remote stress fields are observed. Evaluation of the contribution of each of these factors to the net hardening effects [20] has shown that the main contribution is from the substructural hardening due to the formation of small-angle fragment boundaries and lath martensite crystals. The formation of a highly fragmented and highly defected structure may in turn lead to a redistribution of carbon atoms between the bulk and the boundaries of the fragment. As a result, the carbon concentration in the defective sites may occur to be sufficient for the formation of cementite. The extra hardening of the modified layer may result from the accumulation of abnormally large anisotropic deformation caused by a multiple action of the stress wave which provides in fact a reversed loading of duration about 10^{-6} s. These factors are just responsible for the formation of regions with an abnormally high microhardness.

3.2 Modification of the tribotechnical characteristics of steels and alloys

Tribotechnics covers a set of problems concerned with friction and wear. In practice, resistance to wear is more important than hardness, and the former is not always determined unambiguously by the latter. To elucidate the effect of irradiation on the tribotechnical characteristics, metal-metal [27] and metal-polymer [28] friction couples conventionally used in cryogenic vacuum pumps were chosen.

3.2.1 Surface hardening and modification of the tribotechnical characteristics of the type ШХ15 steel

Specimens of the type ШХ15 steel (1% C, 1.5% Cr) of size 2×8×8 mm with an HRC hardness of 58–60 were irradiated with an LEHCEB having the parameters as follows: pulse duration τ_p = 0.15–0.8 μs, average electron energy 10–20 keV, energy density E_s = 0.6 J/cm^2, and number of pulses N = 200–300. For every fixed pulse duration, the energy density corresponded to an initially molten-off surface. As a result of the cyclic beam action, a hardened zone similar to that observed in the steel 45 specimens was formed (see Subsec. 3.1.1).

For the sake of comparison, in some test specimens were irradiated with a scanning continuous electron beam with an accelerating voltage of 15 kV, a beam current of 50–60 mA, and a scanning speed of 3 m/min. The beam diameter was varied within the limits 1–2 mm, which allowed the surface layer to be quenched from both the solid and the liquid state. The hardening tracks were marked with a step of 2–3 mm, i.e. without overlapping, normal to the line of intersection of the operating surface. As a result, a discrete periodically hardened structure was formed on the operating surface.

The wear rate of irradiated specimens was measured on the frictional machine CMT-1. The frictional scheme that models well the actual conditions of the operation of the friction units in cryogenic vacuum pumps is shown in Fig. 10a served as counterbodies were cylinders of diameter 45 mm and height 20 mm made of the type 12XH3A steel (0.12% C, 0.8% Cr, 3% Ni), having subjected to cementation to a depth of 0.8 mm, quenching, and tempering (HRC 55). Sliding was performed with a load of 100 MPa at a velocity of 1 m/s in the presence of two types of lubricant. The wear was not in excess of 5 μm, which corresponded to the requirements for this friction unit. The wear rate was found by weighting.

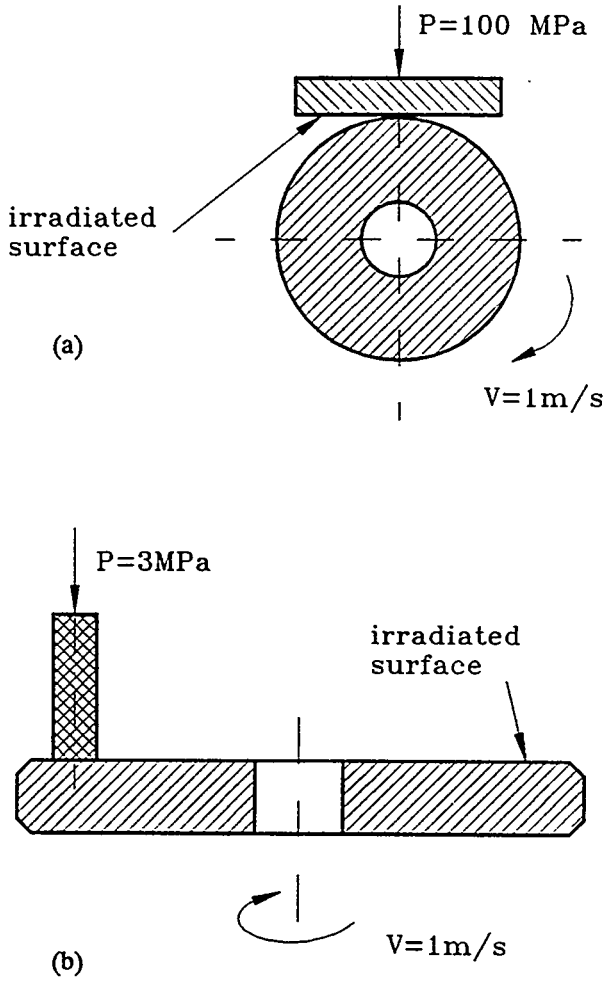


Figure 10: Friction schemes used for measuring the tribotechnical properties of steels and alloys irradiated by a LEHCEB.

When the first-type lubricant (type ВРЖ-1-1 oil containing 0.2% of the type МКФ-18 additive) was used, the wear rate of irradiated (0.7 μs, 2.5 J/cm^2, 300 pulses) plates decreased 1.5-fold and the friction torque decreased 1.7-fold compared to reference (unirradiated) couples.

The test results for the same friction couple in the CM-028-type oil with various modes of electron-beam treatment of plates made of the ШХ15 type steel are listed in Table 2 (signs + and/or - indicate the presence or absence of irradiation in the given mode)

From this table it can be seen that the least wear of the specimens corresponds to two modes of treatment: a continuous irradiation (quenching from melt) and a pulsed irradiation (0.7 μs, 2.5 J/cm^2). For this pulsed mode no wear could be found by weighting for some specimens. The wear rate of the counterbodies (cylinders) therewith decreased about threefold. The improvement of the

Table 2: Effect of e-beam treatment on tribological characteristics of metallic friction couples.

Irradiation modes				Wear rate, 10^{-4}, g/h		Friction torque, N×m
Continuous	Pulsed			specimen ШХ 15	counter-body	
	τ_p, μs	E_s, J/cm^2	N			
-	-	-	-	0.2	1.7	0.43
+ (without melting)	-	-	-	0.1	0.2	0.62
+ (with melting)	-	-	-	0.6	1.2	0.51
-	0.15	0.6	100	0.33	0.45	0.50
-	0.3	1.2	100	0.4	0.8	0.5
-	0.7	2.5	200	0	0.5	0.62
+ (without melting)	0.7	2.5	100	0.3	0.7	0.69
- (with melting)	0.7	2.5	100	0.3	1.3	0.6

tribological characteristics is related in the main to the formation of a homogeneous microcrystalline structure with a smoothed relief by fast quenching from melt.

In the rest modes, electron beam irradiation either does not improve the tribotechnical characteristics of the friction couple under testing of deteriorates them. The deterioration may be associated with the increased friability of the quenched structures having appeared in the surface layer upon electron-beam treatment. From Table 2 it can also be seen that the wear of counterbodies is observed to reduce for almost all modes of treatment, however the friction torque therewith increases to some extent. The latter seems to be related to the fact that the melt-off of the surface smooths out microprotrusions thereby increasing the contact area of the rubbing bodies.

The results obtained suggest that with a proper choice of the LEHCEB parameters one can substantially improve both mechanical and tribotechnical properties of metallic friction couples.

3.2.2 Effect of the pulsed e-beam treatment of metallic materials on the tribotechnical properties of metal-polymer friction couples

The more stringent requirements placed on metal-polymer friction couples used in microcryogenic engineering are dictated by the extreme conditions of their operation (absence of lubricant, wide temperature limits). In view of this a search for new techniques for treating metallic counterbodies is currently continued with the aim to increase the lifetime of this type of friction units.

This subsection describes the results of an investigation of the possibility to improve the mechanical and tribotechnical characteristics of metal-composite (based on carbon and PTFE) systems by treating the counterbodies with LEHCEBs. Used as counterbodies were plane specimens (disks of diameter 50 mm and thickness 5 mm) of steels (types steel 45, 30X13, 38XMIOA, and 12X18H10T) and the type BT6 titanium alloy (Ti-6%Al-4.5%V) with an initial roughness R_a = 0.2-0.4 μm. The operating surfaces of the counterbodies were irradiated with LEHCEBs in the initial melt-off modes (0.7-0.8 μs, 2-3 J/cm^2, 10-200 pulses). The wear rate of polymer specimens (cylinders of diameter 5 mm and height 10 mm) were determined by the "pin-disk" scheme (Fig. 10b) with a load of 3 MPa and a sliding velocity of 1 m/s.

The measurements have demonstrated that a cyclic electron beam action results in a surface hardening of steel counterbodies. The hardened layer thickness reaches 200–250 μm and the degree of hardening strongly depends on the material and the preliminary thermal treatment. In martensitic steel the highest degree of hardening (up to ~1500 kg/mm^2) is achieved, like in carbon steels, not at the surface but at a depth of 30–50 μm. For the 12X18H10T type austenitic stainless steel the microhardness maximum is observed at a depth of about 70 μm (Fig. 11).

For titanium alloys, LEHCEB irradiation allows an increase or decrease in the surface layer microhardness depending on the original structure of the alloy and the character of preliminary or subsequent thermal treatment.

The wear rates of the polymer and the friction coefficient measured for various counterbodies treated with LEHCEBs are listed in Table 3. From this table it can be seen that electron-beam irradiation of counterbodies either does not reduce or increase the wear of the polymer. The increase in the wear of the polymer is related to the enhanced roughness of its surface after quenching from melt. Actually, when the operating surface of the polymer was subsequently treated mechanically (finished), its wear was the same as that measured prior to irradiation. In view of the fact that the LEHCEB treatment increases the hardening of the surface layer, it can be concluded that in order

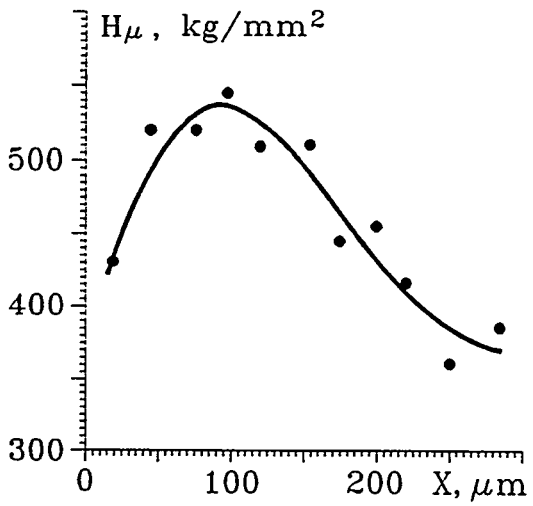


Figure 11: In-depth distribution of the microhardness of a 12X18H10T steel specimen irradiated with a LEHCEB ($\tau_p = 0.7$ μs, $E_s = 2.7$ J/cm^2, N = 200).

to improve the mechanical properties of this type of friction couples it is necessary to finish the operating surface after irradiation.

As a contrast, the surface melt-off of titanium alloys reduces the wear rate of the polymer. This is related in the main to the smooth-out of the initial relief (Fig. 12). Note that this smooth-out effect was also observed for titanium alloys irradiated with intense ion beams [26]. Moreover, the irradiating LEHCEB efficiently cleans the surface layer from impurities (oxygen, carbon). Thus, multiple melting and crystallization result in the formation of a homogeneous fine structure with a smoothed surface relief and free from hard titanium oxides and carbides.

Thus, the LEHCEB irradiation of metallic counterbodies in the surface melt-off modes improves the mechanical and, when using titanium alloys, the tribotechnical characteristics of metal-polymer friction couples.

3.3 Increasing the durability of cutting tools, including those with wear-resistive coatings, by LEHCEB irradiation [29]

Increasing the durability of cutting tools is one of the most urgent concerns in machine building. Since LEHCEB irradiation allows efficient hardening of the surface layer of steels as well as doping of this layer from a preliminary applied coating [30] not changing essentially the original geometry of the article, it would be natural to suppose that this type of treatment could be used to increase the

Table 3: Effect of LEHCEB treatment on the tribological characteristics of metal-polimer friction couples.

Counterbody material	Hardness prior to irradiation, HRC	Wear rate polymer, 10^{-4}, g/h	Friction coefficient
steel 45	46	0.6	0.07
steel 45*	-	1.15	0.08
30X13	50	0.30	0.06
30X13 *	-	0.65	0.07
38XMЮA	47	0.36	0.05
38XMЮA*	-	0.38	0.05
12X18H10T	-	0.67	0.06
12X18H10T*	-	0.89	0.11
BT6	-	0.42	0.02
BT6	-	0.35	0.02

* - after irradiation

service life of conventional cutting tools (drills, mills), including those coated with high-melting-point nitrides.

The durability of cutting tools was examined on drills of diameter 6.8 mm and length 120 mm manufactured from the type P6M5 high-speed steel. To reduce the spread in starting durability, drill lots with a small spread ($\pm 3\%$) in coercitive force were selected. The phase composition and the microhardness in the beam-affected zone were investigated on plane specimens of the P6M5 steel of diameter 20 mm and thickness 10 mm, having subjected to conventional thermal treatment (quenching and triple tempering).

Some plane specimens and drills were coated with TiN using the plasma ion deposition technique on the Bulat-type installation HHB6.6-И1. The surfaces of plane specimens and drills were preliminarily subjected to chemical cleaning. Then they were placed in the installation chamber where ionic cleaning, heating, and deposition of the wear-resistive coatings were performed. The coating was deposited with an arc current of 100 A, accelerating voltage of 200 V, and operating gas (nitrogen)

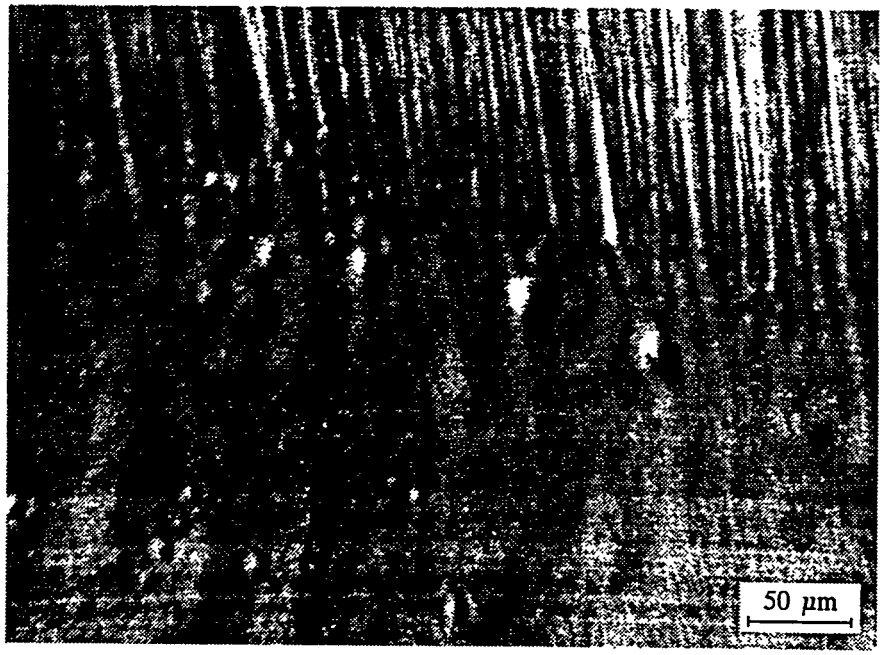


Figure 12: The SEM image of surface of BT3-1 titanium alloy irradiated by a LEHCEB; $\tau_p = 0.7$ μs, $E_s = 2$ J/cm^2, $N = 10$ (seen on the top are marks of original mechanical processing near the beam edge).

pressure of 3×10^{-3} mm Hg. The coating thickness therewith was 3–4 μm.

Some other specimens and drills were coated by the same technique with zirconium-hafnium nitride (80 vol.% Zr and 20 vol.% Hf) to a thickness of 3–4 μm.

Once TiN and (Zr+Hf)N coatings had been deposited, the drills were irradiated with an LEHCEB having the parameters as follows: $\tau_p \approx 0.7$ μs, $E_0 \approx 15$ keV, and $E_s \approx 2.5$ J/cm^2. The pulse interval was 10 s and the number of pulses was $N = 5$–200. Plane specimens with the same coatings were treated with an electron beam separately. For the sake of comparison, some drills on delivery and some uncoated specimens were treated only with an LEHCEB having the above parameters.

The drills were tested for durability on a drilling machine of the 2H125 type. Subjected to mechanical treatment was the type 12X18H10T stainless steel; the treatment mode was as follows: the cutting speed 10 m/min, the advance speed 0.1 mm/rev, the drilling depth 12 mm, the cooling agent 5% water solution of the type ET-2 emulsion. Taken as a characteristic of the durability of the drills was the time in which the wear of the back surface reached 0.8 mm. The wear magnitude was determined using the type ИМЦ 150×50.6 toolmaker's microscope with digital indication. The measurements were accurate to 0.002 mm.

Plane specimens were examined after irradiation by measuring the depth distribution of microhardness using the type ПМТ-3 hardness meter with a load of 50 g and by determining the change in the phase composition in a surface layer of thickness $\approx$ 12 μm using the type ДРОН-1 X-ray diffractometer.

The measurements have shown that in this case, like in the case of martensitic carbon steels, the LEHCEB action on the type steel P6M5 specimens results in the formation of a hardened zone of thickness up to $\approx$ 250 μm with two maxima of microhardness at depths of about 50 and 150 μm. At the surface in itself, the change in microhardness is only slight, if at all. Measurements of microhardness at a depth of 20 μm in the type P6M5 steel specimens with and without titanium nitride coatings, treated with LEHCEBs are listed in Table 4.

Table 4: Effect of e-beam treatment on the microhardness of the surface layer for specimens made of P6M5 steel with wear-resistive coatings.

Specimen treatment	Microhardness, kg/mm^2	
	before irradiation	after irradiation
Quenching + tempering	780	950
Quenching + tempering + deposition of TiN	770	1210
Quenching + tempering + deposition (Zr+Hf)N	790	1280

From Table 4 it can be seen that using only LEHCEB irradiation increased the microhardness of the surface layer by a factor of about 1.2. Doping from a preliminarily deposited TiN coating provided an additional increase in microhardness by a factor of about 1.3.

The test results for drills with and without TiN coatings, treated with LEHCEBs ($N = 50$), are listed in Table 5.

From Table 5 it can be seen that the durability of the uncoated drills increased on irradiation by a factor of about 1.5. Irradiation of the TiN-coated drills increased their durability 1.6 times as compared to the drills with the same coatings but not subjected to irradiation.

Table 5: Effect of e-beam tretment on the durability of drills made of P6M5 steel with wear-resistive coatings.

Drill teratment prior to irradiation	Drill durability, min	
	before irradiation	after irradiation
Quenching + tempering	11	17.2
Quenching + tempering + deposition TiN	14.3	23.2
Quenching + tempering + deposition (Zr+Hf)N	17.1	28.4

It should be noted that increasing the number of pulses over N = 10–50 did not increase the efficiency of the electron-beam treatment of drills. Therefore, subsequently the treatment was carried out as a rule with $N = 50$.

Irradiation of specimens with (Zr + Hf)N coatings increased the microhardness of the surface layer by a factor of about 1.6 as compared to the starting one. The durability of drills with the same coatings in turn increased on irradiation about 1.7 times as compared to unirradiated tools.

Preliminary investigations have shown that for the type P6M5 steel with TiN or (Zr + Hf)N coatings treated with an electron beam with the given parameters, the temperature of the surface layer is somewhat in excess of the melting point of the steel ($\approx$ 1450 °C) and noticeably exceeds the eutectic temperature of the Fe-Ti (1085 °C) and Fe-Zr-Hf ($\approx$ 900 °C) systems. As a result, the thin steel layer disposed directly beneath the ceramic coating melts, the titanium nitride (zirconium-hafnium nitride) dissolves in the liquid phase, and the surface layer of the material becomes enriched with titanium and nitrogen (or zirconium, hafnium, and nitrogen). Actually, prior to irradiation the tools and the test specimens had a yellow color typical of nitrides. This color persisted after the action of one or two pulses, but as the number of pulses was increased, it in fact disappeared and the surface of the specimens and drills acquired a luster typical of molten-off steels.

X-ray structure analysis has shown that whereas the TiN lines can be seen on X-ray pictures of the coated specimens, these lines practically disappear on irradiation of the specimens with 10 pulses.

The saturation of the surface layer of steel articles with titanium and nitrogen, and notably with zirconium, hafnium, and nitrogen, substantially increases their microhardness and wear resistance. In order that the doping be efficient, the ceramic coating should be thin since only then it has time to dissolve in the substrate melt on pulsed electron-beam irradiation. The possibility of the liquid-phase mixing of coating-base systems with formation of metastable phases, including amorphous phases, has been demonstrated on the example of a Ta-Fe system [30].

Another decisive factor in increasing the microhardness of the surface layer and the wear resistance of cutting tools is the substructural hardening of the material under the cyclic action of the bipolar stress waves initiated by the LEHCEB due to thermoelasticity [18, 20].

Thus, the LEHCEB treatment of cutting tools increases their microhardness and wear-resistive. Preliminary deposition of wear resistance ceramic coatings of varied composition and properties noticeably increases the efficiency of pulsed electron-beam treatment.

Analysis of the data on the action of pulsed laser [31] and ion beams [32] on solid alloys available in the literature and our preliminary experiments show that the LEHCEB treatment also show promise for increasing of the durability of ceramic-metal (cemented carbides) cutting tools, including those with preliminarily deposited wear-resistive coatings.

3.4 Other examples of using LEHCEBs for improving the operational features of parts and tools

In optimum modes of LEHCEB hardening of steels, the thickness of the molten layer is not larger than 1 mm. So this treatment may serve as a final technological operation in manufacturing valuable pieces and tools.

Industrial tests have demonstrated that the pulsed electron-beam treatment is promising for increasing the lifetime of cutting tools (drills, milling cutters) and tools used in plastic metal working (drift-pins, punches). The results obtained in specific LEHCEB applications for increasing the lifetime of tools are listed in Table 6.

Figure 13 presents sample tools whose lifetime increased 2–3-fold after LEHCEB treatment. As a contrast to the above-described friction units, where the principal part is played by a thin surface layer, the lengthening of the lifetime of cutting and die-stamping tools occurs due to the hardening of thicker (up to 0.3 mm) layers of the material.

In general, the results obtained allow the conclusion that using the pulsed electron-beam treat-

Table 6: Applications of low-energy high-current electron beams for decreasing the wear of pieces and tools.

Application field	Material	Treatment conditions	Result
Drills for stainless steels and titatium alloys	High-speed steel covered with titanium nitride	0.8 μs, 15 keV, 2.5 J/cm^2, 50 shorts	1.7-fold increased lifetime
Milling cutters for carbon steels	Ibid	Ibid	Ibid, 2.5-fold
Knifes of industrial stichers	Steel with 0.8% C	Ibid	Ibid, 2-fold
Punches for making holes in brass sheet	Steel with 1% C	Ibid	Ibid, 3-fold
Drift-pins for smoothing inner cylindrical surfaces of roller-bearing-steel martrices	Steel with 1% C and 1.5% Cr	Ibid	Ibid, 2-fold

ment for improvement of service characteristics of parts and tools, including those with protective coatings, is promising.

4 Conclusion

The report describes the techniques for production of LEHCEBs and the principle of operation and the design of a LEHCEB source whose parameters have not still been achieved on other sources of this type throughout the world. Investigations of the surface modification of metallic materials irradiated with LEHCEBs have shown that:

(1) For the cyclic electron beam action on carbon and alloy steels, the phenomenon of abnormally deep (to $\sim$ 300 μm) and strong (to $\sim$ 1800 kg/mm^2) hardening accompanied by their near-surface layer with a nanocrystalline structure has been discovered.

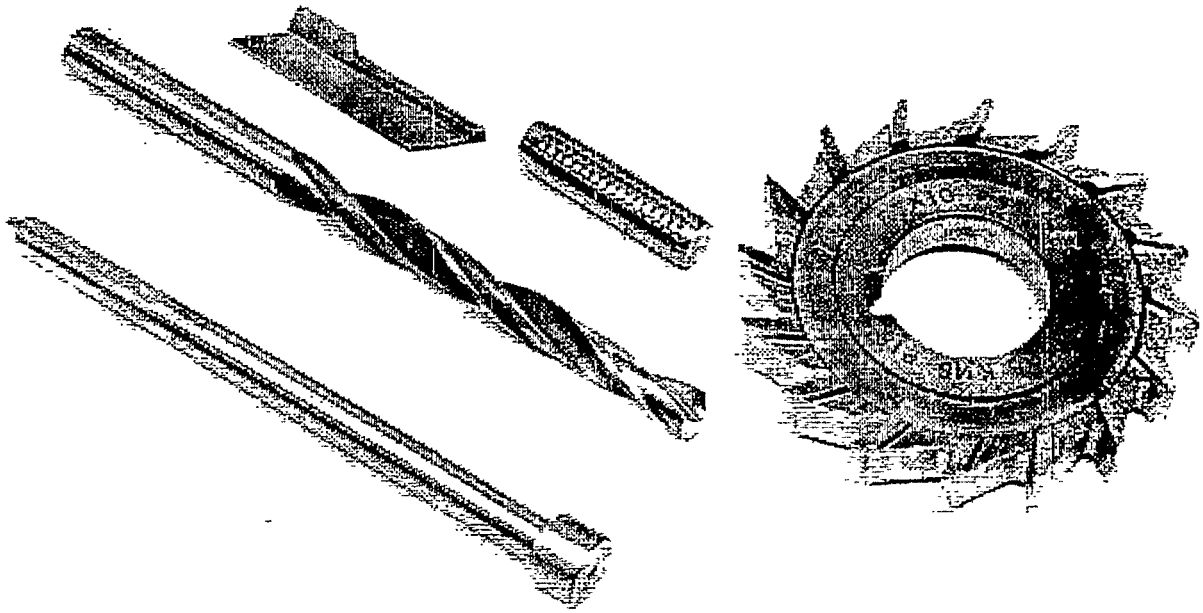


Figure 13: Cutting and plastic-metal-working tools irradiated by a LEHCEB.

(2) The irradiated surfaces of steels have a smoothed microrelief and show increased wear resistance.

(3) The LEHCEB irradiation of cutting tools made of high-speed steel and covered with nitrides of high-melting-point elements increases the tool microhardness and lifetime.

These results form the basis for the development of an unique electron-beam technology for surface modification of parts and tools manufactured from tool steels and hard alloys.

Subsequently, within the frames of this contract it is planned to use LEHCEBs to improve the service characteristics of parts and tools made of tool steels and hard alloys, including those with wear-resistive coatings, by creating interface regions where the material composition, structure, and properties vary gradually from the coating to the base. An option for the production of this functionally graded interface in tool steels involves the operation sequence as follows:

(1) Preliminary (prior to the deposition of a coating) treatment of the surface with an LEHCEB. This treatment results in efficient hardening of the surface layer to a depth up to ~ 300 μm, efficient cleaning of the surface, and the formation of a surface relief favorable for deposition of a coating.

(2) Deposition of a coating of a nitride of some high-melting point element to a thickness of $\sim$ 1 to 5 μm using a standard technology (by the plasma-ion or magnetron method).

(3) Melting of the coating-base system to produce a sublayer where the phases of both the

coating and the base will be present after crystallization. After mixing of the coating with the substrate, the microhardness near the surface increases to $\sim$ 1300 kg/mm^2. Moreover, cutting tools (drills,mills) show substantially increased durability.

(4) Deposition of a coating of required thickness on the sublayer. The graded interface will provide an enhanced performance of the article as a whole.

It is also planned to suggest and realize various versions of using LEHCEBs to improve the strength properties of carbide-based tools, including those with wear-resistive coatings.

A Designation of steel types

SU (Russia)	USA
ст. 45	1045
ШХ15	52100
Р6М5	M3
У8А	W1-0.8C Extra
У12А	W1-1.2C Extra
12Х18Н9	302

References

[1] A.F.Shubin, V.P.Rotshtein, and D.I.Proskurovsky, Plastic deformation of a metal under the action of an intense electron beam of duration 10^{-8}–10^{-7} s. - Izv. Vyssh. Uchebn.Zaved. Fizika, 1974, No. 7, pp. 50–53.

[2] V.P.Rotshtein, L.S.Bushnev, and D.I.Proskurovsky, The dislocation structure of a cooper irradiated by an intense electron beam of duration 10^{-8}–10^{-7} s. Ibid, 1975, No. 3, pp. 130–131

[3] A.R.Kirkpatrick, Method and apparatus involving pulsed electron beam processing of semiconductor devices. - US Patent, No. 3.950.187, Apr. 13, 1976.

[4] A.C.Greenwald, A.R.Kirkpatrick, R.G.Little, J.A.Minnucci, Pulsed electron-beam annealing of ion-implantanted damage. -J. Appl. Phys, 1979, V. 50, No. 2, pp. 783–787.

[5] B.A.Koval, G.A.Mesyats, G.E.Ozur, et al., Generation of high-current, nanosecond, low-energy electron beams. - Pis'ma Zh. Techn. Fiz., 1981, v.7, No. 20, pp. 1227–1230.

[6] G.A.Mesyats and D.I.Proskurovsky, Pulsed Electrical Discharge in Vacuum. - Springer-Verlag, Berlin, 1989, 293 p.

[7] D.V.Iremashvili, T.A.Osepashvili, and P.I.Kakuchaya, Formation of highly intense microsecond electron beams. - Pis'ma Zh. Tech. Fiz., 1975, v.1, No. 11, pp. 508–511.

[8] G.E.Ozur and D.I.Proskurovsky, Formation of submicrosecond low-energy, high-current electron beams in a plasma-anode gun. - Ibid., 1988 v 14 No. 5, pp. 413–416.

[9] G.E.Ozur and D.I.Proskurovsky, On the current density of the HCEB formed in a dynamic double layer. - Ibid., 1990, v. 16, No. 4, pp. 46–49.

[10] G.E.Ozur and D.I.Proskurovsky, Generation of Low-Energy Electron Beam in the Diode with Plasma Anode. - Proc. XIV Intern. Symp. on Discharges and Electr. Insulation in Vacuum, Santa Fe, USA, 1990, pp. 665–670.

[11] M.Yu.Kreindel, E.A.Litvinov, G.E.Ozur, and D.I.Proskurovsky.- Non-steady-state processes in the initial stage of formation of a high-current electron beam in a plasma-filled diode. - Fizika Plasmy, 1991, v. 17, No. 12, pp. 1425–1439.

[12] G.Leggieri, A.Luches, V.Nassiri, et al., Pulsed electron beam for silicon annealing. - Vacuum, 1982, V. 32, No. 1, pp. 9–10.

[13] A.S.El'chaninov, B.A.Koval, G.A.Mesyats, et al., A high-current pulsed source of nonrelativistic electrons. - Prib. Tekh. Exper., 1987, No. 5, pp.122–125.

[14] V.I.Itin, B.A.Koval, N.N.Koval, et al., Surface hardening of iron alloys under the action of an intense electron beam. - Izv. Vyssh. Uchebn. Zaved. Fizika, 1985, No. 6, pp. 38–43.

[15] T.S.Bazhenova, V.I.Itin, B.A.Koval, et al., Electro-chemical behavior of the 12X18H10T steel irradiated by pulsed electron beam. - Zashchita Metallov, 1988, v.24, pp. 466–469.

[16] I. M. Goncharenko, V. I. Itin, S. V. Isichenko, et al. Increasing of corosion resistance of the 12X18H10T steel irradiated by low-energy high-current electron beam. Ibid., 1993, v. 29, No. 6, pp. 932–937.

[17] V.I.Itin, I.S.Kashinskaya, S.V.Lykov, et al.- The mechanism of steel hardening upon the cyclic action of a low-energy high-current electron beam. - Pis'ma Zh. Tekhn. Fiz., 1991, v. 17, No. 5, pp. 89–93.

[18] Yu.F.Ivanov, V.I.Itin, S.V.Lykov, et al., Stress wave dissipation and structural transformations in steels irradiated by a pulsed electron beam. - Dokl. Akad. Nauk SSSR, 1991, v. 321 No. 6, pp. 1192–1196.

V.I.Itin, Yu.F.Ivanov, S.V.Lykov, et al., Dissipation of stress wave energy and structural modification of steels irradiated by a low-energy high-current electron beam. - Proc. of 9-th Intern. Conf. on High-Power Particle Beams (BEAMS 92), Washington, DC May 25–29, 1992, v. 3, pp. 1942–1947.

[19] Yu. F. Ivanov, V. I. Itin, S. V. Lykov, et al. Structural analysis of heat affected zone of steel 45 irradiated by a low-energy high-current electron beam.- Fizika Metallov i Metallovedenie, 1993, v. 75, No. 5, pp. 103–112.

[20] Yu. F. Ivanov, V. I. Itin, S. V. Lykov, et al. Phase and structural changes in steel 45 irradiated by a low-energy high-current electron beam.- Izvestiya RAN, Metally, 1993, No. 3 , pp. 130–140.

[21] E. F. Dudarev, L. A. Kornienko, S. V. Lykov, et al. Dislocation substructure of iron irradiated by a low-energy high-current electron beam.- Izv. Vyssh. Uchebn.Zaved. Fizika, 1993, No. 5, pp. 42–47.

[22] S.V.Lykov, V.I.Itin, G.A.Mesyats, et al., Evolution of stress waves excited in a metal by a pulsed electron beam. - Ibid., 1990, v.310, No. 4, pp. 859–861.

[23] N.N.Rykalin, A.A.Uglov, I.V.Zuev, and A.N.Kokora, Laser and Electron-Beam Treatment of Materials. Handbook. Moscow: Mashinostroenie, 1985, 496 p.

[24] Surface Modification and Alloying by Laser, Ion, and Electron Beams. - Edited by J.M.Poate, G.Foti, and D.C.Jacobson. - 1983, Plenum Press, New York.

[25] Yu. F. Ivanov, M. P. Kashchenko, A. B. Markov, V. P. Rotshtein.- Crytical grain size for nucleation of α-martencite. Preprint No. 16, Tomsk. SD RAS, 1993, 8 p.

[26] R. V. Stinnett, D. C. McIntyre, R. G. Buchheit, et. al. Ion beam surface treatment: a new capability for rapid melt and resolidifi--cation of surfaces. Proc. of 16 Intern. Symp. on Discharges and Electr. Insulation in Vacuum. SPIE, v. 2259, p. 613-618.

[27] G.I.Baranov, I.M.Goncharenko, I.S.Kashinskaya, et al., Surface stregthening and variation of tribotechnical properties of the ШХ15 steel treated by electron beams. - Digest of the 11 All-Union Conf. on Modification of the Properties of Construction Materials by Charged-Particle Beams., v.4, pp.6-8, Sverdlovsk, USSR, 1991.

[28] G.I.Baranov, I.M.Goncharenko, V.I.Itin, et al., The effect of treating metallic materials by low-energy HCEBs on the resistance to wear of metal-polymer friction pairs. - Ibid., pp. 9–11.

[29] V. I. Itin, S. V. Lykov, V. P. Nesterenko, et al. A method for strengthening steel articles. Russian Federation Patent No. 2,009,272.(19) RU (II) 2,009,272C1,12.03.92.

[30] Yu. F. Ivanov, A. B. Markov, D. S. Nazarov, et al.- Pulsed electron-beam mixing of Fe-Ta. Preprint No. 18, Tomsk, SD RAS, 1993, 19 p.

[31] V. M. Gureev, S. I. Yaresko, A. P. Labetin, and A. L. Petrov. Study of the effect of pulsed laser radiation on the structure and phase composition of hard alloys and the operational features of hard-alloy-based tools. - In: Laser Technology and Automatization of Research

Work. Transactions of the Physical Institute of the Russian Academy of Sciences. vol. 198, 1989. pp. 90–110.

[32] G. E. Remnev, V. K. Struts, I. F. Isakov, et al. Strengthening of hard-alloy plates under the action of intense ion beams. - In: Digest of the IIIrd Conference on Modification of the Properties of Construction Materials by Charged-Particle Beams, Tomsk, 1994, vol. 1, pp. 87–89.

Project Title: Genetic Bond between the Melt Properties and the Properties of an Industrial Aluminum Alloy
Principal Investigator: Irena Brodova
Urals Polytechnic Institute
Ekaterinburg, Russia
AM-7682

CLAUSE 1 - STATEMENT OF WORK

Objective:

The purpose of this work is to develop new methods to enhance the properties of an industrial aluminum alloy by melt treatments, including heat-time melt treatment (HTMT) and grain refinement by surface active elements or refractory additions. This shall be accomplished by measuring physical properties such as kinematic viscosity and density of the liquid alloy and then using this data to determine the critical processing temperatures of the melt. These include temperatures and anomalous property changes related to melt structure. The crystallization of this alloy shall also be studied as a function of melt processing parameters by techniques such as penetrating gamma radiation and differential thermal analysis.

Tasks:

The Contractor shall:

1. Provide a report describing the experimental plan that will be used to conduct the investigation described above.

2. Conduct the melt experiments and studies of this alloy including:

HTMT (heat-time melt treatment)
Grain refinement by surface active elements or refractory additions
Measuring physical properties such as kinematic viscosity and density of the liquid alloy. Use this data to determine the critical processing temperatures of the melt, including temperatures and anomalous property changes related to melt structure.
Studying the crystallization of this alloy as a function of melt processing parameters using techniques such as penetrating gamma radiation and differential thermal analysis.

Provide the test data/results for the experiments/studies described above.

3. Characterize the structure and properties of the resulting castings as a function of the melt treatments and provide a final report analyzing the results of the experiments/studies.

INSTITUTE OF METAL PHYSICS
URAL DIVISION OF RUSSIAN ACADEMY OF SCIENCES

620219, Ekaterinburg, S. Kovalevskaya str. 18, GSP-170

Report upon completion of Task 2 for Contract AM-7682

"Test data and results"

Contractor Representative I.G. Brodova

Phone: 007-3432-499-111

Fax: 007-3432-445-244

12.05.95.

RUSSIA

1. THE INVESTIGATION OF THE INFLUENCE OF THE HEAT-TIME TREATMENT ON THE PHYSICAL PROPERTIES IN LIQUID STATE AND CASTING STRUCTURE Al-17%Si ALLOY

INTRODUCTION

Hypereutectic silumins are widely used for producing pistons in the internal- combustion engines, possesing the high strength and hardness at high temperatures, the low coefficient of thermal expansion.

It is known that the structure of the qualitative hyper silumins castings is characterized by uniform distribution of the dispersed primary silicon crystals, absence of rough intermetallic compounds, absence or insignificant development of major silicon segregation and etc. [1]. Decreasing of the phase linear size leads to increasing of the high temperature strength and plasticity. As a result, the inclination of cold and hot cracks formation decreases.

The effective method of structure regulation of industrial cast alloy is to prepare the melt for crystallization by heat-time treatment and to use regimes of crystallization based science. It is necessary to know about the melt physical property investigations for using this method.

1.1. EXPERIMENT

The hypereutectic aluminum alloy Al-17%Si is the object of the investigations. The melt physical property investigations were fulfilled by following methods:

1.1.1. Kinematic viscosity was measured by the method of the trash of a crucible with melt [2]. The investigations were carried out by the following plan: specimens were heated to 1150°C, were maintained at this temperature to removal an oxide skin from specimens surface then were cooled to the temperatures close to the melting point but not crystallization. After such preparing of the melt kinematic viscosity was measured during the specimens heating to 1200°C and further cooling.

1.1.2. The melt density (d) was measured by the method of penetrating γ-ray [3]. The heating and cooling politherms were made when the alloy was heated to 850 and 1200°C. The melt was

maintained in maximum heating temperature conditions during 10 minutes. Cooling speed was 3-5°C/min.

1.1.3. Differential thermal analyze (DTA). Apparatus VDTA-8M3 has been used. The experiments was fulfilled in BeO crucible in a tungsten cell. The chamber was filled with a high purity helium to 0.2bar, speed of cooling was 20°C/min. Thermal effects discovered were identified according to [4,5].

1.1.4. The metallography analyzis of the casting structure was carried out by a microscope MIM-10. The volume of the phase was measured by a point method (fields of vision were 50). The linear sizes were measured by a secant method (number of secants was 50). The absolute error of the methods did not exceed 1%.

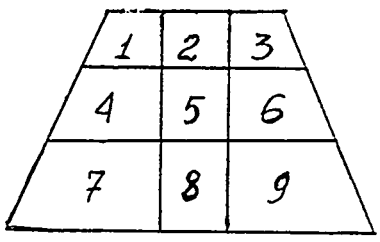
The specimens were etched by $HF+HNO_3$ reactive. The chemical composition of the alloy, produced by the customer, is showed in tab.1.1.

Table 1.1

The chemical composition of the investigation alloy

element	Si	Fe	Cu	Mg	Mn	Zn
the element content, %	17.0	< 0.5	4.5	0.55	< 0.1	< 0.5

The templet 7mm thickness was cut out to study the silicon segregation. Considerable inhomogenety in distribution of the primary silicon through the templet section and a great number of pores were discovered during the microstructure investigations. The low and central parts of the templet were practically deprived of the primary silicon. Taking into account this fact the additional chemical analysis was carried out. The results were showed in diagram and in tab.1.2. Taking into account the primary silicon segregation, the further researches were made on the specimens with the silicon about 17%.



The diagram of the specimen selection for the chemical analyzis

Table 1.2

The dates of the spectral analyzis

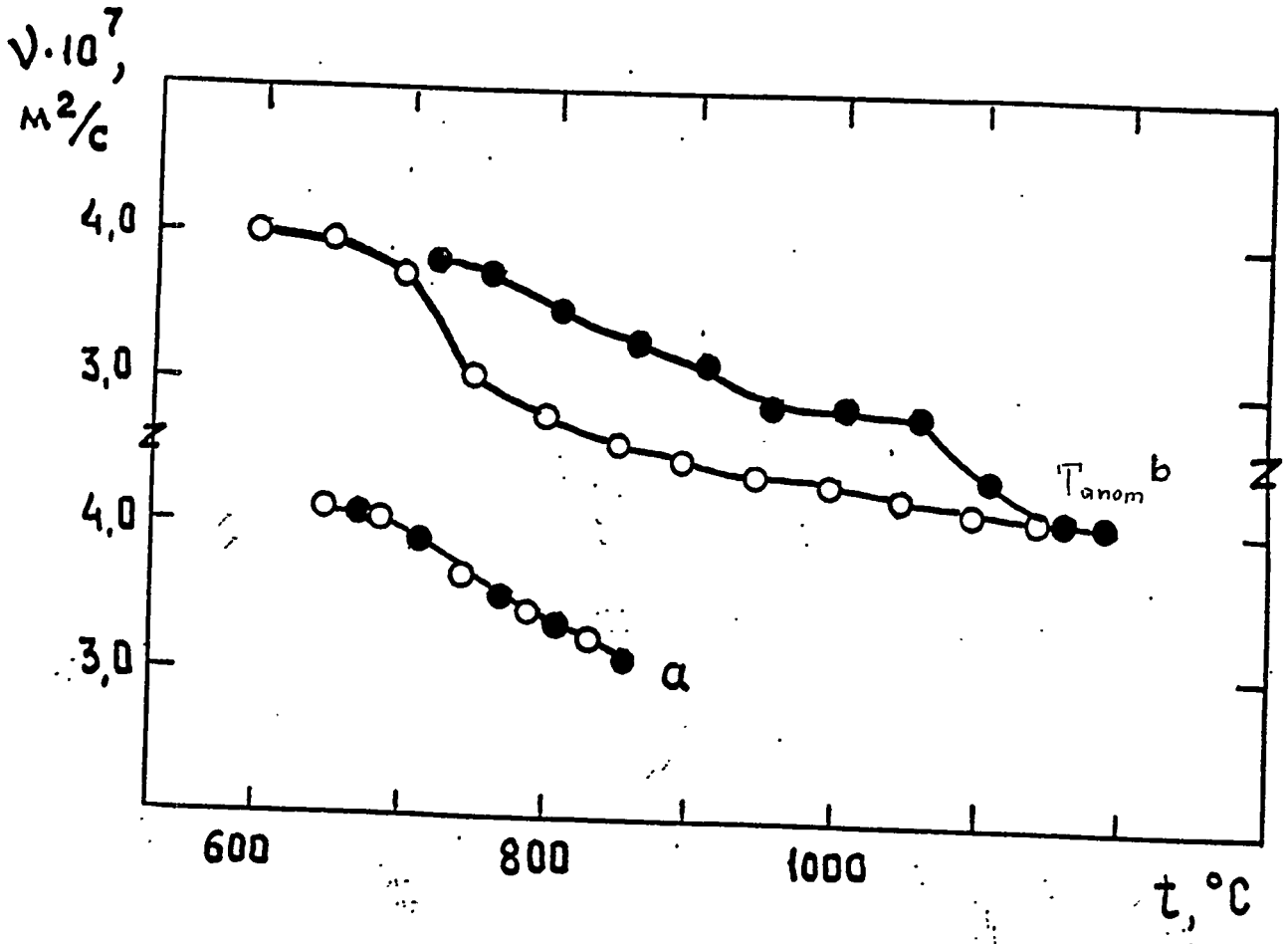
The number of the probe	The element content, %			
	Si	Fe	Mn	Mg
1	10.24	0.69	0.06	1.14
2	10.24	0.73	0.05	0.94
3	10.27	0.64	0.05	1.08
4	16.40	0.70	0.06	0.87
5	10.46	0.62	0.06	0.92
6	14.96	0.62	0.06	0.98
7	18.42	0.83	0.06	0.83
8	18.54	0.73	0.05	0.87
9	16.50	0.62	0.05	0.87

1.2. Results

1.2.1. The results of the kinematic viscosity investigations. The Al-17%Si alloy viscosity polytherms look as if the aluminum alloys one (fig.1.1). The increasing of the melt heating temperature leads to monotone decreasing of viscosity. The hysteresis of kinematics viscosity do not observe at the melt heating temperature 850°C (fig.1.1a), the heating and cooling polytherms coincide. During the heating of the melt to 1200°C, there is a break on $\nu(t)$ at 1060°C (fig.1.1b) ; Viscosity value sharply decreases during the further melt heating to 1200C. The further cooling leads to viscosity polytherms having many branches. The temperature where polytherms have many branches is 1150°C. $\nu(t)$ value makes a jump at the temperature 740°C and in the low temperature interval ($740°-t_1$) agree with the values during heating.

The breaks on viscosity polytherms give evidence about presence

The melt heating temperature influence
on the kinematic viscosity



● - heating; o - cooling

a - the melt heating temperature 850°C

b - the melt heating temperature 1200°C

Fig. 1.1

of the structure transformation taking place in the Al-17%Si melt during heating (1060-1150°C) and cooling (740-700°C).

1.2.2. The results of the density investigations.

The experimental data about Al-17%Si alloy density d(t) behavior are showed on the fig.1.2, 1.3.

The density behavior in 750-1200°C temperature interval is showed on the fig.1.2. The increasing of the melt heating temperature leads to the density decreasing. There is a break on d(t) heating polytherms at 1060°C. The politherms have many branches during the further heating of the melt to 1200°C.

The density values during cooling do not coincide with this one during heating.

The alloy density changes during cooling depending on the melt heating temperature are showed on the fig.1.3. Lets mark the following typical temperature intervals:

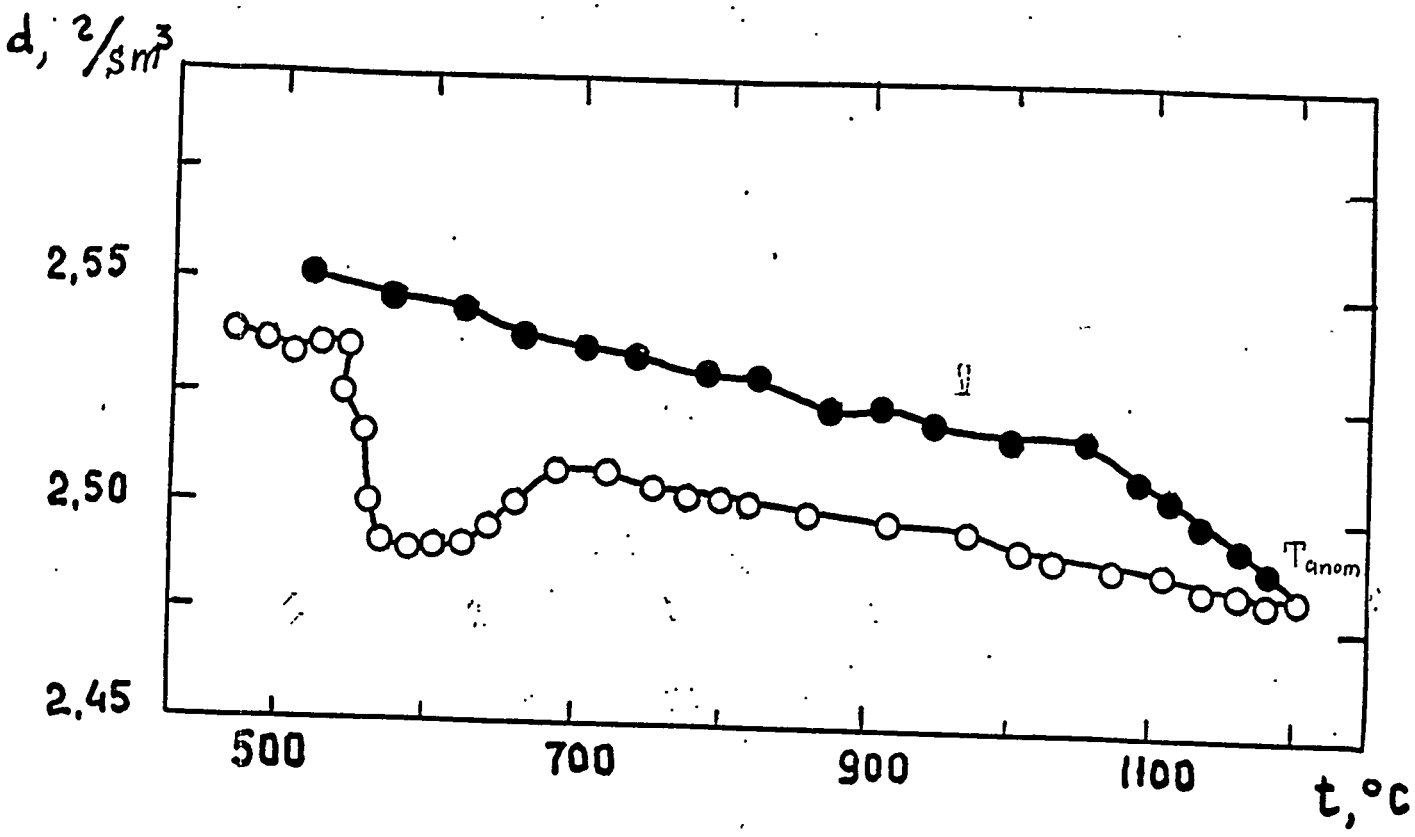
- t_m-t_l - the melt density increasing while temperature decreases.
- t_l-t_e - the decreasing of density during the primary silicon crystallization.
- t_e-t_s - the density increasing during the many components eutectic crystallization.

The further cooling of the solid alloy leads to some increasing and stabilization of the density.

The increasing of the alloy density in (t_m-t_l) interval corresponds to the classical temperature dependence for metallic melts. The Al-17%Si alloy crystallization begins with the primary silicon precipitation at liquidus temperature (t_l). Here is the break on the politherms. The temperature decreasing in (t_l-t_e) interval accompanied with the alloy density reducing. Such decompression of the investigated alloy deals with increasing of the crystallized silicon volume which have the smaller density. Sharp increasing of Al-17%Si alloy density is observed at the temperature of eutectic transformation (t_e), and come to the end at solidus temperature (t_s). The many components eutectic is crystallized in (t_e-t_s) temperature interval during eutectic transformation.

The influence of the melt state on the character of Al-17%Si alloy crystallization was studyed on the specimens, which were heated to different temperatures. The character of the density-

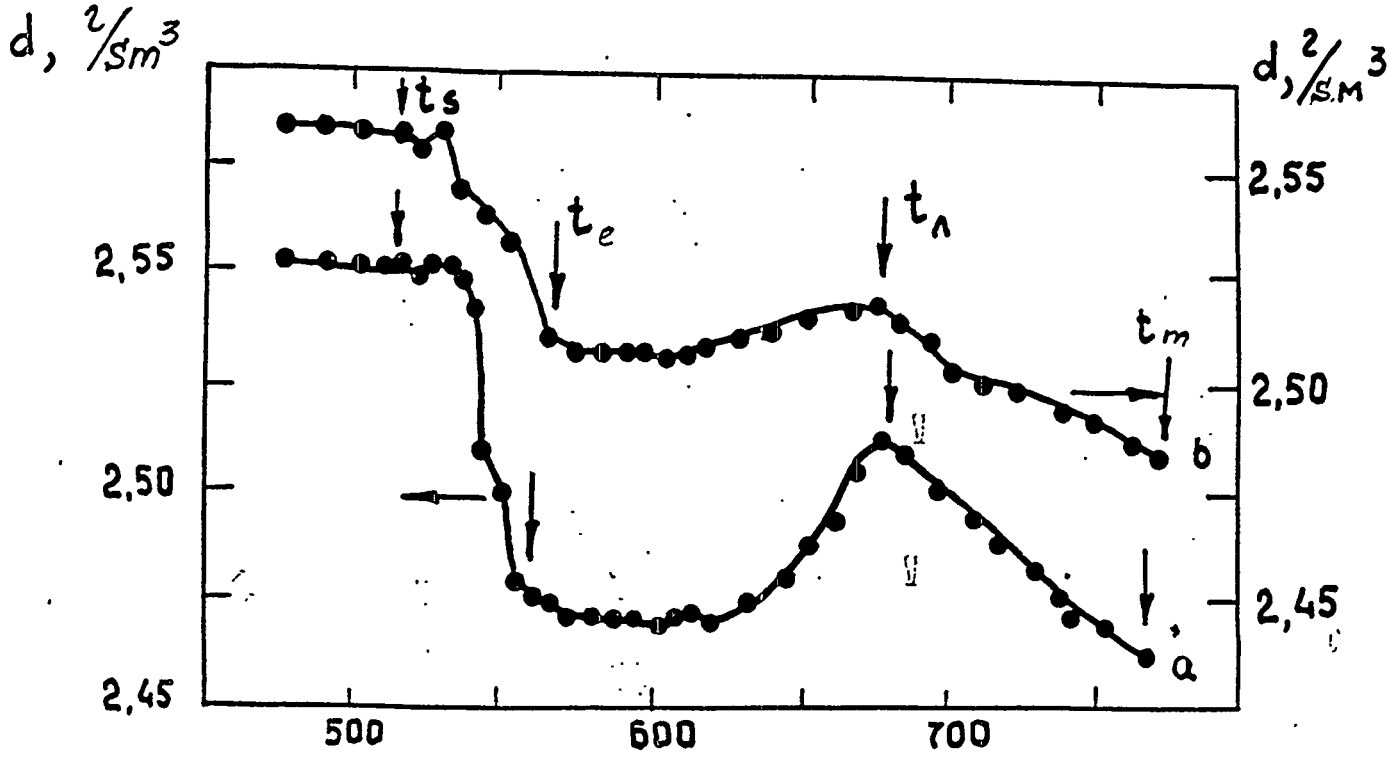
The density politherms of the melt
at heating and cooling



● - heating; ○ - cooling

Fig. 1.2

The influence of the melt heating temperature
on density during cooling



a - the melt heating temperature 850°C
b - the melt heating temperature 1200°C
where: t_m - the liquid melt temperature;
t_l - the liquidus temperature;
t_e - the temperature when eutectic separation begins
t_s - the solidus temperature;

Fig. 1.3

temperature dependence does not change. Increasing of the maximum melt temperature from 850°C to 1200°C leads to certain narrowing of $(t_l - t_e)$ temperature interval of the primary silicon precipitation, from 62 to 52°, due to the decreasing of liquidus temperature. The temperature when precipitation begins and solidus temperature are constant. The increasing of Al-17%Si alloy crystallization interval is 6%. The data of density investigations are showed on the tab.1.3.

Table 1.3

The maximum melt heating temperature influence on the typical points of d(t) dependence

heating temperature of melt, °C	temperature °C			density (d), g/sm^3			density changing during crystallization stages (Δd), g/sm^3		
	T_l	T_e	T_s	d_l	d_e	d_s	Δd_{l-e}	Δd_{e-s}	Δd_{l-s}
850	685	573	510	2.510	2.470	2.552	-0.040	0.82	-0.042
1200	675	573	510	2.516	2.506	2.558	-0.010	0.52	-0.042

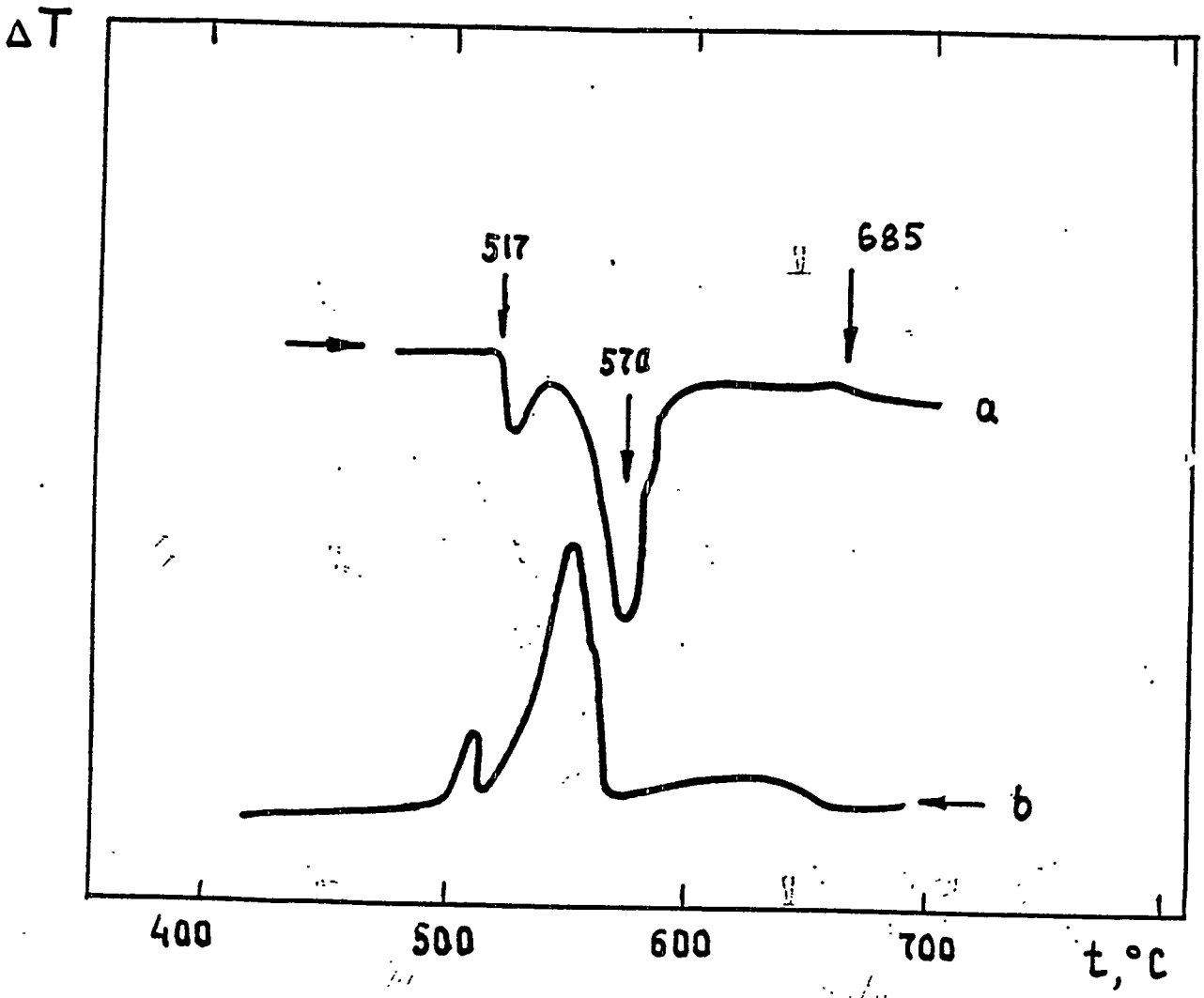
1.2.3. The results of DTA allow to confirm:

There are three typical phase transformation (fig.1.4).

- The solution phase based copper. The solution beginning temperature was 517°C.
- The melting of many components eutectic. The melt beginning temperature was 51°C.
- The solution of the primary silicon. The solution beginning temperature was 685°C.

The characteristic curves received during the cooling of the alloy, which were made under different temperature conditions are showed on the fig.1.5. In all cases the alloys crystallization begins with the primary silicon precipitation. The first peak on the DTA curve corresponds to this fact. Then aluminium-silicon euthectic formation begins, sharp peak with a maximum height corresponds to this fact. The form of the peak is nonsimmetrical, because of the formation of intermetallic compounds based iron and the eutectic silicon precipitation simultaneously at the begining of crystallization. The crystallization of the alloy finished with

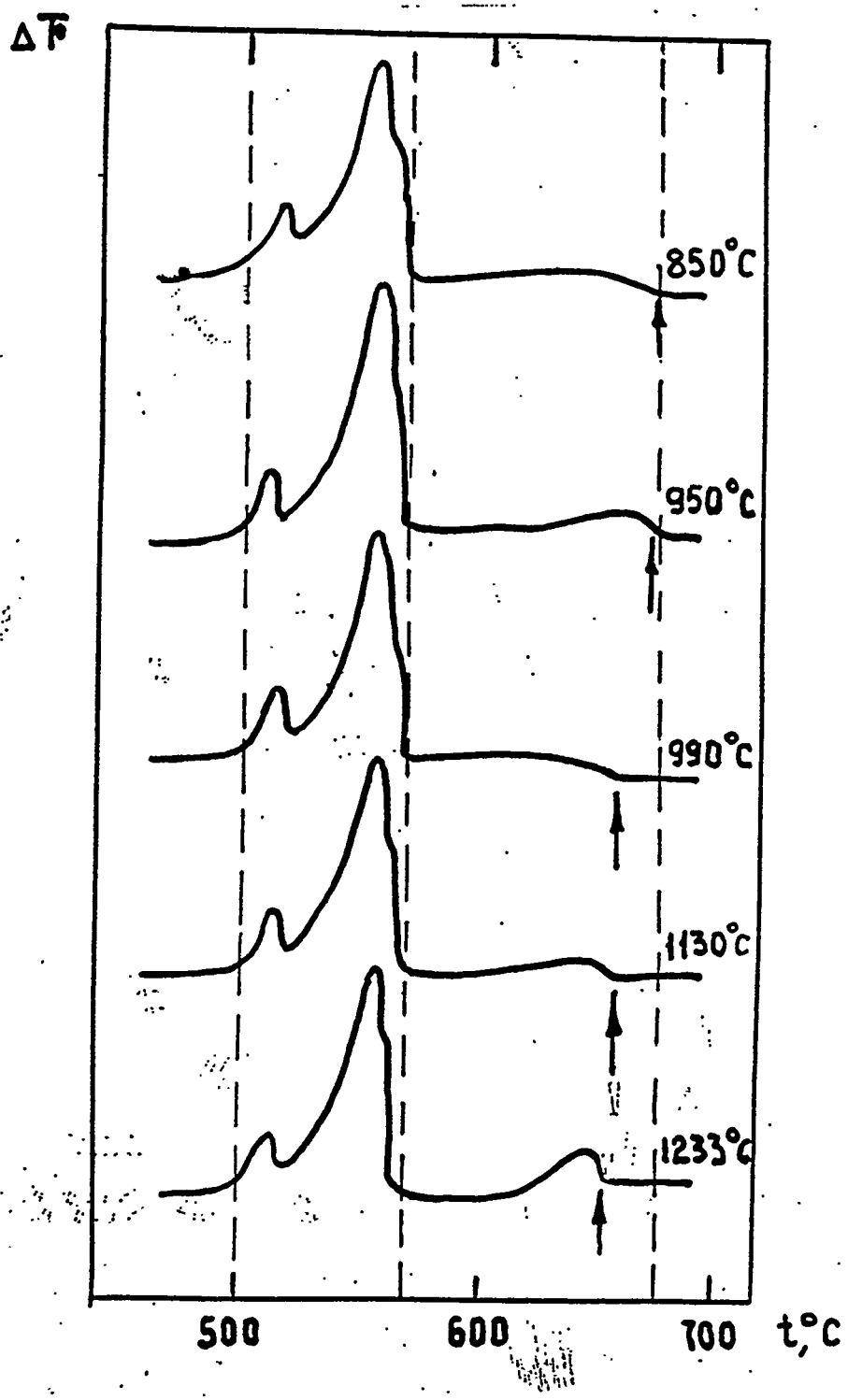
The politherms of the DTA during heating and cooling



a - heating; b - cooling

Fig. 1.4

The melt heating temperature influence on the DTA politerms during cooling



The numbers neare curvers - are the melt heating temperature

Fig.1.5.

the formation of eutectic phase based copper. The precipitation temperatures of the last third phases do not depend on changing of the maximum melt heating temperature , but the liquidus temperature changes. The liquidus temperature decreasing, when the maximum heating temperature of melt increasing from 850 to 1200°C. The increasing of Al-17%Si alloy crystallization interval is 7%.

1.2.4. The metallography analyzis of the specimens after DTA has showed that their structure consists of the large primary silicon preferentially polyedric morphology and mqny components eutectic consisted of silicon and two types of intermetallic compounds (fig.1.6 - 1.9).

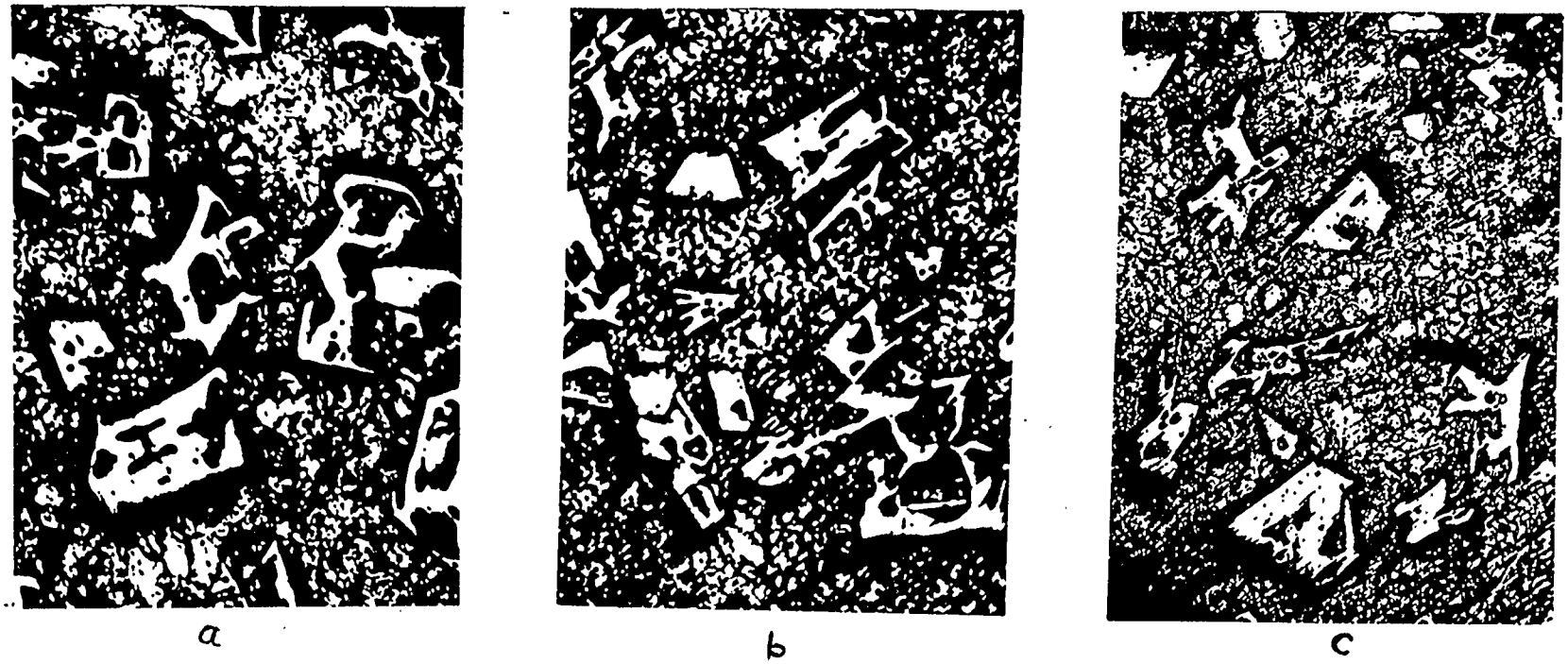
The silicon eutectic have the plate morphology. The intermetallic compounds are two types: extensive fields of white colour with complicated morphology and more dark needles. The chemical structure of alloy and analyzis of literature permit to suppose, that this phases have following stoichiometry: the phase of white colour - $CuAl_2$, and the needle phase - $FeSiAl_5$ [6].

The metallography analyzis has shown, that the maximum melt heating temperature noticeably influences the specimens structure under the identical heat physicsis conditions, the volume, morphology and size of the phases change (tab.1.4, fig.1.10 - 1.11)

The volume of primary and eutectic silicon, intermetallic compounds based iron and copper changes while T. increases (fig.1.10). The primary silicon volume decreases and the eutectic one increases during the heating to 950°C. And the volume stabilization is seen during the heating to 990°C and higher. And behavior of the intermetallic compounds volume is analogous. The volume of intermetallic compounds based iron decreases and based copper increases during the heating to 950°C. And the volume stabilization is seen during the heating to 990°C and higher.

The linear sizes of the phases change by the same law, when the temperature increases (fig.1.11). If the melt was heated to 950-1060°C, decreasing of the linear sizes of the primary silicon and the eutectic silicon linear sizes is observed. The primary silicon and the eutectic silicon sizes stabilized during the heating over 1060°C. The intermetallic compound sizes especially based iron decreases essentially if the melt was heated to 950-1060°C, and the sizes of intermetallic compounds are constant during the melt heating above 1060°C.

The melt [illegible] influence on the microstructure
of Al-Si-Cu alloy (the primary silicon), x50



a

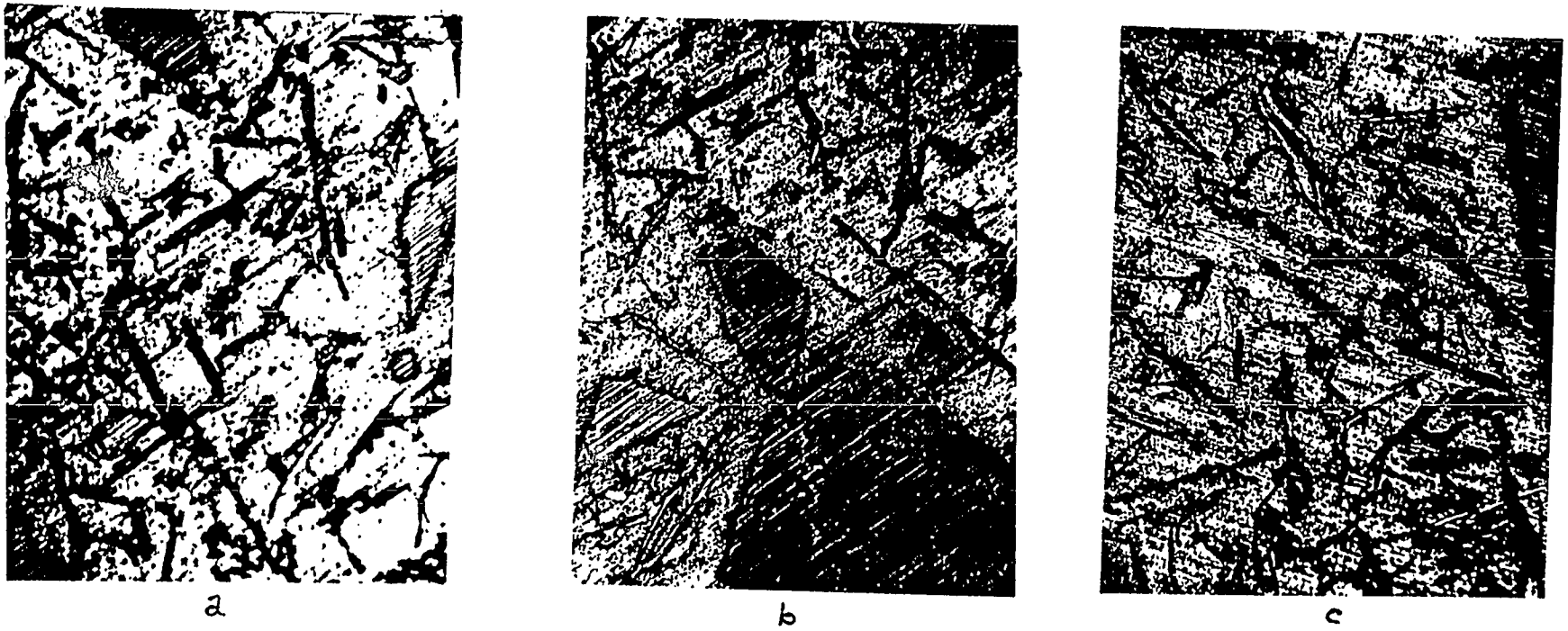
b

c

a - the melt heating temperature 950°C
b - the melt heating temperature 880°C
c - the melt heating temperature 1230°C

Fig. 1.9.

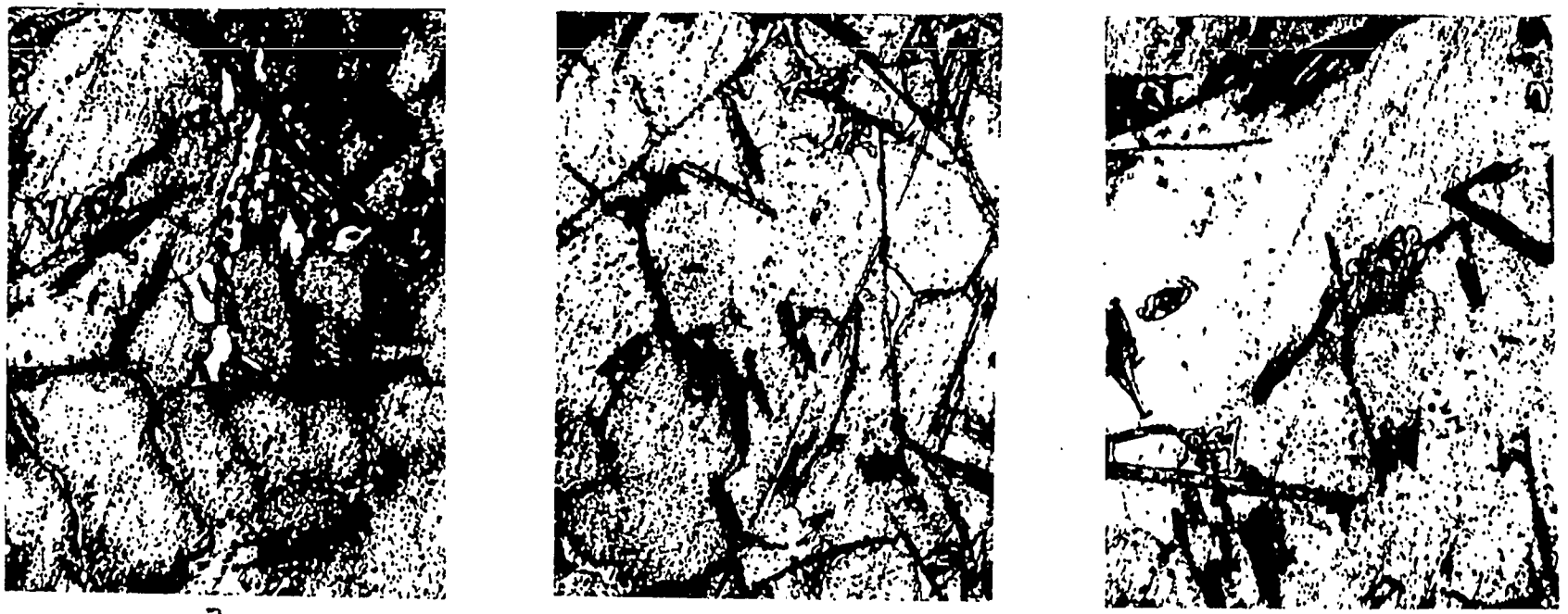
The melt heating temperature influence in the microstructure of Al-Si 9% alloy (the eutectic silumin, ~12%)



a - the melt heating temperature 950°C
b - the melt heating temperature 990°C
c - the melt heating temperature 1020°C

Fig.1.7

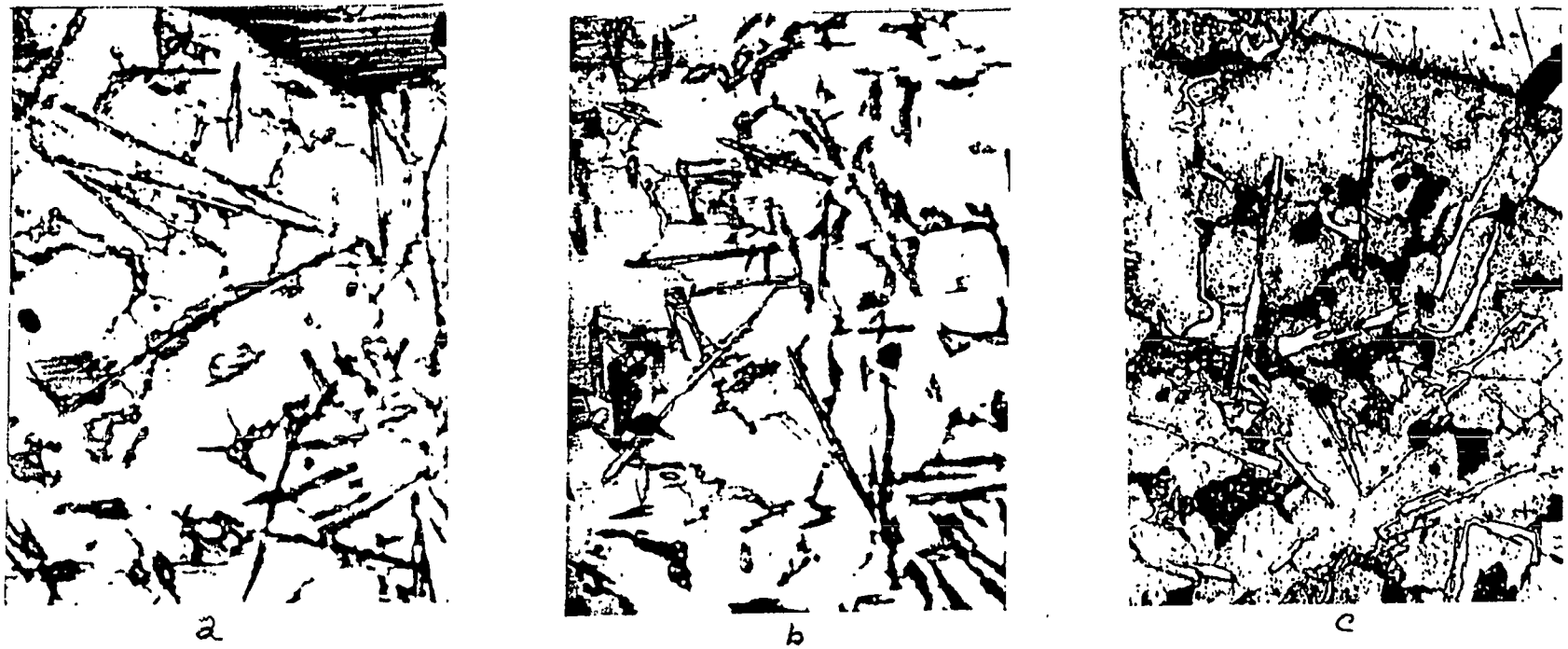
The melt heating temperature influence on the microstructure of Al-12%Si alloy (intermetallic compound $CuAl_2$), x400



a - the melt heating temperature 850°C;
b - the melt heating temperature 990°C;
c - the melt heating temperature 1233°C;

Fig. 1.8

The melt treatment temperature influence on the microstructure
of Al-17Si-4Cu alloy (intermetallic compound Fe3SiAl). x400



a - melting temperature 1000°C
b - melting temperature 1050°C
c - melting temperature 1100°C

Fig.1.9

Table 1.4

The maximum melt heating temperature influence on the speciemen structure

heating temperature of the specimen °C	primary silicon		eutectic silicon		intermetallic compounds			
					$CuAl_2$		$FeSiAl_5$	
	the pattern volume, v.%	the max. linnear size, mkm	the pattern volume, v.%	the max. linnear size, mkm	the pattern volume, v.%	the max. linnear size, mkm	the pattern volume, v.%	the max. linnear size, mkm
850	17.2	490.0	4.1	50.0	1.90	80.0	0.85	100.0
950	15.8	470.0	5.3	45.0	1.95	80.0	0.65	90.0
990	14.8	350.0	5.5	45.0	2.0	70.8	0.60	80.0
1130	14.3	290.0	5.8	39.0	2.20	60.1	0.51	70.0
1233	13.9	270.0	6.2	38.0	2.40	60.0	0.50	60.0

The influence of the maximum melt heating temperature on the phases volume

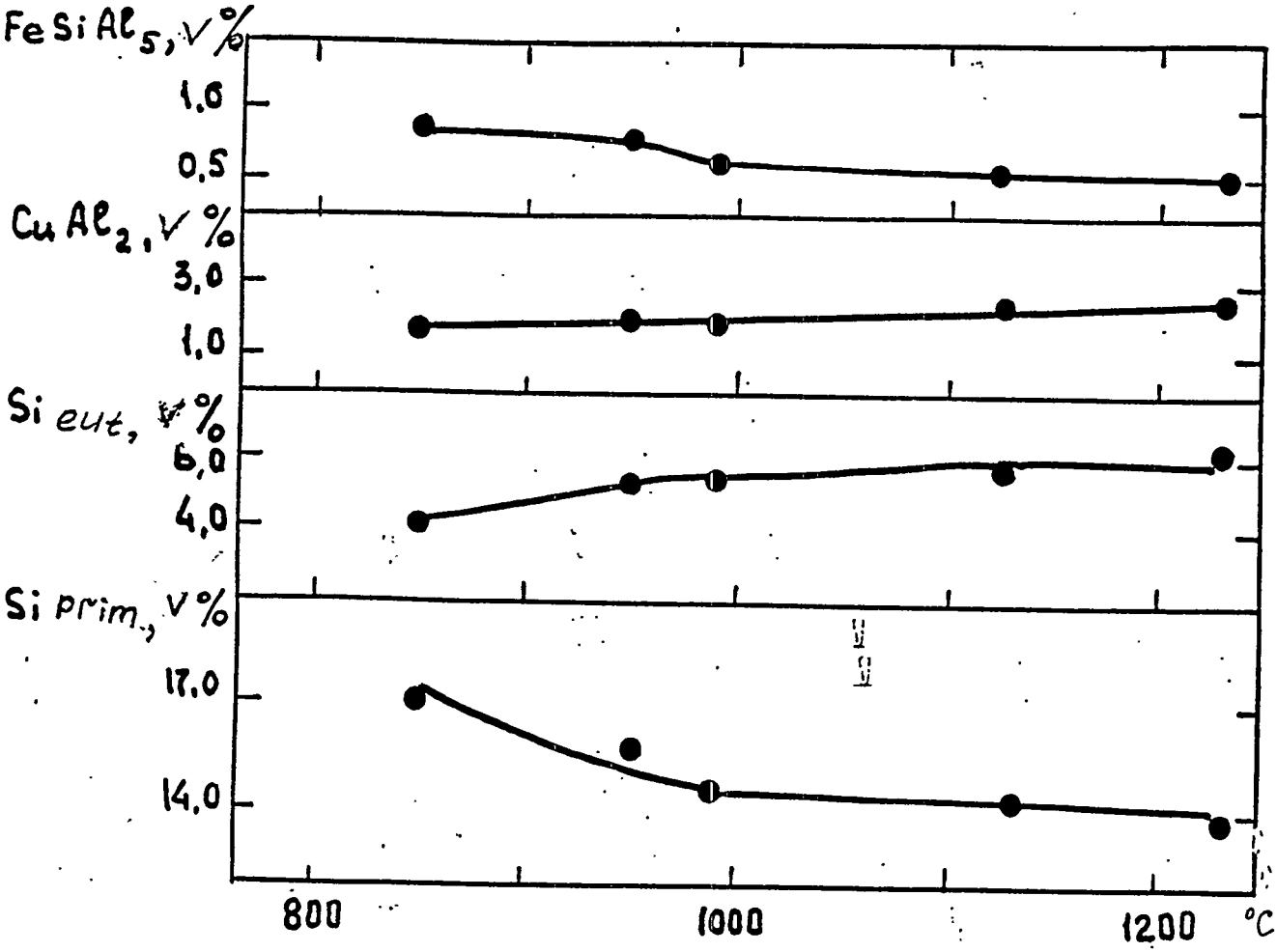


Fig. 1.10

The influence of the maximum melt heating temperature on the linear sizes of the phases in specimens

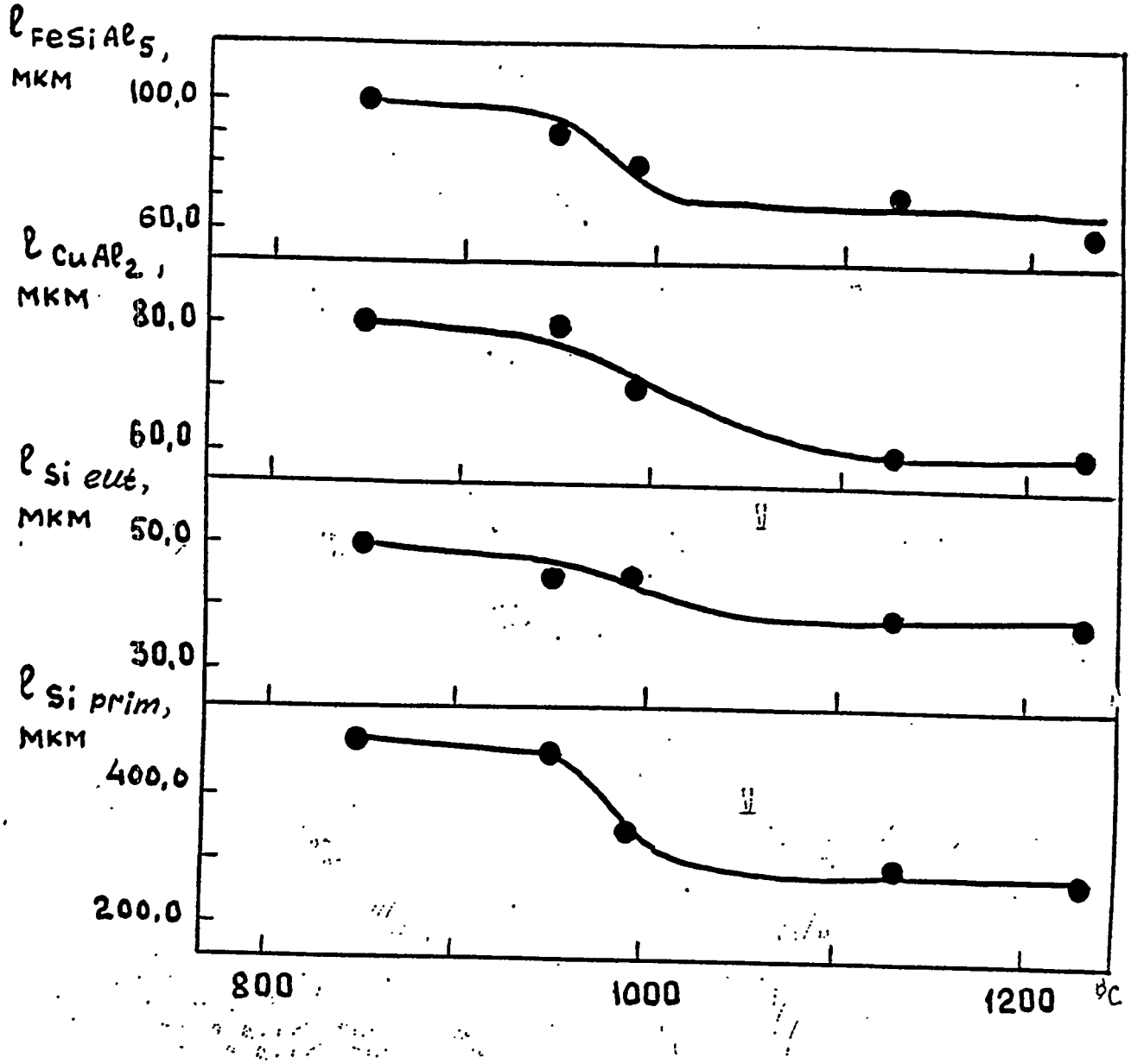


Fig. 1.11

CONCLUSIONS

1. The hypereutectic Al-17%Si alloy in liquid and solid state is characterized by heterogeneity because of uniquality of internuclear connections. The research results of the temperature dependences of kinematic viscosity and density of the melt is testified about its micronon-uniform structure. The temperature intervals of the melt structure transformations were determined on the kinematic viscosity politherms: during the heating (1060-1150°C); during the cooling (740-700°C). And on the density politherms- during the heating 1060-1200°C.

2. There are the conclusions that Al-17%Si alloys crystallization happens in three stages:

- The primary silicon precipitation.
- The many components eutectic precipitation.
- Precipitation of the intermetallic compounds based copper.

The increasing of the melt heating temperature does not influence the solidus temperature and the temperature when eutectic precipitation begins, but the temperature of the primary silicon precipitation decreases. The research results of the temperature dependences of density and DTA are testifyed, that the increasing of the melt heating temperature leads to the narrowing of crystallisation interval due to $T_{л}$ reducing; this narrowing is 6% on the density data and 7% on the DTA data.

3. The interrelation between liquid and solid state was established for Al-17%Si alloy. The increasing of the melt heating temperature is accompanied by the structure changes, the phases volumes and especially their linear sizes change. The most optimum structure is observed when the melt was heated to 1060°C and over. The primary silicon and intermetallic compound volumes decrease and also their linear sizes reduce.

2 THE STRUCTURE INVESTIGATIONS OF SOLID ALLOY

The aim of the present study is the improvement in a quality of the casting and mechanical properties of *Al-Si* alloys by using special technology. This technology includes a casting after heat time melt treatment (HTMT) and a grain refinement by surface-active elements or refractory additions.

2.1 Preparing of specimens and experimental procedures

The initial material was a pig of an alloy with the American Designation 390. The *Al* alloy had the chemistry *Si* - 17%, *Cu* - 4.5%, *Fe* < 0.5%, *Mg* - 0.55% *Mn* - 0.1%, *Zn* < 0.1% in weight percents. This alloy was remelted in a resistance furnace through a large macrosegregation of silicon. The remelting was carried out in alundum crucible at 750 °C with isothermal time interval for 30 min. Then the melt was solidified in a chamotte mould (120 mm in length, 20 mm in width, 10 mm in height). The specimens for the investigations were prepared from this ingots according to the following technique:

Preliminary melted, 10 g. of metal (ingot) was heated to a certain temperature T in a alundum crucible, a master alloy was introduced in an amount depended on the alloy composition, the melt was stirred and held for time interval τ_1 in a furnace at T, and then the melt was cooled down to a certain temperature T_c, held for a time interval τ_2 at T_c and then the alloy was solidified in air, in chamotte mould having the cylindrical form and sizes: 20 mm in diameter and 10 mm in height. The melt temperature range employed was T = 750-1200 °C. $\tau_1 = \tau_2 = 30$ min. Titanium was introduced into a basic

melt by using *Al*-3.6%*Ti* master alloy prepared by standard industrial technology, i.e. by casting a pig from T=1150 °C at a cooling rate V=10 K/c. It's concentration into the alloy was 0.12 wt. % *Ti*. Tin concentration into silumin was 0.2 wt. %.

Six series of specimens was produced. Table 2.1 presents the casting conditions, including HTMT. In the I, III and V series temperatures $T=T_c$=var, in the II, IV, VI series temperature T_c=750°C=const and temperature T=var. The value of V=1 K/c was estimated from the cooling curve, which was recorded by a "КСП-4" potentiometer.

Casting conditions of specimens

Table 2.1

№series	T	№casting	T_c	τ_1	τ_2	*Sn*	*Ti*
I	750	1	750	30	–	–	–
	900	2	900	30	–	–	–
	1100	3	1100	30	–	–	–
	1200	4	1100	30	–	–	–
II	1100	5	750	30	30	–	–
	1200	6	750	30	30	–	–
III	750	7	750	30	–	–	0.12
	900	8	900	30	–	–	0.12
	1200	9	1200	30	–	–	0.12
IV	900	10	750	30	30	–	0.12
	1200	11	750	30	30	–	0.12
V	750	12	750	30	–	0.2	–
	900	13	900	30	–	0.2	–
	1100	14	1100	30	–	0.2	–
	1200	15	1200	30	–	0.2	–
VI	1200	16	750	30	30	0.2	–

The cast structure was investigated in the microsection cutted from a top of ingot with equal distances (see Fig. 2.1).

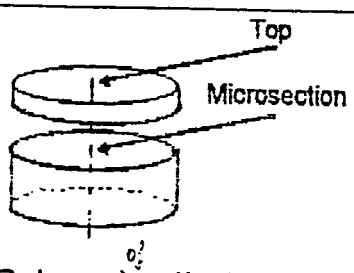


Figure 2.1 Scheme cutted microsection

The quantitative metallography of the alloy structure were obtained by a SIAMS-340 metallography apparatus consisting of a NEOPHOT-2 optical microscope, a television camera, a television set and a IBM PC computer.

The screen images was measured in a window of a computer monitor. In order to get data "статистики" ("statistics") horizontal lines are drawn in according to linear method of a measurement. Histogram of a distribution of section particles is appeared. This histogram shows relative frequency of hit of data into the set of consecutive intervals. Statistic data of the histogram appears in the table "статистики" ("statistics"):

- N - число частиц - quantity of particles (total number of data),
- m - минимум - minimum (minimum sizes of particles);
- M - максимум - maximum (maximum sizes of particles);
- Mo - мода - mode (harmonic mode);
- Me - медиана - median;
- Av - среднее - average (arithmetical mean sizes of particles);
- D - СКО - RMSV (root mean square value);
- A - асимметрия - asymmetry (configuration asymmetry of a histogram);
- E - эксцесс - eccentricity;

- S - площадь - area (area of a window).

In this investigations all measurements were carried out by using 80-times magnification. Final data are results of addition of data of five different images of even specimen.

The X-ray spectrometry analysis of intermetallic compounds phases were carry out on a JCXA-733. The X-ray diffraction phase analysis and the determination of a lattice parameter of aluminum-base solid solution were carried out on a DRON-3 diffractometer.

2.2 Results

2.2.1 The influence of the heat-time melt trearment

Specimens of series I. II was investigated. Regimes of HTMT were choosed by using results of measurements of structure-sensible melt properties (part I).

Two regimes of HTMT was studied:

- the first - $T < T_1$
- the second - $T_1 < T < T_{anom}$, where T_1 = 1050 °C. T_{anom} = 1200 °C.

The third regime of HTMT ($T > T_{anom}$) wasn't researched because of there are great oxidality of the melt and fusible additions of this alloy.

The microstructures of the initial pig and the ingot are shown in Figs. 2.2 *a*, *b* As can be seen, the main structural constituents (primary silicon crystals and the eutectic) are differed low. The growth of faceted crystals is



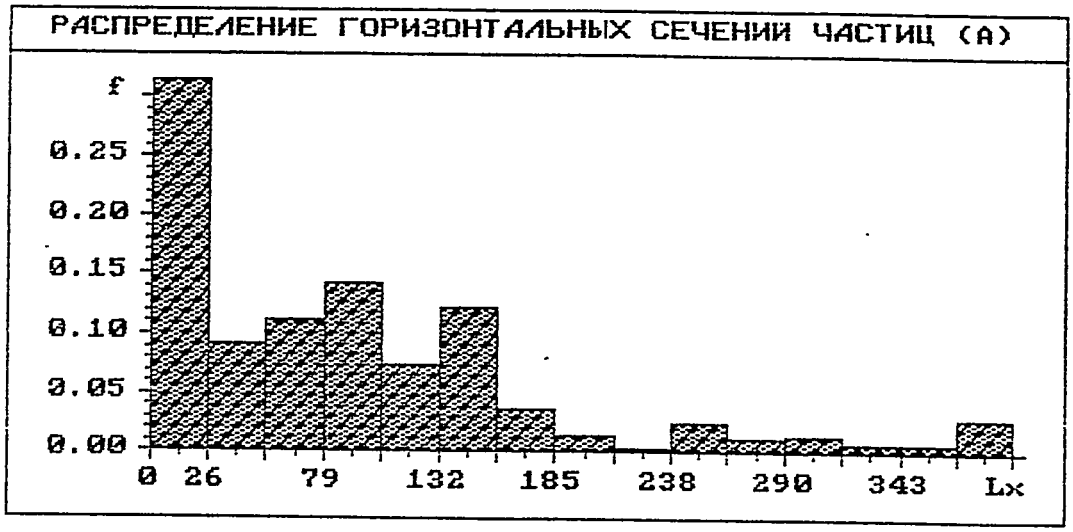
a - pig (x100)



b - ingot (x80)

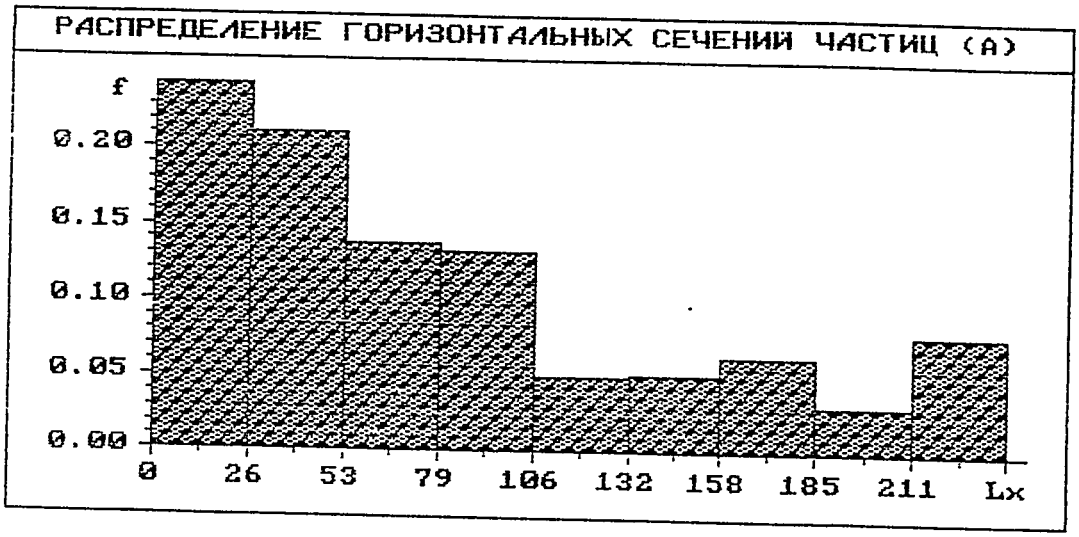
Figure 2.2 Microstructures of pig (*a*) and ingot (*b*) of 390 alloy

Figure 2.3 (*a-d*) Histograms of grain size of primary silicon crystals in specimens casted by using HTMT



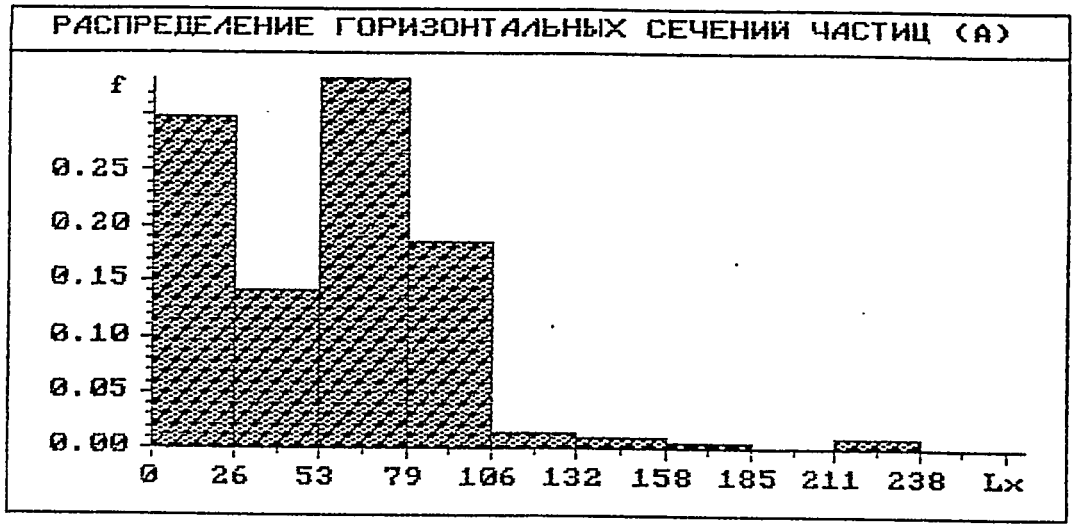
СТАТИСТИКИ (А)	
Число частиц	2640
Минимум	3.300
Максимум	386.110
Мода	3.300
Медиана	72.602
Среднее	93.634
СКО	90.746
Асимметрия	1.483
Эксцесс	2.029
Площадь	3.51E+06

Figure 2.3 *a* (casting №1)



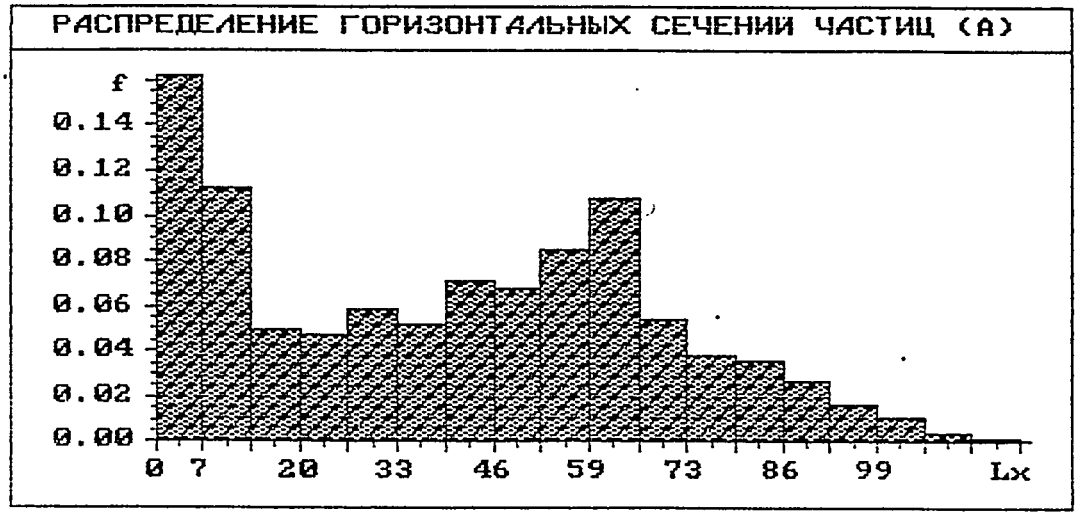
СТАТИСТИКИ (А)	
Число частиц	2980
Минимум	3.300
Максимум	231.006
Мода	3.300
Медиана	59.402
Среднее	80.680
СКО	67.246
Асимметрия	0.848
Эксцесс	-0.400
Площадь	3.51E+06

Figure 2.3 *b* (casting №2)



СТАТИСТИКИ (А)	
Число частиц	2700
Минимум	3.300
Максимум	237.606
Мода	3.300
Медиана	59.402
Среднее	55.069
СКО	39.658
Асимметрия	1.024
Эксцесс	2.992
Площадь	3.51E+06

Figure 2.3 *c* (casting №3)



СТАТИСТИКИ (А)	
Число частиц	4220
Минимум	3.300
Максимум	112.203
Мода	3.300
Медиана	39.601
Среднее	40.410
СКО	27.831
Асимметрия	0.253
Эксцесс	-1.013
Площадь	3.51E+06

Figure 2.3 *d* (casting №4)

observed, although some number of a dendrite crystals are presented. The structure are greatly non-uniform. There are the regions of the hypoeutectic composition consisting of the α-solid solution and so the liquation phases into it.

Histograms of the primary silicon crystals sizes are shown in Figs. 2.3 *a-d* (castings №1-4). The average crystal size (*l*), as function of the temperature (*T*) are given in Fig. 2.4 As can be seen, HTMT according to first regime (castings №1-2) increases the average crystal size, connected with a change of the growth form. Formation of dendritic crystals with high growth rate leads to an increase in *l*. HTMT according to second regime (castings №3. 4) changes the growth form of the crystals: they become faceted square-like and rectangle-like crystals. Fig. 2.5 . illustrates the evolution of morphology of silicon crystals, and Fig. 2.6 shows the dependence of maximum size of primary silicon (*L*) as function of cast temperature (T_c). HTMT causes a equalization in sizes of silicon crystals across the castings. Root-mean square value of crystal sizes are decreased by an increase of *T* (see tables in Figs. 2.3 *a-d*).

Basic eutectic remains without changes. Growth of thin plat-like eutectic silicon is observed. The liquation crystals of intermetallic compounds are in α-solid solution of eutectic (Fig. 2.7 , 2.8).

By X-ray spectrometry analysis it was established that chemistry of intermetallic compound phases are: Al_2Cu and $Al_4Si_2Fe(Mn)$. The temperature treatment of the melt affects on the morphology and the sizes of the crystals. Fig. 2.9 shows the volume fraction of Al_2Cu phases (*V*) as a function of the *T*. It can be seen that high overheating of the melt causes a dispersion in the phases. In specimens produced without HTMT and at low

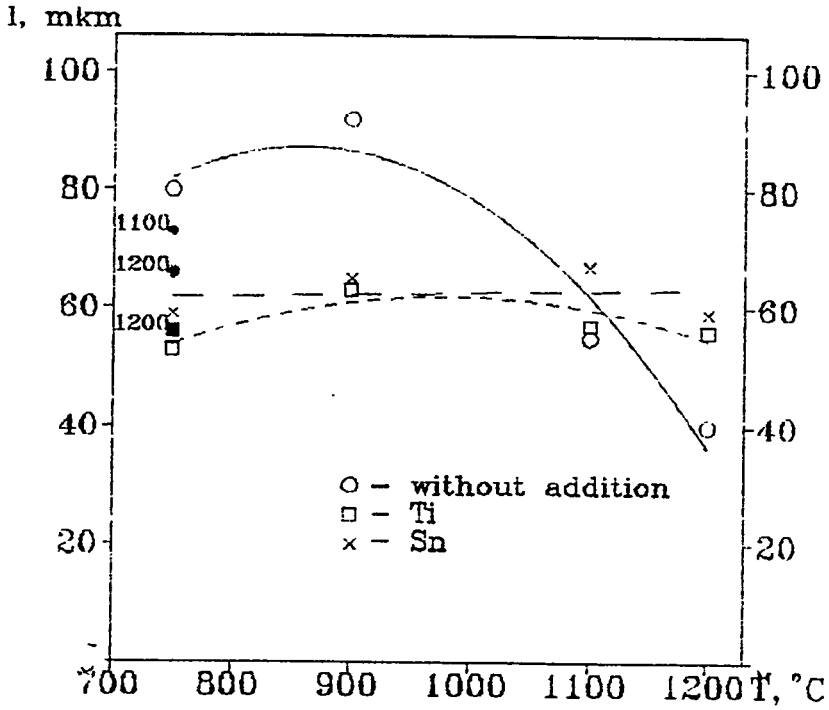


Figure 2.4 Silicon crystals average size as a function of HTMT

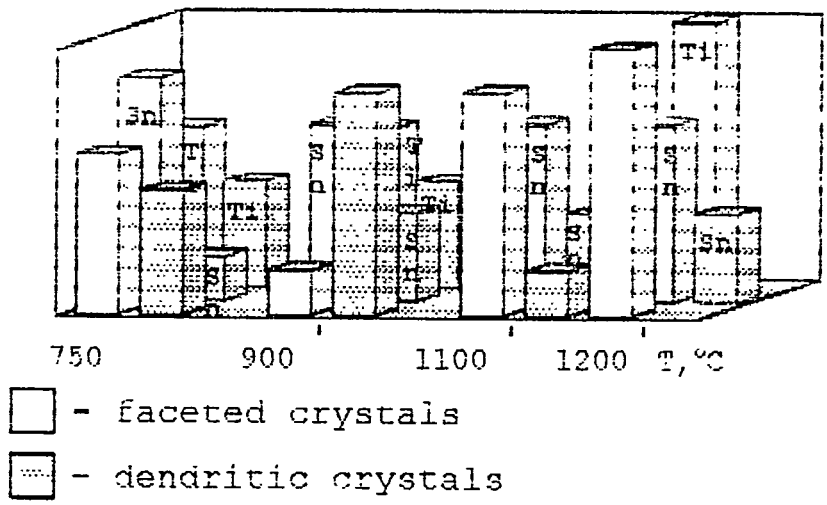


Figure 2.5 Transformation in the morphological features of the primary silicon crystals

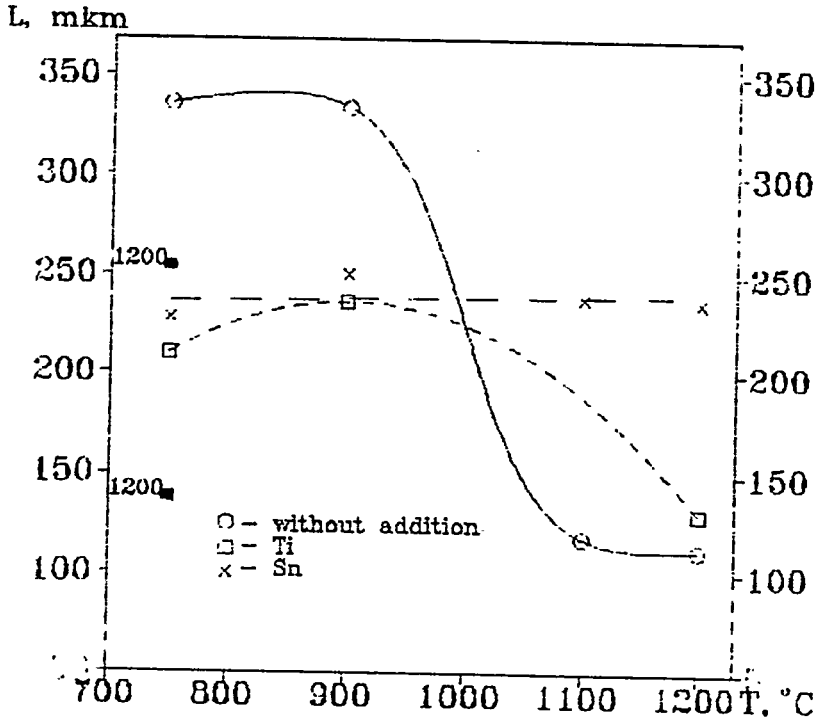


Figure 2.6 Changes in the maximum size of primary silicon crystals in specimens casted at HTMT

temperatures of casting, the growth of isolated faceted plate of Al_4Si_2Fe intermetallic compounds is observed. They are crystallized as primary phases (Fig. 2.7 *b*). For second regime of a HTMT (high overheating) the phase composition of the alloy is changed, Al_5FeSi intermetallic compounds together with Al_4Si_2Fe phases are appeared. The morphology of Al_5FeSi phases have a likeness with chinese hieroglyph (Fig. 2.7 *c*).

Stepped temperature treatment of the melts was used for the second series of specimens. Results of the experiment are illustrated in Figs. 2.10 *a*, *b*, Fig. 2.4 and Fig. 2.6. A temperature of an initial treatment of a melt (*T*) is



a - Al_2Cu (x200)

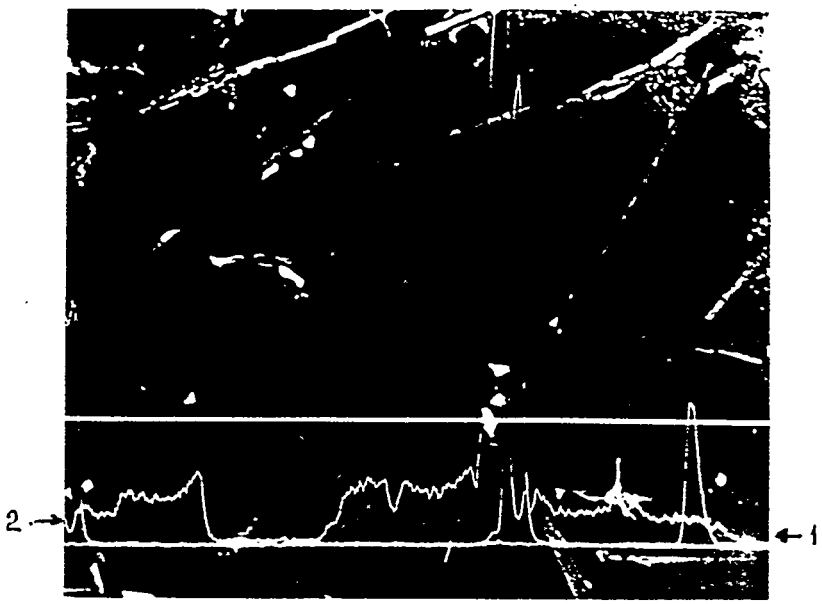


b - $Al_4Si_2Fe(Mn)$ (x 500)

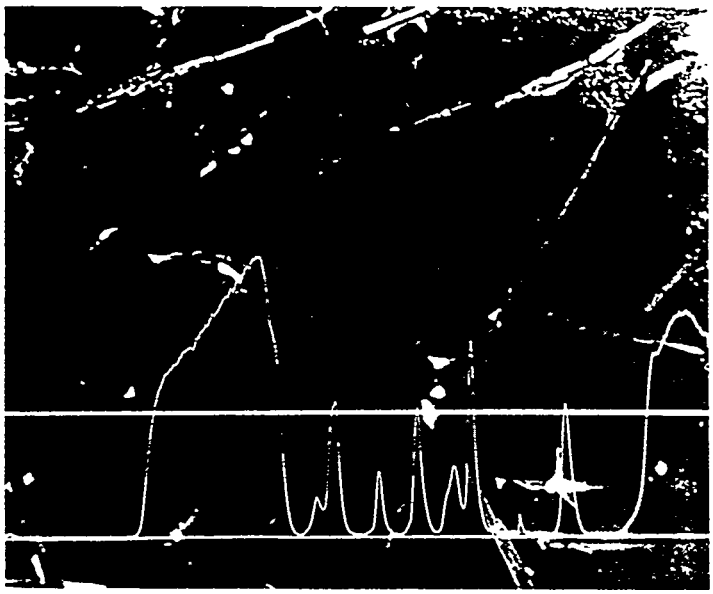


c - Al_5SiFe (x 200)

Figure 2.7 Changes in the morphological features of the intermetallic compounds in cast alloy structure

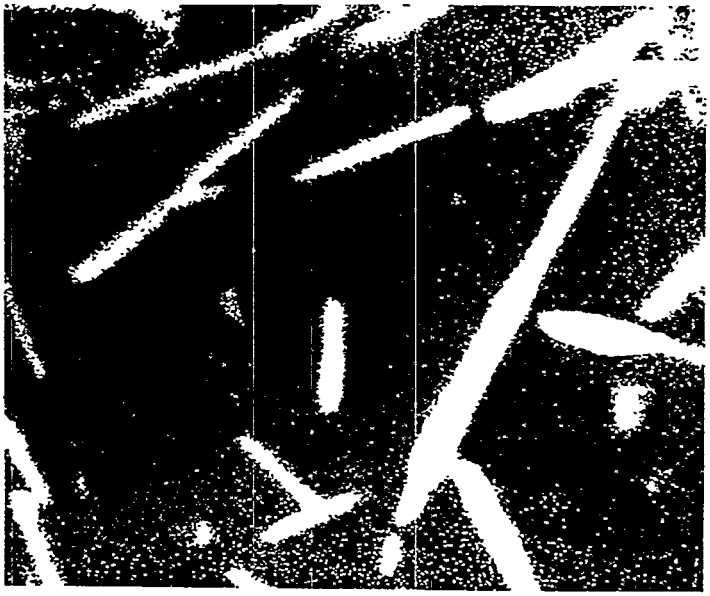


a - secondary electron image, (1 - scanning curve K_{α} Fe; 2 - scanning curve K_{α} Cu)

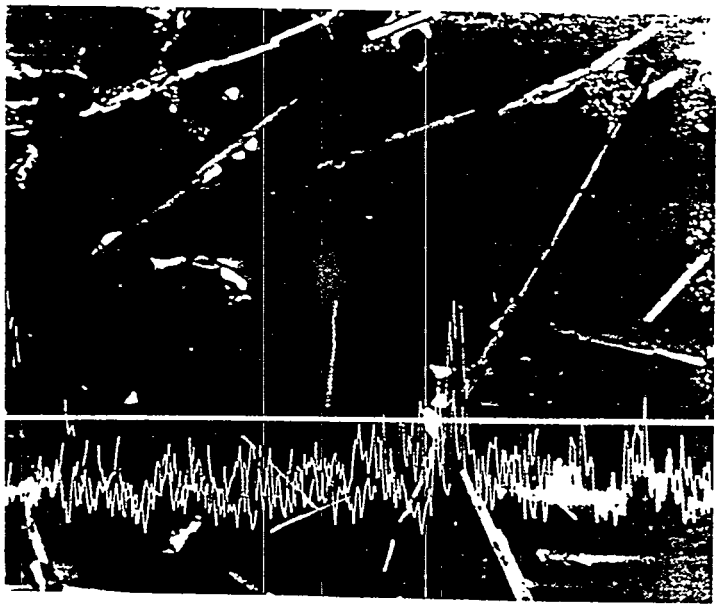


b - secondary electron image, scanning curve K_{α} Si

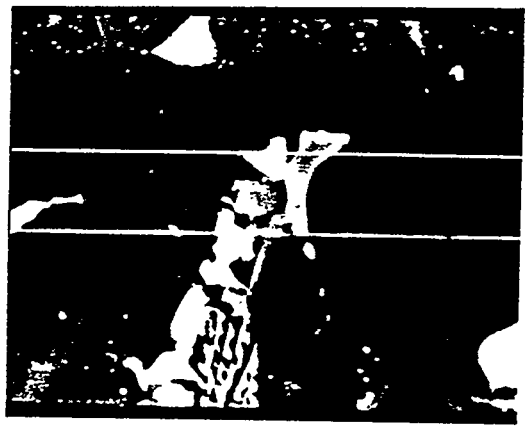
Figure 2.8 *a-f* Intermetallic compounds in the alloy cast structure



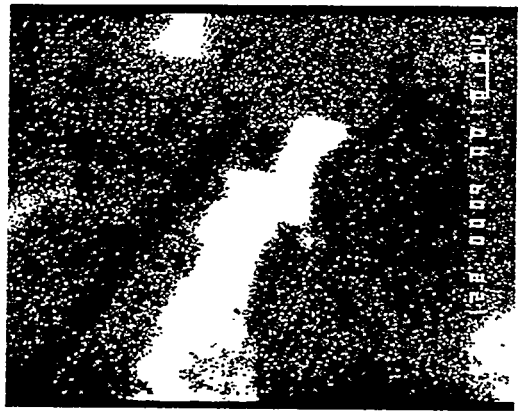
c - X-ray K_{α} Fe radiation



d - secondary electron image, scanning curve K_{α} Mn



e - secondary electron image



f - X-ray K_α Cu radiation

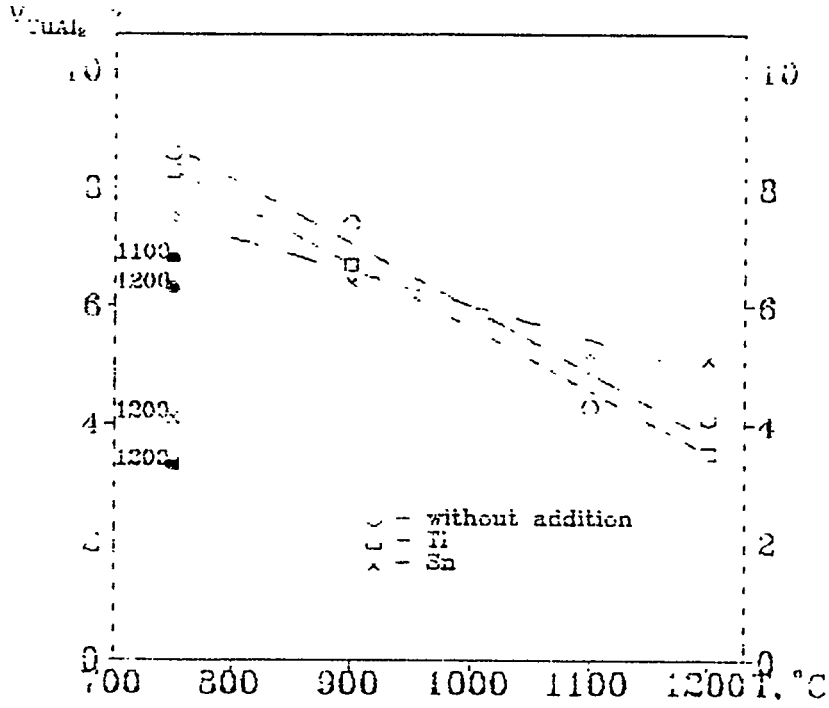
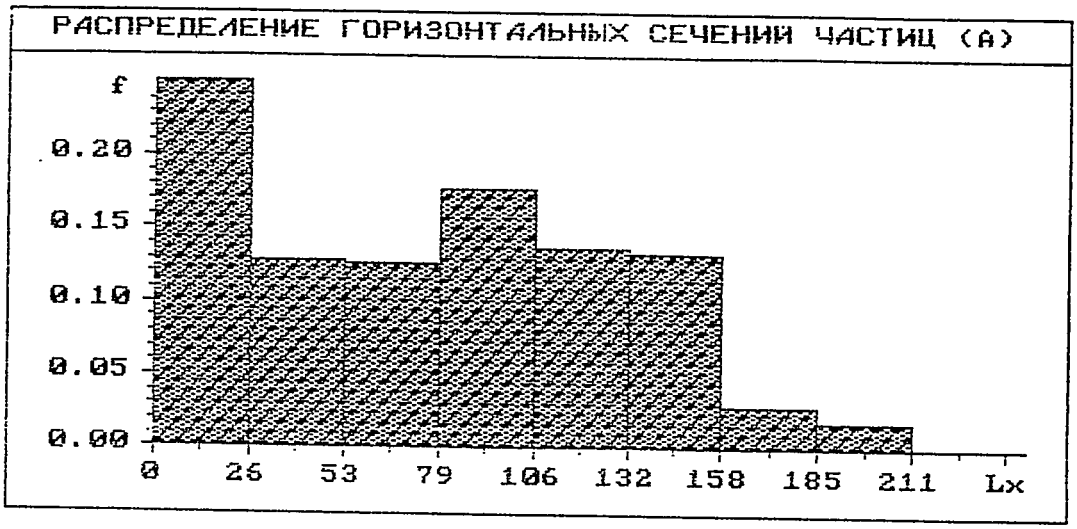


Figure 2.9 Volume fraction of the primary silicon crystals as a function of the HTMT

given near eutectic points. Structure of copper aluminide crystals is shown in Fig. 2.9. It can be seen that the employment of stepped HTMT partially decreases the effect in dispersion of primary silicon.

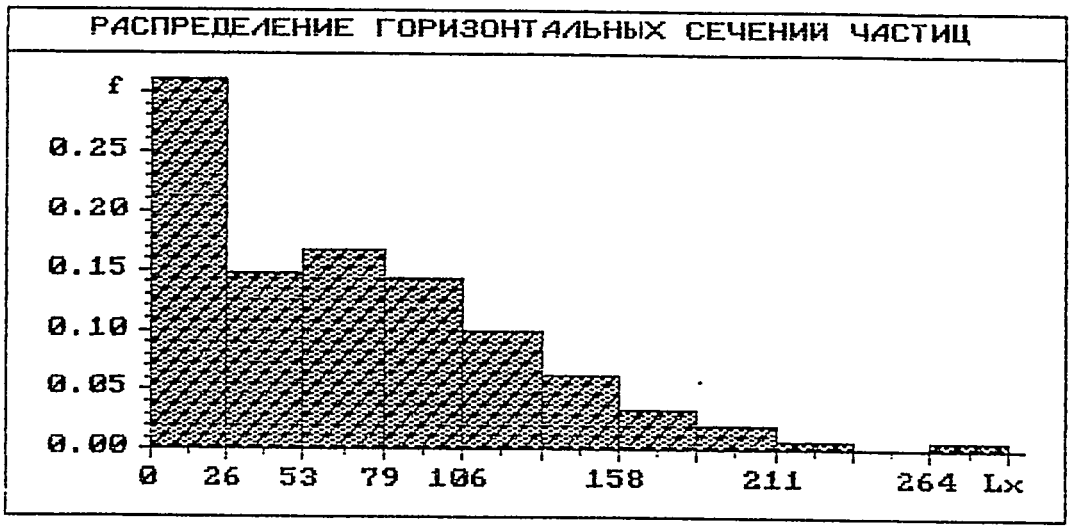
Noted above features of the structure formation of castings may be explain due to the increase of a degree of the melt supercooling by using HTMT [7-9].

Figure 2.10 Histograms of . size of primary silicon crystals in specimens casted by using step HTMT



СТАТИСТИКИ (А)	
Число частиц	4470
Минимум	3.300
Максимум	221.106
Мода	3.300
Медиана	75.902
Среднее	76.884
СКО	53.113
Асимметрия	0.238
Эксцесс	-1.009
Площадь	3.51E+06

Figure 2.10 *a* (casting №5)



СТАТИСТИКИ (А)	
Число частиц	4530
Минимум	3.300
Максимум	277.207
Мода	3.300
Медиана	59.402
Среднее	67.892
СКО	56.059
Асимметрия	0.929
Эксцесс	0.645
Площадь	3.51E+06

Figure 2.10 *b* (casting №6)

2.2.2 Effect of an alloying by refractory additions

Titanium was used as a refractory addition. It was introduced by using binary Al - Ti master alloys.

A typical structure of the master alloys, produced by using the standard industrial technique, i.e. by casting a pig, is shown in Fig. 2.11. Primary crystals of titanium aluminide with a size 75-120 μm non-uniformly scattered across a section of the pig are formed. The X-ray diffraction phase analysis of an intermetallic compounds and determination of the lattice parameter of the aluminum-base solid solution was carried out with a diffractometer by using Co K_α monochromatic radiation. By X-ray diffraction phase analysis it was established that primary crystals are corresponded to Al_3Ti composition

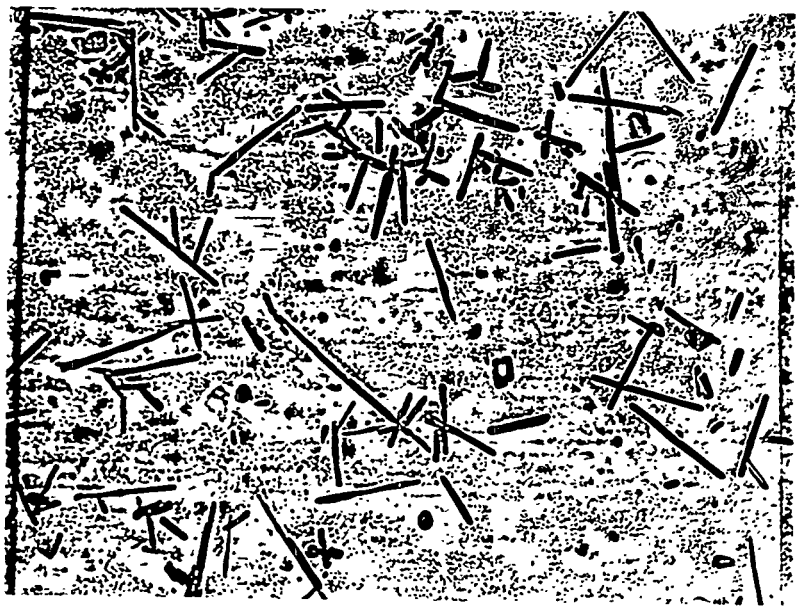


Figure 2.11 Structure of Al - 3.6% Ti master alloy

Figure 2.12 (a-e) Histograms of size of primary silicon crystals in alloy with titanium addition

СТАТИСТИКИ	
Число частиц	648
Минимум	3.300
Максимум	135.304
Мода	3.300
Медиана	52.801
Среднее	54.339
СКО	37.014
Асимметрия	0.141
Эксцесс	-1.311
Площадь	7.03E+05

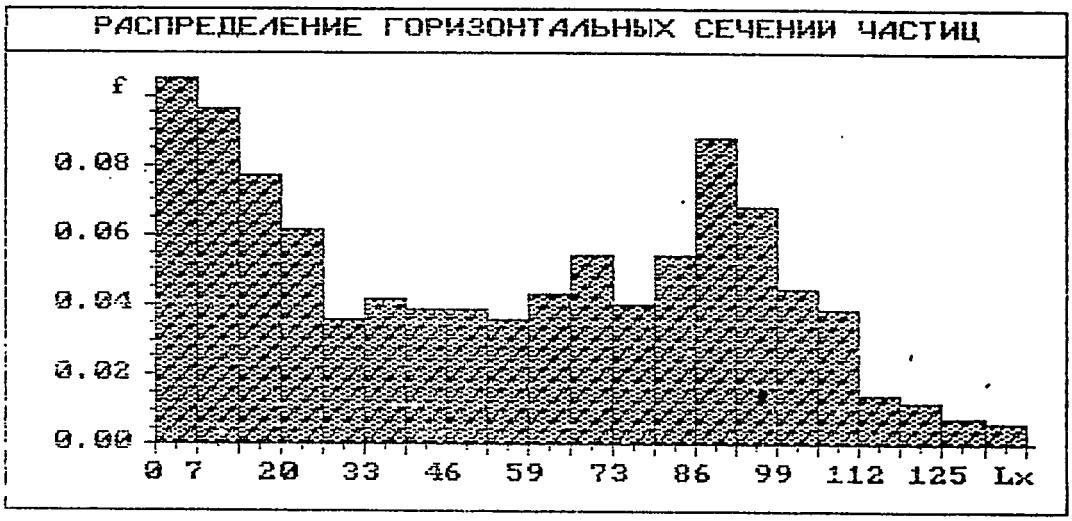
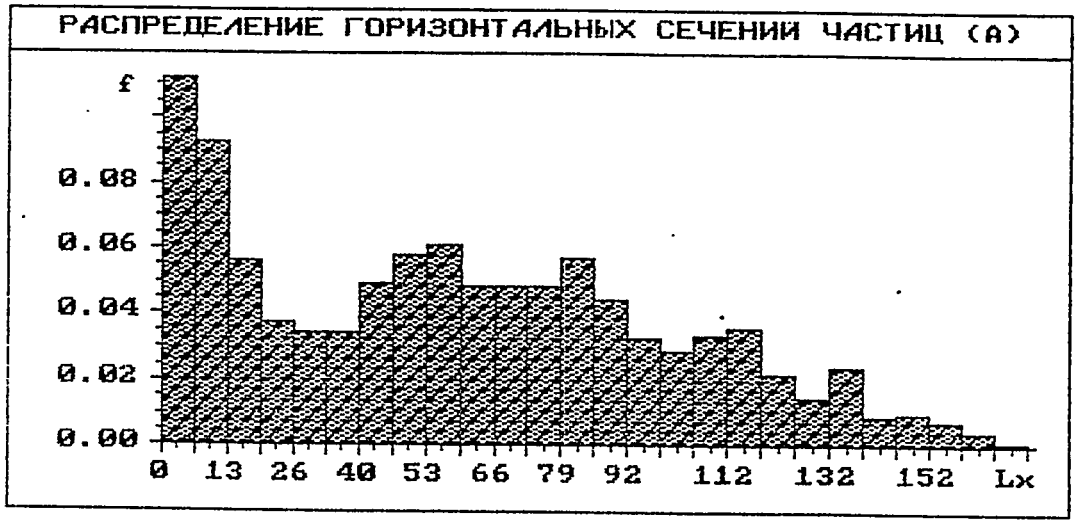


Figure 2.12 *a* (casting №7)



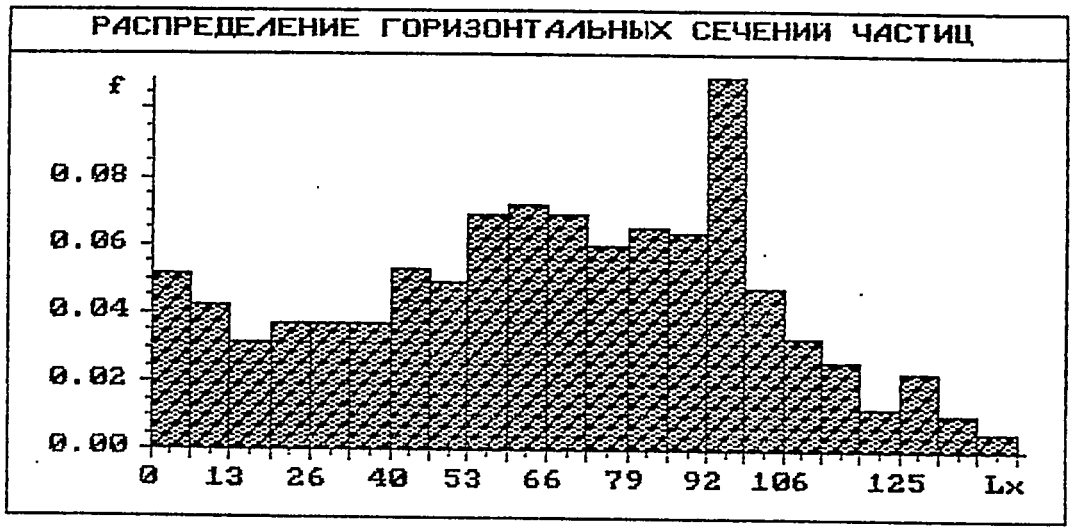
СТАТИСТИКИ (А)	
Число частиц	1925
Минимум	3.300
Максимум	178.205
Мода	3.300
Медиана	59.402
Среднее	66.671
СКО	45.362
Асимметрия	0.349
Эксцесс	-1.075
Площадь	2.81E+06

Figure 2.12 *b* (casting №8)



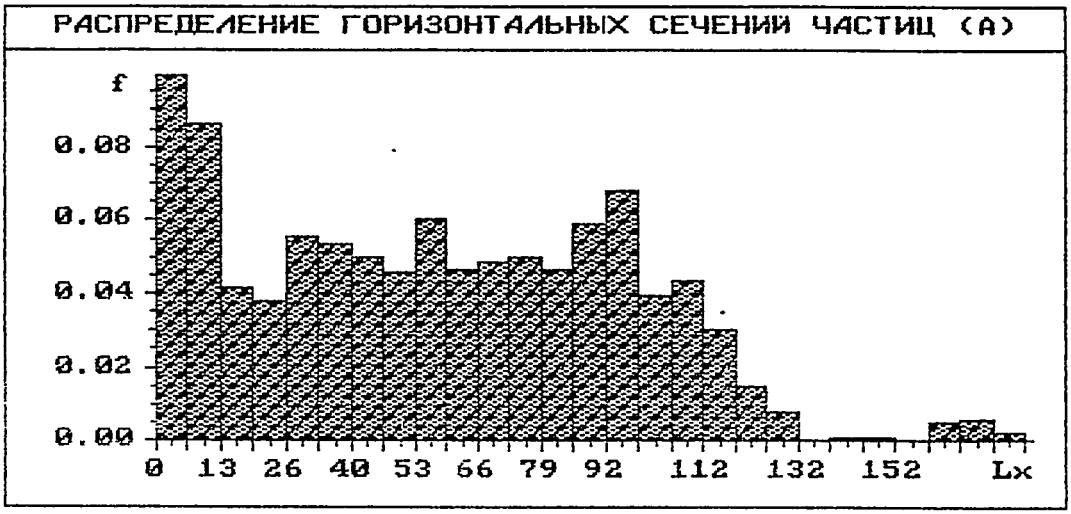
СТАТИСТИКИ (А)	
Число частиц	3276
Минимум	3.300
Максимум	165.004
Мода	3.300
Медиана	52.801
Среднее	58.627
СКО	41.290
Асимметрия	0.382
Эксцесс	-0.818
Площадь	3.51E+06

Figure 2.12 *c* (casting №9)



СТАТИСТИКИ	
Число частиц	570
Минимум	3.300
Максимум	138.604
Мода	92.402
Медиана	66.002
Среднее	66.349
СКО	33.905
Асимметрия	0.00E+00
Эксцесс	-0.801
Площадь	7.03E+05

Figure 2.12 *d* (casting №10)



СТАТИСТИКИ (А)	
Число частиц	1348
Минимум	3.300
Максимум	174.905
Мода	3.300
Медиана	52.801
Среднее	57.536
СКО	38.176
Асимметрия	0.314
Эксцесс	-0.644
Площадь	3.51E+06

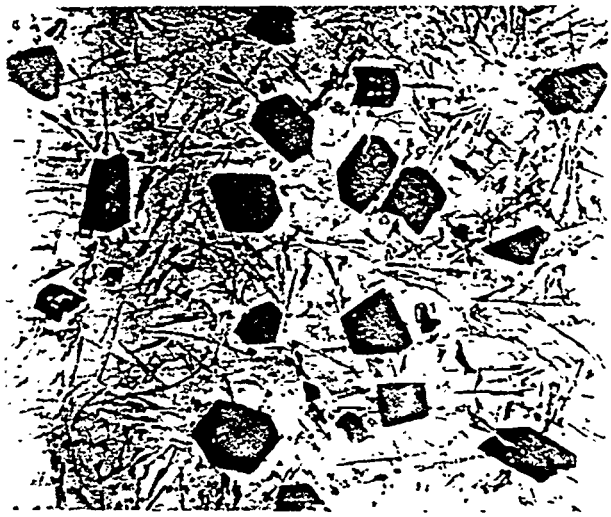
Figure 2.12 *e* (casting №11)



a - casting №1

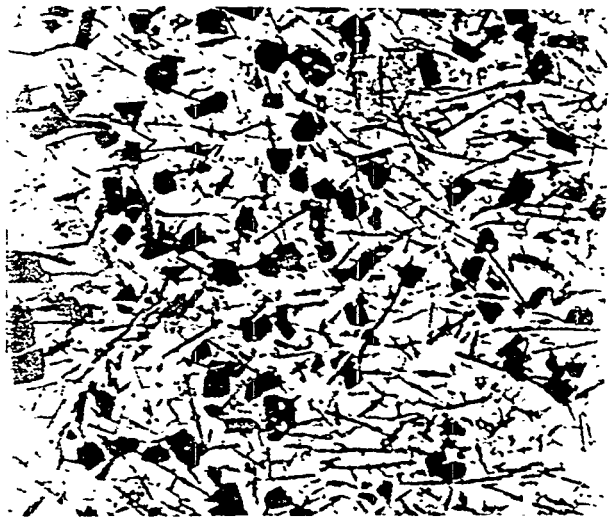


b - casting №7 (Ti)



c - casting №12 (Sn)

Figure 2.13 Changes in the alloy structures after the addition of tin or titanium (x80)



a - casting №4



b - casting № 9 (Ti)

Figure 2.14 Changes in the alloy structure after HTMT (x80)

and a tetragonal lattice having DO_{22} crystal structure and the parameters a = 0.5435 nm and c = 0.8591 nm. In the ingots with 0.12 wt % titanium the structural components are conserved, however, modifications in the sizes, the morphology and the quantity of phases are observed (III series, №7-9 castings and IV series, №10,11 castings). Figs. 2.4 and 2.6 shows the changes in linear sizes of silicon crystals (by corresponding conditional marks (□)), and Fig. 2.5 illustrates the transformation in them growth forms. The comparison of the results of casting №1 and casting №7 notes about refining influence of the addition on a formation of primary phases (Figs. 2.13 *a*, *b*). Crystals sizes of the primary silicon are increased by factor of 2 (Figs. 2.12 *a* - *e*). It is observed the smoothing of the composition in a section of the specimens therefore fields of a hypoeutectic structure are absent.

It is importantly to point out the role of titanium in a nucleation and a kinetic growth of phases of *Al - Si* main eutectic. The decrease in the crystals sizes of eutectic silicon, the modification of the eutectic and the increase of its volume fraction are observed. Primary intermetallic compound phases with titanium don't found, that is an evidence of a supplementary alloying and a hardening of α-solid solution.

The HTMT and the alloying low effect on the formation conditions of primary silicon crystals (Figs. 2.13 *b*, 2.14 *b*), however it is change the dispersion of the whole structure, in particular iron, cooper and silicon phases (Fig. 2.9). Large crystals of $Al_4Si_2Fe(Mn)$ phase growing in the form of needles practically completely are absent and more small Al_5FeSi crystals are present..

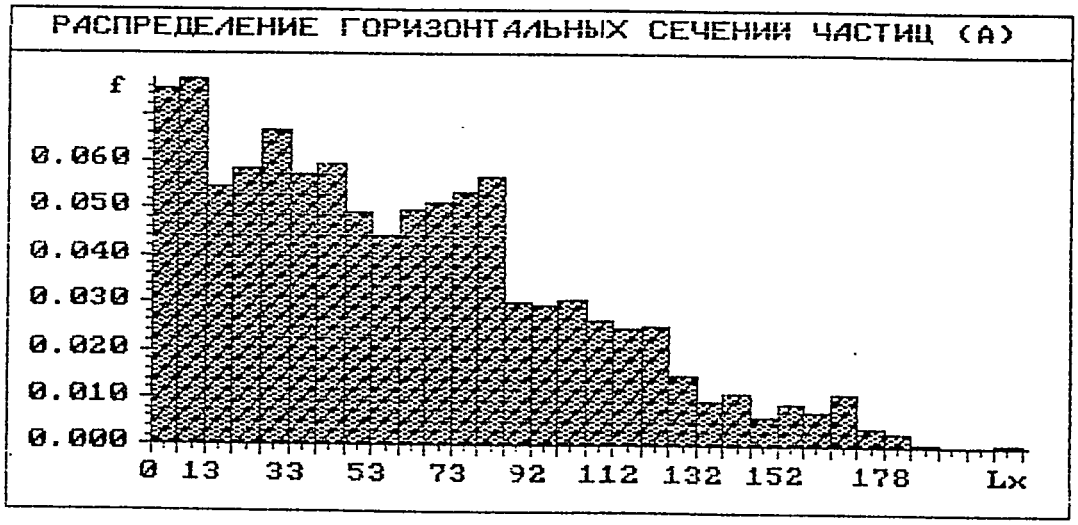
2.2.3 Effect of an alloying by surface-active additions

Tin was used as a surface-active addition which was introduced into initial alloy with concentration 0.2 wt. %. This quantity of the surface-active addition was founded experimentally earlier [10]. The modifying effect on the structure was studied without HTMT (castings №12) and by using HTMT (from 13 to 16 castings). Changes of characters of structures are shown in Fig. 2.13 *c*, Figs. 2.4-2.6, Fig. 2.9 and histograms (Fig. 2.15). Addition of 0.2 wt. % tin into alloy produces a significant effect on the morphology of primary silicon crystals, stabilizing faceted crystal growth, and decrease in the sizes.

The employment of HTMT and microalloying (from 13 to 16 castings) doesn't lead to supplementary change in conditions of a nucleation and a growth of primary silicon crystals (Figs. 2.4, 2.6). We see that a character of a distribution of liquation phases sizes in *T is* conserved (Fig. 2.9).

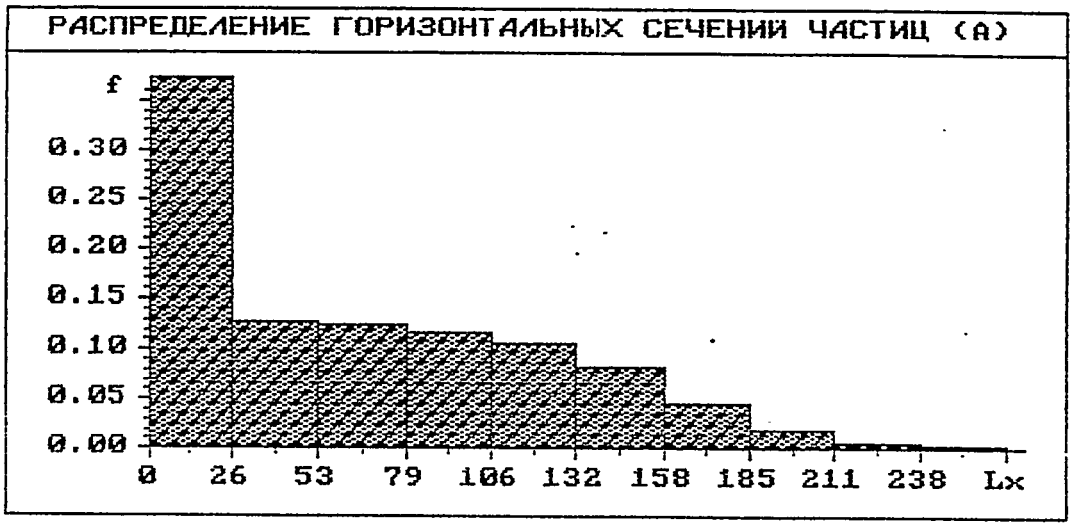
Thus, an alloying of silumin melt by surface-active elements changes the conditions of a nucleation and growth kinetic of phases refining the solid alloy structure.

Figure 2.15 (a - e) Histograms of size of primary silicon crystals in alloy with tin addition



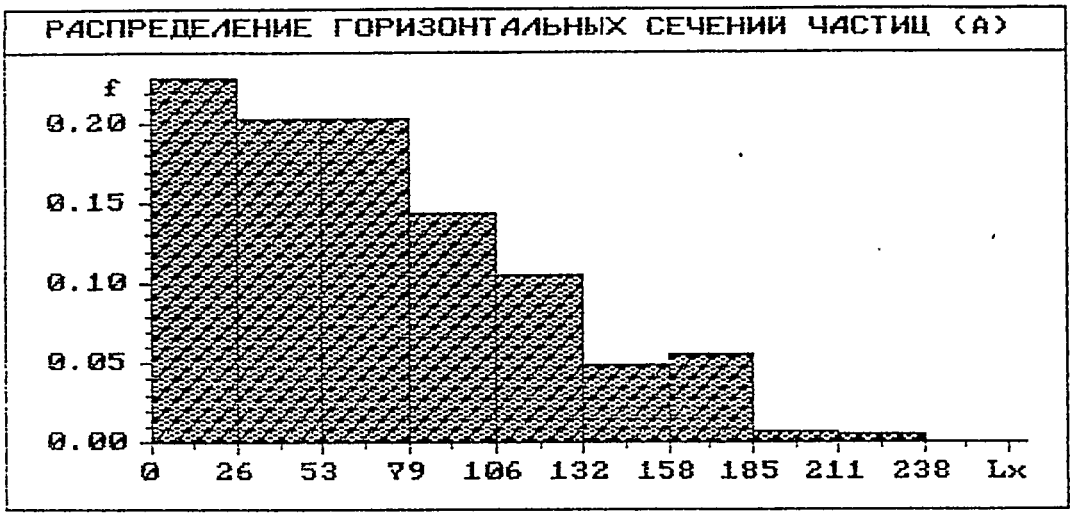
СТАТИСТИКИ (А)	
Число частиц	1808
Минимум	3.300
Максимум	204.605
Мода	3.300
Медиана	52.801
Среднее	59.465
СКО	42.100
Асимметрия	0.680
Эксцесс	-0.194
Площадь	2.81E+06

Figure 2.15 *a* (casting №12)



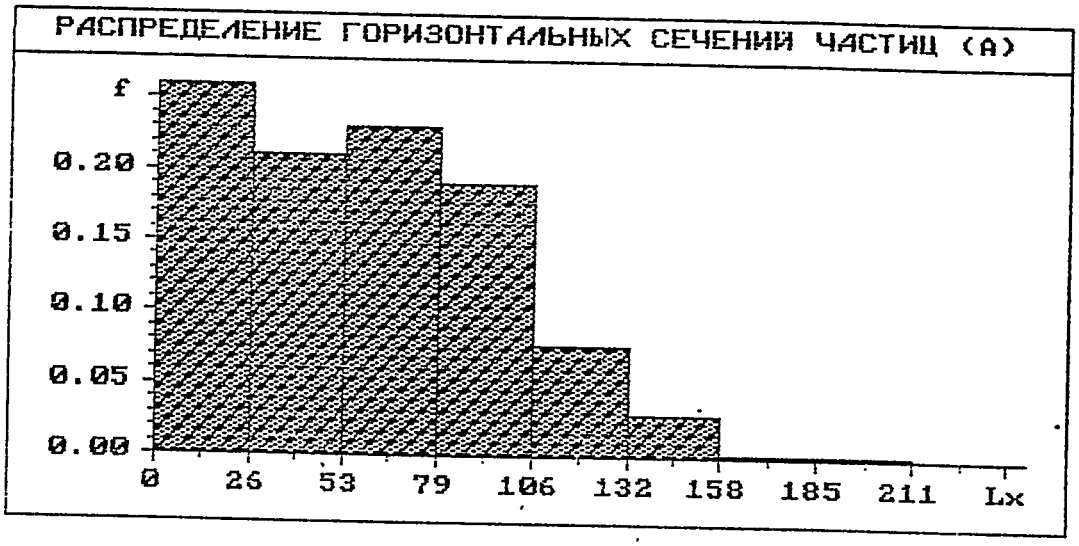
СТАТИСТИКИ (A)	
Число частиц	2697
Минимум	3.300
Максимум	260.707
Мода	3.300
Медиана	52.801
Среднее	65.132
СКО	56.753
Асимметрия	0.710
Эксцесс	-0.435
Площадь	2.81E+06

Figure 2.15 *b* (casting №13)



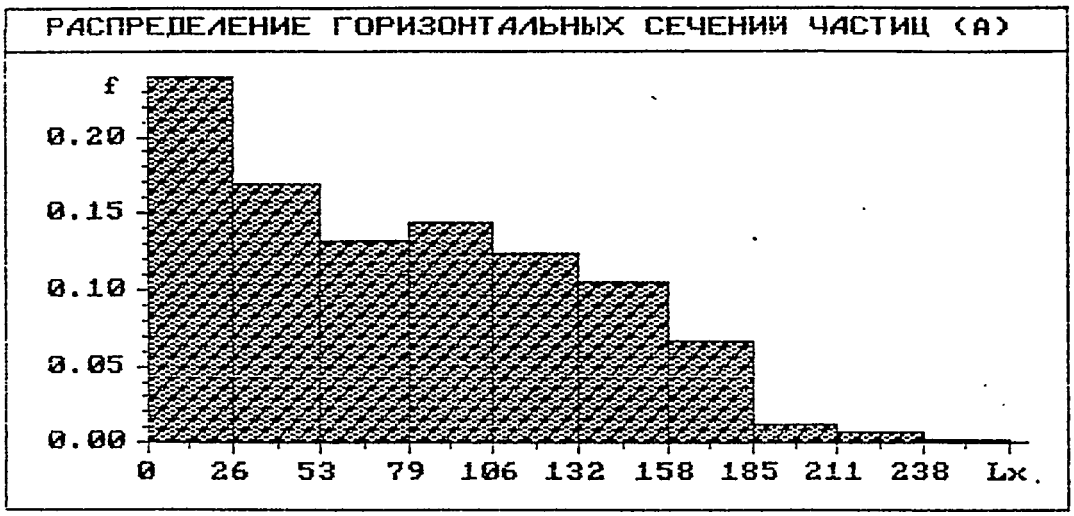
СТАТИСТИКИ (А)	
Число частиц	3056
Минимум	3.300
Максимум	247.507
Мода	6.600
Медиана	59.402
Среднее	69.101
СКО	48.592
Асимметрия	0.732
Эксцесс	-0.030
Площадь	3.51E+06

Figure 2.15 *c* (casting №14)



СТАТИСТИКИ (А)	
Число частиц	4878
Минимум	3.300
Максимум	234.306
Мода	3.300
Медиана	56.102
Среднее	58.871
СКО	38.667
Асимметрия	0.497
Эксцесс	-0.055
Площадь	4.92E+06

Figure 2.15 *d* (casting №15)



СТАТИСТИКИ (А)	
Число частиц	2515
Минимум	3.300
Максимум	247.507
Мода	6.600
Медиана	69.302
Среднее	77.036
СКО	54.666
Асимметрия	0.493
Эксцесс	-0.677
Площадь	2.81E+06

Figure 2.15 *e* (casting №16)

2.3 Conclusion

— The influences of different regimes of HTMT on the structure of castings from 390 alloy were investigated. It was shown, that overheating of the melt up to temperatures under T_{anom} (I regime) does not change the structure of the alloy essentially. Overheating of the melt up to temperatures near T_{anom} leads to the stabilization of faceted forms of a growth and decreases sizes of primary silicon crystals by factor of 2.5. It was demonstrated that HTMT can improve the leveling of the composition and macrostructure of castings and decrease in sizes of liquation phases.

— The effects of small additions on crystallization of silumins were studied. It was shown, that additions of tin and titanium into alloy produces an effect on sizes of primary phases (average size of primary silicon crystals decreases by factor of 1.5 - 1.7). Addition of titanium into silumin causes a decrease in the sizes of eutectic silicon crystals and a grain refinement of eutectic.

— Complex effects of HTMT and alloying lead to supplementary modification of the structure by means of a decrease of a thickness of a liquation eutectic layers between dendrites of α phase.

REFERENCES

1. Taran U.N.. Mazur V.J. The structure of eutectic alloys. M.. Metallurgy. 1978. p. 623.

2. Tyagunov G.V., Tsepelev V.S., Kushnir M.N. and etc. The apparatus for kinematic viscosity measuring of the metallic melts// Plan laboratory. 1980. №10. p.p. 914-920.

3. Khakimov O.P. The influence of the melt state on formation of the cast alloys based iron and aluminium structure and properties. The Dissertation on competition doctor of sience. Ekaterinburg. 1994. p. 120.

4. Vertogradsky V.A., Egorova A.S. Interpretation of the differential analysis thermal curve// engineer-physical magazine. 1979. v.36. №3. p.p. 481-486.

5. Vertogradsky V.A., Ricova T.P. Investigation of the phase transformation in the superalloy melts by the differential thermal analysis. High temperature and heat resistance alloy based nickel. M.: Science. 1984. p.p. 223-227.

6. Mondolfo L.F. The aluminum alloys structure and properties. M.: Metallurgy. 1979. p. 639.

7. Brodova I.G., Popel P.S. and etc. Influence Structure of Melt for Crystallization of Silumin. - Rasplavy, 1987, vo.1, №3, pp. 31-35.

8. Brodova I.G., Esin V.O. and etc. Morphological Peculiarities and Properties of Hypereutectic Silumin. - Fiz. Met. Metaloved, 1988, vol. 65, №6, pp. 31-35.

9. Brodova I.G., Polents I.V. and etc. On the Formation of the Cast Structure of Supercooled Al-Ti Alloys. - The Physics of Metals and Metallography, 1992. vol. 73, №1, pp. 63-67.

10. Brodova I.G., Bashlikov D.V. and etc. Effect of small tin additions on the structure of hypereutectic silumin. - The Physics of Metals and Metallography, 1995, vol. 79, №4, pp. 425-429.

Project Title: Growth of Nickel (Ni) Base Single Crystal Superalloys At High Pressures
Principal Investigator: Vladimir Esin
Institute for Physics of Metals
Ekaterinburg, Russia
AM-7683

CLAUSE 1 - STATEMENT OF WORK

Tasks:

The Contractor Shall:

1. Grow single crystals of Ni base superalloys and aluminum (and Al-Cu) at pressures of 0 to at least three (3) atmospheres, using the Contractor's unique apparatus. The Contractor shall provide 12 samples per alloy.

2. Obtain maps of the structure of specimens using x-ray topography and x-ray shadow techniques. When structure due to liquation is detected, the alloys solute concentration along with x-ray microprobe analyzer data and x-ray diffraction data shall be obtained. Provide a brief report detailing the experimental results.

3. Modify an existing two-dimensional unsteady computer program, which simulates dendritic growth and morphology. Modification shall simulate the effects of pressure on the kinetics of dendritic growth. Provide a report on model modification and theoretical results, and the computer code for this computer program.

4. Deliver a final report that discusses all work performed and make recommendations reached.

Sandia National Laboratories
Attn.: Lee Bertram

M/S 9043. Org.8743
P.O.Box 969
Livermor, CA 94551

Fax to L.Bertram
Fax No. 510 294-2999

Ref.: Contract No AM-7683

Institute of Metal Physics
Ural Division of Russian
Academy of Sciences.
18. S.Kovalevskaya str.
Ekaterinburg, GSP-170
620219, Russia
Fax No 007-3432-445-244

BRIEF REPORT ABOUT TASK 2

(Contract No AM-7683)

The X-ray diffraction topography, shadow microroentgenography, X-ray diffraction analysis of the lattice parameter and X-ray microprobe were used to investigate the structure of single crystals of model **Al-Cu** alloys and **Ni**-base superalloys grown from the melt by Bridgman method at gas pressures of 0 to 3 atmospheres.

The studies were made at five series crystals.

Series 1 : Single crystals of Al-3.5 % (mass) Cu alloys 120 mm long and 20 mm in diameter. Growth rate - R=1 mm/min. P : 0.0; 1.0; 1.5; 2.0; 2.5 and 3.0 atm. (samples № № I-6).

Series 2 : Single crystals of Al-4% (mass) Cu alloys 120 mm long and 20 mm in diameter. Growth rate R=0,5 mm/min. P : 0.0; 1.0; 1.5; 2.0; 2.5 and 3.0 atm. (samples № № 7-I2).

Series 3 : Single crystals of Ni-base superalloy MAR-M200-type 80 mm long and 15 mm in diameter. Growth rate R=3 mm/min. P :1.00; 1.25; 1.50; 1.75; 2.00; 2.25; 2.50; 2.75 and 3.00 atm.(samples № № I3-2I).

Series 4 : Single crystals of Ni-base superalloy MAR-M200-type 80 mm long and 15 mm in diameter. Growth rate R=1 mm/min. P : 1.5; 2.0 and 2.5 atm.(samples № № 22-24).

Series 5 : Crystals of Ni-superalloy MAR-M200-type with higher carbon concentration 80 mm long and 10 mm in diameter. Growth rate R=1 mm/min. (samples № № 25-26). P : 1.0 and 1.5 atm.

All crystals were grown with <100> orientation of the solid-liquid interface from the same seeds in every series.

The crystal growing thermal conditions remained inveriable in every series.

The studies were condacted on plane (100) sections made on an electric spark cutter. They were parallel and perpendicular to the direction of crystal growth. Transverse sections were always cut out at the same distance from the seed because the thermal conditions in growing crystals by Bridgman's technique varied along the specimen length of the crystal.

The X-ray diffraction studies were conducted by taking topographs on a RCDT scanning chamber based on a GUR-4 goniometer. All topographs were received in Cu - K_α radiation from (400) planes.

The shadow roentgenography studies were conducted using radiation from Cu- sharp focus X-ray tube at specimens 0.25 mm thickness for Al-Cu alloys and 0.15 mm thickness for Ni-base superalloys.

The X-ray diffraction date of the lattice parameter are obtained from the (400) lines using Co-K_β monochromatic radiation by DRON-3 diffractometer.

The X-ray microanalysis were conducted by Microscan-MK-PA, JSM-U3 and Superprobe-733 technique.

The main results are illustrated by following figures.

Fig.1. X-ray diffraction topographs of the longitudinal and transverse sections of crystals Al-Cu alloy series 1.

Fig.2. X-ray diffraction topographs of the longitudinal sections of crystals Al-Cu alloy series 2.

Fig.3. X-ray diffraction topographs of the longitudinal and transverse sections of crystals Ni-base superalloy series 3.

Fig.4. X-ray diffraction topographs of the longitudinal and transverse sections of crystals Ni-base superalloy series 4.

Fig.5. Shadow microroentgenographs of the across cuts of Al-Cu crystals series 1. (black network shows high Cu segregation region leading to formation of eutectic phase - $CuAl_2$).

Fig.6. Shadow microroentgenographs of the longitudinal cuts of Al-Cu crystals series 2. (black network shows high Cu segregation region).

Fig.7. Shadow microroengenographs of the across cuts of Ni-base superalloy crystals series 3. (Light network correspond to interdendritic space; small black crosses show carbide phase - MeC.)

Fig.8. Dependences of lattice parameter (a) of the solid solution on the pressure (P) for Al-Cu crystals series 1.
Curve 1-distance from the seed 20 mm;
Curva 2-distance from the seed 60 mm.

Fig.9. Change in the lattice parameter (a) along crystals (L) at verious pressures for Al-Cu crystals series 2.
Arrows show position of cellular-dendritic transition.

Fig.10. Dependences of the lattice parameter (a) of the solid solution on the pressure (P) for Ni-base superalloy crystals series 3.
Curve 1-distance from the seed 20 mm;
Curve 2-distance from the seed 60 mm.

Fig.11. A typical profiles of Cu distribution along cross-sections primary arms of dendrites at verious pressures for Al-Cu crystals series 1.

Fig.12. Distribution of Cu in region cellular-dendritic transition at longitudinal sections of crystals series 2.
1-the cellular growth;
2-the dendritic growth.

Fig.13. Distribution of Al (1) and Nb (2) in interdendritic space for crystals series 3. at verious pressures.

Fig.14. Microprobe traverse across primary arms of dendrites for crystals series 3.
1- common sight;
2- distribution of Nb.

Fig.15. Distribution and concentration (mass.%) of verious soluble components at transverse section of crystal series 3 (P=0.275 MPa).

Fig.16. Macrostructure of the longitudinal sections Ni-base superalloy with higher carbon concentration series 5.

Fig.17. Scheme of cutting (section) of single cristals.

Intensivity of liquation may be characterized by the ratio of concentration of soluble components in interdendritic space to concentration of those in primary arm. These data are presented in table.

P MPa	Al	Ti	Nb	W	Co	Cr
0.275	0.91	1.8	1.9	0.92	0.91	0.96
0.300	0.99	3.0	3.4	0.91	0.88	0.96

The results of X-ray analysis have shown:

1. The single crystals of Al-Cu alloys series 1 solidify with the formation of the dendritic structure typical for growth of the dendritic ensembles.

2. In the series 2 initial part of the single crystal was solidified with the formation of the cellular structure and other part with the formation of dendritic structure. Position of the cellular-dendritic transition boundaries is depended on pressures.

3. The single crystals of Ni-base superalloys have complex chemical composition and specific structure. It solidifies with formation of a single crystal γ-phase having cellular-dendritic growth morphology. Interdendritic spaces is filled with eutectic γ'-phase and simultaneously of monocarbide phase.

4. The specimens of series 5 is not single crystals because of high carbon concentration leading to the formation of carbide phase which is centres of crystallization at two-phase zone. However it show influence of pressure on the alloy structure very well.

5. As follows from above data the high pressures in all cases influence on the structural perfection of single crystals every alloy, lattice parameters and the liquation processes leading to segregation of alloy solution components, that must also have changed the amount and distribution of the intermetallics and carbide phases.

10.05.95 V.O.Esin

Principal Investigator

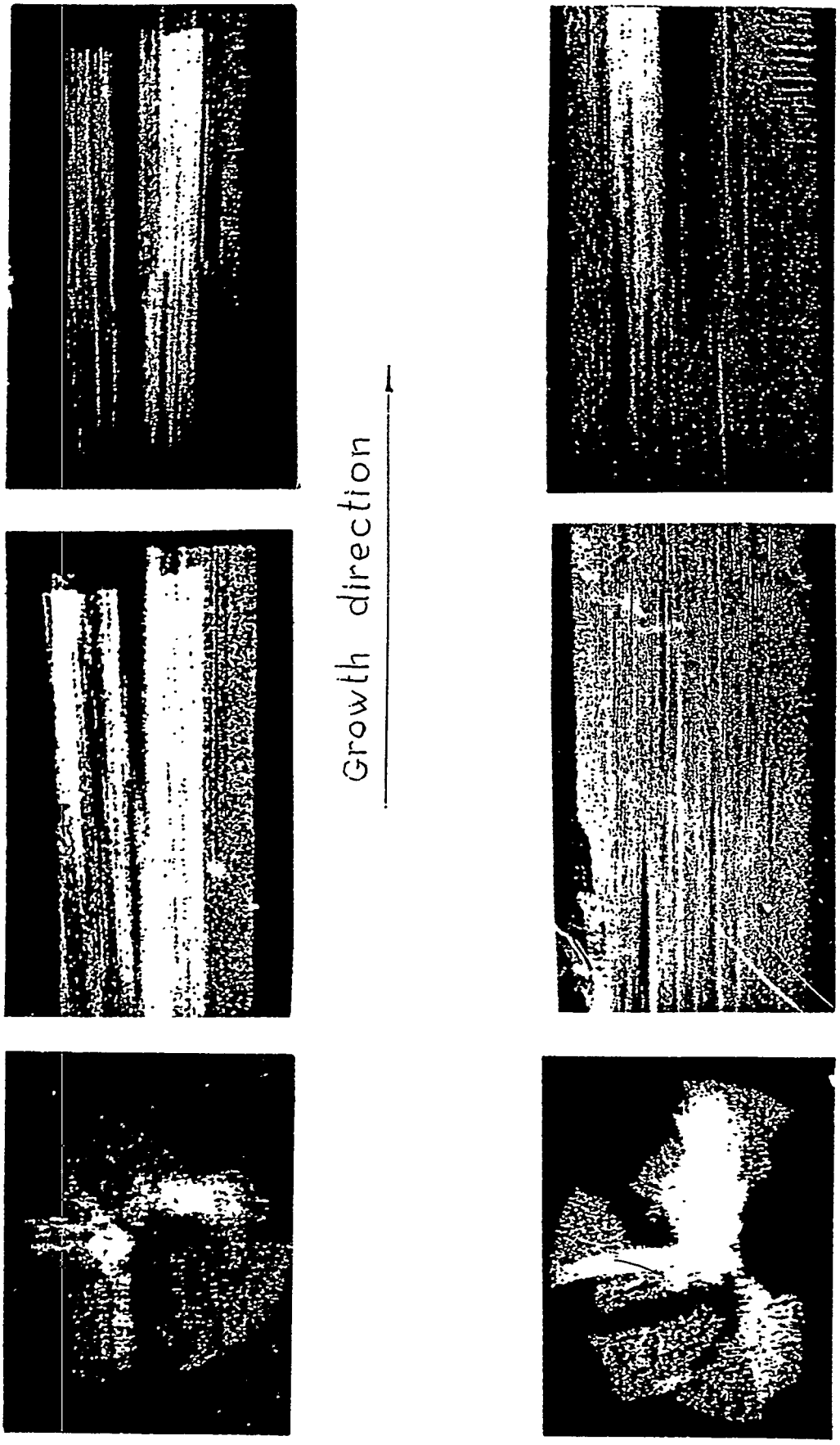
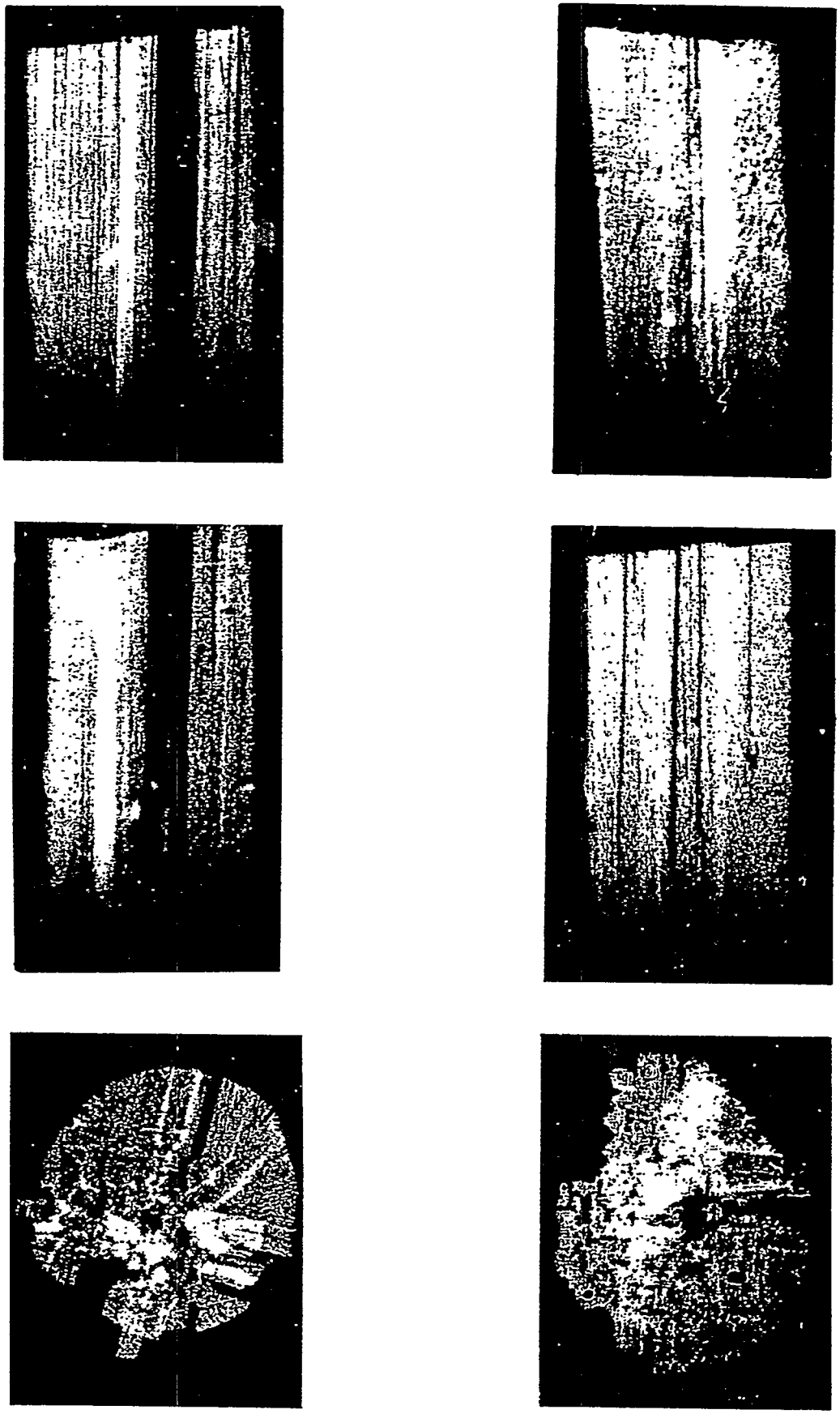


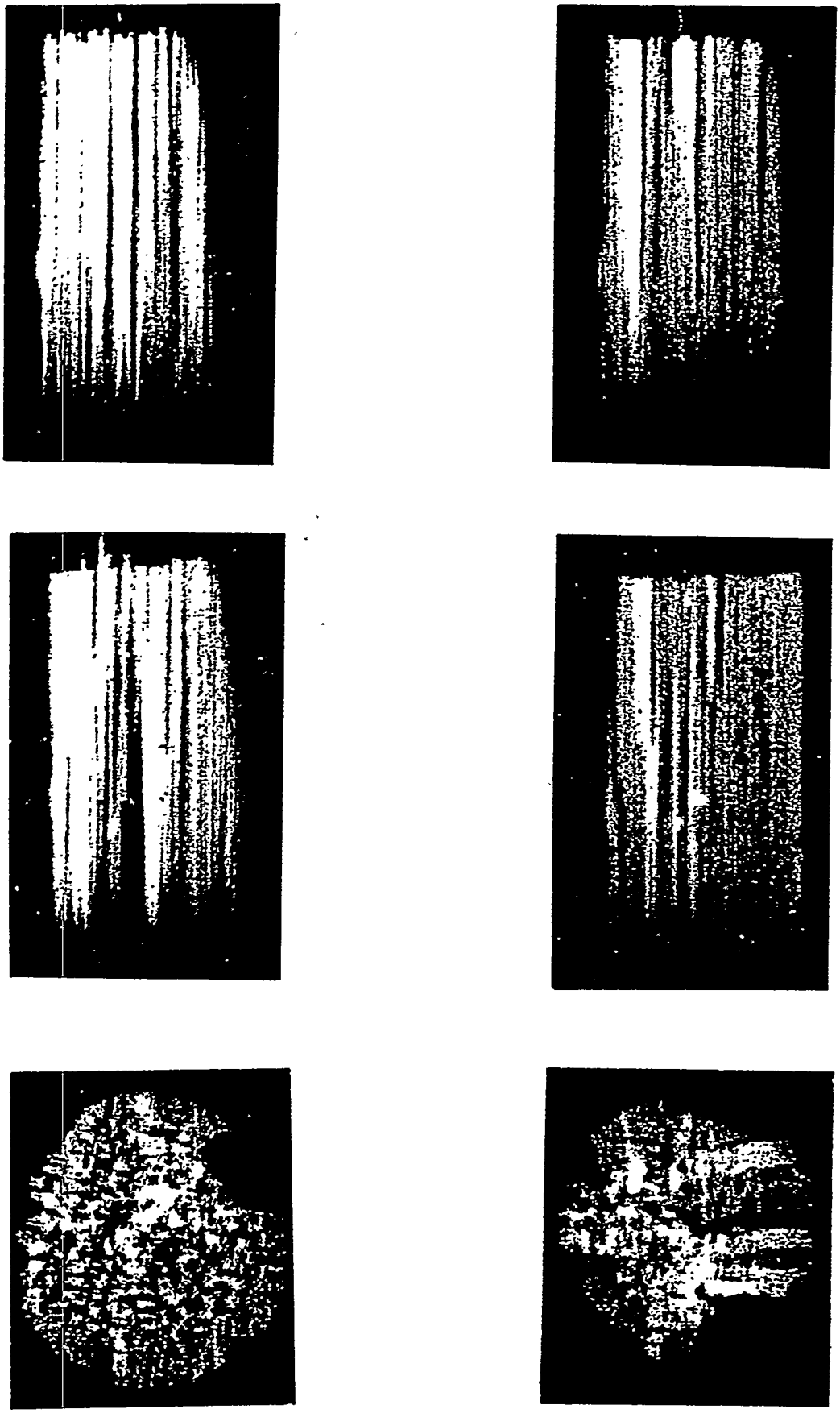
Fig. 1. × 2



P= 0.15 MPa

P= 0.20 MPa

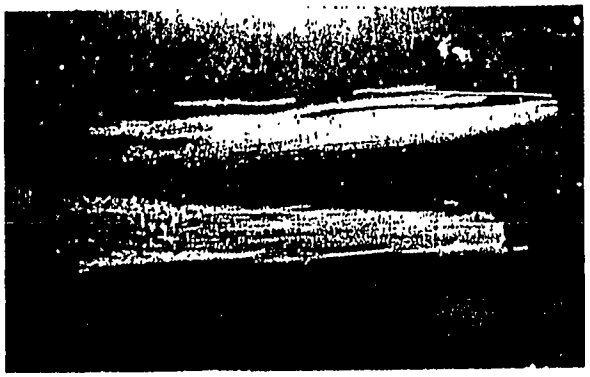
Fig. 1.



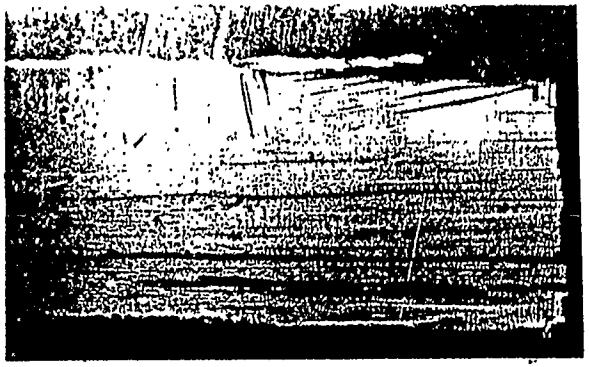
P = 0.25 MPa

P = 0.30 MPa

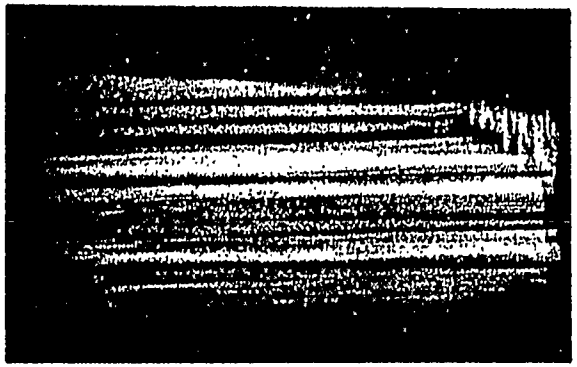
Fig. 1.



P = 0.15 MPa

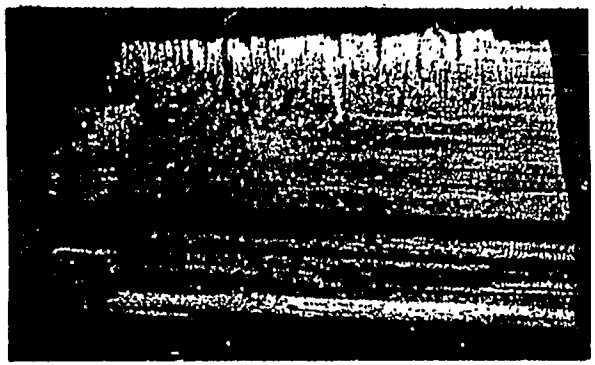


P = 0.10 MPa

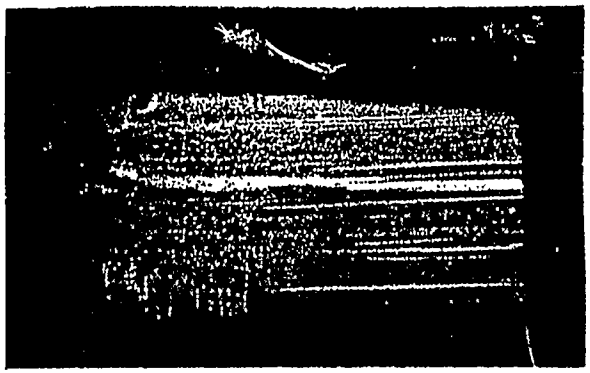


P = 0

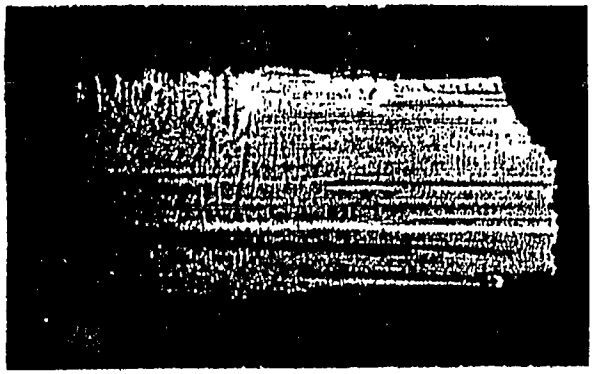
Growth direction



P = 0.30 MPa



P = 0.25 MPa



P = 0.20 MPa

Fig. 2. ×2

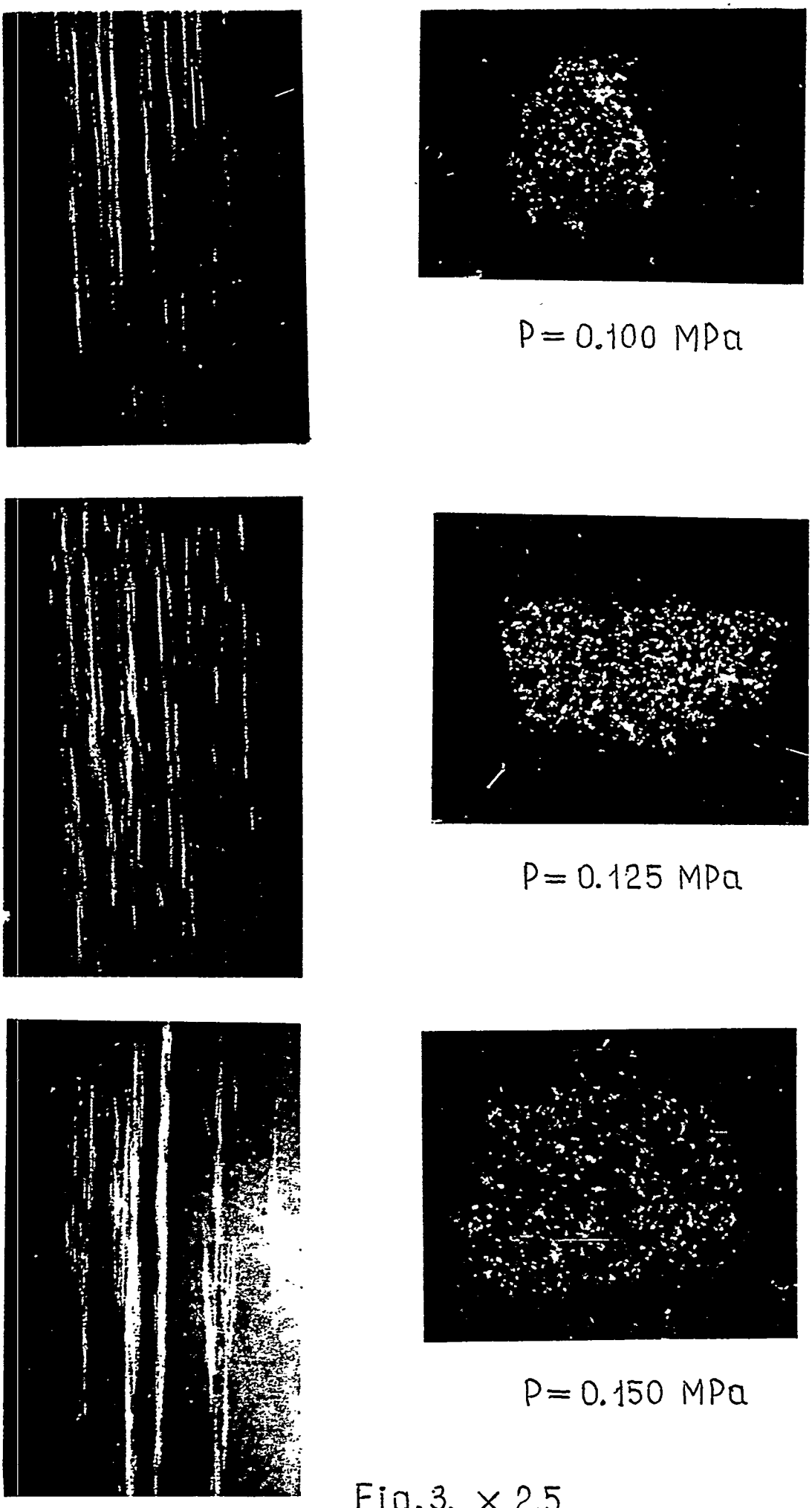
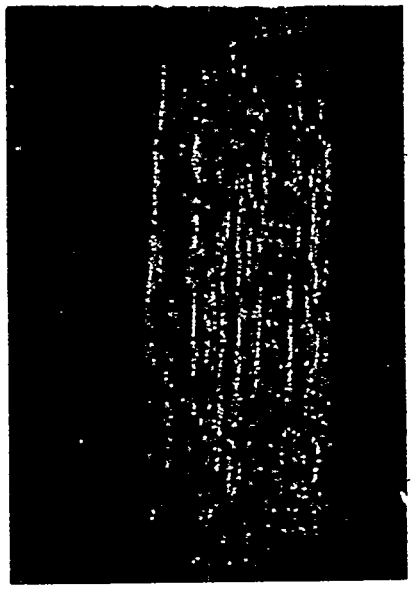
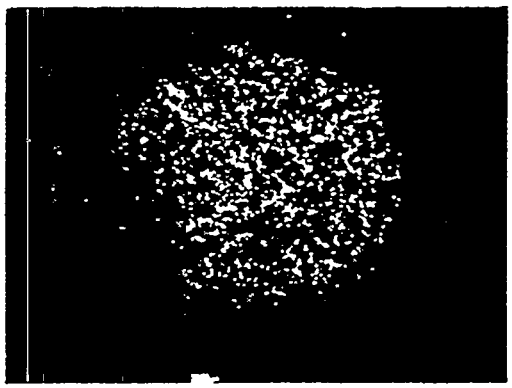
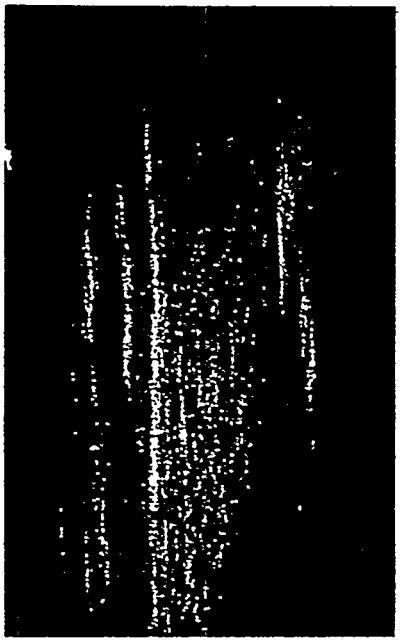


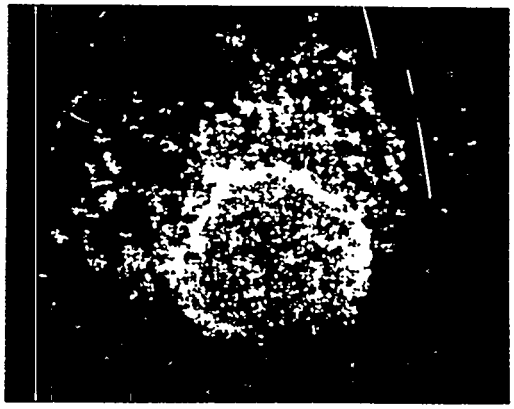
Fig.3. × 2.5



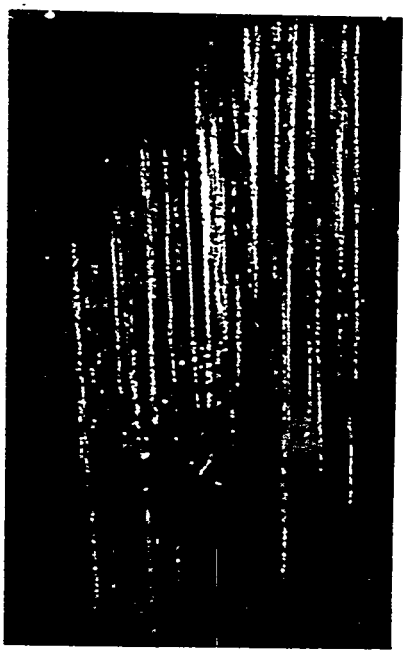


P=0.175 MPa





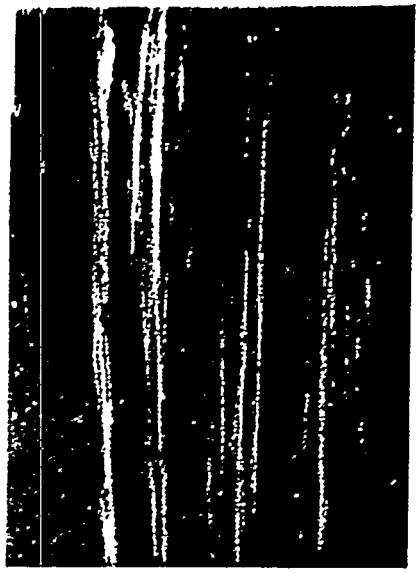
P=0.200 MPa

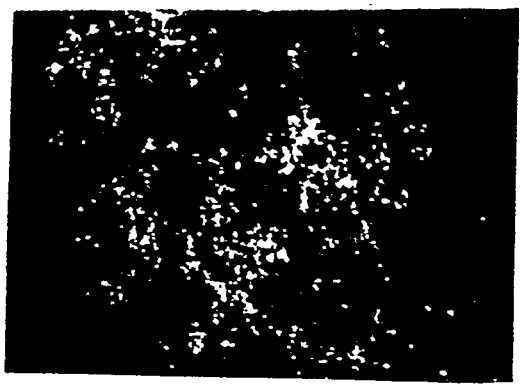




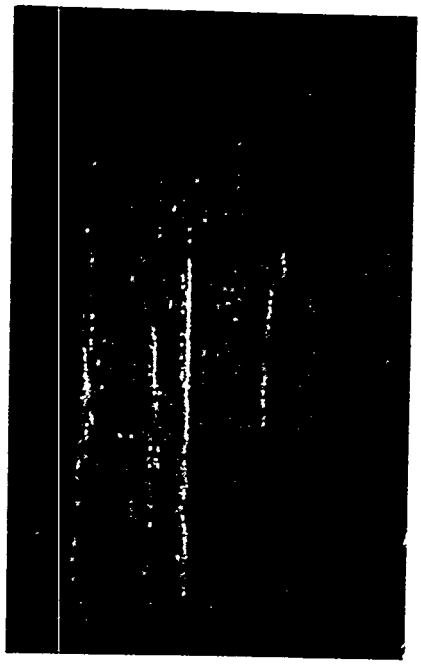
P=0.225 MPa

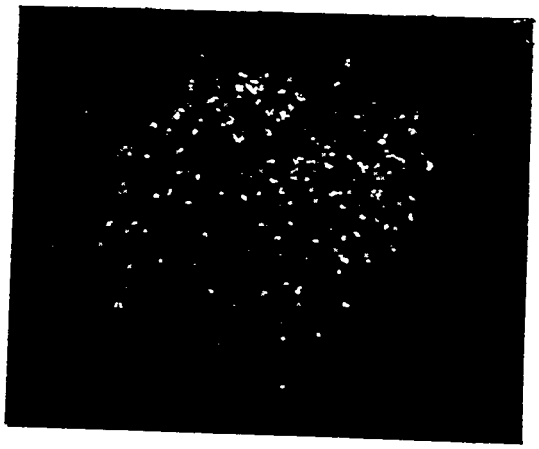
Fig. 3.



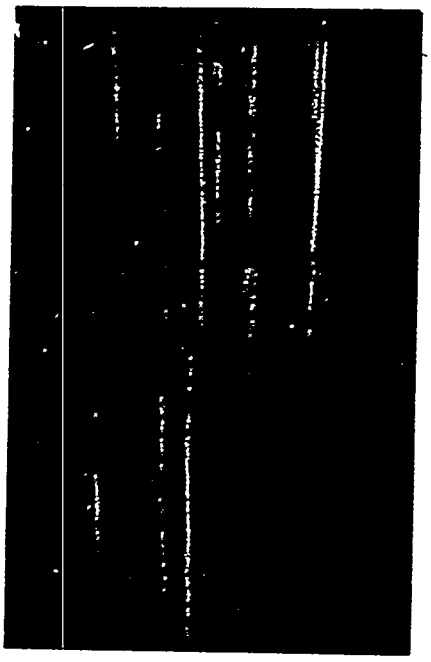


P=0.250 MPa





P=0.275 MPa

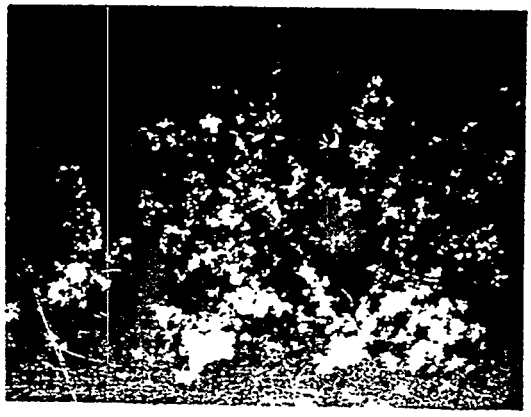




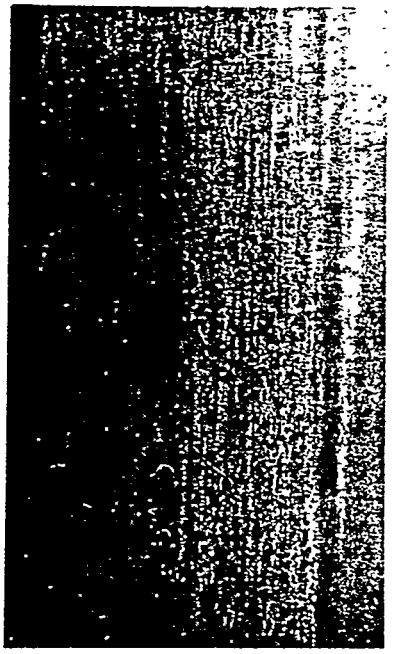
P=0.300 MPa

Fig.3.

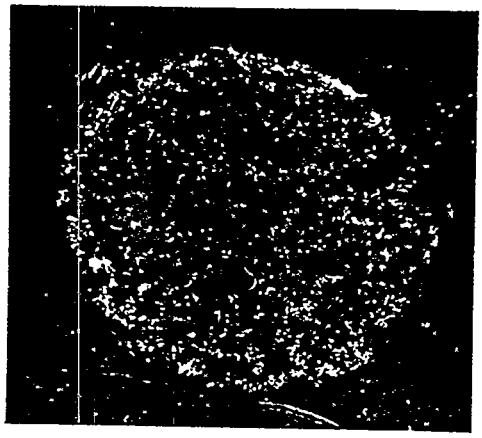




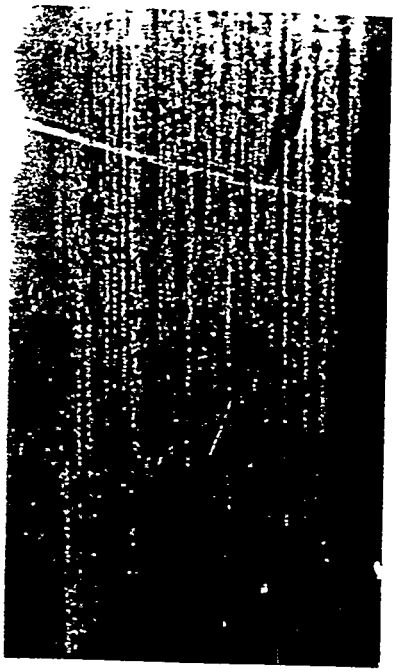
P=0.15 MPa

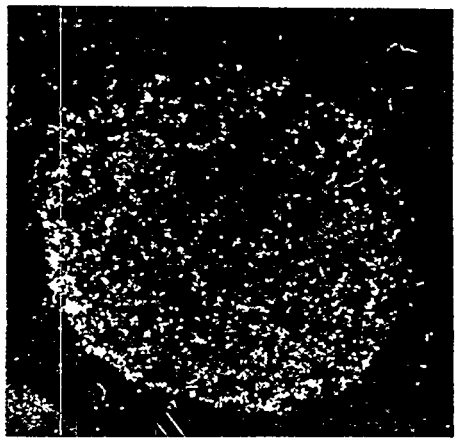


Growth direction



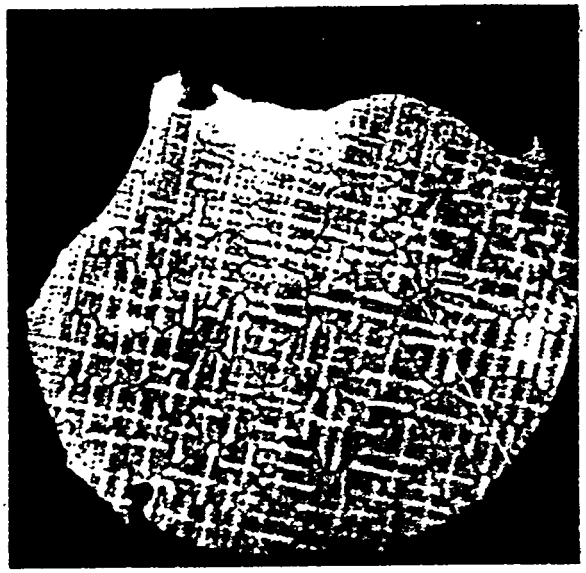
P=0.20 MPa



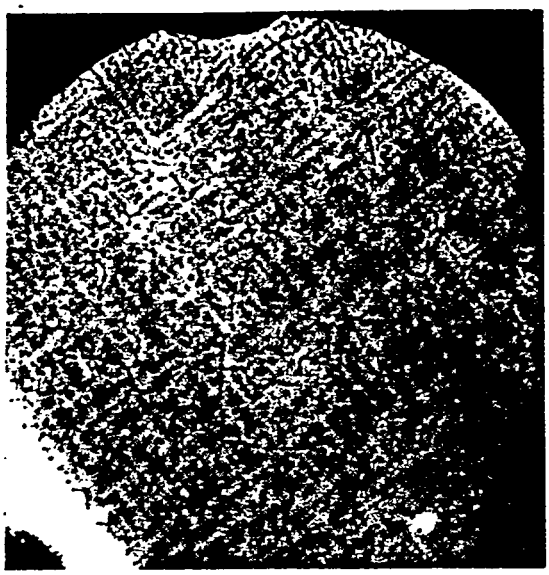


P=0.25 MPa

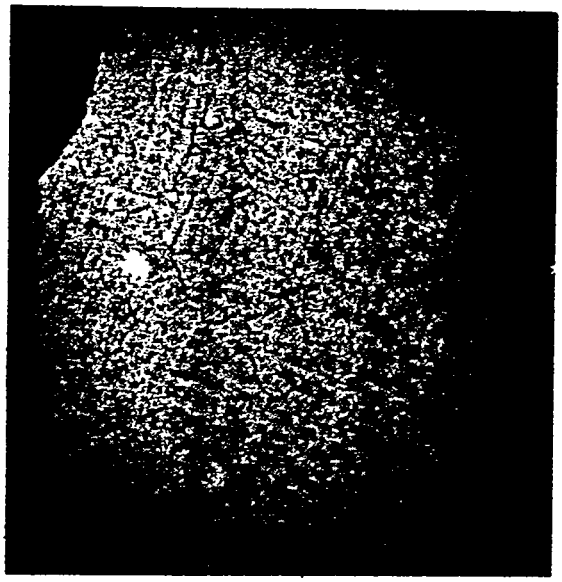
Fig.4. × 2.5



P = 0



P = 0.10 MPa



P = 0.15 MPa

Fig.5. x8

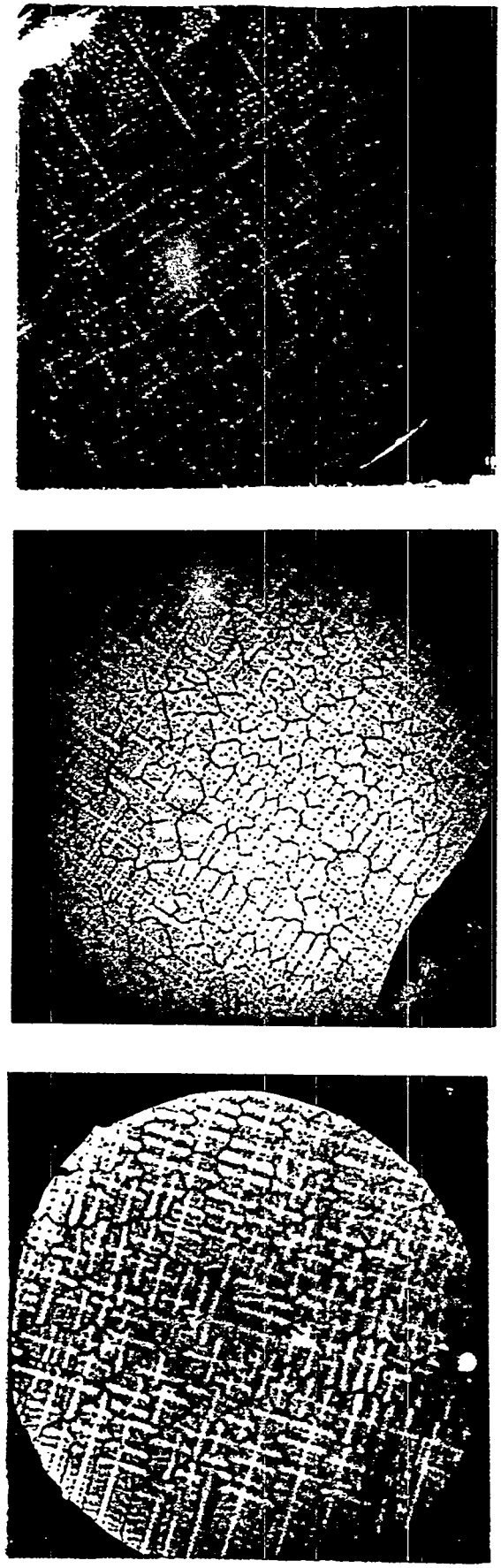
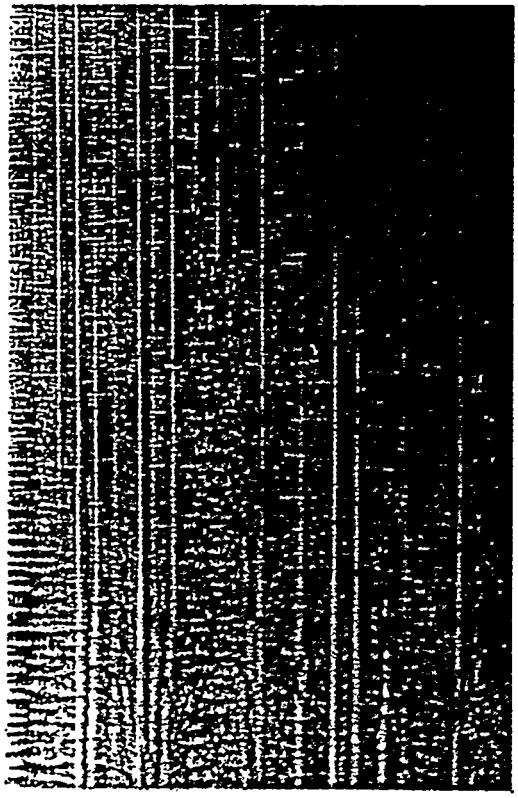
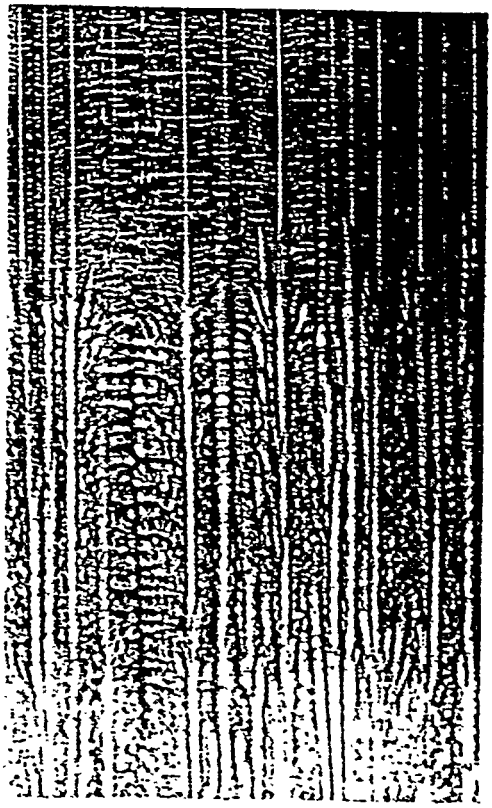


Fig. 5.

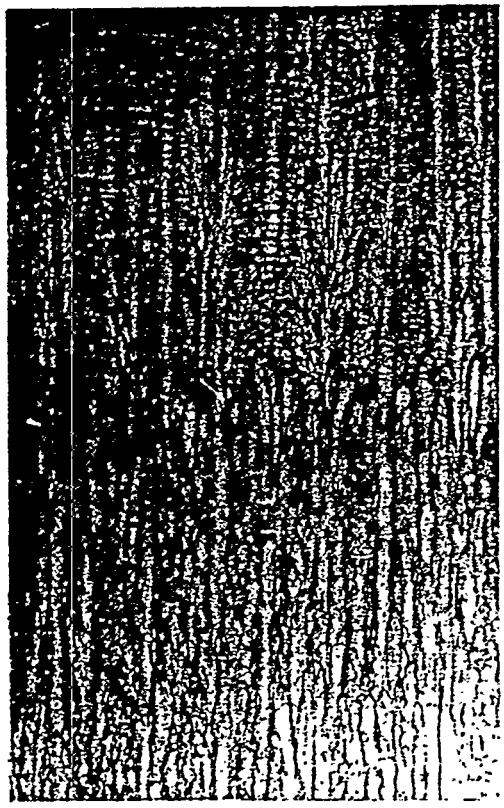


P = 0

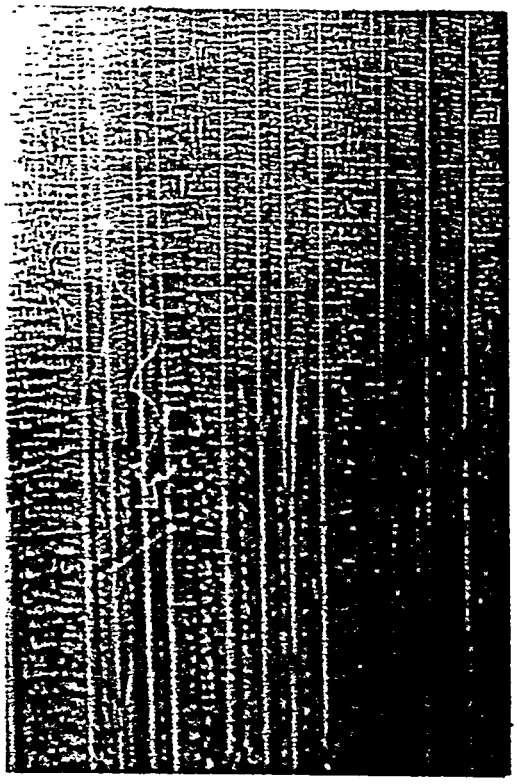


P = 0.10 MPa

Growth direction

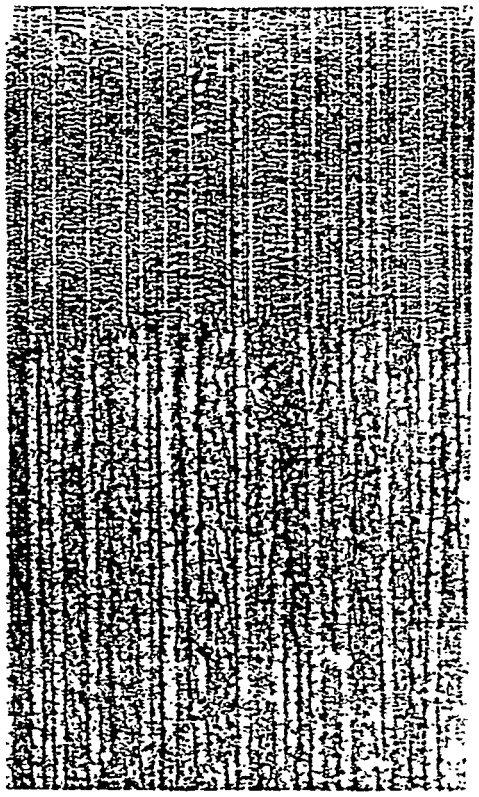


P = 0.15 MPa

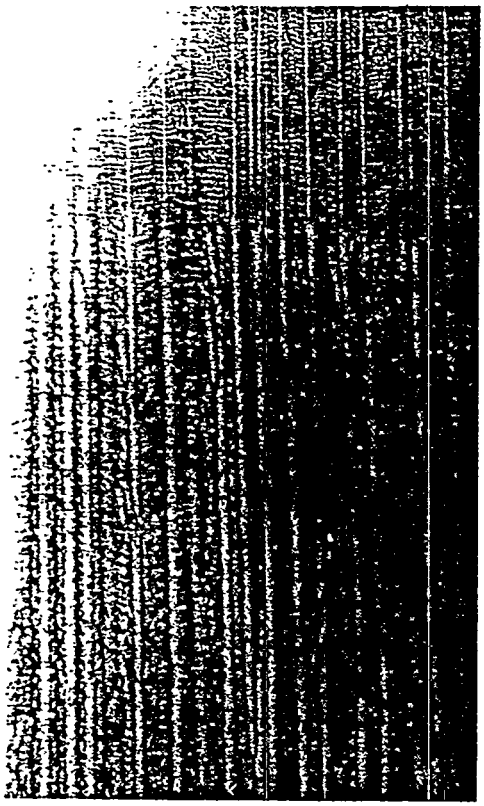


P = 0.20 MPa

Fig.6. x 10

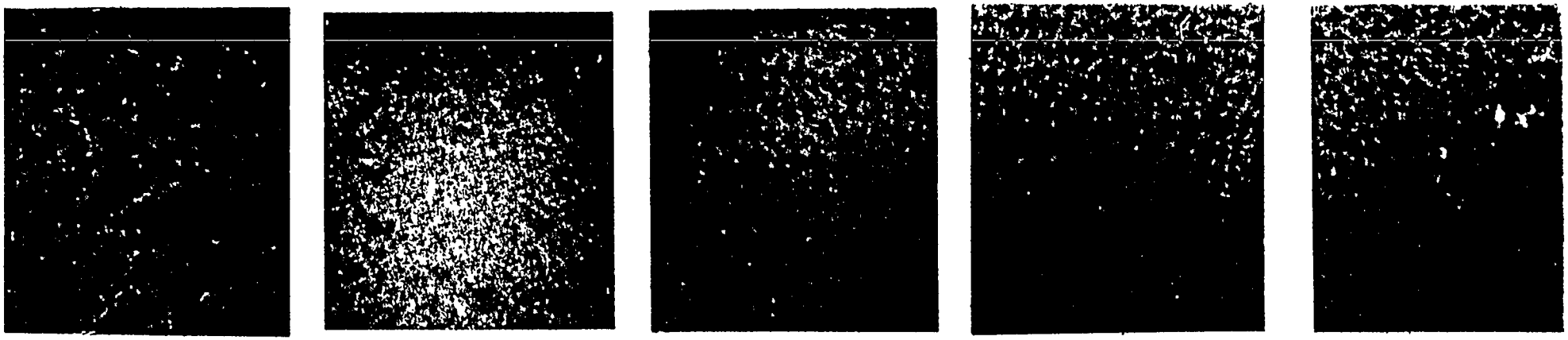


P = 0.25 MPa

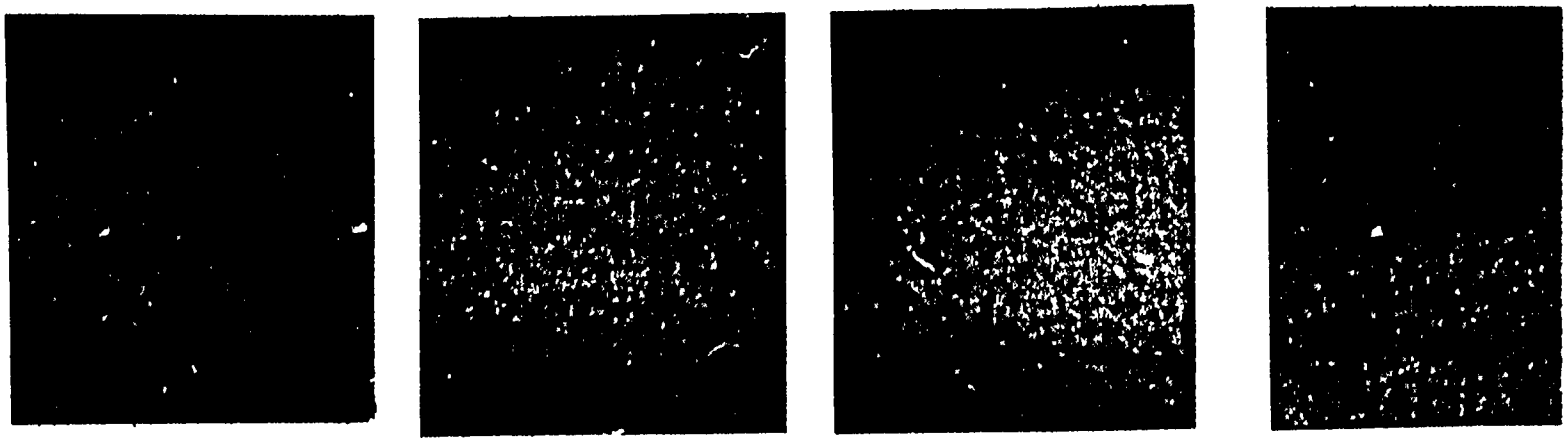


P = 0.30. MPa

Fig. 6.



P = 0.200 MPa P = 0.175 MPa P = 0.150 MPa P = 0.125 MPa P = 0.100 MPa



P = 0.300 MPa P = 0.275 MPa P = 0.250 MPa P = 0.225 MPa

Fig.7. × 14

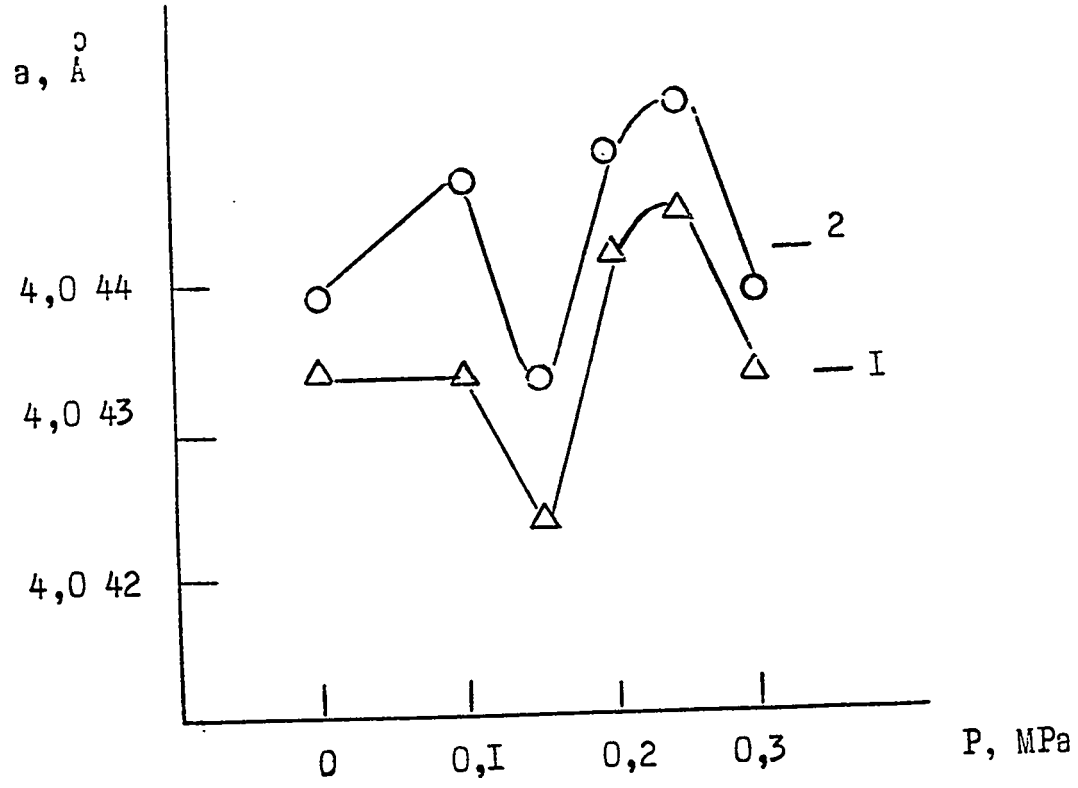

a, Å
4,0 44
4,0 43
4,0 42
2
I
0
0,I
0,2
0,3
P, MPa

Fig. 8.

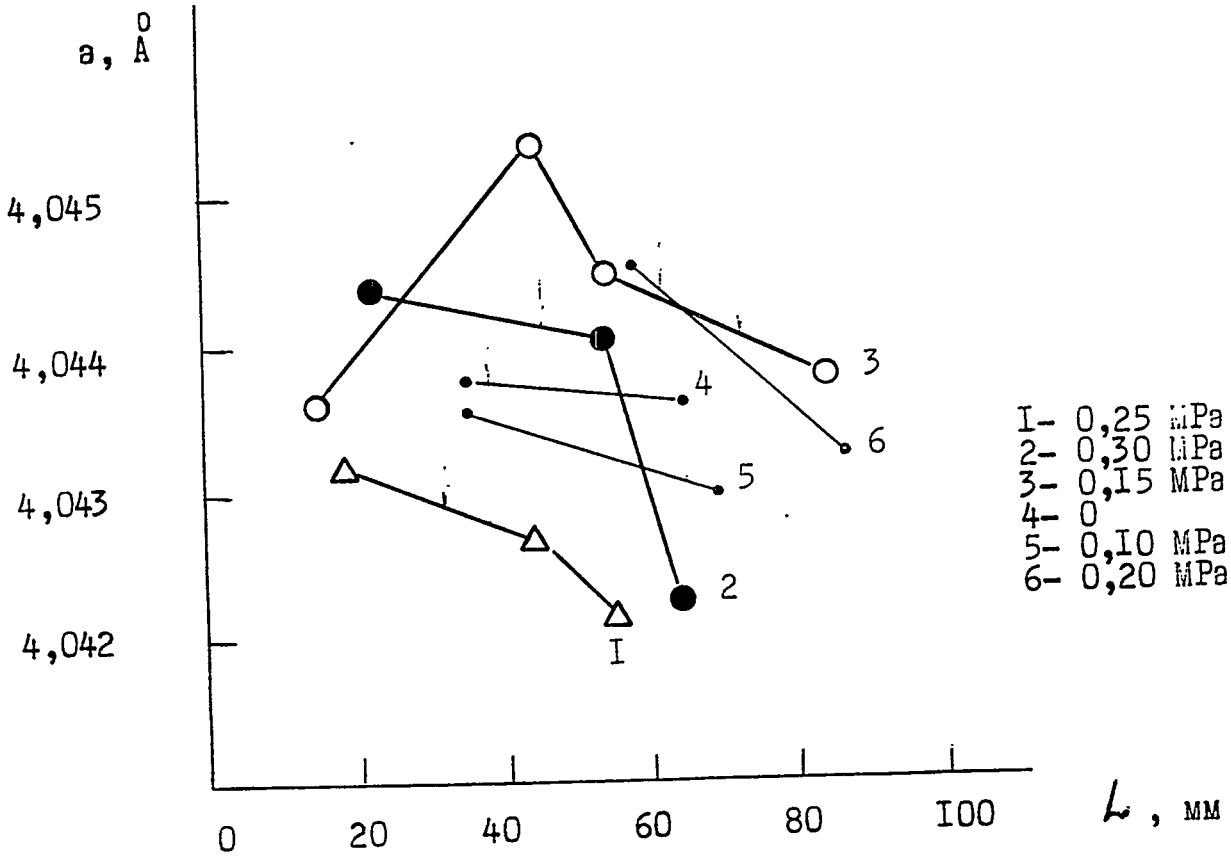

a, Å
4,045
4,044
4,043
4,042
3
4
6
5
2
I
0
20
40
60
80
I00
L, мм
I- 0,25 MPa
2- 0,30 MPa
3- 0,I5 MPa
4- 0
5- 0,I0 MPa
6- 0,20 MPa

Fig. 9.

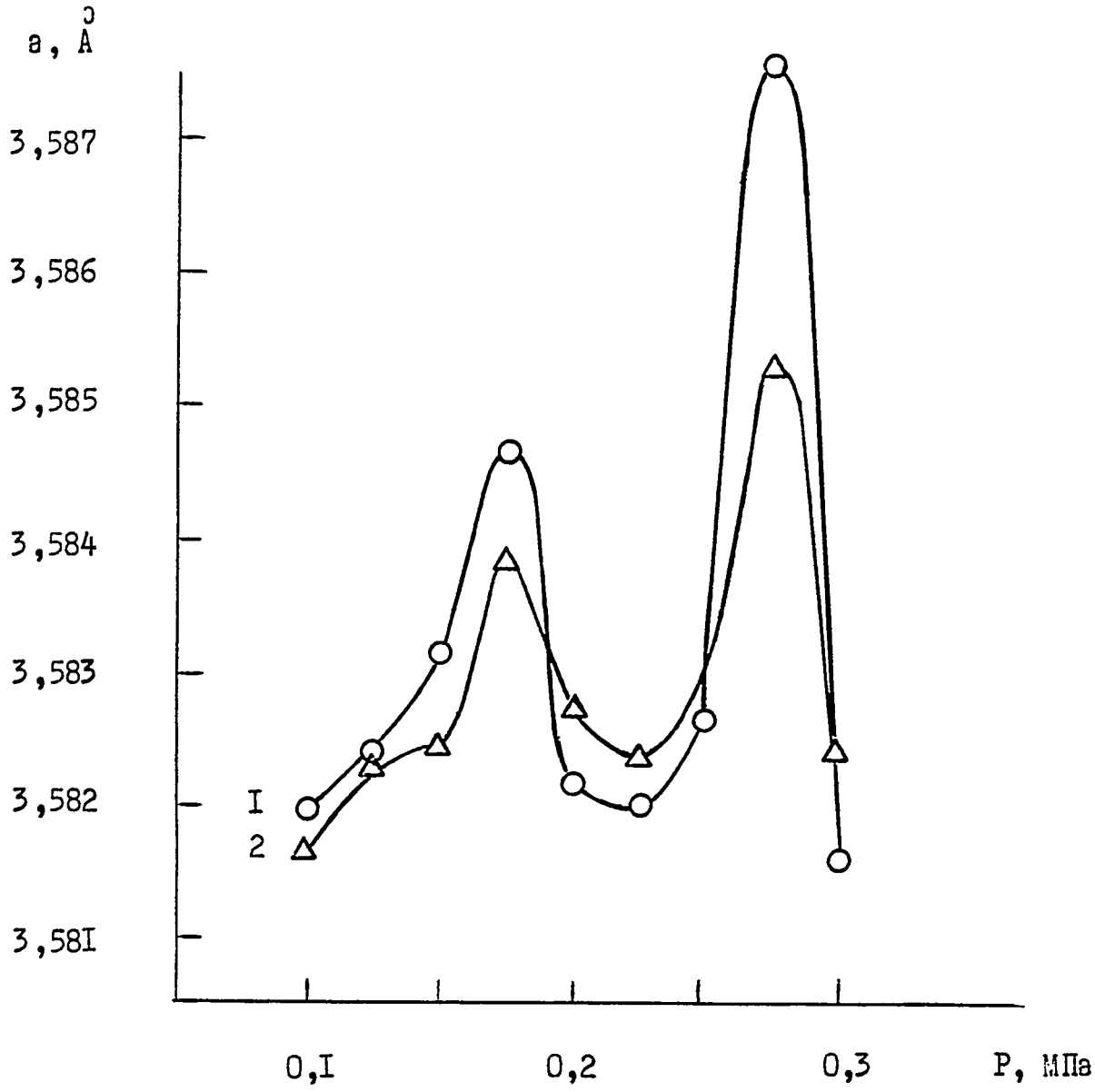


Fig. 10.

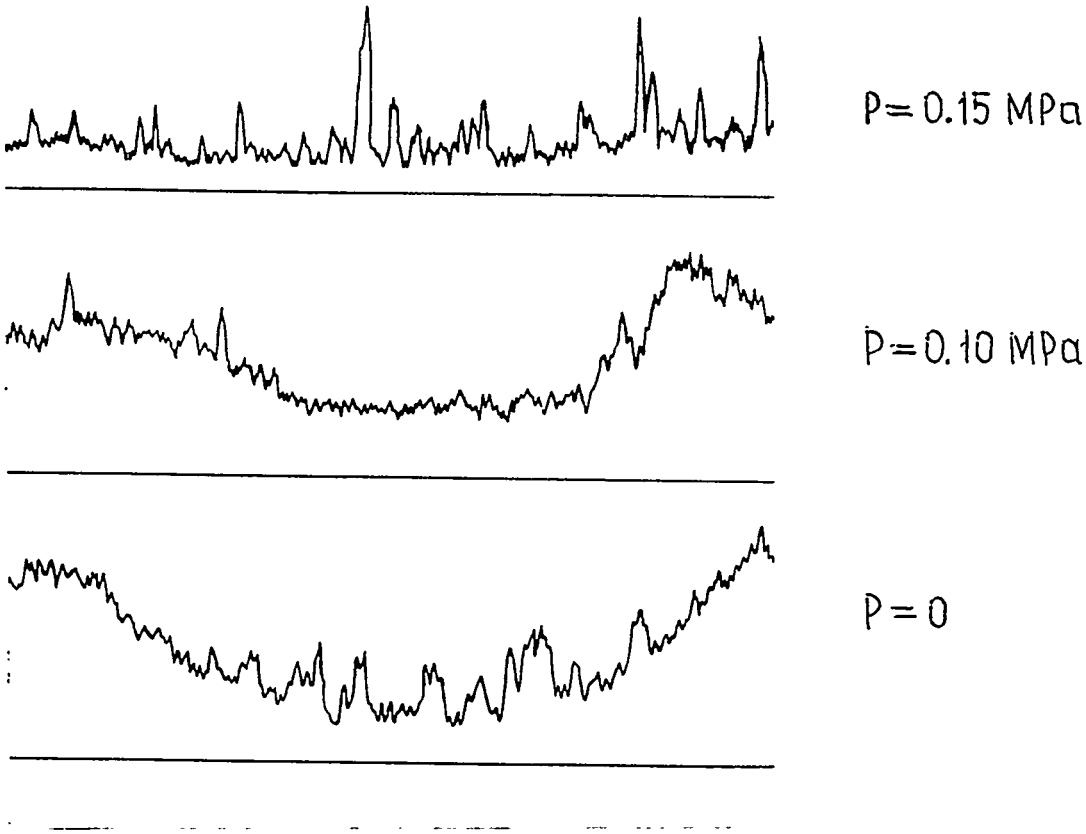
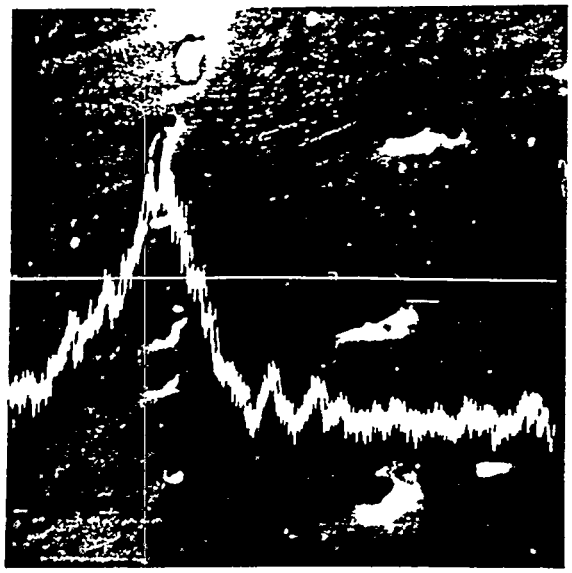
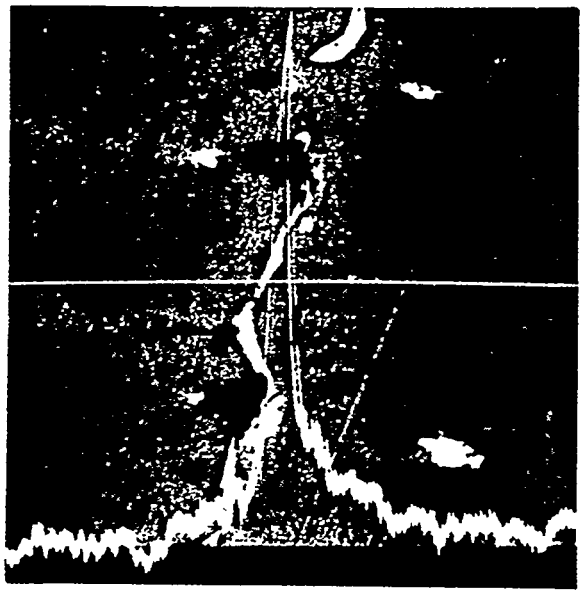


Fig. 11.
(Microscan MK-PA)

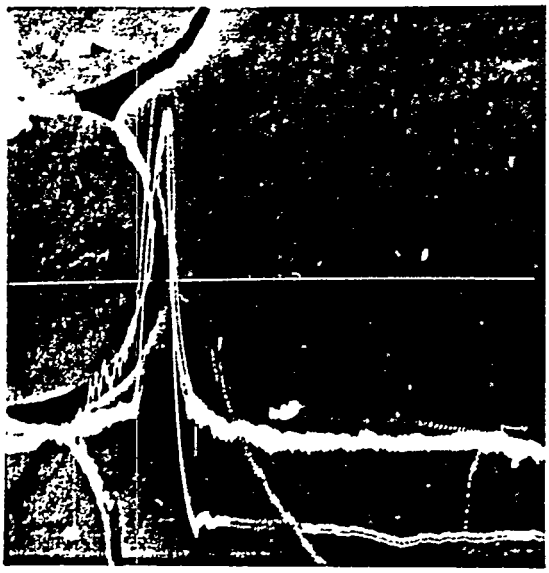


P= 0.150 MPa (1)

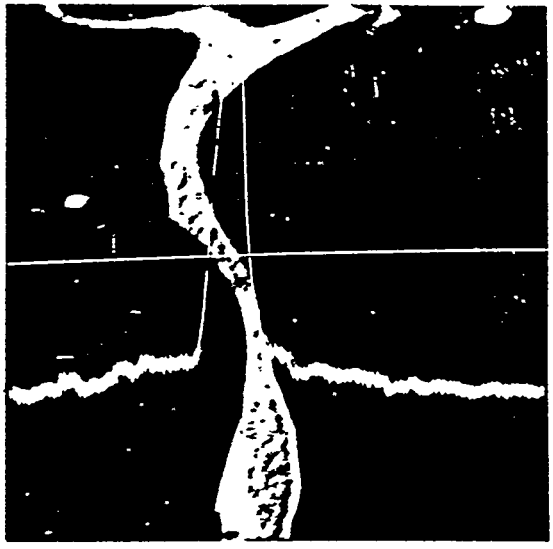


P= 0.250 MPa (1)

1



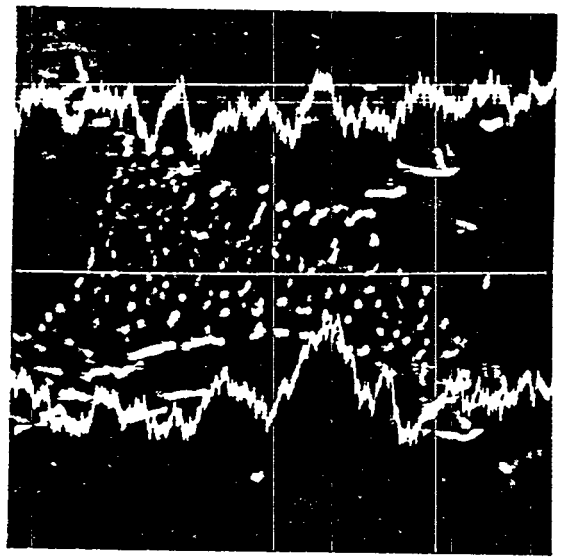
P= 0.150 MPa (2)

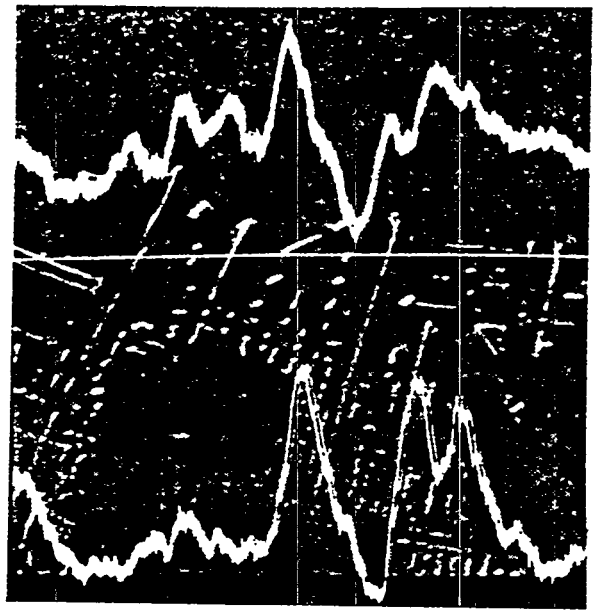


P= 0.250 MPa (2)

2

Fig. 12. × 390 (JSM-U3)





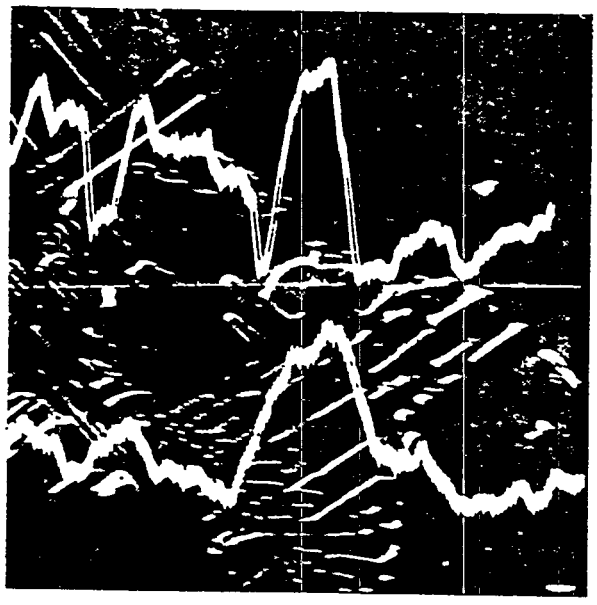


Fig. 13. x 650 (JSM-U3)

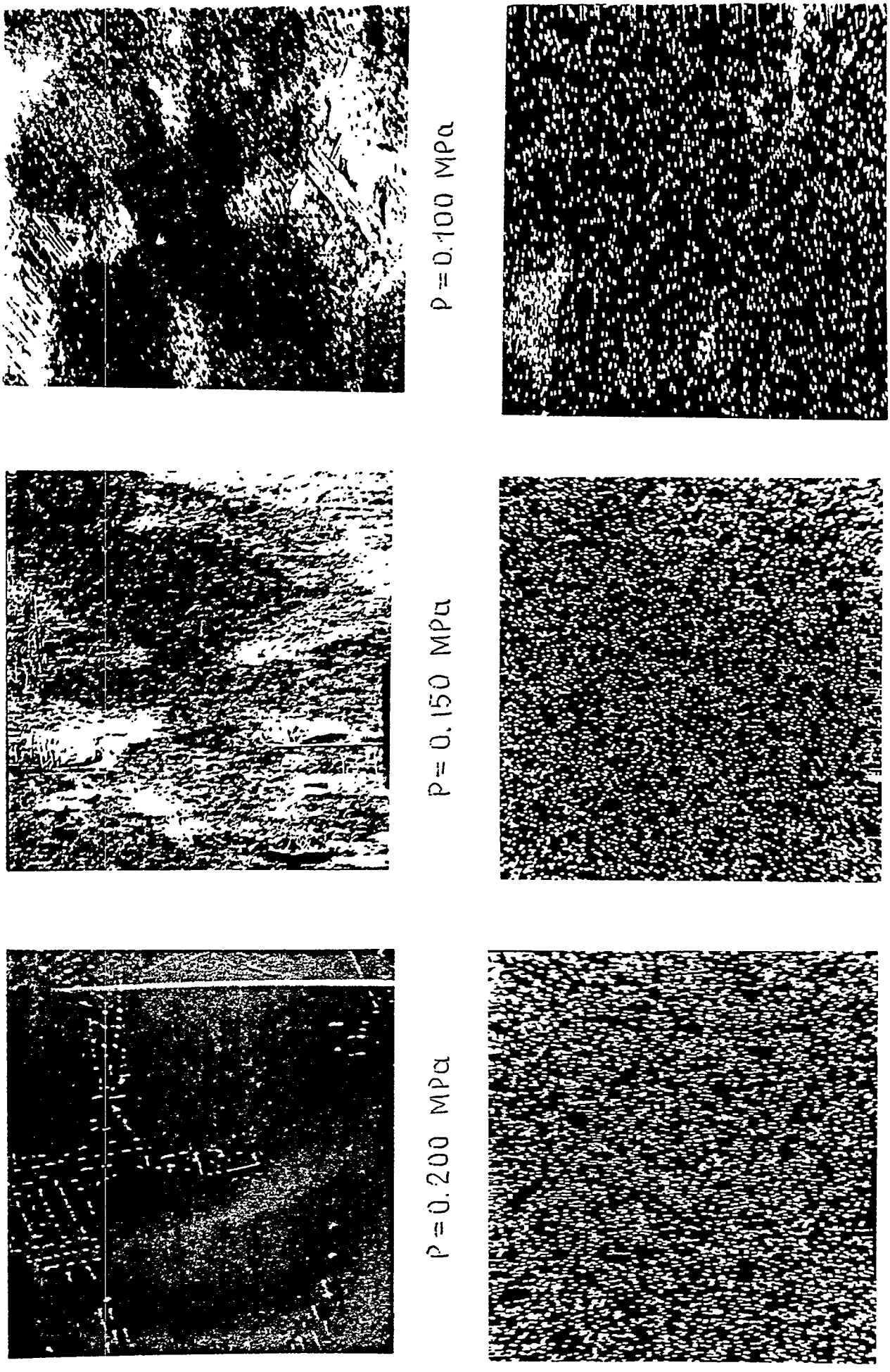
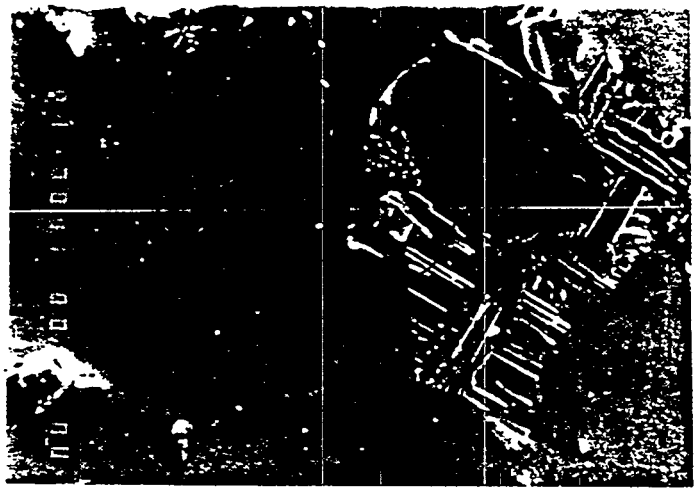
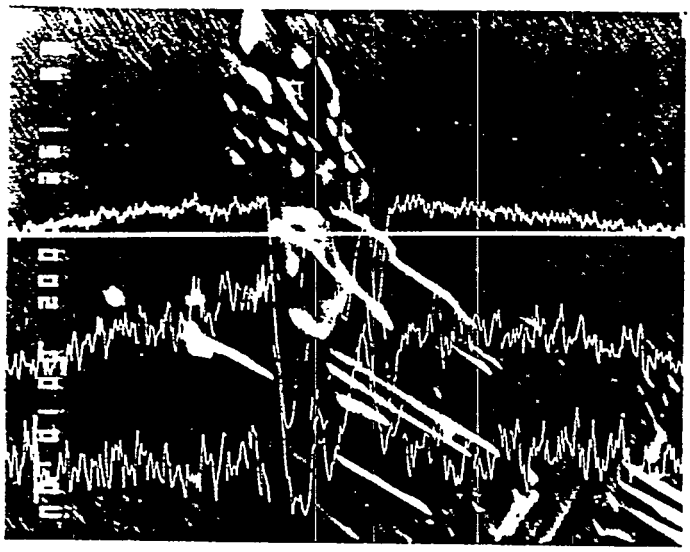


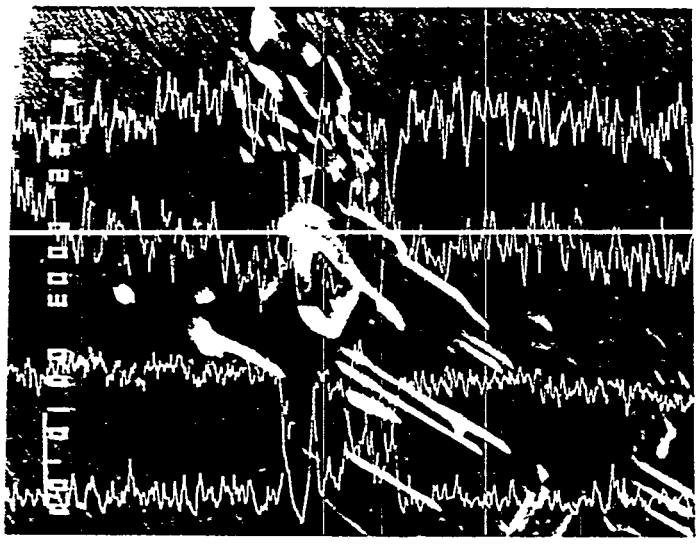
Fig. 14. x 650 (JSM-U3)





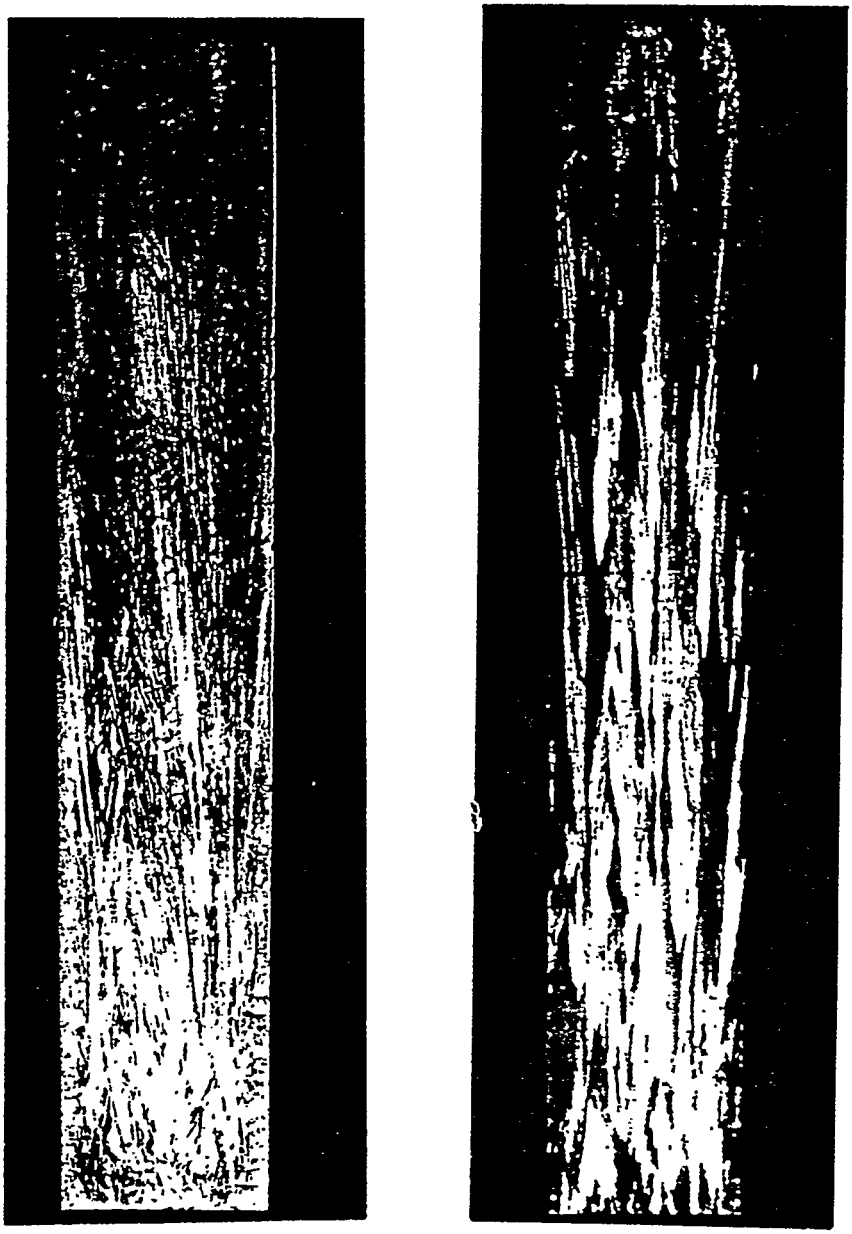
P = 0.275 MPa

- Ni { 53.7 % – 1 ; 51.1 % – 2
- Al { 5.8 % – 1 ; 5.3 % – 2
- Ti { 0.13 % – 1 ; 0.32 % – 2



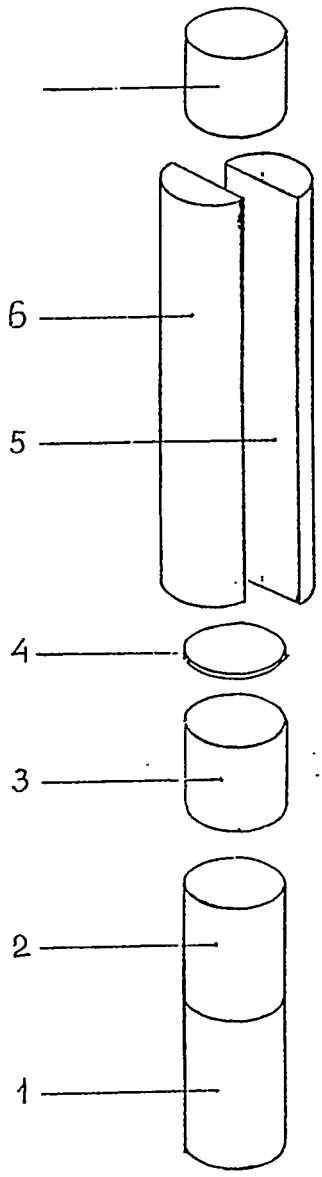
- W { 9.9 % – 1 ; 8.3 % – 2
- Cr { 5.0 % – 1 ; 5.15 % – 2
- Co { 10.7 % – 1 ; 9.6 % – 2
- Nb { 0.72 % – 1 ; 2.7 % – 2

Fig. 15. (Superprobe-733)



P = 0.10 MPa P = 0.15 MPa

Fig. 16. ×3



1 - unmelted part of the seed

2 - melted part of the seed

3 - transverse section of cristal for X-ray diffraction topography and microanalysis

4 - across cut for shadow microroentgenography

5 - longitudinal section of cristal for X-ray diffraction topography, microanalysis and lattice parameter

6 - the samples for Sandia

Fig. 17.

Project Title: Applications of Damage/healing Theory as Applied to Self-healing Bearings and to Semi-continuous Wiring Drawing.
Principal Investigator: Eduard Gorkunov
Mechanical Engineering Research Institute (IMACH)
Ekaterinburg, Russia
AM-7684

CLAUSE 1 - STATEMENT OF WORK

Tasks:

The Contractor shall:

1. Produce and provide to Sandia samples of titanium bar and wire as follows:

3-5 rods = 8 to 10 mm in diameter
150mm to 200mm in length
wire = 0.5 to 2mm in diameter
1000mm to 1500mm in length

These samples shall be formed from titanium sponge by the semi-continuous extrusion method.

2. Construct and provide to Sandia two bearings in accordance with the specifications given by Sandia. The bearings shall be in the size range of 3cm to 4cm in diameter. One bearing shall be tested by the Contractor, and the other bearing will be tested by Sandia, each under severe loading conditions.

3. Provide a mathematical model of damage accumulation in the contact boundary layer. Also provide an accompanying document that details the Kolmogorov damage/healing analysis.

4. Deliver a final report that discusses all work performed.

Project Title: Investigation of the Role of Ectons in the Vacuum Arc
Principal Investigator: Gennady Mesyats
Institute of Electrophysics
Ekaterinburg, Russia
AM-7685

CLAUSE 1 - STATEMENT OF WORK

Tasks:

The Contractor shall:

Provide a report describing the project plan, including a description of the following items:
proposed model for experimental data analysis
proposed experiments for measuring ecton lifetime and erosion rate during vacuum arc operation
proposed computer simulation of vacuum arc operation
proposed design of theoretical model of the microprocesses involved in vacuum arc operation

2. Develop the analytical model for experimental data analysis and provide a report on the model.

3. Experimentally measure ecton lifetime under different conditions of cathode temperature, cathode material and inter-electrode gap. Also, measure erosion rate due to ecton activity for different cathode temperatures and materials. Provide a report describing the experimental results.

4. Perform computer simulation of vacuum arc operation based on a two-dimensional magneto-gas dynamic approach, taking into account both electron and multi-ion components. Use a one-step modeling of both erosion and plasma expansion. The simulation shall describe the current density distribution, electron temperature distribution and the potential distribution in the electrode gap.

5. Develop the theoretical model of the microprocesses in the plasma jet. The model shall enable the calculation of integral characteristic of the vacuum arc (arc current and potential distribution in the electrode gap), and explain the local concentration of current density re-distribution in the plasma jet. Provide a final report describing the complete theoretical model and integral vacuum arc characteristics.

Report for a Contract number
AM 7685 (English version)

INVESTIGATION OF THE ECTON ROLE IN VACUUM ARC.

TASK 2.

Analytical model for the experimental data analysis.

1. Introduction.

A vacuum arc is an electrical discharge plasma generated from the electrode material [1,2]. In other words, the conductive material feeds into the gap region due to the erosion process on the electrode. This is exactly the reason that the erosion processes play such an important role in the vacuum arc operation.

The processes responsible for the vacuum arc phenomenon take place on the cathode and near the cathode region. The location of the vacuum arc operation is known as a cathode spot [1-3]. The cathode spot would be experimentally observed by either erosion traces or by a bright glow on the cathode.

Cathode spots, known as "first type", are of a specific interest. These spots would move rapidly over the cathode surface and produce erosion traces in the form of separate microcraters. In this paper we will refer to such "first type" cathode spots as just the cathode spots (CS).

G.A.Mesyats developed a hypothesis that the processes in CSs were of a non-stationary, cyclic behavior, in much the same way as the phenomenon of explosive electron emission [4-6]. It was proposed that the microcraters resulted from explosive evaporation of the cathode material due to the magnitude of the Joule heating, with the high-density electric current flowing due to an intense electron emission from individual spots on the cathode surface. As the microcrater radius increases, the current density decreases, and the emission/evaporation process subsequently stops. However, such a process sets the stage for a new similar process to be initiated and developed. To describe such processes a new term was introduced -- an explosive emission center. In subsequent publications, [7,8], this term was abbreviated to "ecton" - Explosive Center and Emissive Center.

In presenting our material we shall adhere to the following plan. First, we shall briefly describe the basic experimental data available on the vacuum arcs. Second, based on the ecton model, we shall try and explain some of these experiments.

2. Basic experimental data on vacuum arcs.

The CS trace, as visible with the electron microscope, is a chain or band containing the microcraters of several micrometers in size (Fig. 1a and 1b). The radii of microcraters and their relative positions depend on purity of the cathode surface and the value of arc current. In case the cathode surface is pure, the CS trace is seen as a chain of the craters sequentially superimposed on each other, with the center of each crater being located at the edge of the previous one. Shown are the traces of the metal being splashed out of the crater, that causes the microtips and microdrops to appear.

a)

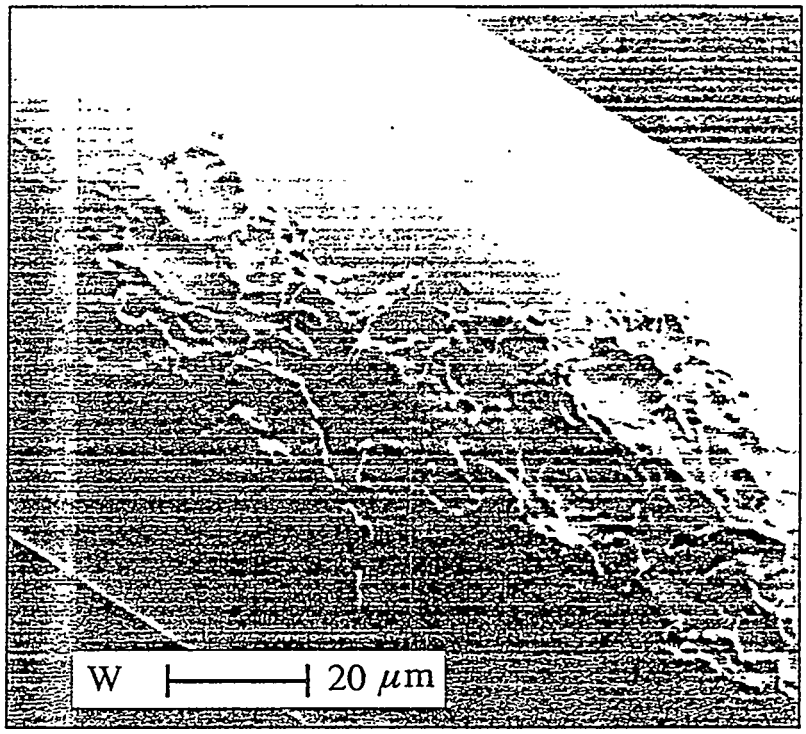


Fig. 1 a). The cathode spot trace on the pure cathode surface. (W, i = 45 A).

b)

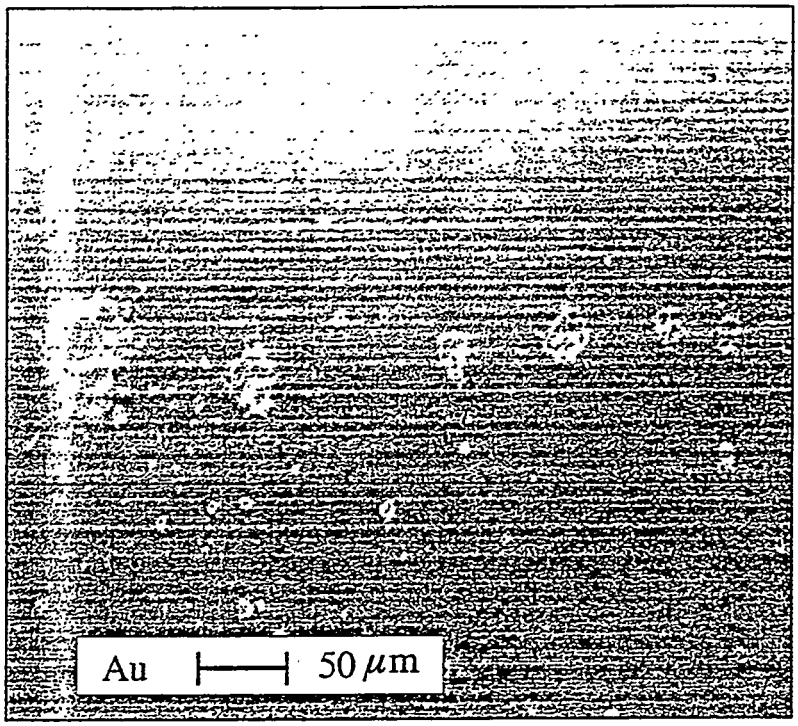


Fig.1 b). The cathode spot trace on the oxidized surface of the cathode (Au, i= 3 A).

If there are dielectric inclusions and films on the cathode surface, which is likely under the poor vacuum conditions, then the cathode spot trace is seen as a great number of the small separated microcraters. In this case the size of crater depends on the arc current value (See Fig.2).

The cathode spot erosion products are the drops of liquid metal, the ions, and neutral particles. Investigations made for the drop fraction of the erosion products have shown the following regularities. [13-18] The drop size ranges widely, from a fraction of micron to hundreds of microns. The number of drops decreases as their sizes increase. The velocity of drop scattering depends on the drop size, and such a dependence can be approximated by the inverse proportion to the square root of the size. The velocity value is ~ 10^6 cm/sec. The angular distribution of the scattering drops has its maximum in the direction parallel to the cathode surface. As the discharge current decreases, the drop fraction of the erosion products is reduced. The number of drops leaving the cathode is ~ 10^7 drops per 1 Coulomb.

The experimental investigation made for the ion fraction of the erosion product has given the following results. [1,2,5-17, 19-22]. The fraction of current corresponding to the ions emitted from the spot is 8-10 % of the arc current, being independent of the arc current. The ionization degree is near 2 in the average. The velocity of ion flowing is ~ 10^6 cm/sec, and is essentially independent of the arc current and the properties of cathode material. The angular distribution of the ion flow has its maximum in the direction perpendicular to the cathode surface. The recoil force of the ion-plasma stream is near proportional to the current and is 10-50 din/A. The specific ion erosion changes very slightly with current and is 10^{-4} - 10^{-5} g/C. The erosion fraction corresponding to the neutral particles is a moderate value -- a few per cent [15-17].

The spot would move chaotically [1-3]. With a tangential magnetic field being applied, the spot starts moving in the direction opposite to that dictated by the Ampere rule. It has experimentally been shown that the CS has a tendency to move in the direction of maximum tangential magnetic field. The spot movement velocity depends on the state of the cathode surface, and ranges within 10^3 - 10^5 cm/sec.

Arc instability. Threshold currents.

The vacuum arc is characterized by its spontaneous extinction [1,2]. The arc extinction is of a random behavior, and can be characterized by an average time of burning, with certain conditions specified. The average burning time as a function of arc current follows the exponential curve. The arc current has its threshold value. When the arc current is less than the threshold value, the arc can not operate. It has been established that the threshold currents are proportional to the cathode material melting temperature multiplied by the square root of the thermal conductivity, with the pressure being ~60 mm Hg. When the current is equal to the doubled threshold value, the spot starts splitting: one spot falls into two spots and so on.

The voltage drop on the arc comprises of the cathode voltage drop, the voltage drop near the cathode region, the voltage drop in plasma, the anode voltage drop, and the voltage drop near the anode region. The arc voltage depends on the electrode materials, mostly the cathode material, and ranges within 10 - 30 V. [1-3] The voltage varies with time, with the oscillations being of a giga-Hertz frequency. The lower level of voltage is well defined and invariable with time -- so, it is this value that is interpreted as the arc voltage drop. The upper level fluctuates, with the fluctuation amplitude increasing as the current decreases. According to the changes in the electrode gap, the voltage drop on plasma is negligible. Special probe measurements have shown that the greater part of the voltage drop is due to the cathode and the near cathode region -- a so-called "cathode voltage drop". Some of the experiments could

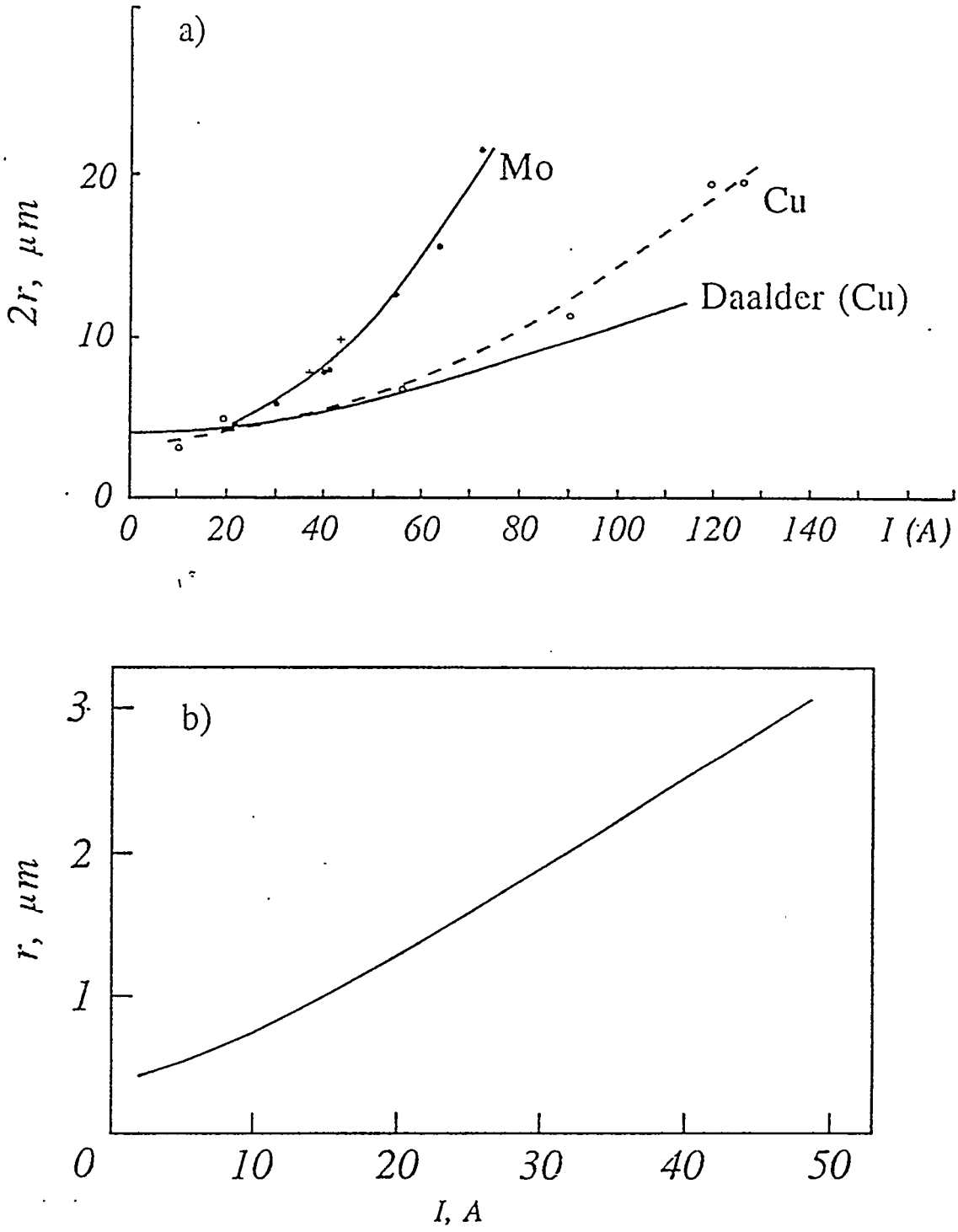


Fig. 2. Ecton crater radius r vs the cathode current I:
a) - experimental data;
b) - theoretical curve according to the equation (37).

not reveal any dependence of the voltage drop on the arc current, while in the other measurements there was a moderate increase in the voltage drop observed. For example, the current increase from 1 to 30 A caused the changes in voltage from 1 to 2 V. The arc voltage and current are characteristics of the energy consumed to sustain the discharge [23-25]. It is known that almost all the energy from an outer source is dissipated in the electrodes, with the anode consuming twice as much energy as the cathode. Detailed measurements have shown that the cathode consumes ~30 % of the energy given out by the arc, independently of the cathode material and current value.

Temporal characteristics of the CS as a cyclic process. [1,2,4-6,9,26]

The experimental observations on the separated microcraters on the cathode indicates a cyclic behavior of the processes in CSs. Knowing the number of microcraters and the time of arc operation, one can decide on the cycle time. This time was determined to range from a few nanoseconds to several tens of nanoseconds. There was a glow observed on the cathode, which was discontinues in its behavior, with the period of a few nanoseconds.

3. Model for the erosion process.

Mathematical model for the ecton.

It is quite natural to think that the microcrater is of a hemispherical shape. Such a supposition will allow for the spherical symmetry approach to the problem. Besides, using the spherical symmetry makes it possible to study the processes occurring not only on the bulky cathode (a lune on a plane), but also on the cathode tip (a truncated cone). (Fig. 3). Any real surface of the cathode is characterized by microtips. Under certain conditions an ecton can be initiated on the top of such a microtip. As one can see on the microphotos, (Fig. 1), the melted metal, under the action of the plasma pressure, can produce microtips. The equations describing the ecton operation can be written as follows:

$$\rho c \frac{\partial T}{\partial t} = \frac{1}{r^2}\frac{\partial}{\partial r}\left(\lambda r^2 \frac{\partial T}{\partial r}\right) - \frac{i c_e}{e \Omega r^2}\frac{\partial T}{\partial r} - \left(\frac{i}{\Omega r^2}\right)^2 \chi_0 T \; ; \qquad (1)$$

$$T_{|t=0} = T_0 \quad ; \quad T_{r\to\infty} = T_0 \; ; \qquad (2)$$

$$T(r_{mel}, t) = T_{mel} \quad ; \quad \lambda \nabla T_{sol} - \lambda \nabla T_{liq} = \frac{\rho}{m} v_{mel} \varepsilon_{mel} \; ; \qquad (3)$$

$$v_{vap} = v_0 \exp\left(\frac{-\varepsilon_{vap}}{k T}\right) \; ; \qquad (4)$$

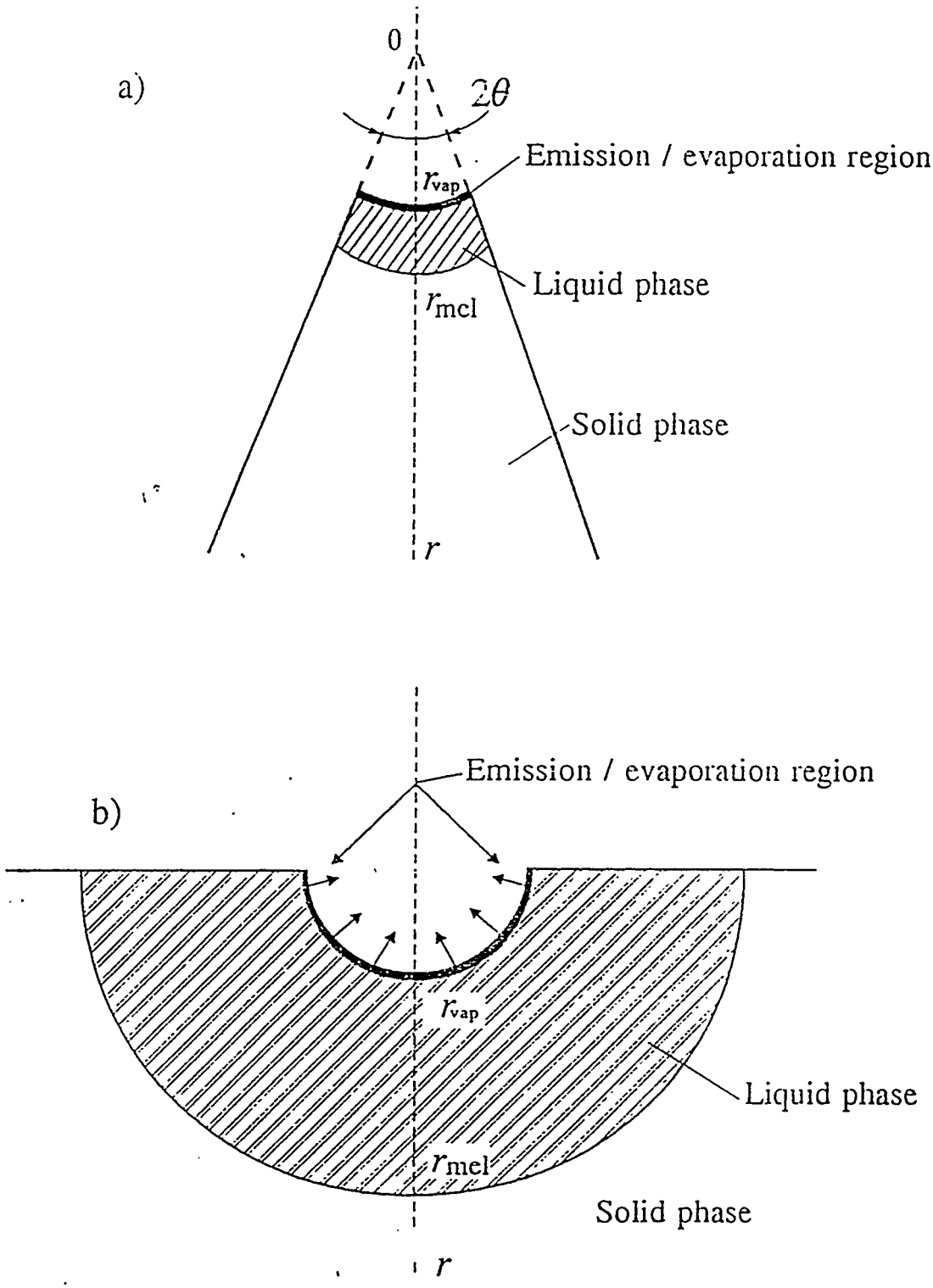


Fig. 3. The ecton geometry: a) - on the tip; b) - on the plane.

$$-\lambda \nabla T_{r=r_{vap}} = -\frac{\rho}{m} v_{vap}\left(\varepsilon_{vap} + 2kT\right) - \frac{j_{em}}{e}\left(\varphi - 2kT\right) + \frac{j_i}{e}\left(\varphi_i - \varphi - \varphi_c - 2kT\right) + \tag{5}$$

$$- \frac{j_e}{e}\left(\varphi + 2kT_e\right) \quad ;$$

$$\varphi = \begin{cases} kT \ln\left(\dfrac{AT^2}{i}\Omega r_{vap}^2\right), & \varphi > \varphi_0 - \Delta\varphi \\ \varphi_0 - \Delta\varphi \end{cases} ; \tag{6}$$

$$i = \begin{cases} \Omega r_{vap}^2 A T^2 \exp\left(\dfrac{-\varphi}{kT}\right), & \varphi = \varphi_0 - \Delta\varphi \\ i_{ect}, & \varphi > \varphi_0 - \Delta\varphi \end{cases} ; \tag{7}$$

$$j_{em} = \frac{i}{\Omega r_{vap}^2} \quad ; \tag{8}$$

$$j_i = e_i n\left(\frac{kT_e}{2\pi m}\right)^{1/2} \quad ; \quad n \approx \frac{\rho v_{vap}}{m\left(kT_i/m\right)^{1/2}} \quad ; \tag{9}$$

$$j_e = e n\left(\frac{kT_e}{2\pi m_e}\right)^{1/2} \exp\left(-\frac{\varphi_c + \varphi}{kT_e}\right) \quad ; \tag{10}$$

Where, T is the cathode temperature; ρ is the cathode material density; c is the specific heat; λ is the thermal conductivity coefficient; χ_0 is the temperature coefficient of specific resistance; $\Omega = 2\pi(1-cos\theta)$ - the solid angle; $c_e=\pi^2k^2T/2\varepsilon_F$ is the electron heat capacity; k is the Boltzmann constant; ε_F is the Fermi energy; m is the atomic weight of the cathode material; T_{mel} is the melting temperature; v_{mel} - is the velocity of melting front; ε_{mel} is the melting energy per atom; v_{vap} is the velocity of evaporation front; v_s is the transverse velocity of sound in the cathode material; ε_{vap} is the binding energy for the cathode material atoms; φ is the effective work function; i_{ect} is the current through an ecton; φ_0 is the cathode work function; $\Delta\varphi =(e^3E)^{1/2}$ is the Schottky factor of the work function due to the Debye - McKone electric field E [1]; j_i is the current density (the ion current flowing from the near cathode region to the cathode); j_e is the electron current density (the electron current flowing from plasma to the cathode); φ_c is the voltage drop at the cathode; φ_i is the ionization potential; T_e and T_i are the electron and ion temperatures of plasma, respectively.

The equation (1) is the internal energy balance equation. The equation does not take into account the proportionality of electric current density to the temperature gradient, the proportionality of the

thermal flux to the electric field intensity, and the effect of phonon entrainment [27]. Special numerical calculations have shown that these effects can be neglected. The equations (2) are to specify the initial conditions and to state the fact that the temperature is constant at a sufficiently far distance from the spot of ecton operation. The equations (3) describe the melting front. The signs $|_{sc}$ and $|_{liq}$ indicate the boundary conditions from the liquid and solid phases, respectively. The equation (4) describe the evaporation front. There are some surface energy sources at the edge of evaporation front: cooling due to the evaporation and electron emission, heating due to the electron and ion flows from the cathode plasma. The current density in ecton is supposed to make for the temperature high enough for the thermal emission current to be sufficiently high. In other words, with ecton operating, there is a virtual cathode at the emission-evaporation front. As soon as the condition is violated, the current density depends heavily on temperature (the exponential law); such a situation is unstable, and the ecton operation ceases. These processes are stated by the equations (6) and (7).

From the mathematical point of view the problem (1) - (10) is a non-linear double problem of Stefan. The exact solution can be found only with the use of the numerical approach. So, we will consider comparatively simple, descriptive physical models, in order to avoid mathematical complexity.

The Joule model

Let us assume that the heat transfer is negligible. It is obviously true for a tip of a sufficiently small solid angle Ω. So, we can change the equation (1) as

$$\rho c \frac{\partial T}{\partial t} \approx \frac{i^2 \chi_0 T}{\Omega^2 r^4} \quad ; \qquad T|_{t=0} = T_0 \quad , \tag{11}$$

and the solution will then be

$$ln\frac{T}{T_0} \approx \frac{\chi_0 \int_0^t i^2 dt'}{\Omega^2 \rho c r^4} \quad . \tag{12}$$

The equation (12) states that at the instant t, with the radius r, the temperature is greater than T. The equation (12) can be written as follows:

$$r = \left(\frac{\chi_0 \int_0^t i^2 dt'}{\Omega^2 \rho c \, ln(T/T_0)} \right)^{1/4} \quad . \tag{13}$$

The equation (13) can be considered as that to determine the r-isotherm T at the instant t. If $T_c = \varepsilon_{vap}/k$ then we can find the r_c - the depth to which the cathode is heated up until it is destroyed.

$$r_c \approx \left(\frac{\int_0^t i^2 dt'}{\Omega^2 h} \right)^{1/4} \quad , \tag{14}$$

where r_0 is the specific action needed to destroy the material. The volume of destruction can be calculated as

$$V = \Omega \int_{r_0}^{r_c} r^2 dr = \frac{\Omega}{3}\left(r_c^3 - r_0^3\right) \quad , \tag{15}$$

where r_0 is the initial radius. With $r_c^3 >> r_0^3$, keeping in mind $M=\rho V$, we will then have, for the mass removal

$$M = \frac{\rho}{3\Omega^{1/2}}\left(\frac{\int_0^t i^2 dt'}{h}\right)^{3/2} \quad . \tag{16}$$

The specific erosion can be estimated as

$$\gamma = \frac{M}{\int_0^t i\,dt'} = \frac{\rho}{3\Omega^{1/2}}\left(\frac{\int_0^t i^2 dt'}{h\left(\int_0^t i\,dt'\right)^{4/3}}\right)^{3/2} \quad . \tag{17}$$

Assuming that

$$\frac{dr_c}{dt} \approx v_{vap} \quad , \tag{18}$$

and using the equations (14) and (4), one can estimate the evaporation surface temperature

$$T = \frac{\varepsilon_{vap}}{k\,ln\left(\frac{4v_c}{i^2}\left(\int_0^t i^2 dt'\right)^{3/4} h^{1/4}\Omega^{1/2}\right)} \quad . \tag{19}$$

The cross-section of a radius r_c can be written as

$$S_c = \Omega r_c^2 = \left(\int_0^t i^2 dt' / h\right)^{1/2} \quad . \tag{20}$$

Note that S_c does not depend on geometry and is determined by properties of the cathode material and by the current through the ecton. The corresponding current density will then be

$$j_c = \frac{i(t)}{S_c} = \left(\frac{i^2}{h\int_0^t i^2 dt'}\right)^{1/2} \quad , \tag{21}$$

decreasing with time, with any non-transcendent dependence $i=i(t)$. The magnitude of j_c is dependent on properties of the cathode material and on the ecton operation time. The decrease in the current density according to (21) suggests that this is the prerequisite to the duration of the ecton operation. In the above we neglected the thermal conductivity effect. Such a neglecting can be analytically expressed as follows:

$$at \ll \left(\frac{\int_0^t i^2 dt'}{\Omega^2 h} \right)^{1/2} , \tag{22}$$

where $a=\lambda/\rho c$ is the thermal diffusivity coefficient. Otherwise, with

$$at \gg \left(\frac{\int_0^t i^2 dt'}{\Omega^2 h} \right)^{1/2} , \tag{23}$$

the cathode material mass removal and the emission should stop. The equation (23) determines the time of ecton operation. Let the current through an ecton be constant and equal to i. Then we will have

$$r_c = (i^2 t/h)^{1/4} / \Omega^{1/2} \quad ; \tag{24}$$

$$M = (\rho/3\Omega^{1/2})(i^2 t/h)^{3/4} \quad ; \tag{25}$$

$$\gamma = (\rho/3\Omega^{1/2})(i^2 t/h)^{3/4} / (it) \quad ; \tag{26}$$

$$T = (\varepsilon_{vap}/k) / \ln\left[4\Omega^{1/2} v_s / (i^2 t/h)^{1/4}\right] \quad ; \tag{27}$$

$$S_c = (i^2 t/h)^{1/2} \quad ; \tag{28}$$

$$J_c = i(h/i^2 t)^{1/2} \quad . \tag{29}$$

Having the equation (23) in mind, we will have

$$t \approx i^2/(\Omega^2 a^2 h) \quad . \tag{30}$$

With high Ω magnitudes, in case the thermal conductivity effect can not be neglected, we can suggest the following. Let us assume that heating up the microtip and its subsequent failure are initiating factors for the ecton. Then the discharge can be considered as the case "a lune on a plane". Since $\varepsilon_{vap} >> \varepsilon_{mel}$, one can assume that the emission/evaporation zone is much less than the melting zone. The extension of melting zone is necessary to know, for it dictates the microcrater's size. The intensity of the Joule heating source is decreasing as r^{-4}, so that an intense generation of energy occurs in the immediate vicinity of the emission zone, with the emission/evaporation process being short as compared to the melting process. Thus, we can use an approach of the instant point heating source to obtain the current dependence of melting zone radius. If at the instant $t=0$ at the point $r=0$ the heat generated is Q, then, with the heat is being conveyed to the semisphere, [28], we will obtain

$$T - T_0 = \frac{Q}{4(\pi a t)^{3/2} \rho c} \exp\left(-\frac{r^2}{4at}\right) . \tag{31}$$

The temperature reaches its maximum at the point r_* with $t=r^2/6a$. For the melting temperature being the maximum temperature, we will then have

$$T_{mel} - T_0 = Q/\left(6.8\,\rho\, c r_{mel}^3\right) \quad , \tag{32}$$

and thus we have

$$r_{mel}^3 = Q/\left(6.8\,\rho\, c\, T_{mel} - T_0\right) \quad . \tag{33}$$

At the initiate period of ecton operation the evaporation front is moving with the velocity greater than the cooling rate. The energy generated during this period can not be efficiently conveyed to the cathode bulk and, therefore, the energy can not contribute to the melting process. This is in force until the time

$$t_0 = i^2/\left(4\pi^2 a^2 h\right) \quad . \tag{34}$$

for $\Omega=2\pi$ from the equation (30). The corresponding r_0 can be written as

$$r_0 = i/\left[2\pi\left(a h\right)^{1/2}\right] \quad . \tag{35}$$

Since, according to the equations (12) and (31) the temperature heavily depends on radius and time, the quantity Q can be determined as

$$Q = \int_{t_0}^{t_1} dt \int_{r_0}^{r_1} \frac{i^2 \chi_0 T}{4\pi^2 r^4} 2\pi r^2 dr \approx \frac{i^2 \chi_0 T}{2\pi} \int_{t_0}^{\alpha t_0} dt \int_{r_0}^{\beta r_0} \frac{dr}{r^2} = \frac{i^2 \chi_0 T\, t_0 (\alpha - 1)(\beta - 1)}{2\pi\, r_0\, \beta} \quad , \tag{36}$$

where $\alpha > 1$ and $\beta > 1$. These parameters can be used as correlation coefficients to match the theoretical predictions with the experimental data. The value of T in the equation (36) is taken from the equation (27), with $t=t_0$. Then, from (33) we will obtain:

$$r_{mel} = \left\{ \frac{(\alpha - 1)(\beta - 1)\,\varepsilon_{vap}\,\chi_0}{27\pi\,\beta\, k a^{3/2} h^{1/2}\, \rho\, c\, T_{mel}\, ln\left[\left(2 v_e / a^{3/2} h^{1/2}\right) i\right]} \right\}^{1/3} i \quad . \tag{37}$$

Figure 2b shows r_{mel} as a function of i for copper. It is seen that at high currents the function is linear, while at low currents rmelt slightly decreases, which is in good agreement with the above experiments. (See Fig. 2a).

It is worthy of note that the equation (37) can be applied to the metals of high electrical and thermal conductivities (Cu, AL), while, in the case of transient metals (W, Mo), the materials of lower electrical and thermal conductivities, such a result can not be used.

It is necessary to make a distinction between two tasks: to determine the melting zone radius r_{mel}, and to determine the emission/evaporation radius r_e. Though for the tip of a comparatively small solid angle Ω the melting front is but slightly ahead of the destruction front, it is not the case for the plane geometry. Substituting the equation (35) in (34) and with the definitions of a and h in mind, we thus will have

$$ij \approx \Omega \ln\left(\frac{T_c}{T}\right)\frac{\lambda}{\chi_0} \; ; \qquad (\Omega = 2\pi) \tag{38}$$

$$jr_c \approx \left(\ln\left(\frac{T_c}{T}\right)\frac{\lambda}{\chi_0}\right)^{1/2} \; , \tag{39}$$

where j is current density through the ecton at the terminal stage of its operation at the point r_c. It should be noted, however, that the problem of the current density in the cathode spot is open for further discussion [1-9] and certainly demands special attention.

It is right to write for the terminal stage of ecton operation:

$$\frac{d}{dt}(at) \geq \frac{dr_c}{dt} \; : \tag{40}$$

$$v_c \exp\left(-\frac{\varepsilon_{vap}}{kT}\right) \approx \frac{dr_c}{dt} \; ; \tag{41}$$

$$i = \Omega r_c^2 A T^2 \exp\left(-\frac{\varphi}{kT}\right) \; . \tag{42}$$

In general, $\varphi = \varphi_0 - \Delta\varphi$, but to determine $\Delta\varphi$, it is necessary to take into account the equations for plasma parameters. However, to determine the ecton life time t, the temperature at the emission/evaporation front T, and the effective work function φ, we can restrict ourselves with consideration of a mathematically complete set of equations: (40), (41), and (42).

It is our opinion that a notation of a so called virtual cathode could be very useful in this case. Such a notation can demonstrate an abrupt changes in the emission current during the process of ecton operation. So, for the specific erosion, variable with time, we can write

$$\gamma = \frac{\rho v_c}{AT^2}\exp\left(\frac{\varphi - \varepsilon_{vap}}{kT}\right) \; . \tag{43}$$

In this case the parameter ε_{vap} means a certain energy necessary to remove an atom from the cathode, to ionize the atom and to transfer the ion into the cathode plasma. Assuming that the potential barrier for electrons and the potential well for ions are equal factors in the emission process, we will have from (43)

$$\gamma = \frac{\rho v_c}{A\left(\varepsilon_{vap}/k\right)^2}\left(\ln\left(\frac{1}{v_s}\frac{dr_c}{dt}\right)\right)^2 \; ; \qquad \left(\exp\left(\frac{\varphi - \varepsilon_{vap}}{kT}\right) \approx 1\right) \; . \tag{44}$$

In all the above we supposed the current through ecton to be known. In reality, however, it is not the case, and it will be shown later.

4. On the mechanism of ecton self-sustaining under the pure surface conditions.

According to the above, the cathode erosion traces are a chain of craters. So, on a pure surface the new ectons are initiated at the microstructures developed by the previous ectons at the periphery of the cathode spot. When splashing out, a part of the melted metal expand as drops. So, in the publication [29] a model of the emission center initiation was considered as the electrical explosion of the neck of the liquid metal drop breaking off. Such a hypothesis was developed earlier in [5]. In this paper we will analyze the operation conditions of such an ecton regeneration mechanism.

The current density in the neck region j_p is obviously connected with the average current density j_d through the drop surface: $j_p = j_d(S_d/S_p)$, where S_d and S_p are drop surface and the neck cross-section, respectively in the region of maximum constriction. (Fig. 4)

Considering a drop with the neck as an electrical probe inserted in the cathode plasma, and using the (9) and (10) we will then have for the electron and ion currents, respectively:

$$j_i \approx (10^5 — 10^6)\ \text{A/cm}^2;\quad j_e \approx (10^6 — 10^7)\ \text{A/cm}^2,\ \varphi_c + \varphi \approx 15\ \text{V}. \tag{45}$$

Figure 5 shows the curves for the field emission current densities being $j_{em}(T_c, E) = 10^6 — 10^7$ A/cm^2, where T_c is the cathode temperature. E - the field intensity on the surface. The minimum of T_c corresponds to $E \approx (8\pi n T_e)^{1/2}[(\varphi_c + \varphi)/T_e]^{1/4}$, with the emission electrons decreasing the field intensity E.

The analysis of the stability of the neck shape made in [29] has shown that the neck is stable if the characteristic length along the z-axis, along which the neck radius is changed, is equal to or less than the neck radius r_p.

Analysis of the heat evolution in the neck has made it possible to reveal that a pronounced increase in the neck temperature can be observed only for $r_p \sim 2q\pi^{-1}$. Therefore, the condition for intense heat release in the neck region can be written as $r_p \leq 2q\pi^{-1}$ or

$$\sqrt{\frac{\chi_0 S_p}{\lambda S_p}}\,\frac{j_e r_p}{(1-\cos\theta)} \geq 1\ , \tag{46}$$

It has been shown in [29] that the thermal conductivity effect can be neglected in (49), and the characteristic time of the neck heating up can be estimated as $\tau_j \approx \rho c\,(\chi_0 j_p^2)^{-1}$.

Note, that when the left part of the (46) is but slightly greater than the right part, it is possible to assume that $j_d \approx j_e$.

The time until the drop breaks off, which was obtained from the analysis of the neck shape stability, has proved to be greater than the characteristic time of the neck heating τ_j. This allows one to conclude about reality of the ecton initiating mechanism due to the neck overheating.

It should be pointed out that in the equation (45) the values of the reverse electron current from plasma to the cathode proved to be greater than the ion current, with the reverse electron energy density being 10^7 - 10^8 W/cm. This provides for the cathode being heated up to the elevated temperatures, which causes an intense field emission to appear. The highest temperatures of the metal surface are attained at

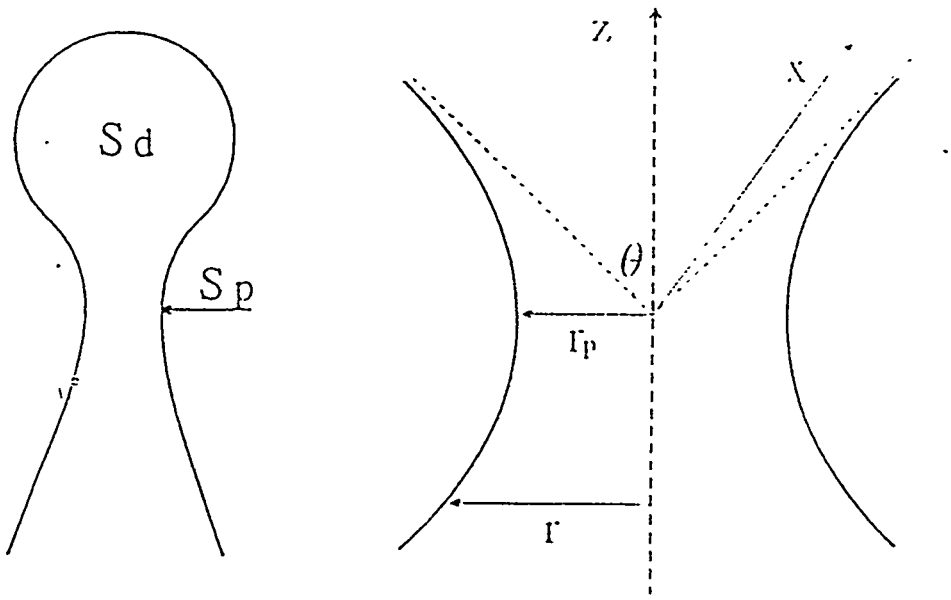


Fig. 4. The drop configuration: a) with the neck development b) the neck.

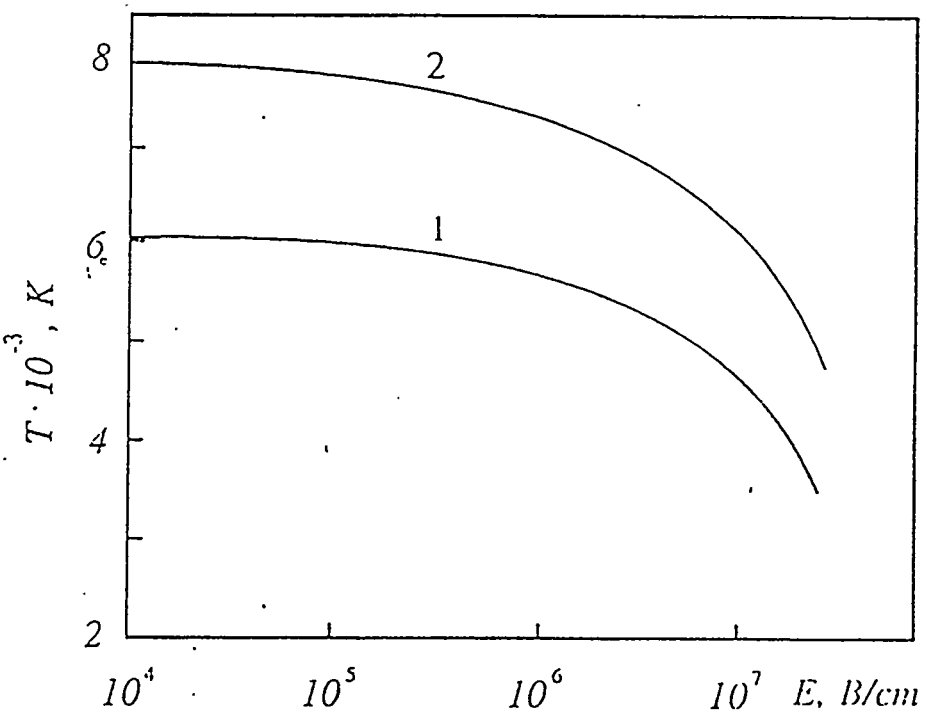


Fig. 5. Cathode temperature T vs the electric field intensity E on the metal surface at the thermal assisted field emission current density j_{em}: 1 - $j_{em} = 10^6$ A/cm^2, 2 - $j_{em} = 10^7$ A/cm^2.

the central part of cathode spot. With distance from the spot center, the temperature should decrease resulting in the decrease of the field emission current. So, it is natural to think that at the periphery of the cathode spot the fast plasma electron contribution to the total current density is dominating over the ion and field emission contributions. and the current through the center spot is partly flowing as reverse plasma electrons.

G.A. Mesyats developed a new approach to the ecton problem. [7,8]. By analogy with the glow discharge. a criterion for the arc cycle self-sustaining was proposed as

$$\gamma_d i_m \tau_e \geq 1 \quad . \tag{47}$$

where $\gamma_d = 10^7$ drops per Coulomb -- the specific erosion due to the drop fraction; i_m -- is the current through an ecton. equal to the double threshold arc current; τ_e is the time of ecton operation. Further is assumed that the total arc cycle time is comprised of the τ_e and τ_i, where t_i is the time of the ion current flowing trough the cathode region, when φ_c increases and, according to (10), the electron current J_e from plasma decreases drastically. The voltage "flash-ups", observed at the vacuum discharges, give an evidence of this [6]. The time τ_e can be estimated from (30) at $i=i_m$. To determine the values of r_c, M, j_c the equations (24), (25) and (29) were used. The specific erosion γ can be described as

$$\gamma = \frac{M}{i_m(\tau_e + \tau_i)} = 2\rho(1-\alpha)\,a^{1/2} / 3h^{1/2} \quad , \tag{48}$$

where $\alpha=\tau_i/(\tau_e+\tau_i)$. The ion current contribution can be written as

$$\gamma_i = \frac{Ze}{A}\gamma \quad . \tag{49}$$

where Z is the average ionic charge; A is the atomic weight.

Since the liquid microtip geometry (the angle Ω) is known but approximately, the more exact value of the angle Ω is proposed to be determined from the τ_e. (the equation (47)), or from the experiment.

Conclusions

The above analysis on the cathode phenomena, accompanying the initiation and operation of vacuum arc. has shown that the most of the results can be explained in terms of the proposed ecton approach. The relationships have been obtained to estimate the ecton life time, the specific erosion of the cathode. the current density through the ecton, the temperature at the emission/evaporation front, etc.

It has been shown that all the parameters are dictated by thermophysical and electrophysical properties of the cathode material. It has been stated that during the process of ecton operation there are conditions set for a new ecton (or ectons) to appear. The analysis of the ecton regeneration mechanism has been performed.

We proposed the analytical model for the experimental data analysis on the ecton role in vacuum arc operation. However, to study the ecton role in more detail, it is necessary to investigate the cathode plasma characteristics, which is the purpose of our further work to be performed under the contract.

References

1. I.G. Kesaev. Cathode Processes of an Electric Arc.- Moscow, "Nauka",1968. (in Russian).

2. Vacuum Arcs. Ed. by J.M. Lafferty. J. Wiley & Sons, 1980.

3. G.A. Lyubimov and V.I. Rakhovsky. Cathode spot of vacuum arc. - Uspekhi Fiz. Nauk, vol. 125, N 4, pp. 665-706, 1978. (in Russian)

4. S.P. Bugaev. E.A. Litvinov, G.A. Mesyats and D.I. Proskurovsky. Explosive Electron Emission. - Uspekhi Fiz. Nauk, v. 115, N 1, pp 101-120, 1975. (in Russian)

5. E.A. Litvinov, G.A. Mesyats and D.I.Proskurovsky. Field Emission and Explosive Emission Processes under Vacuum Discharges. - Uspekhi Fiz. Nauk, v. 139, N 2, pp. 265-302, 1983. (in Russian)

6. G.A. Mesyats and D.I.Proskurovsky Pulsed Electrical Discharge in Vacuum. Springer, Berlin-Hidelberg, 1989.

7. G.A. Mesyats. Ectons in electrical discharges. - Pisma Zh. Eksper. Teor. Fiz., v. 57, pp. 88-90, 1993. (in Russian)

8. G.A. Mesyats. Ectons in vacuum arc. - Pisma Zh. Eksper. Teor. Fiz., v. 60, pp. 514-517, 1994. (in Russian)

9. V.F. Puchkarev and A.M. Murzakaev. Current density and the cathode spot lifetime in a vacuum arc at threshold currents. - J. Phys. D, v. 23, N 1 pp. 26-35, 1990.

10. K.Jakubka and B.Juttner. On the Influence of Surface Conditions on Initiation and Spot Types of Unipolar Arcs in Tokamak. - J. Nucl. Mater., v. 102, pp. 259-266, 1981.

11. J.E. Daalder. Diameter and Current Density of Single and Multiple Cathode Discharges in Vacuum. - IEEE Trans. Power. Appar. Syst., v. PAS-93, pp. 1747-1757, 1974.

12. B. Juttner. Erosion Craters and Arc Cathode Spots in Vacuum. - Beitr. Plasma Phys., v. 19, pp. 25-48, 1979.

13. Ya.Ya. Udris. Disintegration of Materials by an Arc Cathode Spot. - Radio Eng. Electron Phys., v. 8, pp. 1050-1056, 1963.

14. B.N. Klyarfel'd, N.A. Neretina and N.A. Druzhinina. Metal Sputtering by the Cathode Spot of a Vacuum Arc. - Sov. Phys. Tech. Phys., v. 14, pp. 107-115, 1969.

15. D.T. Tuma, C.L. Chen and W.D.Davis. Erosion products from the cathode spot region of a copper vacuum arc. - J. Appl. Phys., v. 49, N 7, pp. 3821-3851, 1978.

16. J.E. Daalder. Erosion and origion of charged and neutral species in vacuum arcs. - J. Phys. D, v. 8, pp. 1647-1659, 1975.

17. J.E. Daalder. Components of cathode erosion in vacuum arcs. - J. Phys. D. v. 9, pp. 2379-2395, 1976.

18. T. Utsumi and J.H. English. Study of electrode products emitted by vacuum arcs in form of molten metal particles.- J. Appl. Phys., v. 46, N 1, pp. 126-131, 1975.

19. C.W. Kimblin. Vacuum arc ion currents and electrode phenomena. - Proc. IEEE, v. 49, pp. 546-555, 1971.

20. C.W. Kimblin. Erosion and ionization in the cathode region of vacuum arcs.- J. Appl. Phys., v. 44, N 7, pp. 3074-3081, 1973.

21. W. D. Davis and H.C. Miller. Analysis of the electrode products emitted by DC arc in a vacuum ambient. - J. Appl. Phys., v. 40, N 5, pp. 2212-2221, 1969.

22. A.A. Plyutto and V.N. Ryzkov. High speed plasma beams in vacuum arcs.- Zh. Eksper. Teor. Fiz. v. 47, pp. 494-507, 1964. (in Russian)

23. H.C. Miller. Contraints imposed upon theories of the vacuum arc cathode region by specific ion energy measurements.- J. Appl. Phys., v. 52, N 7, pp. 4523-4530, 1981.

24. W.G.J. Rondeel. Cathodic erosion in the vacuum arc.- J. Phys. D, v. 6, N 14, pp. 1705-1711, 1973.

25. J.E. Daalder. Energy dissipation in the cathode of a vacuum arc. - J. Phys. D v. 10, N 16, pp. 2225-2234, 1977.

26. B. Mazurek and J.D. Cross. Fast cathode processes in vacuum discharge development. J. Appl. Phys., v. 63, N 10, pp. 4899-4904, 1988.

27. E.M. Lifshits and L.P. Pitaevsky. Physical kinetics. Moscow, "Nauka", 1979. (in Russian)

28. G. Carslou and D. Eger. Thermal conductivity of Solids . Moscow, "Nauka", 1964.

29. E.A. Litvinov, G.A. Mesyats, A.G. Perfyonov, A.I. Fedosov, On the mechanism of vacuum arc cathode spot self-sustaining, Zhurnal Tech. Phys., vol. 55, 1985, pp.2270-2273.

ICPIG – 95 (Hoboken, NJ)

Ecton Processes in Vacuum Arc.

Gennady A. Mesyats
The Institute of Electrophysics,
Russian Academy of Sciences,
Ural Division, 34, Komsomolskaya St.,
Ekaterinburg, 620219, Russia

It is established that when microexplosions occur on a cathode there is a so-called explosive electron emission (EEE) observed [1]. Such an emission is realized through individual short portions (the electron avalanches) which we have named "ectons" [2]. The duration of electron current of such a portion is dictated by the time needed to cool down the emission center, that causes the EEE to stop.

We will proceed from the assumption of Kesaev [3], that the cathode spot consists of separate cells from which the current i_n, equal to the doubled arc current i_m, is flowing. An ecton is formed by interaction between the liquid metal stream and plasma. When the current exceeds a certain threshold value, the liquid metal stream produces a drop. This drop, even before its break-off, leads to the increase in density of the ion current from plasma in the stream-drop joint. This results in a great energy concentration in the joint and initiates an ecton due to the Joule heating of the joint. We consider the arc cycle to consist of two processes. The first one, of a duration t_e, is the process of ecton operation. The second one, of a duration t_i, is due to the ion current flowing within the cathode region. During the t_i period the formation of a new liquid metal stream is completed, which causes a new ecton to emerge. The process thus becomes self-sustaining. If the new ecton is produced, with a drop breaking-off, then the criterion for the arc cycle to be self-sustaining is written as

$$\gamma_d t_c i_m \geq 1 \qquad (1)$$

where γ_d is the drop number per 1 Coulomb; $t_c = t_e + t_i$ is the time of arc cycle; $i_m = 2i_t$ is the minimum current in cell; i_t is the threshold current of the arc.

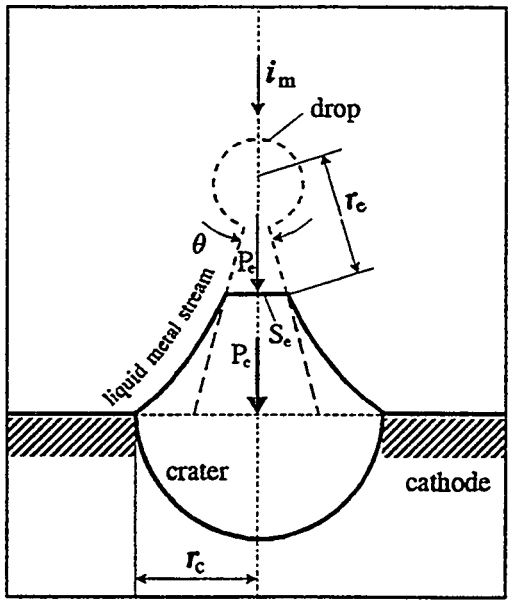


Fig. 1

Thus, let a liquid metal stream, of a conic shape with an angle of a taper θ, results from the arc operation. Then the time of ecton operation t_e, the specific mass removal γ_m, the current density at the end of the ecton operation j_e are determined from the Joule model of the cone heating, (Fig.1). [6]

$$t_e = i_m^2 / \pi^2 \alpha^2 \bar{h} \theta^4 \qquad (2)$$

$$\gamma_m = 2\rho (1-\alpha) a^{1/2} / 3\bar{h}^{1/2} \qquad (3)$$

$$j_e = \pi a \bar{h} \theta^2 / i_m \qquad (4)$$

where a is the thermal diffusivity, $\bar{h}$ is a specific action characterizing the explosion of metal; $\alpha = t_i/t_c$, $\theta = 0.74$.

Based upon the ecton mechanism of the vacuum arc operation one can explain the effect that involves a force acting to extend the distance between the cathode and anode during the arc operation [7]. To describe the process specifically there is a characteristic f introduced, which is actually the force value per unit current. Let us

consider the time of ecton operation te during which the velocity of plasma flowing varies from zero to v_p, that yields

$$f = m_e v_p / 2\, t_e\, i_m \qquad (5)$$

Having in mind that $m_e/t_e i_m = \gamma_m$ is the specific erosion of the cathode, we thus have

$$f = \gamma_m v_p/2(1-\alpha) \qquad (6)$$

We will substitute γ_m from (3) and thus have,

$$f = \rho a^{1/2} v_p/3\bar{h}^{1/2} \qquad (7)$$

It can readily be shown that at the end of the process of the ecton operation the plasma pressure put on the surface S_e will be

$$P_e = fj_e = \pi\sqrt{\rho}\, a^{3/2} v_p \bar{h}^{1/2}/3i_m \qquad (8)$$

The plasma pressure within the liquid metal zone will then be $P_c = P_e S_e/S_c$, where S_c is the crater surface. Taking into account that the crater is formed due to the thermal conductivity within the time interval t_e, we will have $S_e/S_c = \theta^2/4$. Therefore, it will be right to write

$$P_c = P_e \theta^2/4 \qquad (9)$$

As a result of the above we can, using the idea of ectons, find a number of the vacuum arc cathode spot parameters and establish a correlation between the parameters.

The comparisons of the predictions with experiments have been made for the copper electrode arc. Upon completion of the ecton operation, the current density is evaluated from the equition (4) which yields $j_e \cong 2.2 \cdot 10^8$ A/cm^2. The value is in agreement with those obtained by many workers [1, 3, 7]. The usual practice, however, is to evaluate the current density through the radius r_c of a crater on the cathode surface and through the current flowing. With the radius being estimated according to the equition $r_c = 2\,(at_c)^{1/2}$ we have the value $r_c \cong 2 \cdot 10^{-4}$ cm. This corresponds to the data from [5], with the arc current ranging as $i < 10$A. In this case the apparent current density will be $i_m/\pi r_c^2 = 2.7 \cdot 10^7$ A/cm^2, [5].

Let us now consider the dynamic characteristics of the cathode spot. We can, using the equition (7), obtain the value of the specific force f~100 din/A. This value is nearly five times as great as the experimental data by Tanberg [7]. Upon the analysis of this work [7] we concluded that the specific erosion of the copper cathode was γ_m ~0.15 10^{-4} g/C which was 3-7 times as low as the most reliable measurements available [3-5]. This can be explained by the fact that there was a contaminated cathode used in the work [7], and a spot of the first type was operating on the cathode. However, in the measurements made through the works [3-5], a cathode was the well purified copper electrode on which a second type spot was operating with a considerably higher value of the γ_m. The small value of γ_m in [7] resulted in the reduced values of the force f according to the equition (6). For example, Kesaev has found that f~50 din/A.

According to the equition (8) the pressure P_e amounts to ~$4 \cdot 10^9$ Pa, and the pressure P_c~$0.5 \cdot 10^9$ Pa. The latter is close to the value measured in [1] for the graphite cathode.

REFERENCES

1. G.A. Mesyats and D.I. Proskurovsky, Pulsed Electrical Discharge in Vacuum. Berlin: Springer-Verlag, 1989.

2. G.A. Mesyats, Pis'ma v JETV, 1993, v.57, N 1,2, pp. 88-92 (in Russian)

3. I.G. Kesaev, Cathode processes of electrical arc. Moscow: Nauka, 1968 (in Russian).

4. C.W. Kimblin, J.Appl.Phys., 1973, v.44, N 7, pp. 3074-3081.

5. J.E. Daalder, J.of Phys. D. Appl. Physics, 1975, v.8, p. 1647-1659.

6. G.A.Mesyats, Pisma v JETV, 1994, v.60. N7, pp.514-577 (in Russian).

7. R. Tanberg, Phys. Rev. , 1930, v.35, pp.1080-1089.

1. Noise measurements of the emission center lifetime in a vacuum arc cathode spot

1.1 Introduction

The nonstationary behavior of the vacuum arc cathode spot is one of its principal properties. The spot continuously moves over the cathode surface and never resides at one and the same place. This motion is stepwise in character, i.e., one emission center stops operating at one place and another emission center appears at a new place. The velocity of this motion is high (~5 10^4 cm/s) for a contaminated cathode surface; for a clean surface it is lower (~5 10^3 -10^4 cm/s). On a contaminated surface, a large number of craters with sizes of 0.1 - 1 μm are formed, with the distance between them being several times greater then the crater size. The craters on a clean surface have sizes on the order of 10^{-6} m, and each next crater is at the edge of the preceding one [1,2,3].

Therefore, it is natural to introduce the lifetime of a cathode spot as its characteristic and to define this time as the time for which the spot resides at one and the same place.

This quantity is determined experimentally by several means, namely,

(1) by fluctuations of the voltage,

(2) by fluctuations of the glow intensity,

(3) by high-speed photographing of the cathode spot,

(4) by the method of cathode spot autographs.

(1) It is known that the voltage across an arc is unstable and features bursts whose number is the larger, the lower the discharge current [1,4]. This instability is less pronounced for a contaminated cathode surface than for a clean one. These voltage bursts correspond to the "attempts" of the arc to cease; each burst exerts a recovering action on the discharge. With each voltage burst a new crater appears. The authors of [5] has demonstrated that the fluctuations of the gap voltage are related to the processes occurring at the cathode. Supposing that each voltage burst corresponds to the death of a cathode spot, the authors of [1,6] have estimated the lifetime of a cathode spot on copper as 2-10μs.

(2) The authors of [1,8,9] in their investigation into the fluctuations in the intensity of the discharge glow, supposing that the cathode spot lifetime is the time between two glow intensity bursts, have obtained that the lifetime falls in the range 2-20 μs.

(3) The cathode spot lifetime defined as the time during which the spot resides at one and the same place was measured using methods of high-speed photography, by [10,7] who have obtained this time to be equal to 2-10 μs.

(4) One more independent method for the determination of the lifetime of a cathode spot is the method of autographs where clean and smooth cathode surfaces are subjected to the action of a single arc current pulse; in the process, waveforms of the

current through the gap and the discharge voltage are recorded. From these waveforms, the time for which the discharge has been operating is determined. Then the trace left by the cathode spot on the surface (autograph) is photographed with the use of an electron microscope. With the known discharge operation time and having counted the number of the craters that had appeared for this time, an average lifetime is determined. To obtain a more precise result, the cathode spot is forced to move additionally in an external transverse magnetic field. Using this technique [2,4], the cathode spot lifetime was found to lie in the range 5-40 ns and increase with cathode temperature [2]. For a molybdenum cathode, the formative time of an emission center was estimated to be 1-3 ns.

The cathode spot lifetimes measured by the method of autographs and by other methods differ by two orders of magnitude. This suggests that merely different discharge characteristics were measured. By the discharge glow fluctuations and voltage bursts, the "attempts" of the arc to extinguish are indicated. For low arc currents, they take place with an average interval of 1 μs. During this time, several tens of emission centers have appeared and then ceased on the cathode, each of them having left one crater [2]. The lifetime of the emission center is supposed [2] to correspond to low-voltage (5-10 V) oscillations that occur during the time between the voltage bursts reaching the power supply voltage[1].

The authors of [12] have obtained Fourier spectra for the arc voltage, but they have found no peculiarities in them.

The results of the studies carried out by the method of autographs suggest that the search should be made in another frequency region and, furthermore, for low discharge currents, in order that a joint action of many emission centers do not distort the pattern of the process. These investigations call for wideband circuits to power the discharge and measure its parameters, which were not used in previous experiments.

The present work was focused at studying with high temporal resolution (~ 1 GHz) the noises of a low-current discharge on a clean surface of W, Cu, and Al cathodes. The goal was to obtain an information about the lifetime of an emission center in a vacuum arc cathode spot.

Actually, most of the investigators mean by a cathode spot the bright luminous region at the cathode surface and measure the lifetime of this region, while it is known that this region involves several simultaneously operating emission centers, each leaving one crater on the cathode surface. The higher the arc current, the larger the number of fragments in the cathode spot, so that the current per fragment is in fact an invariable quantity of the order of a few amperes. Theoretical models of the operation of a cathode spot are constructed just as applied to these emission centers rather than to the cathode spot as a whole.

---

[1] In a number of studies it has been shown that the gap voltage fluctuations are related to the cathode processes (birth and death of cathode spots). Therefore, it seemed purposeful to perform a frequency analysis of the discharge voltage aimed at the determination of the cathode spot lifetime.

To make theoretical estimates, it is required to know the lifetime of one emission center rather than that of the whole cathode spot that consists of several closely located and existing simultaneously emission centers (fragments, by Kesaev's terminology).

Furthermore, the case of a surface where uncontrollable contaminants are present in the form of dielectric films offers no interest from the theoretical viewpoint. To verify a model, experimental data should be obtained in pure vacuum conditions (superhigh oil-free vacuum) for a degassed cathode surface cleaned by multiple arcing. Moreover, the discharge current should be low in order that only one emission center exist.

1.2 Experimental setup and technique

The experiments were carried out in a cylindrical vacuum chamber, 85 mm in inner diameter, made of stainless steel. The experimental chamber is shown schematically in Fig.1. Coaxial inputs of voltage, of 75 Ω wave resistance, are circularly positioned at the chamber sides. The two high-voltage inputs are to impress a pulse voltage, up to 40 kV in amplitude, onto the chamber. All inputs are movable and connected with the chamber through metallic bellows. The measurements were performed with a microscope, while observing through the sight hole. The chamber was pumped down to 10^{-3} Torr, with an absorption forepump followed by an ion pump. An oil-free high vacuum was thus obtained, with the residual pressure being 10^{-8} Torr.

Small sizes of the chamber provide for a bandwidth of 1 GHz. Figure 2 shows an oscillogram for a voltage pulse with a short risetime before entering the camber and after passing through it. Shown is the resulting distortion of the pulse loading edge.

Within the chamber, each input has an electrode holder 2 mm in diameter, made of stainless steel. Wire electrodes and a probe are fastened to the holders. The anode is 200 μm in diameter. The trigger electrode is a needle made by electrochemical pitching, with the tip 10 μm in diameter. The anode is at a distance of 350 μm from the cathode. The collecting surface of the probe is at a distance 450 μm from the cathode. But for the cathodes made of aluminum and copper, all electrodes were made of tungsten wires. The wires were pretreated by electrolytic polishing. The high melting point of tungsten allows the purification and degasification to be performed immediately before the experiment, warming the wires up to 2000 K in vacuum by passing current through the wires for a few minutes.

The copper and aluminum electrodes were prepared as follows. A portion of the metal was fastened to the tip of a V-form tungsten wire. The wire was then heated in vacuum until the metal started to melt, producing a droplet. It was such a droplet of the metal that served as a cathode. Immediately prior to measurements, the cathode surface was purified by multiple pulses of the arc current.

The tungsten cathodes were prepared by heating the tip of a wire up to the melting point with the current emitted from an auxiliary cathode, with the result that a spherical droplet of the metal formed at the tip. One of the versions of electrode design is shown in Fig. 3. A tungsten wire 75 mm in diameter is used as a probe, with the insulation made of

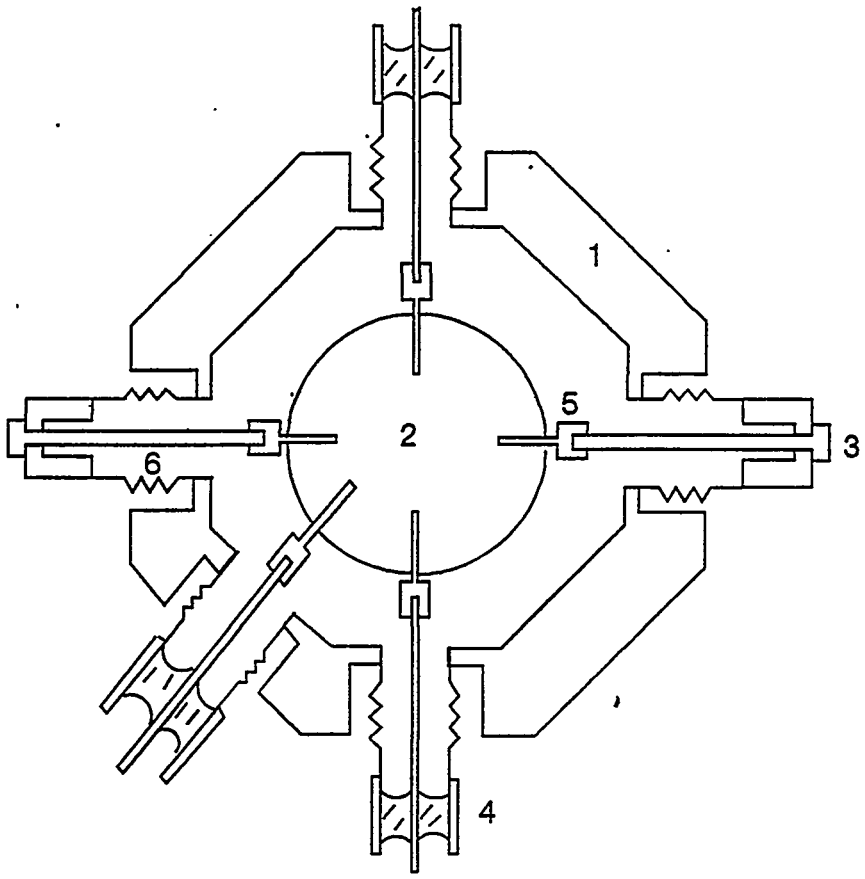


Fig. 1. Experimental vacuum chamber: 1- vacuum chamber; 2 - Sigth hole; 3 - High voltage input; 4 - Movable voltage input; 5 - Holder; 6 - Metallic bellows.

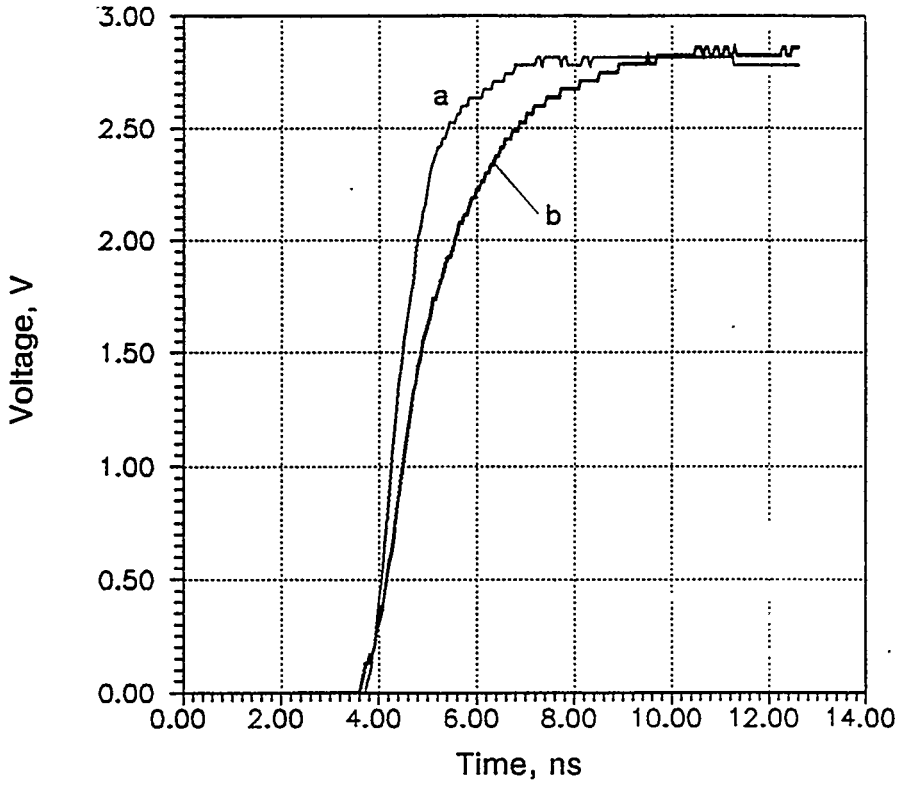


Fig. 2. Oscillogram for a voltage pulse with a short risetime before entering the chamber (a) and after passing through it (b).

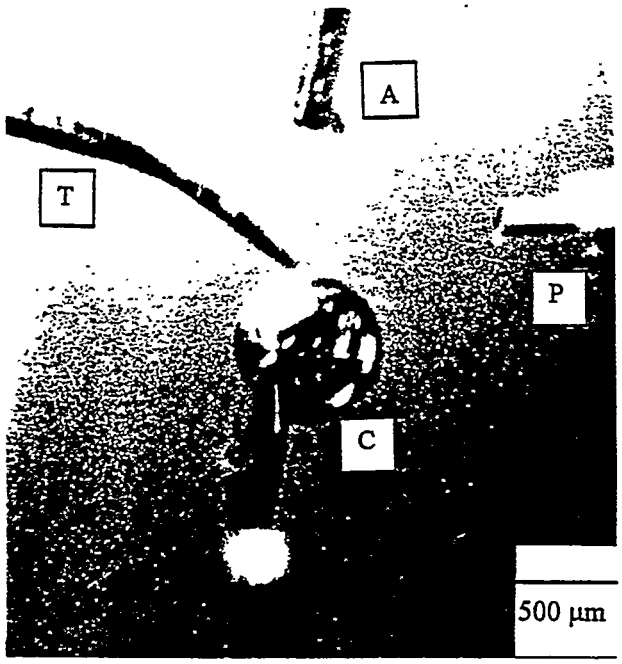


Fig. 3. Electrode design: A - anode; C - cathode; T - trigger pin; P - probe.

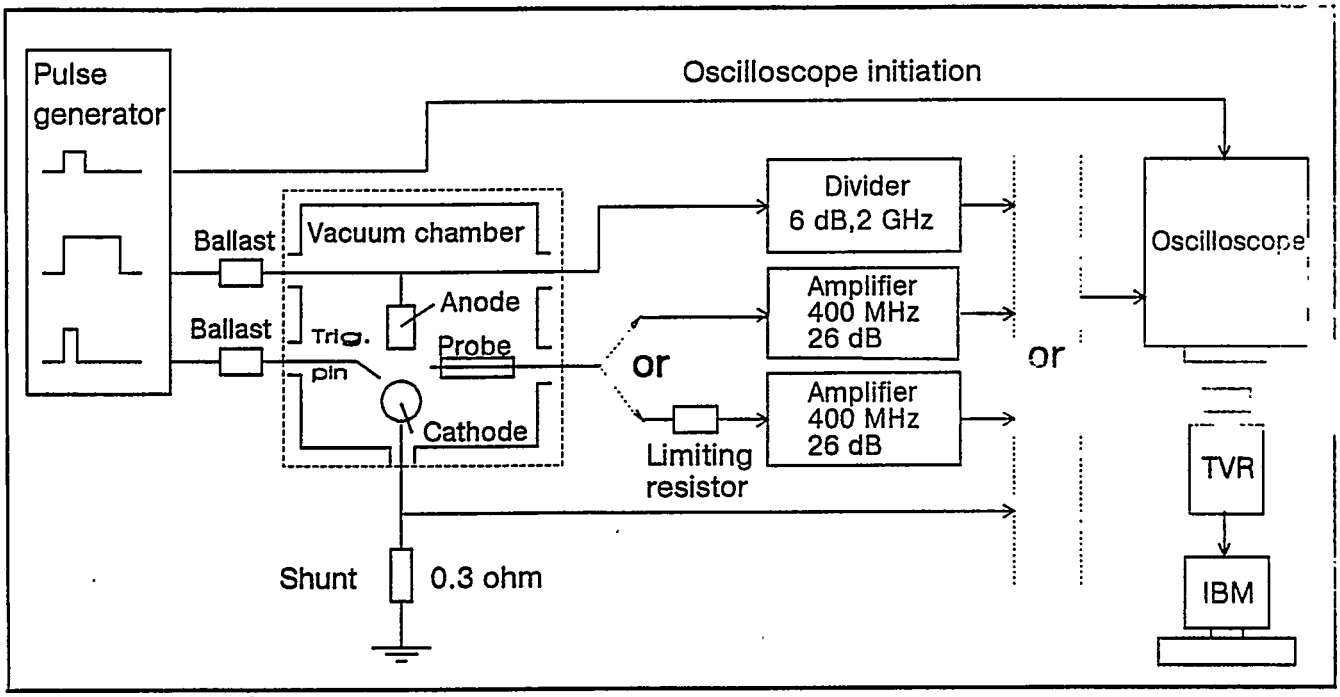


Fig. 4. Experimental arrangement

alundum, the diameter of the insulated probe being 200 μm, the length of the uninsulated part of the probe ~ 100 μm. The insulated part of the probe is 18 mm in length; and in the time of measurement, the arc plasma expanding into vacuum has no time to reach the opposite uninsulated part of the probe. So, only the insulated part of the probe reacts to the arc plasma particles.

Due to the difficulties arising in measuring the temperatures of Cu and Al cathodes with so small sizes, we have to use the following technique. All V-form wires were made identical in length, diameter, and shape. Different pure metals, the melting temperatures of which are known, were placed on the different wires. The wires were heated until the metal on the tip started to melt. In doing so, the current flowing through the wire was recorded. Based on the results, a calibrating curve was constructed, that was then used in determining the temperature to which the cathode should be heated.

The temperature of a tungsten cathode was measured through the sight hole of the chamber with an optical pyrometer. A correction of 100° C was made to the temperature measured, as recommended in [13]. In each test only a one parameter of the discharge was recorded: or the discharge current, or the discharge voltage, or the floating probe potential, or the current on to the probe being under the cathode potential in plasma. A schematic diagram of the electrical measurements is shown in Fig. 4.

The pulse generator contains two pulse forming lines made of coaxial cable with a wave resistance of 75 Ω, and one common triggered spark gap. Initially, the cables are charged through a limiting resistor to 20-40 kV. When the spark gap operates, every line forms a voltage pulse across the load, with the risetime being ~1 ns and the duration equal to the electric length of the cable. For external circuits, the generator has an internal resistance of 75 Ω, with the emf being equal to the initial voltage. The generator produces two rectangular pulses of high voltage at a time, with a duration of 1300 and 40 ns. The pulse of duration 1300 ns is used to power the discharge, with the arc current being determined by the limiting resistor in the anode circuit. The 40-ns pulse is applied to the trigger electrode; the current of the trigger pulse is limited by the resistor in the trigger circuit; and it is 5 A. All resistors are carbon ones of low internal inductance. The arc is initiated by a trigger pulsse applied to the cathode-trigger electrone gap; this gap is broken down and the resulting plasma propagating toward the anode at a velocity of $\sim 10^6$ sm/s. Thus the anode-cathode circuit is closed, and as the trigger pulse terminates (in 40 ns), the discharge continues operating in the cathode circuit.

Simultaneously with the high-voltage pulses, a low-voltage pulse is produced by the generator, the pulse being used to start up the measuring equipment.

The discharge voltage is recorded by a fast oscillograph through a voltage divider (10 dB) with the bandwidth 2 GHz.

The discharge current is measured with an oscillograph using a shunt based on low-inductance carbon resistors.

To measure the floating probe potential, a resistor of R=6.6 kΩ is connected into the probe circuit, at a distance of 80 mm from the tip. The signal was then applied to the oscillograph input. So, the oscillograph made a record of the voltage from the voltage

divider formed by R_p and R_{inp}, where R_{inp}=50 Ω is the input resistance of the oscillograph. The probe potential can be calculated if the load sharing coefficient is known.

In measuring the floating probe potential a floating condition should be met, that is the resistance in the probe circuit should be much higher than the resistance of the plasma/probe layer. The fulfillment of this condition was experimentally verified as follows.

Two runs of measurements were conducted: with all other conditions being equal in the first run R was taken equal to 6.6 kΩ, and in the second run 10 kΩ. The probe potentials calculated from those runs differed from one another by a value less than the instrumental error. So, the resistor of R=6.6 kΩ is sufficient to meet the floating condition. The current from the plasma onto the probe was measured an applying the signal from the probe directly onto the input of the oscillograph, so that the probe was connected with the cathode through the input resistance of the oscillograph (50 Ω). However, due to the low value of the current, the probe potential was neglected as compared to the cathode potential, and the probe made records of the ion current from plasma.

Due to the weak signals in the probe measurements, an amplifier with a bandwidth of 400 MHz and an amplification factor of 25 dB was used.

The measuring system consists of a fast oscillograph with a bandwidth of 5 GHz and a fixed sensitivity of 0.8 V/cm. An oscillogram is read out of the screen of the oscillograph by means of a teledetector and is then stored in a computer memory. Each oscillogram is made of 256 dotes. The discreteness step along the vertical axis is considerably less than the beam width on the oscillograph screen.

The oscillograms are subjected to the Fourier analysis and autocorrellation analysis. The oscilograms were processed using the fast Fourier Transform and thus individual spectra were obtained. After that, an averaging by some number (more often 30) of individual spectra was performed.

The autocorrelation analysis consisted in that that for each oscillogram an individual autocorrelation function G_i was constructed as

$$G_i(t_s) = T^{-1}\int_0^T p(t)p(t-t_s)dt \ ,$$

where t_s is the shift in time, $p(t)$ is the discharge parameter under investigation,

For t_s=0, this function was normalized to unity. Then an autocorrelation function G_a (t_s) was calculated as an average of the individual functions G_i (t_s). It was supposed that if the signal involves some characteristic repetitive process, this should show up in the G_a (t_s) plot in the form of local maxima at ts corresponding to the period of the process.

1.3 Experimental results and discussion

Noise measurements for the discharge parameters have been performed for copper, aluminum, and tungstren at two cathode temperatures: 300 K and a temperature being about half the melting temperature. The latter temperature was 600 K for Al, 800 K for Cu, and 1800 K for W. The discharge current was chosen such that the discharge operate in average during 600 ns until its self-extinguishing. This discharge operation time is quite sufficient to perform measurements. The measuring equipment (oscillographs and a teledetector) was started 300 ns after the discharge initiation, in order that the stray processes in the measuring circuits caused by the high-voltage trigger pulse of duration 40 ns be completely attenuated.

Figure 5 shows the current amplitude spectrum for a 4-A copper arc measured at a cathode temperature T_c=300 K and averaged by 30 measurements. The spectrum has no peculiarities; moreover, this spectrum was not reproduced from one measurement series to another and, when averaged by a large number of pulses, became a more and more monotonic curve. For this reason, we did not perform discharge current spectrum measurements for Al and W.

Figure 6 presents a typical voltage waveform for a 4-A copper arc recorded at a cathode temperature T_c=300 K. Low-voltage oscillations around an average voltage level of about 20 V can be seen. The voltage amplitude spectrum for a copper arc measured at T_c=300 K is shown in Fig.7a. The spectrum has been obtained as an average of 30 spectra of individual oscillograms and showed high reproducibility from one measurement series to another. Figure 7b shows the copper arc voltage spectrum obtained for the same current but for a cathode temperature increased to 800 K. The spectra corresponding to different temperatures are distinct: the spectrum for the increased temperature has a peculiarity at a frequency corresponding to the period 38 ns, while for the spectrum obtained at T_c=300 K, a peculiatity appears in 20 ns; the spectrum of the heated cathode has retained the peculiarity corresponding to 25 ns. The appearance of the spectra allows the conclusion that the local maxima characteristic of the spectrum shift toward the lower frequencies as the cathode is heated.

The voltage spectrum measured for an in arc on tungstrem (Fig.8) shows a simular behavior on varying cathode temperature. For T_c=300 K, this spectrum has locccal maxima at 38 ns, 25 ns, 21 ns while for T_c=1500 K local maxima correspond to 57 ns, 23 ns, and 13 ns.

The results of measuring the voltage spectrum for an arc on an Al cathode are indefinite. The spectra measured in different test series repeated each other and we failed to indicate stably reproducible local maxima. It seems that the cathode surface was not cleaned from oxides even by multiple arc current pulses. The reason for this may be the fact that the aluminum cathode was made of a thin oil strip fastened to the tip of a V-form tungstren electrode. In the process of fabricating, the aluminum cathode was made to have the shape of a drop, so it had a comparatively large volume per unit surface area, while for the original foil the area per unit volume was large. As a result, the drop surface might contain oxides in more amounts than the original foil surface.

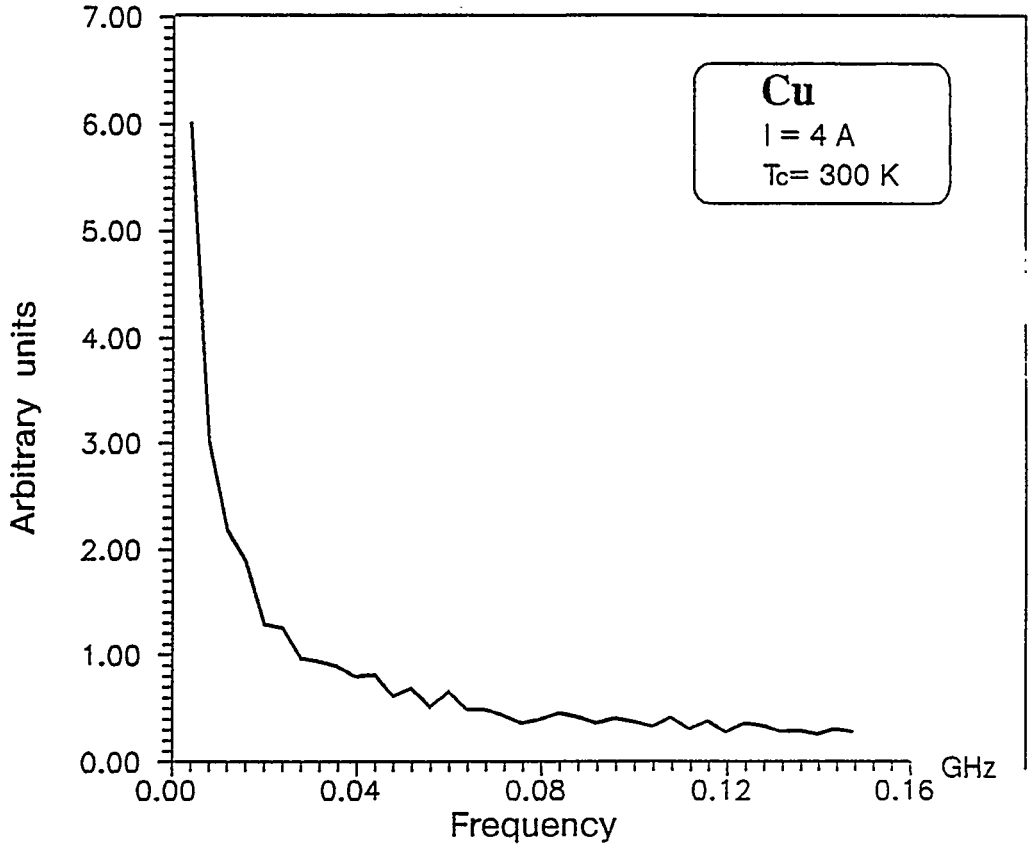


Fig. 5. Amplitude spectrum of the arc current for a copper cathode. Arc current 4 A.

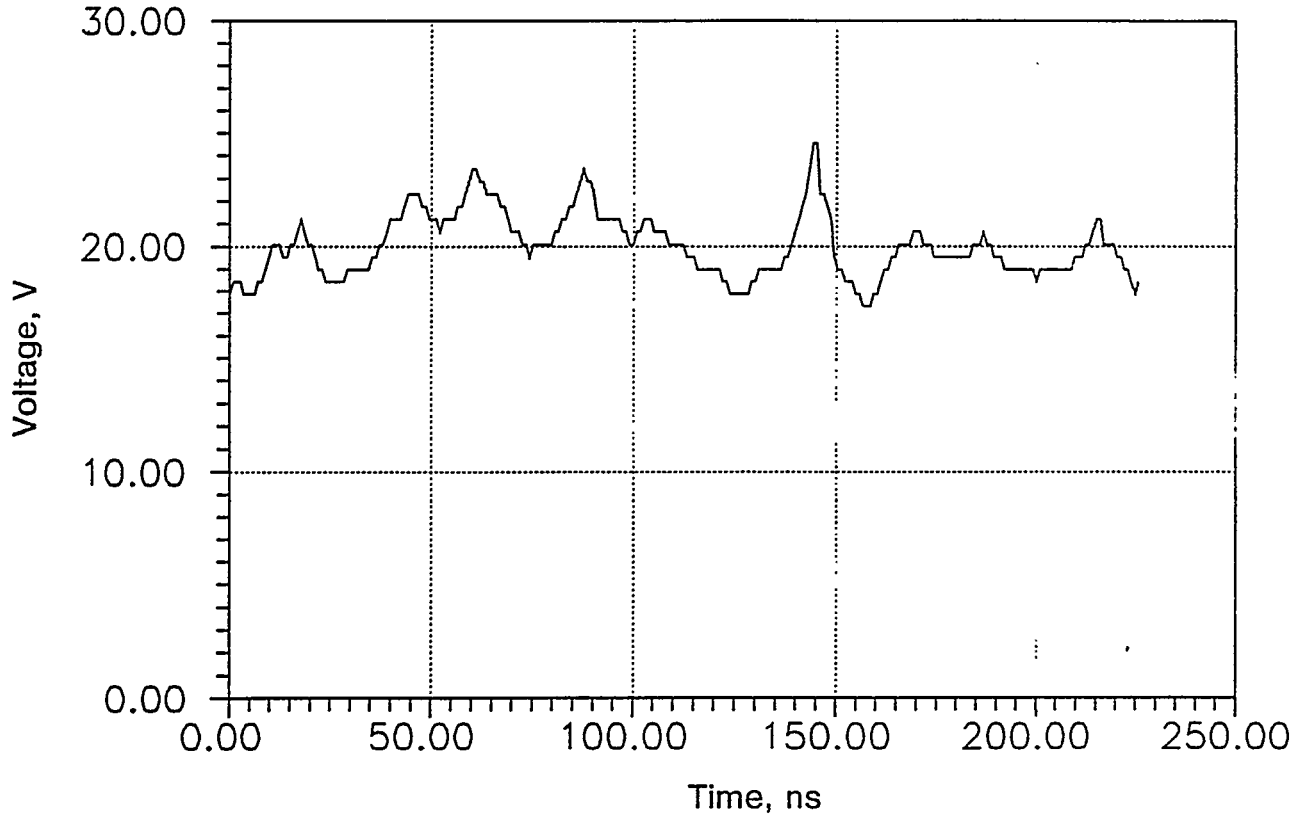


Fig. 6. Typical voltage waveform for a 4-A copper arc recorder at a cathode temperature 300 K.

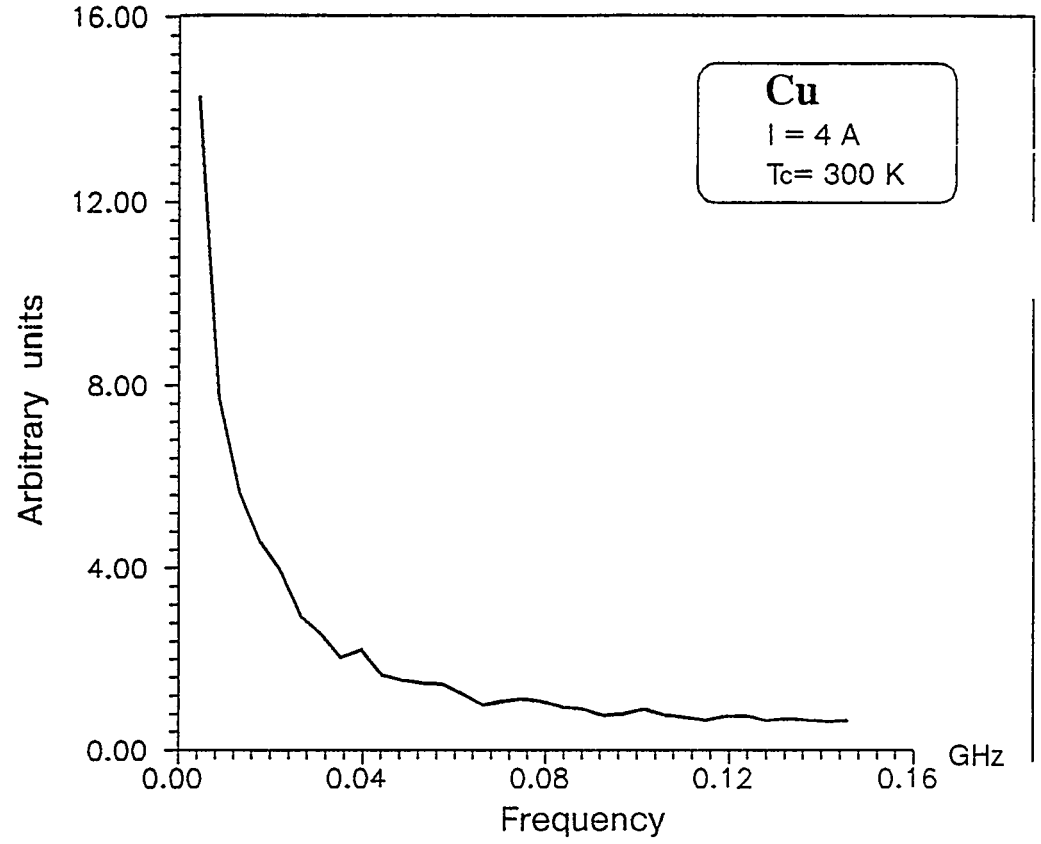


Fig. 7a. Amplitude spectrum of the arc voltage for a cooper cathode at T_c= 300 K. Arc current 4 A.

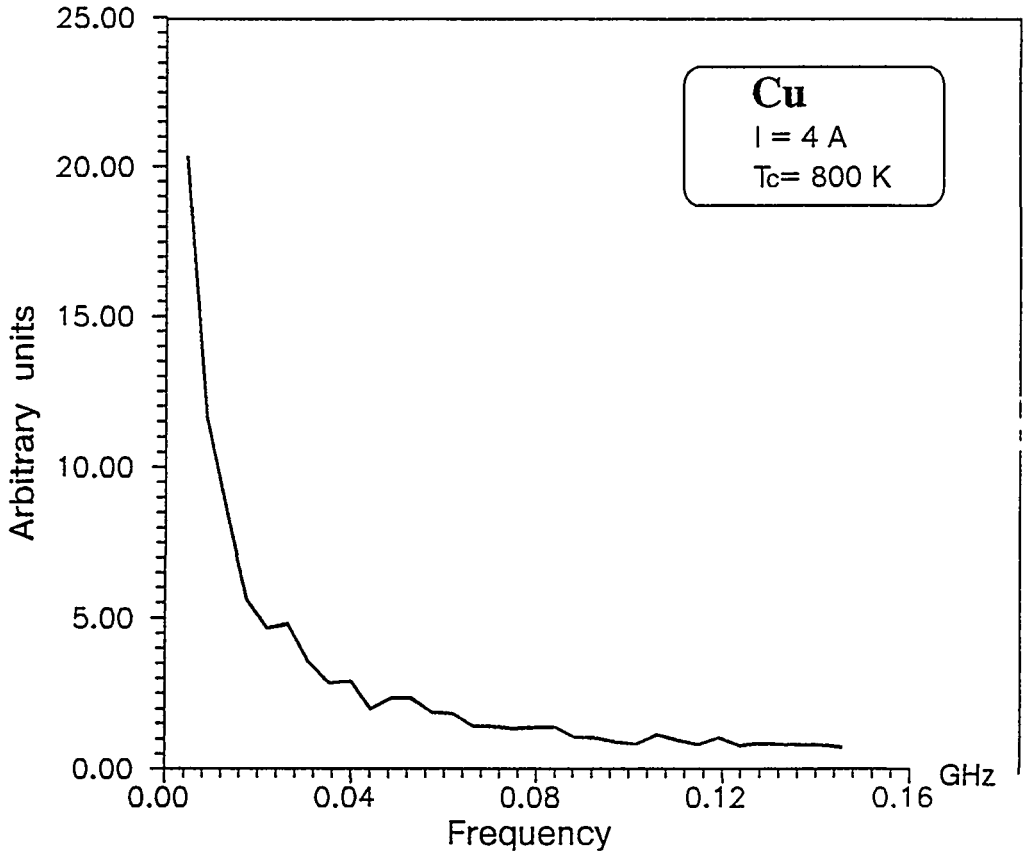


Fig. 7b. Amplitude spectrum of the arc voltage for a cooper cathode at T_c= 800 K. Arc current 4 A.

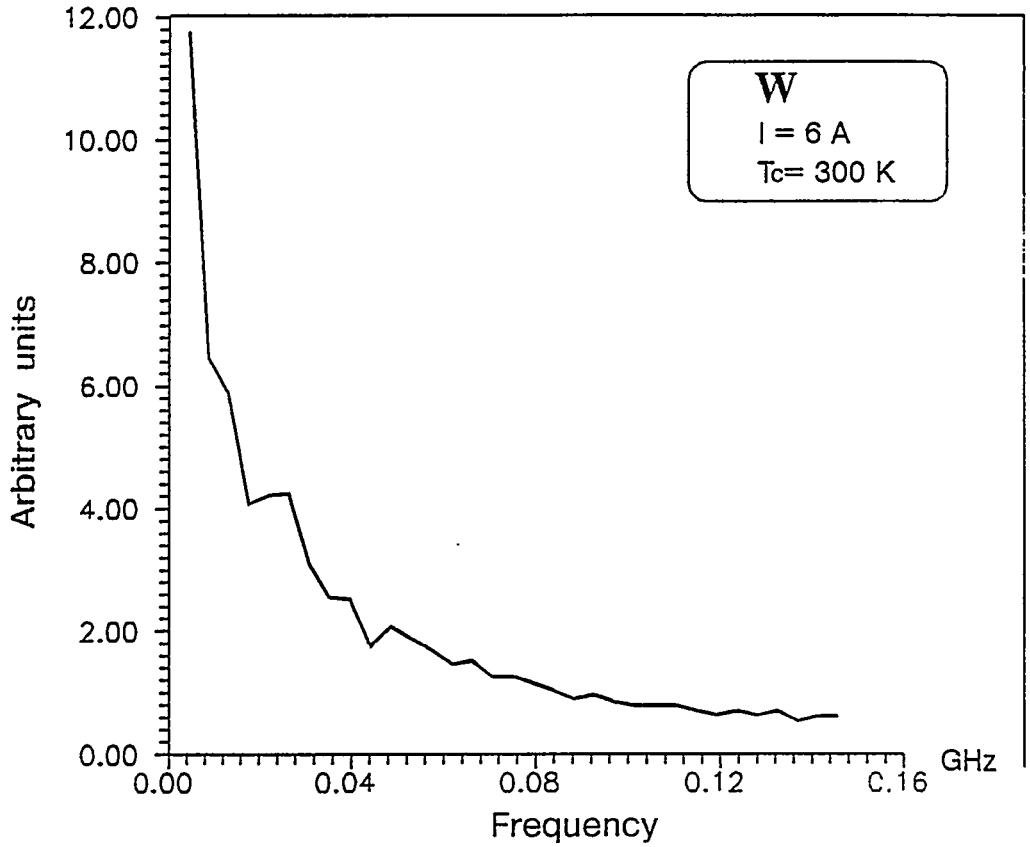


Fig. 8a. Amplitude spectrum of the arc voltage for a tungstrem cathode at T_c= 300 K. Arc current 6 A.

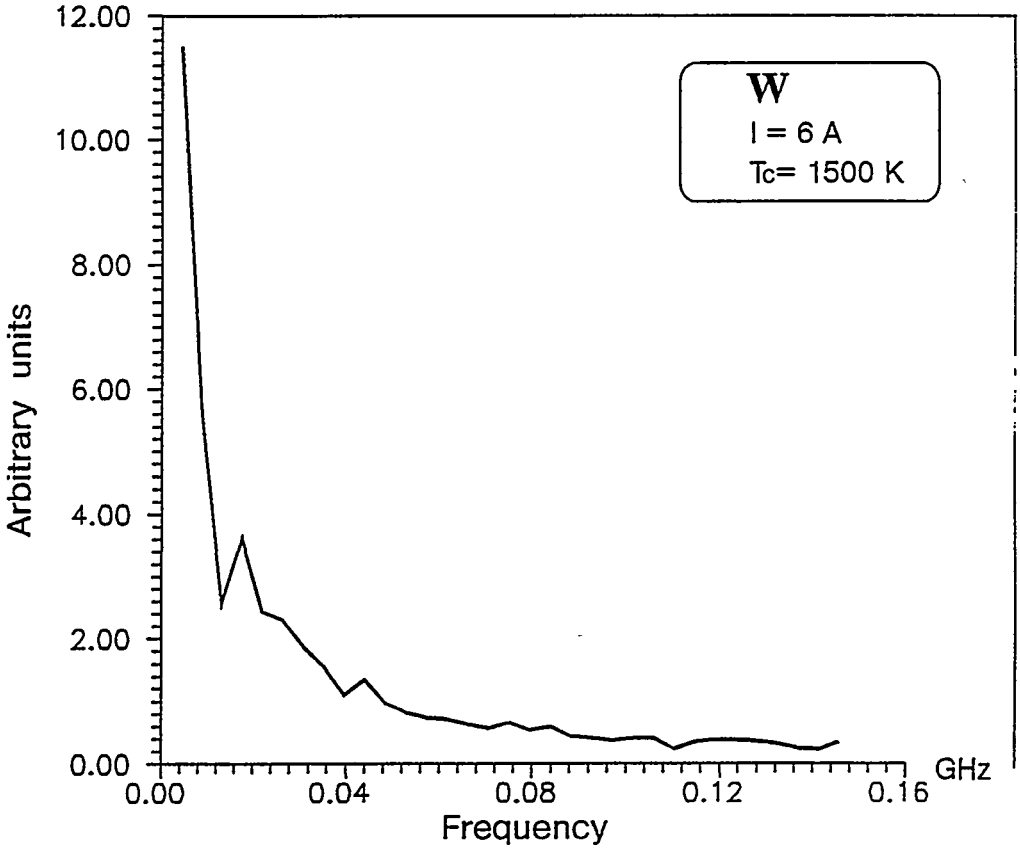


Fig. 8b. Amplitude spectrum of the arc voltage for a tungstrem cathode at T_c= 1500 K. Arc current 6 A.

Experimentally, no effect of the gap spacing on the arc voltage spectrum has been found for anode-cathode separation varied from 0.2 to 0.6 mm.

The average spectra of the floating probe potential have been observed to be identifical to those of the gap voltage. It seems that this can be accounted for by the fact that, in the absence of oscillation in anode fall potential in the frequency range under investigation, the plasma potential measured by the probe follows the gap voltage oscillations. The spectra of the current onto the probe being at cathode potential and immersed into plasma, when averaged by a grate number of individual spectra, show no peculiarities and have the form of smooth, exponentially falling curves. This behavior of the current onto the probe can be accounted for by known fact [14] that ions are emitted from the cathode spot region in the form of sharp jets with the cone angle 10 -20 degrees, with the jet out flow direction being distributed in a random law. If a burst of the current onto probe corresponds to the incidence of a cathode plasma jet on the probe, the signal will also vary according to a random law.

The experimental results obtained testify to the presence of repetitive fluctuations in the discharge voltage whose characteristic times are several tens of nanosecond and their repetition period decreases with increasing cathode temperature. At the same time, it is well known that the arc voltage fluctuations are related to the crater formation on the cathode surface [1,4,5]. It was also been established [2] that the average time between two sequential events of the microcrater formation on a pure surface of a tungsten cathode is 25-30 ns for the cathode temperature T_c=300 K and arc current 5 A and it increases with cathode temperature. For the same arc current and a cathode temperature of 1200 K this time is about 100 ns. A comparison of the above literature data and the results of our measurements performed for tungsten allows the conclusion that the technique we used provides an information about the lifetime of an emission center in a vacuum arc cathode spot, i.e., the time during which the current in the discharge gap is sustained due to the operation of the emission center. As this time has gone, the emission center ceases to operate at its place and a new emission center appears at another place.

The present work is in fact a target experiment aimed at answering the question whether the data on the lifetime of a cathode spot emission center (which is meant as an object leaving one crater on the cathode surface) can be obtained using the frequency analysis of fluctuations for one or other parameter of the discharge.

The sole now avaiable experimental method for the determination of the lifetime of a single emission center is the method of cathode spot autographs used by Juttner [11] and Puchkarev and Murzakaev [2]. However, this method is applicable only to refractive metals whose surface can be cleaned from contaminants by heating to high temperatures in superhigh vacuum. For the rest materials, a sole reliable technique for cleaning the cathode surface from contaminants seems to be the use of the arc itself [15], but in this case the method of autographs is of cause inapplicable. At the same time, it is well known that the surface contaminants affect the cathode spot parameters such as the chaotic motion velocity, the lifetime, the crater size and number, etc.[16].

Therefore, it is of great interest to develop some other method for the determination of the emission center lifetime which would be applicable for any cathode material.

An autocorrelation analysis of the recorded voltage waveforms has shown that despite the fact that for many individual waveforms the autocorrelation function shows periodicity for the sigual that follows (see Fig.9) an averaging by several tens of individual correlation functions yields a smooth falling curve (see Fig.10). Thus, the autocorrelation analysis turned out to be a noninformative tool for the processing of noise data.

2. Cathode erosion rate measurements

2.1 Introduction

A vacuum arc operating with a moderate current, when the anode spot does not form, carries the current through the gap only due to the evaporation of the cathode material[1]. Thus, the cathode erosion is the fundamental property of a cathode-initiated discharge in vacuum. The erosion rate is generally expressed in terms of micrograms per coulomb charge transfer.

The erosion rate is used in fact in any theoretical model of the cathode spot either to verify the predictions or to estimate the principal parameters of the cathode spot such as the spot temperature, the cathode plasma density, etc.

Despite the fact that the erosion rate is comparatively simple to measure, the data obtained by different researchers are largely different. These differences refer to both the magnitude of the erosion rate and its dependencies on the discharge current, pulse duration, and cathode diameter.

The best-studied cathode material is copper for which the erosion rate measurements vary in the range from $4.7 \cdot 10^{-7}$ [16] to $1.3 \cdot 10^{-4}$ g/C [17]. It has been established [17,18,19,20] that the erosion rate depends on the discharge current. In [17] it is reported that as the current was varied from 400 to 600 A. the erosion rate varied from 130 to 200 μg/C, while the authors of [21] observed only a slight increase in erosion rate for the same current range. The authors of [22,23] measured an increase in erosion rate by 5-10 % for a 5-7-fold rise of current.

Daalder [24], having analyzed a great body of his own measurements and the data available in the literature, arrived at the conclusion that the erosion rate increases with the product of the discharge current and the discharge operation time. The Daalder's results indicate that the erosion rate increases with the duration of the current pulse. He has also discovered the dependence of the erosion rate on cathode diameter: the smaller the diameter, the larger the erosion rate.

On the other hand, it is well known that the dielectric films present on a cathode surface play a significant part in the process of cathode erosion. This problem was specially investigated by [25,15]. They have found that the erosion rate for a cathode

[1] It is pointed out [28] that the anode spot formation can be expected for currents of 600 A and above

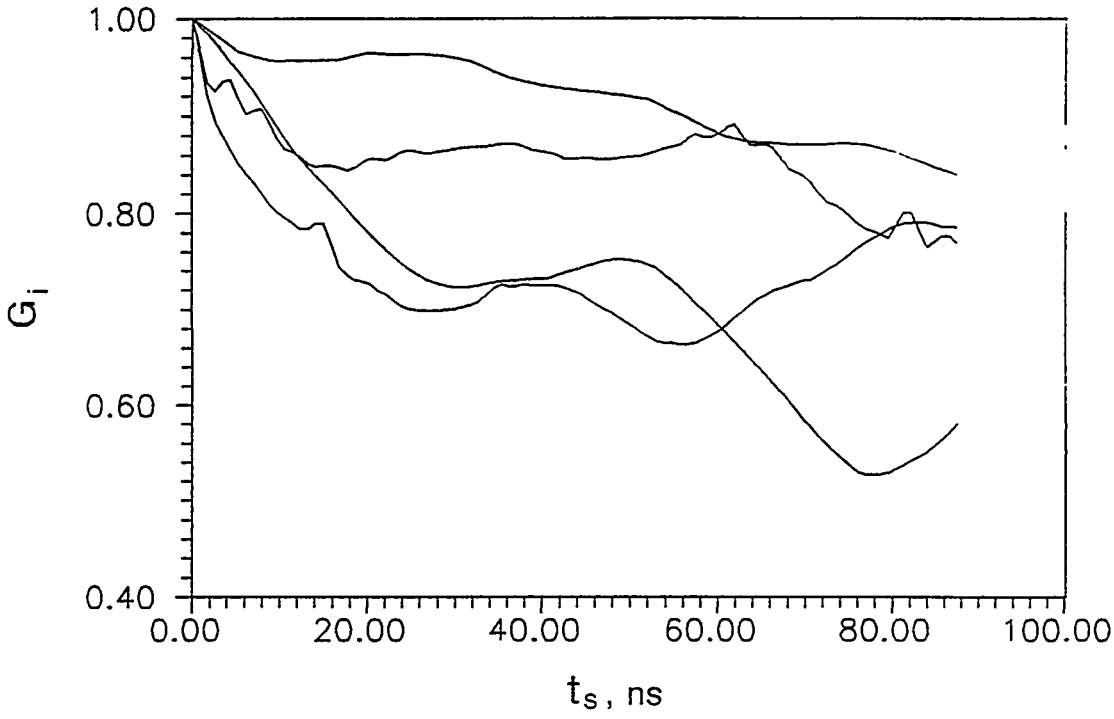


Fig. 9. Autocorrelation function for the signals of arc voltage. I = 4 A.

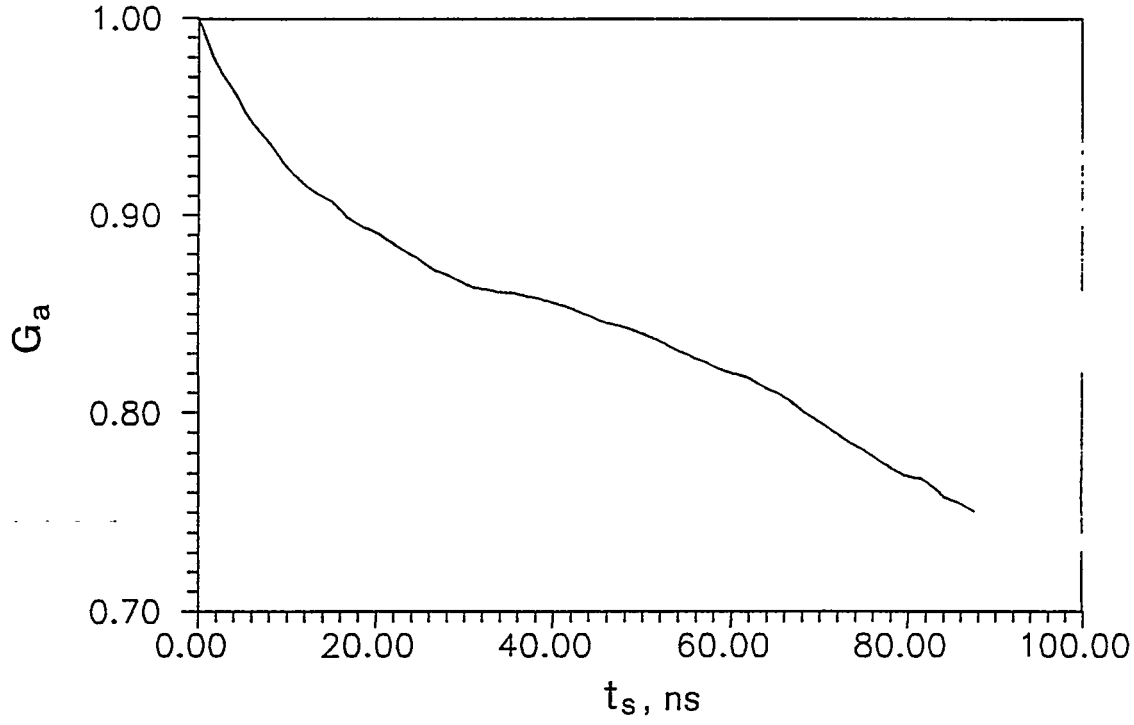


Fig. 10. Average form of the autocorrelation function of the arc voltage.

covered with a dielectric film is substantially lower compared to a cathode with a clean surface. The dielectric film erodes first; the metal beneath the film is damaged only weakly. Only when the arc itself removes the dielectric film from the surface, the discharge continues operating in the metallic vapor. Alchert and Juttner have established that the cathode erosion is strongly affected by the oil vapor present in the chamber (in the case when an oil pump is used for pumping out; the cathode surface therewith is contaminated with the continuously precipitating oil vapor). This, like in the case of dielectric coatings, results in a decrease in the sizes of the craters, an increase in their number, an increase in the velocity of the chaotic motion of the cathode spot, and in a decrease in erosion rate. A cathode spot is known to consist of closely located fragments (emission centers), each leaving one crater on the cathode. These emission centers operate simultaneously; the current per emission center is on the order of a few amperes and depends on the cathode material.

The data available in the literature have been obtained for the most part in the oil vacuum, i.e., the surface cleanness was not controlled.

The cathode surface contaminants strongly affect the cathode processes of the discharge: the velocity of the spot motion over the cathode surface increases, the average crater size decreases, while the craters increase in number. This suggests that there exist two types of cathode spot:

- the first-type spots operating on contaminated cathode surfaces and the second-type spots operating on clean surfaces. Characteristic of the first-type spots is low erosion rate; according to the data of [16], it is 4 10^{-7} g/C;
- the second-type spots produce a more substantial erosion with a rate on the order of 10^{-3} -10^{-4} g/C.

The large spread in the measured erosion rates can be accounted for just by the fact that there were no control of the cathode surface contamination. It has been shown [15] that the techniques for cleaning the surface used conventionally in high vacuum technology fail to provide a clean electrode surface. A reliable cleaning effect can be achieved by using multiple arcing. However, this technique gives no results for an oil vacuum worse than 10^{-5} Pa since in this case the surface appears to be contaminated with the precipitated oil vapor in a very short time. Most of the erosion rate measurements were performed under oil vacuum conditions; in this case the dependence of the measured erosion rate on the charge having carried by the cathode can be accounted for by the gradual increase of the cathode surface cleanness in the course of experiment. The similar dependence of the erosion rate on the electrode size can be explained by the fact that the cathode surface was eventually completely cleaned from contaminants which resulted in that that only second-type spots operated at the end of the experiment, while initially the spot existed on an incompletely cleaned surface, being sometimes a first-type spot and sometimes a second-type spot. This explanation is qualitatively supported by the experiment [11] where a copper cathode of diameter 25 mm was completely cleaned by a charge of 10^4 As having passed through the cathode, while in the Daalder's experiment [24], the total charge having passed through an identical cathode was $3*10^2$ As, which perhaps testifies to the fact that in the latter case the electrode surface was contaminated.

It can also be supposed that the erosion rate depends on cathode temperature. The cathode spot during its operation heats the surface. and the higher the discharge current and the longer the pulse, the more intense is the surface heating near the cathode spot, which may lead to a more intense splashing of the metal in the form of microdrops or a more intense evaporation of the metal from the cathode regions just left by emission centers.

The existing theoretical models that describe the operation of a vacuum arc cathode spot refer in a fact to a single emission center (fragment) of the cathode spot. They are based on the assumption that the metal surface is clean and that it contains no gas either dissolved in the metal or adsorbed at its surface. Thus, a cathode erosion experiment should be carried out in oil-free high vacuum with currents close to the current passed through a single fragment in order that there were no influence of one emission center on another. Such an experiment should be carried out with short discharge operation times, such that the cathode surface have no time to heat up within the current pulse duration, i.e., the emission center operate on a cold cathode surface.

Increasing discharge current increases the number of simultaneously existing cathode spot fragments, the current per fragment varying insignifically.

Initially, we intended to work with the arc current pulse duration 10^{-3} s, but we would have then to use a bulk cathode in order to avoid its heating during the discharge. A large-area cathode would require for its cleaning a too large number of arcings (see Refs. 15,11,26), and the problem of the surface cleanness would remain unresolved. So we have decided that an experimentation with a short pulse duration (10^{-6} s) would be more useful as the base for the construction of a theoretical model. In this case, first, the surface temperature remains unchanged during the arc current pulse and, second, the cathode can be made small (100 μm in diameter) in order that the surface be cleaned by arc discharges in a few first pulses and subsequently the arc operate on a clean cathode, with the number of cleaning pulses being much smaller than the total number of pulses used in the experiment.

2.2 Experimental setup and technique

All experiments were carried out in the vacuum chamber described above. The chamber was pumped out with an adsorption pump and an ion pump. After warming up the chamber to 200°C during 12 hours, the pressure was $<10^{-8}$ Torr, the vacuum was oil-free.

The technique to manufacture cathodes of Al, W and Cu is similar to that used in performing noise measurements. During 3 hours all the cathodes were getting degasified at temperatures 700 K, 800 K , and 1500 K for Al, Cu, and W, respectively. Before placing the cathodes into the chamber, they were weighed with an accuracy of 2 μg. The cathodes were fastened to the holders with special clamps made of Ta foil, to prevent the surface from damage during the process of installation and removal of the cathodes.

An electropolished tungsten wire 200 μm in diameter, served as an anode. with its end surface being faced to the cathode. The trigger electrode was a tungsten needle produced by electrochemical pitching, with the radius of the tip being less than 10 μm.

The arc discharge was initiated by applying a voltage of amplitude 20 kV and duration 40 ns; the voltage being applied to the cathode/trigger gap.

A voltage pulse of amplitude 20 kV and duration 1300 ns arrives at the cathode coincidentally with the trigger pulse.

The discharge current and the duration of arcing were recorded by an oscillograph by means of a low-inductive shunt of 0.34 Ω. The duration of arcing was always 1300 ns and could be determined with a pulse generator. The transferred charge transfer was defined as the product of the current times the duration of arcing times the number of pulses. The measurements were performed for a current of 5A at two different temperatures of the cathode. Measurements for a current of 50 A were also performed to make a comparison with other works. The erosion rate was determined at two different temperatures: at room temperature and at a temperature close to the melting point.

The temperature range was limited by the requirement that there should be no considerable mass loss from the cathode due to the evaporation of the cathode material. The following temperatures were chosen: 700 K for Al, 800 K for Cu, 1800 K for W. The cathodes were heated by the current from a stabilized source. The temperatures of the Al and Cu cathodes were estimated from the data of the calibration curve (Sec.1.2) obtained during the preparation of the cathodes. The temperature of the W cathode was estimated by means of an optical pyrometer.

The erosion rate was found based on the known charge and the mass removed from the cathode in the course of experiment. The accuracy in determining the mass loss was dictated mostly by the instrumental error of the analytical balance used; the error was 2 μg, which for our experimental data of 10 μg mass loss proved to be 20%. This error should be added by the error arising in measuring discharge currents. The current is characterized by oscillations which are 10% of the average value. Therefore, the total error in estimating the erosion rate is 30%.

2.3 Results and discussion

Erosion rate measurements were performed for copper, aluminum, and tungsten cathodes with the discharge currents 5 and 50 A and two cathode temperatures: 300 K and an elevated temperature. The cathode temperature was not made too high in order that the evaporation of the cathode be unappreciable in the total test time (25 hours for the current 5 A). The elevated temperature was 700 K for Al, 800 K for Cu, and 1800 K for W.

Table 1 presents our erosion rate measurements and, for comparison, the data obtained by Kimblin, Daalder, and Plyutto et al., since they are invoked most often in the literature where the erosion rate in vacuum arcs is discussed. Also given in Table 1 are the

data of Jttner [11] on the cathode erosion in vacuum breakdown, because they were obtained in Jttner experimental conditions most similar to ours. The cathode erosion rate has been found to be independent of discharge current in the range 5 - 50 A within the experimental error 20-30%. At the same time, its strong dependence on the cathode temperature has been discovered.

Table 1. Erosion rate μg/C

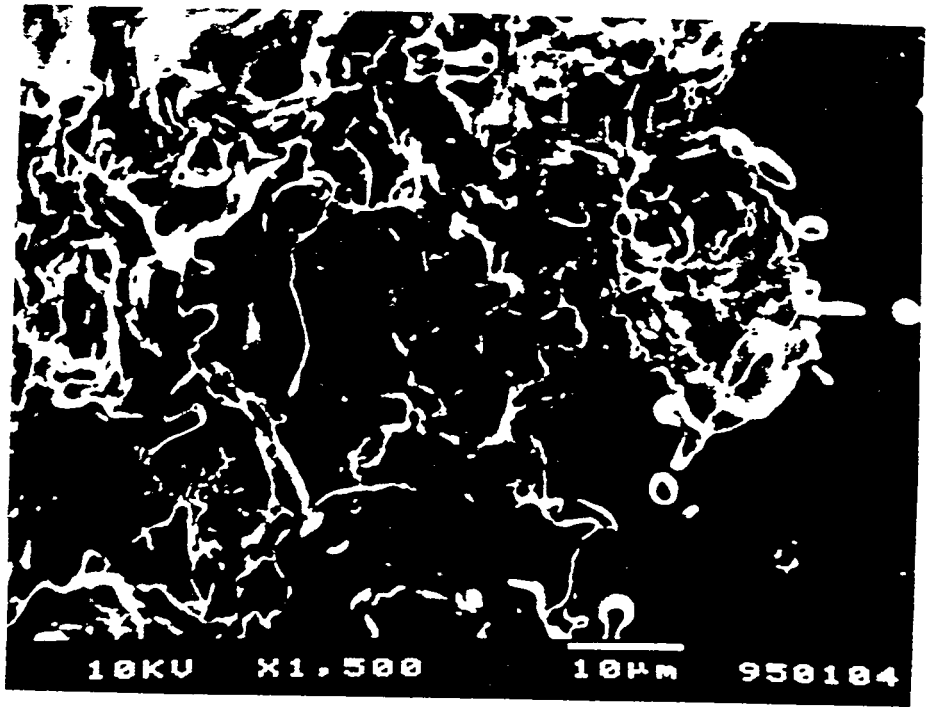
Cathode material	Cathode temperature	Our results		Kimblin	Daalder	Plutto et al	Juttner
		I_a=5 A	I_a=50 A	I_a=100 A	I_a=33 - 200 A	I_a=200 A	I_a=10-100A
Cu	300 K	44 ± 20	40 ± 10	115	40 - 60	130	50
Cu	800 K	130 ± 45	130 ± 40				
Al	300 K	90 ± 35	90 ± 20			120	100
Al	700 K	120 ± 45	120 ± 30				
W	300 K	110 ± 40	110 ± 30	62			136
W	1800 K	210 ± 65	210 ± 30				

Figure 11 shows micrograhps of some regions of the surface of a copper cathode taken after the action of a 50-A arc for the cathode temperatures 300 and 800 K. It can be seen that the crater size increases with temperature. The craters on the cold surface were 5 - 15 μm in size, while on the heated surface the crater size reached 25 μm. It can also be seen for the heated surface that the metal was intensely splashed out from the cathode spot region, sometimes in the form of large (up to 200 μm in size) particles. For the cold surface, such splashing was not observed.

Figure 12 presents a micrograph of a copper cathode taken after the action of 2500 pulses with a current of 50 A. The eroded surface region is a circle with clearly pronounced edges. This character of surface damage suggests that originally the surface was clean. Otherwise the cathode spot should appear at larger distances from the site of arc ignition because of the breakdown of the dielectric films on the cathode surface. It is well known that a cathode spot may operate on the cathode even when it is not "directly visible" from the anode, this effect being more pronounced for a contaminated cathode surface (see, e.g., [27]). For our experiment this is not the case and the cathode spot operates only near the site of arc ignition and only on the surface preliminarily cleaned by preceding current pulses. Thus, the character of the cathode damage shows that our erosion rate measurements were performed for clean metallic cathode surfaces.

From Table 1 it can be seen that the erosion rates obtained for cold cathodes are most close to the results of Juttner [11] obtained for a high-voltage breakdown under the conditions of superhigh vacuum. The fact that the erosion rates measured by us are somewhat lower than those measured by Juttner can be explained by that in the Juttner's experiment the discharge operated at the wire tip of diameter 10 μm (for tungsten ..20 μm) or, in the case of Al, at the edge of a foil strip of thikness 10 μm. At the same time, the crater size is typically about 10 μm, i.e., it is close to the foil thickness, which can

a)



b)

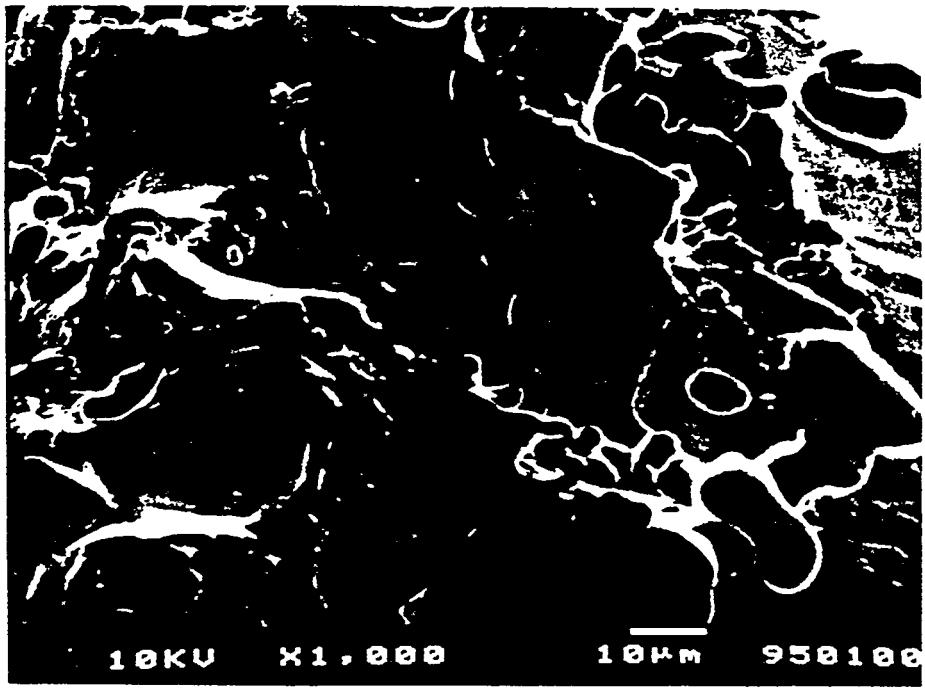


Fig. 11ab. SEM micrographs of Cu cathode after a 50-A arc. Cathode temperature 300 K (a) and 800 K (b).

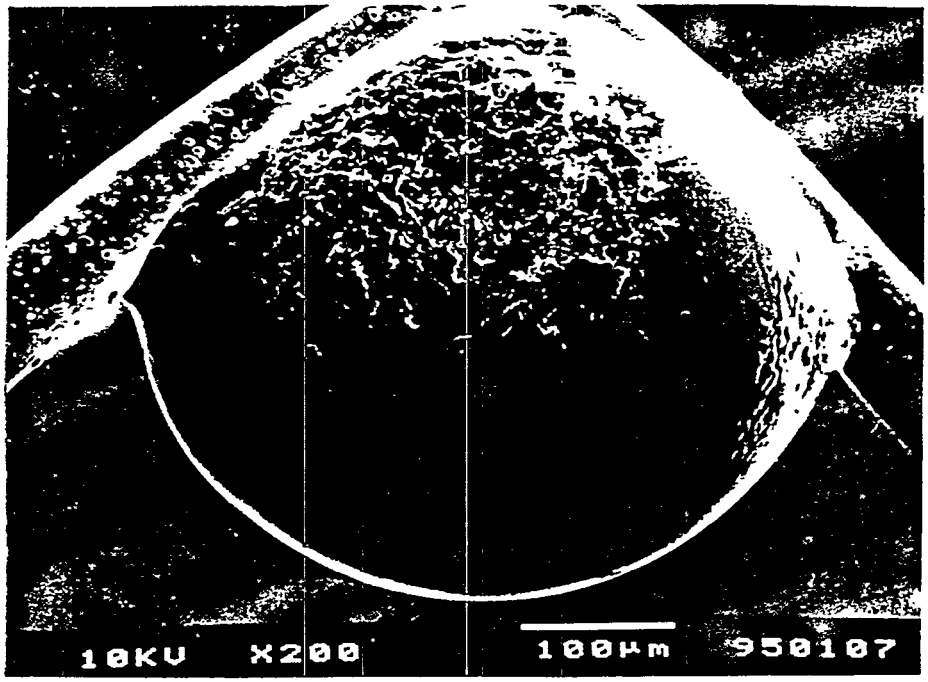


Fig. 12. SEM micrograph of a Cu cathode after 2500 arc discharges (1300 ns) of current 50 A .

result in an enhanced emission of the metallin the form of microdrops. Our results show no dependence of the erosion rate on the arc current . In the literature, attention has been drawn not once to the similarity of the cathode processes in a vacuum breakdown (a discharge in vacuum which has not yet gone into the arc stage, i.e., the discharge plasma has not bridged the anode cathode gap, the gap voltage therewith being high, namely, some tens of kilovolts) and in a vacuum arc. The agreement between the results on the erosion rate obtained by us and by the authors of [11] is an additional evidence supporting this viewpoint. That is the phisical processes occurring in both types of discharge have the same nature.

On the other hand, our data on the erosion rate are also close to the data obtained by other researches. According to Daalder's data, if the charge transferred in a pulse is lower than 1 C, the erosion rate is weakly dependent on the charge. In our experiment, the transferred charge was 10^{-5} -10^{-4} C. Thus, the independence of the erosion rate on the transferred charge, starting from a certain value of charge, discovered by Daalder has been confirmed qualitatively.

3. Conclusion

To summarize, we dwell briefly on some inferences from the experimental data obtained in studying the erosion rate and the lifetime of a vacuum arc cathode spot. The most important one is that the physical processes responsible for the erosion of the cathode material are simular in nature for a vacuum arc and a vacuum breakdown. This is testified by the fact that our results are in fact the same as those obtained for the erosion rate in a vacuum breakdown [11]. It is well known that the reason for the vacuum breakdown of a short gap is the explosive destruction of microprotrusions on the cathode and the expansion of the resulting plasma into the electrode gap. It is justifiable to suppose that simular processes took place in our experiments aimed at studying the erosion rate during the operation of a vacuum arc. This is also evidenced by the measurements of the emission center lifetime performed based on noise spectra. The peculiarities in these spectra seem to appear due to the nonuniform income of plasmoids into the electrode gap. Emission centers appear, then disappear, and then give rise to the birth of new emission centers.

In our opinion, these results support the vacuum arc model we have proposed earlier, which is based on the explosive emission of portions of the metal, occurring in local regions at the cathode surface; we have named the resulting charged particle blobs "ectons".

At the same time, some our observations, such as the strong dependence of the erosion rate annnd the emission center lifetime on the cathode temperature, call for a comprehensive analysis and further investigation which is planned to do subsequently in the context of the work under contract.

4. References

[1] I.G. Kesaev 1968. Cathode Processes of the Electrical Arc (Moscow, Nauka) (in Russian)

[2] V.F. Puchkarev and A.M. Murzakaev J.Phys.D.: Appl.Phys.23 (1990) 26-35.

[3] B.Juttner. Formation time and heating mechanism of arc cathode craters in vacuum. J. Phys. D.: Appl.Phys., 14 (1981) 1265-75.

[4] V.F. Puchkarev, D.I. Proskyrovskii, A.M. Murzakaev Zhurn. Teh. Fiz., vol.57, no.12, 1987, pp.2324-2329 (in Russian).

[5] Y.H.Fu. The influence of cathode surface microstructure on PC vacuum arc. J.Phys.D.: Appl.Phys. 22 (1989), 94-102.

[6] B. Juttner, E. Freund , Pursch H. Preprint ZIE 78-2, Berlin, April 1978.

[7] F.I. Bushik, B. Juttner Pursch. Beitr. Plasma Physic. 19 (1979).

[8] V.I. Rachovsky IEEE Trans. Plasma Sci. PS-4 (1976) 81.

[9] V.I. Golub, V.V. Kantsel, V.I. Rachovsky Proc.2 Int. Conference on Gas Discharges, London, 1972, p.224.

[10] B. Juttner Preprint ZIE 79-9, Berlin, September 1979.

[11] B.Juttner. Preprint ZIE, 78-14, 1978.

[12] S.N. Nazarov, V.I. Rachovsky, V.G. Zhurbenko. Voltage drop over a vacuum arc and the cathode spot brightness. XII-th Int. Symp. on Discharges and Electrical Insulation in Vacuum, Paris, 1988, p.148.

[13] F. Rosebury, Handbook of Electrone Tube and Vacuum Techniques, Massachusetts, 1964.

[14] V.M. Khoroshin, I.I. Aksenov, I.I Konovalov. Zhurn. Teh. Fiz.,vol.58, no.6.

[15] J.Atchert et al. Beitrage ous der Plasma Physic, vol.17, no.6, p.419, 1977.

[16] G.A.Lyibimov and V.I.Rachovsky. Usp.Fiz.Nauk. vol.125,no.4,p.665, 1978.

[17] A.A.Plutto, V.M.Ryzhkov, and A.T.Kapin. Sov.Phys.- JETP,20,328 (1965)

[18] B. Klyarfel'd at al. 1969. Sov. Phys. - Tech. Phys. 14, 796-799.

[19] V.V. Kansel' 1968. Sov. Phys. - Tech. Phys. 13, 814-817.

[20] Z. Zaluski and J. Kutzner 1972, Proc. Vth Int. Symp. on Discharges and Electrical Insulation in Vacuum, Poznan, Poland, p.275-281.

[21] W.G.J.Pondeel J.Phys.D. Appl. Phys., 1973, vol.6, 1705-1711.

[22] D.Y.Fang, A.Nurnberg, U.H.Bauder, R.H.Behrish. Journ. Nucl. Mater. (1982) 111 & 112, pp.517-521.

[23] S.K.Sethuranam, P.A.Chatterton, M.K.Barrault. Journ. Nucl.Mater., (1982), 111 & 112, pp.510-516.

[24] J.E.Daalder, J.Phys.D. Appl.Phys., vol.18, 1647 (1975)

[25] J.Achert at al 1977 Beitr. Plasma Phys. v.17, 419-431

[26] B.Juttner. Proc. XI Int. Symp. on Discharges and Electrical Insulation in Vacuum, p.155.

[27] Debora R. Porto, S.W.Kimblin, Tuma D.T. J.Appl.Phys. vol.53, no.7, 1982, 4740-4749.

[28] H.Craig.Miller. Proc.XI International Symposium on Discharge and Insulation in Vacuum. (Berlin), 1984, pp.115-122.

Project Title: Measurement of Viscosity of Liquid Metals
Principal Investigator: V. L. Lisen
Institute of Metallurgy
Ekaterinburg, Russia
AM-7686

CLAUSE 1 - STATEMENT OF WORK

Tasks:

The Contractor shall:

1. Provide a report describing the testing apparatus and test procedure that will be used to measure the viscosity at ambient pressure of five (5) Sandia selected and provided Fe or Ni base alloys as a function of temperature from the solidus temperature to the maximum temperature at which the measurements will be made.

2. Using x-ray techniques, measure the viscosity at ambient pressure of five (5) Sandia selected and provided Fe or Ni base alloys as a function of temperature from the solidus temperature to 300(C above the liquidus temperature. Measurements shall be made at temperature intervals subject to the anomalous behavior of the data. This will be decided in-situ by the Contractor. It is understood that measurements in the mushy region could erroneous because the presence of crystallites. Provide the test data and results.

3. Provide a final report analyzing the results of the test.

AM 7686

THE VISCOSITY MEASUREMENT OF LIQUIDS BY X-RAY METHOD

Here is the substance of the viscosity measurement method being offered. The standard and the liquid under investigation are exposed to X-Ray radiation one after another. The diffraction peaks of the standard and the liquids under investigation are produced,then the intensity values of compared diffraction peaks are aligned,the areas under the tops of these peaks are determined (the base of these tops is the constant interval of the scattering vector). Then the liquid viscosity is calculated according to the equation:

$$\nu_{inv} = \nu_{st}\, \Pi_{inv} / \Pi_{st} , \qquad (1)$$

where ν_{st} - is the standard viscosity at given temperature T, m^2/sec;

Π_{st} - is the area under the diffraction peak of standard at T, relative units;

ν_{inv} - is the viscosity of the liquid under investigation at T, m^2/sec;

Π_{inv} - is the area under the diffraction peak of the liquid under investigation at T, relative units.

Measuring the melt s viscosity,it is expedient to use the first peak as its intensity is maximal in comparing with the other peaks of the diffraction curve and the error in values of its intensity does not exceed 0.6%.

The offered mode can be realized in the plant shown in fig.1. The plant is a high-temperature Θ-Θ diffractometer with Bregg-Brentano focusing, with a stationary sample and a monochromator in a diffracted beam.

The vacuum high-temperature X-Ray chamber consists of two water-cooled demountable semi-cylinders 6 and 7, a gear-transmission system and a step-by-step engine,which rotates arms 9 uniformly and sinchronously towards one another the X-Ray tube 10 and the pulse counter 11 being fixed on them. In the removable top part of the chamber 6 there is a slot 12mm wide for X-Ray passage.The slot is closed with a thin beryllium (aluminium) plate.

The turning angle range of the X-ray tube 10 and the pulse counter 11 is from 0^0 tu 75^0 .The interval of angular movement in the automatic mode is multiple of the minimal step of the engine and is 0.015^0.During the scanning of the angle Θ the X-Ray tube and the pulse counter are automatically stopped at a nesessary angle.The intensity values at each point are registered into the computer's memory.

During the continious recording of the diffraction curve the interval is equal to the entire movement range of the X-Ray tube and the pulse counter.

Molybdenum (Tungsten) heater 1 of byfilar-type and a thermal screen-system 2 with a slot allow free passing of the primary and diffracted X-Ray beams and let heat up the melting pot 5 with a sample up to 2273K.

The melting pot 5 lies on the molybdenum rest 4 which is puted on a mobile piller 3. There is a through hole inside the piller 3 through which the W-Re termocouple 8 goes and stops against the melting pot's bottom.The melting pot's material is Al_2O_3,BeO,SiO_2,C,Mo,ZrO_2,Fe etc.

The piller can be moved vertically as far as 30mm by a special elevating device which consists of a microscrew,two gears and a step-by-step engine.The piller 3 is connected with the bottom part of the chamber 7 by bellows.

To implement the discribed mode of viscosity measurement the X-Ray plant operates as follows.

The sample (or its components) in solid state is put into the melting pot 5. The air is evacuated from the camber (up to $6*10^{-4}$Pa), the chamber is filled in with argon (helium), heated up to the melting of the sample and more up to the given temperature. The primary X-Ray beam is formed by means of collimator and then drops on the liquid sample under investigation through the slot in the top semi-cylinder 6 of the chamber.

The X-Ray tube 10 and the pulse counter 11 are placed into horizontal position ($\Theta=0^0$) the direct primary X-Ray beam's intensity I_0 is defined, then the molibdenum rest 4 with the melting pot 5 is moved with mobile piller 3 so, that in the result of blocking of the direct X-Ray beam by surface

of the liquid sample, the intensity I registered by pulse counter decreases twice: $I=I_0/2$.

After this procedure the melt surface alignes with the geometrical axis of the chamber, around which the X-Ray tube 10 and the pulse counter 11 rotate.

Then the X-Ray tube and pulse counter start rotating uniformly and sinchronously with the help of the step-by-step engine.The primary X-Ray beam drops on the horizontal surface of the sample at the angle Θ.Having reflected from the sample's surface at the angle Θ,the X-Ray beam passes frealy through the berillium plate,then it is reflected from a monocrystall (pyrolitical graphite) and is registered by the pulse counter.

The signals from electric circuits of the angle-marker and of the pulse counter are transformed into digital form in the unit of discrete signals input and processed by micro-computer according to the following algorythm:

$$I_i = I\ (S_i),$$

where $S_i = 4\Pi\ \mathrm{Sin}\Theta/\lambda$ -is the scattering vector, corresponding to the i-th pulse of the angle-marker, $\mathring{A}^{-1}$;

$\Theta = 1.5^{\circ} + (i-1)\cdot\Delta$, Δ -is the angular interval multiple of 0.015°.

λ -is the wave-length of the X-Ray characteristic radiation Mo K_{α}.

For all metallic systems the first maximum of diffraction curves is entirely places in the angle-interval $1.5^{\circ} \leq 0 \leq 15^{\circ}$, that correspondes to the change of the vector S_i from $0.46\mathring{A}^{-1}$ to $4.6\mathring{A}^{-1}$.

Then, changing the diffraction angle from 1.5° to 15°, we record the diffraction curve of the standard over this range at the points with the step Δ multiple of the minimal step of the engine.

In recording the first diffraction peak for metallic systems, the exposition time τ was 20sec., and the angular step Δ was 0.15°.

We plot the intensity $I_{i,st}/\tau$ (pulse/sec.) against the scattering vector $S_i, (\mathring{A}^{-1})$, i.e. $I_{ist}(S_i)$-is the curve A fig.2.

The maximum intensity $I_{ist}(S_1)$ of the diffraction curve A fig.2 is defined. The diffraction curve B' (different liquid,

different composition) is recorded for $S_i = 0.46 \div 4.6 \overset{0}{A}^{-1}$, noting the maximum value of its first peak $I_2'(S_2)$ fig.2. The X-Ray tube and the pulse counter are positioned at the diffraction angle, corresponding to S_2. Operating with the same collimator the plate current is changed so, that the intensity $I_2'(S_2)$ equals $I_{1,st}(S_1)$, i.e.

$$I_2(S_2) = I_{1,st}(S_1)$$

Afterwards without changing the plate current, set during the alignment of values of the intensities of the first peaks of the standard and the liquid under investigation, the second diffraction curve B is recorded for $\Theta = 1.5^0 \div 15^0$ ($0.46 \div 4.6 \overset{0}{A}^{-1}$) fig.2.

In the same way we produce the whole set of the diffraction curves for other compositions, other liquids, whose first peak values are normalized, i. e.

$$I_n(S_n) = I_{n-1}(S_{n-1}) = \ldots = I_2(S_2) = I_{1,st}(S_1)$$

Then, out of the first peak of the curve A we cut off the figure $A_1B_1C_1$ by a straight line 1 parallel to the abscissa. The value of this figure's base is

$$\Delta S_1 = S_{12} - S_{11} = \Delta S,$$

where S_{11} and S_{12} are the abscissas of the points A_1 and C_1 (the crossing points of the curve A and the straight line 1) fig.2.

For the normalized curve B we select such a line 2 parallel to the abscissa, which cuts off the figure $A_2B_2C_2$, whose base is

$$\Delta S_2 = S_{22} - S_{21} = \Delta S_1 = \Delta S,$$

where S_{21} and S_{22} are the abscissas of the points A_2 and C_2 (the crossing points of the curve B and the straight line 2) fig.2.

The exsperience of the processing of the intensity curves has shown, that for the metallic systems $\Delta S \approx 1.1 \overset{0}{A}^{-1}$.

For all the $j = 1, 2, \ldots, n$ of the diffraction curves we build the figures $A_jB_jC_j$ in the sume way, their base being the constant scattering vector:

$$\Delta S = \Delta S_n = \Delta S_{n-1} = \ldots = \Delta S_2 = \Delta S_{1,st}$$

The areas Π_j of figures $A_jB_jC_j$ are found, each liquid viscosity is defined according to the area values with the

help of the above equation (1).

Taking into account the proportional correlation between $\sqrt{}$ and Π, it is sufficient to know the viscosity of the liquid under investigation at least at one temperature T_{inv}. It means, that having determined one of the values $\sqrt{}_{inv}$ at T_{inv} by the above method, we produce the set of values

$$\Pi_1(T_1), \Pi_2(T_2), \Pi_{inv}(T_{inv}), \Pi_j(T_j).$$

Reference

The Patent N1520412, applicated 27.11.87. C1001 23/206 "The mode of the viscosity measurement of a liquid". E.M.Kern,N.A.Vatolin,V.L.Lisin etc. Published in the invention bul.,1989, N41. in the invention bul.,1989,N41.

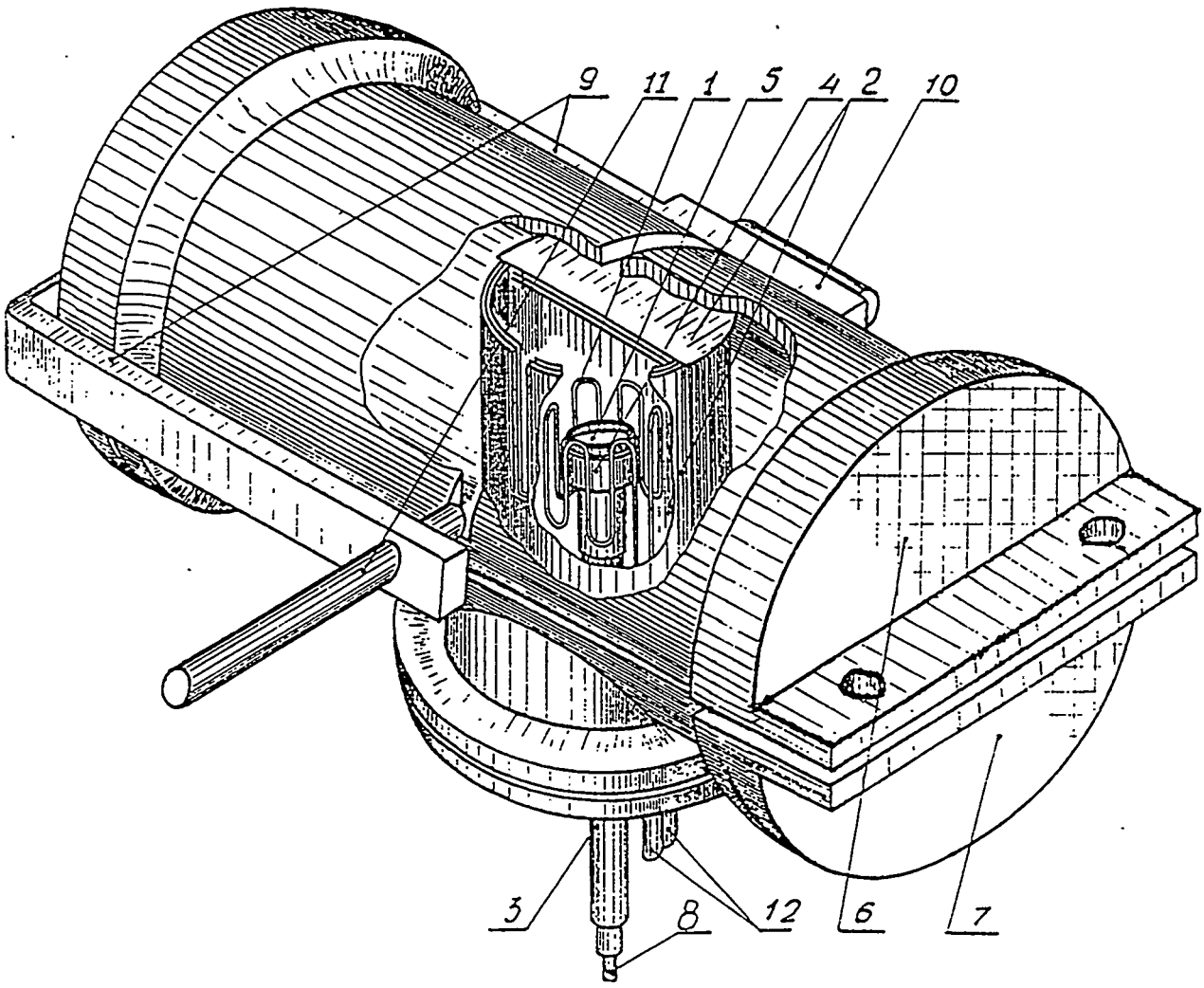


Fig.1.

1. The heater; 2. The screen, 3. The piller; 4.The molybdenous rest for the melting pot; 5.The melting pot; 6.The top semi-cylinder; 7.The lower semi-cylinder; 8.The termocouple W-Re; 9.The arms; 10.The X-Ray tube; 11.The pulce counter; 12.The current leads.

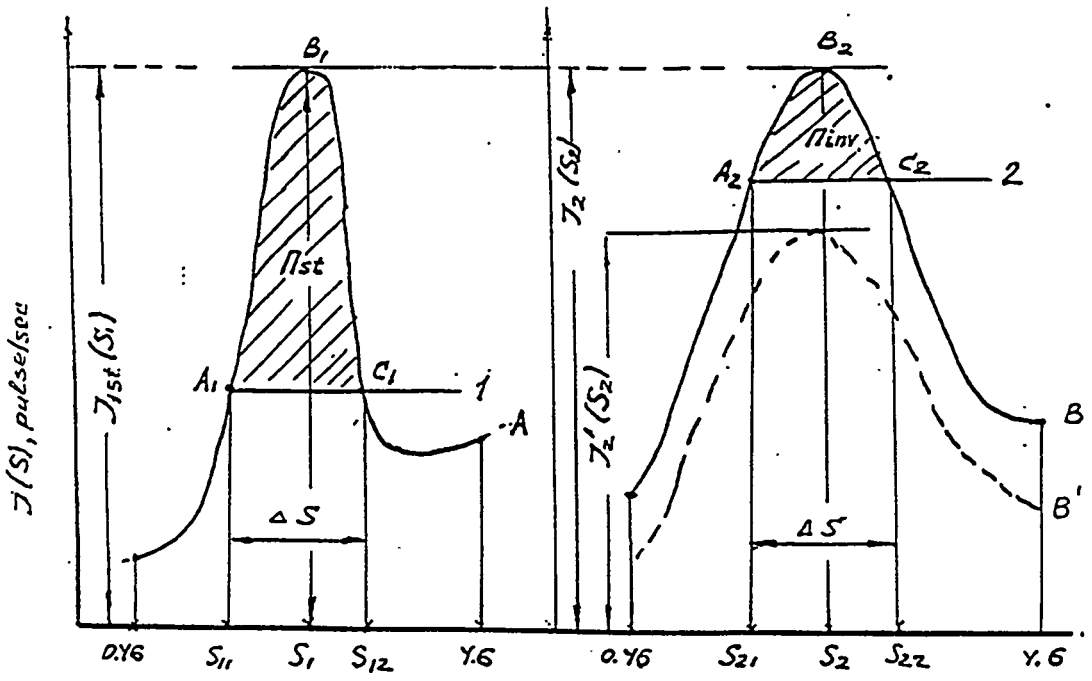


Fig. 2.

The normalization of the first peak's intensity of the standard and the liquid under investigation. A - is the difraction curve of the standard; $I_{1.st}(S_1)$ - is the maximum intensity of the curve A; B' - is the unnormalized curve of the liquid under investigation; I'_2 (S_2) - is the intensity of the curve B' of the liquid under investigation; B - is the normalized curve of the liquid under investigation; I_2 (S_2) - is the intensity of the curve B of the liquid under investigation; Π_{st} - is the area of the figure $A_1B_1C_1$ of the standard; Π_{inv} - is the area of the figure $A_2B_2C_2$ of the liquid under investigation.

THE VISCOSITY MEASUREMENT OF LIQUIDS BY X-RAY METHOD

Here is the substance of the viscosity measurement method being offered. The standard and the liquid under investigation are exposed to X-Ray radiation one after another. The diffraction peaks of the standard and the liquids under investigation are produced,then the intensity values of compared diffraction peaks are aligned,the areas under the tops of these peaks are determined (the base of these tops is the constant interval of the scattering vector). Then the liquid viscosity is calculated according to the equation:

$$\eta_{inv} = \eta_{st}\, \Pi_{inv} / \Pi_{st} , \qquad (1)$$

where η_{st} - is the standard viscosity at given temperature T, m^2/sec;

Π_{st} - is the area under the diffraction peak of standard at T, relative units;

η_{inv} - is the viscosity of the liquid under investigation at T, m^2/sec;

Π_{inv} - is the area under the diffraction peak of the liquid under investigation at T, relative units.

Measuring the melt s viscosity,it is expedient to use the first peak as its intensity is maximal in comparing with the other peaks of the diffraction curve and the error in values of its intensity does not exceed 0.6%.

The offered mode can be realized in the plant shown in fig.1. The plant is a high-temperature Θ-Θ diffractometer with Bregg-Brentano focusing, with a stationary sample and a monochromator in a diffracted beam.

The vacuum high-temperature X-Ray chamber consists of two water-cooled demountable semi-cylinders 6 and 7, a gear-transmission system and a step-by-step engine,which rotates arms 9 uniformly and sinchronously towards one another the X-Ray tube 10 and the pulse counter 11 being fixed on them. In the removable top part of the chamber 6 there is a slot 12mm wide for X-Ray passage.The slot is closed with a thin beryllium (aluminium) plate.

The turning angle range of the X-ray tube 10 and the pulse counter 11 is from 0^0 tu 75^0 .The interval of angular movement in the automatic mode is multiple of the minimal step of the engine and is 0.015^0.During the scanning of the angle Θ the X-Ray tube and the pulse counter are automatically stopped at a nesessary angle.The intensity values at each point are registered into the computer's memory.

During the continious recording of the diffraction curve the interval is equal to the entire movement range of the X-Ray tube and the pulse counter.

Molybdenum (Tungsten) heater 1 of byfilar-type and a thermal screen-system 2 with a slot allow free passing of the primary and diffracted X-Ray beams and let heat up the melting pot 5 with a sample up to 2273K.

The melting pot 5 lies on the molybdenum rest 4 which is puted on a mobile piller 3. There is a through hole inside the piller 3 through which the W-Re termocouple 8 goes and stops against the melting pot's bottom.The melting pot's material is Al_2O_3,BeO,SiO_2,C,Mo,ZrO_2,Fe etc.

The piller can be moved vertically as far as 30mm by a special elevating device which consists of a microscrew,two gears and a step-by-step engine.The piller 3 is connected with the bottom part of the chamber 7 by bellows.

To implement the discribed mode of viscosity measurement the X-Ray plant operates as follows.

The sample (or its components) in solid state is put into the melting pot 5. The air is evacuated from the camber (up to $6*10^{-4}$Pa), the chamber is filled in with argon (helium), heated up to the melting of the sample and more up to the given temperature. The primary X-Ray beam is formed by means of collimator and then drops on the liquid sample under investigation through the slot in the top semi-cylinder 6 of the chamber.

The X-Ray tube 10 and the pulse counter 11 are placed into horizontal position ($\Theta=0^0$) the direct primary X-Ray beam's intensity I_0 is defined, then the molibdenum rest 4 with the melting pot 5 is moved with mobile piller 3 so, that in the result of blocking of the direct X-Ray beam by surface

of the liquid sample, the intensity I registered by pulse counter decreases twice: $I=I_0/2$.

After this procedure the melt surface alignes with the geometrical axis of the chamber, around which the X-Ray tube 10 and the pulse counter 11 rotate.

Then the X-Ray tube and pulse counter start rotating uniformly and sinchronously with the help of the step-by-step engine.The primary X-Ray beam drops on the horizontal surface of the sample at the angle Θ.Having reflected from the sample's surface at the angle Θ,the X-Ray beam passes frealy through the berillium plate,then it is reflected from a monocrystall (pyrolitical graphite) and is registered by the pulse counter.

The signals from electric circuits of the angle-marker and of the pulse counter are transformed into digital form in the unit of discrete signals input and processed by micro-computer according to the following algorythm:

$$I_i = I\ (S_i),$$

where $S_i = 4\Pi\ \mathrm{Sin}\Theta/\lambda$ -is the scattering vector, corresponding to the i-th pulse of the angle-marker, $\mathring{A}^{-1}$;

$\Theta = 1.5^{\circ} + (i-1)\cdot\Delta$, Δ -is the angular interval multiple of 0.015°.

λ -is the wave-length of the X-Ray characteristic radiation Mo K_{α}.

For all metallic systems the first maximum of diffraction curves is entirely places in the angle-interval $1.5^{\circ} \leq 0 \leq 15^{\circ}$, that correspondes to the change of the vector S_i from $0.46\mathring{A}^{-1}$ to $4.6\mathring{A}^{-1}$.

Then, changing the diffraction angle from 1.5° to 15°, we record the diffraction curve of the standard over this range at the points with the step Δ multiple of the minimal step of the engine.

In recording the first diffraction peak for metallic systems, the exposition time τ was 20sec., and the angular step Δ was 0.15°.

We plot the intensity $I_{i,st}/\tau$ (pulse/sec.) against the scattering vector $S_i, (\mathring{A}^{-1})$, i.e. $I_{ist}(S_i)$-is the curve A fig.2.

The maximum intensity $I_{ist}(S_i)$ of the diffraction curve A fig.2 is defined. The diffraction curve B' (different liquid,

different composition) is recorded for $S_i = 0.46 \div 4.6 \overset{0}{A}^{-1}$, noting the maximum value of its first peak $I_2'(S_2)$ fig.2. The X-Ray tube and the pulse counter are positioned at the diffraction angle, corresponding to S_2. Operating with the same collimator the plate current is changed so, that the intensity $I_2'(S_2)$ equals $I_{1,st}(S_1)$, i.e.

$$I_2(S_2) = I_{1,st}(S_1)$$

Afterwards without changing the plate current, set during the alignment of values of the intensities of the first peaks of the standard and the liquid under investigation, the second diffraction curve B is recorded for $\Theta = 1.5^0 \div 15^0$ ($0.46 \div 4.6 \overset{0}{A}^{-1}$) fig.2.

In the same way we produce the whole set of the diffraction curves for other compositions, other liquids, whose first peak values are normalized, i. e.

$$I_n(S_n) = I_{n-1}(S_{n-1}) = \ldots = I_2(S_2) = I_{1,st}(S_1)$$

Then, out of the first peak of the curve A we cut off the figure $A_1B_1C_1$ by a straight line 1 parallel to the abscissa. The value of this figure's base is

$$\Delta S_1 = S_{12} - S_{11} = \Delta S,$$

where S_{11} and S_{12} are the abscissas of the points A_1 and C_1 (the crossing points of the curve A and the straight line 1) fig.2.

For the normalized curve B we select such a line 2 parallel to the abscissa, which cuts off the figure $A_2B_2C_2$, whose base is

$$\Delta S_2 = S_{22} - S_{21} = \Delta S_1 = \Delta S,$$

where S_{21} and S_{22} are the abscissas of the points A_2 and C_2 (the crossing points of the curve B and the straight line 2) fig.2.

The exsperience of the processing of the intensity curves has shown, that for the metallic systems $\Delta S \approx 1.1 \overset{0}{A}^{-1}$.

For all the $j = 1, 2, \ldots, n$ of the diffraction curves we build the figures $A_jB_jC_j$ in the sume way, their base being the constant scattering vector:

$$\Delta S = \Delta S_n = \Delta S_{n-1} = \ldots = \Delta S_2 = \Delta S_{1,st}$$

The areas Π_j of figures $A_jB_jC_j$ are found, each liquid viscosity is defined according to the area values with the

help of the above equation (1).

Taking into account the proportional correlation between $\sqrt{\nu}$ and Π, it is sufficient to know the viscosity of the liquid under investigation at least at one temperature T_{inv}. It means, that having determined one of the values $\sqrt{\nu_{inv}}$ at T_{inv} by the above method, we produce the set of values

$$\Pi_1(T_1), \Pi_2(T_2), \Pi_{inv}(T_{inv}), \Pi_j(T_j).$$

Reference

The Patent N1520412, applicated 27.11.87. C1001 23/206 "The mode of the viscosity measurement of a liquid". E.M.Kern,N.A.Vatolin,V.L.Lisin etc. Published in the invention bul.,1989, N41. in the invention bul.,1989,N41.

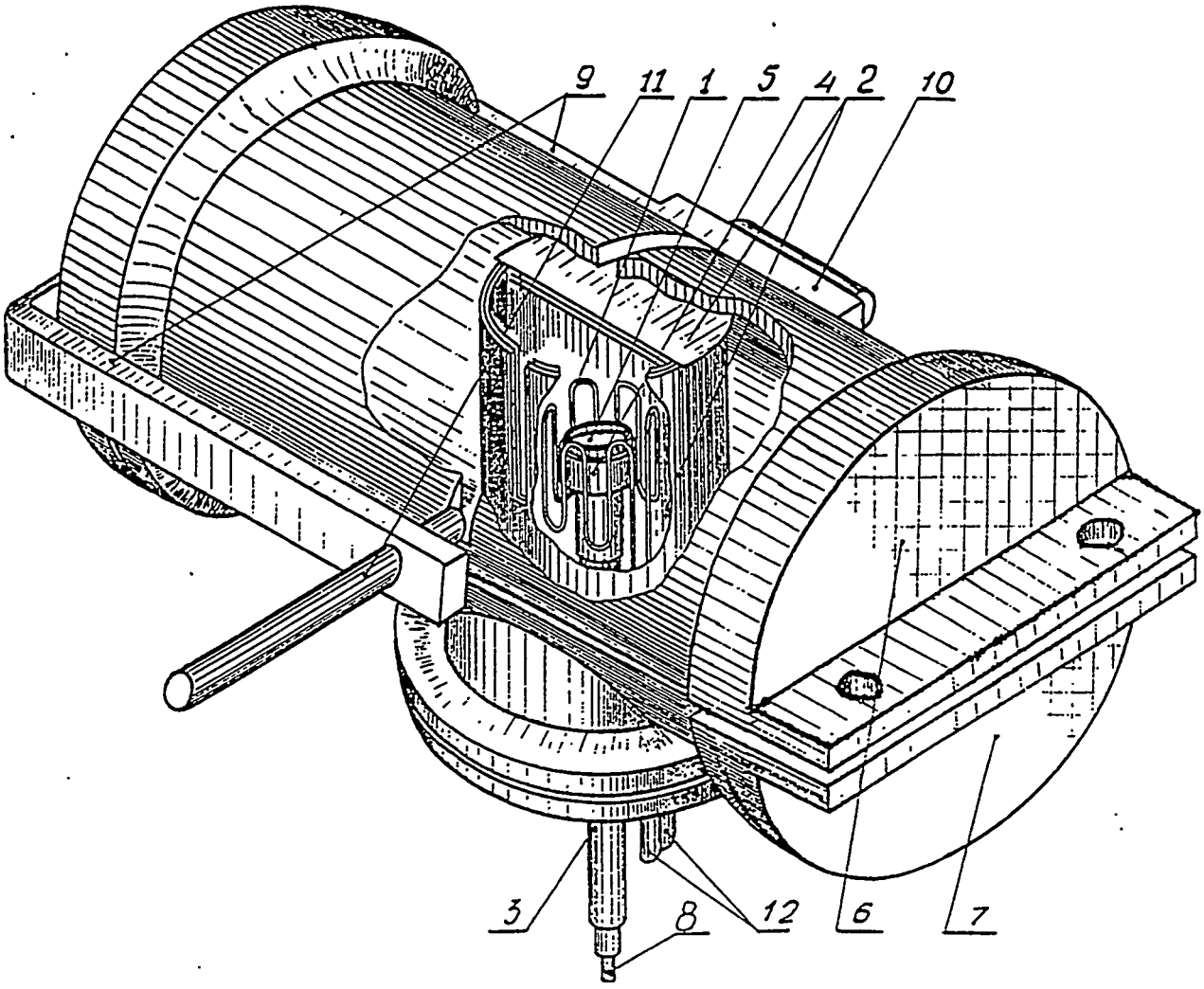


Fig.1.

1. The heater; 2. The screen; 3. The piller; 4.The molybdenous rest for the melting pot; 5.The melting pot; 6.The top semi-cylinder; 7.The lower semi-cylinder; 8.The termocouple W-Re; 9.The arms; 10.The X-Ray tube; 11.The pulce counter; 12.The current leads.

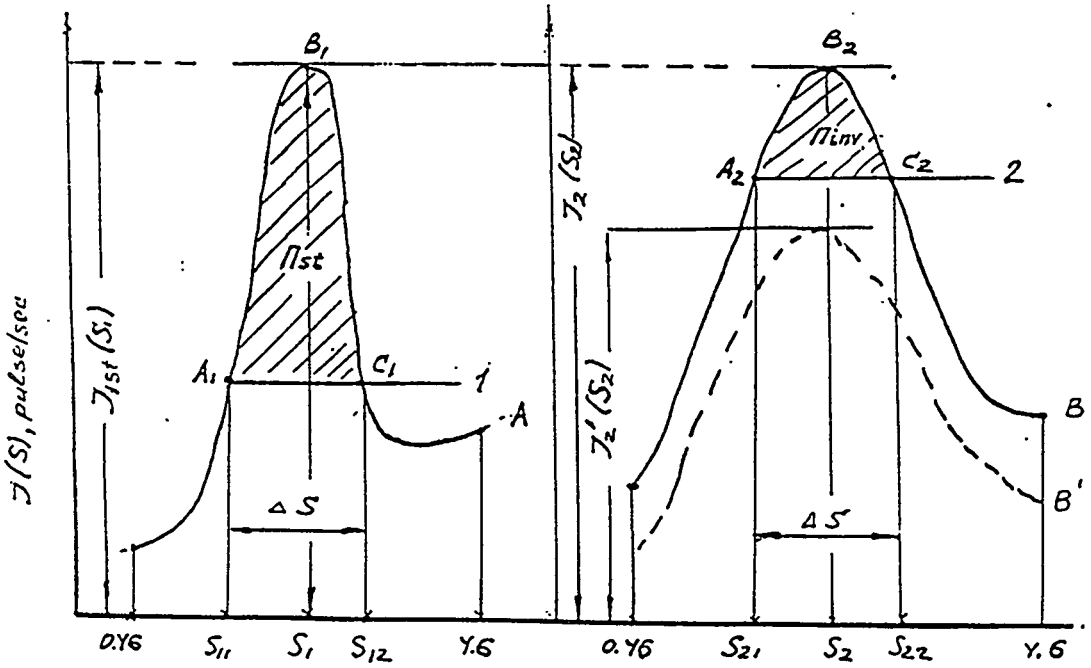


Fig. 2.

The normalization of the first peak's intensity of the standard and the liquid under investigation. A - is the difraction curve of the standard; $I_{1.st}(S_1)$ - is the maximum intensity of the curve A; B' - is the unnormalized curve of the liquid under investigation; $I'_2(S_2)$ - is the intensity of the curve B' of the liquid under investigation; B - is the normalized curve of the liquid under investigation; $I_2(S_2)$ - is the intensity of the curve B of the liquid under investigation; Π_{st} - is the area of the figure $A_1B_1C_1$ of the standard; Π_{inv} - is the area of the figure $A_2B_2C_2$ of the liquid under investigation.

DISTRIBUTION:

1 US Department of Energy
Attn: John Hnatio
NN-1, x66319
Forrestal Building, Rm. GA087
1000 Independence Ave., SW
Washington, DC 20585

54 USIC
Attn: Mike Deagan, President
1524 Victoria Farms
Vienna, VA 22182

1 MS 0360 A. R. C. Westwood, 1000
1 MS 0467 Dennis Croessman, 5091
1 MS 0609 William Moffatt, 1841
1 MS 0725 Thomas Hunter, 6900
1 MS 1409 Alton Romig, 1800
1 MS 1134 Brian Damkroger, 1833
30 MS 1134 Frank Zanner, 1833
1 MS 9018 Central Technical Files, 8523-2
5 MS 0899 Technical Library, 13414
1 MS 0619 Print Media, 12615
2 MS 0100 Document Processing, 7613-2